Advances in Hybrid Water-Lubricated Journal Bearings for Use in Ocean Vessels

by

Brian Douglas Heberley

B.S., Webb Institute (2001)
M.E.M., Old Dominion University (2008)
S.M., Massachusetts Institute of Technology (2011)
NAVAL ENGINEER, Massachusetts Institute of Technology (2011)

Submitted to the Department of Mechanical Engineering
in partial fulfillment of the requirements for the degree of

Doctor of Philosophy in Mechanical Engineering

at the

MASSACHUSETTS INSTITUTE OF TECHNOLOGY

June 2013

The author hereby grants to MIT permission to reproduce and to distribute publicly paper and electronic copies of this thesis document in whole or in part in any medium now known or hereafter created.

Author . . . .
Department of Mechanical Engineering
May 18, 2013

Certified by. . . . .
Alexander H. Slocum
Pappalardo Professor of Mechanical Engineering
Thesis Supervisor

Accepted by . . . .
David E. Hardt
Chairman, Department Committee on Graduate Theses

Advances in Hybrid Water-Lubricated Journal Bearings for Use in Ocean Vessels

by

Brian Douglas Heberley

Abstract

The outboard bearings that support shafts in naval ships and submarines present unique challenges to designers, shipbuilders, and operators. Such bearings must operate continuously and reliably in demanding environments at speeds that vary from below 1 rpm to well over 100 rpm. Water-lubricated bearings typically used for these applications operate hydrodynamically and are prone to adverse effects at lower speeds such as increased abrasive and adhesive wear as well as stick-slip shaft motion. This project focuses on developing a hybrid journal bearing capable of operating with hydrostatic pump pressure at lower rpm, while still maintaining the capability for hydrodynamic operation at higher rpm. Benefits of such a system include extending the periodicity between outboard bearing replacements, less abrasion and scoring damage to the propulsion shaft, and preventing stick-slip shaft motion.

To enable the in-water replacement of bearings without removal of the propulsion shaft, a partial arc (<180 degree wrap) configuration is required. This partial arc constraint introduces several unique manufacturing difficulties. To address this, a novel manufacturing process has been developed that enables the rapid fabrication of high precision bearings with diameter and roundness errors of less than 0.001" (25.4 microns) on a nominal diameter of 3.24" as measured with a Coordinate Measuring Machine - greatly exceeding the published tolerances of conventional methods.

A unique experimental test rig was designed and built in order to measure the performance of 15 different prototype bearing designs. The rig is capable of submerged bearing testing in both hydrostatic and hydrodynamic modes of operation, with fundamental parameters such as speed, torque, loads, pressures, flow rates, and shaft position recorded. The operating characteristics of the bearings were then analyzed to identify key features and variables affecting bearing performance.

Certain bearing designs were found to be inherently stable for side loading conditions, without the use of compensation typically used in hydrostatic bearings. This

finding led to bearings designed with simplified hydrostatic features and fluid supply systems. Such designs were found to have minimal degradation in hydrodynamic performance, making them particularly suitable for use as hybrid bearings. The key design drivers identified in this work are combined with ancillary factors to discuss the feasibility of hybrid bearings for use in marine applications.

Thesis Committee Member: Douglas P. Hart
Title: Professor of Mechanical Engineering

Thesis Committee Member: Captain Mark Thomas, USN
Title: Professor of the Practice

Thesis Supervisor: Alexander H. Slocum
Title: Pappalardo Professor of Mechanical Engineering

Acknowledgments

I would like to thank several people and organizations that played a role in allowing me to complete this work.

The U.S. Navy Engineering Duty Officer community for allowing me to spend the time at MIT to conduct this research. I would also like to thank the staff and classmates in the 2N program that have provided fantastic support over the last several years. I will endeavor to see that the Navy realizes a return on the investment in put into me throughout my career.

The sponsors of this research:

- The Defense Advance Research Projects Agency (DARPA)

- Propulsor Technology, Inc. (PTI)

- The Office of Naval Research (ONR)

Various members of the navy technical community:

- Craig Madden and Capt. Bill Needham, USN (Ret.) from NSWCCD

- Kevin King, Rick Teichman, and Cynthia Ericksen from NSWCCD-SSES

- Justin Pollack and Capt. Pat Keenan, USN (Ret.) from NAVSEA 00C

- Capt. Chris Warren from DARPA

- Dr. Airan Perez from ONR

- Ralph Nevells, Bob Bate, Judith Locke, Kevin Mills, Douglas DeAngelis, and LCDR Dave Hanthorne from PNSY

Other personnel at various commercial entities:

- Drew Devitt from New Way Air bearings

Contents

List of Figures

13

17

19

20

List of Tables

Chapter 1

Introduction

The main propulsion shaft in a ship is used to link the power output of the prime mover to the propeller where energy is transferred into the water. The components that support the shaft are very complex and must satisfy numerous requirements. The entire system must be able to support loads from the shaft and propeller as well as transmit thrust from the propeller to the ship, at speeds that vary from approximately 0.1 rpm (when on the turning gear) to well over 100 rpm in either direction. Since the shaft penetrates the hull, the system must also be capable of preventing uncontrolled flow of water into the hull. Reliability of the system is vital - most large commercial ships and many Navy ships only have one shaft and do not have a redundant system for full propulsion. In the case of navy ships, the system must also withstand large dynamic shock loads and be designed to stringent acoustic noise signature requirements.

The outboard bearings that support the shaft (such as stern tube, propeller and strut bearings) present unique challenges. Figure 1-1 and 1-2 show the location of such bearings in the propulsion shaftline of a ship and a submarine. Since these bearings are exposed to seawater and contaminates such as mud, sand, and silt they can be susceptible to abrasive and adhesive wear. Prior to 1960, the majority of ships used water-lubricated bearings in the form of *Lignum Vitae* (a dense hardwood of the genus *Guaiacum*) staves. During the 1960s, a shift to oil lubricated bearings began due to shortened lifespans of the wood bearings resulting from an increased ship size.
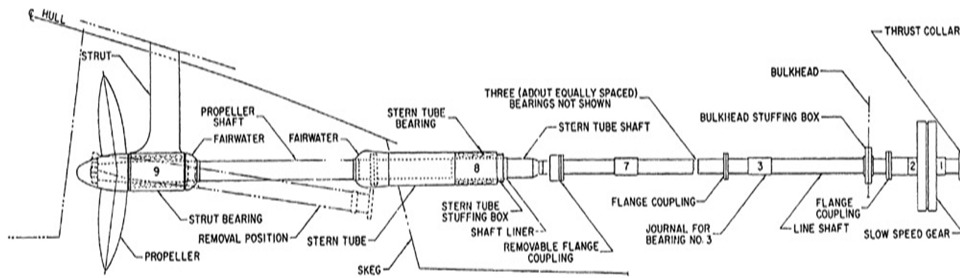
Figure 1-1: Typical Ship Shaftline Bearings and Components [11]
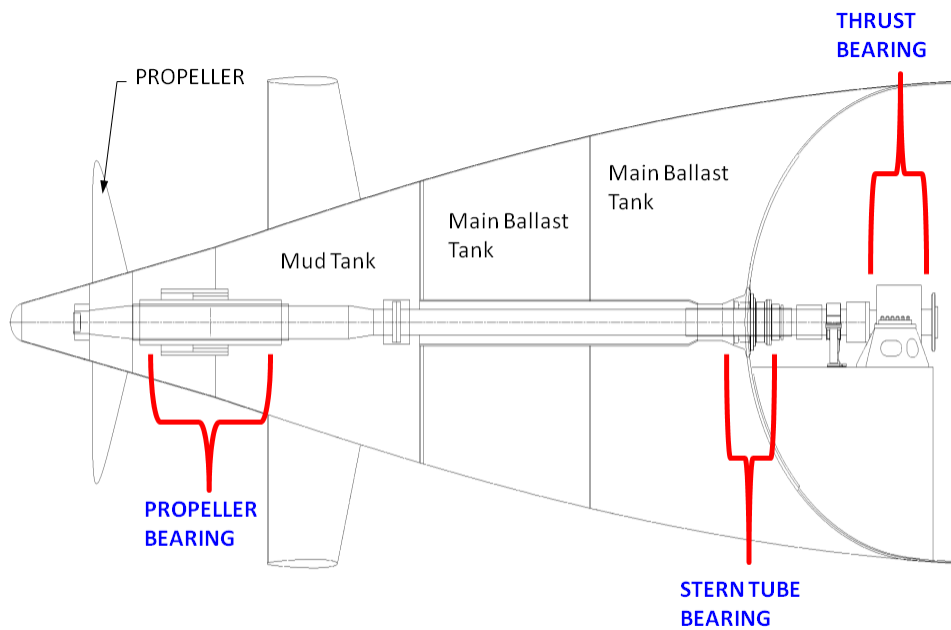
Figure 1-2: Typical Submarine Shaftline Bearings and Components

To this day, most large commercial ships employ oil-lubricated white metal bearings. Oil-lubricated bearings are not without their drawbacks. Although they tend to be more efficient than water-lubricated bearings, they require complex oil supply systems and seals to prevent both oil leakage to the environment and water leakage into the bearing.[1] A failure of any of these systems can result in an oil spill or a complete bearing failure.

The increasing severity of fines imposed from leaking oil into the environment as well improvements in materials has led to the start of a gradual change back towards water-lubricated bearings. Most navies and coast guards have long used water-lubricated bearings primarily for their simplicity and the fact that they tend to fail in a non-catastrophic manner. Figure 1-3 shows examples of water-lubricated bearings.

(a) Stave Bearing   (b) Partial Arc Bearing
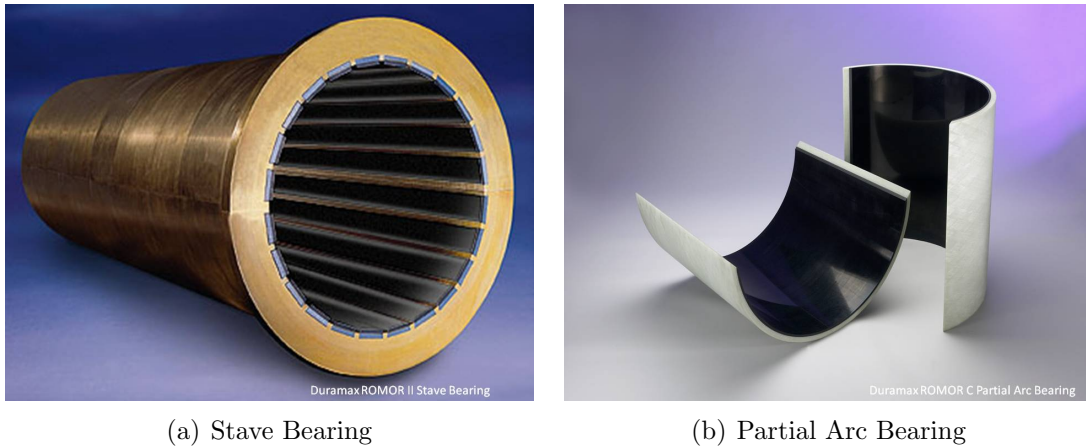
Figure 1-3: Typical Water-Lubricated Bearings

Using water as a lubricant provides many advantages, such as a high heat capacity of the working fluid, a readily available supply, and no environmental pollution [21]. There are, however, drawbacks associated with its use in bearings for ships. Using water as a lubricant also means that the shaft is directly exposed to a corrosive seawater environment. To protect against corrosion and the possibility of a shaft failure

---

[1]Harrington reported that a typical commercial ship of 22,000 shp can expect an efficiency improvement of approximately 0.2 percent through the use of oil-lubricated instead of water-lubricated bearings [11]

(the consequences of which can lead to a disastrous loss of the whole ship), shafts that are supported by water-lubricated bearings are typically sleeved in some form of corrosion resistant metal such as Cu-Ni or Inconel. Such sleeves are very expensive and add additional costs to ships.

Because of the high coefficient of friction experienced in the boundary-lubrication region of a water-lubricated bearing, intermittent shaft rotation (known as stick-slip shaft motion) is often observed in speeds below 10 rpm. This intermittent motion can result in gear backlash noise and a degradation in the acoustic signature of a ship [11]. Stick-slip motion is not the only unfavorable result of low rpm shaft operations. A common failure mode of outboard bearings is due to the abrasion and adhesion wear from either surface asperities or contaminants. This wear is typically a problem during slow speed operation when the film layer is thin enough to allow wear by particles or direct contact between bearing and shaft. At higher speeds the film thicknesses are usually sufficient enough to prevent such damage to the bearing. Mooring evolutions and use of the jacking gear in port means that low speed operating conditions can not always be avoided. Because water-lubricated bearings are directly exposed to the environment, they are at risk of ingesting foreign debris. Figure 1-4 shows examples of bearing failures.

(a) Plain journal bearing failure

(b) Stave bearing failure due to ingestion of foreign debris

Figure 1-4: Water-lubricated Bearing Failures

There have been historical studies done to quantify the likelihood and economic impacts of bearing failures. Arpi and Winn analyzed ship data from Lloyd's Register to provide failure rates for both oil and water-lubricated bearings [3]. The results of this work is shown in Figure 1-5.[2] This work is quite dated and encompasses data from vessels built between 1960 and 1979, so the results do not take into account advances in marine bearing technology. More recent experiences of American Bureau of Shipping engineers indicate that while advances in bearings design and ship production (especially in regards to alignment of the shaft) has reduced the failure rates, they still occur. Although commercial ABS experience with water-lubricated bearings is limited, non-stave water-lubricated bearings do not seem to last more than 5 to 10 years before requiring replacement [30].
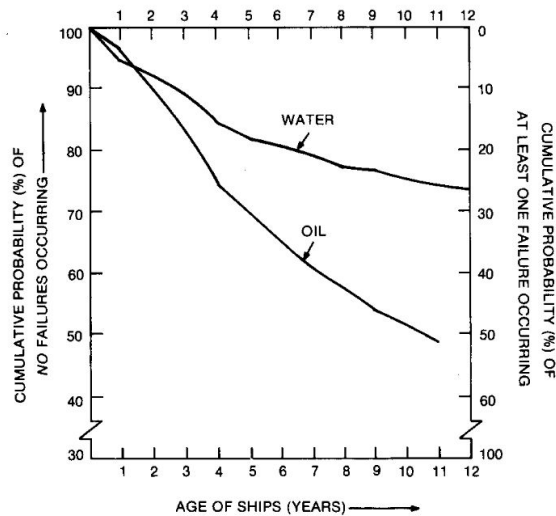
Figure 1-5: Cummulative Failure Rates for Stern-Tube Bearings with Shaft Diameters Greater than 500 mm

The consequences of a bearing failure can be quite severe from both operational and economic perspectives. Arpi and Winn found that the combined cost of repair and lost time for a bearing replacement in a commercial vessel may exceed $640,000 in CY-2013 dollars. Quantifying the cost of a bearing failure for a naval platform is more

---

[2]The failure rates of the water-lubricated bearings may be under reported, since a significant part of the data set includes stave bearings that do not result in a complete failure of the bearing if they degrade, but do require replacement at the next scheduled drydocking or overhaul.

difficult, but the amount of lost time if the vessel must be drydocked, the propeller removed, and the shaft pulled can be significant. By one estimate, the average minimum cost to drydock a U.S. Navy vessel is approximately $1,000,000 [13]. It is clear that extending the expected life of marine propulsion bearings can be a significant positive contribution to vessel owners and operators. These costs can be reduced through the use of a partial arc bearing (comprising less than 180 degrees of bearing engagement) or through the use of staves because they do not necessarily require the shaft to be removed for bearing replacement.

Different techniques can be used to minimize the impacts of operations at low speeds that lead to bearing failures. These include reducing the size and amount of contaminants by filtration if a forced lubrication water supply is installed, and the use of hydrostatic bearings. Unlike hydrodynamic bearings that require relative motion between shaft and bearing to generate a lubrication film separating the shaft from the bearing, hydrostatic bearings utilize pressure from a pump to create the fluid film.

This work focuses on the development of a hybrid bearing that can prevent the low speed abrasive wear and stick-slip motion by using hydrostatic operation at low rpm, while still maintaining the capability for hydrodynamic operation at higher rpm.

Chapter 2

Fluid Film Bearing Background, Theory, and Nomenclature

2.1 Lubrication Regimes

Fluid film bearings are designed to operate using either hydrodynamic or hydrostatic lubrication. In hydrodynamic lubrication, the surfaces of a bearing are separated by a film of lubricant created by the relative motion between the journal and the bearing. This relative motion pulls a wedge of lubricant at sufficient velocity to generate a pressure large enough to separate the surfaces. This hydrodynamic film does not require fluid to be supplied at an elevated pressure. With a decrease in velocity, lubricant viscosity, or an increase in the load on the bearing, the film may become thin enough that surface asperities on the journal and bearing begin to contact each other - a condition known as mixed lubrication. At even smaller film thicknesses on the order of the molecular dimension of the lubricant, the condition is known as boundary lubrication. These regions are shown in Figure 2-1 in a graphic representation of a Stribeck curve.

Boundary lubrication occurs when there are very low relative speeds between surfaces. When this occurs, the speed and viscosity are not able to create a film pressure capable of supporting the applied load on the bearing. This results in the gap between
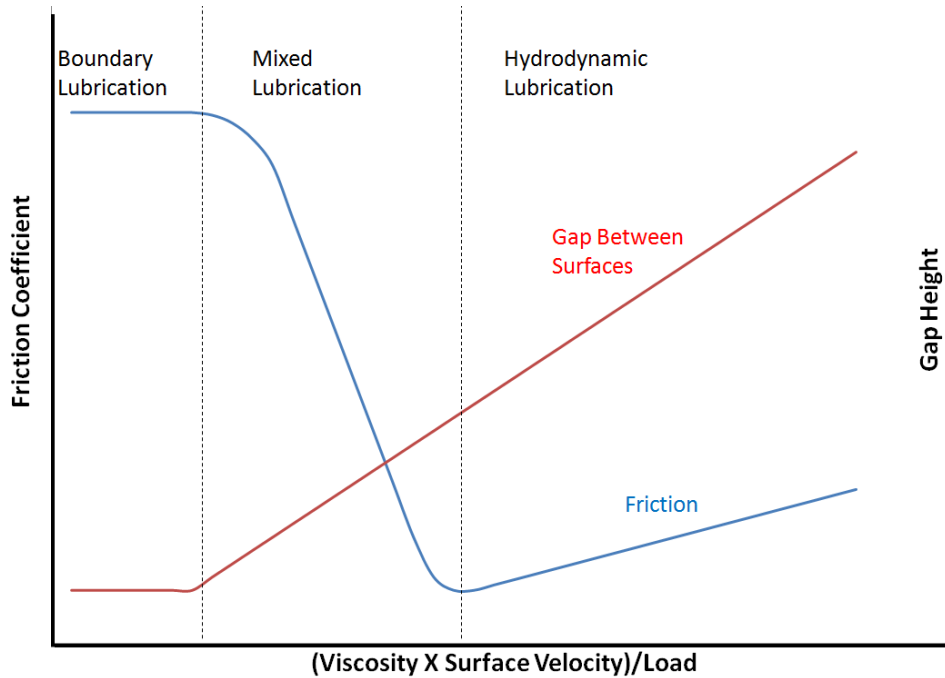
Figure 2-1: Stribeck Curve

surfaces to decrease and cause the asperities on the surfaces to penetrate each other with plastic deformation (depending on loads). Operation in this regime results in increased friction, temperature, and wear. Friction coefficients in the boundary lubrication regime are typically on the order of 0.2 to 0.4 and is highly dependent on the composition and finishes of the bearing and journal materials. In between hydrodynamic and boundary lubrication is the region known as mixed lubrication - named so because it is a mixture of hydrodynamic effects and boundary lubrication effects. This region also results in increased wear and friction, albeit at lower severities than boundary lubrication.

Because of the adverse effects of friction and wear, prolonged operation in the mixed or boundary lubrication is highly undesirable for a fluid film bearing. For a properly designed hydrodynamic bearing, it is only during starting and stopping that boundary and mixed lubrication are seen. When surface speeds in a bearing are such that operation in the boundary or mixed regimes can not be avoided, hydrostatic lubrication - which utilizes an external pressure supply to generate a fluid film between
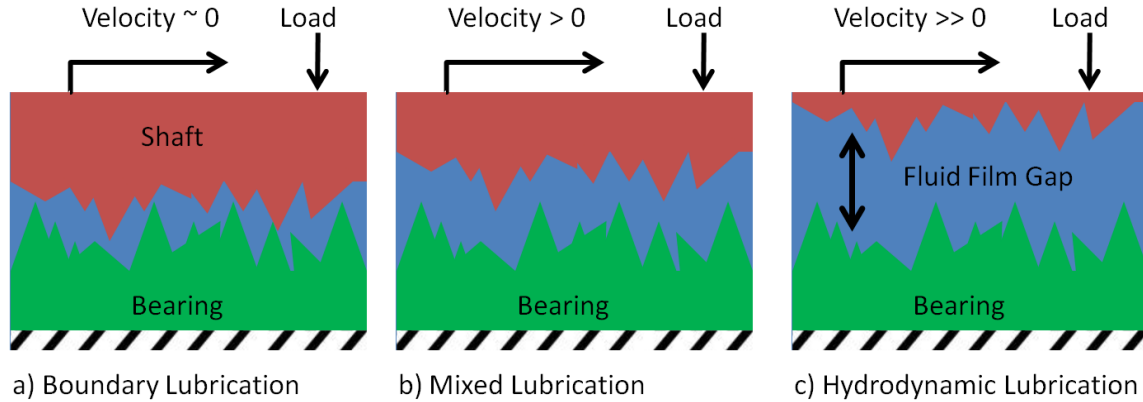
Figure 2-2: Fluid Film Gap for Lubrication Regimes

surfaces - can be used since it does not require relative motion between journal and bearing surfaces.

2.1.1   Effect of Surface Roughness on Lubrication Regime

As Figure 2-1 shows, the gap between the bearing and shaft surfaces generally increases with rotational speed. The magnitude of this gap is one of the driving factors behind what lubrication regime the bearing is operating in. The reason for this is because when the gap is small, there is no longer a full film of fluid between surfaces. Instead, there starts to develop contact between the asperities of the bearing and shaft materials as shown in Figure 2-2. In the boundary lubrication regime, the fluid gap is negligible and the response of the bearing is dominated by the material properties of the two materials. The fluid gap becomes significant in the mixed lubrication regime, but it is not large enough to completely prevent the surface asperities from touching - leading to wear and friction. In hydrodynamic lubrication the fluid gap becomes large enough such that there is no longer any physical contact between surfaces, and the bearing response is purely a function of fluid dynamics.

There are many ways to characterize the material texture of a surface. An actual surface profile can consist of form error, waviness, and roughness. All of these can be significant in influencing the performance of a bearing, but for most bearings that

35

are manufactured without significant form or waviness errors the surface roughness is the dominant factor. There are several methods to calculate surface roughness such as stylus contact profilometry, interferometry, and various forms of microscopy.

Surface roughness is most typically reported as the average roughness (usually denoted as R_a), which is the average deviation of individual surface point heights and depths from the mean elevation of the surface profile. Another commonly utilized measure of roughness useful in journal bearings is the root-mean-square (rms) roughness (usually denoted as R_q). There are other measures of roughness that can be used such as the peak-to-valley height of the surface (indicating the max deviation in the surface and usually denoted as R_t), the skewness (measuring the relative symmetry of the height variations), and kurtosis (measuring the relative sharpness of the peaks). The production method of manufacturing the bearing is the major factor behind the ultimate surface roughness of a bearing or shaft. There are general thumbrules that are applicable for determining the ratio between R_q and R_a [14]. For example, gausian distributions have a ratio of $\frac{R_q}{R_a}$ equal to 1.25 which is applicable for many surface finishes, while honing processes have a ratio equal to 1.45.

Determining the roughness of the bearing and shaft surfaces allows for a rough estimate in the required minimum film thickness h_{min} needed to achieve operation in different lubrication regimes. Hamrock uses a dimensionless film parameter Λ for this [9]:

$$\Lambda = \frac{h_{min}}{\left(R_{q,a}^2 + R_{q,b}^2\right)^{1/2}} \tag{2.1}$$

where $R_{q,a}$ and $R_{q,b}$ are the rms finish of the two surfaces. Values for Λ vary with the lubrication regimes. Rough values indicating the ranges for these are:

1. Hydrodynamic Lubrication: $\Lambda > 5$

2. Mixed Lubrication: $1 < \Lambda < 5$

3. Boundary Lubrication: $\Lambda < 1$

The values listed above are general estimates, but can vary depending on actual operation. Surface roughness is not always a constant, particularly when softer bearing materials are utilized. After prolonged operation in boundary or mixed lubrication regimes the high asperities peaks in the softer material (such as babbitt) can gradually wear down, effectively improving the surface finish to a lower roughness. This is the reason that bearings typically undergo a running-in process before full unrestricted operation ensues.

Another condition at lower Λ values can occur when soft bearing materials are utilized. In this case, the actual bearing material may elastically deform when subjected to large point loads. This can lead to local changes in the shape of the surfaces and effect the hydrodynamic film. This is a typically not a major issue for conformal surfaces (like journal bearings), where the load is distributed over a relatively large area. For water-lubricated bearings that have a small projected area loading, the magnitude of this issue is further minimized. In spite of these low loads, elastic deflection of the material can occur - particularly when synthetic rubber is used as a bearing surface.

It is clear to see that the quality of surface finishes on both the shaft and bearing material is vital to promoting hydrodynamic operation. It is for this reason that very good surface finishes are specified and used for marine bearings. Shaft sleeve and bearing finishes are typically ≤ 32 to 64 μinches R_a. Based on equation 2.1, this means the h_{min} will typically be on the order of 0.0002 to 0.0005 inches (or lower) to promote hydrodynamic lubrication.

2.2 Hydrostatic Lubrication

Hydrostatic lubrication does not require relative motion between journal and bearing surfaces. Instead, lubricant is introduced into the load bearing gap at a pressure sufficient to separate the surfaces with a fluid film. The simplified basic principle of
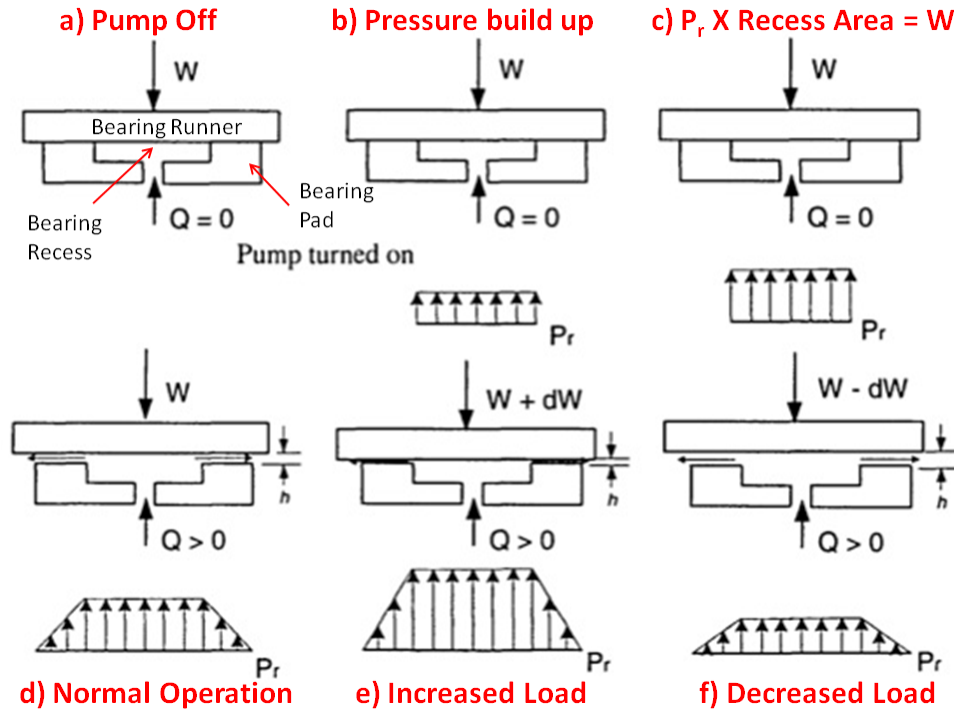
Figure 2-3: Hydrostatic Bearing Operation

operation of these bearings is shown in Figure 2-3.

In Figure 2-3a, the pump is off with the bearing runner resting on the bearing pad. Then the pump is turned on, allowing recess pressure (P_r) to build up (Figure 2-3b). Pressure in the recess builds up to a point where the force - equal to the recess area times pressure - is large enough to lift the load (W) applied on the runner (Figure 2-3c). This is called the 'lift' pressure. Once the bearing runner is lifted off the bearing pad to a gap of height h, normal operation commences and flow (Q) begins through the system as shown in Figure 2-3d. Because of the flow rate through the bearing and across the bearing pad, a pressure drop exists between the bearing recess and the exit of the bearing pad.

In a condition where an increased load is applied (Figure 2-3e) the gap height h will decrease, resulting in a rise in recess pressure until it is high enough to support the increased load. In the opposite condition (Figure 2-3f) where load is decreased the

gap height h will increase causing the recess pressure to drop until the applied load is matched by the bearing pressure applied on the bearing area.

Hydrostatic bearings provide distinct advantages over hydrodynamic ones, including:

- No wear (theoretically)

- High load capacity, stiffness, and damping

- Low friction at slow speeds, and no static friction

These advantages are offset by disadvantages associated with complex, expensive, and power consuming lubrication supply systems. In spite of these drawbacks, hydrostatic bearings have been widely used in various applications including precision machine tools, nuclear reactor coolant pumps, dynamometers, and large rotating equipment such as telescopes and radar antennas [4].

When multiple recesses are used in hydrostatic bearings, each individual recesses usually requires its own individual pressure source or a way of compensating the pressure from a single source. This is because when a single pressure source supplies two recesses, one is more likely to lift than the other due to geometric or loading differences. Once one lifts, flow will commence through that recess limiting the ability of the pressure source to increase its pressure sufficient to lift the other recess. The use of a compensating element, which limits or restricts the flow to each individual recess, allows pressure to build up in all recesses to a value sufficient to lift them.

Compensation in hydrostatic bearings is typically done with external flow restrictions such as flat edge pins, capillary tubes, orifice restrictors, or flow control valves. These systems all require fine tuning of the resistance network for the bearing to operate properly. They also are very susceptible to clogging from contaminates in the lubrication fluid which can lead to complete bearing failure [28]. Because the lubricating fluid of the outboard bearings of ships and submarines is seawater and often has entrained contaminants, this presents a serious problems for implementing hydrostatic

bearings. Filtration systems can provide a clean supply of seawater, but a failure of the system - especially in a muddy harbor - can lead to a single point failure in the propulsion train. Alternatives to the use of compensating devices is to use a single hydrostatic recess, individual pumps for each recess, or self-compensation that uses bearing clearances to regulate pressure instead of external systems. In-depth discussion of compensation for hydrostatic bearings and the different methods used to achieve it are available from many different sources [25, 26, 28].
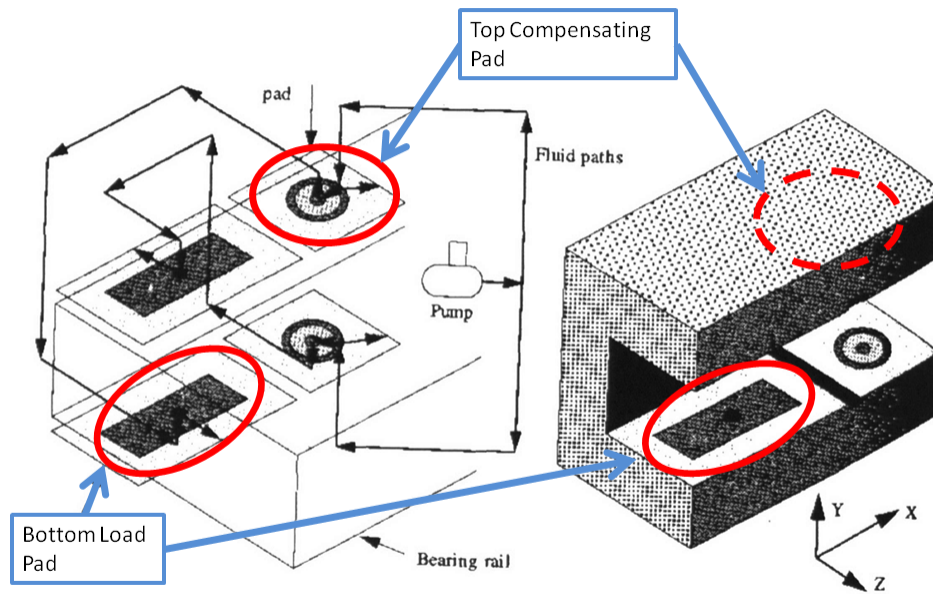
A. H. Slocum, *Precision Machine Design*. Dearborn, Michigan: Society of Manufacturing Engineers, 1992.

Figure 2-4: Self-Compensating Hydrostatic Bearing Concept

The concept of self-compensating bearings is displayed in Figure 2-4. The 'C' shape would straddle a rectangular bearing rail and flow is supplied to an inlet of compensating pad from a pressure supply. The compensating pad consists of the inlet (fed by the pump), a land, and a recess on the other side of the land. Flow enters the inlet, across the land and into the recess. The recess pressure and flow is then routed to the opposite side of the bearing where it supplies a load pad. The operation of the bearing is described below:

1. A single pump supplies pressure to the compensating pad inlets on the top and bottom of the bearing.

2. A centered bearing rail moves towards the top of the bearing due to an upward force. This causes the fluid gap between the rail and the top compensating land to decrease, while the fluid gap between the rail and the bottom land increases.

3. This causes a larger pressure drop across the top compensating land and smaller pressure drop across the bottom compensating land. This results in a smaller pressure in the top compensating recess and bottom load pad. In addition to this, there is a larger pressure in the bottom compensating recess and top load pad.

4. This difference in load pad pressures causes a restoring force that opposes the upward force on the rail until a stable operating point is reached.

Self-compensation removes the need for complex inlet restrictors and is passive. Surface self-compensation takes the concept one step further by using connecting grooves on the surface of the bearing instead of individual piping to route flow and pressure between the compensating pad and load pad. This is beneficial for a water-lubricated bearing because there are no internal routing connections that may become clogged from debris or growth and subsequently affect performance. Any such contaminants will be sheared away from the bearing during normal operation and allows for the use of seawater.

Surface self-compensation journal bearings have been previously used in high speed machine tools [27, 29], and recent work by Wong has showed the potential for water-lubricated partial-arc surface self-compensated journal bearings [33].

2.3 Hydrodynamic Lubrication

2.3.1 Overview

Hydrodynamic lubrication is a direct result of relative motion between two surfaces.
Depending on the geometry and relative orientation of the two surfaces there usually
exists an area where there is a converging region between the two. The combination of
this converging shape, relative motion, and fluid viscosity result in a positive pressure
that provides for the existence of the fluid film. The manner in which a hydrodynamic
journal bearing operates is shown in Figure 2-5.[1]

(a) $\omega = 0$ (b) $\omega > 0$

(c) $\omega >> 0$
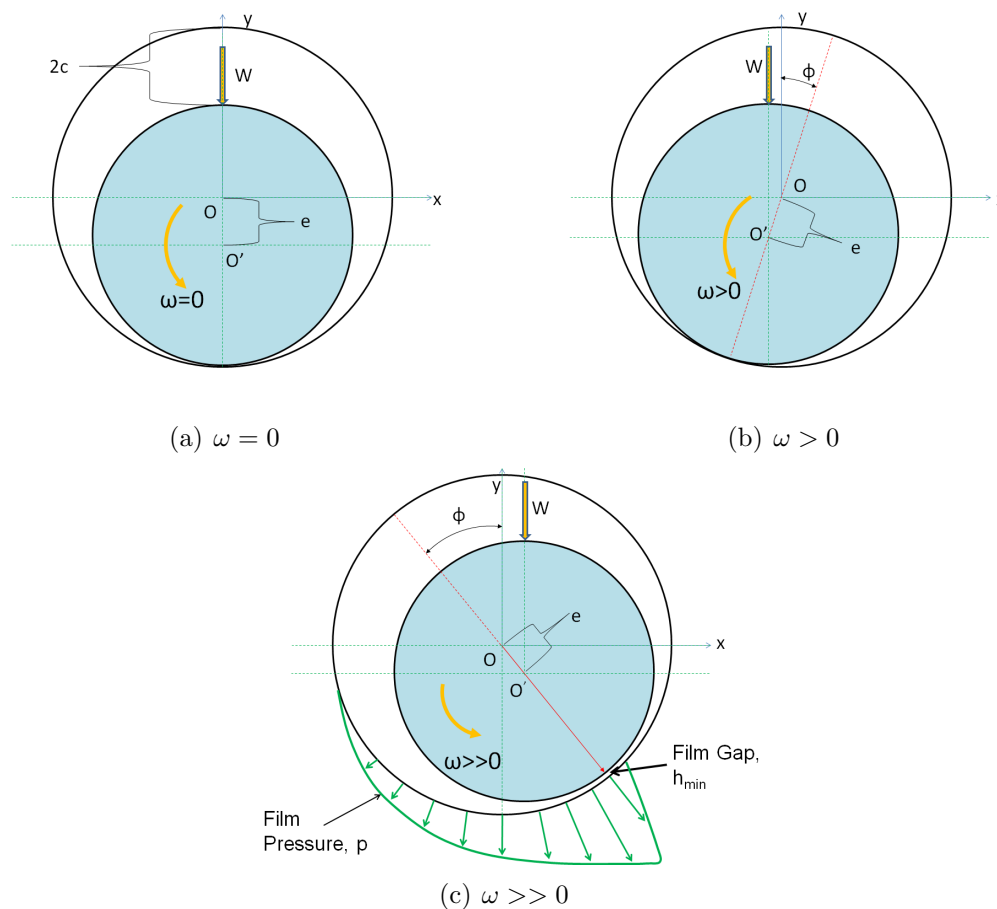
Figure 2-5: Operation of Hydrodynamic Journal Bearing

A shaft initially at rest with an angular velocity (ω) equal to zero and an applied
radial load (W) will be located at the bottom dead center (BDC) of the bearing

---

[1]Bearing clearances are greatly exaggerated for clarity.

(Figure 2-5(a)). In this condition the eccentricity ratio (ϵ) is equal to one and is defined as:

$$\epsilon = \frac{e}{C} \tag{2.2}$$

where e is the displacement of the shaft center from the bearing center, and C is the radial clearance of the bearing. When the shaft initially starts rotating there is a friction force developed in the physical contact between the shaft and bearing (Figure 2-5(b)). This causes the shaft to ride up the bearing away from the direction of rotation. This continues until the shaft speed increases to the point where fluid is pulled into the wedge shape between the two surfaces - generating a pressure.

As the speed increases, so does the pressure until it is sufficient to lift the shaft off the bearing and maintain a fluid film between the surfaces for hydrodynamic lubrication (Figure 2-5(c)). In this condition, the distribution of the film pressure pushes the bearing in the direction of rotation. This combined with the size of minimum film gap (h_{min}) leads to the shaft operating at an attitude angle (ϕ). As mentioned in section 2.1.1, this minimum film gap must be larger than the combined heights of the surface asperities.

2.3.2   Viscosity, Petroff's Equation, and Sommerfeld Number

For bearings that operate with a fluid film, the shear stresses (τ) in the fluid are the driving cause of frictional force. The relationship between the shear stress in a fluid and the rate of shear is viscosity. It is best illustrated by the simple case of two flat plates experiencing a velocity-induced flow with one plate stationary and one moving, as depicted in Figure 2-6. In this figure the top plate moves at a velocity U parallel to the lower fixed surface. A film of fluid thickness h separates the plate and a frictional force F is required to shear the fluid between the plates of an area A. If the assumption that there is no-slip conditions at the plate boundaries is made, this relationship can be summarized by the equation:

$$\tau = \frac{F}{A} = \mu\frac{U}{h} \tag{2.3}$$

In this equation μ is the absolute (or dynamic) viscosity of the fluid, typically expressed in Reyn's ($\frac{lb_f s}{in^2}$). For Newtonian fluids μ is constant regardless of $\frac{du}{dy}$, which is the shear rate or velocity gradient. An alternative measure of viscosity, known as kinematic viscosity (ν) is defined as absolute viscosity divided by density:

$$\nu = \frac{\mu}{\rho} \tag{2.4}$$
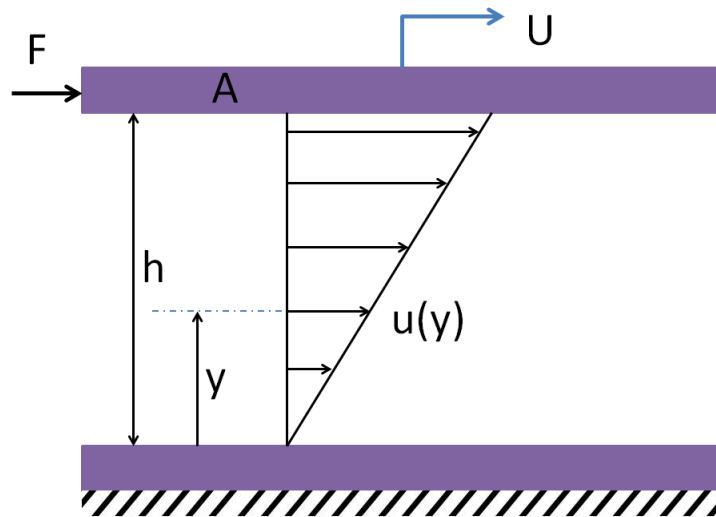
Figure 2-6: Velocity Induced Couette Flow

The relationship in equation 2.3 is useful in the analysis journal bearings. A concentric shaft in a bearing with geometry of length L, radial clearance c, shaft radius r_s and bearing radius r_b as shown in Figure 2-7 can be considered. If this shaft is operating at N revolutions per second then the tangential velocity of the surface (in feet/second or inches/second) is equal to:

$$U = 2\pi r_s N \tag{2.5}$$

Substituting this into equation 2.3 yields the equation for shear stress in the fluid

44
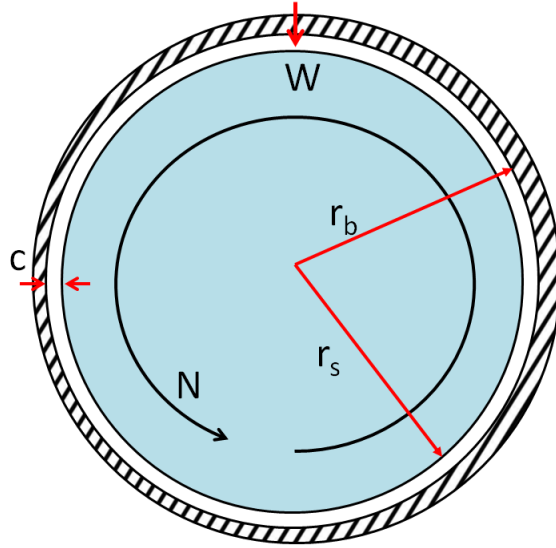
Figure 2-7: Concentric Shaft Example

film:

$$\tau = \mu \frac{2\pi N r_s}{C} \tag{2.6}$$

By multiplying τ by the area of the bearing $(2\pi r_s L)$, the tangential force needed to shear the fluid is obtained. When this force is multiplied by r_s, the torque T needed to shear the fluid is:

$$T_{shear} = \frac{4\mu N L \pi^2 r_s^3}{C} \tag{2.7}$$

If a load W is imparted on the shaft, the condition can be expressed as the projected area loading on the bearing. The projected area loading, designated by P and normally expressed in psi, is defined as the amount of load per unit of projected bearing area:

$$P = \frac{W}{2L r_b} \tag{2.8}$$

This load condition can be related to force by using a friction coefficient, f, which can than be used to find the torque due to friction in a bearing:

$$T_{friction} = fWr_s = 2fr_s^2LP \tag{2.9}$$

Equating equations 2.7 and 2.9 and solving for friction yields Petroff's equation:

$$f = 2\pi^2 \frac{\mu N}{P} \frac{r_s}{C} \tag{2.10}$$

Petroff's equation is dimensionless and can be split into two different dimensionless parameters. The first, $\frac{r_s}{c}$ is known as the clearance ratio is a key design variable in bearing design. For oil lubricated hydrodynamic bearings, a clearance ratio on the order of 1000 is typically used. For marine water-lubricated hydrodynamic bearings, much lower clearance ratios on the order of 200 to 400 are often used[2]. The second dimensionless parameter, $\frac{\mu N}{P}$, defines the bearing operating characteristics and makes up the x-axis of the Stribeck curve.

A modification of Petroff's equation is the Sommerfeld number. This is oftentimes called the bearing number and is denoted by S:

$$S = \left(\frac{r_s}{C}\right)^2 \frac{\mu N}{P} \tag{2.11}$$

The Sommerfeld number is typically used in non-dimensional tables and graphs that allow designers to easily select hydrodynamic bearings based on operating loads and speeds. The Sommerfeld number works in the hydrodynamic lubrication regime, but does not accurately capture the characteristics of a bearing that is operating in the mixed or boundary lubrication regimes - surface speeds are more typically used for differentiating between operating conditions in those regimes.

---

[2]Larger clearances are usually desirable for marine bearings. They provide for easier alignment during construction and maintenance, can accommodate hull distorting maneuvers more easily, and most importantly provide margin for different thermal expansions that occur between shafts and bearings for vessels that operate between extreme environments.

2.3.3 Reynolds Equation

In tensor form, the Navier-Stokes equation describing a fluid particle's acceleration is:

$$\underbrace{\frac{Du_i}{Dt}}_{\substack{\text{Lagrangian}\\\text{acceleration}}} = \underbrace{\frac{\partial u_i}{\partial t}}_{\substack{\text{Eulerian}\\\text{acceleration}}} + \underbrace{u_j \frac{\partial u_i}{\partial x_j}}_{\substack{\text{Convective}\\\text{acceleration}}} = \underbrace{-\frac{1}{\rho}\frac{\partial p}{\partial x_i}}_{\substack{\text{Pressure}\\\text{gradient}}} + \underbrace{\nu\frac{\partial^2 u_i}{\partial x_j \partial x_i}}_{\substack{\text{Viscous}\\\text{dissipation}}} + \underbrace{\frac{1}{\rho}F_i}_{\substack{\text{Body}\\\text{forces}}} \tag{2.12}$$

Consider a fully developed flow between two plates, as shown in Figure 2-8.
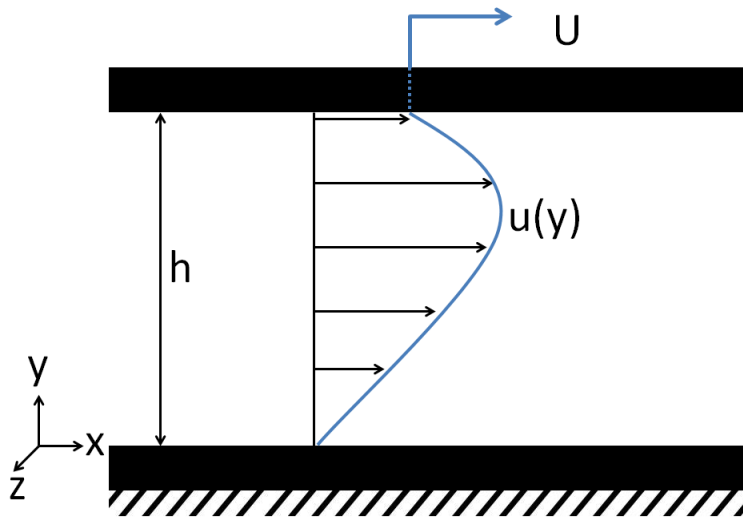
Figure 2-8: Fully Developed Laminar Flow

This can be broken out into individual components for x, y, and z directions. For the x direction, equation 2.12 becomes:

$$\rho\left\{\frac{\partial u}{\partial t} + u\frac{\partial u}{\partial x} + v\frac{\partial u}{\partial y} + w\frac{\partial u}{\partial z}\right\} = -\frac{\partial p}{\partial x} + \mu\Delta u + F_x \tag{2.13}$$

This equation can be greatly simplified by making several assumptions:

1. The lubricant is a Newtonian fluid and viscosity does not vary as it moves through x.

2. The inertia forces are small compared to the viscous shear forces (i.e. low Reynolds number and laminar flow) and may be neglected.

3. Lubricant is incompressible, allowing mass conservation to be directly related to volumetric flow.

4. The pressure in the film is a function of x and does not vary with y. This is typically valid for the small film thicknesses in bearings.

5. The pressure and flow do not vary in the z direction.

6. Changes in the vertical height are small so body forces can be neglected.

7. The flow is fully developed and does not vary with time.

An additional simplification made for journal bearings is to neglect the effects of curvature. This is an acceptable assumption due to the fact that the film thickness, h, is much smaller than the radius of curvature. Combining all of these simplifications allows equation 2.13 to be reduced to:

$$\frac{\partial p}{\partial x} = \mu \frac{\partial^2 u}{\partial y^2} \tag{2.14}$$

By applying no-slip boundary conditions to the walls, the velocity profile of the lubricant as a function of y can be determined:

$$u(y) = \frac{1}{2\mu} \frac{\partial p}{\partial x} \left(y^2 - hy \right) + \frac{U}{h} y \tag{2.15}$$

Integrating across the thickness of the lubricant allows the volumetric flow rate (Q) to be found:

$$Q = \frac{Uh}{2} - \frac{h^3}{12\mu} \frac{\partial p}{\partial x} \tag{2.16}$$

Applying the assumption of an incompressible fluid ($\frac{\partial Q}{\partial x} = 0$) leads to the classic Reynolds equation that is applicable for one-dimensional flow:

$$\frac{\partial}{\partial x}\left(\frac{h^3}{\mu}\frac{\partial p}{\partial x}\right) = 6U\frac{\partial h}{\partial x} \tag{2.17}$$

If the assumption that flow in the z-direction is not valid (i.e. for a short bearing or land), then the full form of equation 2.17 is:

$$\frac{\partial}{\partial x}\left(\frac{h^3}{\mu}\frac{\partial p}{\partial x}\right) + \frac{\partial}{\partial z}\left(\frac{h^3}{\mu}\frac{\partial p}{\partial z}\right) = 6U\frac{\partial h}{\partial x} \tag{2.18}$$

There are no general solutions to this equation, but it forms the basis behind numerical approximations by finite difference programs such as Raimondi and Boyd [23].

2.3.4   Reynolds Number

Since the Reynolds equation is predicated on the assumption that laminar flow exists, the validity of that assumption should be considered if that equation is to be used to model bearing performance. The Reynolds number is a non-dimensional ratio between inertial and viscous forces and for the flow inside the clearance of a hydrodynamic journal bearing it is defined as:

$$Re = \frac{UC}{\nu} \tag{2.19}$$

where U is the surface speed of the journal and C is the radial clearance of the bearing. At a critical Reynolds number, the flow will begin a transition from laminar to turbulent flow. This transition is not immediate, but gradually occurs over a certain range of Reynolds numbers until a fully turbulent flow occurs. Accompanying this transition is an increase in the resistance to shear of the lubricant film, which also results in an increase in the hydrodynamic friction of the bearing. The exact point at which this transition occurs is not exact, but experimental results from a 3 inch water-lubricated journal bearing show that the transition starts at a Reynolds number of approximately 750 and reaches full turbulence at a value of around 1600 [8].

For oil lubricated bearings that use a fluid with a high viscosity, maintaining laminar

flow is rarely an issue unless extremely high speeds are employed. Water has a very low viscosity, but fortunately propulsion shafts operate at relatively slow speeds.[3] A check of the Reynolds number for the bearings tested in this project was done. Table 2.1 shows the Reynolds number for various test speeds and compares the values to a nominal ship scale bearing. Values in the table are based on the test rig shaft diameter of 3.2305", a nominal ship scale shaft diameter of 28", a clearance ratio of 375, and water at 20° C.

Table 2.1: Expected Reynolds Numbers in Test Bearing and Corresponding Ship Scale Bearing

Model Scale RPM	Re_{model}	Ship Scale RPM	Re_{ship}
25.0	12	3	100
100.0	46	12	399
188.0	87	22	751
250.0	115	29	999
400.0	184	46	1598
500.0	230	58	1998
	300	75	2596
	399	100	3462
	499	125	4327
	599	150	5193

The test bearings in this project operate well below the critical Reynolds number even at the highest test speeds. The full scale bearing is another issue. Transition to turbulence can be expected to occur at approximately 22 RPM - roughly equivalent to a 1/3 bell for many vessels. Fully turbulent operation would be seen at approximately 46 RPM. This indicates that ship bearings operate with turbulence throughout much of the speed range.[4]

Consideration must be given for extrapolating any predictions in hydrodynamic performance from the test bearing to full scale. Fortunately for this project - focused primarily on low speed operation of the shafts where the transition between mixed

---

[3]The slow speeds used in main propulsion shafts is primarily due to propellers being more efficient at lower RPMs.

[4]These numbers will be influenced by the actual clearance ratio in the ship scale bearing. A clearance ratio of 375 lies within the typical range for water-lubricated marine bearings.

and hydrodynamic lubrication regimes occur - the assumption of laminar flow is valid at very low speed ranges. In particular, comparing the relative hydrodynamic performance between different test bearings should be completely valid since the test bearings will always be in the laminar flow regime.

Chapter 3

Modeling of Hydrostatic Bearing Performance

This chapter focuses on the different ways in which hydrostatic bearings can be modeled, but a brief mention of the different techniques available for modeling hydrodynamic journal bearings is warranted.

There does exist analytical solutions for hydrodynamic journal bearings such as the Full Sommerfeld and Half Sommerfeld solutions. These solutions make the assumption that there is no axial flow and provide acceptable accuracy for bearings that have very long length to diameter (L/D) ratio (or infinitely long). Several approximate solutions for bearings of a finite width are described by Fuller [8]. Numerical solutions using finite difference methods based on equation 2.18 include those by Raimondi and Boyd [23].

3.1 Lumped Parameter Modeling

The lumped parameter method divides a hydrostatic bearing into different regions where the flow can be modeled as a one dimensional, fully developed flow. Because hydrostatic models assume stationary surfaces, equation 2.16 can be simplified by removing the surface velocity term U. Assuming a width of a plate in the z direction

(L_z), the equation for flow through two plates becomes:

$$Q = -\frac{L_z h^3}{12\mu}\frac{\partial p}{\partial x} \tag{3.1}$$

If the pressure gradient is integrated over the length of the plates in the x direction, the difference in pressure over the plate can be determined:

$$\Delta P = Q\frac{12\mu L_x}{h^3 L_z} \tag{3.2}$$

It is at this point an electric circuit analogy to Ohm's law is made equating flow rate (analogous to current), pressure drop (analogous to voltage drop), and hydraulic resistance (analogous to resistance).

$$R_{Rectangle} = \frac{\Delta P}{Q} = \frac{12\mu L_x}{h^3 L_z} \tag{3.3}$$

This concept of the hydraulic resistance of a rectangular pad can be extended to that of an annulus with an inner radius (r_i) and outer radius(r_o):

$$R_{Annulus} = \frac{6\mu}{\pi h^3}\ln\frac{r_o}{r_i} \tag{3.4}$$

These basic equations for hydraulic resistance allow a hydrostatic bearing to be discretized into rectangular and circular geometries that are representative of the bearing. These resistances are then combined to create an fluid resistance network allowing for pressures, flows, and resistances to be found. An example showing this process for a 3 Port Hydrostatic journal bearing is shown in Figure 3-1.

The lumped parameter modeling method was used in designing the surface self-compensated bearings for this project. A MATLAB program was created for each of those bearings that calculated the hydraulic resistances of the various lands in the bearings. The individual bearing designs and descriptions are provided in chapter 6. More in depth description of the lumped parameter method for solving hydrostatic bearings can be found in several good references [28, 15, 33].
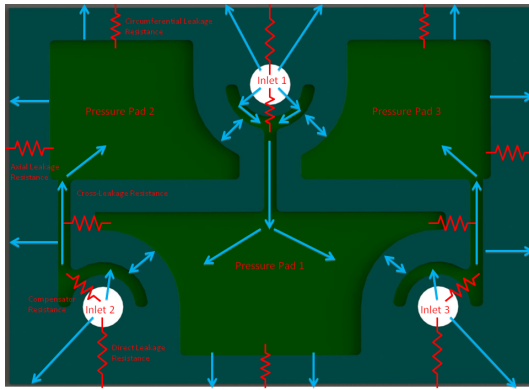
(a) 3 Port Hydrostatic Concept
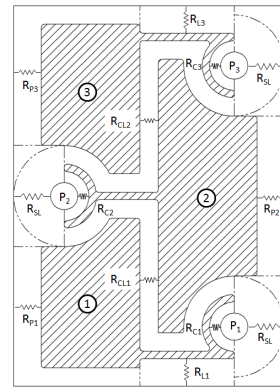
(b) Discretizing Resistances [33]
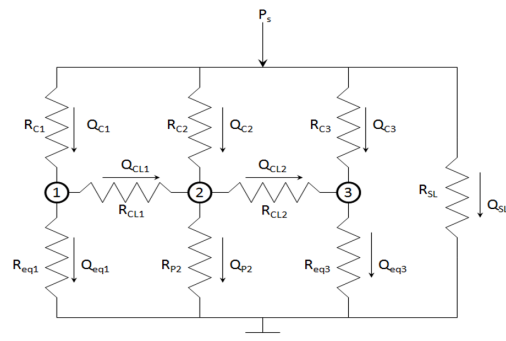
$$R_{eq1} = \frac{R_{P1}R_{L1}}{R_{P1}+R_{L1}} \qquad R_{eq3} = \frac{R_{P3}R_{L3}}{R_{P3}+R_{L3}}$$

(c) Fluid Resistance Network [33]

Figure 3-1: Lumped Parameter Discretization Process

3.2　Geometry Effects of Eccentric Shafts
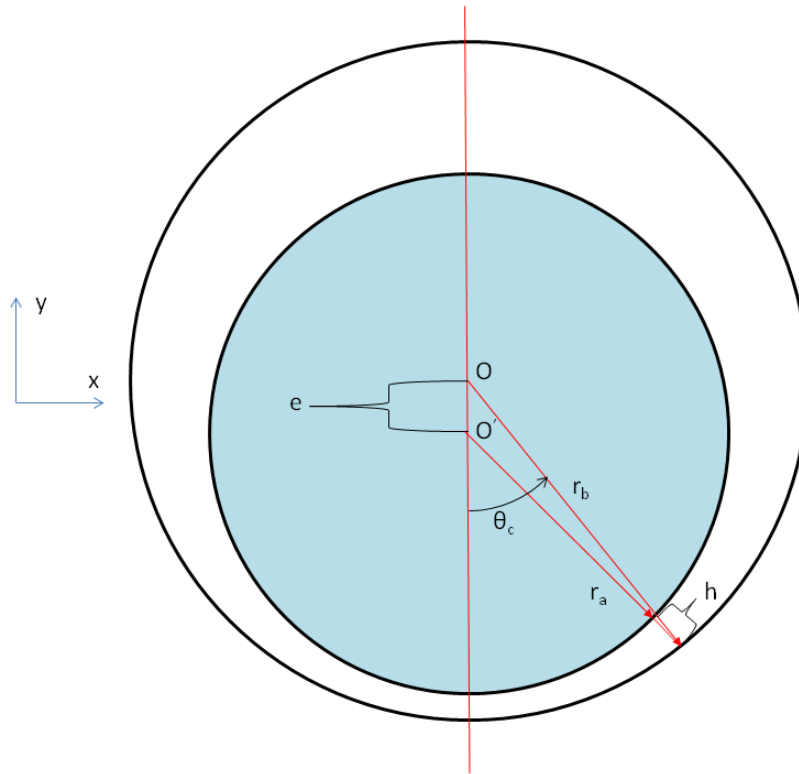
Figure 3-2: Geometry of an eccentric shaft in a bearing

For a bearing that has an eccentric shaft position the surfaces of the shaft and bearing are not parallel with each other. The effective gap size between these surfaces varies depending on both the attitude angle and eccentricity of the shaft. The general geometry of a bearing with an eccentricity is shown in Figure 3-2 where O' is the center of the shaft and O is the center of the bearing. The radial clearance of the bearing is:

$$C = r_b - r_a \tag{3.5}$$

and eccentricity ratio is defined as:

$$\epsilon = \frac{e}{C} \tag{3.6}$$

It can be shown that the gap between journal and bearing, h, is a function of ϵ and θ_C:

$$h = C\left(1 - \epsilon \, cos \, \theta_c\right) \tag{3.7}$$

where θ_c is the relative angle from the minimum clearance.

This relationship can be used to model the behavior of fluid flow within sections of a journal bearing with varying gap thicknesses due to eccentricity ratio. If there is a raised land spanning the bearing surface from point s1 to s2 as shown in Figure 3-3, then the gap at any point on the land can be defined as:

$$h = C\left[1 - \epsilon \, cos\left(\frac{s}{r_b}\right)\right] \tag{3.8}$$

where s is the arc length distance from θ_c. This can be analyzed for a land that has flow across it circumferentially as well as for a land that has flow across it axially.

3.2.1 Land with Circumferential Flow

For the case of a land of length L_z placed lengthwise (along z axis in Figure 3-3) on the bearing surface with a flowpath that goes across the land circumferentially (i.e. flow from point p1 to p2), equation (3.8) can be substituted into equation (3.1) to find the pressure gradient:

$$\frac{dp}{ds} = -\frac{12\mu Q}{L_z} \frac{1}{C^3 \left[1 + \epsilon \, cos\left(\frac{s}{r_b}\right)\right]^3} \tag{3.9}$$

This pressure distribution provides a means to determine the hydraulic resistance across the land and the forces on the land. The total pressure drop can be found by integrating across the land:

$$p1 - p2 = \frac{12\mu Q}{C^3 L_z} \int_{s1}^{s2} \frac{1}{\left[1 + \epsilon \, cos\left(\frac{s}{r_b}\right)\right]^3} \partial s \tag{3.10}$$

57
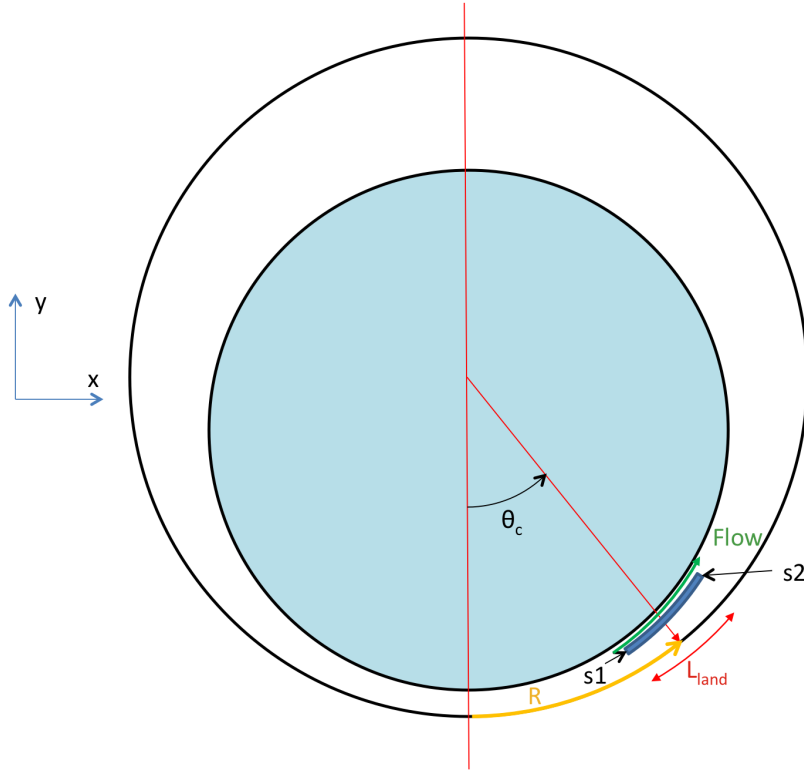
Figure 3-3: Diagram of circumferential fluid flow over a land in an eccentric shaft

This leads to the equation to find the hydraulic resistance:

$$R_c = \frac{12\mu}{C^3 L_z} \int_{s1}^{s2} \frac{1}{\left[1 + \epsilon \, cos(\frac{s}{r_b})\right]^3} \partial s \qquad (3.11)$$

The use of these equations are particularly useful in evaluating the response the hydrostatic lift bearing (section 6.9), forming the basis for a tool used to predict the forces generated in that design. Knowing that the fluid inlet flow and pressure is distributed axially along the BDC of the bearing and that there are atmospheric pressure conditions along the circumferential exits of the bearing allows the pressure distribution to be determined at any angle along the bearing surface. These pressures enable the vertical and horizontal forces imposed by the fluid on the shaft to be calculated. Modeling in this fashion is a simple 2D slice of the bearing, but when integrated over the length of the inlet slot the entire bearing response can be modeled. As will be shown in section 6.9, the use of a 2D model to predict the performance of

a 3D bearing introduces errors because the axial pressure distribution due to leakage from the ends of the bearing will not be accurately captured. This model did, however allow for key insights into the effect of shaft location on the pressure profile in the bearing.

3.2.2   Land with Axial Flow
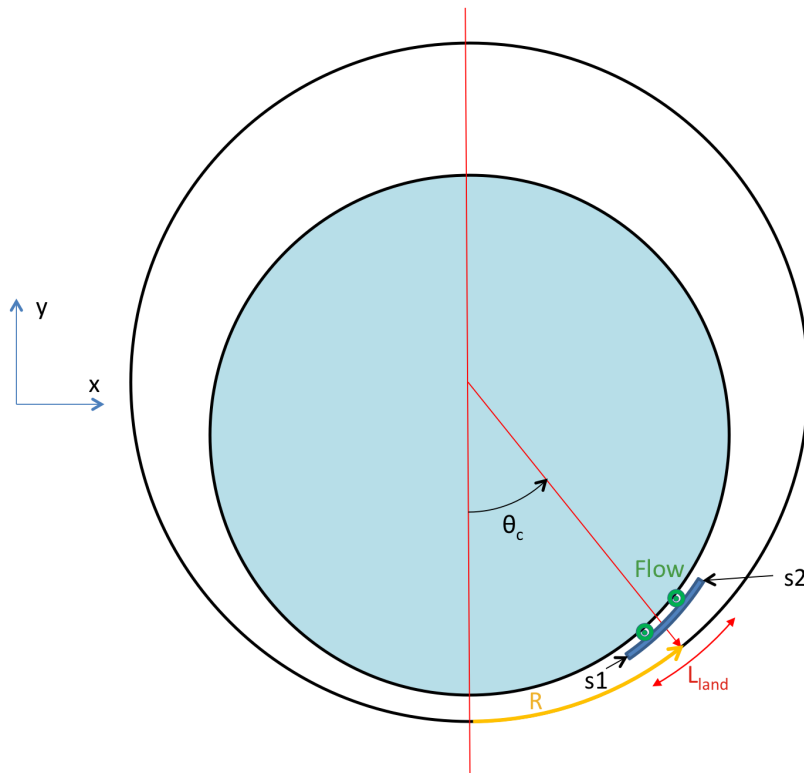
Figure 3-4: Diagram of axial fluid flow over a land in an eccentric shaft

The case of a land of exposed to axial flow along a length of land L_{land} (with flow into the page as shown in Figure 3-4) can also be analyzed using a similar process as in section 3.2.1. Substituting equation (3.8) into equation (3.1) and solving for flow Q as a function of position on the arc length of the land:

$$Q(s) = \frac{C^3}{12\mu} \left[1 - \epsilon \; cos \left(\frac{s}{r_b} \right) \right]^3 \frac{dp}{dz} \qquad (3.12)$$

If there is no axial or vertical tilt of the journal relative to the bearing, then it can

be assumed that the pressure gradient is constant over the length of the land L_z.

$$\frac{dp}{dz} = \frac{\Delta P}{L_z} \tag{3.13}$$

The total flow can than be found:

$$Q = \frac{\Delta P C^3}{12\mu L_z} \int_{s1}^{s2} \left[1 + \epsilon \; cos(\frac{s}{r_b})\right]^3 \partial s \tag{3.14}$$

This allows the hydraulic resistance to flow to be determined.

$$R_a = \frac{12\mu L_z}{C^3} \int_{s1}^{s2} \frac{1}{\left[1 + \epsilon \; cos(\frac{s}{r_b})\right]^3 \partial s} \tag{3.15}$$

3.2.3   Comparison to Flat Plate Resistance

The full hydraulic resistance equations found in sections 3.2.1 and 3.2.2 are complicated to evaluate directly. Because of this, the flat plate resistance is often used instead of the full integral equations when analyzing hydrostatic journal bearings. This simplification is adequate when the bearing operates at very low eccentricity ratios, but can result in significant errors if one is not careful.

To quantify the magnitude of the error between the flat plate resistance and the full solution equation, the ratio of equations (3.11) and (3.15) can taken over equation (3.3) for a given gap height defined by the radial clearance in equation (3.5). The full equations were numerically evaluated for a range of ϵ, θ_c, and land length (L_{land}) values. The MATLAB script used to provide these numerical integrations is provided in appendix A.1.

This resistance ratio is shown for both axial and circumferential flows for a land length equal to the bearing radius in figures 3-5 and 3-6. As expected, the full solutions converge to the flat plate approximation as shaft eccentricity goes to zero. In almost all cases an increase in eccentricity ratio results in a substantial departure from the flat
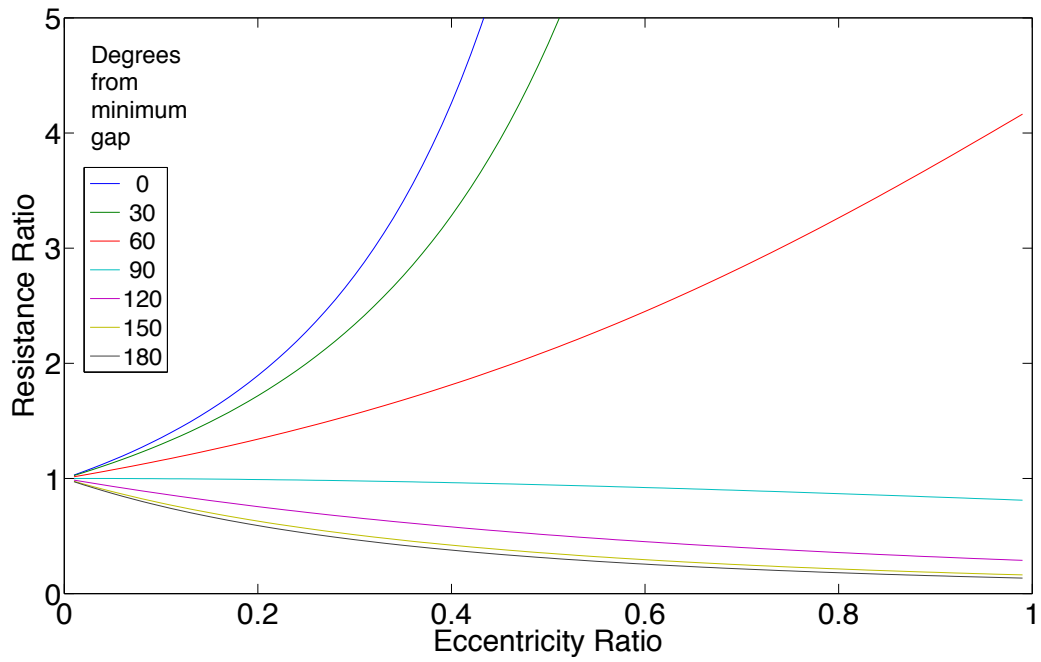
Figure 3-5: Resistance ratio between full journal solution and flat plate approximation for axial flow with $\frac{L_{land}}{r_b} = 1$
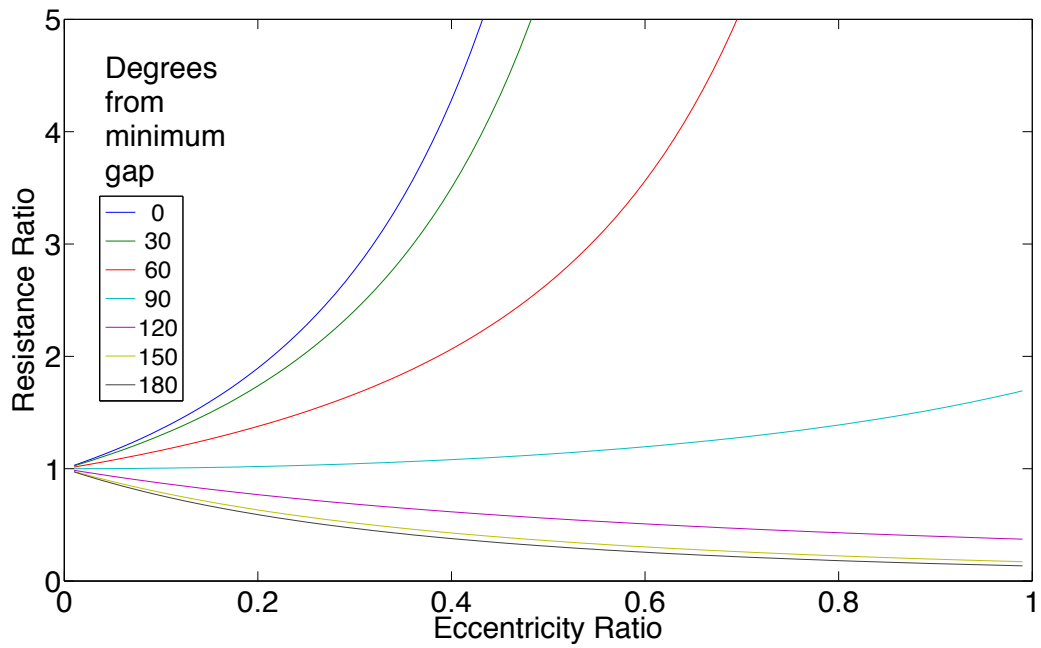
Figure 3-6: Resistance ratio between full journal solution and flat plate approximation for circumferential flow with $\frac{L_{land}}{r_b} = 1$

plate simplification. For θ_c values close to zero, this error rapidly increases to orders of magnitude errors with an increase in eccentricity ratio due to the gap becoming 'pinched' off by the shaft. When the gap becomes larger than nominal for θ_c greater than 90 degrees, the flat plate approximation predicts greater resistance values than actual. The magnitude of error is generally insensitive to land lengths with the exception of extremely long lands (on the order of 180 degrees of arc or longer).

This analysis illustrates the caution that needs to be taken by a designer when utilizing a flat plate assumption for bearings that will operate at points with even modest eccentricity ratios. Although most of the surface self-compensated hydrostatic bearings designed in this project utilized the flat plate approximation for hydraulic resistance, the Two-Port bearing (section 6.6) used the full integral equations to evaluate the resistances to aid in its design for an eccentricity ratio greater than zero.

3.3   Numerical Methods

Significant effort was expended early in the project to model the 3 port surface self-compensating bearing designs (sections 6.3 and 6.4) using computational fluid dynamics (CFD) programs. The ANSYS software package provides two different CFD solvers, FLUENT and CFX. There were great difficulties in obtaining numerical solutions for the complex hydrostatic bearing designs. Several major reasons for this are listed below:

- Mesh Size. To fully capture the size and complexity of the surface self-compensated bearings required an extremely large model. A significant driver behind this is that to accurately model the flow profile between lands and shaft requires a mesh of several layers. These land areas are of a very small length scale (on the order of 0.002 to 0.004") in thickness, but several orders of magnitude larger in length and width (on the order 0.25 to 4"). The groove and recess areas are of significantly larger thickness (on the order of 0.05"), but of similar lengths

and widths as the lands. An increased localized mesh density is also required in order to capture the effects of the flow transitioning between land and recesses regions. Both unstructured and structured meshes were attempted with model sizes exceeding 4.2 million elements in size - approximately the limit of the laboratory FEA computer.[1] Figure 3-7 shows one of the mesh models used in CFX simulations.
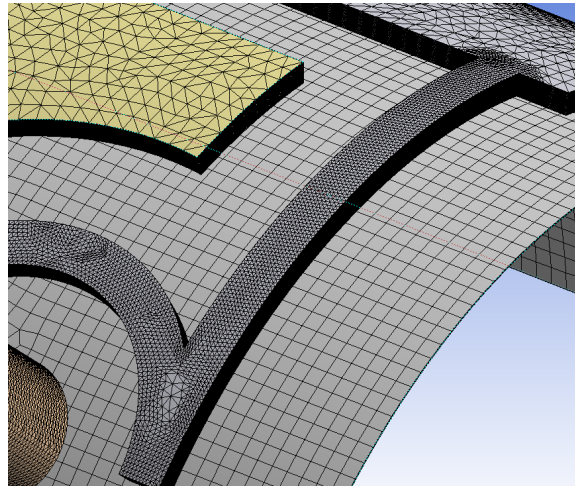
Figure 3-7: Screen Shot of CFD Mesh for 3 Port Hydrostatic Bearings in ANSYS CFX

- Mesh Dynamics. The mesh is dynamic in that the shaft moves relative to the bearing - creating the need for a mesh that can be reconfigured after each time step in a simulation. This presented difficulties with some forms of structured mesh modeling, as well as led to program crashes when the fluid gap disappeared if the surfaces contacted each other - a condition that happens in reality.

- Fluid-Structure Interactions (FSI). Although the FSI between lubricant and shaft can be considered to be negligible, the FSI between lubricant and the relatively soft and compliant bearing materials used can not be. This requires the use of coupled structural FEA program in working in tandem with the CFD program. Although the ANSYS suite has this capability, this is not a

---

[1]The computer used for CFD calculations was an i7 six-core machine with 24 GB of RAM custom built specifically for this project.

trivial problem and increases model size, complexity, and computational time significantly.

After several months with no discernible progress made in modeling the bearings with CFD, it was decided to pursue empirical experiments to determine bearing performance since experimental data was required to validate any CFD results that would be obtained. The later bearing designs removed the surface self-compensation features and the many transitions between inlets, lands, and recesses. Since these were contributing factors behind the failure to create a working CFD model, for these simplified bearings CFD modeling may be possible. CFD would also allow any turbulent conditions that may be present during hydrostatic operation in the significantly larger full scale size to be captured. In addition to CFD programs that use finite element methods, the potential to use a finite difference method based on equation 2.18 for the simplified hydrostatic bearing designs is quite feasible.

Chapter 4

Test Rig Design and Data Collection

4.1 Testing Requirements

The primary focus area of the research in this project was identifying the behavior of the hybrid bearings in the transition region between mixed and hydrodynamic lubrication regimes. This required that a dedicated test rig be designed and built to obtain empirical data to quantify the performance of the bearings. Key data required from the test rig include:

- Shaft speed.

- Bearing load.

- Hydrostatic bearing inflow pressure.

- Pressure at various locations on bearing surface.

- Hydrostatic bearing inflow rate.

- Torque.

- Shaft location relative to bearing surface.

65

The first three items needed to be controlled as design and operational variables. The last four items vary as a function of the controlled inputs and the actual design of the bearings, which include the topology of the surface features, geometric tolerances, form errors, the bearing material, and surface finish.

There were additional derived requirements for the test rig. With the intended application being marine water-lubricated outboard bearings, the test rig needed to be able to test the bearings in an environment representative of the end use. This resulted in a requirement for the bearing to be submerged in water, allowing for self-lubrication to occur during hydrodynamic testing when hydrostatic pumps were not supplying fluid to the bearings. The operating speeds of interest for the test bearings is the transition between hydrodynamic and mixed lubrication regimes (see Figure 2-1). The torque experienced at these operating speeds is the lowest that occurs in bearings. To differentiate between the relatively low torque values, the inherent torque (or 'tare' torque) in the test rig needs to be minimized. This would ensure that small changes in torque at different operating speeds and conditions would be a result of the test bearings and not test rig itself.

4.2 Initial Concept

Several different conceptual test rig designs were considered based on the requirements for data collection and bearing testing. The primary design variants that were initially considered are described below:

1. Vertical Test Rig. A rig utilizing a vertically mounted shaft that extends into a water tank was an option. The radial load on a test bearing could be applied horizontally on a test bearing by pulling or pushing against the test shaft. A tank for submerged bearing operations could be located below a suspended test shaft (and associated support bearings and drive assembly), or the shaft could penetrate a tank located above the test rig. The second version would require a shaft sealing system.

2. Horizontal Test Rig. A system employing a horizontally configured test shaft was investigated. This rig would have a centrally located water tank with the test shaft penetrating the tank through shaft seals. Support bearings and drive assembly would be located outside the tank. In this configuration the radial load could be applied either directly to the shaft through the support bearings, or through the test bearing by pushing or pulling on it when configured on the shaft.

3. Articulating Test Rig. A test rig design that could be quickly reconfigured for both dry and submerged testing was developed. This rig would not require shaft seals, but would expose many parts of the test apparatus to water. A design where the tank would move into the test section was considered, as was a design where the test section of the bearing would be lowered into a stationary tank.

The third option was ultimately chosen as the test rig design. The primary factor behind this decision was the concern with the effect that shaft seals would have on the test rig. The seals would increase the 'tare' torque on the test rig and reduce the ability to differentiate between small torque values. Another issue with shaft seals is their reliability. The test rig would be in a laboratory location with close proximity to expensive experimental equipment, so the effects that a shaft seal failure and accompanying water leak would have on other test equipment was a concern. The articulating concept had many positive attributes that help in selecting it as a design:

- The shaft and other equipment could be stored in a dry environment when not testing.

- The test bearings could be tested in a dry configuration without draining water from the tank.

- Access to the test bearings would be relatively unobstructed by a testing tank, allowing for easier modifications and changes of bearings.

- The use of radial air bearings that would provide virtually zero 'tare' torque.

The original concept of the test rig is shown in Figure 4-1. The design employs an outer frame that spans a water tank with a testing section attached to the frame by a pivoting hinge. This allows the test section to be lowered into the water tank for submerged operation and stowed above water when not testing. A single column force tester is used to pull on a test bearing, which is located on the bottom of the test shaft.

(a) Rig Configured for Submerged Testing   (b) Testing Section
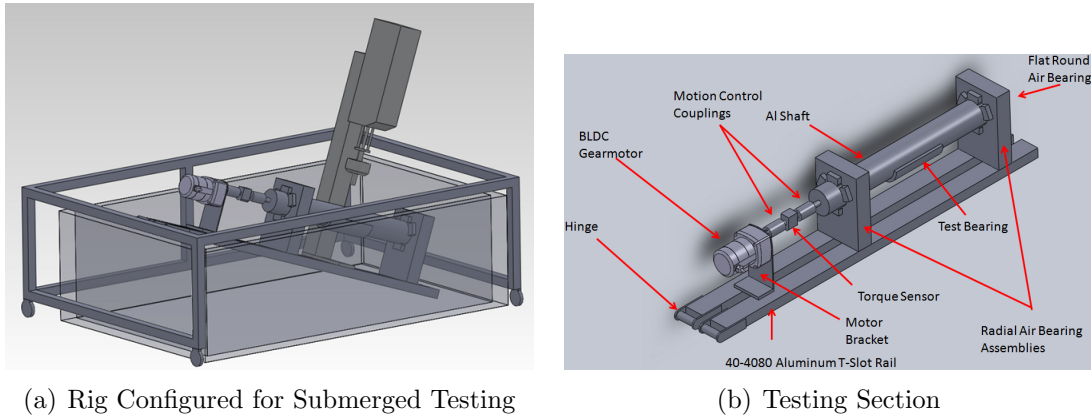
Figure 4-1: Original Concept Design of Test Rig

4.3 Test Rig Description

This section provides a detailed description of the design calculations and the test apparatus. The design and construction of the test rig was evolutionary process, with some design decisions deferred to later in construction. This allowed for critical path items that required longer lead time to be designed, built, and/or ordered early in the design.

4.3.1 Air Bearings

Air bearings utilize a very small film of pressurized air to provide an interface between surfaces. The NewWay® air bearings used in the test rig provide air through a porous carbon medium that allows for a relatively uniform pressure profile across the entire face of the bearing. Unlike contact roller bearings, this allows for virtually no friction

or wear providing long term, repeatable performance. The decision to use air bearings for the support bearings of the test rig ocurred early in the design process. This was result of many factors including:

- Availability of shop air throughout MIT.

- Negligible friction forces.

- High reliability.

- High stiffness.

- Low vibration and noise.

- Low Maintenance.

1. **Radial Support.** NewWay® offers two types of air bearings designed for supporting radial components such as shafts: Air bushings and radial air bearings.[1] Air bushings are offered in common internal diameter (ID) sizes. The largest bushing size available had a 3 inch ID. The original test bearing diameter being considered was in the 4 inch (approximately 100 mm) ID range. The use of bushings would therefore require a step down in the shaft to employ them. An additional drawback to using bushings was a more critical alignment process during test rig construction and a lower receptiveness to shaft deflections and misalignment that would be caused by the test bearing loads during operation.

Radial air bearings were chosen for use in the test rig. A picture of a radial air bearing and the spherical ball mounting screw system is shown in Figure 4-2.[2] The ID of the bearings are precision machined to match up to a shaft which makes the selection of a shaft and radial air bearings integral with each other. The original plan was to manufacture a test shaft and have the air bearings machined to fit the shaft. Because NewWay® had a supply of pre-built shafts

---

[1]www.newwayairbearings.com

[2]The radial air bearing shown has the radius across the length of the bearing. The actual bearings utilized in the test rig have the radius across the width of the bearings.

Figure 4-2: NewWay® Radial Air Bearing and Mounting Screw

available that would suite the test rig (see section 4.3.2), the air bearings were designed to be matched up to a shaft with an ID of 3.2305 inches.

The air bearing size selected was 50mm wide by 100mm long. This was the largest size that could effectively accommodate the 3.2305 inch ID shaft. These bearings have a load capacity of 801 N (180 lbf), and a stiffness of 110 N per micrometer. The goal of these bearings is to support the shaft and oppose the force imparted on the shaft by the test bearing. This meant that the capacity of the bearing test rig (and ultimately the maximum projected area loading on the bearing) would be limited by the load capacity of the air bearings. Two main bearing configurations were considered when designing the bearing arrangement:

- The first arrangement employed two sets of four air bearings each. Within each set, three of the bearings were configured on the top section of the

shaft. The remaining bearing was located at the bottom dead center (BDC) position of the shaft. This arrangement can be seen in Figure 4-1(b)

- The second arrangement employed two sets of three air bearings each. Two bearings were located to the left and right of the top dead center (TDC) position of the shaft and the remaining bearing located once again at BDC.
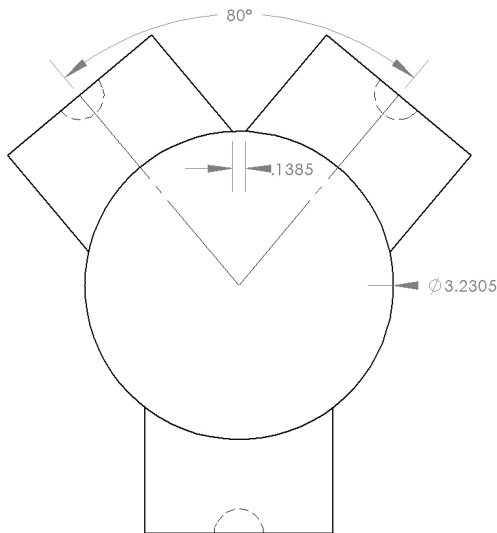
(a) Radial Air Bearing Geometry   (b) Picture of Radial Air Bearings
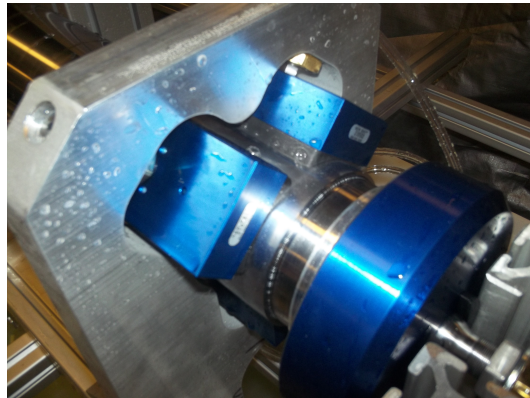
Figure 4-3: Radial Air Bearing Assembly

These configurations would provide the maximum bearing area on the top area of the shaft to oppose the force from the test shaft. A minimum angular separation between bearings of 80 degrees was used. This resulted in a circumferential distance between the contact areas of the air bearings of approximately 1/8 inch. The first configuration resulted in a maximum load capacity in the direction of the test bearing loading of 485 lbf (corresponding to a projected area load of 23.2 psi). Even though there was one less bearing per assembly, the second configuration had a maximum load capacity of 552 lbf (corresponding to a projected area load of 26.44 psi).[3] Neither one of these configurations would be capable of loadings reaching the projected area loading of 40 psi, which is

---

[3]Because of the geometry, the four bearing configuration had a lower load capacity due to the fact that two of the bearings had to be located at 80 and 280 degrees from TDC.

considered the standard value for water-lubricated ship bearings.

There were concerns over the ability to achieve an even loading on bearings
with the four set configuration. The three bearing configuration would auto-
matically achieve an even loading due to it being an exactly constrained kine-
matic connection. Because of the uncertainty in evenly loading a set of four
bearings, the greater load capacity, and the cost savings associated with using
2 less bearings, the decision to use the three bearing configuration was obvious.
The final bearing configuration used is shown in Figure 4-3.

The radial air bearings use two 1.25 inch 6061 T6511 aluminum plates as
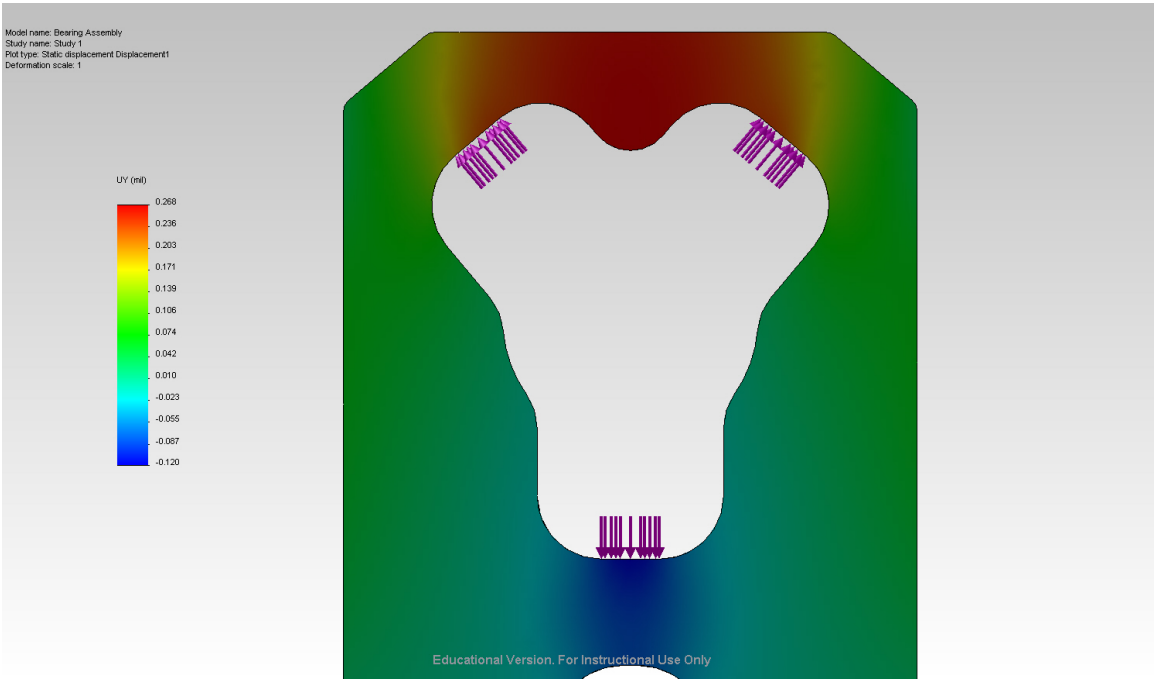
Figure 4-4: Deflection of Air Bearing Block at 552 lbf Load

mounting blocks. The pattern and shape of the mounting blocks were cut us-
ing a waterjet and mounting holes in the blocks were drilled and taped using
a 3 axis mill. The use of a monolithic aluminum plate for the mounting block
provides ample support for the radial air bearings, allows the air bearings to
preload each other, and is strong enough that stresses and deflections do not

alter the performance of the bearing. The results of an FEA analysis on the block using the maximum load capacity of 552 lbf is shown in Figure 4-4. At maximum bearing loading, FEA predicts the magnitude of deflections to be 0.00039 inches which is of the same order of the air bearing gap. FEA also predicts the maximum stress in the block to be 1,260 psi (well below the 40,000 psi yield strength). Both of these values indicate that the block is lightly loaded and does not deflect greatly.

2. **Axial Support.** Because the test rig pivots at an angle into a water tank during testing, a portion of the weight of the shaft has to be axially constrained. To accomplish this, an additional flat round air bearing is used as a thrust bearing. The required thrust bearing load is equal to:

$$RequiredLoad_{ThrustBearing} = Weight_{Shaft} * \sin\theta_{rig} \qquad (4.1)$$

where θ_{rig} is 20 degrees. Accounting for the stainless-steel shaft and aluminum end caps that are attached to the shaft, $Weight_{Shaft}$ is 50 lbf. This results in a required load of 17 lbf for the thrust bearing.

A 125mm (4.92 inch) diameter flat round air bearing was selected for use as the thrust bearing due to the fact that a spare bearing and mounting hardware were available in the laboratory. This bearing is oversized for the 3.2305 inch (82.05mm) shaft, so would not be expected to be able to develop it's rated load of 650 lbf due to a large portion of the air bearing surface not being in contact with a mating surface. NewWay® round air bearings within the range of 80 to 125mm diameter have load capacities of approximately 32 psi. Assuming that the 3.2305 inch mated portion of the 125mm diameter flat round bearing would be able to support loads at 32 psi, the calculated thrust bearing capacity is approximately 262 lbf, well above the required load capacity of 17 lbf.

The test shaft needed an end cap in order to mate with the flat round air

bearing. This thrust end cap was designed to have recesses for six 8-32 socket head bolts that would thread into the test shaft. There were concerns with the potential for air hammer occurring in the bolt hole recesses. To prevent air hammer, leakage paths were provided in the end cap from the bolt recesses to the circumference of the end caps. The end cap design is shown in Figure 4-5. It was constructed out of 6061 aluminum and the fabricated piece and shaft are shown in Figure 4-7.
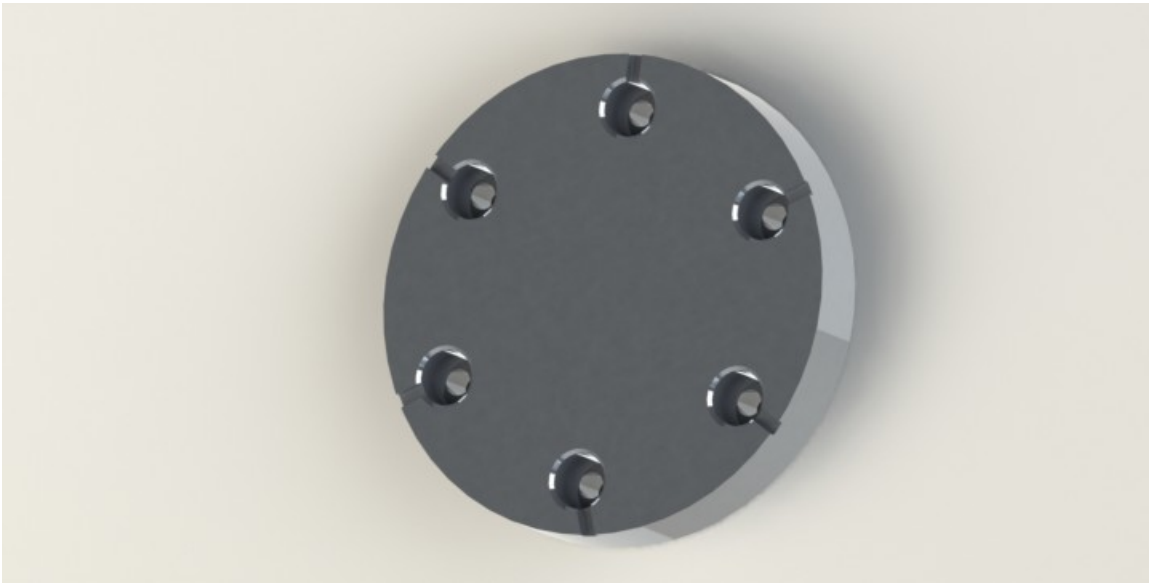
Figure 4-5: Thrust End Cap Design

3. **Air Supply.** The air bearings all utilize 0.25" OD / 0.125" ID polyurethane air tube. Barbed fittings are used for terminal connections to the air bearings themselves, and push-to-connect fittings are used elsewhere in the system. A pressure regulator is configured upstream of the air bearings to supply air at the recommended inlet pressure of 60 psi. The air use specifications for the air bearings (based on 60 psi) are shown in Table 4.1 below:

The total air requirement of 65.6 SCFH (1.09 SCFM) is supplied by a 6 HP Craftsman air compressor with an accumulator capacity of 33 gallons. The compressor is rated at 8.6 SCFM @ 40 psi and 6.4 SCFM @ 90 psi. Assuming

Table 4.1: Air Use Requirements in Air Bearings

Bearing Type	QTY	SCFH (each)	SCFH(Total)
50mmX100mm Radial	6	10	60
125mm Flat Round	1	5.6	5.6
TOTAL			65.6

an estimated capacity of 7.3 SCFM @ 60 psi, the predicted duty cycle of the air compressor is 15%. During operation of the test rig, the average duty cycle is 17%.

4.3.2 Test Shaft

The shaft is a critical component for the testing of bearings. It serves as the mating surface of the bearing and must be capable of satisfying several requirements:

- The surface finish must be hard to prevent scoring due to contact with the bearing or debris in the water.

- Strong enough to handle anticipated torsional, shear, and bending loads.

- Be corrosion resistant to ensure a long operational life.

- Have a high quality surface finish to reduce asperities that hinder hydrodynamic lubrication.

1. **Shaft Load Calculations.** The limiting loads for ship propulsion shafting is typically not torsion loads, but rather the bending loads due to the large overhung weight of a propeller. Bending loads also dominate for the test shaft used in the test rig. To bound the maximum anticipated torsion load that the shaft and other shaftline components would experience, the torque that would develop in the boundary lubrication regime was estimated. The torque that a shaft (or bearing) experiences is:

$$Torque = fR_{shaft}W_{load} \tag{4.2}$$

where f is the friction coefficient, W_{load} is the load applied normal to the shaft, and R_{shaft} is the radius of the shaft. The static friction coefficient of Ultra High Molecular Weight (UHMW) Polyethylene (PE) and steel varies between 0.15 and 0.25. As a check, an experimental test of the dry static friction value of the UHMW PE bearing built by Wong [33] yielded an f equal to 0.2. Using the value of 0.2 for friction, the maximum bearing load of 552 lbf, and the shaft diameter of 3.2305", a maximum anticipated torque of 178 in-lbf was calculated. This value was used as the design torque load for the shaft and associated systems. The torques experienced in actual bearing testing in the mixed and hydrodynamic lubrication regimes are much lower than this calculated maximum. Using this design torque value, the torsional stress in the shaft can be calculated:

$$\tau_{max} = \frac{T R_{shaft}}{I_p} \tag{4.3}$$

where I_p is the polar moment of inertia for the shaft, which for a solid cylindrical section is:

$$I_p = \frac{\pi R_{shaft}^4}{2} \tag{4.4}$$

The bending moment load in the shaft was estimated using the assumption that the test bearing load is a point load and the air bearings provide simple supports. In reality the bearing load will be distributed relatively evenly across the length of the bearing (with the exception of the extreme axial ends of the bearing), but the point load assumption results in a conservative estimate of stresses and displacements. The air bearing simple support assumption is appropriate because the spherical ball mounts do not allow the bearings to impart a moment to the shaft. For a simply supported beam with a point load located at the midpoint of the beam the maximum bending stress, shaft deflection, and

slope of deflection can all be easily calculated:

$$\sigma_{max} = \frac{M_{max} R_{shaft}}{I} \tag{4.5}$$

$$\Delta Y_{shaft} = \frac{W_{load} x}{48EI} \left(3L_{shaft}^2 - 4x^2\right) \tag{4.6}$$

$$\delta_{shaft} = \frac{W_{load}}{16EI} \left(L_{shaft}^2 - 4x^2\right) \tag{4.7}$$

where M_{max} is the maximum bending moment in the shaft, E is the modulus of elasticity, I is the moment of intertia, x is the axial distance along the shaft from one of the ends, and L_{shaft} is the length of the shaft. For a cylindrical shaft:

$$M_{max} = \frac{W_{load} L_{shaft}}{4} \tag{4.8}$$

$$I = \frac{\pi R_{shaft}}{4} \tag{4.9}$$

2. **Surface Finish.** Navy shafts have a 32 μinch R_a (or better) surface finish. The American Bureau of Shipping specifies a minimum finish of 125 μinch R_a, although in practice finishes are typically much better than this[19]. The air bearings require a surface finish of 16 μinch R_a or better which set the upper threshold for surface finish on the test shaft. A higher quality surface finish has asperities of lower height which ultimately reduces the shaft speed at which hydrodynamic lubrication occurs, making it more advantageous. There is cost-benefit tradeoff in selecting surface finish however; a better surface finish results in a more costly shaft so there is a limit to the quality of the surface finish that would be selected.

3. **Test Shaft Selection.** The initial plan called for a four inch OD test shaft to be fabricated using machine shops at MIT, however there were no lathes capable of handling a shaft of the desired diameter and length on campus. During the course of soliciting proposals from machine shops, NewWay® indicated that they had a supply of shafts that might be suitable for the test rig. These
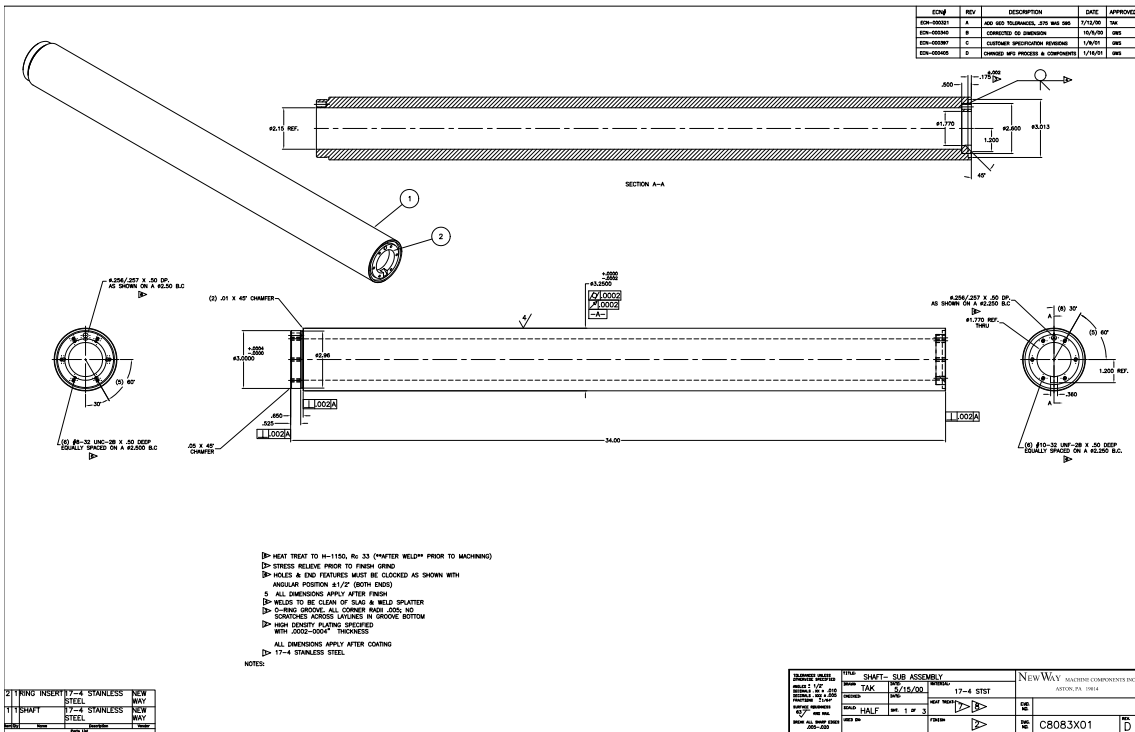
Figure 4-6: Test Shaft Design

Table 4.2: Material Characteristics of Test Shaft

Characteristic	Value	Unit
Shaft Material	304 Stainless Steel	
Coating Material	Nickel Plate	
Yield Stress	31,200	psi
Elastic Modulus, E	28,000	ksi
OD	3.2305	inches
ID	2	inches
Length	34	inches
Coating Thickness	0.0003	inches
Surface Finish	4	Ra

shafts were originally designed and built for a NewWay® client in the silicon industry but due to design changes from the client they were not used. The design drawings of these shafts is shown in Figure 4-6, with the characteristics of the shaft presented in Table 4.2.

Calculations were done to ensure the shaft would be acceptable for use in the test rig. Stresses and deflections were found to be satisfactory. Even though the shaft is hollow, the deflections and stresses are driven greatly by moment of inertia. The stresses and deflections in the shaft were only 17.2% greater than those for a similar dimeter solid shaft while weighing only 62% of the solid shaft weight. Table 4.3 shows the values of the test shaft performance as a result of a 552 lbf test bearing load. It is clear that little benefit is gained by using a solid shaft. The deflections are very minimal with a change in gap height at max load of only 0.00013" (corresponding to 6.5% of a 0.002" radial clearance in a bearing). Because of these small values, the effect of the shaft deflection on bearing performance is minimal.

Table 4.3: Test Shaft Characteristics with a 552 lbf Bearing Load

Characteristic	Test Shaft	Solid Shaft	Unit
Yield Stress	31,200	31,200	psi
Elastic Modulus, E	28,000	28,000	ksi
Max Torsional Stress (τ_{max})	31	27	psi
Max Bending Stress (σ_{max})	653	557	psi
Deflection at Midpoint of Test Bearing	1.61	1.38	1/1000 inch
Deflection at End of Test Bearing	1.48	1.26	1/1000 inch
Gap Height Difference in Bearing	0.13	0.11	1/1000 inch
Shaft Weight	48.6	78.9	lb

The NewWay® shaft was found to be suitable for use in the test rig, but an anodized solid aluminum shaft was also considered. A new aluminum shaft would allow the use of larger scale 4 inch diameter test bearings and would weigh approximately the same as the hollow stainless shaft. Because of aluminum's lower modulus of elasticity, the deflection in a 4 inch shaft would be

almost twice the deflection in the 3.2305 inch stainless shaft. This fact led to the selection of the stainless steel shaft for use in the test rig.

4. **End Caps.** The NewWay® shaft has bolt holes drilled into the ends of the shafts as part of its original design for use in industry. To utilize the shaft in the test rig, end caps were fabricated. One end cap is the mating surface for the flat round thrust air bearing (described in section 4.3.1). The other end cap provides for the transmission of torque from the drive motor. Figure 4-7 shows the end caps and one end of the shaft prior to assembly. Stainless bolts are used to connect the aluminum end caps to the stainless shaft.
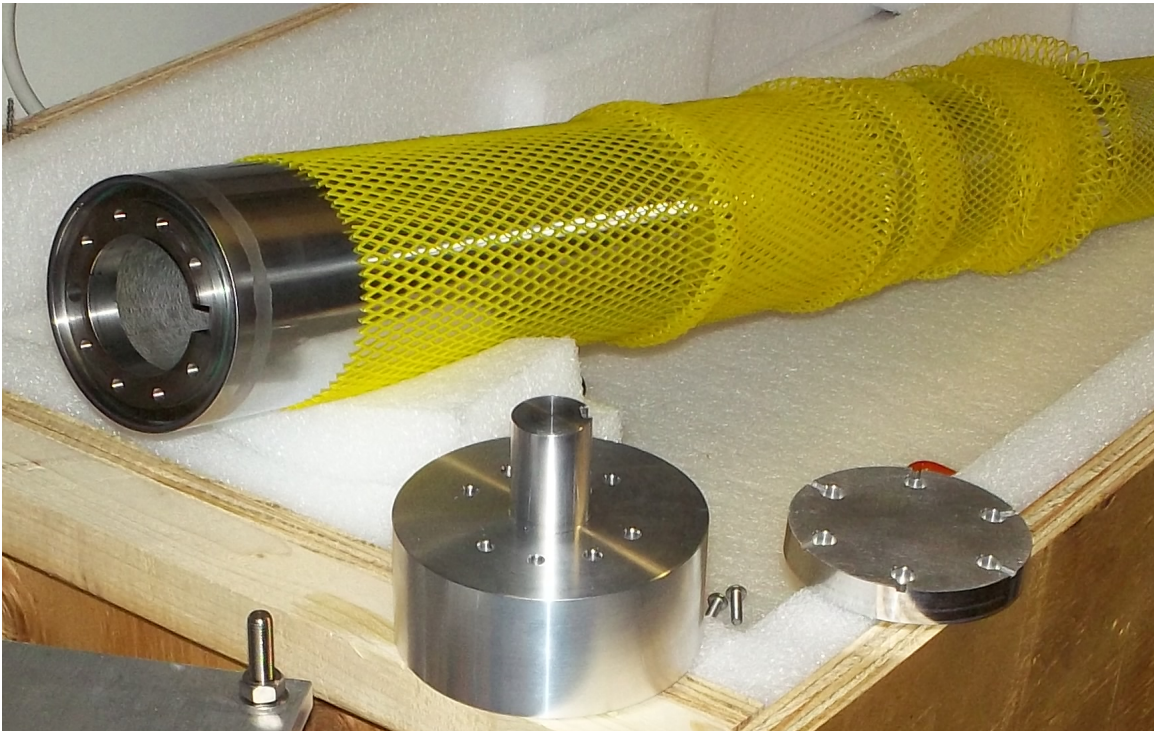
Figure 4-7: End Caps and Shaft

The torque end cap had to be precisely machined in order to minimize any eccentricity between the shaft and end cap, which would ultimately result in vibrations being imparted on the torque sensor and motor. The 3.2305" OD of the shaft is a precision surface so that was selected as a locating feature, with the end cap sliding over. A sliding fit is used between the OD of the shaft and

the ID of the torque end cap in accordance with ANSI B4.2 *Preferred Metric Limits and Fits*[2]. The machined ID of the torque end cap wis 3.2315 inches. The torque end cap has a 1 inch neck down with a 1/4 inch keyway for transmitting torque to and from the shaft. The end cap uses eight 10-32 button head socket bolts for attaching to the shaft, which are sufficient for mating the part to the shaft at the design torque.

4.3.3 Torque Sensor

Accurate measurement of the friction forces in the test bearings is required to identify the transition between mixed and hydrodynamic lubrication regimes. With journal bearings, this friction force results in torque. A shaft to shaft rotary torque sensor was therefore required to measure the torque that developed in the bearing. Torque sensors use a flexure device with a strain gages that are used to generate a DC voltage output signal proportional to applied torque. Torque sensors often have encoders to allow for measuring rotational speed, but because the rpm in the test rig is directly measured from the drive motor the extra cost of an encoder was not warranted.

1. **Mounting Configuration.** Rotary torque sensors have two basic configurations: fixed mounted and floating. Figure 4-8 shows the two variants.[4]

(a) Fixed Mount Torque Sensor   (b) Floating Type Torque Sensor
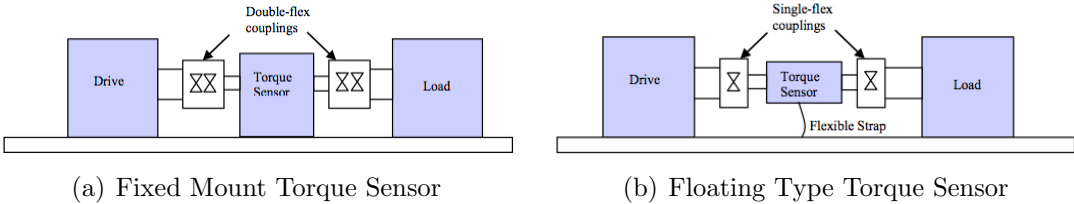
Figure 4-8: Rotary Torque Sensor Types

In a fixed mount, the torque sensor is attached to a support piece in-line with the system drive and load with the alignment of the support piece being critical. Fixed mount torque sensors are better suited for high rpm applications

---

[4]Figures from Interface, Inc.

where the misalignment between driver and load does not vary. They also have advantages over floating types in applications where either the drives or loads are frequently changed, which would result in a floating type sensor loosing a support.

In a floating mount, the torque sensor is supported by the drive and load connections. A cable, or other means of preventing the torque sensor from rotating is required, as are flexible couplings that allow for minor misalignment between the drive motor, the torque sensor, and the load. Unlike fixed mount torque sensors, thrust loads are not imparted on the bearings of the floating type torque sensors, promoting a longer operating life. The decision to use a floating type torque sensor was made for several reasons:

- The test rig operates at relatively low RPMs with to the area of interest being the transition between mixed and hydrodynamic lubrication regimes.

- The test bearing causes deflection in the test shaft which leads to varying angular, axial, and parallel misalignment between the motor and the shaft. This misalignment is more easily accepted in a floating type sensor.

- The test shaft is a permanent installation. The drive motor is capable of being changed, but this is a very infrequent event.

- Fixed mount torque sensors are more expensive for a given capacity.

2. **Torque Sensor Characteristics.** A FUTEK TRS300 FSH01988 torque sensor was selected for use in the test rig. The accuracy and resolution of torque sensors are usually given as a percent of rated output. Because of this, a torque sensor with low torque rating and range provides the best accuracy for very small torque values such as those seen in the hydrodynamic regime. The specifications of the TRS torque sensor is shown in Table 4.4 and a picture of the torque sensor is shown in Figure 4-13. The torque sensor rating of 20 N-m (177 in-lbf) closely matches the maximum design torque of 178 in-lbf. The maximum operating speed of 3000 rpm is much greater than the test rig design

Table 4.4: FUTEK TRS 300 Torque Sensor Specifications

Characteristic	Value	Unit
Rated Output (R.O.)	177	in-lbf
Overload Torque Capacity	150%	R.O.
Voltage Output	2	mV/V
Nonlinearity	0.2%	R.O.
Hysteresis	0.1%	R.O.
Combined Error	0.3%	R.O.
Max Rotational Speed	3000	RPM
Max Axial Force	124.0	lbf
Max Radial Force	6.8	lbf
Drive Shaft Diameter	19	mm

speed of 500 rpm. The combined error of 0.3% of rated output corresponds to a torque of 0.531 in-lbf. This provides a resolution in the friction coefficient that varies between 0.0006 at maximum bearing load of 552 lbf and 0.016 at 20 lbf (corresponding to a very small projected area load of 1 psi). This resolution is sufficient to identify the orders of magnitude increases in friction coefficient between hydrodynamic and mixed lubrication regimes.

Since the sensor is floating between the drive motor and the test shaft, a method of preventing rotation is required. The connection cable that powers the sensor and returns output voltage provides a nominal counter-torque. During actual operation, this proved to be sufficient to keep the torque sensor from rotating due to the very low friction in the sensor's bearings. The designed method employed to prevent rotation uses 60 lbf monofilament fishing line tethers that are attached to bolts threaded into the torque sensor. One inch long M4 stainless bolts are attached to the sensor and monofilament is anchored to the the test rig frame. This provides a nominal torque rating of 90 in-lbf for each tether for a combined 180 in-lbf, commensurate with the design torque of 178 in-lbf.

The torque sensor requires an excitation voltage of 5 to 11 volts DC. The nominal output voltage of 2mV/V requires an amplifier to provide a high-level sig-

nal output to the test rig's National Instruments (NI) Data Acquisition (DAQ) board. A FUTEK CSG110 amplifier module is used to provide the signal amplification from the torque sensor as well as the 10 volt DC excitation voltage. The amplifier is located in-line between the sensor and the DAQ board and is designed to work with 2 mV/V FUTEK sensors.

3. **Calibration.** The torque sensor comes from the factory with a certificate of conformance to specifications, but requires field calibration. For calibration, the motor end of the torque sensor was mechanically locked in place and a removable bar clamp was attached to the test shaft. A series of torques were applied to the shaft by placing various weights at positions on the bar clamp to provide torque in both the clockwise and counter-clockwise directions. An 11 point calibration curve was generated with torques up to 10 ft-lbf in both rotation directions. This fully encompasses the torque range in the mixed and hydrodynamic lubrication transition regimes. The sensor's torque per volt relationship was determined and proved to be very linear with an R^2 value of 0.9999.

   Prior to, and after, individual bearing tests the zero torque value was recorded. This zero torque value, along with the torque per volt value allows torque to be calculated from the output voltage recorded by the DAQ board during test runs.

4.3.4 Drive Motor

The test rig drive motor provides a means of rotating the test shaft at consistent, measurable speeds under load. The motor has to be capable of speeds high enough to reach hydrodynamic lubrication in the bearings. Estimation of the speed at which hydrodynamic lubrication occurs (also known as shaft lift-off) is difficult to predict since it depends on many variables, with the dominant one being the surface speed between mating surfaces. A thumbrule often used in water-lubricated marine bearings is a surface speed greater than 3.5 ft/sec will result in hydrodynamic lubrication. For

the 3.2305 inch test shaft, this corresponds to a shaft rotational speed of 249 RPM. Another empirical method for predicting the lift-off speed is presented by Vogelpohl by the following equation:[31]

$$N_T = \frac{W_{load}}{C_T \mu V_{bearing}} \tag{4.10}$$

where N_T is the lift-off speed in RPM, W_{load} is the bearing loading pounds, C_T is a factor related to lubricant flow as well as geometric quantities such as clearance and minimum film thickness, μ is the absolute viscosity in microreyn, and $V_{bearing}$ is the bearing volume ($=\frac{\pi L D^2}{4}$). A value for $C_T = 1/4$ is most often used. Vogelpohl's equation predicts a lift-off speed of 286 RPM. With no better method of estimating the lift-off speed in the bearings, the relatively close agreement between the thumbrule and Vogelpohl provided a resonable expectation of the actual lift off speed occuring in the vacinity of 275 RPM.

For a rotational motor, power is the product of torque and rotational speed. Thus, a motor capable of developing the max design torque at relatively high anticipated testing speeds (100-300 RPM) requires much more power than a motor designed to develop the max design torque at zero RPM. Because torque in the transition region between mixed and hydrodynamic lubrication is much lower than that in the boundary lubrication regime, a smaller motor with a lower torque and power rating could be utilized.

A Brushless DC (BLDC) gearmotor is used as the drive motor. BLDC motors have several features that make them advantageous for the test rig:

- They are reversible, allowing for clockwise and counter-clockwise testing of bearings.

- The speed can be adjusted and has very good regulation that is generally independent of load.

- They do not use brushes and commutators, which can wear out with use and require periodic maintenance. In other types of DC motors brushes and commutators can introduce noise. Since they do not have them, BLDC motors provide quite operation which is critical for detecting small torque values in testing.

- They are not sensitive to harmonics like an AC motor is.

The primary disadvantage with using BLDC motors is that an electronic motor controller is required to control commutation in the motor. Commutation in a BLDC motor occurs by sequentially switching the current in the stator phase windings, which generates a rotating magnetic field causing the motor to rotate as the rotor magnets follow the magnetic field. With advances in power electronics, this is no longer a significant disadvantage.

1. **Motor Characteristic.** A BODINE 3369 BLDC gearmotor is used as the primary drive in the test rig. The rig also allows for a separate BODINE 3383 BLDC gearmotor to be used for very slow speed testing when neccesary. This process is accomplished by swapping motors. The motors have a common bolt pattern allowing a single motor bracket to be used. The motor controller is also capable of controlling either motor. The specifications for the motors are provided in Table 4.5.

Table 4.5: Characteristics of BLDC Gearmotors

Characteristic	Model 3369	Model 3383
RPM (max)	500	83
Rated Voltage	130V	130V
Motor HP	3/8	1/4
Rated Torque (in-lbf)	42	135
Peak Torque (in-lbf)	86	318
Gear Ratio	5:1	30:1
Output Shaft	3/4"	3/4"

At lower speeds the, BLDC gearmotors experience motor cogging. In the model

3369 motor, the motor cogging becomes appreciable below speeds of approximately 25 RPM and in the single digit RPMs for the model 3383 motor. Fortunately, the majority of testing occurs at speeds greater than 25 RPM, which allows the 3369 motor to be used for most tests.

2. **Motor Controller.** A BODINE 3911 filtered SCR speed controller is used to control the output of the BLDC gearmotor. A BODINE 3984 isolation and interface board is used for input voltage signals from the NI DAQ board that provide input to the controller for motor speed, direction, and power. The 3911 speed controller has the following features and characteristics:

- Operates from 120 Volt AC input.

- Provides up to 130 Volt DC output for the motor.

- Has a closed loop speed regulation circuit that maintains a 1% maximum change in motor speed from 0-100% of rated load.

- Dynamic braking for quickly stoping the motor.

- 12 pulse per revolution tachometer output signal for indication of motor speed.

- Speed is manually controllable by potentiometer or electronically by an external input voltage.

- User-adjustable potentiometers can set torque limit, minimum speed limit, maximum speed limit, acceleration time, and deceleration time.

- DIP switches to limit current, allowing it to control different sized BODINE BLDC motors.

Both the 3911 motor controller and 3984 isolation and interface board are mounted in a separate electric enclosure. Wire penetrations into the enclosure for input voltages, logic circuits, power, and output are all protected by cord grips that provide strain relief for the cables and protect against water and dust intrusion. The enclosure is shown in Figure 4-21.

3. **Wiring.** The one-line wiring schematic for the motor controller is shown in Figure 4-9. Power is supplied by a standard 110 VAC receptacle which feeds both the speed controller and isolation interface module from a terminal block. A 15 amp circuit breaker on the line is used for overcurrent protection of the entire system and the interface module is protected individually by a separate fuse. The speed controller and motor chassis are grounded through the 110 VAC receptacle.
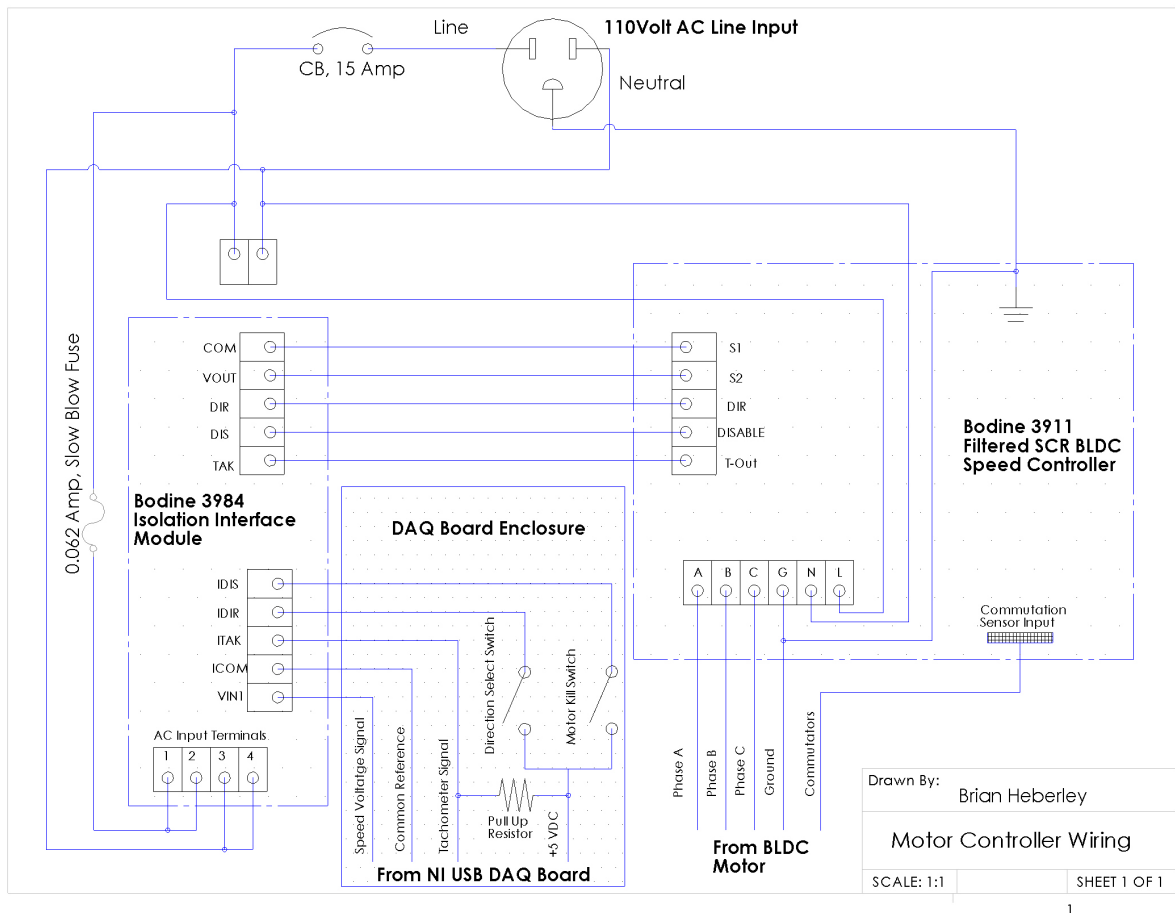
Figure 4-9: Motor Controller Wiring Schematic

Internal wiring connects the interface module outputs to the corresponding speed controller inputs, and a chassis cable is used to connect the speed controller outputs to the motor. The chassis cable connects directly to the BLDC

motors through a waterproof circular connector. On the speed controller end there are three phase wires, a ground wire, and a 6 strand multi-cable connector for the commutation leads.

The 3984 interface and isolation board provides a digital tachometer pulse output that is approximately 0.8 msec wide. Twelve pulses correspond to one motor revolution. A 4.7 KΩ pull-up resistor is used between the interface module and the NI USB DAQ board to allow the output to be measured. The tachometer signal is digitally processed in LABVIEW to provide motor RPM when running.

The motor speed, motor direction, and a motor kill switch are all controlled through external inputs into the motor controller. Motor speed is controlled by a LABVIEW program which provides a variable analog DC input voltage (from zero to 10 volts) from the NI USB DAQ board. The motor controller has a linear RPM per volt relationship which aids in selecting and maintaining desired motor speed. This relationship was determined by using the motor controller tachometer signal and checked using a hand-held optical tachometer. Both the motor direction and the kill switch, which disables the motor, are operated through single-pole single-throw (SPST) switches that are hard mounted on the side of the DAQ board enclosure.

The 3911 speed controller has DIP switches that allow the motor controller to be used with BLDC motors that uses 60 or 120 degree commutation. The DIP swiches change the sensor phasing and the AC input current limit to the motor. In addition to adjusting the DIP switches when changing motors, a line fuse is swapped to an appropriately sized one.

Potentiometers are located on the 3911 speed controller for internal adjustments that control the acceleration and deceleration response time of the motor, the minimum and maximum motor speed, and the torque limit of the motor.

During routine bearing testing, the torque limit is adjusted to provide a lower torque than the maximum. Even though the individual test rig components are designed to withstand the maximum motor torque, this provides additional margin against damage.

The internal wiring of the motor controller is shown in Figure 4-10.
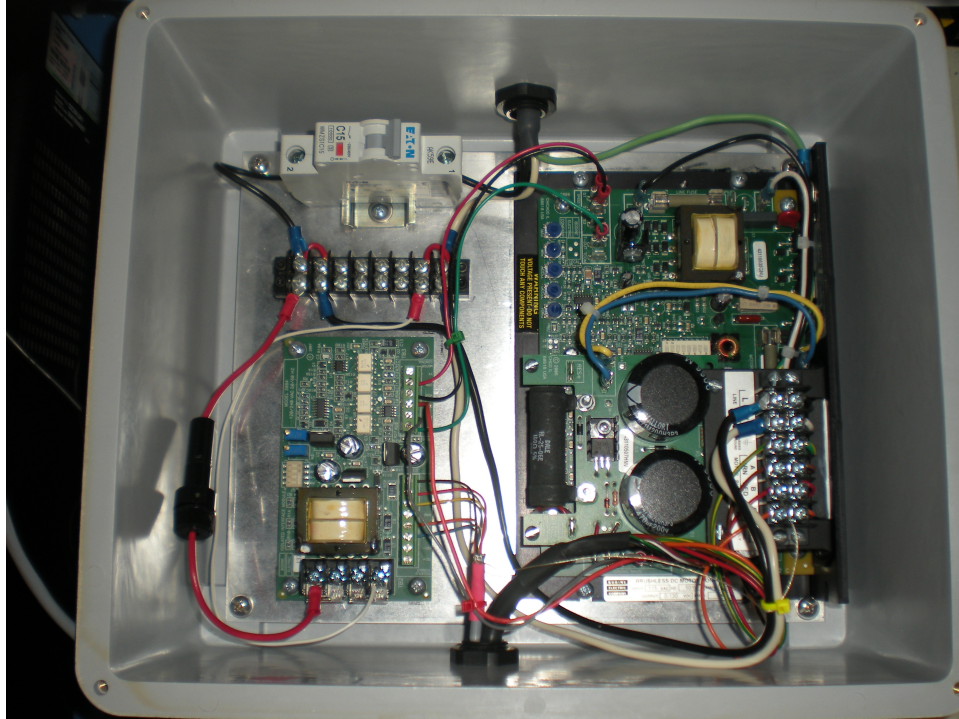
Figure 4-10: Picture of Motor Controller Wiring

4.3.5 Flexible Couplings

A pair of couplings are needed to transmit the torque from the drive motor to the test shaft. Flexible couplings are typically employed to account for misalignment between the coupled shafts that can result from manufacturing tolerances, improper mounting of components, or dynamic loads. The misalignment between shafts is one of three types, or a combination of them. The types are shown in Figure 4-11[5] and described below:

---

[5]Figure from Armstrong Pumps

- Parallel misalignment. Also known as offset or radial misalignment, this is a result of lateral distance between the shaft centers of rotation.

- Angular misalignment. Also known as gap misalignment, this is due to the relative difference in the angles of the shaft centerlines.

- Axial misalignment. This is due to movement of one shaft along it's axis relative to the other shaft. This is typically caused by thermal expansion.
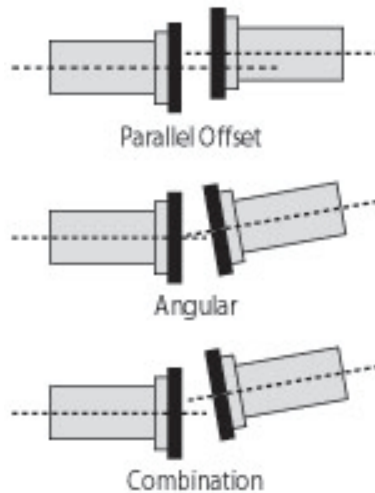
Figure 4-11: Types of Shaft Misalignment

For floating type torque sensor applications, a single-flex coupling that only accounts for angular misalignment is typically used. Double-flex couplings that can accommodate both angular and parallel misalignment are normally used for fixed mount torque sensors.

1. **Misalignment Calculation** The misalignment in the shafts of the test rig is a result of two main causes. The first, which is static, is caused primarily due to the mounting of the drive motor and the adjustment screws on the air bearings that control the location and attitude of the test shaft. The second cause of misalignment is a dynamic relative movement between the test shaft and the motor mount. This dynamic movement is a caused by flexing in the test shaft and deflection in the test rig rails when a load is applied to the test bearing. A greater load in the test bearing results in a larger dynamic misalignment.

To bound the maximum dynamic misalignment of the test rig, the predicted deflections at the maximum bearing load of 552 lbf were calculated using a simply supported beam assumption. The bearing load places a force in one direction while an opposing force is imparted on T-Slot rails that the bearing assemblies and motor are mounted to. Equation 4.7 for slope of deflection for a simply supported beam is applicable for both the test shaft, and the T-Slot rails (using appropriate modulus of elasticity and moment of inertia values). Bending stresses are negligible at locations outside of the air bearing assemblies. Because of this, the difference in slopes of deflection between the test shaft and T-Slot rails is the maximum angular misalignment that the flexible couplings need to accommodate. The parallel misalignment is found from the change in offset in the shafts caused by the difference in slopes at the coupling locations. The maximum dynamic parallel misalignment in the system occurs at the point farthest from the forward air bearing, corresponding to the flexible coupling between the drive motor and the torque sensor. Axial misalignment is relatively small because thermal fluctuations during testing are minimal. A visual representation of the test rig deflections is shown in Figure 4-12[6] and the calculated dynamic misalignment in the test rig is provided in Table 4.6.

Table 4.6: Dynamic Misalignment in Test Rig

Characteristic	Value	Unit
Angle at Forward Air Bearing Assembly		
Test Shaft	0.009	Deg
T-Slot Rails	-0.030	Deg
Maximum Angular Misalignment	**0.039**	**Deg**
Vertical Deflection at Forward Coupling		
Test Shaft	-0.0019	Inch
T-Slot Rails	0.0056	Inch
Maximum Parallel Misalignment	**0.0076**	**Inch**

---

[6]Deflections in drawing are not to scale.
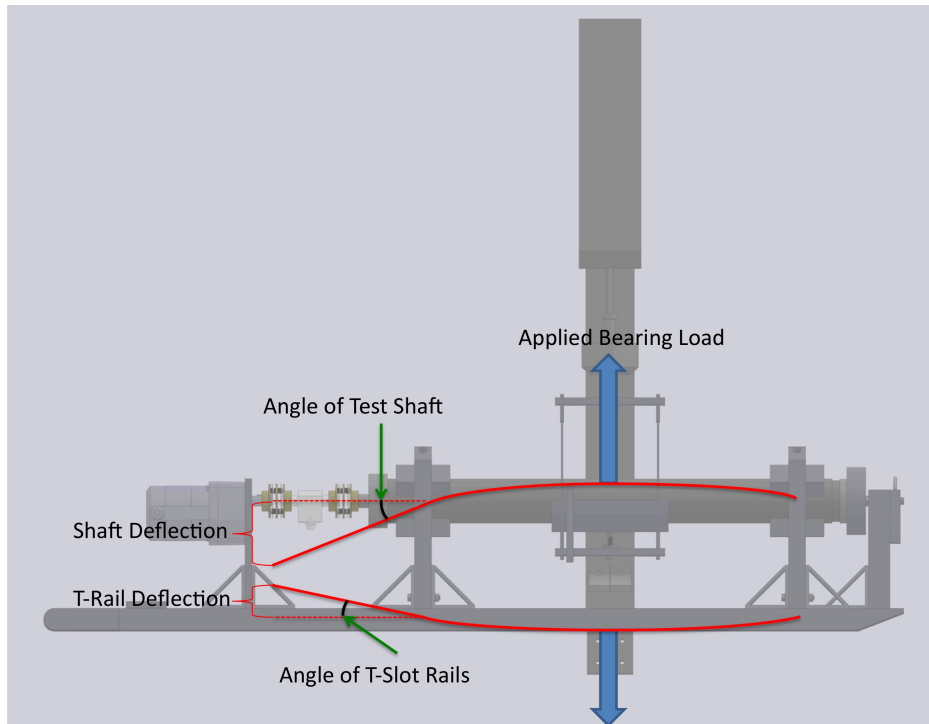
Figure 4-12: Visual Representation of Test Rig Deflections

2. **Flexible Coupling Selection.** Several functional requirements from the flexible couplings are:

- One coupling needs to mate up to the 3/4" drive motor shaft and the 19mm torque sensor shaft. The other has to mate up to the 1" torque end cap of the test shaft and the 19mm torque sensor shaft.

- Both couplings must be capable of handling the maximum design torque of 178 in-lbf.

- Accommodate the maximum misalignment that would be experienced.

- Be torsionally rigid with no or minimal backlash to prevent bearing frictional forces from inducing torsional oscillations.

- Have a long operational life in an environment where they would be exposed to water.

- Impart no or minimal friction into the system even at design misalignments.

Because of variation in parallel and angular misalignment due to dynamic loading of the bearing, double-flex couplings are used even though the torque sensor is of the floating type. A pair of RENBRANT Fleximite® flexible disc couplings are used in the test rig. Flexible disc couplings utilize multiple thin discs that are bolted to the outer rim of shaft hubs. These discs flex under load to account for misalignment. These couplings are capable of accommodating the anticipated misalignment in the test rig, the maximum design torque, and possess the other desired characteristics. Figure 4-13 shows a picture of the flexible couplings connecting the motor, torque sensor, and test shaft. Table 4.7 shows the characteristics of the couplings.
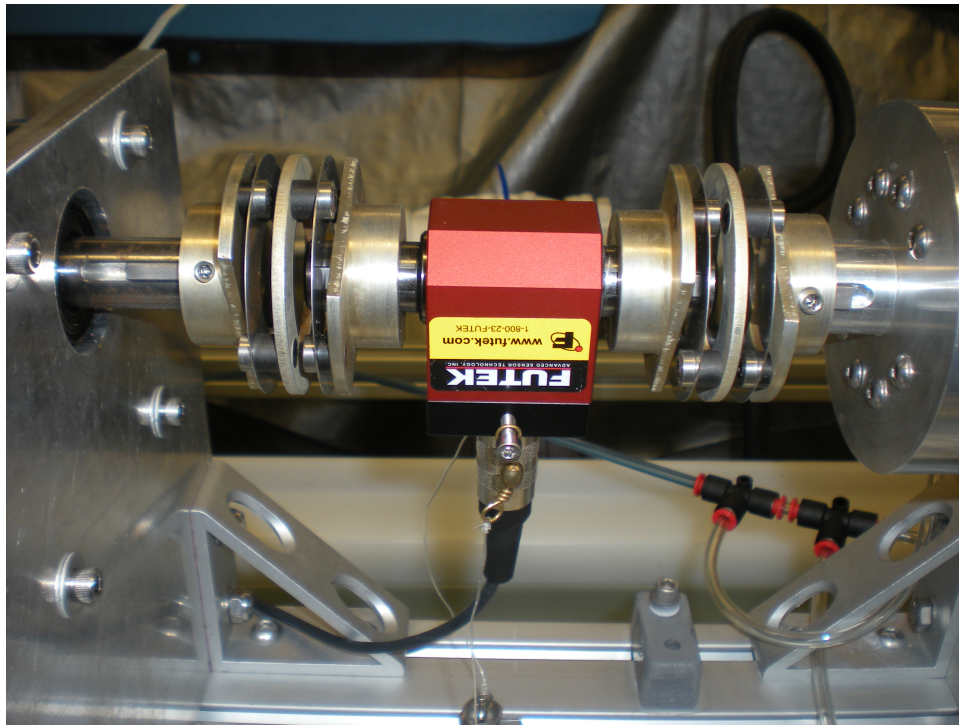
Figure 4-13: Flexible Couplings

3. **Alignment.** The drive train of the test rig was assembled on a precision granite surface plate. The air bearings and test shaft were first installed on the air bearing assembly blocks and installed on the T-Slot rails. Shop air was used for acceptance testing and pre-tensioning of the air bearings. The drive motor was then installed onto the motor bracket and connected to the T-Slot rails.

Table 4.7: Characteristics of RENBRANT Fleximite® Couplings

Characteristic	Value	Unit
Model Size	5	
Allowable Angular Misalignment	2	Deg
Allowable Parallel Misalignment	0.010	Inch
Allowable Total Indicated Runout	0.02	Inch
Maximum Torque	240	in-lbf

A visual check between the test shaft and drive motor was done to provide a rough alignment.

With the motor and test shafts installed on the rig, runouts on all shafts were measured using a dial indicator. The drive motor shaft and test shaft had runouts less than 0.0005". The torque end cap had a measured runout of 0.002", which indicated that the test shaft and end cap were not concentric. An aluminum 19mm diameter shaft was fabricated for use between the flexible couplings (in lieu of the torque sensor) during the alignment procedure. Vertical and horizontal stack height measurements were conducted along the axial length of the drive train. This allowed for parallel misalignment to be directly measured, and angular misalignment between the shafts to be calculated.

The air bearing ball mounting screws (seen in Figure 4-2) were iteratively adjusted to alter the height and attitude of the test shaft until it was concentric with the drive motor shaft, indicating a satisfactory static alignment. The 19mm shaft was then replaced by the torque sensor and the entire test rig was run. The test rig was checked at various speeds to ensure that the eccentricity from the 0.002" runout in the torque end cap did not excite natural frequencies in the torque sensor and flexible couplings. Other than a slight motion in the torque sensor that can be attributed to the runout, there are no problems with the overall alignment.

There are keys in connections between shafts and hubs in the flexible couplings. To account for axial misalignment in the drive train of the test rig, the set screws that solidly connect the hubs to shafts were left slack to allow for the shafts to move within the hubs.

4.3.6   Force Tester

Navy and commercial propulsion shaft bearings must support the weight of the shaft and the overhung weight of the propeller. This results in a radial load that is typically a steady load in the vertical direction[7]. Water-lubricated bearings are usually designed to support a projected area load of 40 psi. As mentioned in section 4.3.1, the air bearings were only able to support a load of 552 lbf (corresponding to 26.44 psi projected area load).

Instead of having a static bearing that has to support the weight of a shaft, the test rig was designed to have a static shaft with a varying load applied to the bearing. An ADMET eXpert 5604 single column universal testing machine is used to apply a varying force to the test bearing, up to the 552 lbf maximum rating of the test rig air bearings. The details for the testing machine are provided in Table 4.8. The testing machine was selected because it was on hand, having been used in an earlier test rig[33]. It was custom built for a lower travel speed to allow for fine control of the crosshead displacement. The testing machine utilizes its own control system known as MTESTQuattro®. This system consists of an external interface box (shown in Figure 4-21) and a PC-based software application. The interface box provides power, sends/receives data signals to the testing machine, and receives data from the load cell. The load cell used is an INTERFACE 1210-ACK-1K-B rated for 1000 lbf with an accuracy of 0.04% of rated output. The interface box has a servo loop with a Proportional Integral Derivative (PID) filter for control of the applied

---

[7]Appreciable dynamic loads in the vertical direction have historically been seen in the bearings of large commercial ships with high block coefficients and 5 bladed non-skewed propellers due to propeller/wake-field interactions

Table 4.8: ADMET eXpert 5604 Force Tester Characteristics

Characteristic	Value	Unit
Model Size	ADMET eXpert 5604	
Load Capacity	1000	lbf
Maximum Travel Speed	2	Inch/min
Minimum Travel Speed	.005	Inch/min
Total Crosshead Travel	12	Inch
Load Cell	Interface 1210-ACK-1K-B	

load.

The MTESTQuattro® software is operated from the computer workstation to impart the desired loads on the bearing. The software allows for custom test programs to be generated. One such program was created for bearing testing applications to provide a given consistent load on the bearing even if the bearing displacement changes with the size of the fluid gap. The PID gains, the data sampling rate, and the force loading rate (lbf/min) were adjusted by trial and error to obtain a satisfactory response in the force tester.

The software has the capability to log data forces and crosshead displacement over time, but this is not done during testing for several reasons. Because in actual application the projected load on the bearing is constant, short term variations in load during individual test runs were not directly investigated[8]. Crosshead displacement is not recorded due to bearing position being recorded by eddy current probes (discussed in section 4.5) and the fact that there are resilient spring components between the crosshead and the bearing.

4.3.7 Bearing Support System

A means is needed to transmit the force generated in the testing machine to the test bearing. The load cell and force tester are both capable of bi-directional loads, which

---

[8]The response of bearings to different load conditions were investigated.

allows for a load to be applied by pushing on a bearing located on the top of the test shaft or by pulling on a shaft located on the bottom of the test shaft. The test rig utilizes the method of pulling on the bearings. This method is used primarily because placing the bearing below the test shaft allows for the bearing to be submerged at a lower water level than if the bearing was on top. This means that the test shaft is inclined at a lower angle than if the bearing was on top. This also allows for a shallower tank.

Several methods were considered to pull on the test bearing that would allow for the vertical load to be applied; two of these included utilizing slings or a ball mounted screw located at the bottom dead center (BDC) of the bearing (shown in Figure 4-14). Not only does a suitable system have to transmit the vertical load, but also the torque from the bearing. Additional issues were the ability of the pulling mechanism to allow fluid supply and pressure lines to be connected to the back of the bearing housings, the magnitude of the localized deflections in the bearing housing that might occur due to the pulling mechanism itself, and providing a resilient spring between the load cell and the test bearing. After considering these factors and calculating the anticipated bearing housing deflections with FEA, neither of the solutions in Figure 4-14 was selected.

(a) Sling System   (b) Ball Mount System
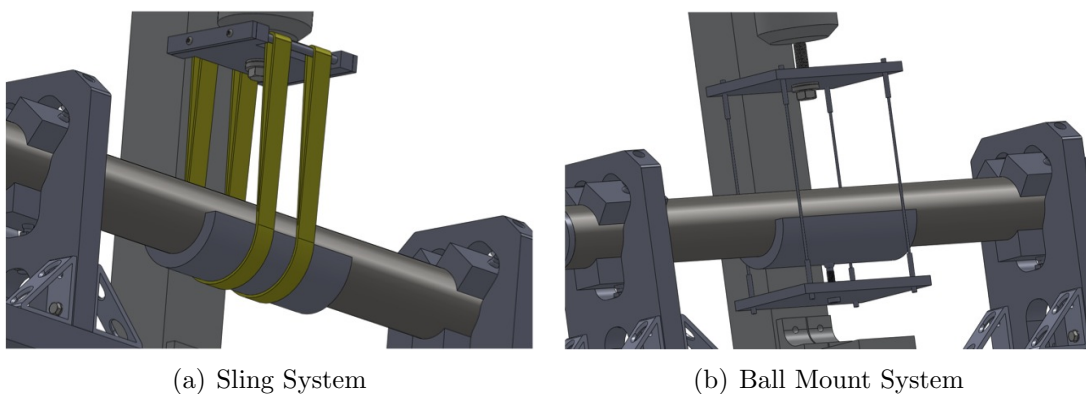
Figure 4-14: Potential Bearing Pulling Mechanism Solutions

1. **Hoist Mechanism Description.** The hoist mechanism that is used to pull the bearing on the shaft utilizes two aluminum plates connected by four 3/16" coated stainless steel lanyards. Each of these lanyards has a working load limit of 740 lbf, providing ample safety margin to the 552 lbf test bearing load limit. The hoist mechanism configuration is shown in Figure 4-15. The lanyards have 1/4"-20 threaded connections on either end allowing the height between plates at the lanyard locations to be adjusted and secured with nuts. The top plate is connected to the INTERFACE load cell through a 5/8"-18 UNF bolt. A spherical washer is used at the location of the bolt head to allow for tilting of the top plate relative to the load cell. This provides the ability to compensate and self align due to bearing movement during operation.

Because four lanyards are required to transmit force from the top plate to the bottom plate, there was a concern over the ability to evenly load the lanyards. To evenly load the lanyards a 'wobble plate' separated from the top plate by a 1/4" ball bearing seated in 1/4" spherical recesses located in both plates is used. In this setup, the lanyards are attached to the 'wobble plate' and allow for the plate to tilt as needed to evenly distribute loads in the lanyards.

Some Navy ships utilize a self-aligning mount to accommodate for misalignment between the bearings and shaft not only during installation, but also during transient maneuvers that can cause the hull and bearing to flex and move relative to the shaft. The self-aligning mount works by employing a soft rubber (shore A durometer of approximately 39-45) along the outside of the bearing housing, which allows the bearing surface to compensate for rake/slope of the shaft. A similar concept is used in the test rig design wherein the bottom plate of the test shaft hoist mechanism supports a rubber casting. The rubber is cast in a mold box made from melamine board with an aluminum bearing housing on it to generate the bearing seating surface of the mount. The rubber used is a FREEMAN 1035 two part polyurethane with a 35A shore hardness.
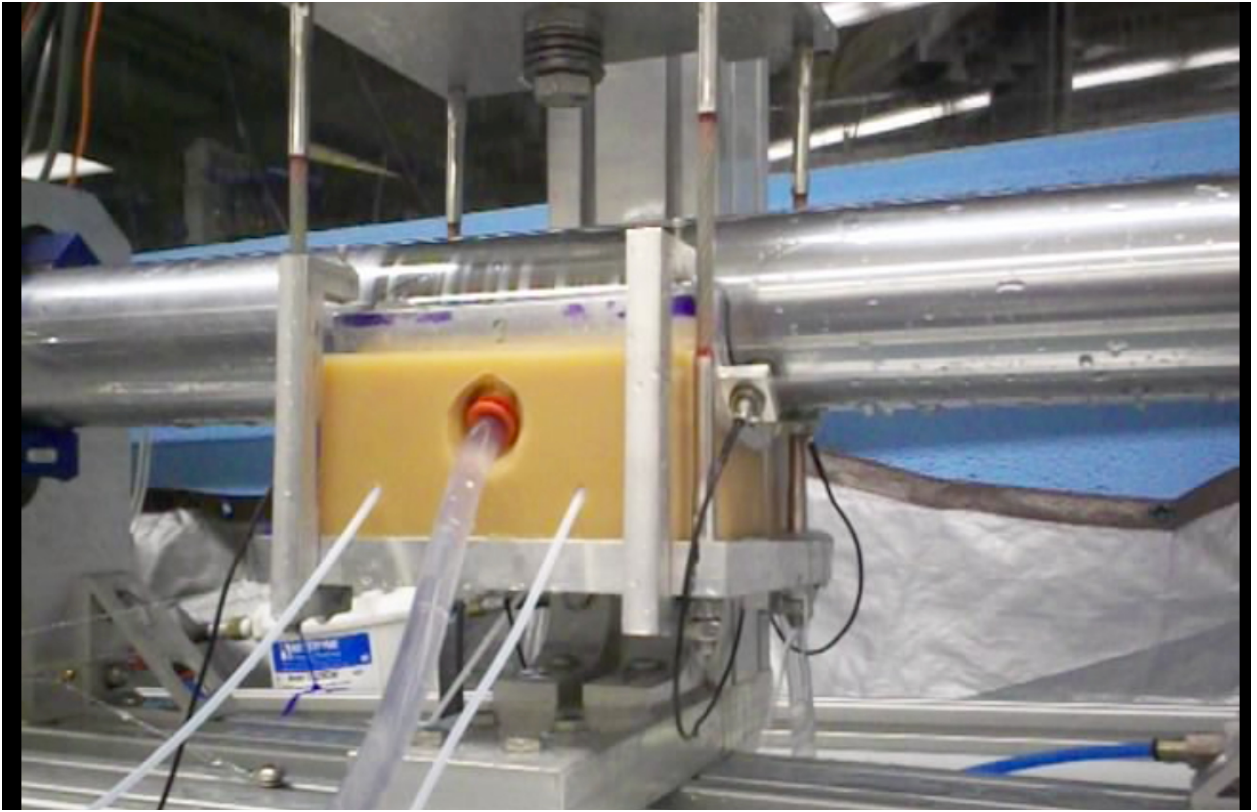
Figure 4-15: Hoisting Mechanism

The rubber is degassed during the mixing process to remove entrained air, then cast into a mold that is coated with release agent to facilitate separation of the rubber from the mold once set.

To make the penetrations needed for fluid supply lines and pressure ports, two methods were employed. The first method involved using acetal blanks that were bolted into the back of the bearing housing to form a void in the rubber during casting (see Figure 4-16(a)). The second method, which proved to be more flexible when small changes to bearing configurations was needed, involved using thin aluminum tubes of slightly larger size than the fluid and pressure lines. These tubes were bored out and sharpened on a lathe to form a cutting edge. The tube was then spun at a low speed on the lathe while the rubber mold was pressed into tube at the desired locations to cut plugs out of the mold (see Figure 4-16(b)).

(a) Blank Method   (b) Cutting Method
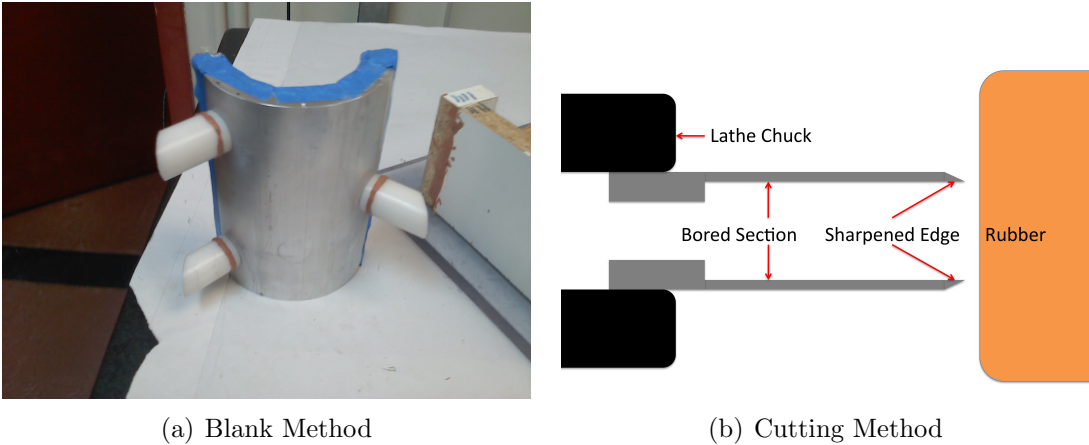
Figure 4-16: Methods for Creating Cutouts for Flow in Self-Aligning Mold

The universal testing machine is inherently a displacement controlled mechanism. When combined with a hydrostatic or hydrodynamic bearing that has a very large stiffness at operating conditions this can create problems with the testing machine hunting to achieve the desired load. To effectively change the universal testing machine from a displacement controlled device to a force controlled device, a resilient spring is needed to provide a relatively consistent load

over small changes in displacement. To provide a spring in the force control system the test rig originally employed sets of belleville disc springs between the top plate and the load cell in addition to the spherical washer.

2. **Support System Performance Characteristics.** Stainless steel belleville springs with a 565 lbf working load (roughly equal to the max design bearing load on test rig) were selected for use in the test rig. The springs have a deflection of 0.017" at the working load. Disc springs can be stacked singularly, in parallel, or in series to provide different force responses. When stacked in series they double the displacement for the same force. A set of eight belleville springs were therefore stacked in series to reduce the stiffness in the system, yielding a total deflection of 0.136" at working loads (equivalent to a stiffness of 4154 lbf/in) from the disc springs alone.

In addition to the disc springs, the polyurethane rubber self-aligning mount
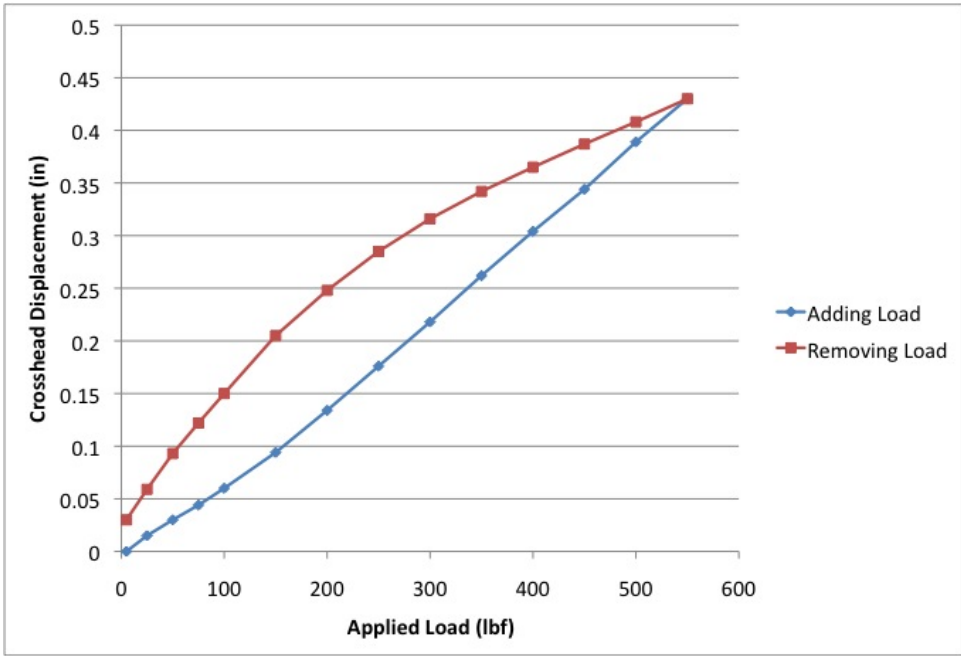
Figure 4-17: Self-Aligning Mount Displacement with Load

also acts as a spring. During calibration of the eddy current probes, the stiffness of the self-aligning mount was found to be 1280 lbf/in. The mount displays viscoelastic properties as expected from a rubber polymer and displays hysteresis effects (see Figure 4-17). During later stages of testing it was determined that the self-aligning mount acts as a sufficient spring by itself that the belleville washers are not required and were subsequently removed.

Concerns existed regarding the interaction between the self-aligning mount and the bearing housing. Because it provides an elastically averaged support surface for the bearing housing, the amount of deflection that occurs in the housing (and therefore the bearing surface) due to an applied load is minimal. To bound the magnitude of the effect that the mount has on the housing, a FEA study was done using a Mooney-Rivlin hyper-elastic material model to characterize the response. Since Mooney-Rivlin coefficients for rubber in the mounts is not available, estimates of the coefficients based on the shore hardness were used [9].

Different 550 lbf loading condition profiles were analyzed including a line load at the bottom dead center (BDC) of the bearing, a parabolic pressure load distribution, and a uniform pressure load distribution. The parabolic distribution is most representative of the pressure profile during actual bearing operation while the line load is representative of the pressure profile during static load calibration. The magnitude of the housing deflections from these loads is provided in Table 4.9.

Table 4.9: Estimated Housing Deflections due to Self-Aligning Mount

Load Distribution	Housing Deflection(1/1000 inch)	Direction
Parabolic	0.16	Expansion
Uniform	0.58	Expansion
Line	0.266	Contraction

Figure 4-18 show the stresses in the housing and the contact pressures from

[9]Values were obtained from E.F. Gobel's Rubber Springs Design

the self-aligning mount for a 550 lbf parabolic load distribution in the bearing. It is clear that stresses and pressures are quite low, supporting the very small housing deflections. For the test rig, the deflections are considered negligible.

(a) Housing Stresses   (b) Contact Pressures
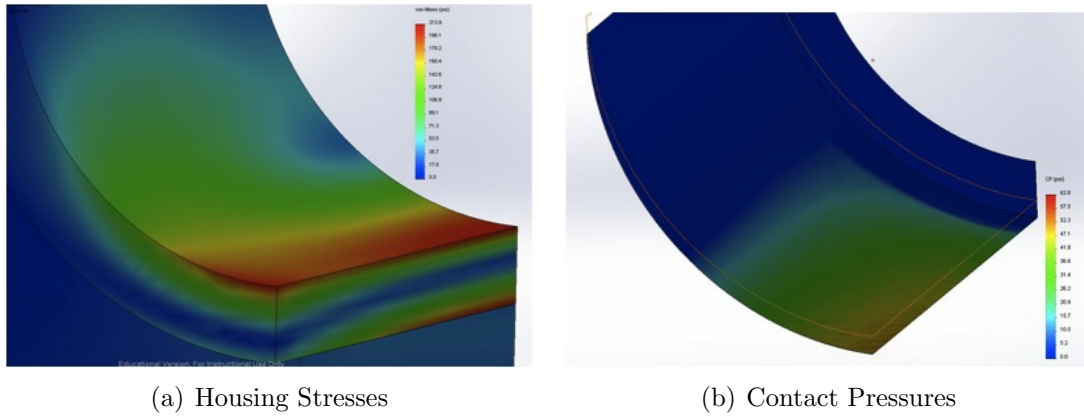
Figure 4-18: Effect from Self-Aligning Mount with 550 lbf Parabolic Bearing Load Distribution

4.3.8   Tank

To provide a representative environment for bearing testing, a rectangular water tank is used that allows the bearing test section to be submerged during operation allowing for natural lubrication during hydrodynamic testing. Selecting the length and depth of the tank was based on maintaining a relatively low tilt angle on the shaft when conducting submerged testing. This resulted in a long, relatively shallow tank. The width of the tank was driven by the need to allow the entire test rig to rotate into the tank without interference. This included providing margin to allow for the fluid supply and pressure tubing to be free of interference from the sides of the tank.

A 102 gallon polypropylene tank is used for testing. The dimensions are 60"L X 24"W X 18"H with a 1/4" wall thickness, with a 1-1/2" X 1-1/2" lip that extends around the top of the tank. Once received, the tank was filled with water outdoors to perform a leak and integrity check. There was noticeable (approximately 1") outward bowing of the tank on each side with the tank full. This caused a concern with the plastic creeping over long periods of time when full that would potentially cause a

failure of the tank and flooding in the location of the test rig. To mitigate against this possibility, an external support frame of T-Slot 40mm extrusion was built around the lower lip of the tank.

The test rig and tank are located in MIT's Laboratory for Electromagnetic and Electronic Systems (LEES lab) in the basement of building 10. The basement location was selected based on the availability of floor space and the presence of floor drains should a leak occur. A secondary containment, consisting of an external frame of 1-1/4" PVC pipe supporting a tub created by a heavy duty tarpaulin, is utilized to further protect against leakage.

The tank is filled using a garden hose connected to a spigot in the LEES lab. Due to the basement location and absence of natural sunlight the growth of algae is not a problem. The collection of dust and bugs in the tank is controlled by the continuous use of an aquarium surface filter and the operation of the fluid supply system and recirculation line during the frequent bearing testing. Evaporation of the water over time does occur, requiring the tank to be topped off with additional water approximately once a month. For removal of water, a LITTLE GIANT 20 gpm submersible pump is used that discharges water into a drain line in the lab.

4.3.9   Frame

The test rig is constructed of and supported by a frame built of 80/20® 40mm T-Slot aluminum extrusion. The choice of the aluminum T-Slot extrusion as a frame was a result of having a supply of 40mm T-Slot extrusions and fittings on hand, the flexibility it provides in making future modifications to the test rig, and the corrosion resistant properties of aluminum.

An exterior frame of square 40mm extrusion is mounted on swiveling castor wheels and bridges the tank that is located on the floor. The wheels allow the entire test rig to be moved away from the tank, allowing for it to serve as a multi-purpose water

testing tank for other experiments. The testing section of the rig that houses the air bearing assemblies, shaft, motor, force tester, and instrumentation is mounted on two double width 80mm extrusions. This testing section is connected to the exterior frame by 180 deg perpendicular hinged pivots that allow it to drop the bearing section into the water.

The testing section is raised and lowered into the tank by a marine winch that is hooked to a U-bolt on the thrust bearing assembly (see Figure 4-19). During non-test periods, the test rig is supported in the raised position by a cross-bar of T-Slot extrusion placed across the exterior frame allowing the testing section to rest on it. A sheet of Ultra High Molecular Weight (UHMW) Polyethylene is adhered to the interior bottom of the tank where the testing section rails rest on the bottom, protecting against wear on the actual tank from repeated raising and lowering of the test rig into the water.

Since significant portions of the test rig will be submerged and exposed to water, corrosion was a concern during the design and construction of the test rig to ensure a long operating life. The framing sections, associated brackets, and fittings are aluminum. All bolts are either 18-8 or 304 stainless steel. The test section that lowers into the water is protected by two magnesium sacrificial anodes that are directly bolted to the 80mm rails. The magnesium was selected due to the use of freshwater in the tank, which has a low electrical conductivity - therefore a high negative galvanic potential is needed for an effective anode. The exterior frame of the tank is not directly exposed to water and electrically isolated from the test section by plastic washers in the hinged pivots. Because of this, the anodes used to protect the fluid supply system are adequate to protect the external frame.

4.3.10   Side Force Apparatus

A removable side force module is used to allow for the application of a side force during bearing testing. This is used to simulate a load that would be seen under
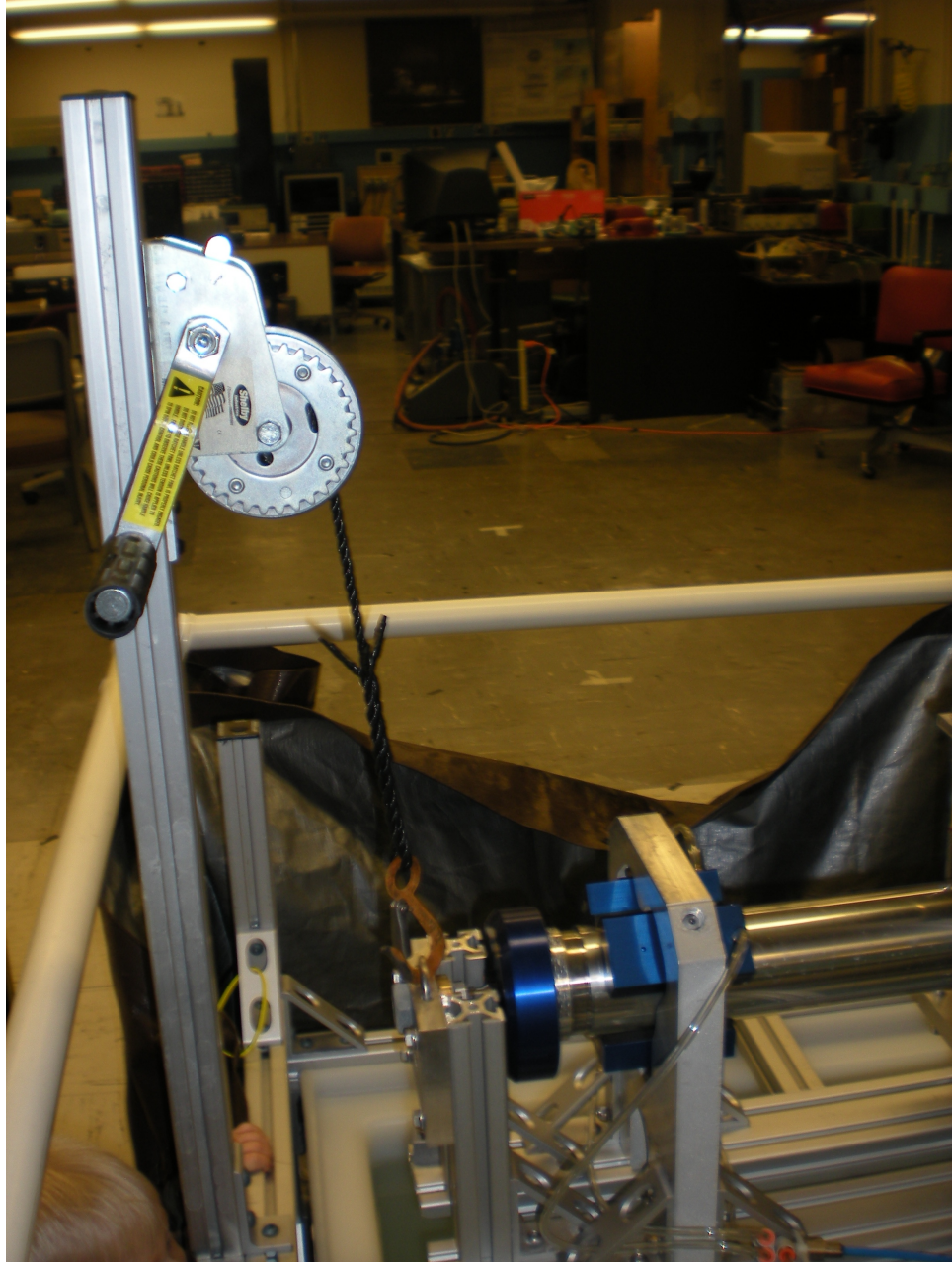
Figure 4-19: Winch Assembly

conditions of a ship heeling or rolling in heavy seas. It is a simple system consisting of two pulleys that are used to apply force to the forward and aft lanyards of the bearing support. Monofiliment line is tied to the lanyards and laced through the pulleys. A set of 2.5 lbf and 10 lbf gym weights are used to apply a variety of loads and moments to the test bearings. When side force testing is not being conducted, the device is removed to allow for easier access to the test bearings. The apparatus can be seen in Figure 6-5, which shows the bearing under side force testing.

4.3.11   Data Acquisition System

A total of 16 sources of data are electronically recorded during testing. They are:

- Motor RPM

- Bearing torque

- Four flowmeters

- Four eddy-current probes

- Six pressure transducers

Although it is a test variable, bearing load is not directly recorded since the load does not vary for individual tests. The bearing load is annotated in a test matrix spreadsheet and in the data file name.

To record the data, a National Instruments USB-6218 Data Acquisition (DAQ) board is used in conjunction with a LABVIEW program. The DAQ board is capable of sampling at 250,000 samples per second with a total of 32 analog inputs. With 16 data channels, this means that the individual sensor sampling rate can be as high as 15,625 Hz (250,000 divided by 16 channels). The actual sampling frequency used during later stages of testing was 12,000 Hz. This high sampling frequency protects against aliasing of the data and is capable of fully capturing any short-time transients that might occur during testing.

The motor tachometer, torque sensor, and eddy-current probes are all recorded with two analog inputs, with the voltage difference between the two providing the sensor's data signal. The flowmeters and pressure transducers are configured to measure the voltage of a single analog input signal relative to a common analog input ground that is the DC supply voltage for those sensors. This means that a total of 22 analog inputs of the DAQ board are utilized. The DAQ board also provides 2 analog outputs. One of these outputs is utilized to pass a voltage signal to the motor controller for the speed signal.

Data cables are muliti-conductor with a foil shield and drain wire. Only the ends terminating at the DAQ board are grounded. This avoids ground loops in the sensors that might cause noise - frequency analysis of the data shows very little harmonic noise in the signal. Connections from the sensors are first collected on a breadboard mounted on top of the DAQ board. Jumpers are then used to connect the breadboard to the DAQ board ports. The breadboard also provides for connecting the wiring for the DC supply voltage to the sensors, the motor controller direction and disable switches, and tachometer signal pullup resistor. The entire DAQ board assembly is housed in an enclosure. Penetrations in the enclosure utilize cord grips to protect against water and dust intrusion. The DAQ enclosure can be seen in Figure 4-20.

4.3.12 Operating Station

The test rig is operated and controlled from one central location. The motor controller, DAQ board enclosure, ADMET force tester controller, power supplies, and the computer workstation that operates the LABVIEW and MTESTQuattro software are all located on a VIDMAR cabinet adjacent to the test rig (shown in Figure 4-21). The fluid supply system control header (described in section 4.4) is also adjacent to the operating station, allowing for full control of the fluid supply system. A pressure gauge and control valve for the air bearings is visible from the operating station. Con-
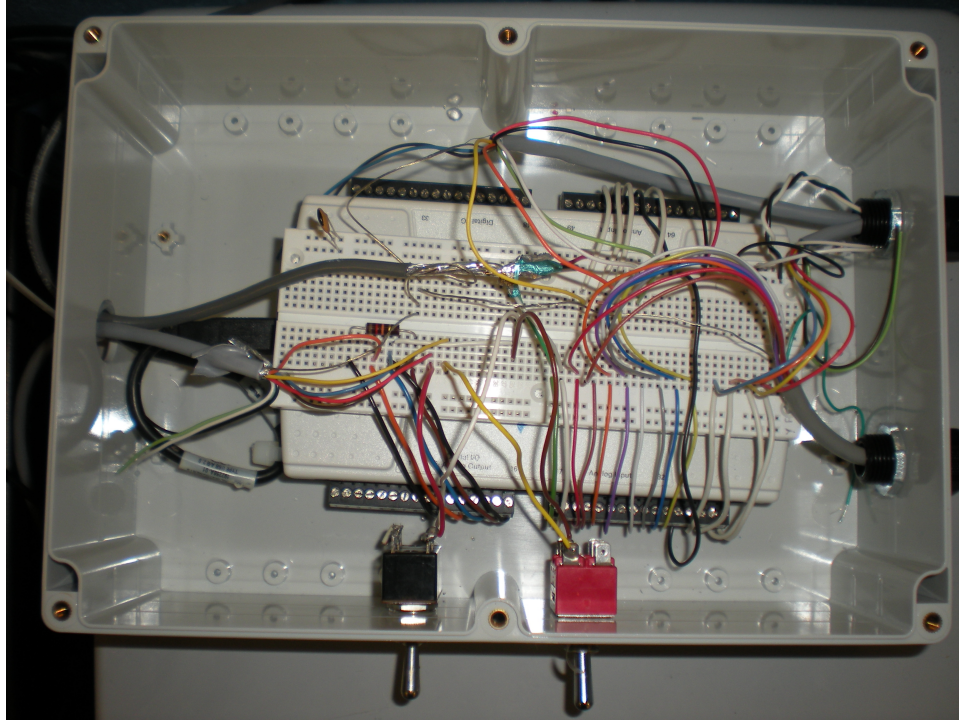
Figure 4-20: DAQ Enclosure

trol of the force tester is controlled from the workstation as described in section 4.3.6.

The test rig motor and data collection system is operated through the LABVIEW program, with data files from tests saved locally on the computer workstation hard drive for later processing. The LABVIEW program provides real-time output of all recorded sensor outputs with the exception of shaft position, which is post-processed. The operator can electronically monitor vital parameters during testing in addition to visually observing the test rig. This allows the operator to immediately respond to abnormal conditions that might occur during testing.

4.4   Fluid Supply System

The test rig employs a dedicated fluid supply system to provide pressurized water to the hydrostatic bearings. Figure 4-22 shows the fluid network diagram[10]. The

---

[10]The schematic shows the configuration with three bearing inlet ports. Depending on the test bearing configuration, one or two of these ports are blocked off.
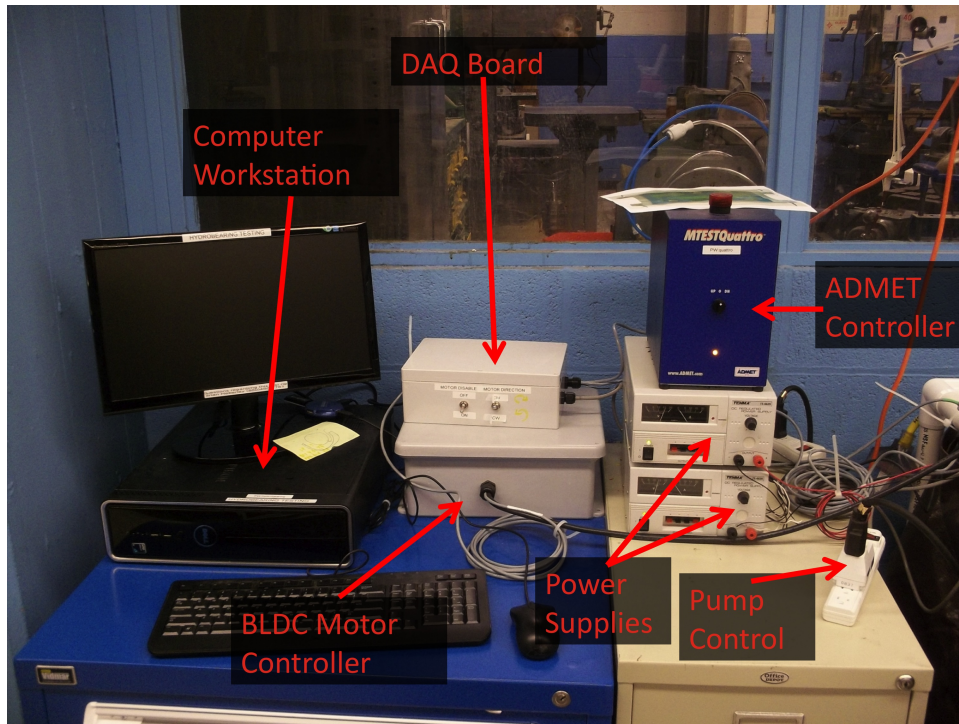
Figure 4-21: Operating Station

pressure source is an electric motor driven centrifugal pump. A system of valves and sensors is used to route and monitor the fluid to the bearing inlet ports. The fluid system is also used to filter debris and circulate the water in the tank to prevent it from becoming stagnant.

4.4.1 Fluid System Component Descriptions

A description of the components used in the fluid supply system is provided below.

1. **Pump.** The pump is a SHURFLO COMBB5X centrifugal impeller pump driven by a 1.5 HP electric motor. The electric motor operates at 3450 RPM and 110 volts, drawing 17 amps at full load. The pump develops a deadhead pressure of 67 feet (29 psi). Figure 4-23 shows the pump curve and a picture of the pump installed in the rig. A two inch non-collapsible hose is used for the pump inlet, discharging into a 1/2 inch NPT connection. Because the pump is not self-priming, it is located approximately eight inches below the water level in the tank to ensure the inlet remains flooded and to assist in providing a net
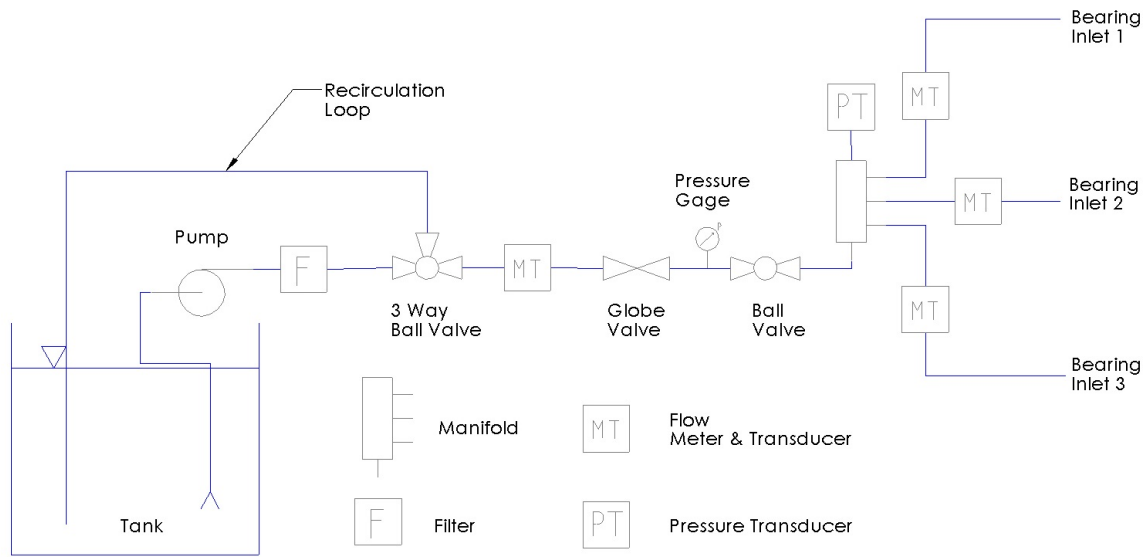
Figure 4-22: Schematic of Fluid Supply System

positive suction head (NPSH).
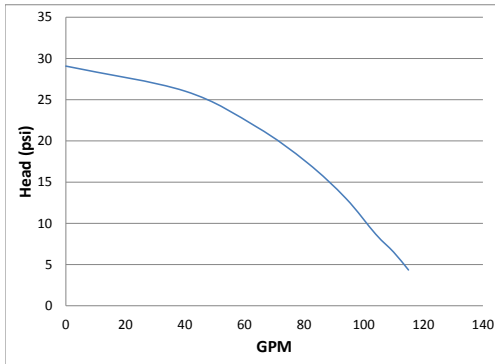
(a) Pump Curve
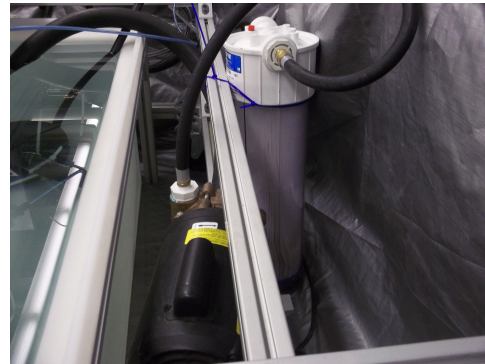
(b) Pump and Filter

Figure 4-23: Centrifugal Pump

2. **Filter.** A Keystone CG20 high capacity cartridge-type water filter is used re-
move debris from the water. A 50 micron (0.00197 inch) filter element is used.
This size was selected due to the design clearances on some of the bearings tested
being 0.002 inches. The removal of debris larger than the clearance should pre-
vent foreign material from becoming lodged in the bearing and causing damage

during operation. A finer filter would be advantageous for long term bearing operation in harsh environments, but would increase the pressure drop across the filter and possibly require a larger pump. Because of the relatively short testing periods and clean freshwater used in the test rig, a 50 micron filter proved adequate. For a full scale implementation with larger design clearances it would be possible to use a more course filter such as the 125 micron strainers typically used in the shaft seal water lubrication systems of naval vessels[17].

3. **Valves.** Three different valves are installed on a header adjacent to the test rig operating station to allow for control of the fluid to the bearing. Figure 4-24 shows the control header and the valves associated with the fluid system.
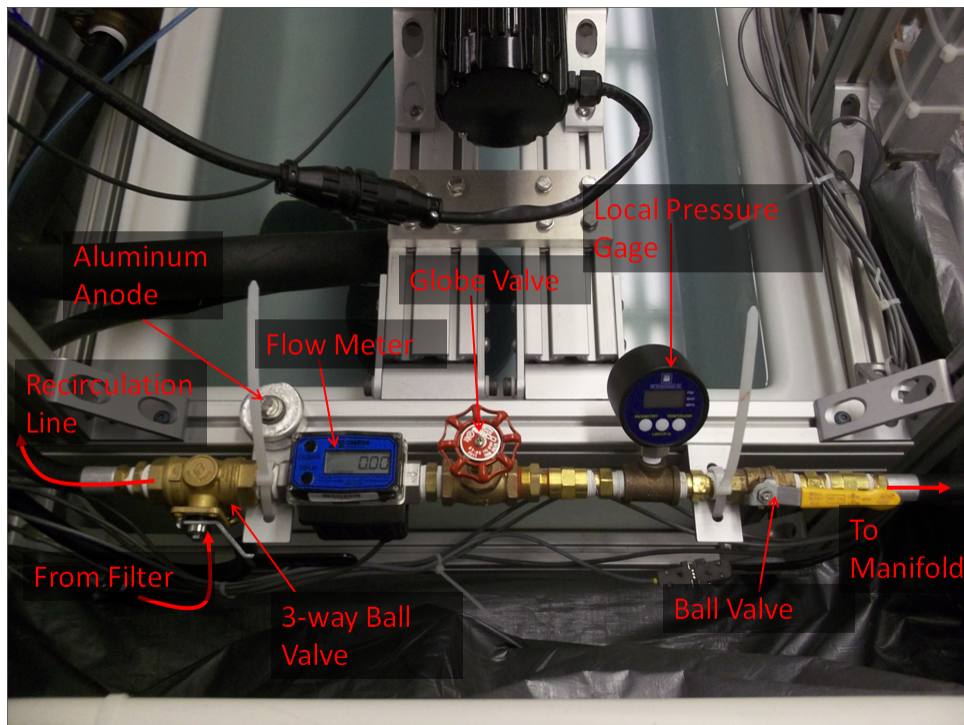
Figure 4-24: Fluid Control Header

- *Three-Way Ball Valve.* A three-way ball valve is used to direct water to the bearing or to a recirculation line pumping water directly back into the tank. The recirculation loop is used for warming up the pump prior to testing, filtering the water in the tank, and preventing long term deadhead operation of the pump when flow is secured to the bearings.

- *Globe Valve.* Globe valves are designed for throttling flow. This provides precise control over the amount of flow that goes to the test bearing, allowing for fine control over testing parameters.

- *Ball Valve.* A ball valve is used for isolating flow into the test bearing. This allows for a testing of the local pressure gage upstream of the valve to check for proper deadhead operation of the pump and a quick means of securing flow to the bearing should any of the downstream piping elements spring a leak.

4. **Flow Meters.** Four Omega FTB790 series turbine flowmeters are used to mea-
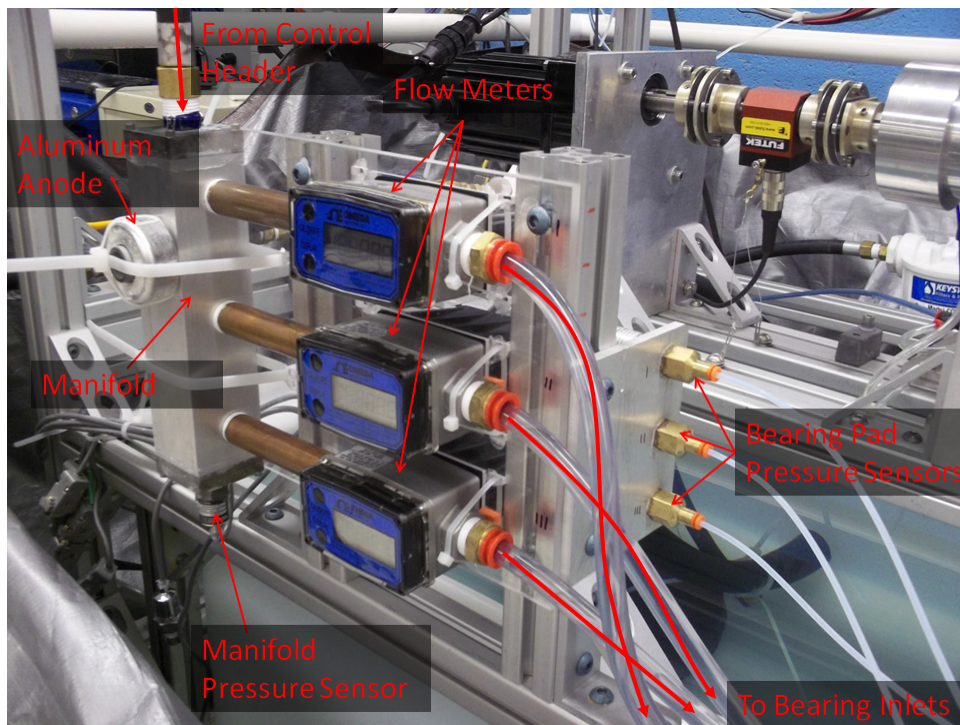
Figure 4-25: Fluid Manifold

sure flow rates in the fluid system. One is used to measure the total flow in the control header and three are used to measure the individual flows to the bearing inlet ports (dependent on the test bearing configuration). The control header flowmeter is shown in Figure 4-24 and the three inlet port flow meters are shown in Figure 4-25. The characteristics of the flow meters used are provided in Table 4.10. The flowmeters come factory calibrated for freshwater at 70^oF

and are rated to be accurate within 2% of indicated reading. FLSC790-MA modules are installed on each flowmeter for remote data recording of the flow signals with the DAQ system. A 13.8 volt DC supply voltage is provided to each module and a voltage output of 1-4 volt DC is sent to the DAQ board for data recording. The modules are calibrated to each individual flowmeter. This is done by altering the flow to each flowmeter by iteratively plugging the exits to the flowmeters and adjusting overall flow using the globe valve in the control header, developing calibration data correlating flow rate to output voltage.

Table 4.10: Flow Meter Characteristics

Meter	Model	QTY	Size	Linear Range (GPM)	Max Pressure Drop (psi)
Control Header	FTB792	1	3/4 inch	2-20	7.5
Bearing Inlet	FTB791	3	1/2 inch	1-10	8

Because turbine flowmeters are intrusive flow measurement devices, they have a measurable pressure-drop across them that varies with flowrate. The specified maximum pressure drops indicated in Table 4.10 is for the flow at the maximum rate within the linear range. To find pressure drops at different flow rates, viscosities and specific gravities for turbine flowmeters, the following equation is used [20]:

$$\Delta P_2 = \Delta P_1 \left(\frac{\rho_2}{\rho_1}\right)^{.81} \left(\frac{\mu_2}{\mu 1}\right)^{.27} \left(\frac{Q_2}{Q_1}\right)^{1.82} \qquad (4.11)$$

where ρ is specific gravity, μ is viscosity in centipoise, and Q is flow rate in gallons per minute. Since the fluid does not change, ρ and μ remain constant simplifying the equation to:

$$\Delta P_2 = \Delta P_1 \left(\frac{Q_2}{Q_1}\right)^{1.82} \qquad (4.12)$$

During calibration of the fluid systems it was found that the pressure drop associated with the FTB791 flowmeters was much greater than expected and

did not correspond directly with OMEGA's specifications and empirical equations. The actual pressure drop measured across the flowmeters as a function of flowrate is shown in Figure 4-26. A power regression was used to match up to the calibration data and refine equation 4.12:

$$\Delta P_{flowmeters} = 0.1745 \left(Q_{Flowmeter} \right)^{1.904} \tag{4.13}$$

Flow altering devices such as elbows and valves that are located upstream and
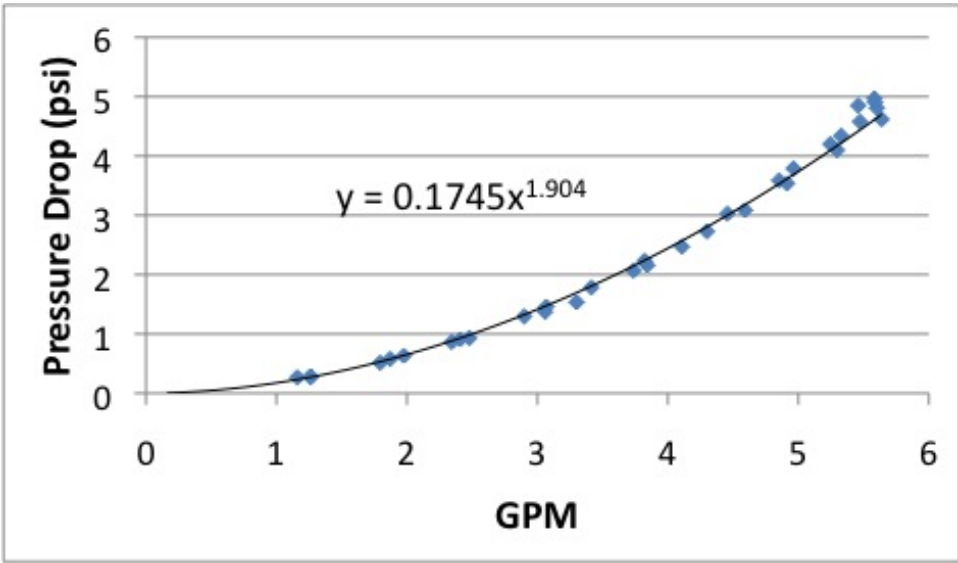
Figure 4-26: Measured Pressure Drop Across FTB791 Flowmeters

downstream of the flowmeters can affect accuracy. Because of this, five-inch long copper sections of straight pipe (seen in Figure 4-25) are installed upstream of the bearing inlet flowmeters to meet the manufacturers recommendation of an upstream straight pipe length equal to 10 times the internal diameter of the turbine. Downstream recommendations are for a straight pipe length equal to five times the internal diameter of the turbine. The bearing inlet flowmeters discharge into a flexible clear tubing that do not have severe bends which allows for a relatively straight downstream run of piping. It should be noted that the control header flowmeter does not meet the recommended length for sections of straight piping upstream or downstream of the flowmeter. This is due to size

Table 4.11: Calibration Flowrates in Gallons Per Minute (GPM)

Run	Control Header	Inlet 1	Inlet 2	Inlet 3	Inlet Sum	| % Error |
1	0	0	0	0	0	
2	8.74	2.82	2.94	2.98	8.74	0.0%
3	7.15	2.31	2.41	2.45	7.17	0.3%
4	5.1	1.69	1.74	1.77	5.2	2.0%
5	2.26	0.8	0.76	0.77	2.33	3.1%
6	8.72	2.82	2.94	2.96	8.72	0.0%
7	3.8	3.76	0	0	3.76	1.1%
8	5.58	5.54	0	0	5.54	0.7%
9	6.65	6.6	0	0	6.6	0.8%
10	3.3	0	3.25	0	3.25	1.5%
11	5.42	0	5.38	0	5.38	0.7%
12	6.78	0	6.72	0	6.72	0.9%
13	4.58	0	0	4.55	4.55	0.7%
14	5.86	0	0	5.8	5.8	1.0%
15	6.74	0	0	6.66	6.66	1.2%
Average						**1.0%**

constraints resulting from the desire to have all valves on the control header within easy reach of the operating station.

As configured, the sum of the bearing inlet flowmeters should equal flow through the control header flowmeter. During calibration runs shown in Table 4.11, the percent error between bearing inlet and control header flowmeters averaged 1.0% with a maximum recorded error of 3.1%. This provided confidence in the accuracy of flow measurements for the test rig.

5. **Pressure Sensors.** In the fluid supply network, pressure sensors are used to read and record pressure at various points in the fluid system and bearings. A local digital SSI Technologies MG1 pressure gage is used on the control header (shown in Figure 4-24). This gauge has no recording capabilities but does provide real-time feedback to the operator, allowing one to check and verify anticipated response when manipulating valves in the fluid network.

A total of six Measurement Specialties MSP300-100 pressure transducers are used to record pressure data during tests. Originally there was only one transducer, which was located in the flow manifold to allow for determining the inlet pressure to the bearings themselves. The other transducers were added later to allow for actual pressures to be measured at various locations in the bearing surface itself. They are located on a mounting bracket external to the bearings. The configuration of the transducers can be seen in Figure 4-25. The external mount transducers are connected to the test bearings via 1/8 inch tubing to allow for pressure readings at any part of the bearing depending on the bearing configuration. The pressure transducers are not waterproof, but were modified by sealing vulnerable gaps in the sensors with silicon. In addition to this, the transducers were mounted outside of fluid flow paths and protected from inadvertent spray by aluminum and acrylic brackets.

The MSP300-100 pressure sensors are rated up to 100 psi gage pressure and supplied with a 13.8 volt DC voltage. The output signal voltage of 1-5 volt DC is sent to the DAQ board just like the flow sensor modules. The sensors specified accuracy is 1% of full scale voltage (combined non-linearity, hysteresis, and repeatability), providing a confidence in pressure readings of +/- 1 psi. Utilizing the fluid supply system configuration, a two point calibration procedure was used for the pressure transducers. Because of the linearity of the sensors, this was deemed to be sufficient. Zero pressure was obtained by providing a open path to atmosphere from the pressure sensors. A pressure of 29 psi was applied to the sensors by deadheading the pump (which has a known output pressure at zero flow) to the sensors themselves. By doing so the slope of the volts per psi relationship and intercept was determined.

During calibration and operation, purging air from the pressure transducer lines is necessary to obtain accurate measurements. This is done automatically for the manifold pressure transducer due to it being mounted at the bottom of

manifold. For the five external mounted pressure transducers, this iss accomplished by operating the test rig with pressure in the 1/8 inch tubing leading to the transducers sufficient to induce a flow through the lines. The lines are disconnected from the transducer connections until all the air was expelled from the line at which point the lines are installed back on the transducers.

6. **Hoses and Fittings.** National Pipe Taper (NPT) fittings are used exculsively due to their ability to seal connections when mated together. To assist in sealing connections, teflon tape (also known as 'dope' tape) is applied to all male threads. Various hoses and fittings are used in the fluid system to connect the various components:

   - *Rubber Hose.* Rubber 1/2 inch ID hose is used to connect the pump outlet to the filter, the filter to the 3-way ball valve, the ball valve to the manifold, and is used for the recirculation line back to the tank.

   - *Couplings and Reducers.* Various male-to-male, male-to-female, and female-to-female connectors are used to mate up the components in the system. 3/4 inch to 1/2 inch reducers are also used for the connection to the 3/4 inch 3-way ball valve (the 1/2 inch hose from the pump and to the 1/2 inch recirculation line) and for the connection from the 3/4 inch globe valve to the local pressure gage.

   - *Push-To-Connect Fittings.* Push-to-connect fittings are used in sections that are routinely removed for calibration or reconfiguring the test rig for different bearings. These fittings provide a quick means of connecting and disconnecting tubing and provide a watertight seal for the relatively low pressures (less than 100 psi) seen in the test rig. 1/2 inch fittings are used in the outlet of the bearing inlet flow meters and the actual bearing inlets themselves. 1/8 inch fittings are used on the external mounted pressure transducers and the outside of the bearings at the location of pressure measurements for the bearings, as shown in Figure 4-27.

   - *Flexible Tubing.* In between the push-to-connect fittings, flexible tubing is
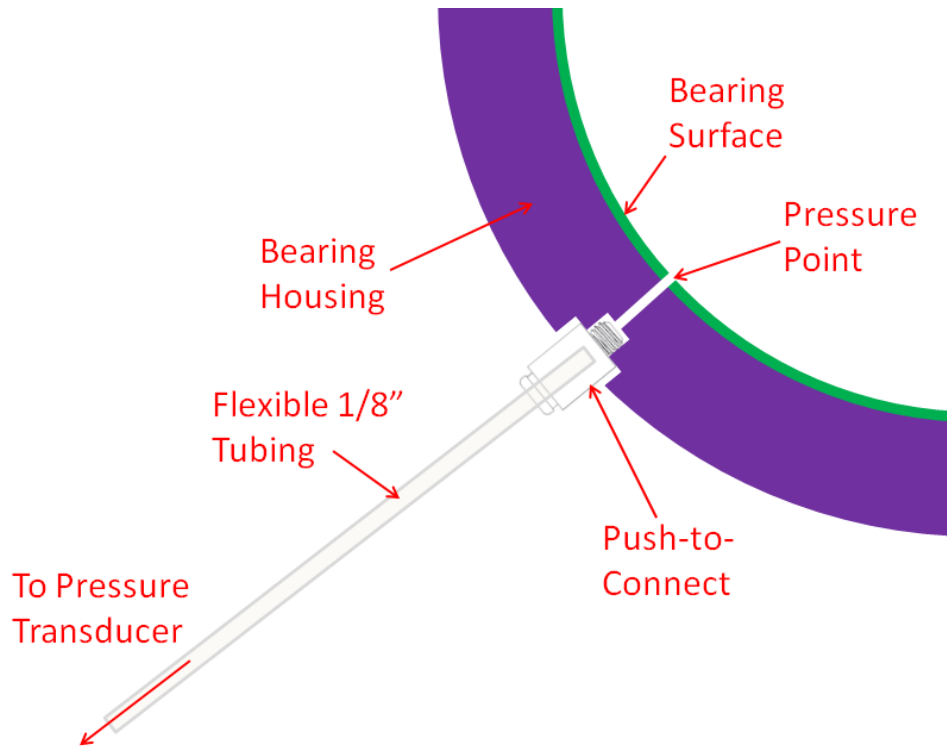
Figure 4-27: Bearing Pressure Tap Configuration

utilized. Such tubing minimizes the external forces that would be imparted on the bearing from a stiff hose or metal pipe. The tubing sizes are 1/2 inch OD (3/8 inch ID) for the inlet flow into the bearings and 1/8 inch OD (0.73 inch ID) for the pressure lines. The nylon and polyethelyne tubing material used is clear or semi-clear allowing the flow of fluid through the lines to be seen. The tubing can be seen in Figure 4-25.

7. **Manifold.** A manifold is used as a collecting point for fluid directly upstream from the bearing inlet flowmeters. It is constructed of 2 inch square 6061 aluminum tubing with a wall thickness of 1/4 inch and a length of 8 inches. The endplates provide an inlet to the manifold on the top and connection for the pressure transducer on the bottom. Three outlet ports are located on the side for the bearing inlet flows. The internal volume of 24.5 in^3 provides a small reservoir for pressure to equalize before entering each bearing inlet line.

8. **Cathodic Protection.** The metallic parts in the fluid system area are a combination of stainless steel, aluminum, and brass. Because of galvanic coupling between these metals, the aluminum is a sacrificial anode to the stainless steel and brass, which will lead to corrosion and reduce the longevity of the test rig. This is mitigated by using freshwater in the test rig as the working fluid, and by the use of sacrificial aluminum anodes. These anodes can be seen in figures 4-24 and 4-25. One is fastened directly on the manifold and one is bolted on the aluminum 80/20 frame directly adjacent to the control header[11].

4.4.2   Fluid System Pressure Drop Calculations

The flow of fluid through the supply system results in a pressure loss to the water entering the bearing inlets. The amount of this pressure loss is dependent upon many things including:

- Obstructions in the flow such as valves.

- Changes in flow direction through bends, elbows or tees.

- Friction in the piping. This is a function of the internal roughness of the pipe or tubing, the velocity of the fluid, and the viscosity of the fluid.

- Changes in the cross-section of the flow.

This pressure loss is undesirable but a reality of fluid through internal piping. To minimize the magnitude of the pressure loss in the test rig system, piping runs and unnecessary valves and flow restrictions are minimized as much as practical.

The manifold serves as a collection point from which flow into the bearing inlets is sent, and a common pressure in the system that is read and recorded by a pressure transducer. Because there are flow meters, piping, and tubing between the manifold

---

[11]It should be noted that the aluminum used in the sacrificial anodes has a greater negative galvanic potential than the 6061 aluminum used in the fittings and frame of the test rig, which ensures the aluminum anodes will be sacrificed before the 6061 aluminum.

and the bearing inlets, the manifold pressure is not the actual pressure entering the bearing inlets. The accurate determination of the pressure entering the bearing inlets is vital to analyzing the operating responses of different test bearings. The bearing inlet pressures are calculated by estimating the pressure drop seen in the various parts of the fluid system between the manifold and bearing inlet. These are estimated using standard calculations and information for the flow of fluids through valves, fittings, and piping[5]. This process is outlined below:

1. **Flow Rate.** The flow rate of each bearing inlet branch is determined by the flow meter in the branch. This is measured in gallons per minute (GPM) and can be converted to flow velocity by the equation:

$$V_{branch} = \frac{Q_{branch}}{A_{branch}} \tag{4.14}$$

   where Q_{branch} is flow rate in ft^3/s ($1 ft^3 = 7.4805$ gallons), and A_{branch} is the cross-sectional area of the piping in ft^3.

2. **Reynolds Number as a Function of Flow Rate.** The Reynolds number is the non-dimensional ratio of dynamic forces of mass flow to the shearing stresses due to viscosity. It is used as an indicator for determine the laminar or turbulent nature of the flow in a pipe and has a direct effect on the friction of flow in a piping system. It is defined as:

$$R_e = \frac{D_{branch} * V_{branch} * \rho}{\mu} \tag{4.15}$$

   where D_{branch} is the diameter of the section of piping in feet, ρ is the density of the fluid (1.936 slugs/ft^3), and μ is the dynamic viscosity (2.037 X 10^{-5} $\frac{lb_f s}{ft^2}$). Fluid property values are taken for 70°F.

   For engineering purposes, flow in pipes is generally considered laminar for Reynolds numbers less than 2000 and turbulent for Reynolds numbers greater than 4000. A check of the lowest expected Reynolds numbers that are expected

in the bearing inlet flowpaths is shown in Table 4.12. As can be seen for the 0.6 inch ID sections of brass piping, flow rates between 0.5 and 0.742 GPM are in the 'critical zone' between turbulent and laminar flow. The friction factor in this region is indeterminent with the upper limits of friction bounded by the turbulent flow, while the lower limits bounded by the laminar friction equation:

$$f_{friction} = \frac{64}{R_e} \tag{4.16}$$

For flow rates greater than 0.742 GPM, accurate friction factors can be determined. The accuracy of the flow meters in the bearing inlet branches are not linear for flow rates less than 1 GPM (and not readable below 0.5 GPM), so for most cases the use of turbulent friction factors will be appropriate. It should be noted that in the flexible tubing section of the piping that has an ID of 3/8 inch, the reynolds number will always be higher than in the brass piping for flow rates that can be reliably recorded by the flowmeters.

Table 4.12: Expected Reynolds Numbers in Bearing Inlet Flowpaths

Flow Rate (gpm)	Flow Velocity(ft/s)	R_e (Brass Piping)	R_e (Flexible Tubing)
0.5	0.57	2696	4314
0.742	0.84	4000	6400
1	1.13	5392	8628
2	2.27	10785	17255
4	4.54	21569	34511
8	9.08	43138	69021
10	11.35	53923	86277

3. **Friction Factor as a Function of Flow Rate.** Turbulent friction factors are commonly found using Moody diagrams that relate the friction factor to reynolds number and relative roughness. Relative roughness is defined as:

$$\frac{\epsilon_{roughness}}{D_{branch}} \tag{4.17}$$

123

where $\epsilon_{roughness}$ is the absolute roughness (RMS) of the pipe (in feet). Because the system components in question are a section of drawn brass piping and a section of plastic tubing, an absolute roughness value of $\epsilon_{roughness} = 5.0$ x 10^{-6} feet is used in calculations, corresponding to smooth pipes. To aid in numerically calculating pressure drops, the Colebrook equation is used to implicitly find the turbulent friction factors given absolute roughness and pipe diameter:

$$\frac{1}{\sqrt{f_{friction}}} = -2log\left(\frac{\epsilon_{roughness}}{3.7D_{branch}} + \frac{2.51}{R_e\sqrt{f_{friction}}}\right) \qquad (4.18)$$

The Colebrook equation does require root solving, but is superior to using the Moody charts, which cannot be numerically automated. The friction factors are different for the brass pipe and for the flexible tubing due to differences in internal diameter.

4. **Determination of Resistance Coefficients.** A velocity in a pipe can be achieved with a decrease in static head:

$$h_L = \frac{V_{branch}^2}{2g} \qquad (4.19)$$

where h_L is known as head loss typically expressed in terms of feet of static head and g is the gravitational constant. For flow of fluid through a fitting or a valve, a reduction in static head is also seen. This can be expressed through the use of a 'resistance coefficient' K in the equation:

$$h_L = K\frac{V_{branch}^2}{2g} \qquad (4.20)$$

The head loss in valves and fittings is typically dominated by obstructions or changes to the flow, and not the friction losses associated with the length; because of this, K can be considered independent of $f_{friction}$ and R_e. In straight pipe sections a similar head loss occurs, but it is a function of the length of the

pipe and $f_{friction}$:

$$h_L = \left(f_{friction} \frac{L}{D_{branch}} \right) \frac{V_{branch}^2}{2g} \tag{4.21}$$

where L is the length of straight pipe. From equations 4.20 and 4.21 it follows that:

$$K = \left(f_{friction} \frac{L}{D_{branch}} \right) \tag{4.22}$$

Using this relationship, the total head loss in the system can be found by summing the resistance coefficents of all the valves in the system and $\left(f_{friction} \frac{L}{D_{branch}} \right)$ values for all sections the branches. The calculations presented here are for the test bearing configurations that utilized three inlet ports. In determining the resistance coefficients, formulas and values are all taken from Crane's technical paper TP-410 'Flow of Fluids through valves, fittings and pipe'[5].

- *Common Components.* All three flowmeter lines have a common length of brass straight pipe and contraction from the 1/2 inch ID outlet of the flow meters to the 3/8 inch ID flexible tubing. The resistance coefficient of the 0.6 inch ID straight brass pipe section is:

$$K_{bp} = \left(f_{friction} \frac{L}{D_{branch}} \right) = \left(f_{friction(0.6)} \frac{5"}{0.6"} \right) = 8.33 f_{friction(0.6)} \tag{4.23}$$

The resistance coefficient of the contraction is:

$$K_{contract} = 0.5 \left(1 - \frac{d_1^2}{d_2^2} \right)$$
$$K_{contract} = 0.5 \left(1 - \frac{0.375"^2}{0.6"^2} \right) = 0.30469 \tag{4.24}$$

where d_1 is the diameter of the smaller pipe and d_2 is the diameter of the larger pipe. The pressure drop associated with the flowmeters is handled using equation 4.13.

- *Branch 1.* Branch 1 is a shorter and more direct 36 inch length of tubing consisting of a short 6 inch radius 90 degree bend and a larger 18 inch radius 90 degree bend. The first bend (with an r/d = 16) has a resistance

coefficient of:

$$K_{11} = 42 f_{friction(0.375)} \tag{4.25}$$

The second bend has a resistance coefficient of:

$$K_{12} = 0.5\pi \frac{r}{D_{branch}} f_{friction(0.375)}$$
$$K_{12} = 0.5\pi \frac{18"}{0.375"} f_{friction(0.375)} \tag{4.26}$$

- *Branch 2 and 3.* Branch 2 and 3 are longer lengths of flexible tubing with a large 18 inch radius bend, a 13 inch length of straight run, and a short 6 inch radius 180 degree bend leading into the bearing inlets. The large bends are similar to in branch 1 such that the resistance coefficients are the same:

$$K_{11} = K_{21} = K_{31} \tag{4.27}$$

where the first subscript indicates the branch and the second indicates the component of the resistance. The length of straight run has a resistance coefficient of:

$$K_{22} = K_{32} = \left(f_{friction(0.375)} \frac{13"}{0.375"} \right) = 34.67 f_{friction(0.375)} \tag{4.28}$$

The 180 degree bends have resistance coefficients of:

$$K_{23} = K_{33} = (n-1) \left(0.25\pi f_{friction(0.375)} \frac{r}{D_{branch}} + 0.5 K_{90} \right) + K_{90}$$
$$K_{23} = K_{33} = 0.25\pi f_{friction(0.375)} \frac{6"}{0.375"} + 1.5 \left(42 f_{friction(0.375)} \right) \tag{4.29}$$

where K_{90} is the K factor for a single 90 degree bend of r/d, and n is the number of consecutive 90 degree bends.

5. **Calculation of Pressure Drop as a Function of Flow Rate.** The vertical location of the manifold is the same as the vertical location of the test bear-

126

ing. Because of this, there is no hydrostatic component in the pressure drop calculation, leaving only the resistance associated with flow. Combining all the resistance coefficients, the head loss from from the manifold to the bearing inlet ports is found. For branch one, the pressure drop in psi is:

$$h_{L-Inlet} = 0.434 \left(\frac{(K_{bp} + K_{contract}) V_{brass}^2 + (K_{11} + K_{12}) V_{branch1}^2}{2g} \right) + \Delta P_{flowmeter}$$
(4.30)

Where V_{brass} is the velocity of fluid flow through the 1/2" brass section and V_{branch} is the velocity of fluid in the flexible 3/8" tubing section in feet/second. Knowing the pressure of the fluid in the manifold allows the bearing inlet pressure to be estimated:

$$P_{inlet} = P_{manifold} - h_{L-Inlet}$$
(4.31)

4.4.3   Positive Displacement Gear Pump

Towards the later stages of bearing testing, the need for a different fluid supply system was identified. Centrifugal pumps are simple and reliable, but present a drawback in that they have only one operating point based on the hydraulic resistance downstream of the pump. This means that the bearing flow and pressure are linked together and neither can be independently altered without affecting the other. The shutoff head of the centrifugal pump ultimately proved to be limiting in that only 29 psi could be developed in the supply system. By utilizing a positive displacement pump, flow rate can be independently controlled allowing for much greater control over the test bearing.

Rotary gear pumps were chosen because they provide a relatively smooth and continuous flow of fluid, unlike some other positive displacement pumps such as piston or diaphragm pumps. It was also desired to have two identical pumps capable of operating at synchronous speeds. This allows for two separate, but equal flow rates to be applied to the inlet ports of bearings, removing the need for external compensating

devices such as capillaries or orifices.

A pump system was designed utilizing a variable frequency AC drive motor to power two identical gear pumps via a sheave and pulley system. This allowed the pumps to be driven by a common shaft to provide equal flow. The conceptual design of the gear pump system is shown in Figure 4-28(a).
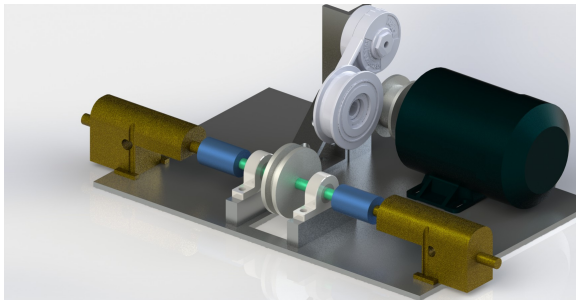
(a) Gear Pump Conceptual Design   (b) Photo of Gear Pump System

Figure 4-28: Gear Pump System

The gear pumps selected were SHURflo BBV1 bronze rotary gear pumps, with carbon graphite bushings suitable for use with water. The pumps are rated for 1.7 gpm at 100 psi when operated at their max speed of 1725 rpm. Because positive displacement pumps can generate extremely high pressures if outlet flow is stopped by an obstruction, these pumps have integrated pressure relief valves. In addition to this, no downstream valves are used with the gear pump fluid supply system.

To power the pumps, a Bodine 42R AC inverter duty motor (model 2235) is driven by a controller that allows speed to be varied between approximately 200 rpm and the maximum motor speed of 3500 rpm. The max speed of the motor is limited by

a dashpot on the controller to correspond to the maximum gear pump speed of 1725 based on the drive reduction from the sheave and pulley system. The motor is rated for 3/8 HP.

The fluid supply system consists of one suction line feeding a common filter. A tee connection on the filter outlet splits the flow to the two gear pumps. The flow of the gear pumps is either combined through an additional tee connection or left as two separate flow paths depending on the testing requirements. The motor speed controller is powered by a 110 VAC receptacle and located at the operator station.

4.5   Measuring Shaft Location
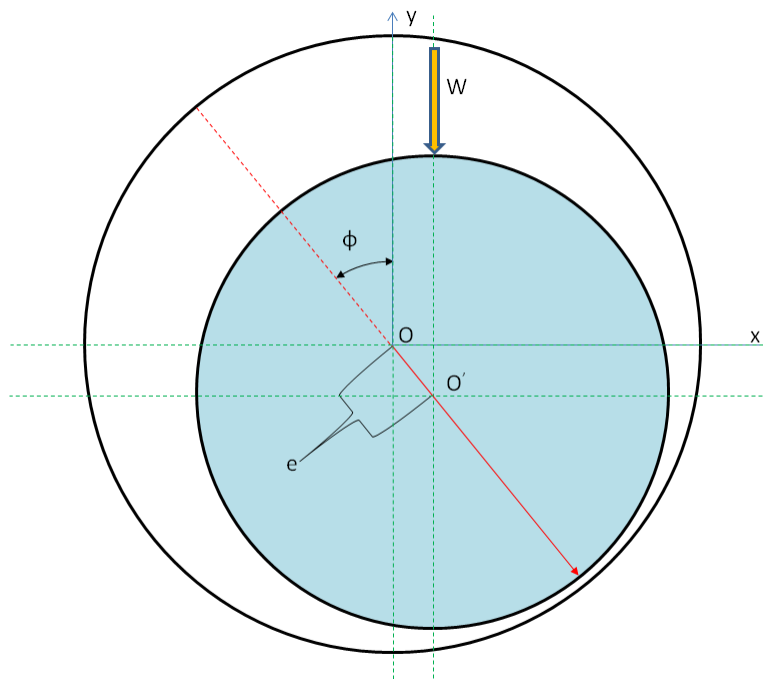
Figure 4-29: Shaft Location Geometry

The position of the shaft relative to the bearing changes as a function of many operating variables. This was first addressed in section 3.2. To define the center of a shaft, O', with respect to the center of the bearing, O, two parameters are needed.

The first is eccentricity ratio, which is defined as:

$$\epsilon = \frac{e}{C} \tag{4.32}$$

The second parameter is called the attitude angle, ϕ, which is the angle between the load direction W and the center line between O' and O. Figure 4-29 shows these parameters.

4.5.1 Eddy-Current Probes

To locate the position of the shaft the test rig utilizes eddy-current sensors, which are non-contact devices that can provide high-precision change in position measurements for conductive targets. Because of their high-resolution and capability to work underwater they are ideal for measuring shaft location. Eddy-current sensors work by driving a high frequency alternating current in a probe that creates an alternating magnetic field. When a metal target is in proximity to this magnetic field, electromagnetic induction causes eddy currents in the target material. These eddy-currents create an opposing magnetic field that resists the field generated by the probe. The basic operating principle of these probes is shown in Figure 4-30. The interaction between these magnetic fields is dependent upon the distance between the probe and target material, which is sensed by electronics that produce a voltage output proportional to the change in distance between probe and target.

The spot size of an eddy-current probe's magnetic field is relatively large. It is therefore recommended that the target surface be at least three times larger than the probe diameter for normal calibrated operation. While larger diameter probes provide a wider usable range of operation, they do so with lower fidelity resolution. Larger probes also have a larger near gap than smaller probes allowing for a larger standoff between probe and target. This last trait is important to ensure that physical contact does not occur between the two and damage the eddy-current probe, or score the test shaft. Based on these competing attributes, as large a probe as possible

(a) Eddy-current principle of operation

(b) Spot size of probe
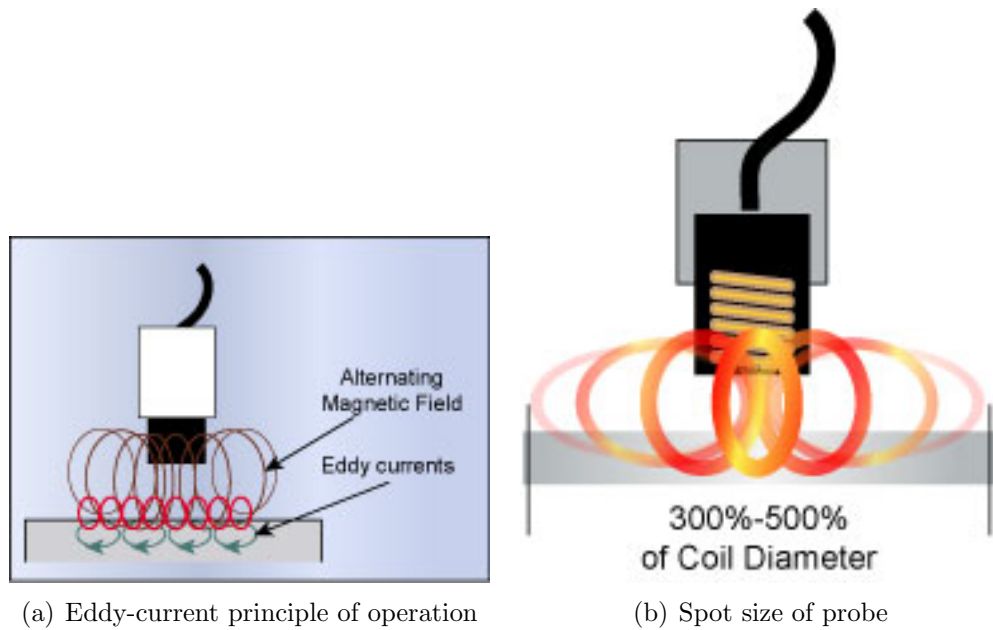
Figure 4-30: Eddy-current probes [6]

is desired to provide adequate standoff, while at the same time provide satisfactory resolution in determining shaft distances from the probes.

Because the target shaft has curvature itself, there is an additional layer of complexity to the proper sizing of the eddy-current probes. This curvature results in an increasing vertical distance between the probe and target the further from the probe center, shown in Figure 4-31. The manufacturer of the eddy-current probes used in the test rig, Lion Precision, recommends that the target diameter be approximately eight to ten times the diameter of the probe to ensure that a proper calibration can be done. A set of four U8 probes are used in the test rig, run by ECL202 drivers mounted on the testing machine mast (shown in Figure 4-32). These probes have the following attributes:

- Diameter = 8 mm

- Range = 0.080 inch

- Near Gap = 0.015 inch

- Nominal Resolution (@15kHz Bandwidth) = 8 μinch

$$D_1 = \sqrt{\left(\frac{D}{2}\right)^2 - (d_2)^2}$$

$$D_2 = \frac{D}{2} - D_1$$

$$D_3 = h + D_2$$

$$Error(\%) = \frac{D_3}{h}$$
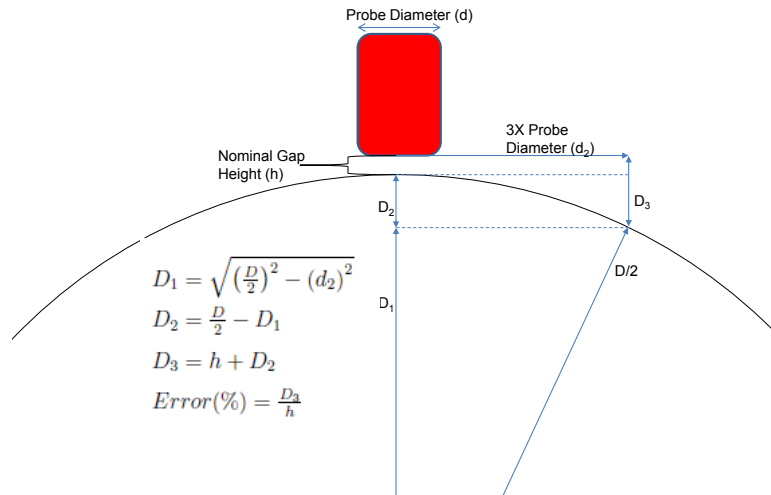
Figure 4-31: Geometry of eddy-current probe with cylindrical target
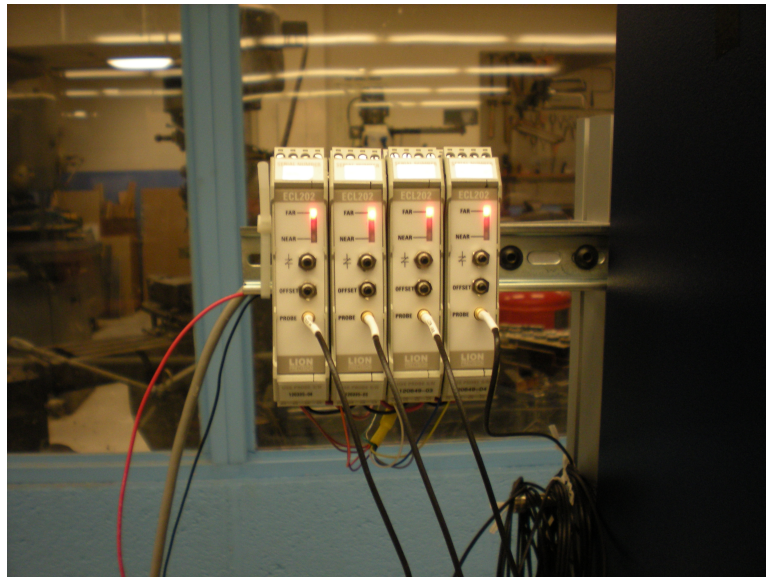
Figure 4-32: ECL202 Eddy Current Probe Drivers

132

- Sensitivity = 5.000 mV/μm (127 V/inch)

These probes provide sufficient standoff distance from the shaft to ensure protection against contact. With a nominal gap on the order of 0.002 to 0.005 inch, the probes also provide an sufficient resolution to determine shaft location even though only 2.5 to 6.3 percent of the range is being utilized. A DC voltage is supplied to the four ECL202 drivers, which are synchronized to each other and provide a 0-10 volt DC output read by the NI USB 6218 DAQ board.

The effect of the curved target and the resulting error in gap height relative to a flat target is quite pronounced, especially as the location of interest gets farther away from the probe center. This effect is shown quite dramatically in Figure 4-33(b), which shows the error between the nominal gap directly beneath the probe as the radial distance from the probe increases [12]. The error changes non-linearly with nominal gap size, with smaller gaps having more error.

Although these errors appear to be quite limiting with a curved target, the output of the eddy-current probes is digitally processed and corrected using a linearizer circuit. The accuracy of the probes is further aided because the probes used in the test rig were calibrated using a spare shaft that is geometrically identical to the test shaft and of the same material and surface finish. Calibration certifications document the probes with linearity errors of less than 0.04 percent and resolution better than 5.25 μinch.

4.5.2 Shaft Position and Orientation Procedure

The four eddy current probes are configured with two probes each at both longitudinal ends of the bearing. At each end, two probes are fixed at 135 and 225 degrees from top dead center (TDC) locations. Figure 4-34 shows the configuration of the eddy-current probes as installed on a bearing housing.

---

[12]This is shown for a probe diameter of 8mm - at the top end of the recommended probe diameter for the test shaft.
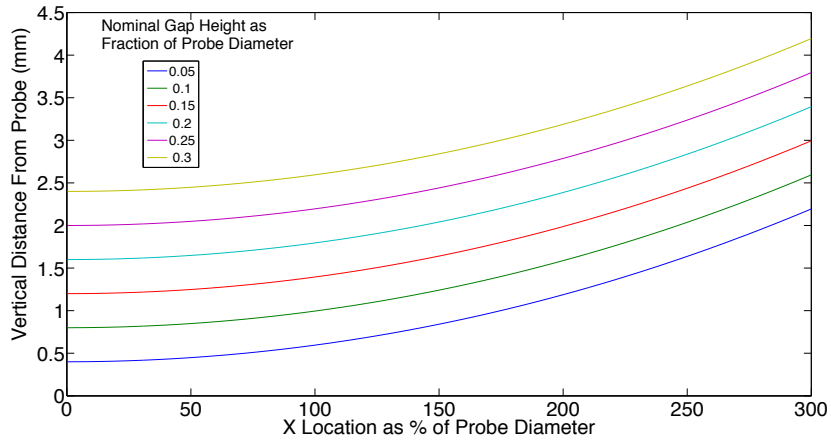
(a) Vertical distance of probe to curved target
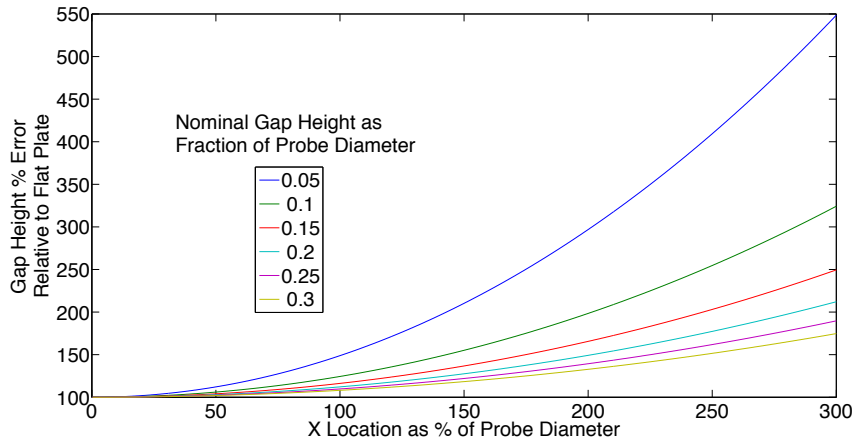
(b) Nominal error a curved target has on gap height relative to a flat plate target

Figure 4-33: Geometric effects for target diameter to probe diameter ratio of 10.25
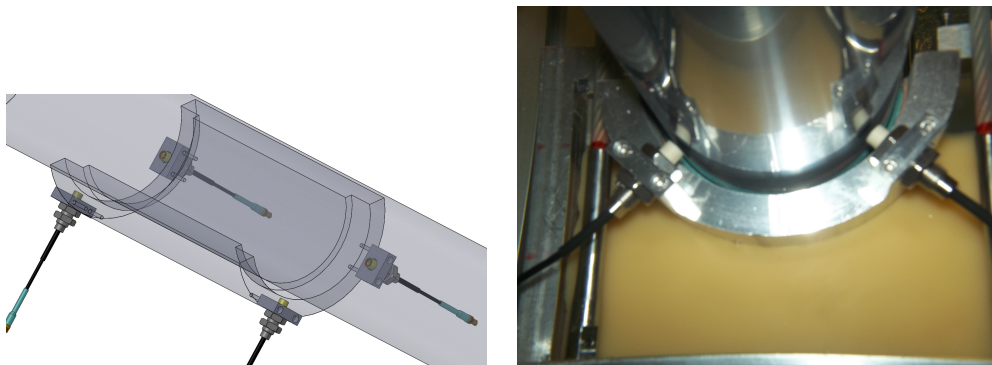
(a) CAD representation   (b) Underwater photograph of installed probes on bearing

Figure 4-34: Configuration of eddy-current probes on test bearing

This configuration is used based on the fundamental principle that two circles can intercept at two distinct points; in this case the two circles represent the distance of the shaft center from the two different probes. One of the resulting intersections is impossible due to the constraint that the shaft cannot physically go through the bearing which leaves only one real intersection - that one being the actual location of the shaft center within the bearing.

The procedure using the probes to locate the shaft utilizes the principle that only relative movement can be detected between test runs. This requires a known starting condition for the shaft. Due to the cylindrical shape of bearings, a fundamental assumption is that the shaft will go to the minimum potential energy state corresponding to the bottom dead center (BDC) location when loaded without shaft rotation. The following outlines the methodology used.

1. When installing the eddy-current probes onto the bearing, the bearing is lightly loaded to pull the bearing onto the shaft at which point the probes are fixed at a location that is within the middle 20 percent of the operating range of the probe. This information is available from an LED range indicator on each of the four ECL202 drivers. This ensures adequate standoff and makes sure that potentially adverse effects from operation at the near or far gap of the probes are not seen. Before conducting test runs a series of calibration runs is done where the bearing is loaded to a range of projected area loads, and voltage measurements of the probes are taken. The bearing is then unloaded, the shaft rotated a set number of degrees and loaded again for another calibration measurement. This is done at every load condition until a full 360 degree rotation is complete. This iteration is done to prevent a material flaw at any location from causing errors in the calibration. These measurement runs are then analyzed and averaged together to obtain reference voltages for calibration for each probe. Any individual calibration measurement that is more than 3 standard deviations from the mean is rerun. In the case of the two probes at

the aft end of the bearing these voltages are called 'P_1' and 'P_2'.

2. The probes are then 'virtually' located on the bearing surface at 135 and 225 degrees from TDC. The distance, $D_{bearing}$, from the bearing center is calculated as:

$$D_{bearing} = \frac{D_{shaft}}{2} + C \tag{4.33}$$

where D_{shaft} is the shaft diameter and C is the nominal radial clearance of the bearing.

(a) The origin is set as the centroid of the bearing, O. The absolute coordinates of the probes relative to the origin, (X_1, Y_1) and (X_2, Y_2), are then found. For the case of probe at 135 degrees from TDC the coordinates are:

$$\begin{aligned}X_1 &= D_{bearing}\frac{\sqrt{2}}{2} \\ Y_1 &= -D_{bearing}\frac{\sqrt{2}}{2}\end{aligned} \tag{4.34}$$

The same is done for the probe at 225 degrees from TDC.

(b) A reference distance for the virtual probe location to the shaft center, O', is then found. This is done by finding the x and y distances from the probe to the center of the shaft in the minimum energy position:

$$\begin{aligned}x_1 &= D_{bearing}\frac{\sqrt{2}}{2} \\ y_1 &= -D_{bearing}\frac{\sqrt{2}}{2} + C\end{aligned} \tag{4.35}$$

This yields the reference probe distance, r_1, that is related to the calibration reference voltage P_1.

$$r_1 = \sqrt{x_1^2 + y_1^2} \tag{4.36}$$

This process is done for all four probes at varoius projected load conditions with the reference voltages (P_1 through P_4), reference distances

(r_1 through r_4), and projected loads saved as calibration values for use in processing test runs. Figure 4-35 shows the geometry governing this calibration process.
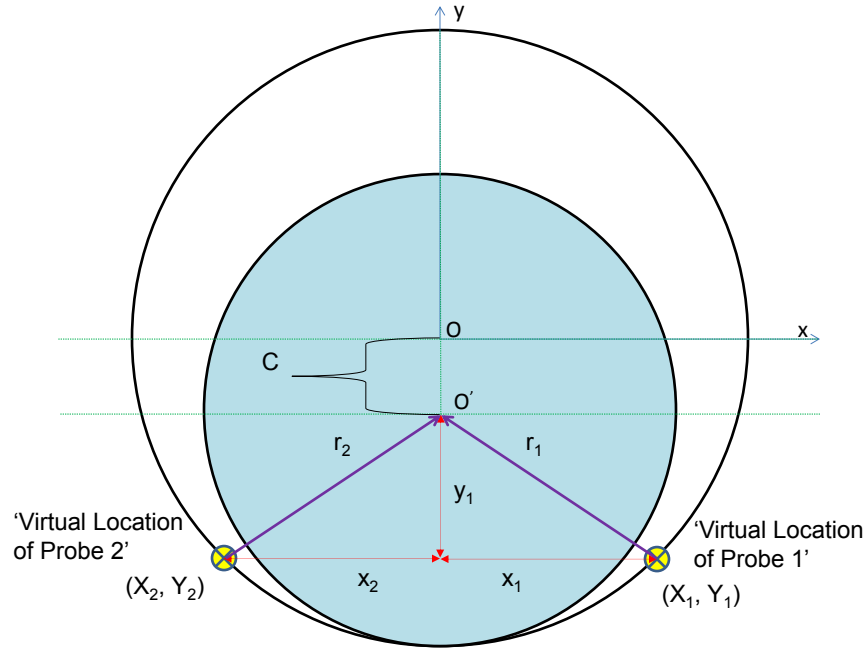
Figure 4-35: Geometry of eddy-current calibration

3. The data from test runs is then processed. The probe voltages that were recorded during the individual test runs are recalled and averaged. In the case of the aft probes these voltages are called 'P_{11}' and 'P_{22}'.

4. The relative difference between the test run and reference distances is calculated by using the difference in voltages. The probes are set up such that a higher voltage indicates a greater distance to the target. In the case of probe 1 this distance, D_1, is calculated as:

$$D_1 = (P_{11} - P_1)/S_8 \qquad (4.37)$$

where S_8 is the sensativity of the probe (127 volts per inch). This value is then

137

used to obtain the actual distance between the probe and the shaft center:

$$R_1 = r_1 + D_1 \qquad (4.38)$$

This is done for the other probe to obtain distance R_2.
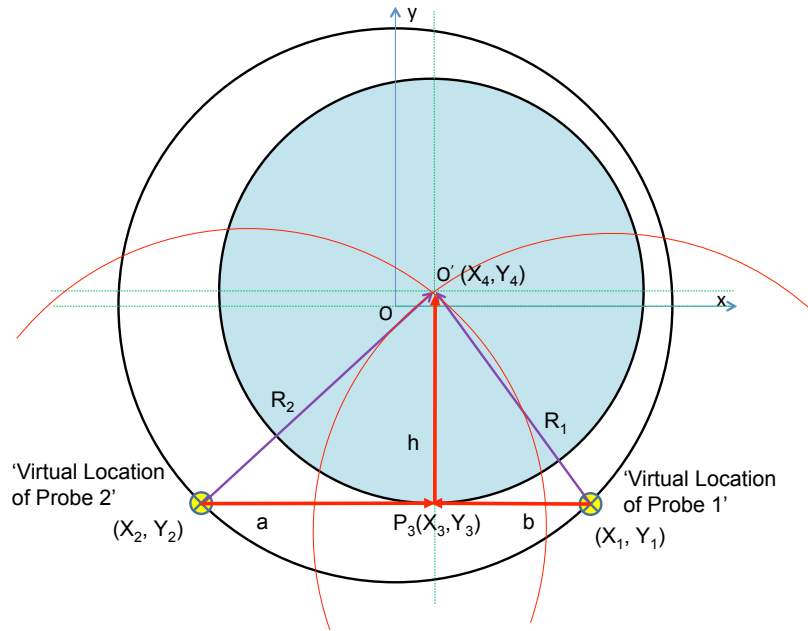
Figure 4-36: Circle-circle intersection for shaft location

5. With known distances from the probes, locating the shaft becomes a problem of finding the intersection of two circles. A representative example is illustrated by Figure 4-36. In this figure the distances between probe and shaft center R_1 and R_2 represent unknown arcs - anywhere on which the shaft center might lie. Because there are two probes there are two intersections of these arcs and there is only one possible intersection due to the shaft being constrained by the bearing. To resolve the location of the shaft center O', consider the two right triangles Probe2-P_3-O' and Probe1-P_3-O' which provides the following

138

relationships:

$$a^2 + h^2 = R_2$$
$$b^2 + h^2 = R_1$$

(4.39)

The distance between probes is also known:

$$a + b = D_{bearing}\sqrt{2}$$

(4.40)

Using equations (4.39) and (4.40) the value of (a) can be found:

$$a = \frac{R_2^2 - R_1^2 + \left(D_{bearing}\sqrt{2}\right)^2}{D_{bearing}2\sqrt{2}}$$

(4.41)

From this both h and X_4 (which is equal to X_3) can be obtained:

$$h = \sqrt{R_2^2 - a^2}$$

(4.42)

$$X_4 = -\frac{D_{bearing}\sqrt{2}}{2} + a$$

(4.43)

and finally Y_4 is found:

$$Y_4 = -\frac{D_{bearing}\sqrt{2}}{2} + h$$

(4.44)

This process is simplified through the use of a MATLAB function 'circcirc' requiring only the inputs of $X_1, Y_1, R_1, X_2, Y_2,$ and R_2.

6. Knowing the coordinates of the shaft location (X_4, Y_4) allows the distance from the bearing center (e), the eccentricity ratio (ϵ), and attitude angle (ϕ) to be determined:

$$e = \sqrt{X_4^2 + Y_4^2}$$

(4.45)

$$\phi = \arctan\left(\frac{X_4}{Y_4}\right)$$

(4.46)

It should be reiterated that this process relies on the assumption that the shaft is located at the BDC of the bearing during calibration. Any deviation from this

assumption will introduce uncertainty in the actual position estimate of the shaft relative to the bearing. This uncertainty can be used to develop error bars on predicted shaft location.

4.5.3   Shaft Tilt

Each pair of eddy-current probes provides information about the shaft location at their axial location on the shaft. When the forward and aft probe locations are combined, the vertical and horizontal tilt of the shaft can be determined using simple geometry. If a profile view is taken of the bearing, as in Figure 4-37, the vertical tilt of the shaft relative to the bearing ($\theta_{tilt-vertical}$) can be found by:
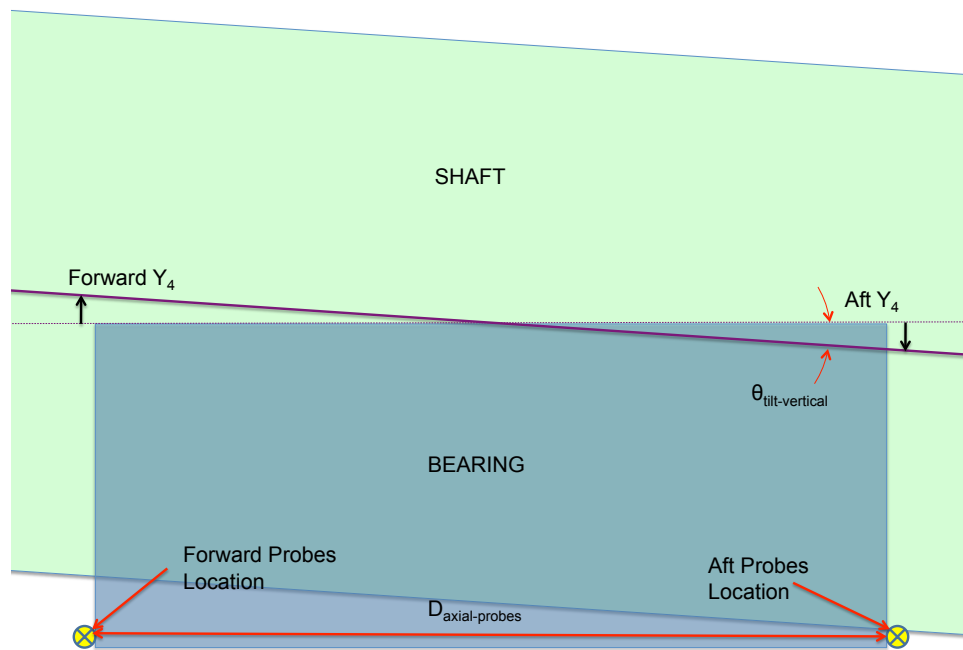
Figure 4-37: Profile view of bearing showing vertical tilt

$$\theta_{tilt-vertical} = \arctan\left(\frac{Y_{4(forward)} - Y_{4(aft)}}{D_{axial-probes}}\right) \tag{4.47}$$

Using a similar process with a plan view of the shaft and bearing, the horizontal tilt ($\theta_{tilt-horizontal}$) can also be determined:

$$\theta_{tilt-horizontal} = \arctan\left(\frac{X_{4(forward)} - X_{4(aft)}}{D_{axial-probes}}\right) \tag{4.48}$$

4.5.4   Calibration Effects

As described in section 4.5.2, calibration data for the eddy-current probes is taken at multiple loading conditions. This is done to account for the combined compression of the bearing material and the deflection of the housing. Although these effects are small, they are measurable and can be accounted for by ensuring that test data is processed with calibration data from a similar projected area load.

As expected, the shaft displacement changes with varying load as it compresses the bearing material. This response is linear over the range of loading conditions that the bearings were tested. Figure 4-38 shows the vertical change in displacement read by the eddy current probes for changes in the projected load of the bearing. The average stiffness of the Turcite bearing material is approximately 42,000 psi projected load per inch displacement for all bearing configurations. The compression of the Turcite is also visco-elastic. An analysis to measure this response was conducted to bound the visco-elastic effect. The change in eddy-current measured displacement was recorded following a rapid increase in projected area loading from zero to 13 psi. After the immediate change in displacement commensurate with the Turcite stiffness, there was a further time-delayed compression of the material of approximately 20 micro-inches. Because this is less than one percent of the gap height, and the nominal resolution of the eddy-current probes is only 8 micro-inch this effect could be considered negligible. Despite this, during calibration and testing runs a settling time was allocated before recording data to account for the visco-elastic effect.

The eddy-current probes have a zero-offset difference when they are in water and in air. This was noticed during side force testing, which occurs with the bearing
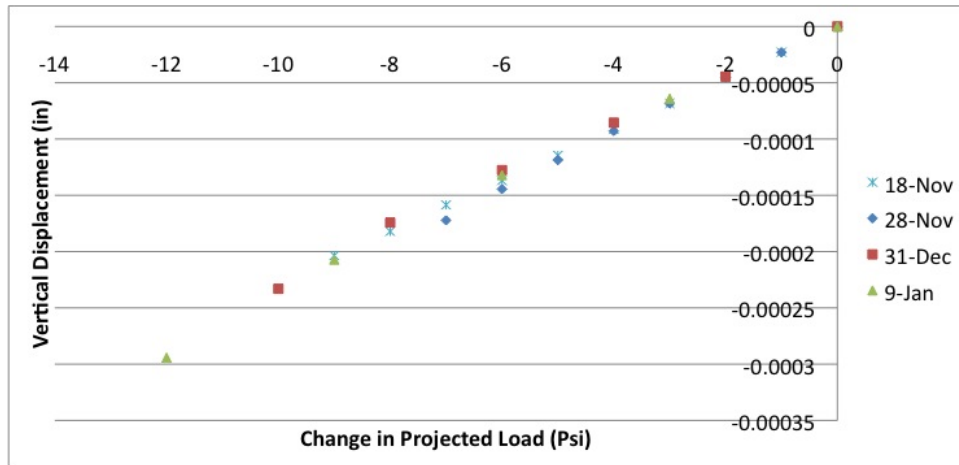
Figure 4-38: Vertical Compression of Bearing due to Changing Loads

not submerged in the tank. The eddy-current probes were initially calibrated with the bearings dry, but when tested with water flowing to the bearing and flowing out between the shaft and eddy-probes an offset of approximately 0.0003 inch was noted. When questioned regarding this, the eddy-current probe vendor indicated that a zero point shift can can occur with the water, but the displacement response (volts/inch) will not be effected.
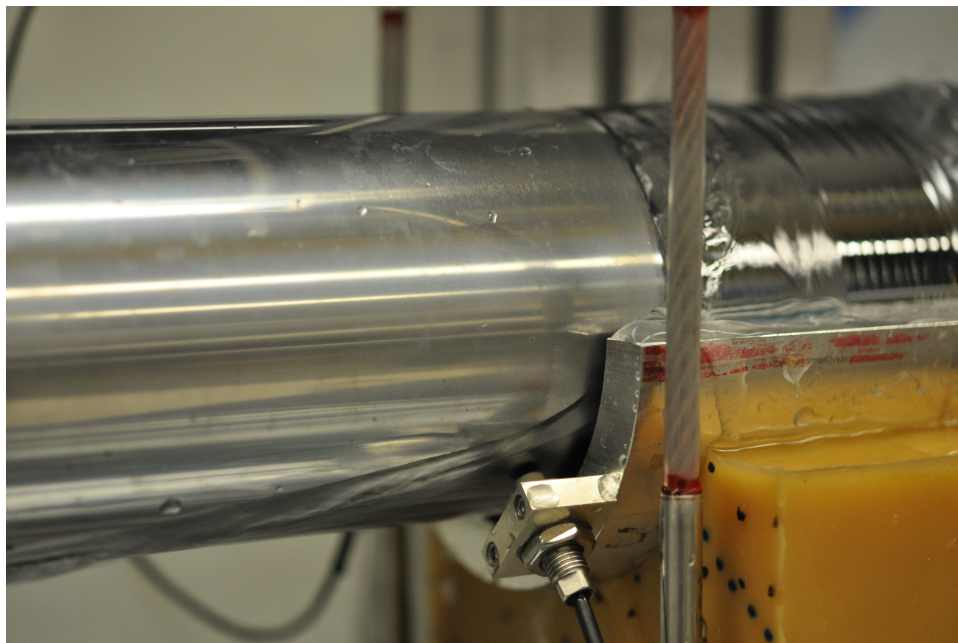
Figure 4-39: Air and water mixture between shaft and eddy probes

To mitigate this phenomena, all eddy-current probe calibrations occur with the bearing submerged in water. This worked in all testing conditions with the exception of side force testing when the bearing was operated in air, but with pressurized fluid supplied to the bearing. In this configuration, some water exiting the axial ends of the bearings flows between the eddy probes and the shaft, but there still exists a small air gap that introduces a small and variable offset to the probes (see Figure 4-39). The magnitude of this offset is extremely small, but does introduce a small amount of uncertainty to the test results based on the manner in which side force testing is conducted.

4.6 Tare Torque
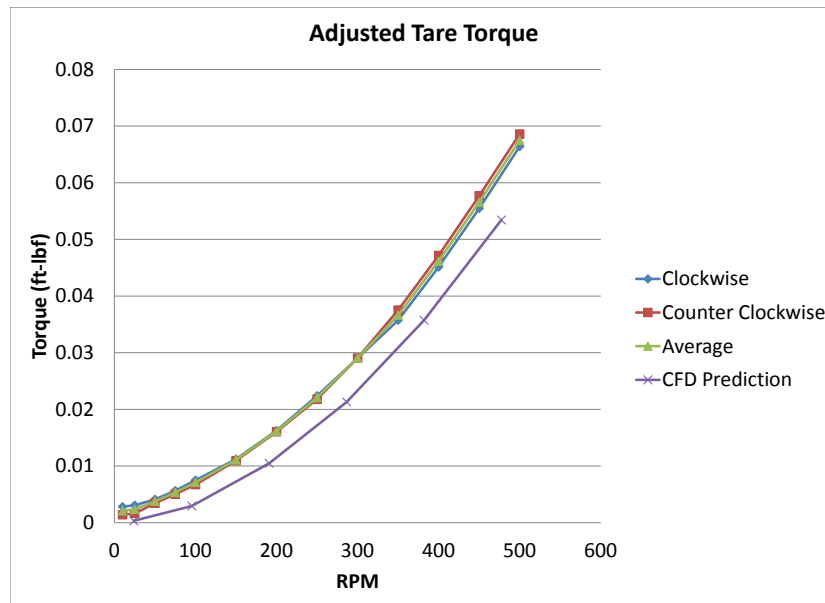
Figure 4-40: Tare Torque of Test Shaft

Due to the virtually frictionless properties of air bearings, there is negligible torque at any speed the test shaft is run, without a test bearing, in air. When submerged into the water, the frictional skin forces created from the shearing forces in the boundary

layer of the water next to the rotating shaft creates a tare torque. This torque is accounted for by subtracting the tare values from the measured torque values with test bearings.

Calculating the friction from the rotating cylinder can not be done in a closed form manner - boundary layer velocity profiles are usually assumed and from this shear stress along the wall can be calculated. The velocity profile and thickness of the layer needs to be experimentally determined and is reliant on velocity of the shaft (dictating Reynolds number and laminar/turbulent regime), fluid viscosity, and the surface roughness of the shaft surface.

Figure 4-40 shows the net measured directional and average tare torque versus shaft speed. Plotted alongside with with the experimental results are Solidworks Flow Simulation CFD predictions based on spinning a 24 inch long cylinder similar to the test shaft in. Although there are differences in results and numerical predictions, the general trends match, lending confidence to the measured results.

Chapter 5

Bearing Manufacturing

5.1 Manufacturing Concept

Because water-lubricated bearings are made of synthetic polymers (in the case of plain journal bearings) or rubber (in the case of stave bearings), it was desired that the bearing material would be a polymer material. Such materials are typically machined (and sometimes cast) to achieve the desired diameter. For non-stave configurations, the bearing material is then affixed to a metallic housing by either a chemical bond such as epoxy, or an interference fit to achieve a 360 degree bearing surface. Interference fits are usually achieved by cooling the bearing material, which has a relatively high thermal coefficient of expansion compared to metals, with dry ice or liquid nitrogen. Coolant grooves, if designed into the bearing, are usually aligned axially and machined on the surface before or after the bearing has been fitted to the housing. The bearing is then ready for an aligned installation into the stern tube of a ship. Final boring of the bearing internal diameter is also sometimes necessary.

The bearings created during this project have two major features that required a unique manufacturing process that is atypical of common ship water-lubricated manufacturing methods:

1. A partial arc (less than 180 degree) configuration.

2. Complex surface groove patterns.

5.1.1 Partial Arc Configuration

Due to the desire to have a bearing design that is capable of an in-water replacement, a partial arc (less than 180 degree wrap) is a requirement. Such a configuration allows the bearing to be removed without the need to pull the tailshaft, which would require drydocking of the vessel. This means that a split bearing configuration is needed, but this introduces difficulties in the manufacturing process for bearings. The first complication is that the use of an interference fit is no longer feasible, because with a less than 180 degree arc of the bearing there would be a tendency for the bearing to 'pop' out of the housing. This results in the need for some form of chemical bonding (such as epoxy) to fuse the synthetic bearing material to the metal housing.

The second issue with a partial arc configuration involves the potentially unpredictable form errors that can result when a bearing that was machined in a 360 degree configuration is split into two pieces. These form errors are a result of residual stresses that exist in the materials. Because of this, a bearing that has satisfactory circularity in a 360 degree configuration might spring to a shape that is unsatisfactory. This effect can be present in both the bearing material as well as the metallic housing. Because of this even a precision machined bearing housing may be warped once it is split and result in a distortion of the bearing face.

Experiments were conducted to quantify the effect that splitting a tube has on dimensional accuracy and form error. A pair of 3.5 inch internal diameter (ID)/4.5 inch outer diameter (OD) aluminum 6061 T651 extruded tubes were measured with a Coordinate Measuring Machine (CMM - described in section 5.3.1) in the unsplit condition, split in half using a vertical bandsaw, and then measured again. The tube sections were approximately 7.5 inches in length and the split sections ended up being housing sections for bearings created for this project. 6061 T651 aluminum is strain relieved as part of the forming process. By using such material, the actual spring in
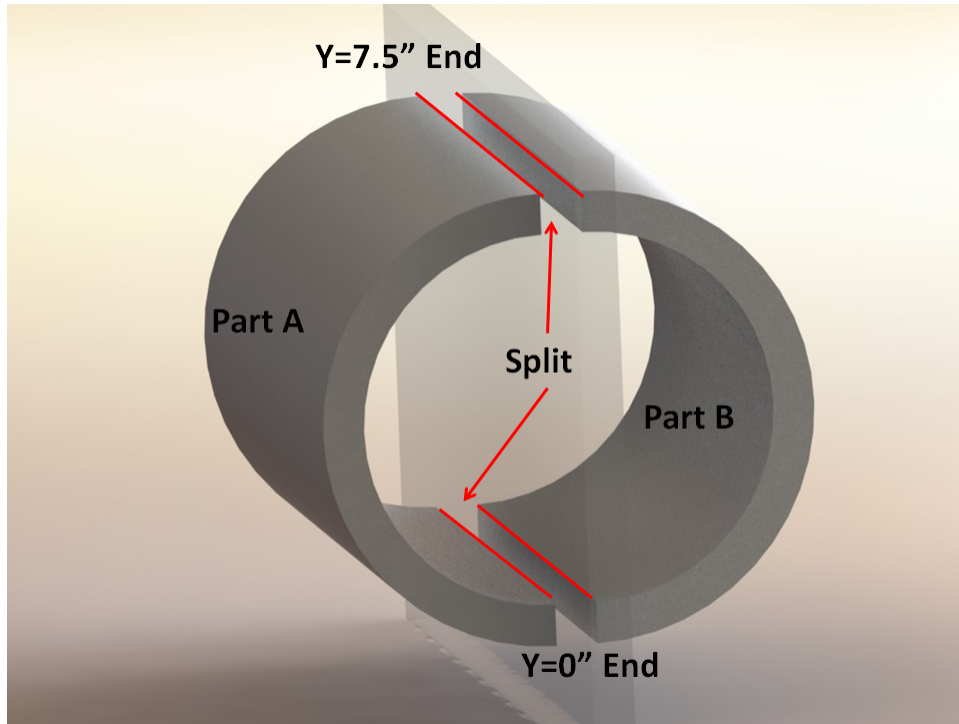
Figure 5-1: Conceptual Split Aluminum Tube

the metal that occurs from splitting it should be minimized. Figure 5-1 shows the configuration of the tubes and how they were split.

The effects of splitting the tubes are provided in Table 5.1. These measurements are from as extruded tubes that were not ID bored. Although boring the ID would reduce the pre-split form errors and introduce additional stresses in the material, the spring of the metal after splitting should be similar. The magnitude of the change in diameter and roundness is dependent on the orientation of the split relative to the existing form error. In all cases that were measured, the form error improves, but is unacceptable nonetheless. This is because even if diameter can be controlled, roundness errors are of similar magnitude to the clearance gaps used in the bearings. An example of the resulting spring in the metal is shown in Figure 5-2. The full results of the runs are provided in appendix D.

To address the issues with the dimensional accuracy of a split housing, the concept of

147

Table 5.1: Geometric Accuracy and Form Error of ID for Split Tubes (inches)

Housing	Piece	y = 0.0" End Diameter	Roundness	y=7.5" End Diameter	Roundness
1	Full Tube	3.4936	0.0028	3.4935	0.0065
1	Part A	3.4887	0.0018	3.4806	0.0031
1	Part B	3.4896	0.0016	3.4825	0.0016
2	Full Tube	3.4929	0.0022	3.4917	0.0051
2	Part A	3.4928	0.0012	3.4961	0.0023
2	Part B	3.4935	0.0022	3.4959	0.0016
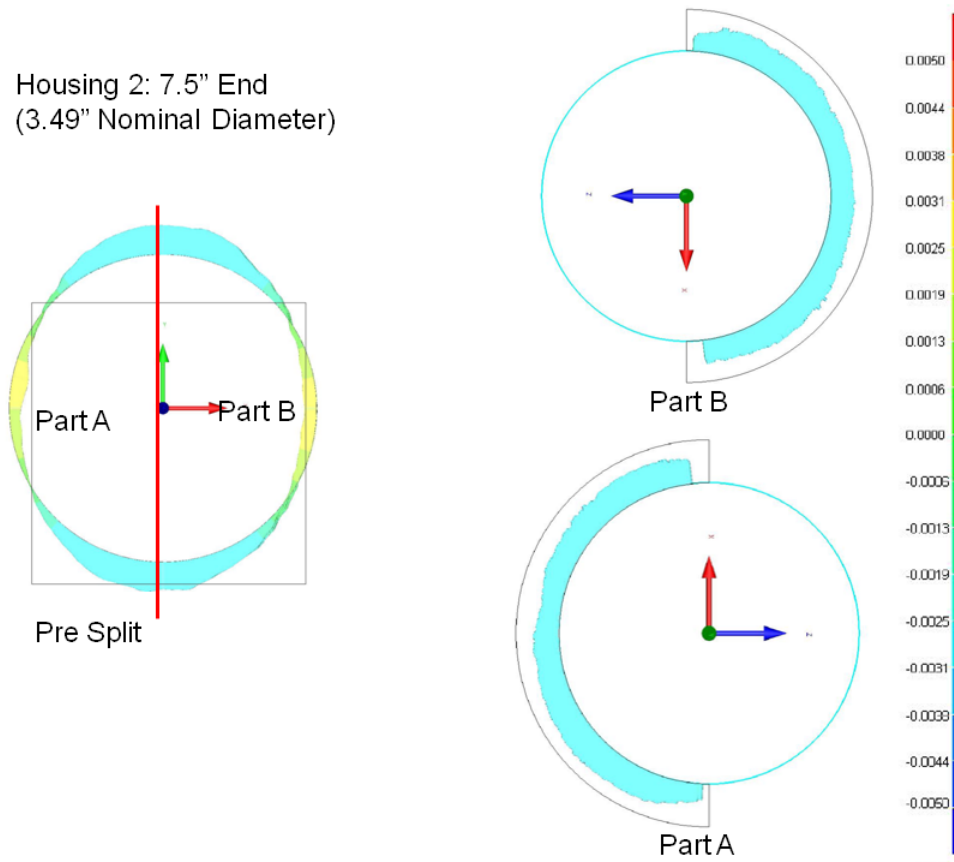
Figure 5-2: Spring Effect on Split Aluminum Tube

potting the bearing into the housing using epoxy is used. If bearing material with a dimensionally acceptable ID is created, an epoxy layer between the OD of the bearing material and the ID of the bearing housing allows the epoxy to account for variations in the housing and provides means of bonding the two pieces without the introduction of stresses from an interference or mechanical fit.

5.1.2   Complex Surface Grooves
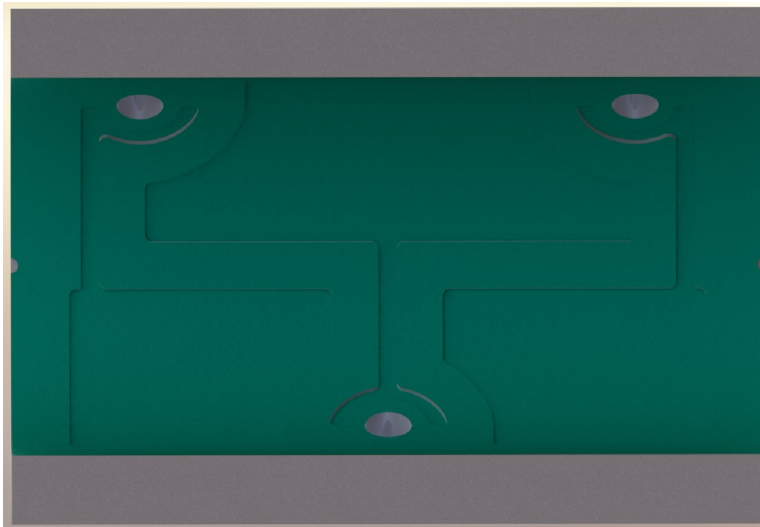
Figure 5-3: Concept Rendering of Hybrid Bearing

Many of the bearings designed and built for this project have complex features that are not easily machined in a cylindrical surface. An example of one of the bearings fabricated is shown in Figure 5-3. Machining the grooves and recesses in a cylindrical bearing requires expensive machinery capable of 4 or 5 axis control. One potential method would be using a CNC mill after the ID has been bored on a lathe or cast to shape. This requires separate machines and fixtures to create the needed features. An alternative method would be to add articulating live mill tooling to a vertical lathe (mill turn machine) to get the additional axis control needed. Such a method would allow the ID to be bored and the surface features milled on one machine. There are several additional complications that can arise with manufacturing in this method. First, the live tooling or milling head would have to fit within the bore of the bearing.

Secondly, boring operations should be done vertically to eliminate an excessive over-hang for long bearings if fixtured at one end of a bearing in a horizontal lathe. Lastly, because full scale bearing sizes can be on the order of 30 inches (or even larger) any machine using such a method will have to be extremely large. Exact cost estimates of such a custom machine are unknown, but could easily reach millions of dollars. No machines at MIT that are capable of performing these tasks were available for use to manufacture these types of bearings, so this process was not a option.

An alternative manufacturing method would be to cast the bearing material into the desired shape. Such a process would require the fabrication of a shaft with protrusions corresponding to the location of the desired grooves and recesses to serve as a face for the mold. Machining a shaft such as this would be costly, but for a class of vessels that will have multiple bearings produced of the same dimensions, this could be quite feasible. This method would not be cost effective for unique custom bearings where only one is built. For this reason this process was not used for this project.

5.1.3 Novel Manufacturing Concept
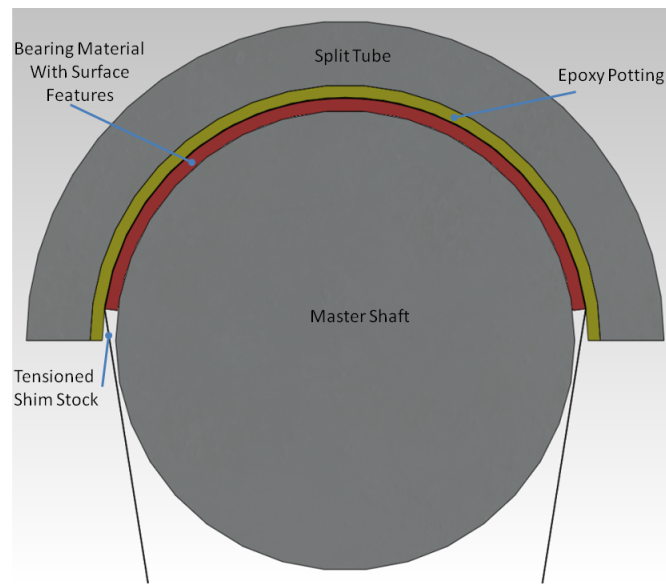
Figure 5-4: Original Manufacturing Concept

Multiple bearings of different surface topologies had to be created for this project. To allow for timely and cost effective fabrication of these bearings a novel bearing manufacturing process was conceived and developed that addresses the two major difficulties outlined above. The basic process is illustrated in Figure 5-4. The original procedural steps in the concept are as follows:

1. The grooves and recesses that make up the hydrostatic surface features are cut into the bearing material (originally Ultra High Molecular Weight Polyethylene) while in a flat configuration. This allows the complex features to be milled into the surface by utilizing a 3 axis CNC machine.

2. The bearing material is then adhesively bonded to aluminum shim stock.

3. The shim stock is tensioned around a pre-built master shaft. The master shaft has a diameter greater than that of the test shaft. The difference in diameters is used to set the diametrical clearance in the bearing. The master shaft and tensioned bearing are then heated in an oven to form the bearing around the shaft.

4. An aluminum tube is bored out to set a nominal epoxy thickness and then split in half.

5. The tensioned bearing material and master shaft are then set into the split aluminum tube with the gap between the two filled with epoxy.

6. The shim stock is cut and the master shaft removed from the bearing. Excess epoxy at the circumferential and axial ends of the bearings is then milled away.

7. Locating holes for inlet fluid and pressure taps are drilled from the inside surfaces of the bearings and then fitting threads are drilled and tapped from the back of the housing.

This process allows for readily available machinery at MIT (or other locations) to perform the very few precision machining steps required to make the bearings. Inherent form errors in the bearing housings become irrelevant by having the epoxy

layer fill in the peaks and valleys of the housing surface. This original concept was not without its own problems, which came to light as attempts to create satisfactory bearings were made. Although the process evolved over several iterations with certain steps added or removed, and some materials changed, the basic concept remained the same.

5.2   Development of Manufacturing Process

5.2.1   Ultra High Molecular Weight (UHMW) Polyethylene (PE) Bearings

Partial arc journal bearings were originally created without hydrostatic features cut into the bearing material. The reason for this was to prove out the manufacturing processes that would be used for future bearings and to allow for the testing of a plain journal bearing. Doing so provided a baseline bearing for comparison and allowed for troubleshooting of the test rig.

Ultra High Molecular Weight (UHMW) Polyethylene (PE) was the original choice for bearing material. This was due to several reasons. It is readily available, and also has several properties that make it advantageous for water lubricated bearings such as a low dry coefficient of friction, high abrasion resistance and a very low affinity for absorption of water.

5.2.1.1   PE-1

Bearing PE-1 was the first attempt to manufacture an UHMW PE bearing potted with epoxy. The 0.093" PE had adhesive backing for a total nominal thickness of 0.1". This material was affixed to 0.002" stainless steel shim stock in a flat condition. The aluminum master shaft was then suspended in the bearing, placed in an oven and heated to 130°C for a period of eight hours , which is slightly below the melting temperature of 138°C and within the recommended forming temperature. This

allowed the PE to form itself around the master shaft as the material became compliant at the elevated temperatures[1]. The material was then slowly cooled to ambient temperature, taking the shape of the master shaft. This material was then potted into a partial arc aluminum housing using DWH 316 putty epoxy.[2]

DWH series epoxy is typically used for static fits in machine assemblies and bonds well to metals. The consistency of the putty also allowed for the epoxy to stick to the walls of the aluminum when prepping the housing for the bearing material. These attributes made it a viable choice as an epoxy material. The recommended thickness of the DWH 316 putty is 0.060 to 0.125". Based on this range, a design thickness of 0.08" was selected. Because the aluminum housing material is a 6061 T651 Aluminum tube extrusion of 3.5"ID and 4.5"OD, the tube had to be bored out to increase the ID to 3.5985" per Table 5.2. This was done on a HAAS CNC lathe (shown in Figure 5-5). The tube was then split in half on a vertical band saw and finally prepped in a milling machine by fabricating longitudinal slots to allow for the epoxy to lock into the housing.

Table 5.2: Calculation of Required Housing ID for Bearing PE-1

Shaft Diameter	3.2305	inches
Shaft Radius	1.6153	inches
Radial Gap	+0.0020	inches
Shim Stock Thickness	+0.0020	inches
Epoxy Thickness	+0.0800	inches
UHMW Thickness	+0.1000	inches
Required Housing Radius	1.7993	inches
Required Housing ID	3.5985	inches

Bearing PE-1 had two major flaws. The first was that the shim stock easily delaminated from the epoxy. Although the DWH epoxy is designed to bond to metal, the

---

[1]The first master shaft had a clearance ratio of approximately 800:1. This bearing clearance is fairly close to the thumb rule of 1000:1 for hydrodynamic bearings, but is a much smaller clearance than typical for water lubricated bearings. Section 7.1 provides more discussion of the effects of bearing clearance.

[2]DWH 316 epoxy is from Devitt Machinery Co. (www.moglice.com)

Figure 5-5: Boring ID of Aluminum Housing on HAAS CNC Lathe

surface finish of the shim stock was too smooth to achieve a satisfactory bond. This failure is shown in Figure 5-6. The epoxy did not appear to have any problems bonding to the aluminum housing, with the longitudinal slits in the housing providing recesses for the epoxy to lock into. Another contributing factor aiding the housing/epoxy bond was that chatter was experienced in the boring bar of the lathe during the final cut, which degraded the surface finish of the housing. This roughened surface finish helped provide a good bonding surface to which the epoxy could adhere to. These features in the housing are shown in Figure 5-7.

The second major flaw occurred because simply using the weight of the suspended master shaft to wrap the UHMW PE bearing material around the shaft proved insufficient to achieve a good form of the bearing. This issue was noted when the master shaft was concentric with the bearing material. The amount of form error was not quantitatively measured because the bearing was peeled from the epoxy before this could occur. The form error was visible to the naked eye however - indicating a flawed

manufacturing process.

<div align="center">(a)   (b)   (c)</div>
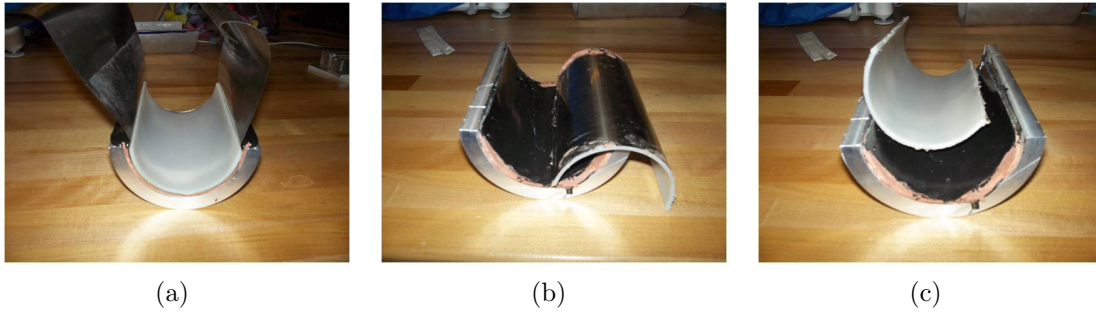
Figure 5-6: Delamination Failure of Bearing PE-1
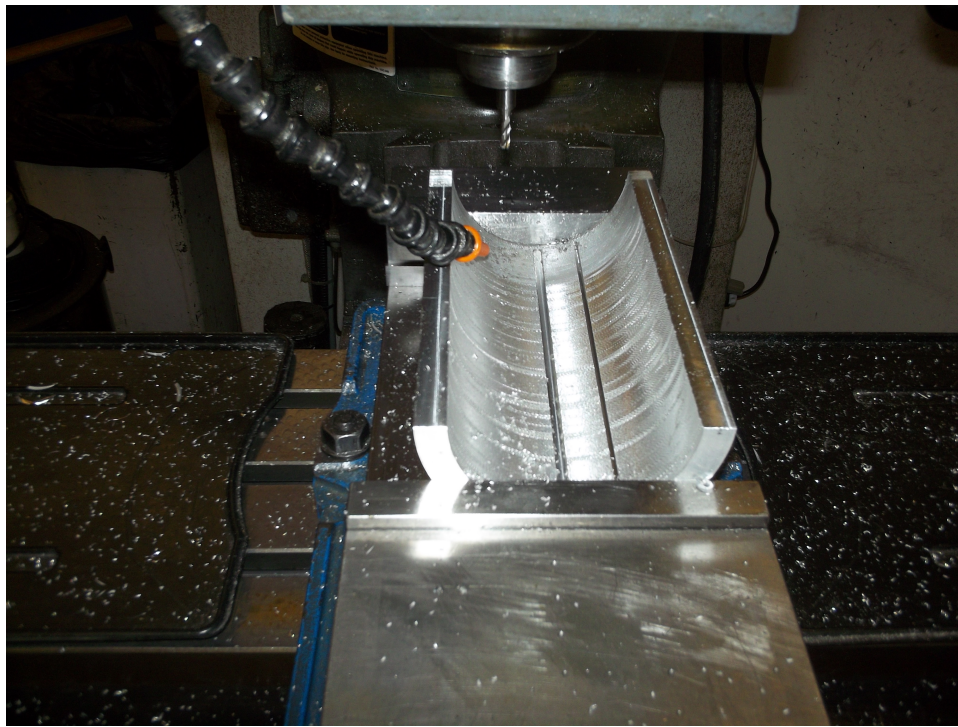
Figure 5-7: Cutting Longitudinal Slits into Housing

5.2.1.2   PE-2

To resolve the form error problem a tensioning device was created to allow for more directed force in shaping the bearing material around the master shaft. The device, shown in Figure 5-8, wraps the intermediate layer (in this case the shim stock) around a tensioning shaft to provide a large circumferential force pulling the the bearing material tight to the master shaft. The apparatus utilizes an aluminum shaft with a slit

in the middle of it, which allows the intermediate layer to pass through it, then get wrapped around the tensioning shaft to generate the force on the bearing material. A ratchet and pawl mechanism locks the shaft into place once tightened with a socket or wrench. The 0.10" wide slit in the aluminum shaft was created using a waterjet and the ratchet gear was affixed to the shaft by an interference fit[3].

(a) Tensioner design with top plate removed (b) Tensioner on PE-2 bearing in oven
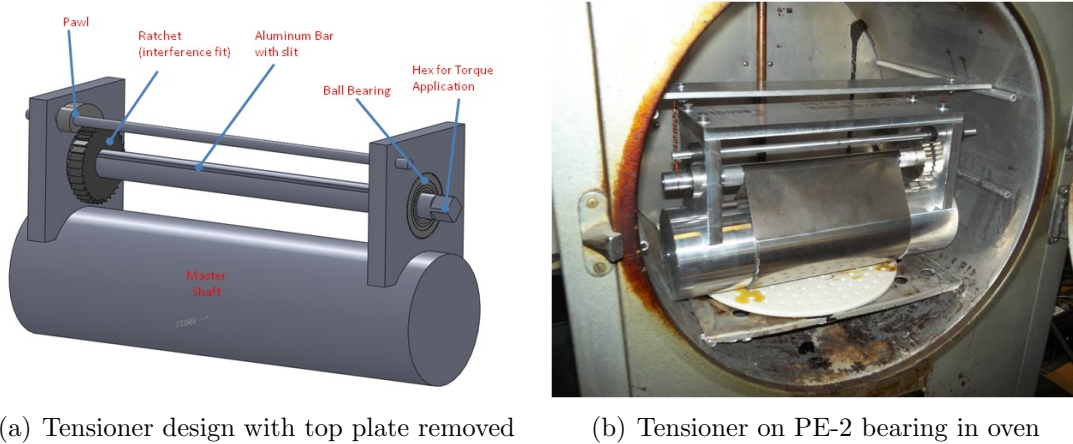
Figure 5-8: Tensioning Device

Bearing PE-2 attempted to fix the delamination of the shim stock from the epoxy by prepping the exterior side of the shim stock with 36 grit aluminum oxide sanding paper to roughen the finish to achieve a satisfactory bonding surface (shown in Figure 5-9). All other manufacturing processes were identical to bearing PE-1. The additional prepping did provide a stronger bond between the epoxy and shim stock, but the bearing material was still able to be peeled from the housing by hand.

5.2.1.3   PE-3

Due to the inability to achieve a satisfactory bond between the epoxy and shim stock even with a roughened surface finish, a more effective solution was needed. The decision to utilize wire mesh in lieu of shim stock as the intermediate layer between bearing material and epoxy was made, the theory being that the epoxy would flow

---

[3]The interference fit was achieved by cooling the shaft in liquid nitrogen and heating the ratchet gear to 200 °C.
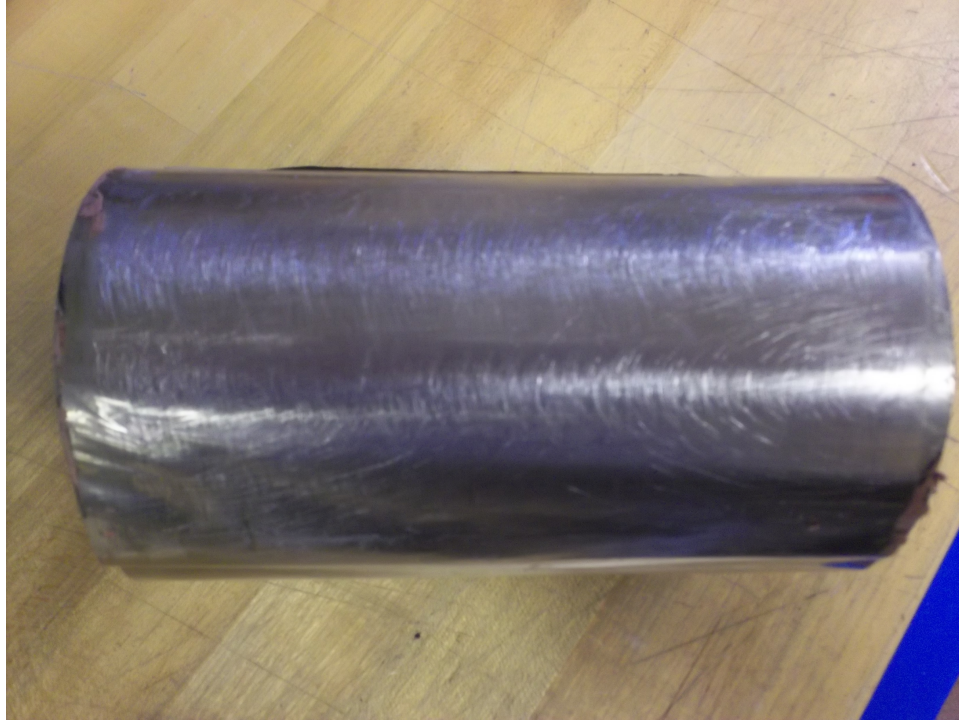
Figure 5-9: Outer layer of shim stock after sanding with 36 Grit Sandpaper

through the mesh and adhere to the adhesive backing on the UHMW PE. A series of tests were conducted on 3/4" x 3/4" coupon samples to test the difference in shear strength as a function of various wire mesh sizes (ranging from 30 to 150 squares per inch) and two different epoxies (DWH 316 Putty and LOCTITE Metal/Concrete Epoxy). These tests utilized an ADMET eXpert 5600 series single column universal testing machine with an 1000 pound capacity load cell. A plot of results is provided in Figure 5-10.

For all samples, regardless of the wire mesh size or epoxy type, the limiting component turned out to be the bond between the UHMW PE and the adhesive backing. It was noted that the adhesive backing was separating from the PE during failure for all samples. Although this trait did not allow the full strength of the epoxy bond to be utilized, it did provide adequate margin against the bearing material shearing from the epoxy. From the equation for torque:
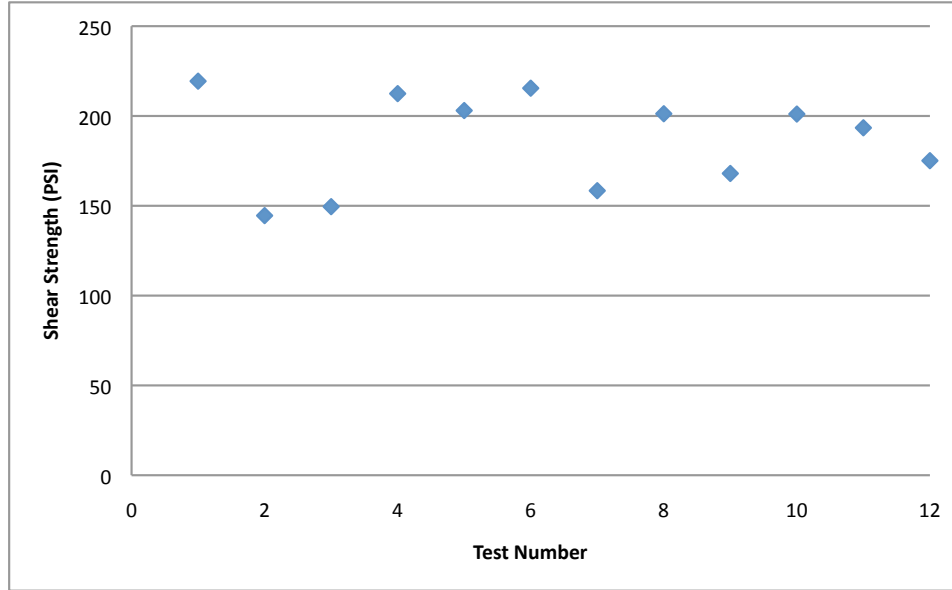
Figure 5-10: Shear Strength of Epoxies

$$Torque = fWr = F_{tan}r \qquad (5.1)$$

where f is the friction coefficient, W is bearing load, r is bearing radius, and F_{tan} is tangential force. The projected area load (P) is a function of W, bearing diameter (D) and bearing Length (L):

$$P = \frac{W}{LD} \qquad (5.2)$$

The definition of shear stress (τ) in the bearing can be defined as:

$$\tau = \frac{F_{tan}}{\pi LD} \qquad (5.3)$$

Rearranging and substituting the relationships in equations (5.1) and (5.2) into equation (5.3) yields:

$$\tau = \frac{fP}{\pi} \qquad (5.4)$$

Using a maximum friction coefficient of 0.2 (corresponding to UHMW PE on mild steel) and a typical water-lubricated bearing value of 40 psi projected area load, the

UHMW PE adhesive backing strength provides ample shear strength as shown in Table 5.3.

Table 5.3: Required Shear Stress for Epoxy Bond

Shaft Diameter	3.2305	inches
Radius	1.6153	inches
L/D Ratio	2	
Projected Area Load	40	psi
Projected Area	20.9	in^2
Bearing Load	834.9	lb$_f$
Friction Coefficient	0.2	
Torque	269.7	in-lb$_f$
Tangential Force	167	lb$_f$
Circumferential Shear Area	65.6	in^2
Required Shear Stress	2.55	psi
Minimum Tested Shear Stress	144.5	psi
Average Tested Shear Stress	186.8	psi

Type 304 Stainless steel mesh of size 70 x 70 squares per inch with a wire diameter of 0.0065" and overall thickness of 0.013" was selected for use on bearing PE-3. Since the mesh size had no discernible effect on the bonding strength of the adhesive backing on the UHMW PE, the size 70 mesh provided adequate flexibility and a relatively large opening between the wires of 0.0078" for the epoxy to flow through. The manufacturing process was similar to bearing PE-2 utilizing the tensioning device, heat treatment to 130°, and potting into a split tube aluminum housing. Figure 5-11 shows the schematic layout of the bearing.

No flaws were initially seen in bearing PE-3. The bearing was installed into the test rig and tests were done up to 300 RPM and projected area loadings of up to 4.7 psi when it quickly became clear that there was a fundamental problem with the bearing's performance. Since the bearing was a plain journal bearing of ≈180 degree arc, the performance was checked against the theoretical prediction utilizing the standard methodology of Raimondi and Boyd [23]. The abnormally high torque values are illustrated by Figure 5-12. Not only was the measure torque much higher than anticipated, but the bearing did not display expected trends.
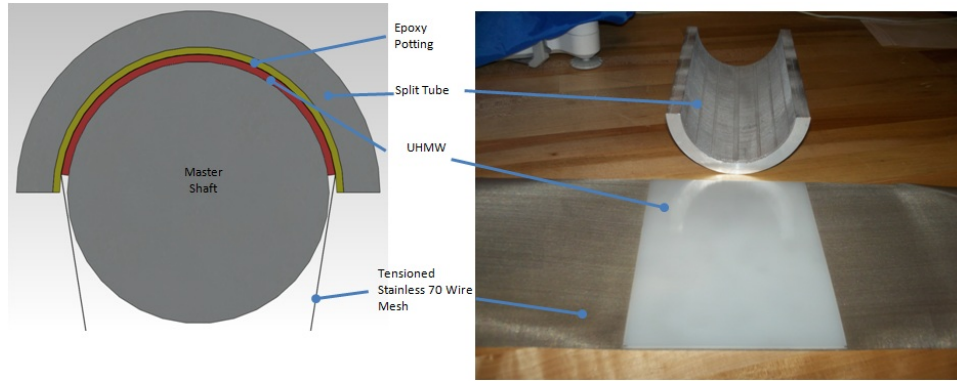
Figure 5-11: Construction details of bearing PE-3
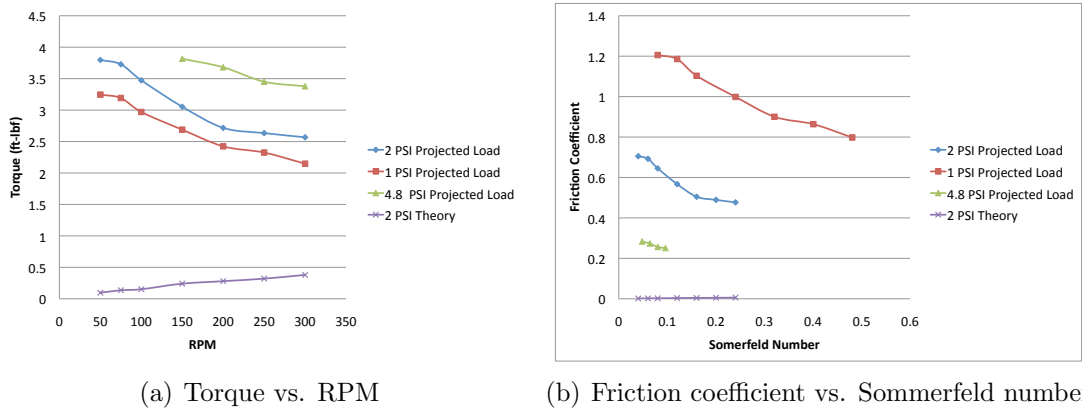
(a) Torque vs. RPM

(b) Friction coefficient vs. Sommerfeld number

Figure 5-12: Torque measurements of bearing PE-3

Testing was halted and the cause of the unexpected results was investigated. When the bearing was removed from the test cradle and applied to the shaft by hand in water, very high torque was observed even without an applied load. Furthermore, the bearing had a 'suction' effect where once the shaft had been rotated, the bearing stuck to the shaft and required a relatively large force to remove it. Bearing PE-3 was taken to Methods Machine Tools in Sudbury, Ma to be measured on a Zeiss Contura CMM to aid in determining the root cause of the performance issue. The form error's in bearing PE-3 turned out to be much worse than expected. Figure 5-13 shows a visual representation of the form error in the bearing. It is clear that a 'valley' was present in the bearing, where the bottom of the bearing was deeper than the intended cylindrical shape and the sides of the bearing (-90 and +90 degrees from

160

TDC) were 'pinched' in. In total bearing PE-3 had a cylindricity error of 0.0058" - completely unacceptable considering the nominal radial bearing gap was only 0.002". It is theorized that the valley and pinching in of the sides created a seal on the shaft and was the cause of the suction effect.
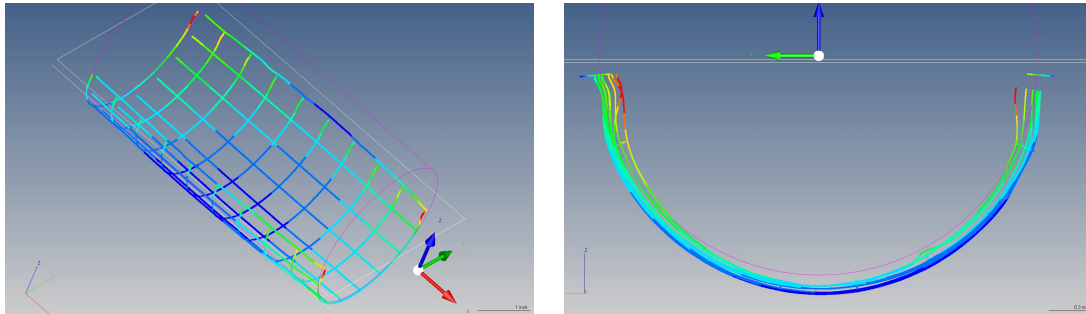
(a) Orthogonal view of form error in bearing PE-3

(b) Axial view of form error in bearing PE-3

Figure 5-13: Visual form error in bearing PE-3

5.2.1.4 Temperature Related Problems

A major manufacturing deficiency was identified by examining bearing PE-3 and the processes making it. It became clear that the UHMW PE had a springing issue with it after being heated to elevated temperature. This was indicative of the material still having residual stresses after being heated into a cylindrical shape. To address this issue, several potential solutions were investigated.

1. **Experimentation with heating and cooling cycles.**

   Attempts to reduce the stresses in the PE were done by heating the material to a higher temperature of 135°C (slightly below the UHMW PE melting temperature of 138°C), decreasing the heatup and cooldown rates, and maintaining a longer 'soak time' at elevated temperature. Despite these experiments, the PE response was still unpredictable appearing to be not only dependent on the heat/cooldown cycle, but also the orientation of the PE relative to the extrusion direction and proximity to the edges. For some samples the PE would spring in, while on others it would spring out. Figure 5-14 shows the spring effect in the

161

PE after a 36 hour soak on the tensioned master shaft at a 135°C temperature.

(a) UHMW PE 5 minutes after removal from master shaft

(b) UHMW PE 24 hours after removal from master shaft

Figure 5-14: Spring Effect in UHMW PE

An additional undesirable effect of the elevated temperatures was the failure of the adhesive backing to the PE. The failure mode ranged from delamination of the adhesive backing from the PE (Figure 5-15(a)) to the complete hardening of the adhesive and the loss of all capability to bond to the wire mesh (Figure 5-15(b)).
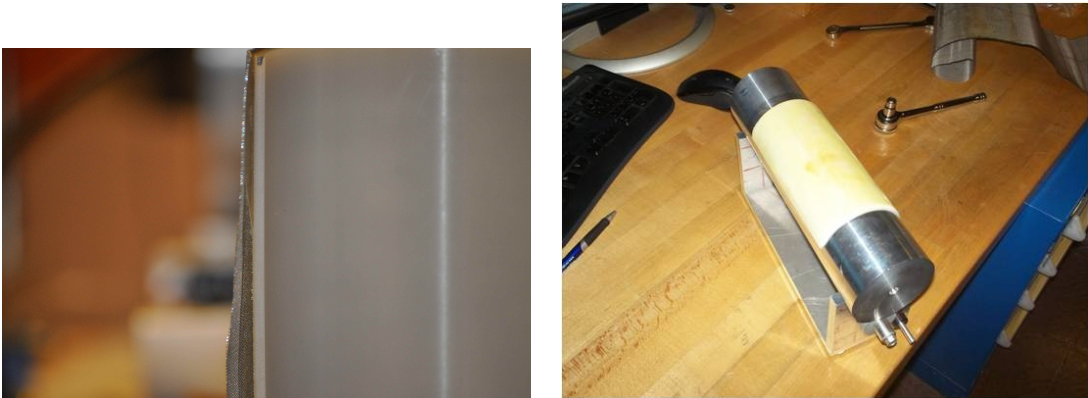
(a) Delamination of Adhesive Backing

(b) Hardening of Adhesive Backing

Figure 5-15: Failure of Adhesive Backing on UHMW PE

The use of adhesive backing on the UHMW PE was made because of the difficulty in achieving a chemical bond with PE. By using PE with an adhesive
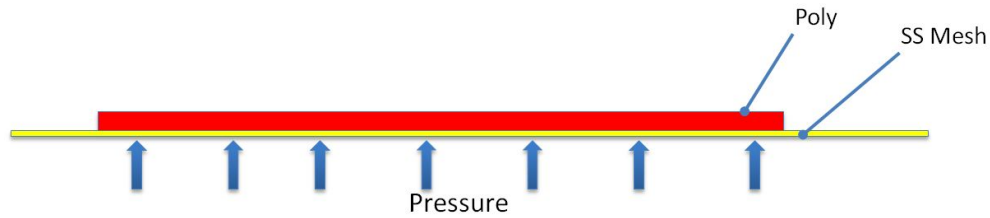
(a) Non-Adhesive UHMW PE Concept

(b) Test Strips on Shaft

(c) Test Strips

Figure 5-16: Non-Adhesive UHMW PE Testing

already applied to it, a difficult step in the bearing manufacturing process could be avoided. An attempt to take non-adhesive backed UHMW PE heated close to melting temperature and 'fuse' course wire mesh by having the mesh flow into the poly was done. The concept and pictures of the test are shown in Figure 5-16. Despite significant tension to force the wire mesh into the PE, the screen was easily peeled from the material after cooling.

2. Cold-Molding of UHMW PE.

Because of the unpredictable spring that occurs in the PE and the degradation of the adhesive, a process where the UHMW was forcibly wrapped around the master shaft without application of heating to relieve residual stresses was attempted. The theory was that although the PE would want to spring outward to regain its original flat form, the aluminum housing and epoxy would resist it. This would result in a slightly elliptically shaped bearing. The mag-

nitude of this effect would be a result of the stiffness of the UHMW PE and the aluminum housing. There are many elliptically shaped hydrodynamic bearing designs (often called 'lemon' bearings), so an outward spring should provide better performance than the completely unacceptable performance of an inward spring.

Since UHMW PE is fairly stiff at room temperature, the cold-molding concept requires a large tension force on the wire mesh to tightly wrap the bearing material around the master shaft. This force is imparted by the tensioning mechanism, which led to concerns over the stiffness of the tensioning shaft. The original tension shaft was made out of aluminum, which has approximately 1/3rd the elastic modulus of steel and therefore would deflect approximately 3 times as much as steel. Examination of Figure 5-13 suggests that a possible cause of the 'valley' along the bottom dead center (BDC) of the bearing is likely due to uneven tension force along the axial length of the wire mesh. A 304 stainless steel shaft was fabricated to replace the aluminum tension shaft. As with the aluminum shaft, an interference fit was used to attach the ratchet gear to the shaft and the slot for the wire mesh was created by a waterjet.

The impact that the tension force of the wire mesh had on the deflection of the tension shaft was analyzed. Figure 5-17 shows the geometry of the wire mesh around the master and tensioning shafts. On subsequent bearings, the average torque required to tension the bearing material around the master shaft was 15 Newton-meters (133 in-lb$_f$). With the tensioning shaft diameter of 0.75", this results in a tangential tension force of 354 lb$_f$ on the wire mesh. Assuming that the horizontal force in the two sides of the tensioned wire mesh must cancel, the tension forces in each side of the mesh can be found. These are 139 lb$_f$ for the left (44.4 degree) side and 215 lb$_f$ for the right (62.5 degree) side. This results in a total vertical force of 288 lb$_f$ pulling the bearing material up (and
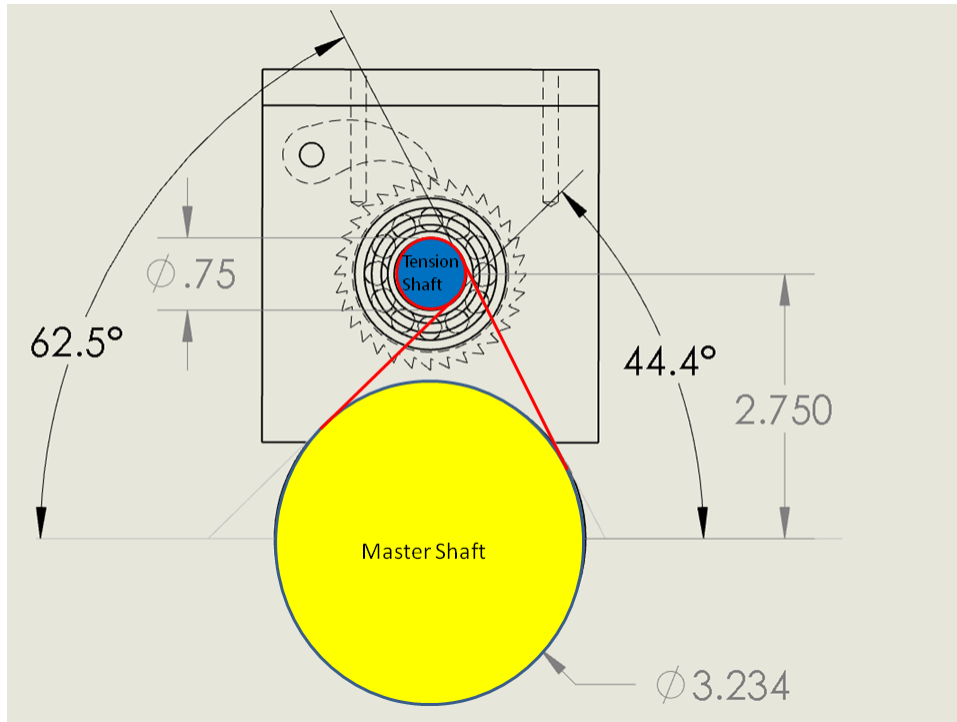
Figure 5-17: Geometry of Tensioning Device

the tension shaft down).

This vertical force acts on the center 7 inches of the tensioning shaft for a distributed load of 41.1 lb$_f$/in, which is supported by ball bearings spaced 9.5" from each other. This simply supported structure is illustrated in Figure 5-18 and equations for the deflection of such a structure can be analytically determined using simple beam theory, applying superposition and readily available beam deflection formulas. A variables that alters the response of the tensioning shaft is the orientation of the slot since this changes the moment of inertia. In addition to the analytic calculations, FEA was done on the shafts for both 304 stainless steel and 6061 T6 aluminum with the slit oriented vertically and horizontally. The FEA deflection results for an aluminum shaft with the shaft oriented vertically is shown in Figure 5-19.

As expected, the aluminum shaft deflects approximately 3 times as much as the
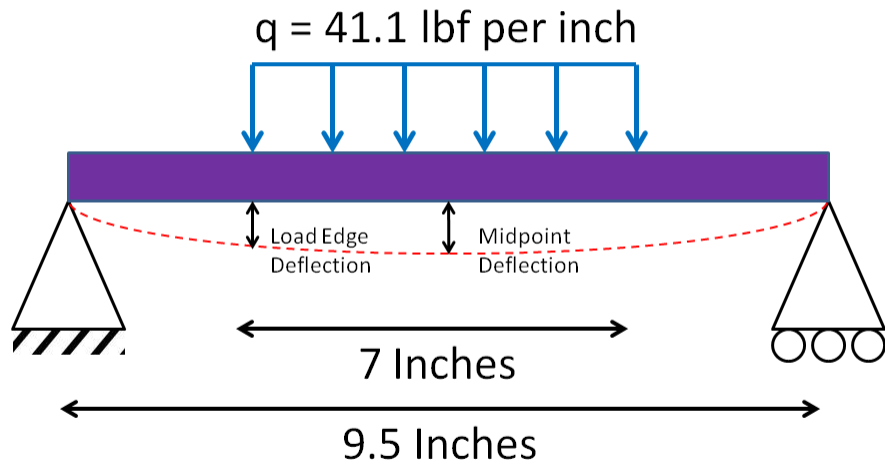
Figure 5-18: Geometry of Tensioning Device
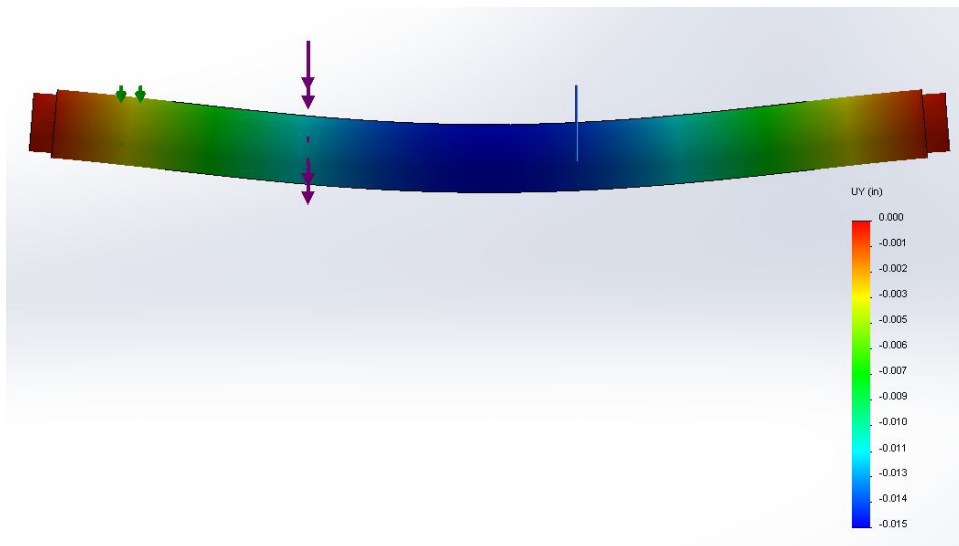
Figure 5-19: FEA Deflection for Aluminum Tensioning Shaft

steel shaft. Overall differences in deflections within the slit are on the order of 0.015 inches for the aluminum shaft and 0.005" for the steel shaft. Although this deflection is of the same order of magnitude as the bearing gaps, the wire mesh provides an elastic averaging effect that accounts for the deflection in the shaft. The expected elongation of the 30x30 wire mesh assuming a uniform load distribution is on the order of the deflection of the shaft. The use of a stiffer mesh composed of thicker wire strands or a higher density weave would reduce the ability of the mesh to ensure proper tensioning of the bearing material to the master shaft. The 30x30 mesh size provided a suitable compromise between being flexible and allowing enough open area for the epoxy to reach the back side of the bearing material. The average deflections predicted by analytical calculations and FEA, as well as the predicted wire mesh elongations are provided in Table 5.4

Table 5.4: Average Tension Shaft Deflection Calculations (inches)

	Aluminum (6061 T6)	Stainless Steel (304)
Analytic Calculations:		
Midpoint Deflection	0.0294	0.0105
Load Edge Deflection	0.0111	0.0040
Difference	0.0183	0.0065
FEA Results:		
Midpoint Deflection	0.0185	0.0065
Load Edge Deflection	0.0050	0.0020
Difference	0.0135	0.0045
Predicted Mesh Stretch:		
30x30 Mesh	0.0096	0.0096
70x70 Mesh	0.0041	0.0041

3. **Alternative Materials.** An investigation of alternative bearing materials was undertaken. The desired attributes a bearing material were:

- Flexible enough to bend into a cylindrical shape by wrapping around a master shaft

- Low affinity for absorbing water

167

- Low frictional properties with steel

- An ability to bond the material to an aluminum housing

- Receptive to machining grooves and recesses into the surface

After considering numerous materials, a material known as Turcite® was selected for further use in bearings.[4] Although this material had some deficiencies, it turned out to be a very good material for this manufacturing process and was the process material for the bearings developed in this project. More detailed information regarding the Turcite® and follow on bearings is in section 5.2.2.

4. **Increased Clearances.** The exacting tolerances required for a bearing with radial clearances on the order of 0.002 inches were adding to the difficulty in fabricating acceptable bearings. The master shaft itself, which was fabricated on a precision HAAS CNC lathe, had a taper error of 0.0002" over a 11 inch length. This alone starts the bearing off with a 10 percent error in form if the bearing could exactly replicate the master shaft. The original clearance ratio of 800:1 was selected primarily a compromise between journal bearing thumbrules that recommend a ratio of approximately 1000:1 and equations based on rotational speed [8, 10]. Further investigation revealed that the 800:1 clearance ratio was much tighter than those typically used for shipboard water-lubricated bearings. A larger clearance was chosen for future bearing iterations, making the relative magnitude of error to be much less for a given manufacturing tolerance. More information regarding clearances is provided in section 7.1.

5.2.1.5   PE-4

While alternative materials were being tested, an additional UHMW PE bearing was constructed in parallel by using the cold-molding technique. This bearing used the same nominal 800:1 clearance ratio as previous bearings and was successfully run as a hydrodynamic bearing. This bearing was not initially examined by a CMM, but based on the improved testing results it was assumed that the cold-molding technique

---

[4]http://www.tss.trelleborg.com

was an improvement over the method requiring heat. In spite of this improvement, the decision to switch to Turcite® was made due to the relative ease of construction using that material.

5.2.2 TURCITE® Bearings

Turcite® B Slydway® (hereafter called simply Turcite®) is a acetal-based, PTFE (polytetrafluoroethylene) filled thermoplastic made by Trelleborg Sealing Solutions. It is a flat linear bearing material marketed as having several features and characteristics that make is excellent for rebuilding guideways and gibs of machine tools. Among them are:

- Low friction without stick-slip

- Self-lubricating

- Heat, wear, and chemical resistant

- Impervious to oiling and moisture

- Safe for dry running in the event of poor or no lubrication

- Dimensionally stable

In normal applications, Turcite® is fixed to a base material with an epoxy bond. One side of it is chemically treated to make it receptive to adhesives. The base material is prepared for bonding by roughening the surface, and then cleaned of oil, grease, dust and rust. Turcite® can then be machined after bonding to achieve a satisfactory surface roughness and/or create lubricating grooves. To the authors knowledge, based on conversations with Trelleborg technical experts, it has never been used in a journal bearing application. Table 5.5 lists its material characteristics.

The manufacturing processes used to create Turcite® journal bearings is based on the same basic steps used in the UHMW PE bearings, incorporating the lessons learned

Table 5.5: Turcite®-B Material Characteristics

Property	Value	Unit
Water Absorption	≤ 0.01	Percent
Thermal Expansion Coefficient	$3.2\text{X}10^{-5}$	$1/^{o}\text{F}$
Hardness	60	Shore D
Modulus of Elasticity	145	psi
Specific Gravity	3.1	
Pressure Load at 1% deformation	1350	psi

from those bearings. This includes utilizing the cold-molding technique with the stainless steel tensioning device, with stainless steel 30x30 wire mesh as an intermediate layer between bearing material and the epoxy layer. Turcite® is available in sheet thicknesses from 1/64" to 1/4". For the bearings in this project, 3/32" thick material was used. The 3/32" sheet material thickness tolerance of +/- 0.005" would normally be unacceptable, but due to the unique tensioning device and epoxy potting method of bearing manufacturing the thickness tolerance is irrelevant. As long as the surface of the bearing material is firmly pulled tight to the master shaft, deviations in the bearing material thickness are accounted for by the epoxy, just like deviations in the housing. This manufacturing process therefore removes the need for precise dimensioning of the housing or raw bearing material, leading to cost savings.

5.2.2.1 Bonding

To adhere the Turcite® to the aluminum housings an epoxy called Waylock II is used. Waylock II, also distributed by Trelleborg Sealing Solutions, is a specifically formulated two-part epoxy for bonding Turcite® to metallic surfaces. To prepare the aluminum housing with the DHW epoxy, the housing was bored out to set the epoxy gap thickness. For the Turcite® bearings, this is not done. The recommended thickness of the Waylock is set by using a supplied spatula with triangular serrations approximately 0.004" deep, which implies a final thickness on the order of 0.002". As Table 5.6 shows, the use of a 3/32" thick sheet of Turcite® leaves a suitable epoxy thickness. The previous UHMW PE bearing housings had grooves milled into the housing with a 1/8" end mill to ensure the epoxy did not shear from the housing.

For these bearings the inside of the housing is sandblasted to roughen the surface to achieve a suitable finish (required roughness is 0.8 to 3.2 μm).

Table 5.6: Calculation of Waylock II Thickness

Split Housing Diameter	3.49	inches
Split Housing Radius	1.745	inches
Wire Mesh Thickness	-0.012	inches
Turcite Thickness	-0.0938	inches
Master Shaft Radius	-1.6195	inches
Nominal Waylock II Gap	0.0198	inches

After sandblasting the housing is cleaned from impurities using a degreasing spray to remove any residual oil or dirt from the bonding surface. The epoxy is then applied to the housing using the Waylock spatula and the tensioned bearing assembly is potted to the housing. Alignment of the bearing to the housing is done using matchmarks previously machined into both the housing and the bearing material to ensure that the bottom dead centers of the two pieces correspond. Once set together, support pieces are mounted to the sides, ends, and top of the housing and tensioning device to prevent movement of the parts. The weight of the master shaft and additional weights on the tensioning device ensures that a light contact pressure iss continuously applied throughout the curing process. Figure 5-23 shows the tensioned bearing and the housing before and after potting with the epoxy. In the figure, pieces of aluminum foil are used to prevent the excess epoxy from directly adhering to the shaft when it flows out the axial ends of the housing.

The full cure time of the Waylock II is approximately 24 hours, after which the tensioning device is removed from the bearing and the excess wire mesh is cut away. Excess epoxy that has been squeezed out the circumferential and axial ends of the bearing are then machined away to prevent it from interfering with bearing testing. For the first bearing this was initially done with a hand held Dremel tool using a grinding attachment, but for later bearings was done using an end mill.
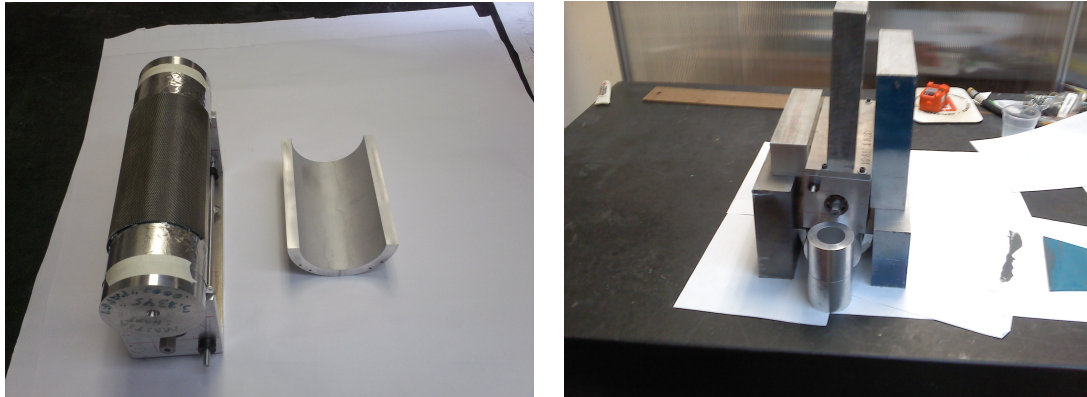
| (a) Tensioned Bearing and Prepared Housing | (b) Bearing Assembly During Curing |

Figure 5-20: Bonding Bearing to Housing

5.2.2.2 Machining

The initial Turcite® bearing was a plain journal bearing and therefore did not require the machining of grooves or recesses into the surface of the bearing. Follow on bearings required such features. The manufacturers specifications state that the material can be easily machined without cooling. During machining of test pieces, it was found that the use of normal machining tools resulted in unacceptable results, primarily due to the generation of a protruding burr that was created above the surface of the material. Although it would be possible to deburr the edges of milled grooves, doing so with consistency would be difficult. For fluid flow reasons, any burr would result in a rupture of a fluid film that flows over it.

Attempts to mill grooves without burrs in the Turcite® with conventional end mills proved impossible to do regardless of any speed/feed combination. It appears the main reason for this is the elastic nature of the polymer which prevents a clean separated chip even with very sharp tools. In effect, the material is pulled by the cutting edge of the mill as it contacts the material. For conventional mills that have an up-cut configuration designed to eject chips away from the bottom of the cut this results in edges with a very ragged lip. Such mills are designed to achieve a very smooth finish at the bottom of the material. For the purposes of these bearings, the bottoms of the grooves and recesses are not nearly as important as the cut quality of the edge
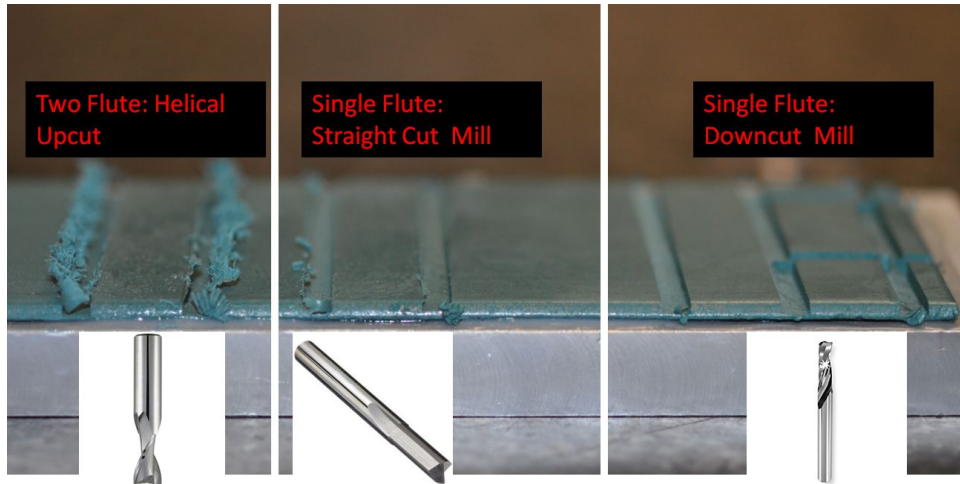
Figure 5-21: Tooling Effects on Turcite Machining

between the top of the material and the side.

Other end mills were tried, including a single flute straight cut mill and a down-cut mill. The straight cut mill provided a vast improvement over the conventional upcut end mill, but still had a noticeable burr. The use of a downcut mill resulted in an excellent quality of cut with no burr at the intersection of the sides of the groove and the top of the material. Various speeds and feeds were attempted with the down-cut mill with no noticeable degradation in the quality of the cut. Figure 5-21 shows the effects of the different mills on machining Turcite®. The details of the end mills selected for machining of bearing grooves and recesses for this project are:

- ONSRUD 64-000 series

- Solid Carbide

- Down-cut

- Single Flute

- For plastic, wood, and aluminum

To machine the Turcite® in a flat configuration, a means of fixturing the material in a flat condition is required. Permanent bonding of the material to a flat plate is not an

173

option since it has to be subsequently rolled into a cylindrical form. Using a vice was also not possible due to the thin compliant nature of the material. Because relatively shallow cuts needed to be made into a very soft material, large cutting forces were not anticipated. This meant that fixturing forces would be relatively small, leaving two viable options:

- Temporary Adhesives

- Vacuum Chuck

The use of a temporary adhesive such as double sided tape could have been used to fixture the material to a flat plate. Although this would work for milling the grooves and recesses, there were concerns of the ability to completely remove the adhesive from the far side of the bearing material and the fixture plate. Any residual adhesive on the Turcite® would have a negative impact on the ability to achieve a good epoxy bond during follow on steps. Leaving residue on the fixture plate would mean that the flatness of the plate would degrade over time and require flycutting or chemical cleaning operations to return the plate to an acceptable condition. This led to the decision to use a vacuum chuck.

Utilizing a vacuum chuck to temporarily hold the Turcite® during milling operations was attractive because it would not leave any residue and would be a very repeatable fixturing operation. The major drawbacks to using a vacuum chuck is the need to buy or make a chuck, and the need for a vacuum pump. The second drawback was not an issue due to the availability of a 10 CFM vacuum pump used for other projects. A custom vacuum chuck was designed and built to save costs and provide a chuck that was ideally suited to the footprint of the bearings.

Figure 5-22 shows the exploded view of the vacuum chuck design. The bottom plate is 3/4" aluminum plate with 1/8" deep vacuum grooves cut into the top of it, and flycut on both sides to achieve good overall flatness and surface finish. The grooves, which serve as a manifold, are 1/4" wide and are located directly below the vacuum
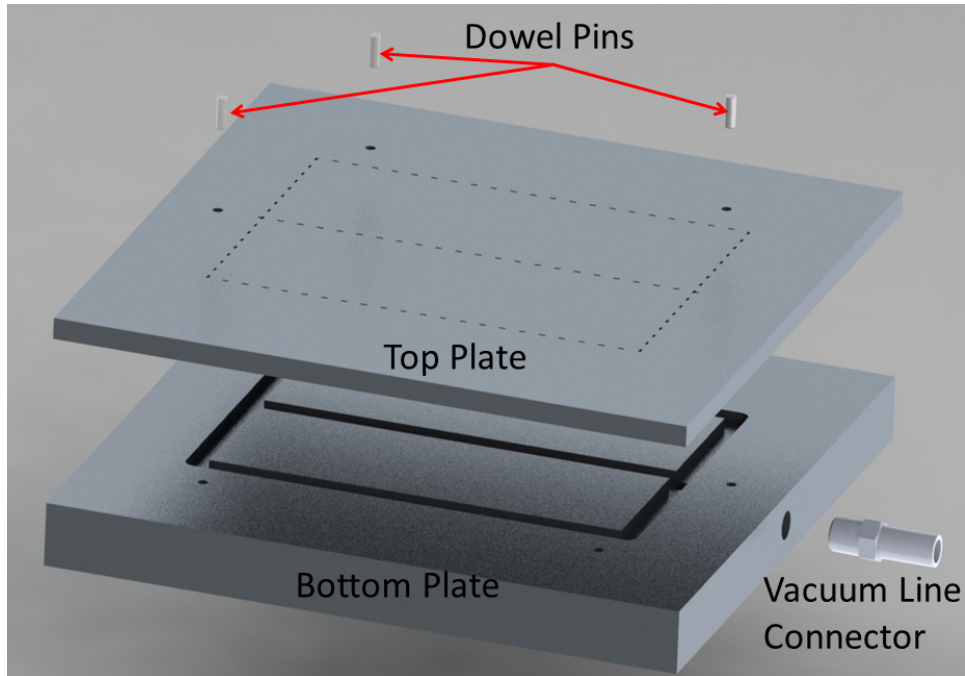
Figure 5-22: Exploded View of Vacuum Chuck

holes in the top plate. The vacuum is pulled through a 3/8" hole, which is drilled and tapped to accept a pipe nipple that connects to the vacuum line of the pump.

The top plate is 1/4" precision ground aluminum with a series of slots waterjetted into it to create the vacuum holes. The slots are approximately 0.08" long by 0.03" wide with a nominal spacing between centers of 1/4". The width of the slots correspond to the kerf of the waterjet, and as such the holes were made by simple linear lines by a waterjet. The outer dimensions of the holes were designed to be approximately 1/2" inside the extremities of the Turcite® bearings fixtured above them. Dowel pins are designed for a semi-kinematic alignment of the bearing material on the top plate.

The top and bottom plates are affixed to each other by a thin layer of double sided tape. The tape serves to keep the two plates together as well as prevent any air from being pulled between the two plates. During machining operations, the chuck plates are held by a vice. The vacuum pump is located on the worktable and connected to

the chuck by a non-collapsible vacuum line. Figure 5-23(a) shows the configuration of the vacuum pump and chuck on a Bridgeport EZTRAK CNC Milling Machine. The vacuum pump is able to consistently maintain a vacuum of at least 28" Hg for extended milling operations, provided a total suction force on the order of 250 lb_f.[5] Although the author was able to peel the sheet off the chuck when initiated from a corner, the chuck is sufficient to keep it firmly adhered during all milling cuts. Figure 5-23(b) shows the actual milling operation of the Turcite®.
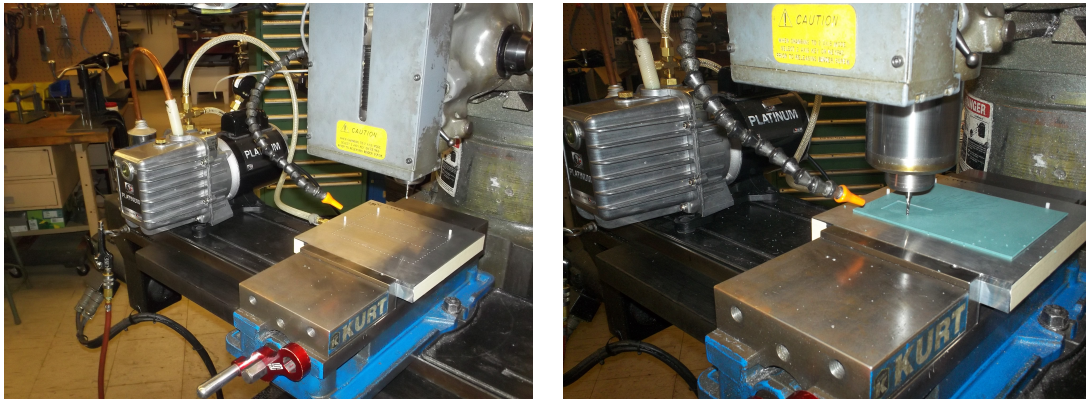
(a) Vacuum Chuck and Pump Installed on Bridgeport EZTRAK CNC Mill

(b) Cutting Recesses into Hybrid Bearing

Figure 5-23: Vacuum Chuck in Operation

5.2.2.3 Post Bonding Steps

After bonding the housing to the bearing material with epoxy, the excess epoxy is milled away to provide a clean bearing surface. Additional machining is required to add the threaded holes for fluid connections. As described in chapter 4.4.1, push-to-connect fittings are used on the back side of the bearing housings for fluid supply and pressure measurement line connections. The supply inlets use 1/4" NPT threads and the pressure measurement lines use 10-32 threads.

To create the threaded holes, the bearings are fixtured to allow the location of the holes to be located on the surface of the bearings. For many bearing configurations

---

[5]The longest continuous use of the vacuum chuck was approximately 20 minutes long during the complex machining of the 3 port bearings' grooves and recesses

the inlet ports locations are machined into the Turcite® while flat, providing location of the holes. Once located, pilot holes are drilled into the bearing surface and all the way through the housing. The pilot hole is followed by larger bits up to the required inlet hole size. Because drill bits pull chips upward, very short pecks are required to ensure that long chips are not formed, which could exit the hole and be thrown outward causing damage to the bearing surface. This is particularly true during the drilling of pressure inlet holes that were on the surface (non-recessed) of the bearings. To alleviate that concern, slightly over sized counterbores for the pressure inlet holes are first milled using a 1/16" down-cut single flute end mill.

After the holes were created from the bearing surface side, the bearings are flipped over and fixtured to allow drilling and tapping from the outside of the housing. Transfer punches or drill bits are used in the existing holes to find the correct location and orientation of the holes from the back side of the bearing. At this point, the holes are drilled to tapping dimensions and subsequently tapped. For the pressure inlet lines that use an O-ring to seal the 10-32 threads, a 3/8" counterbore is created with an end mill to provide a flat seating surface for sealing (this arrangement can be seen in Figure 4-27). The specific geometries used in fabricating these fittings is shown in Figure 5-24. Once the holes were generated and the bearing was ready for testing, the push-to-connect fittings can be installed. The 10-32 fittings are screwed in by hand and the 1/4" NPT are first covered with Teflon tape then tightened by wrench.

5.3 Manufacturing Accuracy

Variations in the surface of a bearing will result in changes to the fluid film shape and subsequently degrade performance. Because of this, bearings require very high precision surfaces that are relatively free from defects such as roundness or cylindricity errors. Additionally, because bearings are designed for a specific radial clearance, differences in diameter can have a huge impact on whether a bearing will operate as designed. This is illustrated by the Reynolds equation where the actual operating
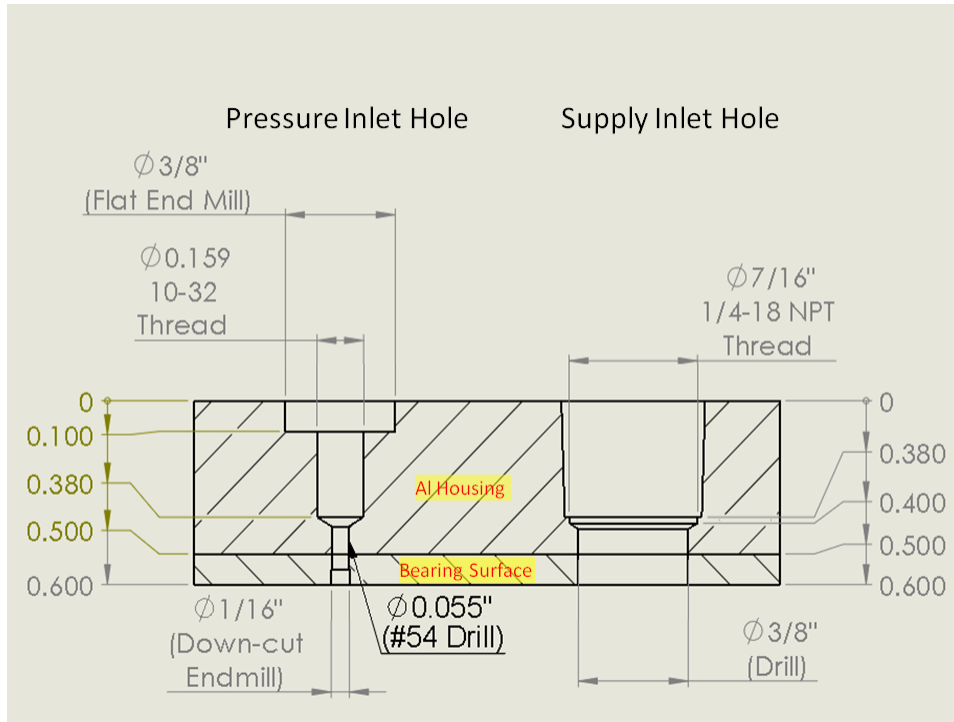
Figure 5-24: Manufacturing Details of Fluid Line Connections

bearing gap (or film thickness) has a cubed relationship to other terms (equation 2.17). In order to accurately determine any causal relationships between different bearing designs, operating conditions, and performance, the magnitude of manufacturing errors needs to be quantified. The very small radial clearances involved in these bearings (on the order of 0.002 to 0.005") made necessary the use of a Coordinate Measuring Machine.

5.3.1 Coordinate Measuring Machine

The measuring of bearings could have been subcontracted out to companies that perform metrology measurement services. This would have resulting in recurring costs and more importantly, a delay between bearing fabrication, obtaining results on the accuracy of the bearing and suitability for use, and subsequent testing. With the bearing design, build, test, and repeat process in this project such delays would have been cumulatively significant and not allowed the aggressive schedule to be met.

It was for these reasons that a Zeiss Eclipse CMM was purchased specifically to obtain the bearing measurement results needed for multiple bearings. The Eclipse is a pre-owned unit that has be modified to include a scanning head allowing for very thorough and precise measurements of the complex geometries of bearings tested in this project. Other CMM vendors and different machines were considered for use, but the Eclipse provided the best value for the project in terms of cost, performance and delivery time. The specifications for the Eclipse CMM are provided in Table 5.7.[6]

Table 5.7: Coordinate Measuring Machine Specifications

Make	Zeiss
Model	Eclipse 550
Probe System	VAST XXT Scanning Head
Operating System	Calypso
MPEE	2.9 + L(mm)/250 microns
Work Volume	19.7" X 21.6" X 22.8"

The maximum permissible error for length (MPEE) specification results in a maximum specified error that is approximately 0.00014" over the length of the test bearings. This worst case scenario is on the order of a 7 percent error for a bearing with a 0.002" gap clearance and only 2.8 percent for a bearing with a 0.005" gap clearance - providing ample accuracy for the bearing metrology measurements. During calibration, the actual accuracy was shown to be significantly better with errors on NIST traceable gages of various shapes and sizes consistently below 1 micron (0.00004").

Figure 5-25 shows the CMM in its installed location at MIT. A polycarbonate enclosure was constructed to protect it from damage from external lab operations and to provide a modicum of environmental protection against laboratory temperature swings. The CMM temperature specifications are 20 +/-2°C (64.4^{o}F to 71.6^{o}F) . A

---

[6]It should be noted that on some initial bearings, measurements were made on a newer model Zeiss Contura CMM with better accuracy than the Eclipse purchased for this project. The Contura CMM was a Zeiss owned demonstration piece located at Methods Machine Tools in Sudbury, MA. It was used for bearing measurements prior to the delivery and installation of the Eclipse CMM at MIT.

Figure 5-25: Zeiss Eclipse CMM Installed at MIT

thermometer is located in the enclosure to record temperatures and the space can easily maintain that temperature. It was found that typical temperature variations in the enclosure are less than 2^oF.[7] To alleviate the effect of temperature variations on measurements, bearings were placed in the enclosure for at least 24 hours to equalize thermal gradients within the bearing itself, and most measurements were conducted at approximately 69 to 71^oF. Because the aluminum housing is significantly stiffer and has a lower temperature coefficient than Turcite®, the bearing material's expansion and contraction is significantly constrained due to it being bonded to the aluminum. Figure 5-26 shows the nominal bearing geometry and expected variation in dimensions due to a 2^oF temperature variations in measurement.
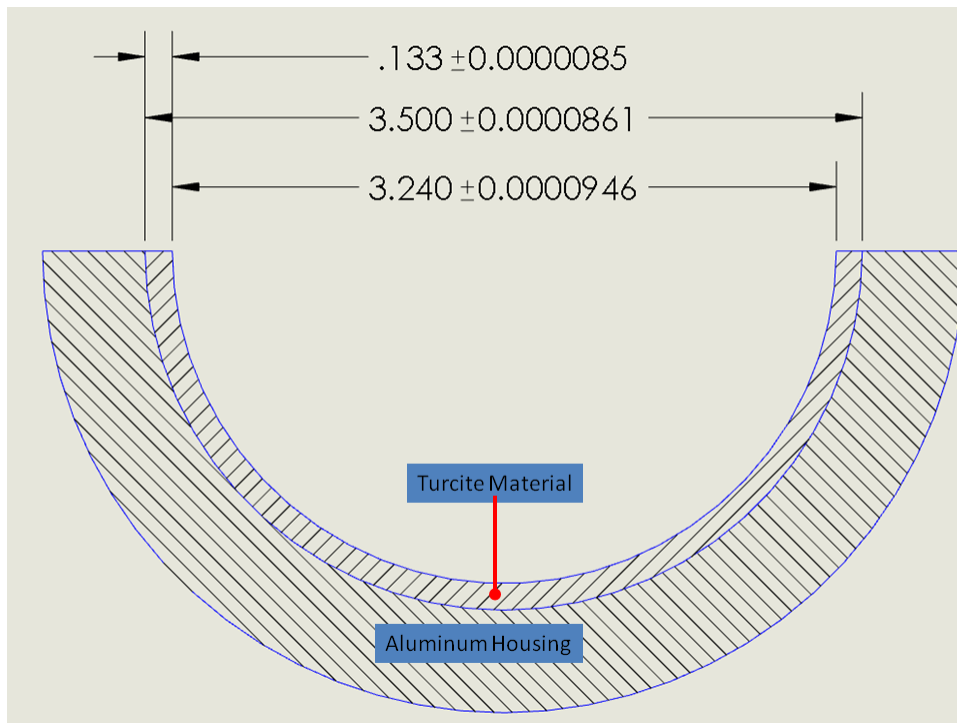
Figure 5-26: Nominal Geometry Variation due to Thermal Fluctuations in CMM Enclosure

Table 5.8 shows the maximum expected measuring uncertainty due to the combined

[7]Temperature ranges are much smaller during spring, summer, and fall months when the A/C units are operating. During the winter months when the A/C system is secured, the heat in the lab space needed to be turned off completely to keep temperatures below the high specification. This was able to provide relatively consistent temperatures, but not as good as during the other months.

Table 5.8: Total Measurement Uncertainty

Thermal Uncertainty		
CMM Enclosure Temperature Variation	2	^{o}F
Aluminum Housing ID	3.5	Inches
Turcite ID	3.234	Inches
Unconstrained Turcite Dimension	0.133	Inches
Housing ID Thermal Uncertainty	0.0861	1/1000"
Turcite Uncertainty	0.0085	1/1000"
Total ID Thermal Uncertainty	0.0946	1/1000"
CMM Accuracy		
Specified CMM MPEE	0.1402	1/1000"
Calibrated Accuracy	0.0394	1/1000"
Total Measuring Uncertainty		
Expected Uncertainty	0.1340	1/1000"

thermal variations in the material and the inherent accuracy of the CMM itself. This uncertainty is an order of magnitude less than the smallest bearing gap of 0.002" and significantly less than the gap of 0.005" for the majority of tested bearings. Because of this high accuracy, there are no significant concerns with the validity of measurement results.

5.3.2 Edge Effects

For the majority of bearings, the grooves and recesses were cut when the bearing material was flat on the vacuum chuck. The subsequent wrapping of the bearing onto the master shaft and adhering of it to the housing left the landed (raised) portions of the bearing material closely matching the geometry of the master shaft. During metrology measurements of the bearings with the CMM, it was found that there was a consistent depression of the bearing material in the immediate vicinity of the edges. Figure 5-27 shows a cartoon depicting an exaggeration of the resulting depression of the edges relative to the landed areas. Although this edge effect was noted for any groove and recess regardless of the orientation of the grooves relative to the bearing geometry, axial grooves had a much larger magnitude of edge depression than circumferential grooves. In addition to the edge effects in grooves, the circumferential and axial ends of the bearing saw similar effects.
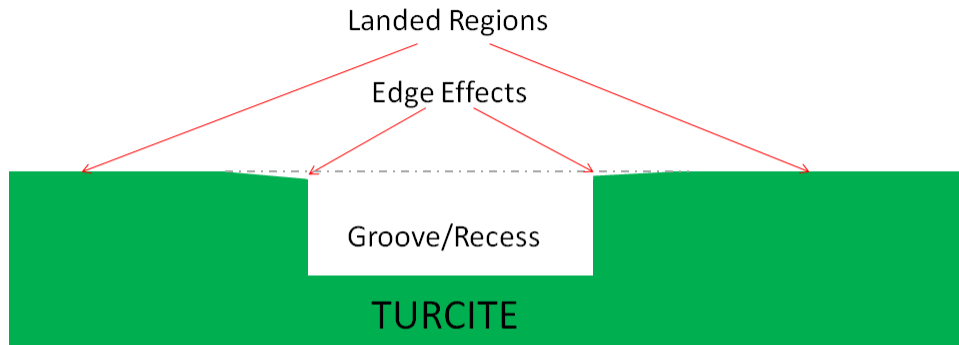
Figure 5-27: Edge Effects of Grooves and Recesses in Turcite® Bearings

In practice, these edge effects are advantageous for bearing operations in the vicinity of grooves. This benefit is because rounding or beveling the edge of a groove has been found to promote the development of a fluid film as opposed to grooves that have sharp edges, which tend to scrape lubricant away from landed regions[8]. For the axial and circumferential ends of the bearings, these edge effects are not desirable because they reduce the resistance to exit flow out of the bearing. To counter this, bearings are made with excess material, approximately 1 inch longer and 10° greater wrap around the master shaft than designed. This provides margin to allow the excess material at the ends and along the circumferential sides of the bearing to be milled away after the epoxy has been set, which removes those edge areas that have depressions.

Axial grooves see depressions of approximately 0.005", while circumferential grooves have depressions on the order of 0.001". This can be seen by Figure 5-28, which
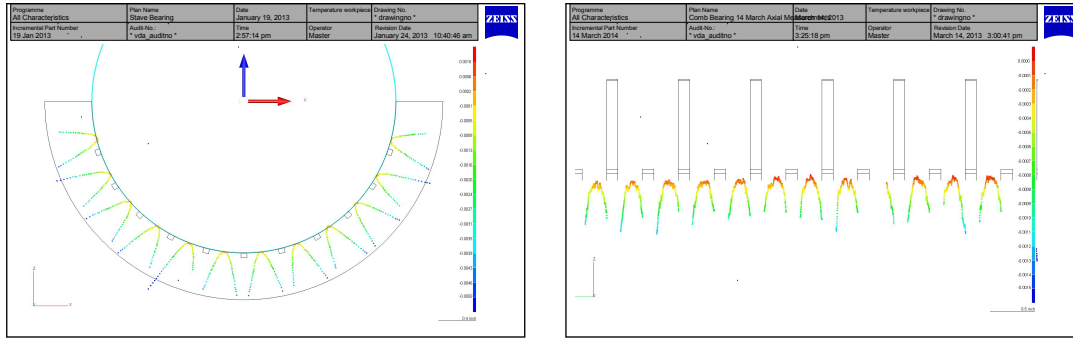
(a) Edge Effects of Axial Grooves in Stave Bearing

(b) Edge Effects of Circumferential Grooves in Comb Bearing

Figure 5-28: Measured Edge Effects

shows the 200 times magnified measured results of a series of axial grooves (as made in a stave bearing configuration in section 6.7) as well as the measured results of a series of circumferential grooves (as made in a 'Comb' style bearing in section 6.8).[8] Many of the bearing configurations have a combination of axial and circumferential grooves in close proximity to each other or intersecting each other. For these complex geometries, the edge effects sometimes extended a fair distance (on the order 3 times groove depth) away from the location of the groove or recess.[9] The areas of depressions disappear and the lands become one uniform height away from the edges. This was very noticeable after hydrodynamic testing where the high points of the bearings had noticeable wear lines of contact that occurred during operation in the mixed and boundary lubrication regimes. Figure 5-29 shows such wear patterns that occurred in a centerlift bearing that had multiple grooves. This effect was also directly measured by CMM.

The edge depressions are due to the poisson effect of the bearing material that is subjected to bending strain as it is forced into a cylindrical shape around the master shaft. The bending places the ID of the material in compression and the OD in tension - very similar to a sheetmetal forming process. In addition to the bending strain,

---

[8]Larger figures are provided in appendix G

[9]This makes sense due to Saint-Venant's principle.
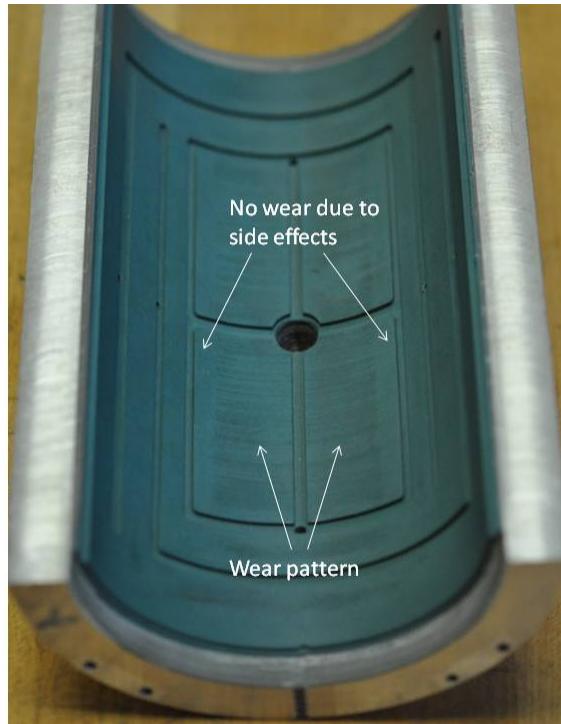
Figure 5-29: Wear Patterns in Centerlift Bearing

the material is also subjected to a compressive strain normal to the surface of the material due to the tensioning device, which pulls the material directly against the shaft. In areas where there are no grooves, the compressive strains are constrained against movement to the sides, leaving the material able to compress only in the direction normal to the surface. In the areas where there are grooves however, the compressive strains result in an expansion of the material into the grooves because there is no constraint against it there. This expansion comes along with a contraction at the interface of the bearing material and master shaft, thereby causing the edge depressions. Axial grooves are effected by both the compressive strain from bending and the normal compressive stresses from the tensioning against the shaft, whereas circumferential grooves are only effected by the compressive stresses from the tensioning against the shaft. This increased compressive strain with axial grooves results in more poisson effect and therefore the greater edge depressions that are seen.

5.3.3 Manufacturing Tolerances

The diameter tolerances of bearings is a very important from a design standpoint. A diameter that is too small can lead to a seized bearing, while a diameter that is too large will have an excessive gap. The machining tolerances of non-metallic materials are generally not as tight as metallic bearing materials such as bronze. Because of this, relatively large design tolerances are typically specified for these materials. For shaft sizes of the diameter of the test rig (3.2305"), diameter tolerances of the bearing of 0.005" are typical of common water-lubricated bearing manufacturers. For full sized applications with shafts over 21", diameter tolerances on the range of 0.01" to 0.016" can be expected.

5.3.3.1 Master Shaft Machining

Although the manufacturing processes outlined in this chapter is largely devoid of precision manufacturing steps, there is a need for a precision machined master shaft. Accurately machining a master shaft requires an appropriately sized lathe that is capable of holding fairly tight manufacturing tolerances. Fortunately most machine shops have lathes capable of doing so. The bearings manufactured in this project utilized aluminum master shafts that were made on a HAAS CNC lathe. A total of 3 shafts were fabricated of varying diameters to allow bearings with different gaps to be manufactured. The designed shaft dimensions and actual machined dimensions are shown in Table 5.9. During machining of the shafts, their diameters were turned and iteratively checked with a micrometer (with a 0.0001" resolution) until the nominal design diameter was achieved. The shafts were then removed from the lathe and checked with the CMM for actual measurements.

There were slight differences (<0.0003") in the measurements between the designed diameter of the shafts and the actual dimensions. These differences are attributed to human error in obtaining accurate micrometer measurements while the shaft was on the lathe. In addition to the difference in mean measured diameters of the shafts, there

Table 5.9: Manufacturing Tolerances in Master Shafts

Shaft	1	2	3	
Nominal Clearance Ratio	800	250	400	
Nominal Design Diameter	3.2345	3.2434	3.2386	Inches
Mean Measured Diameter	3.2345	3.2431	3.2389	Inches
Manufacturing Difference	0.0000	0.0003	-0.0003	Inches
Actual Diametrical Gap	0.004	0.0126	0.0084	Inches
Actual Clearance Ratio	808	256	385	
Measured Roundness Error	0.0002	0.0002	0.0002	Inches

were slight tapers in the master shafts that can be attributed to the inherent accuracy of the lathe. The magnitude of this taper was on the order of 0.0002" over the length of the master shaft. Machining of the master shafts was done without the tailstock live center because it was found that the use of the tailstock introduced significantly more taper than without. Combining the machine taper error and the differences between design and measured diameters, the master shaft is easily machined with a tolerance of less than 0.001". Complete measurements of the master shafts are provided in appendix F.

5.3.3.2 Bearing Replication

The accuracy to which the master shaft can be fabricated is one part of the overall dimensional accuracy of the test bearings. The other, more significant part is the accuracy to which the bearing material can be replicated to the master shaft. A total of nine Turcite® bearings were manufactured. Some of these were modified after initial testing for other test configurations, but the general form of the bearings did not change due to those modifications. Those nine bearings are representative of the manufacturing capabilities of the process. The CMM measurements of the bearing diameters are provided in Table 5.10.[10]

---

[10]Table 5.10 notes:
Note 1: Bearings were formed without any grooves or recesses as plain journal bearings.
Note 2: Bearings had significant grooves and recesses machined prior to forming.
Note 3: Bearings where manufactured without excess margin on sides and ends.
Note 4: Bearing had a layer of release agent sprayed on master shaft prior to bearing tensioning.

Table 5.10: CMM Measured Diameters of Bearings (Inches)

Bearing Configuration	Master Shaft Diameter			Diameter Error	Notes
	3.2345	3.2431	3.2389		
Plain Journal Bearing	3.2346			0.0001	1,3
180 Degree 3 Port Bearing	3.2356			0.0011	2,3
165 Degree 3 Port Bearing		3.2434		0.0003	2,3
Center Lift Bearing			3.2401	0.0012	2
2 Port Bearing			3.2410	0.0021	2
Stave Bearing			3.2390	0.0001	2
Comb Bearing			3.2398	0.0009	2
Hydrostatic Lift Bearing			3.2391	0.0002	1
2 Slot Bearing			3.2397	0.0008	1,4
Max Error				0.0021	
Average Error				0.0008	

As expected, the diameters of the manufactured bearings are all slightly greater than that of the master shafts. The diameter error is remarkably low for bearings that were formed as plain journal bearings. This is primarily due to the fact that there were no interior edge effects to be seen without fluid grooves. The slightly larger diameter error with the 2 slot bearing might be attributed to the fact that a thin layer of mold release agent was sprayed onto the master shaft prior to the bearing material being tensioned around it. The application of release agent onto the shaft was done to prevent epoxy spill-over from adhering to the shaft and causing damage to it. In earlier bearings excess epoxy had occasionally stuck to the master shafts requiring it to be later chipped off - potentially damaging the surface finish and geometry of the shaft. Considering that wet paints are applied in thicknesses on the order of 0.5 to 1 mil (1/1000"), it is not unreasonable to assume that the layer of release agent is responsible in part for the 0.0008" overshoot in diameter for that bearing.

The bearings that had grooves and recesses milled in the flat condition add a level of difficulty in determining the actual bearing diameter. This is due to the edge effects, many of which have several thousandths of an inch depressions as measured by the CMM. The CMM algorithms that calculate diameter take these areas of depression into account to varying levels - resulting in the calculated diameter to be slightly

larger than the minimum inscribed element that could be fit into the landed regions that do not display edge effects.

5.3.3.3 Combined Tolerances

The error associated with fabricating the master shaft and replicating the bearing to the master shaft can be combined to provide the total process tolerance for this manufacturing method. Table 5.11 provides the minimum, average, and maximum expected errors seen in the process. With accuracies below 0.003", this process is well within the range of tolerances of other industrial processes for water-lubricated bearings. Considering the fact that these are for a partial arc split bearing, they are particularly good.

Table 5.11: Total Process Errors in Manufacturing Method

| | Error (inches) | | |
	Min	Average	Max
Master Shaft Machining Error	-0.0003	0	0.0003
Bearing Replication Error	0.0001	0.0008	0.0021
Total Error	-0.0002	0.0008	0.0024

The full CMM measurement results for the bearings is provided in appendix G.

5.4   Comb Bearing Manifold Design

A 'comb' style bearing was designed that required a way to provide a distributed flow of water across a large axial length of the bearing. Unlike other bearings that utilized NPT connections to feed flow into a hole in the bearing, the 'comb' bearing had a series of inlet slots. These inlet slots are the short circumferential slots shown in Figure 5-30. These inlet slots are designed to be fed by one source of fluid. To do so required a manifold to be built on the back of the bearing, and for a custom self-aligning mount to be cast. Drilling a common feed hole into the bearing housing

itself was considered as a source for supply fluid, but due to the relatively thin thickness of the housing (0.5 inches), there were significant concerns over the effect that a large hole running the axial length of the bottom dead center of the bearing would have on the housing stiffness.
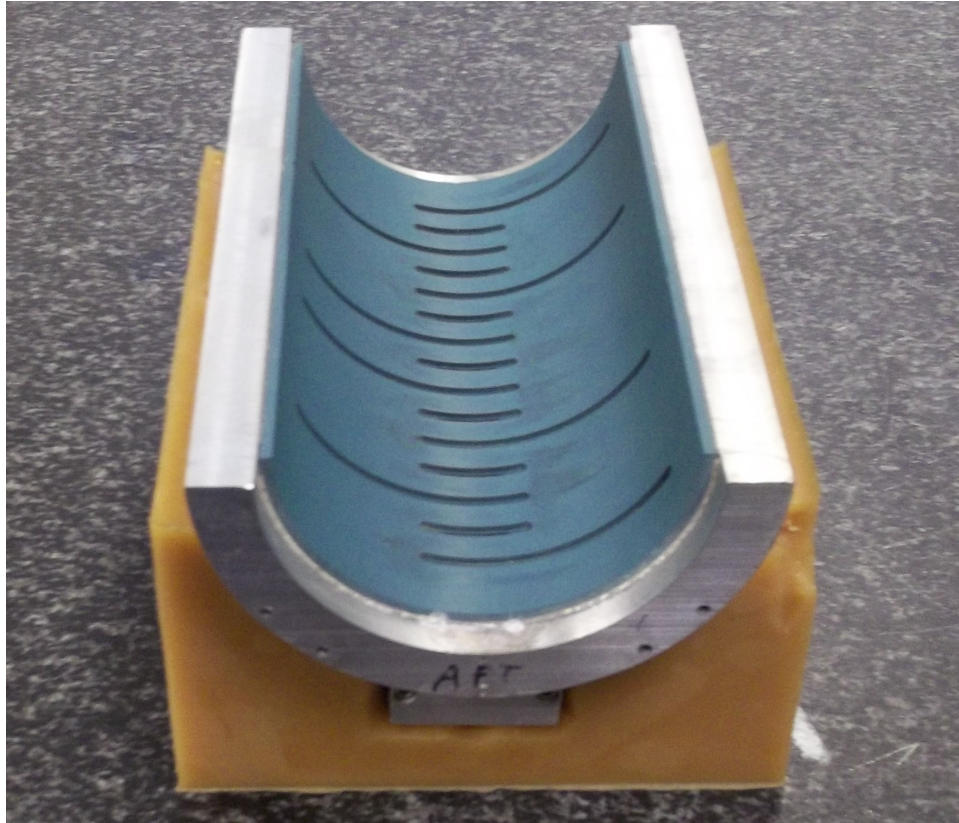
Figure 5-30: Comb Bearing in Self-Aligning Mount

The manifold was constructed of bolted 1/4" aluminum plates with an inlet hole for the fluid supply system on the back end. The manifold had to be attached to the back of the housing in such a way that any bonding stresses did not deform the bearing. With a supply pressure of up to 100 psi in the manifold and a fluid area of 6 square inches, the bond between the manifold and housing would be required to support 600 lbf.

The initial plan was to weld the manifold to the housing prior to the bearing be-

ing potted with epoxy - in this way any thermal stresses from the welding process would not effect the form of the bearing. This turned out to be difficult with the size of TIG welders at MIT because of the thickness of the aluminum housing. With a thickness of 0.5", even a 350 amp welder had difficulty providing enough energy to lay an effective weld. Due to time constraints, using a larger capacity welder was not possible so it was decided to epoxy the manifold to the housing using DEVCON® Plastic Steel Epoxy. With a tensile strength of 2800 psi and a contact area of 3.5 square inches on the manifold, the epoxy provided an suitable watertight bond with ample strength. Using epoxy had the added benefit of allowing the manifold to be added after the bearing was bonded to the housing because there were no thermal stresses introduced.
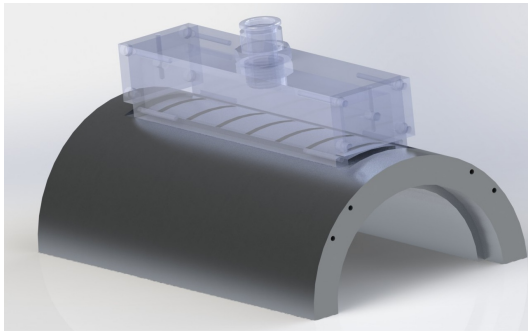
(a) 3D Manifold Design
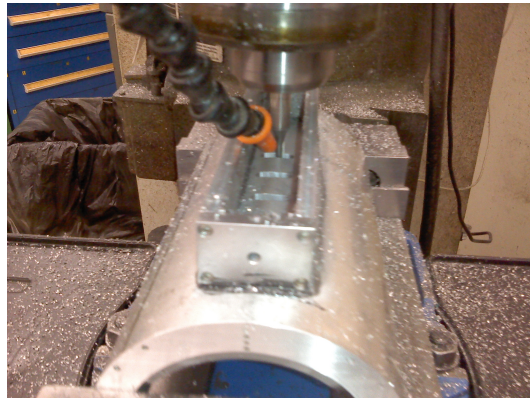
(b) Milling Inlet grooves into Comb Bearing Housing

Figure 5-31: Comb Bearing Manifold

Figure 5-31 shows the manifold design and the slots being milled into the back of the housing after the manifold was adhered to it. The top plate of the manifold is removable to allow for access for machining and the removal of chips. The manifold uses 4-40 screws to secure the individual plates together and silicon to provide a watertight seal between them.

Chapter 6

Test Bearing Designs and Experimental Results

A multitude of bearings were fabricated and tested to quantify their hydrostatic, hydrodynamic, and hybrid operating characteristics. This chapter provides a description of the designs, the rational behind them, and the experimental results that were obtained.

6.1 Overview of Bearings and Testing

Figure ?? shows a photograph of some of the bearings tested in this project. A total of nine different Turcite® bearings were manufactured for this project. Of those nine, two were modified after initial testing to add additional grooves and change the configuration. This included 2 modifications of the Centerlift bearing to see the effect of that different width axial grooves had on bearing performance. The Hydrostatic lift bearing was originally manufactured and tested as a plain partial-arc bearing without grooves, then modified 4 different times to see the effects of different hydrostatic lift configurations. This resulted in a total of 15 different bearing designs that were evaluated experimentally.

Figure 6-1: Various Test Bearing Attributes

Bearings were tested in three main modes of operation:

- Hydrodynamic

- Hydrostatic

- Hybrid

6.1.1   Hydrodynamic Testing
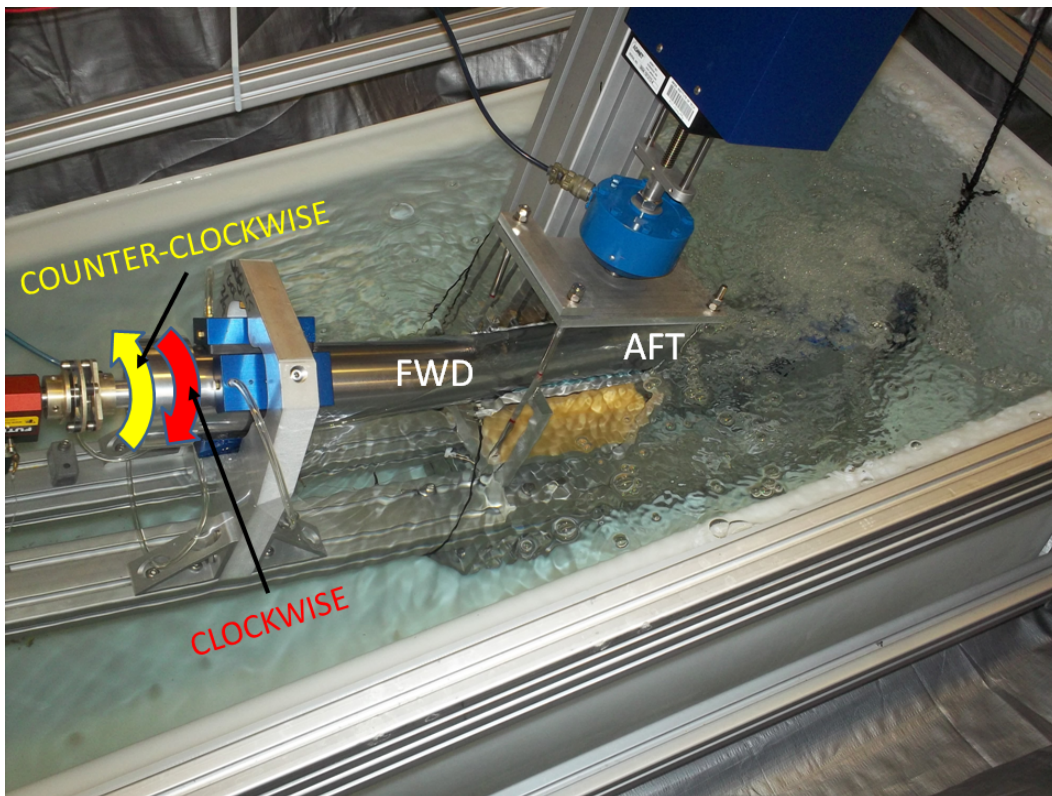
Figure 6-2: Photograph of Hydrodynamic Testing of Plain Journal Bearing

Hydrodynamic testing of the bearings occurred with the test bearings submerged at an angle in the test tank under an applied load. Rotational speeds were varied between 25 and 500 RPM and projected area loads were varied between 1 and 25 psi depending on the bearing configuration. As testing progressed, a projected area loading of 7 psi became a standard load. This tended to be a balance loading condition where even the worst hydrodynamic performing bearings could operate marginally,

allowing for comparison between bearing configurations. Hydrodynamic testing was conducted in both clockwise and counter-clockwise directions. Common speeds used in the test rig for hydrodynamic testing are shown in Table 6.1, including the corresponding full scale RPM for a nominal shipboard shaft sized to 28" in diameter.

Table 6.1: Common Test Rig Hydrodynamic Speeds

Test Rig RPM	RPS	Surface Speed (ft/s)	Full Scale RPM
25	0.42	0.35	2.9
50	0.83	0.70	5.8
75	1.25	1.06	8.7
100	1.67	1.41	11.5
125	2.08	1.76	14.4
150	2.50	2.11	17.3
200	3.33	2.82	23.1
250	4.17	3.52	28.8
300	5.00	4.23	34.6
350	5.83	4.93	40.4
400	6.67	5.64	46.2
450	7.50	6.34	51.9
500	8.33	7.05	57.7

Figure 6-2 shows a plain journal bearing during hydrodynamic testing with the nomenclature used to describe rotation and location along the bearing. The air bubbles from the flat and radial air bearings is visible in the figure. There were initial concerns during the design stage of the test rig regarding air riding up the shaft and effecting test results. This is not a problem since bubbles are whisked away from the shaft well before reaching the test bearing, as shown in Figure 6-3.

Key data that were obtained from hydrodynamic tests include the position of the forward and aft position of the bearing relative to the shaft and the torque due to interaction between shaft and bearing. This allowed for derived data such as friction coefficient, shaft eccentricity, attitude angle, and shaft tilt to be determined. Standard plots used in this project for these data include:
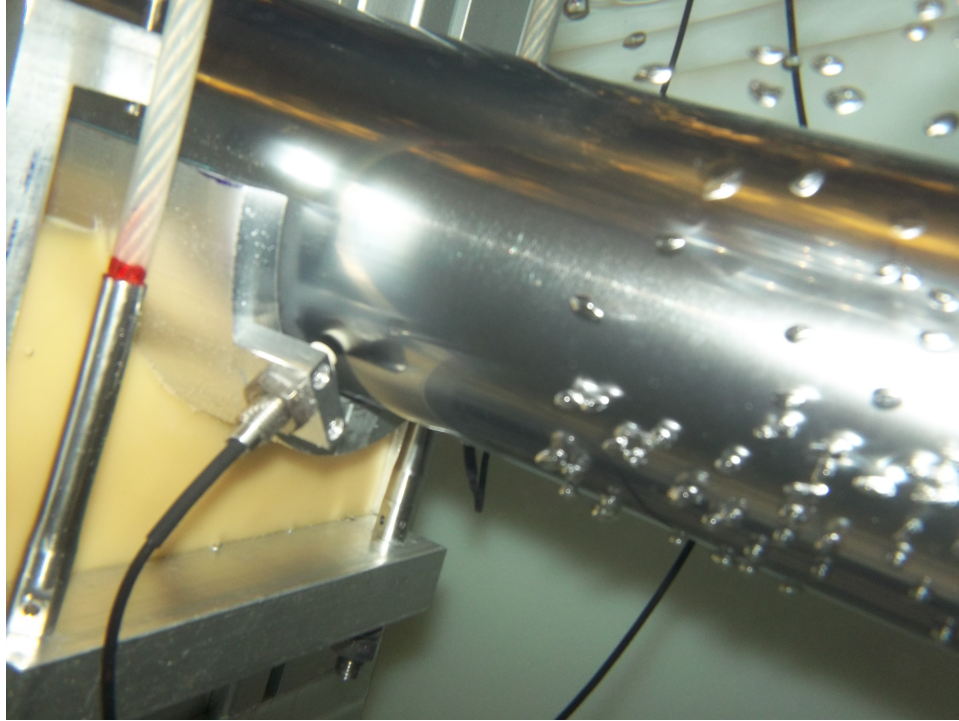
Figure 6-3: Underwater photograph showing air bubbles whisked away from shaft during hydrodynamic testing

1. Friction coefficient plotted against the journal surface speed and Sommerfeld number.

2. Location of shaft relative to the axial midpoint of the bearing.

The *friction coefficient* is a non-dimensional parameter, allowing comparisons to be made for various projected area loads. Hydrodynamic bearings are typically plotted with some variation of the non-dimensional Sommerfeld number (equation 2.11), having viscosity and journal speed in the numerator with loading in the denominator. A focus of this research is to identify and compare the transition between mixed and hydrodynamic lubrication regimes - indicated by the location of minimum friction. The surface speed of the journal is a dominant factor in determining when this occurs. While the Sommerfeld number provides the ability to scale between different size bearings when operation is fully hydrodynamic, surface speed (as an absolute value) can often provides a better indication of when the transition between lubrication regimes will occur. It is for this reason that both Sommerfeld number and

197

surface speeds are used for friction plots.
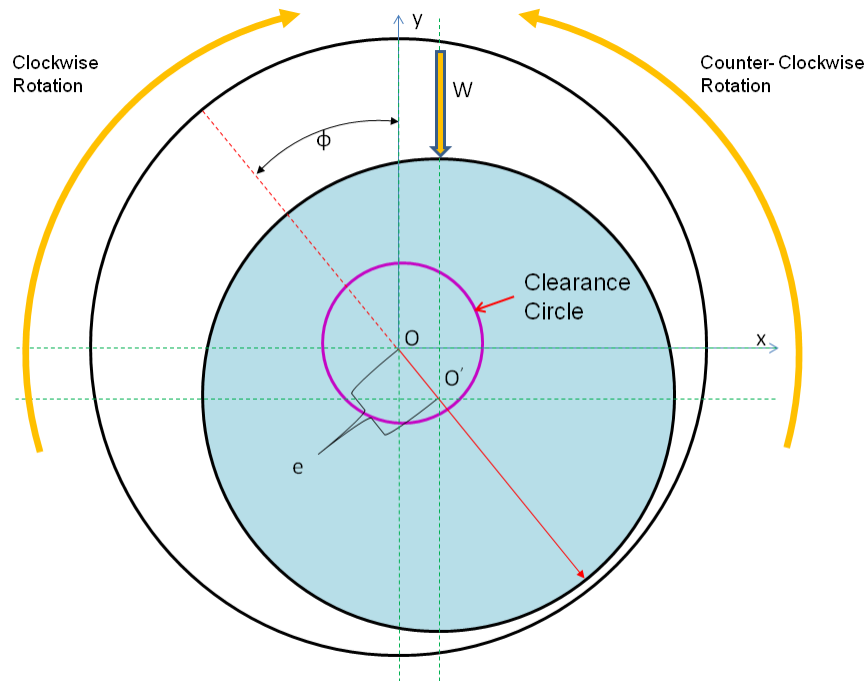
Figure 6-4: Graphic of Bearing Nomenclature

Knowing the shaft location relative to the bearing is needed for determining bearing eccentricity ratio (ϵ), and attitude angle (ϕ). It also allows the film thickness to be determined. Shaft position plots are shown in the form of a clearance circle, where the centroid of the shaft (O$'$) is plotted against the clearance gap around the concentric position of the shaft and bearing (O). Figure 6-4 shows the geometry of the shaft and bearing along with the clearance circle (which is plotted in purple). For standardization, plots are shown looking from the forward section of the bearing in the aft direction.

Most hydrodynamic bearings undergo a break-in period where loads are gradually increased with operating time. This allows for a slow wear down of the very high asperities between contact surfaces, improving the surface finish and hydrodynamic

performance of the bearing. This process can take hours or days.[1] Because of the fast pace of this project involving a multitude of bearings and the fact that the test rig is not designed to be operated unattended, a formal break in of the bearings tested in this project was not done. Only one bearing, the stave configuration, was tested for an extended period of time to determine the effects that a break-in of the bearing had on hydrodynamic performance.

6.1.2   Hydrostatic Testing

Hydrostatic testing occurred primarily with the bearings submerged in the tank. When tested with the centrifugal pump which runs at one speed, projected area loads were varied in increments from a low of 1 psi to 13 psi depending on the bearing's ability to support those loads. Later bearings (Hydrostatic Lift and Two-Slot bearings) were tested with positive displacement gear pumps that had the ability to change operating speed and therefore operating conditions regardless of the projected area load. For these bearings, projected loads were varied as were pump speeds.

(a) Side force test configuration   (b) Curtain to contain excess spray
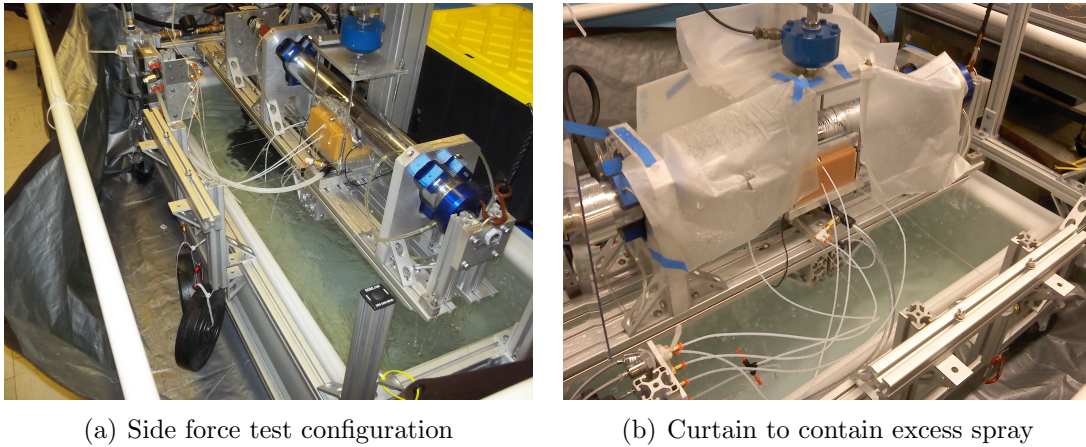
Figure 6-5: Hydrostatic Side Force Testing

Bearings were also tested to determine their ability to support side loads. For these tests, the operating rig was set up such that the bearings were not submerged and operating horizontally in air. In these conditions, the applied side force, the projected

---

[1]MIL-B-17901B specifies a minimum 25 hour break in period for bearings they test.

load, and pump speed (when operating with gear pumps) were varied. In certain operating conditions, the supplied fluid pressure did cause a large amount of spray due to exit flow from the bearing. This required curtains to be setup around the bearing to prevent the wetting of the test rig ancillary electronics. Figure 6-5 shows the hydrostatic side force testing of the bearing and the curtain configuration used to contain spray.

A variety of plots are used to characterize the hydrostatic response of the bearings. Some of the variables of the plots were various operating conditions such as flow rate, projected load, shaft eccentricity, flow horsepower, and load efficiency. Load efficiency (η_{Load}) in hydrostatic bearings is defined as:

$$\eta_{Load} = \frac{P_{projected}}{P_{inlet}} \tag{6.1}$$

where P_{inlet} is the fluid supply inlet pressure to the bearing and $P_{projected}$ is the projected area load.

6.1.3 Hybrid Testing

Hybrid testing, with both hydrostatic pressure and shaft rotation, was conducted with the bearings submerged. In most conditions, the hydrostatic effects completely dominated the bearing response with changes in shaft RPM (even between 0 and 500 RPM) having very minimal effects. Hybrid testing with the bearings out of the water were not done primarily because this prevented normal flow of water into the bearing due to shaft rotation but also because an extreme amount of spray was seen due to the coupling of hydrostatic pressure with shaft rotation.

Transient tests were conducted on some bearings to characterize the dynamic effects of changing speeds, varying loads, and changing the fluid supply flow/pressure. These tests were also conducted with the bearing submerged.

6.2 Plain Journal Bearing - Turcite

6.2.1 Design Basis and Description

The first Turcite® bearing built and tested was a plain journal bearing with a nominal design clearance ratio ($\frac{D_{shaft}}{2C}$) of 800. Although this clearance ratio is much higher than typical for water-lubricated bearings (see chapter 7.1), a tight clearance was selected for the first bearing to provide a bearing more in-line with conventional hydrodynamic bearing clearances. This first bearing was used to prove out the manufacturing process and to serve as a way to validate the proper operation and data collection capability of the test rig because there are numerous references in literature with analytical and experimental results to compare to. This specifications for this bearing are provided in Table 6.2.

Table 6.2: Plain Journal Bearing (Turcite) Specifications

Bearing Configuration	Plain Journal	
Material	Turcite	
Diameter	3.2346	Inches
Radial Clearance	0.0020	Inches
Clearance Ratio	788	
Engagement Arc	175	degrees
L/D Ratio	2	

6.2.2 Test Results

Hydrodynamic testing was done from speeds between 25 and 350 RPM for projected area loads of 2, 5, 10, 15, 20, and 25 psi. For this initial bearing, higher speed tests were not conducted, but for later bearings hydrodynamic testing was done at speeds up to the maximum motor speed of 500 RPM. Figure 6-6 shows the friction coefficient versus surface speed and Figure 6-6 shows the friction coefficient versus Sommerfeld number - both in the counter-clockwise direction.
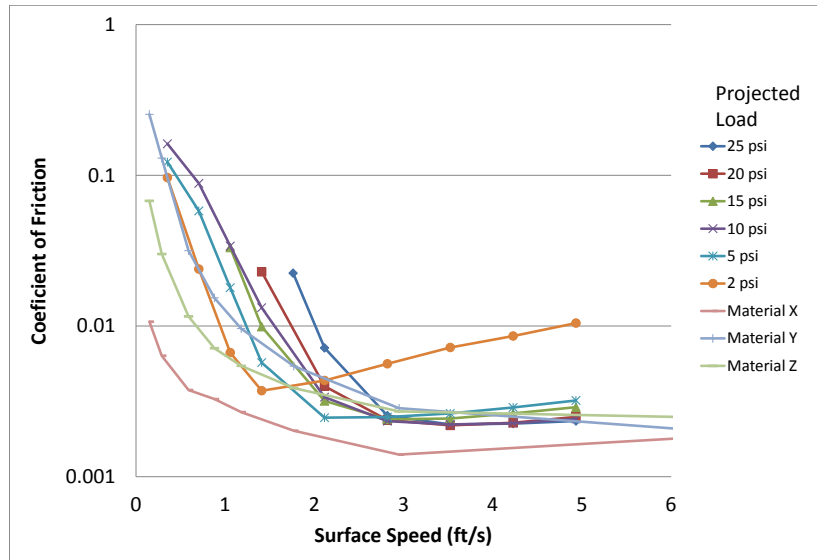
Figure 6-6: Plot of hydrodynamic friction coefficient versus surface speed in plain journal bearing for various projected area loads in the counter-clockwise direction

The friction response of the bearing behaves as expected, with a relatively clear distinction between mixed and hydrodynamic lubrication regimes. Figure 6-6 provides comparison against several bearings tested on a 6.75 inch experimental test rig at Naval Surface Warfare Center, Carderock Division - Ship Systems Engineering Station (NSWCCD-SSES) in Philadelphia. These bearings were of different materials and had undergone a break-in cycle of approximately 150 hours. Although these bearings were tested at a higher projected area load of 40 psi and had lower clearance ratios than the plain journal bearing, the general results are in line with each other and lend confidence in test rig's capabilities.

Figure 6-7 provides comparison against numerical predictions from Raimondi and Boyd[23]. The numerical predictions show a similar trend to experimental results, but a lower predicted friction. Some caveats exist with the numerical predictions such as the fact that direct values do not exist for bearings with L/D values equal

202
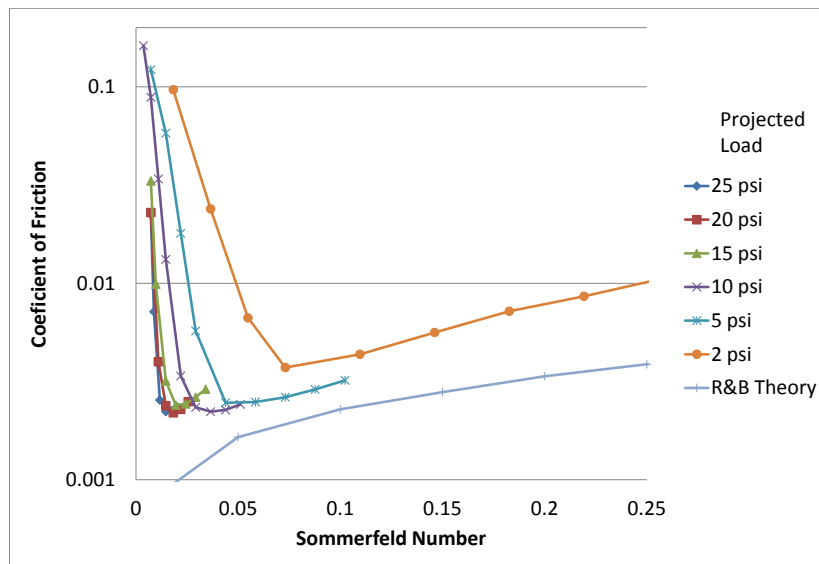
Figure 6-7: Plot of hydrodynamic friction coefficient versus Sommerfeld number in plain journal bearing for various projected area loads in the counter-clockwise direction

to 2. The plotted line is based on interpolated values, which introduces some error. An additional factor is that the numerical values are for extremely low values of Sommerfeld numbers, where the values may not be completely reliable. The Navy experimental values also diverge significantly from theoretical values at the low Sommerfeld numbers tested. Because of these factors, more confidence is placed in the Navy experimental results in Figure 6-6 as a point of comparison.
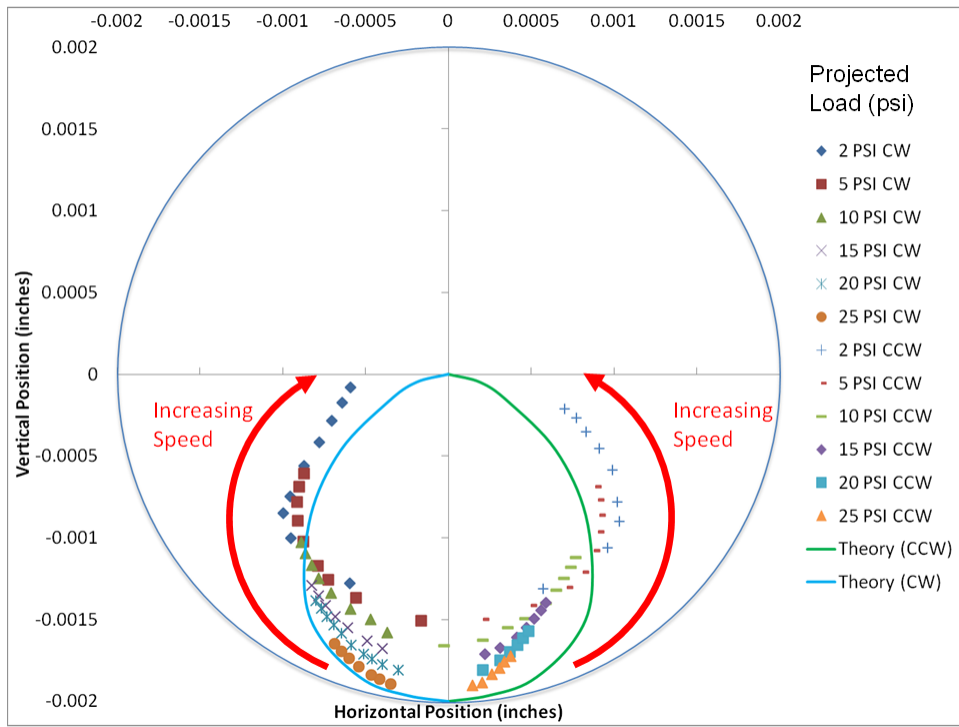
Figure 6-8: Locus of shaft position in plain journal bearing for various projected area loads and speeds, with comparison to theory

Figure 6-8 shows the shaft position for various load conditions and speeds. This plot again shows correlation with predicted trends. The variations between theory - based on numerical solutions - and experimental results are acceptable. At very low projected area loads, there is a small, but increased variation between desired and actual load due to the ability of the force tester to control it, which will introduce errors. Additionally, differences in eccentricity and attitude angle have been seen between predicted and experimental results before[22].

Several observations can be made from these data.

1. Increases in projected area load shift the point of minimum friction (corresponding to the transition between mixed and hydrodynamic lubrication) to higher surface speeds.

2. There is a marked jump in friction as the bearing enters the mixed lubrication regime that is identifiable from the data. This is especially true with a non-log axis.

3. At higher projected area loads (15-25 psi), the Sommerfeld number appears to be a good predictor of the transition between mixed and hydrodynamic regimes.

4. Experimental results indicated higher friction values than theoretical.

5. Water-lubricated ship bearings - when operated at design projected loads of 40 psi and typical operating speeds - can be expected to operate at high eccentricities and low attitude angles.

The plain journal bearing proved to be a good test bearing to validate the test rig and the manufacturing method with Turcite® bearings. This allowed the project to move forward with confidence in the ability to build and test hydrostatic bearings.

6.3   180 Degree 3 Port Bearing

6.3.1   Design Basis and Description

The 180 degree 3 port hydrostatic bearing is a derivative from the work done by Wong[33]. Wong developed and tested a partial arc surface self-compensated hydrostatic bearing using a 3 port external pressure supply system, achieving load efficiencies of approximately 18 to 24 percent. This bearing was tested in a centrally loaded condition without any shaft rotation for various eccentricities.
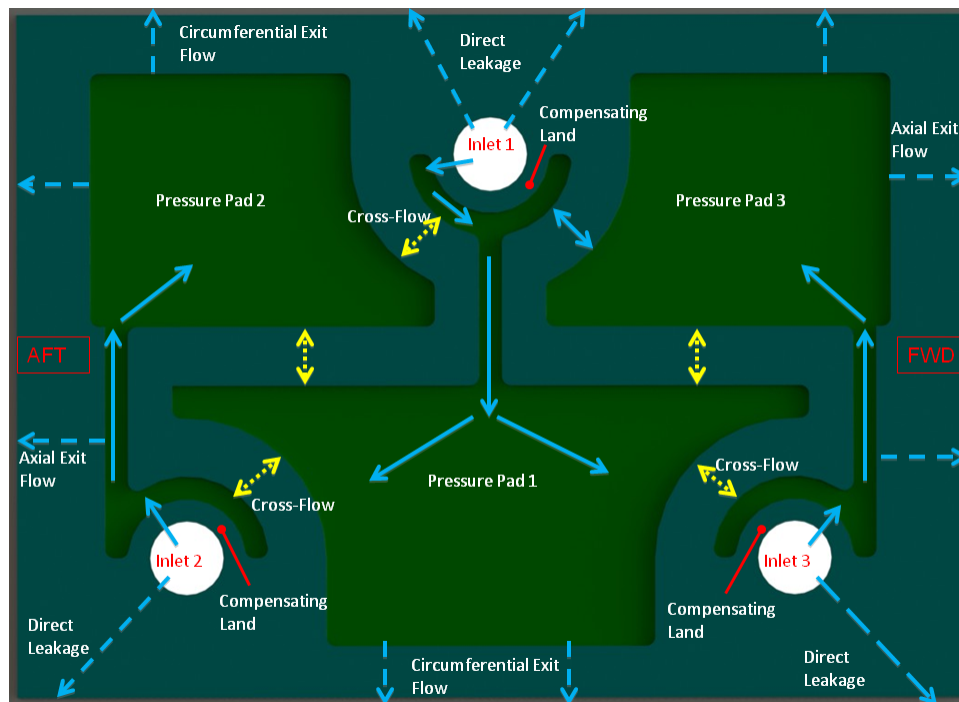
Figure 6-9: Conceptual layout and flowpaths for 3 port bearing configuration

Figure 6-9 shows the conceptual layout of the 3 port bearing configuration. The operation of the bearing is described below:

1. Fluid is supplied to the 3 inlet ports at a common fluid pressure.

2. This fluid flows across the compensating lands into a pressure supply groove and across the bearing to the pressure pads. These pads provide the majority

206

of load support to separate the shaft from the bearing.

3. An eccentric movement of the shaft towards one side of the bearing due to a side load changes the gap clearance across the compensating lands. In the case that the shaft moves towards inlet 1:

  - The compensating gap for inlet 1 narrows, resulting in an increased pressure drop across the compensator.

  - This increased pressure drop results in lower pressure supplied to pressure pad 1, and therefore less force pushing the shaft towards inlet 1.

  - The compensating gaps for inlet 2 and 3 widens, reducing the pressure drop across those compensators.

  - This reduced pressure drop results in a larger pressure supplied to pressure pads 2 and 3, causing an increased force pushing the shaft away from inlet 1.

  - This continues until a balanced operating point is found.

The bearing is also influenced by direct leakage from the inlets, which is wasted energy. Additionally, there are exit flows from the pressure pads and pressure supply grooves in the bearing to the circumferential and axial ends of the bearing. These leakage and exit flow paths are influenced by the width and length of the lands as well as the fluid gap across the lands, which combine to provide a resistance against fluid flow as described in chapter 3.1. In general, these resistances can be lumped together into a resistance across the compensator and resistance to leakage to aid in determining the theoretical operating characteristics of the bearing. Figure 6-10 shows how the lands are discretized and combined to provide a resistance network for analysis.

There is plenty of literature and prior work regarding how to design the compensator and leakage resistances to obtain an optimized result [28, 26]. The dominant variable is the resistance ratio (ζ), defined as:
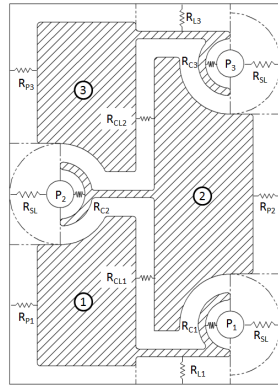
(a) Land resistances of 3 Port Bearing   (b) Resistance Network Schematic
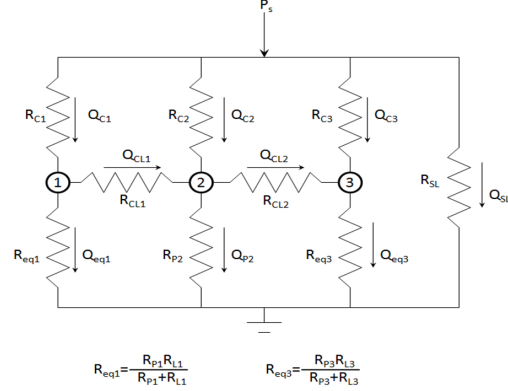
Figure 6-10: 3 Port Bearing Lumped Resistance Network[33]

$$\zeta = \frac{R_{collector}}{R_{leakage}} \tag{6.2}$$

where $R_{collector}$ is the hydraulic resistance of the collector and $R_{leakage}$ is the hydraulic resistance of the leakage paths from the load pad. In general, to obtain a balanced hydrostatic bearing design providing the optimum between load support, stiffness, and ability to compensate for variable load conditions, ζ should be designed to be as close to a value of one as possible. For hydrostatic journal bearings, the resistances are typically calculated assuming a concentric journal and bearing, allowing for the land resistances using the flat plate approximations to be quickly calculated. As described in section 3.2.3, this can introduce large errors - particularly for at higher eccentricities. Despite this, utilizing the flat plate assumption for designing bearings has been done successfully in the past[32, 15, 33].

The 180 degree 3 port bearing was designed using the flat plat approximation to set ζ at approximately 0.946 (close to 1). A further modification to the bearing was done by altering the pressure pads such that they were no longer a complete recess, but rather a land surrounded by a pressure pad groove. The theory is that the landed region improves hydrodynamic performance, and because the pressure pad grooves should all be at approximately the same pressure, there will be very little pressure gradient and result in pressure pad having the same pressure as a fully recessed pad.

208

Figure 6-11: Photo of 180 Degree 3 Port Bearing

The 180 degree 3 port bearing is shown in Figure 6-11, and the specifications for the bearing are provided in Table 6.3.[2]

Table 6.3: 180 Degree 3 Port Bearing Specifications

Bearing Configuration	180 Degree 3 Port Bearing	
Material	Turcite	
Diameter	3.2356	Inches
Radial Clearance	0.0025	Inches
Clearance Ratio	633	
Engagement Arc	180	degrees
L/D Ratio	2	

6.3.2 Test Results

Initial hydrostatic testing of the 180 degree 3 port bearing showed that the bearing had difficulty achieving hydrostatic operation above projected loads of 5 psi. It was

---

[2]The small holes visible in the middle of the pressure pad areas are ports for pressure measurements.

noted that flow was almost entirely stopped at higher loads, indicating that the shaft was sealing off flow from the inlet ports. At the early stage of testing, the rig did not have multiple flowmeters or pressure sensors allowing for the accurate recording of flow into the 3 individual inlet ports or to measure pressure at various locations along the bearing surface. To determine the bearing fluid conditions, flowmeters and additional pressure sensors were added and the experimental testing was repeated.

It was found that the shaft was above the concentric position of the shaft for projected loads less than 4 psi, indicating the shaft was floating above the bearing center at those loads. Loads greater than 5 psi resulted in a the shaft being bottomed against the bearing, leaving a very small desirable operating range between 4 and 5 psi projected loads. At the lower load conditions, total flow rate was very high with values well above 2.5 gpm. Figure 6-12 shows the various pressures for the bearing and Figure 6-13 shows the measured flow rates to the bearing - both as a functions of projected load. The label configuration is as depicted in Figure 6-9.
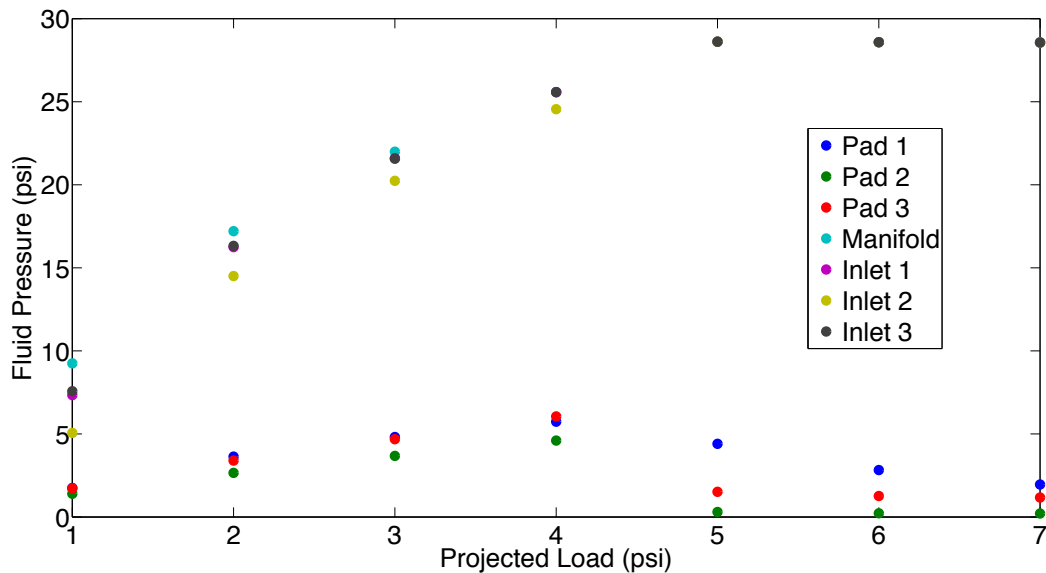
Figure 6-12: Fluid pressures in 180 degree 3 port bearing for various projected area loads

There is a clear change in pressures and flows above 5 psi when the shaft bottoms
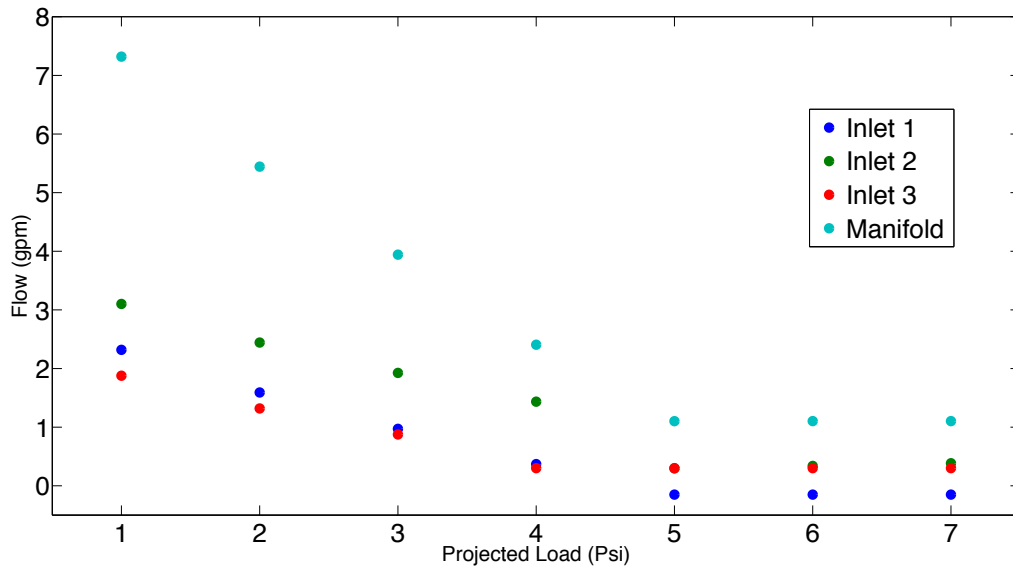
Figure 6-13: Flow rates in 180 degree 3 port bearing for various projected area loads

on the bearing. The inlet pressures all reach the manifold pressure corresponding to the dead head of the centrifugal pump, and the pad pressures drop indicating that flow and pressure is not being maintained in the load pads. Flow rates all reach the 'floor' value of the flowmeters - below which there is no reliable electronic indication of flow.[3] As stated before, flow rates were particularly high. Because the bearing was designed for a resistance ratio (ζ) of approximately 1, the pad pressures were expected to be closer to 50 percent of the value of the inlet ports. The results show that the pad pressures were much lower than this, indicating that there was a pressure drop across the landed region of the pads or some other factor (such as the effect of high eccentricities) was in play. Load efficiencies were also particularly low, with values on the order of 15 to 18 percent.

Hydrodynamic testing of the bearing was conducted at projected loads between 1 and 20 psi and speeds from 25 to 450 rpm. Figure 6-14 compares the friction curves for the two bearings as a function of Sommerfeld number for a given projected load. Its

---

[3]The manifold flowmeter was rated for 2 gpm and above, but could read down to approximately 1 gpm. The inlet flowmeters were each rated for flow down to 1 gpm, but could read to flows of around 1/3 gpm. These lower limits of reading flow are noticeable in Figure 6-13 where they level out and don't change for increased projected loads.
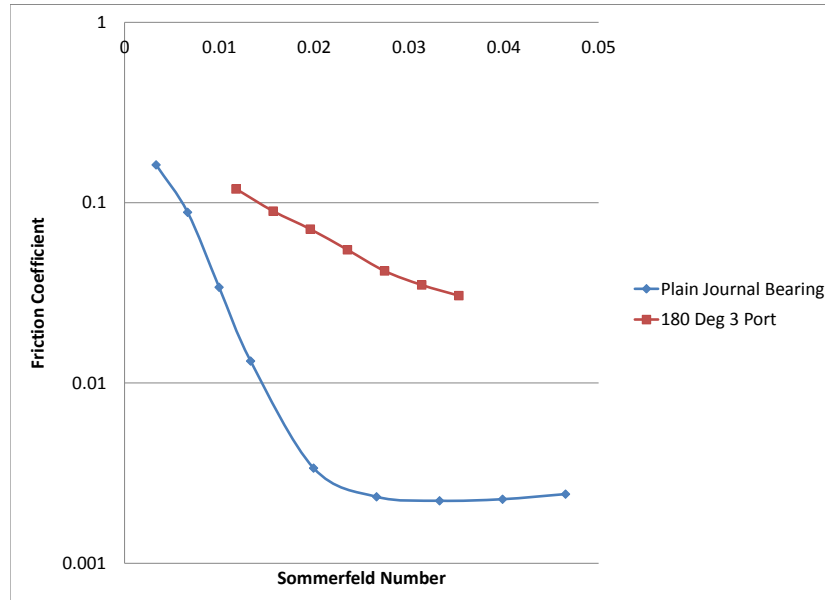
Figure 6-14: Counter-clockwise friction curves for plain journal bearing and 180 deg 3 port bearings at 10 psi projected load as a function of Sommerfeld number

performance was markedly worse than the plain journal bearing in all respects. Transition to the hydrodynamic lubrication regime occurs at significantly higher speeds than the plain journal bearing, and friction values are higher across all loading conditions and speeds. This indicated that the introduction of the many surface grooves had a very substantial effect of the hydrodynamic performance of the bearing, which could ultimately limit its utility.

Hybrid testing of the bearing was also conducted at a variety of speeds and loads. For lower projected loads where the bearing is able to operate hydrostatically, the friction is virtually negligible with the exception of very high rotational speeds.[4]. This flat friction curve turns out to be a very good indicator (along with shaft position) of whether the shaft is actually operating hydrostatically or not. The bearing was also

---

[4]At very high rotational speeds, there is an increase in friction for bearings being supplied with hydrostatic fluid flow and pressure. This is due to the increased shearing of the fluid that occurs with the addition of rotation.
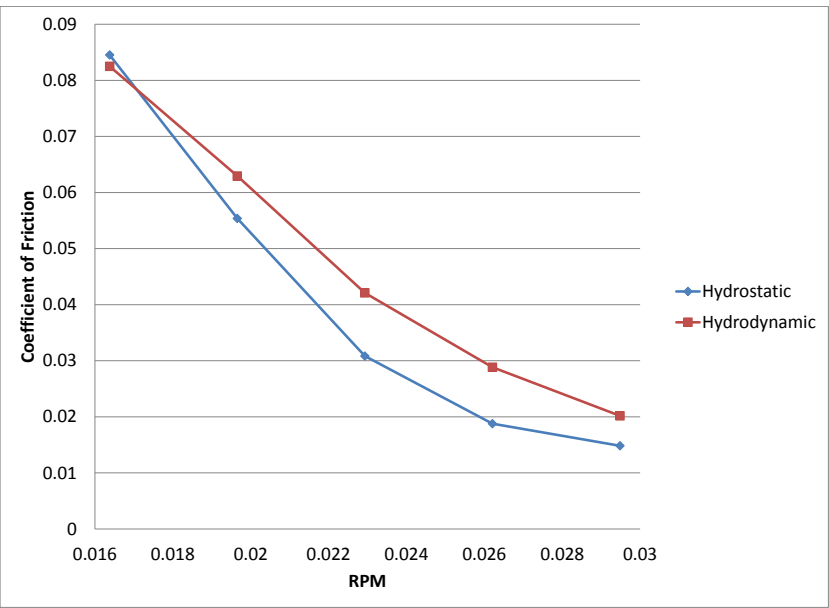
Figure 6-15: Clockwise friction curves for 180 deg 3 port bearings at 15 psi projected load as function of Sommerfeld number, comparing hydrodynamic and hybrid performance

tested at higher projected area loads where the shaft was bottomed out on the bearing during pure hydrostatic testing. Even at these higher load conditions, the addition of hydrostatic fluid pressure had a noticeable reduction in friction for various speeds. This effect diminished at lower speeds until the friction curves met. This is shown in Figure 6-15.[5] This phenomena is due to the added supply pressure acting on the inlet ports and because the hydrodynamic action provides a film gap that allows the supply fluid to flow across the compensator lands and into the pressure pads of the bearing.

The 180 degree 3 port bearing showed a combination of relatively poor hydrostatic performance and a marked decrease in hydrodynamic performance. A second 3 port bearing was designed and built with a few modifications in an attempt to improve upon the performance.

---

[5]The crossing of the friction curves at a Sommerfeld number of approximately 0.016 does not indicate a continued trend, but is rather within the error range of the torque measurements.

6.4   165 Degree 3 Port Bearing

6.4.1   Design Basis and Description

A design review was conducted with the project sponsors to discuss the test results of the 180 degree 3 port bearing and solicit feedback on how to improve the design. Two key points were discussed, and recommendations were made for the next bearing design:

1. The design clearance ratio for the 180 degree bearing was much higher than typical for water-lubricated outboard bearings. A recommendation was made to reduce the clearance ratio (i.e. increase the clearance) significantly. Reasons for this were to bring the clearance ration more in line with standard clearances and because Navy experimental bearing data has shown that increasing the clearance generally results in improved hydrodynamic performance.

2. Naval partial arc bearings use an arc engagement of approximately 165 degrees. The 180 degree bearing was designed and built as close to 180 degrees of arc as possible. It was recommended to reduce the arc to less than 180 degrees to match more typical naval designs. This reduction in arc does come at a cost of less area available for placing hydrostatic features and lands.

To address the recommendation of an increased gap size, a larger master shaft was fabricated to set the clearance ratio at a nominal 250:1. The geometry of the bearing regarding the location, size and shape of the surface features were largely unchanged with the exception that the landed regions inside of the pressure pads were removed. This was expected to have a significant adverse effect on the bearings ability to operate hydrodynamically, but was done to troubleshoot the large pressure drop between inlet ports and pressure pads. If the pressure drop was caused in part by the presence of the lands, then removing them would assist in full pressure being applied to the entire pressure pad. To create the lower arc engagement, the bearing was fabricated in the same way as the 180 degree bearing and the desired arc was obtained by milling away

the circumferential edges of the bearing. Table 6.4 shows the specifications for the 165 degree 3 port bearing.

Table 6.4: 165 Degree 3 Port Bearing Specifications

Bearing Configuration	165 Degree 3 Port Bearing	
Material	Turcite	
Diameter	3.2434	Inches
Radial Clearance	0.0064	Inches
Clearance Ratio	250	
Engagement Arc	165	degrees
L/D Ratio	2	

6.4.2   Test Results

Hydrostatic testing of the 165 degree bearing showed even worse performance than the 180 degree bearing. The combination of larger clearance and smaller land width at the circumference of the bearing resulted in a significant decrease in the resistance against exit flow and leakage. The net result was that bearing flow rates were very high and the bearing was not able to support projected loads greater than approximately 1.75 psi. Figure 6-16 shows the various pressures for the bearing and Figure 6-17 shows the measured flow rates to the bearing - both as a functions of projected load. As before, the label configuration is as depicted in Figure 6-9.

Flow rates were unacceptably high and visual indications from the bearing showed a large amount of the flow appeared to be direct leakage from the inlet ports. This is shown clearly in Figure 6-18, a video screen shot from the 165 degree bearing under hydrostatic test at 1.5 psi projected load. This large direct leakage path was also a contributing factor behind the large pressure drop between inlets and pressure pads and the subsequent low pressures developed in the pads, which resulted in the poor load support ability. This inability to support even modest loads is quantified with the load efficiency values of less than 7 percent.
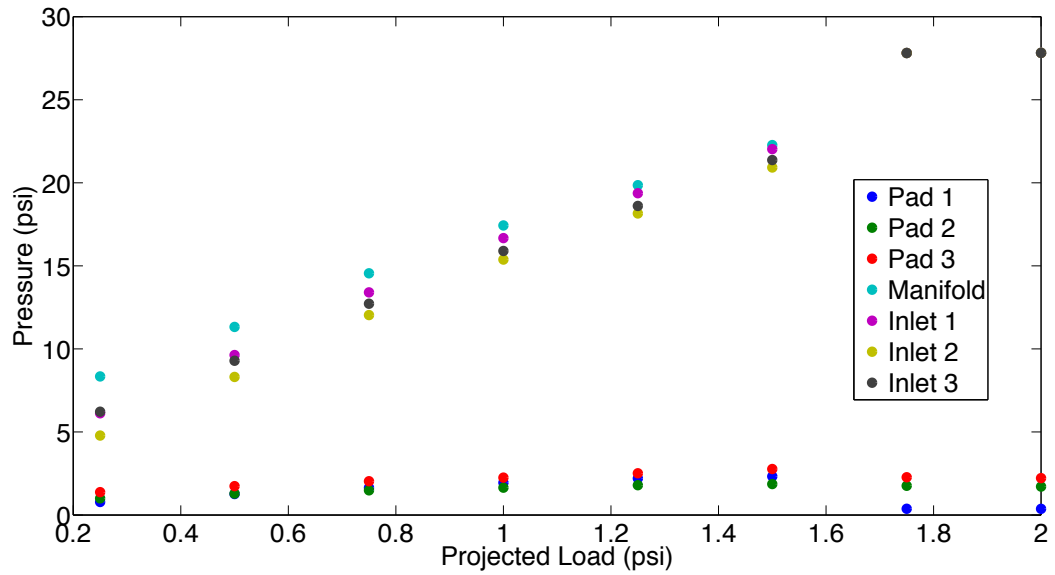
Figure 6-16: Fluid pressures in 165 degree 3 port bearing for various projected area loads
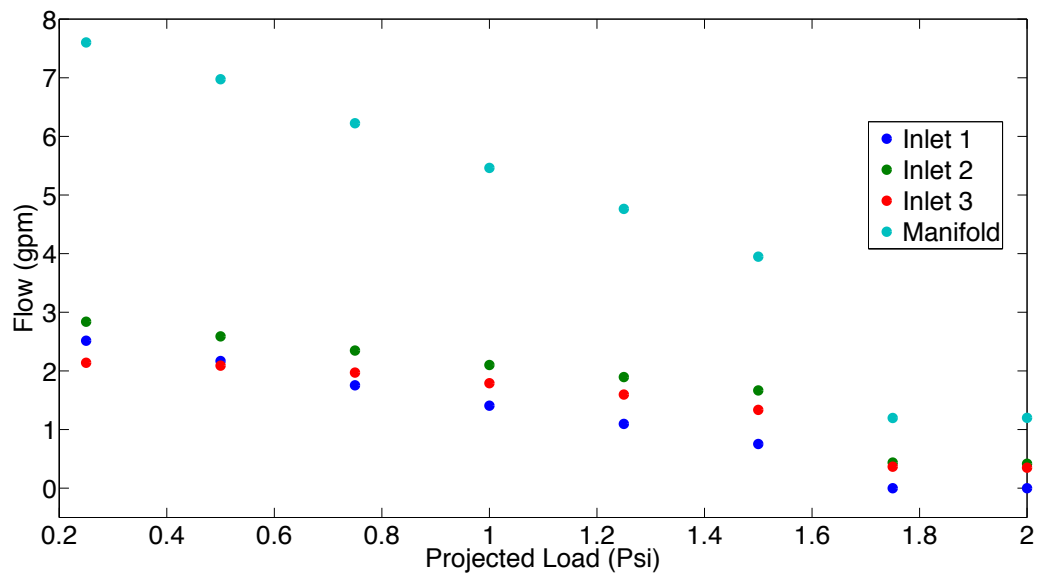
Figure 6-17: Flow rates in 165 degree 3 port bearing for various projected area loads
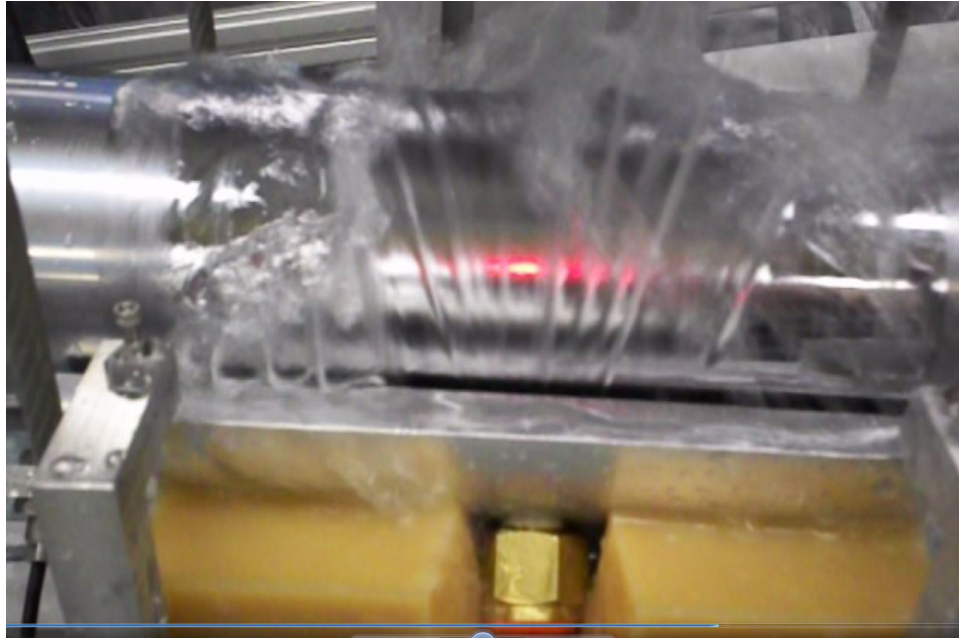
Figure 6-18: Screen shot of high flow rate in 165 degree 3 port bearing at 1.5 psi projected load in hydrostatic operation

Hydrodynamic test results revealed an interesting behavior of the bearing. Because of the relative lack of land regions that are needed for hydrodynamic lubrication, it was expected that the ability to support loads without pump supplied pressure would be very poor. This was generally the case, particularly at higher loads. At lower loads in the clockwise direction however, the bearing displayed a very discrete behavior characterized by two distinct modes of operation. At higher speeds the bearing was hydrodynamic with very little friction, but as speeds decreased the friction jumped significantly. The result was such that the mixed lubrication regime seemed to be skipped entirely at these low load conditions in that direction. At higher loads (above 8 psi projected load), the bearing was unable to achieve hydrodynamic lubrication even at the highest speeds. This response is shown in Figure 6-19. With counter-clockwise rotation, this response was not seen except for very low projected loads below 3 psi and even when the bearing did become hydrodynamic it required much higher rotational speeds than the same loading condition in the clockwise direction. Hydrodynamic lubrication was not achieved at projected loads above 7 psi.
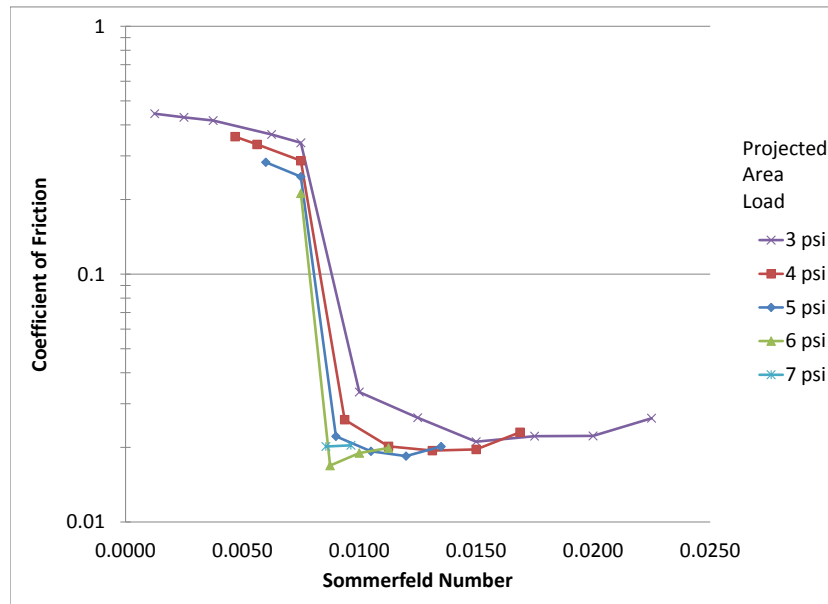
Figure 6-19: Clockwise friction curves of 165 degree 3 port bearing for various projected area loads as a function of Sommerfeld number

It is theorized that the discrete hydrodynamic behavior of the 165 degree 3 port bearing is due to the bearing acting similar to a "Rayleigh Step" bearing. Lord Rayleigh proved that the optimum bearing shape for supporting load is a step of two different thicknesses[24]. The recessed regions meeting up to the landed regions is similar to the profile shown in Figure 6-20. The performance of such bearings is only optimized for one value of film thickness, and is highly dependent upon the ratio of film height to step height as well as the ratio between land widths. Deviations from this optimum condition due to a change in load or speed can result in a significant degradation in the ability of the bearing to support a load[8]. This explains the discrete behavior in the bearing between different loads and speeds, as well as direction (due to the bearing being asymmetrical).

The unique hydrodynamic response of this bearing illustrates some interesting op-

219
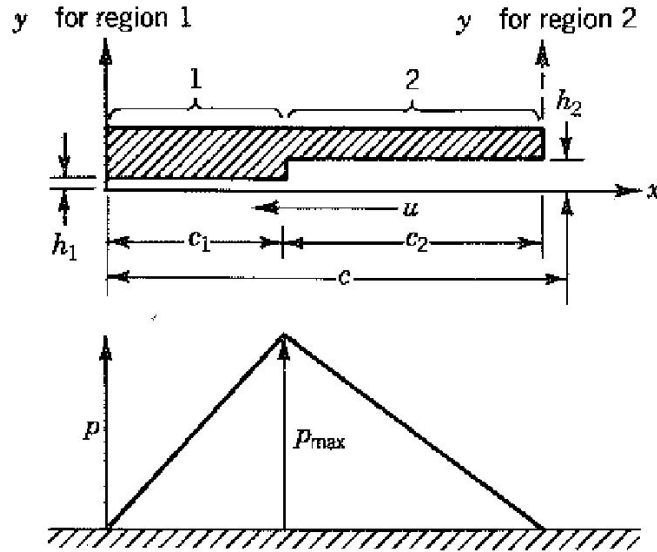
Figure 6-20: Rayleigh step bearing and corresponding pressure profile[8]

portunities for water-lubricated bearing designs. It is possible that a derivation of a step bearing could be designed for a known loading on the shaft and specific shaft speed. For an ocean vessel that may vary shaft speeds over a large range, caution is needed; as was seen in the experimental hydrodynamic results of the 165 degree 3 port bearing, operation outside of a design point can result in very large friction.

Hybrid testing was conducted on the bearing for various speeds, and projected loads up to 5 psi. As with the 180 degree 3 port bearing, in hybrid operation the friction in the bearing when operating hydrostatically is negligible and friction is reduced even at loads exceeding the hydrostatic capacity of the bearing.

The extremely low load efficiencies coupled with the high flow rates in the bearing made this bearing a failure from a hydrostatic perspective. Despite the interesting hydrodynamic behavior observed in this bearing, fundamental changes were needed in the design of the bearing. Possible changes for the basic 3 port bearing design to provide improvements to the response of the bearing include:

1. Locate the inlet ports away from the edges of the bearing. This would reduce

the amount of flow and pressure lost to direct leakage from the bearing, which is effectively lost energy. This would reduce flow rates, but come at the cost of placing the compensating lands closer together. This in effect reduces the ability of the bearing to respond to changing loads.

2. Reduce the width of the compensating lands or fully encircle the inlet ports. This would adjust the resistance ratio, allowing greater pressure to be achieved in the pressure pads and increasing the load support of the bearing.

3. Providing a full 360 degree arc bearing would reduce the flow rate in the bearing and allow greater pressures to be developed. This is not feasible due to the requirement that the bearing be less than 180 degrees.

4. Reduce the clearance in the bearing to provide increased resistance to flow. Due to the bearing materials used and the need for generous gaps for alignment, there is a limit on how small the clearances in the bearing can be, making this an unrealistic change.

The changes would, at best, be able to provide marginal improvements in the bearing design. Instead, a radical departure from the basic 3 port bearing design was made, which resulted in the Centerlift bearing design discussed below.

6.5 Centerlift Bearing

6.5.1 Design Basis and Description

There was an opportunity to attempt to improve the performance of the 3 port bearing designs. As an alternative, there was also an opportunity to develop a new design incorporating the lessons learned from the previous designs, which resulted in the Centerlift bearing. Going back to the original intended application in shipboard shafts, the actual requirements of the bearing were looked at. Although there are side loads in the bearing that develop due to ship heel and rolling, outboard bearings support a relatively consistent vertical load. The main variable that changes operating conditions is the speed of shaft rotation.
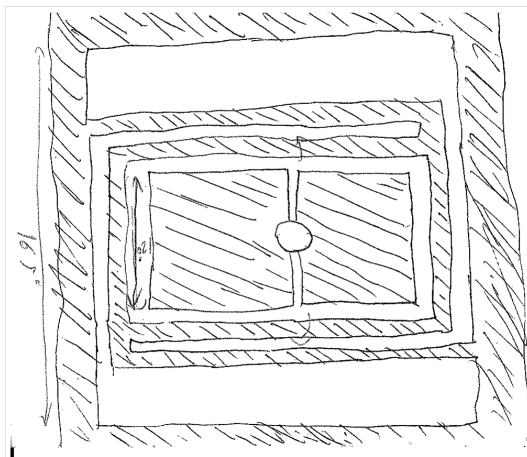
(a) Sketch of Centerlift Bearing Design
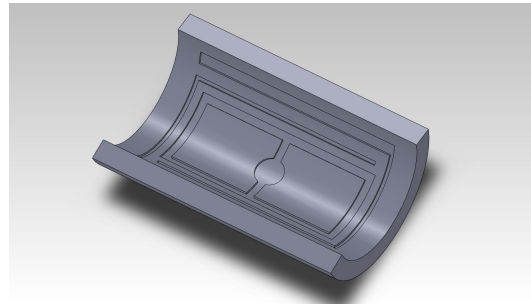
(b) Cad Design of Centerlift Bearing

Figure 6-21: Centerlift Bearing Design

The 3 port bearing was not designed to maximize the vertical load support of the bearing due to the off-center location of the pressure pads. Contributing to this is the fact that the bearing - as a surface self-compensated bearing - has a designed pressure drop across the compensating lands. At its optimum design with a resistance ratio (ζ) of one, only half of the inlet pressure would be passed on to the pressure pads. A fundamental shift in the bearing design was conceived whereby the entire inlet pressure would be utilized to provide vertical load support to the bearing, and surface

self-compensation would be used to provide the ability to respond to side forces. The original sketch of this bearing design is shown in Figure 6-21(a). The basis behind this design is that it would provide a more efficient use of the inlet pressure from the pump directing it to where it is needed most - lifting the shaft from the bearing. Surface self-compensation would be used only to support side loads. The placement of the inlet in the center of the bearing also provides a maximum amount of land area to resist flow and no direct leakage paths to atmosphere, thereby reducing flow requirement to the bearing.

The clearance used in the 165 degree 3 port bearing was quite large, which contributes to the high flow rates seen in the bearing. A larger clearance ratio was desired that would minimize the flow rate in the bearing, while at the same time be similar to actual clearances used in water-lubricated bearings. A design clearance ratio of 400 (on the high end of the range typical for naval applications) was chosen, requiring the fabrication of an additional master shaft.[6]

The shortened arc length of 165 degrees took away surface area to needed to place grooves to route fluid and land area to resist the exit flow from the bearing. Although the bearing area in the vicinity of 90 and 270 degrees provides little hydrodynamic support, that area does provide area that is beneficial to hydrostatic bearings. The design decision was made to increase the arc engagement to approximately 175 degrees. This extra arc would still allow replacement of the bearing without removing the shaft, while providing more area for hydrostatic features. The Centerlift bearing was fabricated to the specifications in Table **??**.

The specific layout, nomenclature, and location of pressure ports in the Centerlift bearing are provided in Figure 6-22. There is a central 'lifting section' of the bearing comprised of a single inlet port surrounded by grooves with hydrostatic lifting lands in the middle. To the sides of this section are compensating lands and the grooves

---

[6]Because of the manufacturing tolerances discussed in section 5.3.3, the actual clearance ratio ended up less than 400.

Table 6.5: Centerlift Bearing Specifications

Bearing Configuration	Centerlift Bearing	
Material	Turcite	
Diameter	3.2401	Inches
Radial Clearance	0.0048	Inches
Clearance Ratio	337	
Engagement Arc	170	degrees
L/D Ratio	2	
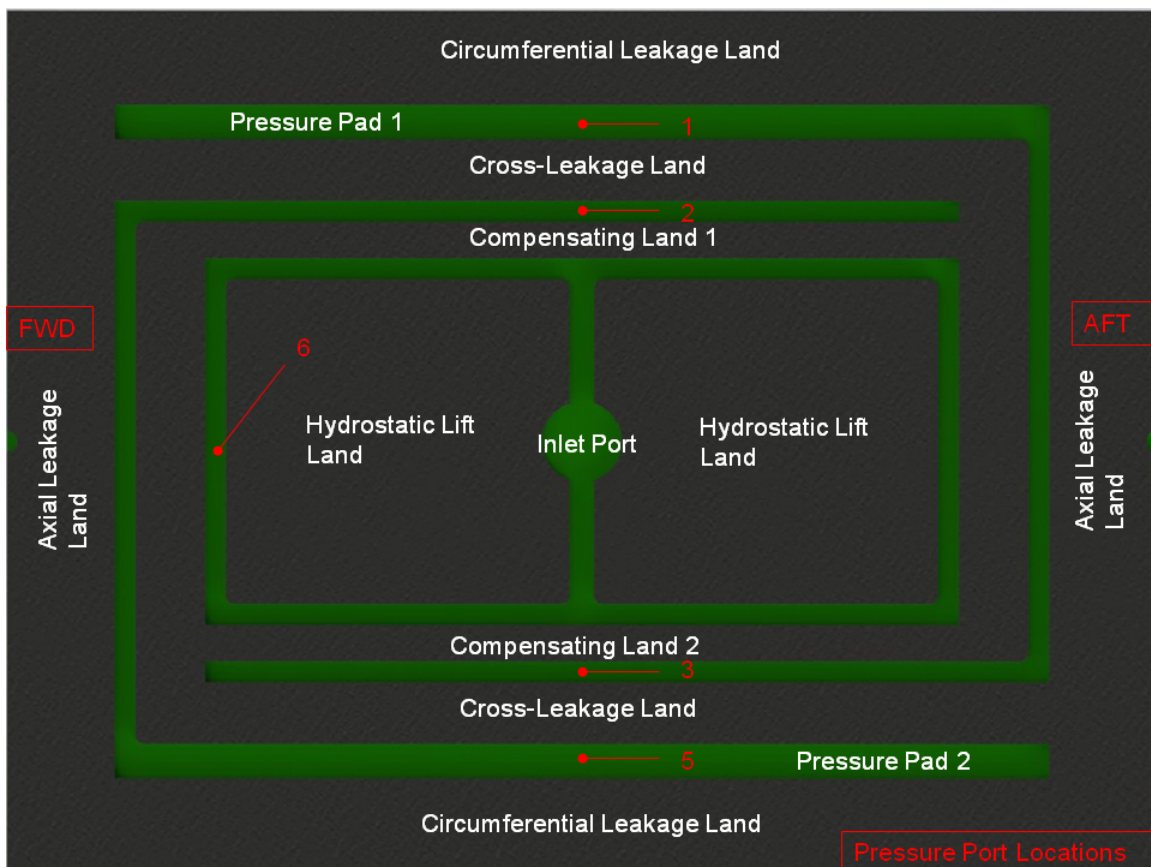
Figure 6-22: Centerlift Bearing Layout

to route pressure to the opposite side of the bearing. The arc between the grooves flanking the hydrostatic lift lands is approximately 60 degrees. This is to provide a large portion of uninterrupted land region along the bottom of the bearing to promote good hydrodynamic performance. Operation of the bearing is described below:

1. At slow operating speeds where hydrodynamic lubrication is insufficient, an external hydrostatic pressure supply provides pressurized fluid to the inlet port.

2. The fluid flows through the recesses around the hydrostatic lift lands, providing a hydrostatic lift capacity roughly equal to the inlet pressure multiplied by the land area. This provides the lift force to separate the shaft from the bearing.

3. If the shaft becomes eccentric towards one side of the bearing (i.e. moves towards compensating land 1) the closing gap between the shaft and compensating land 1 will cause a large pressure drop across it.

4. The large pressure drop across compensating land 1 causes a reduction in pressure in pressure pad 1 and therefore less force pushing the shaft toward compensating land 1.

5. A larger gap between shaft and compensating land 2 causes a smaller pressure drop across it, resulting in a larger pressure in pressure pad 2, and more force pushing the shaft away from compensating land 1.

6. The net result of these effects is a self-correcting force to return the shaft to a concentric position.

6.5.2 Test Results

Hydrostatic testing of the Centerlift bearing showed a significant improvement over the 3 port bearing designs in load support. Load carrying efficiencies were about double that of the 180 degree 3 port bearing, with hydrostatic operation possible up to approximately 10 psi with the centrifugal pump. Figure 6-23 shows the position of the shaft in the clearance circle as a function of projected area load. From the plot,
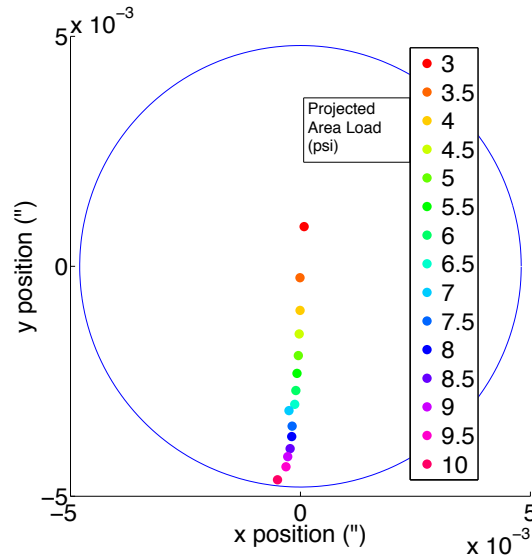
Figure 6-23: Locus of shaft position in Centerlift bearing during hydrostatic testing for various projected area loads (inches)

it is clear that the bearing maintains a relatively centered position from side to side and maintains a fluid film that decreases in magnitude with greater load.

A plot of the flow and pressures as a function of projected area load are provided in figures 6-24 and 6-25. The pressure port locations are as shown in Figure 6-22. Flow rates are appreciably lower than for the 3 port bearings throughout the range of loading conditions. There is a substantial pressure drop seen in port 6 (in the groove of the outer range of the hydrostatic lift land. This indicates that there is either a significant pressure gradient in the grooves themselves, a general drop in bearing pressures with a greater axial distance from the center inlet of the bearing, or some combination of the two. This pressure drop let to several design iterations of the Centerlift bearing in an attempt to increase the pressure seen around the periphery of the hydrostatic lift land region of the bearing. This was done by first adding external fluid routing to the axial ends of the hydrostatic lift lands and then by adding axial slits along the bottom dead center of the bearing to distribute flow directly from the inlet to the axial ends of the lift region.
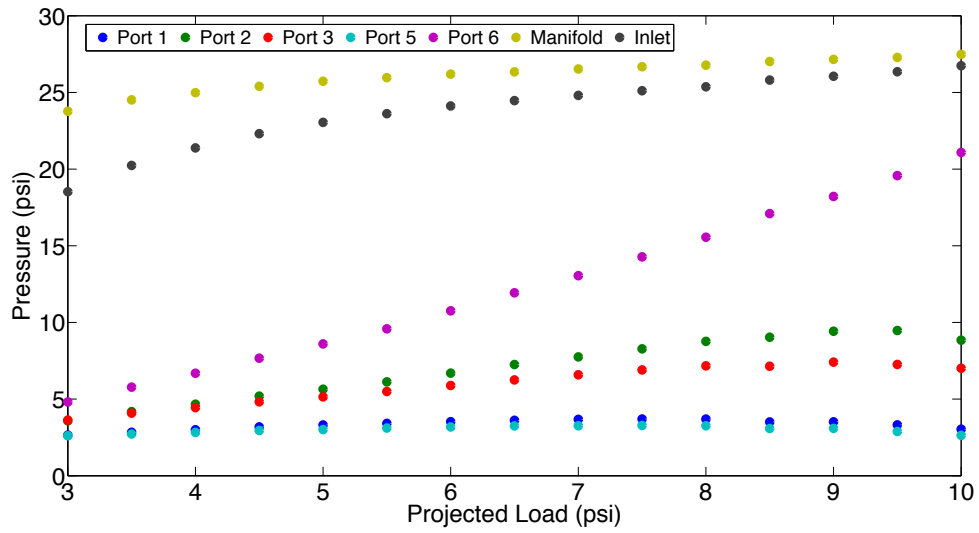
Figure 6-24: Pressures in Centerlift bearing for various projected area loads
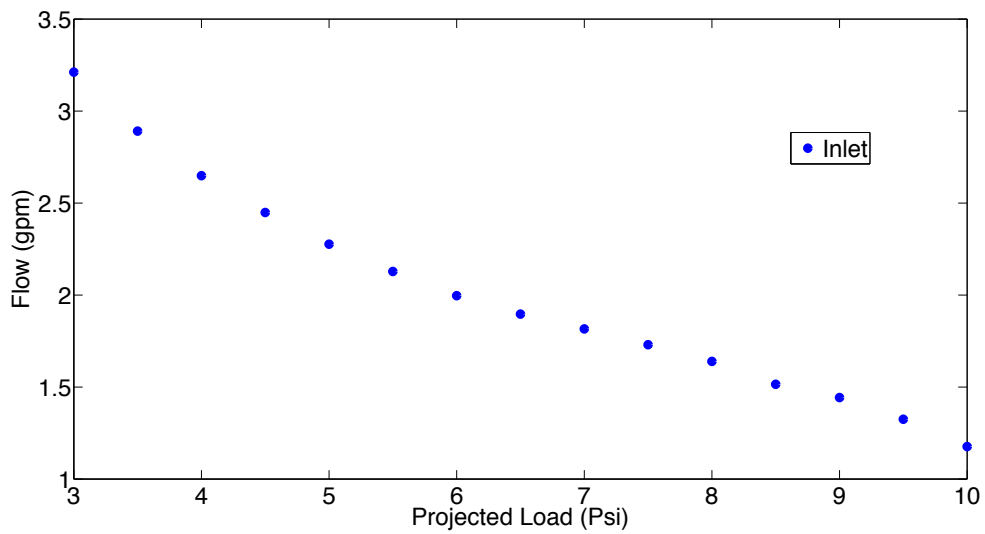
Figure 6-25: Flow rates in Centerlift bearing for various projected area loads

Hydrodynamic testing was done for projected area loads of 3, 5, 7, 9, and 11 psi with speeds from 100 to 450 rpm. Figure 6-26 shows the hydrodynamic friction of the bearing as a function of Sommerfeld number. The minimum point of friction is distinguishable, and the bearings are capable of reaching the hydrodynamic lubrication regime in all load conditions tested with the exception of 11 psi.
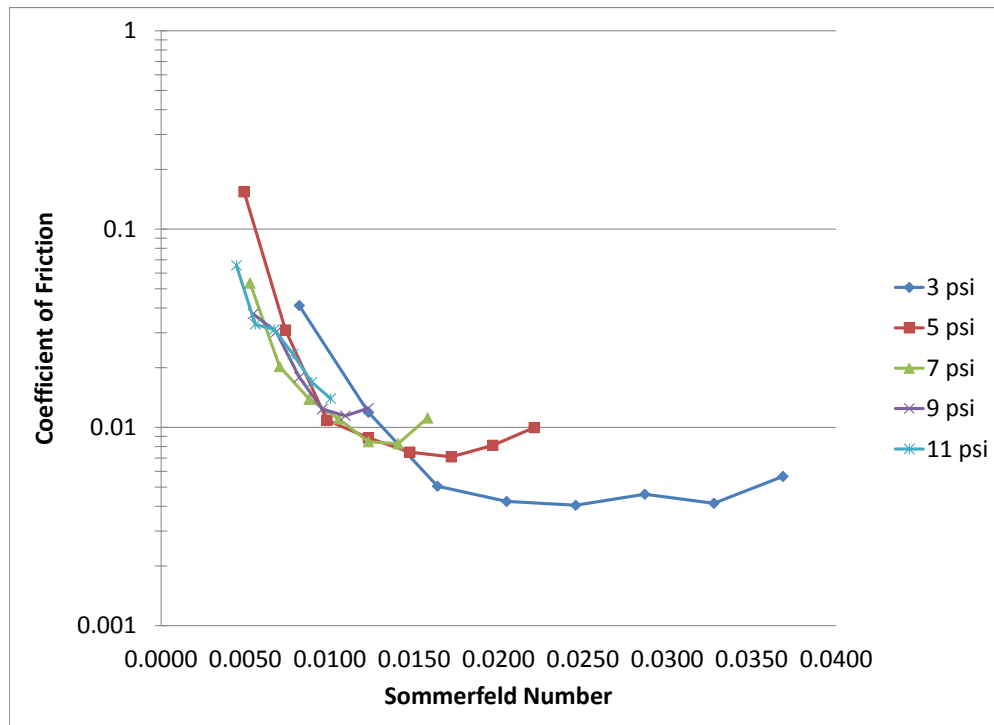
Figure 6-26: Counter-clockwise friction curves of Centerlift bearing for various projected area loads as a function of Sommerfeld number

Performance was degraded compared to the plain journal bearing configuration, but only marginally. This was fairly surprising considering the large amount of grooves that are in the surface of the bearing, despite the fact it had approximately 60 degrees of uninterrupted arc. Figure 6-27 shows the locus of shaft movement in clockwise and counter-clockwise rotation for a projected area load of 7 psi. It is clear that the bearing has a high eccentricity ratio and more importantly a very small attitude
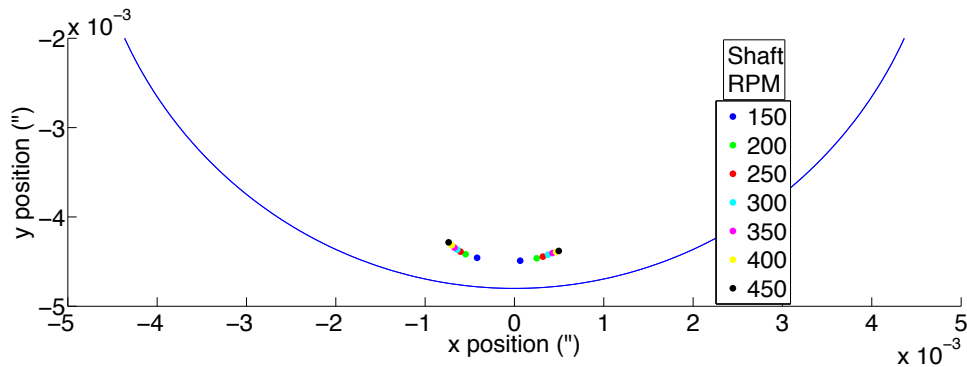
Figure 6-27: Locus of shaft position (inches) in Centerlift bearing during clockwise and counter-clockwise hydrodynamic testing for various RPMs at 7 psi projected area load

angle. Because the attitude angle marks the point of minimum film thickness, the converging wedge profile is not greatly interrupted by the location of the grooves at approximately 30 degrees from BDC. This allows the bearing to retain the majority of the film pressure needed for hydrodynamic lubrication.

This is illustrated best by Figure 6-28, which shows a graphical representation of the pressure distribution during the hydrodynamic operation of a journal bearing. As before, ϕ is attitude angle (or angle of minimum film thickness). Two additional angles are defined:

1. Angle of maximum pressure, ϕ_m

2. Angle of terminating pressure, ϕ_o

The film pressure is what provides the support for separating the shaft from the bearing. Although it is not entirely correct, the attitude angle is often considered to be the angle of terminating pressure. Experimental results verify that this is usually an acceptable simplification[8]. This figure shows that if the bearings attitude angle is small, then axial grooves located at angles greater than that angle should not greatly
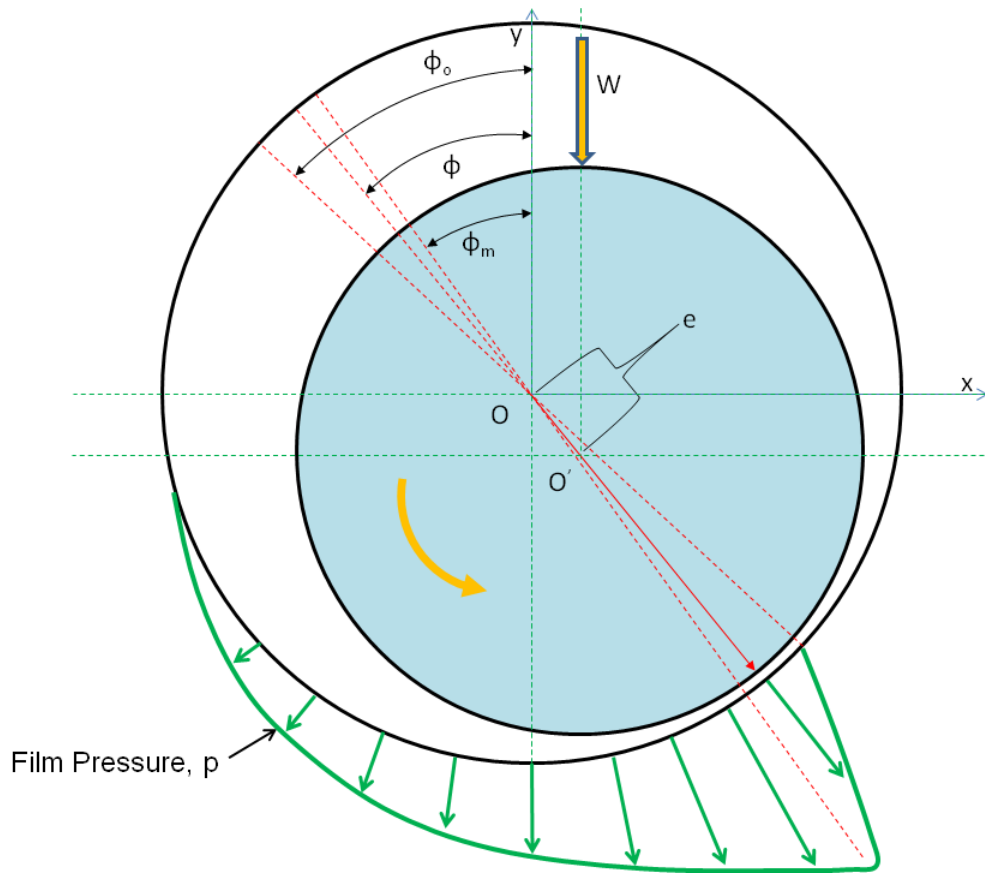
Figure 6-28: Graphical representation of the pressure distribution in a hydrodynamically operating journal bearing with counter-clockwise rotation

affect the hydrodynamic film in the vicinity of the minimum film thickness. There will be some amount of degradation depending on operating conditions due to loss of the starting film pressure on converging side of the bearing. Because water-lubricated shipboard bearings run at very low Sommerfeld numbers, they can be expected to operate with very low attitude angles. This point is key in that it allows for axial grooves to be created that will have very little effect on hydrodynamic performance provided they are located at large enough angle from BDC.[7]

Hybrid testing was conducted for the same load conditions as for hydrodynamic, but with speeds down to 25 rpm. Once again the data revealed a nearly flat, negligible torque when the shaft rotates in load conditions that can be (and are) supported with hydrostatic pressure.

Side force testing was conducted on the bearing to determine its ability to support loads that are not purely vertical. The original side force test apparatus used a single line pulling weights that were connected to a monofilament loop tied to the forward and aft lanyards by a swivel. This setup was found to introduce a moment on the bearing as well as a side force - creating a horizontal tilt in the bearing. Despite this, the ability of the bearing to support side loads was quite good. Figure 6-29 shows the response of the bearing subjected to a standard projected load in the vertical direction, plus an additional side load. As expected, increased projected loads result in a higher eccentricity towards the bearing BDC. The side force, which is applied to pull the bearing to the right while the shaft is held stationary, causes displacement to the side of the bearing. The bearing is capable of maintaining a fluid film with fairly modest side loads. The blacked dashed line indicates where a 5 degree offset from a purely vertical load is - analogous to a 5 degree heel or roll angle on a ship.

---

[7]This generalization becomes more complicated for ocean going ships that can be expected to operate with significant heel angles during high speed turns or heavy seas. This effect will reduce the effective angle at which the groove is located and may cause significant degradation in hydrodynamic performance.
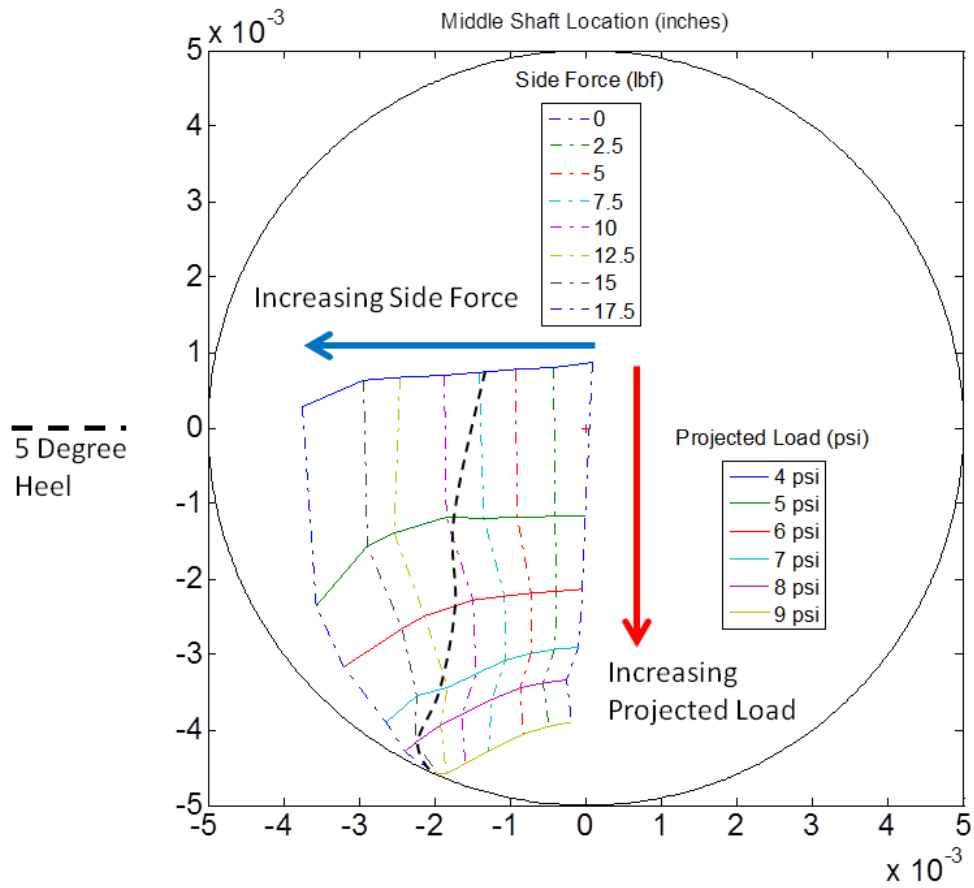
Figure 6-29: Locus of shaft positions (inches) for unmodified Centerlift bearing at various projected loads and side forces
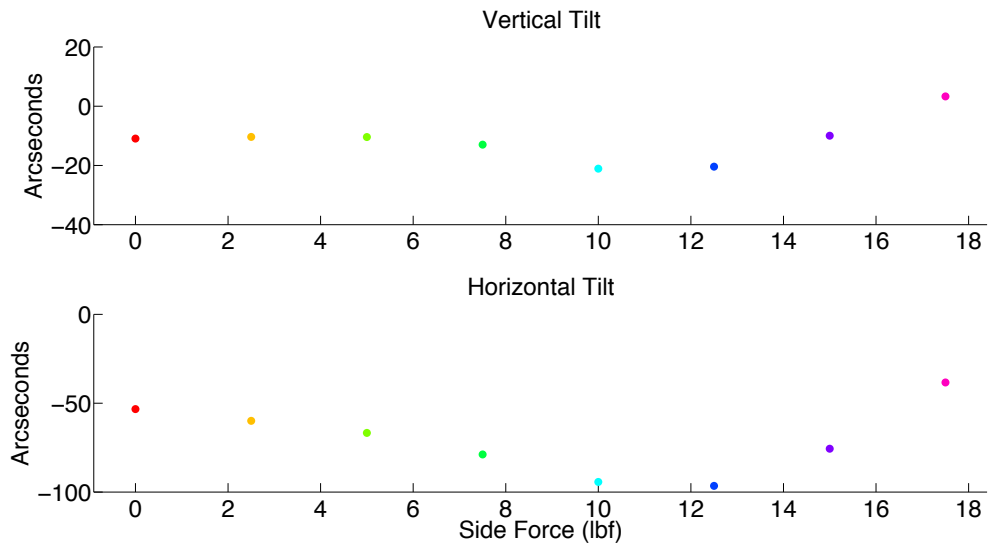
Figure 6-30: Unmodified Centerlift bearing tilt response to side force at 6 psi projected area load
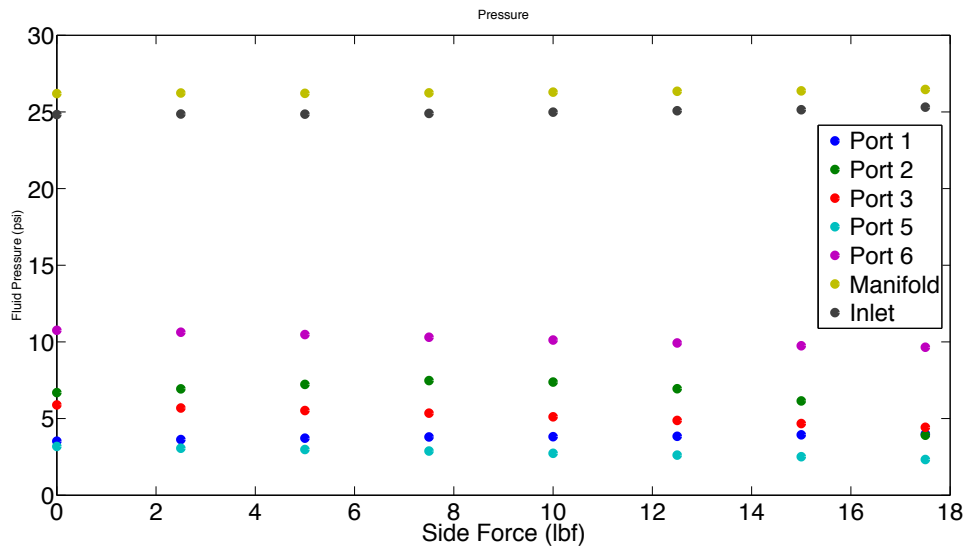
Figure 6-31: Unmodified Centerlift bearing pressure response to side force at 6 psi projected area load

Figures 6-30 and 6-31 show the tilt and pressure response to side loads at 6 psi projected load. Although the self-aligning mount compensates for a small degree of misalignment, there is no inherent tilt stiffness designed into the bearing. This shows up with the bearing having a small, natural tilt in the horizontal direction.[8] Because of the original side load apparatus, the side force induced a moment on the bearing, which increased the tilt of the bearing until one end contacted the side of the bearing at approximately 12.5 lbf side load. This necessitated a modification to the side force apparatus to have two independent lines attached to loads. Figure 6-5 shows the modified configuration. Experimental results showed that there was a slight decrease in flow rates with increased side loads. This is primarily because eccentricity increased with the additional side force loading, which decreases the fluid gap size and increases resistance to flow.

The pressure response raised questions regarding the effectiveness of the self-compensating section of the bearing. Since the bearing was being pulled towards pressure ports 3 and 5 (see configuration in Figure 6-22), based on the self-compensation framework it was expected that pressure ports 2 and 5 would increase, while pressure ports 1 and 3 would increase. It appeared that the exact opposite occurred, indicating that some other effects were dominating the self-compensating response in the bearing. The exact cause was not known, but concerns existed over interactions with the leakage occurring from the axial ends of the hydrostatic lifting region of the bearing as well as the long circuitous path between compensating grooves and load pads. These concerns led to the design of the Two-Port Bearing design.

6.5.3   Modifications to Centerlift Bearing and Results

As discussed in the previous section, the data showed that there was a significant drop in pressure between the inlet and the outer groove in the hydrostatic lift lands. To distribute pressure to the outer edge of the lift region of the bearing, a few modifications

---

[8]An arcsecond of tilt is $\frac{1}{3600}$ of a degree. Over a 1 Mile length this would result in approximately 0.31 inches of misalignment (or approximately 4.85 mm over 1 km).

were done:

1. *Side Flow Modification.* Two 1/8" flexible tubing lines were connected from the inlet supply line to the location of pressure port 6 on the forward end of the bearing, and an identical port located on the aft end of the bearing. The selection of the 1/8" tubing lines was done because using such small lines would not require modification to the surface of the bearing. The small lines would not provide large amounts of flow, but would be able to provide a small amount of flow to distribute pressure to the outer grooves of the lifting region of the bearing. This configuration is shown in Figure 6-32.
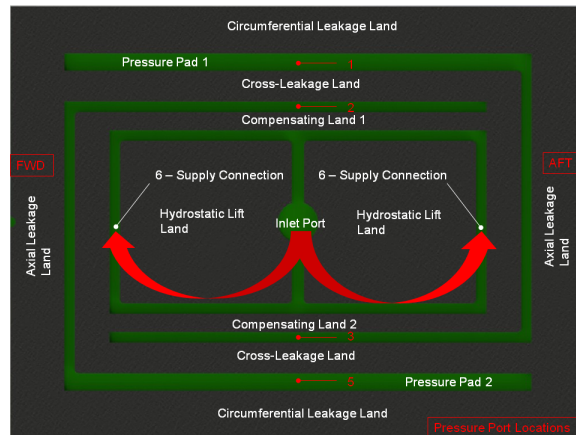
Figure 6-32: Side flow modification showing location of connected flow

2. *Slot Modification.* Two slots were milled into the bearing to provide an additional groove directly from the inlet port to the outer edge of the lifting region. A 1/16 inch wide slot was milled and tested, followed by a 1/8 inch wide slot. Figure 6-33 shows the layout of the modification and a picture of the bearing after modification and testing. The pressure port holes used for the side flow modification are visible in Figure 6-33(b).

For each modified bearing, a full series of hydrostatic, hydrodynamic, and hybrid testing was conducted. Testing showed that the modifications improved the hydrostatic performance of the bearings, but at the expense of added flow rates. To standardize
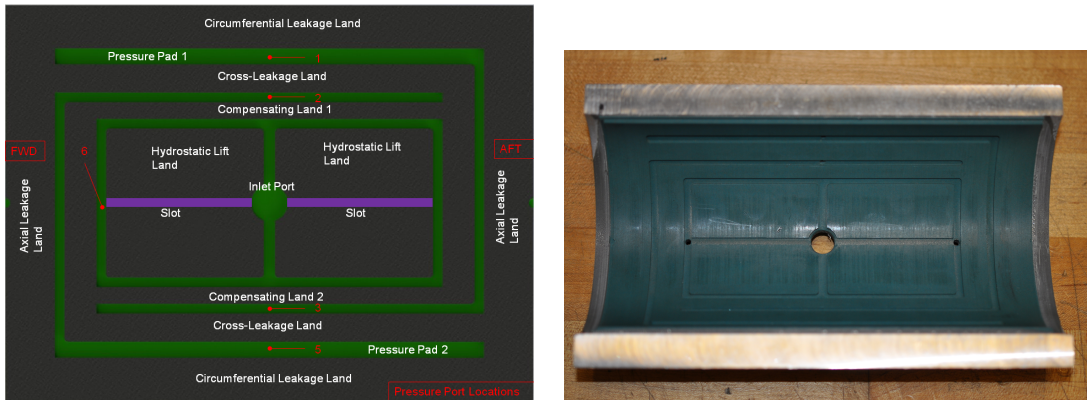
(a) Layout of slot modification to Centerlift bearing (b) Picture of Centerlift bearing after 1/8 unch slot modification

Figure 6-33: Centerlift Bearing Slot Modification

the comparison between the bearings, operating characteristics at an eccentricity ratio of 0.75 are provided in Table 6.6.

Table 6.6: Hydrostatic Performance Comparison of Modified Centerlift Bearings at 0.75 Eccentricity Ratio

Configuration	Projected Load (psi)	Load Carrying Efficiency	Total Flow (gpm)	Inlet Pressure (psi)	Flow Power (HP)
No Slit / No Side Flow	7.7	30.4%	1.7	25.2	0.0250
No Slit / Side Flow	9.1	37.0%	1.96	24.5	0.0281
1/16 Slot	8.7	34.8%	1.86	25.1	0.0272
1/8 Slot	9.3	38.1%	2.09	24.3	0.0296

Although the modifications to distribute pressure more fully around the lifting region did work, there were two main drawbacks to the designs. The first was the increased flow rate, which resulted in a larger power requirement from the pump. The second was a degradation in the hydrodynamic performance of the bearings in the slot modified configurations. Figure 6-34 shows the effect of the different modifications on hydrodynamic friction, with comparison to a plain journal bearing (tested in section 6.9). The difference between the plain journal bearing and the original Centerlift bearing with no slots is very small, with the reasons for this described in the previous section. The introduction of even a small 1/16 inch axial slot effectively cuts a swath

236
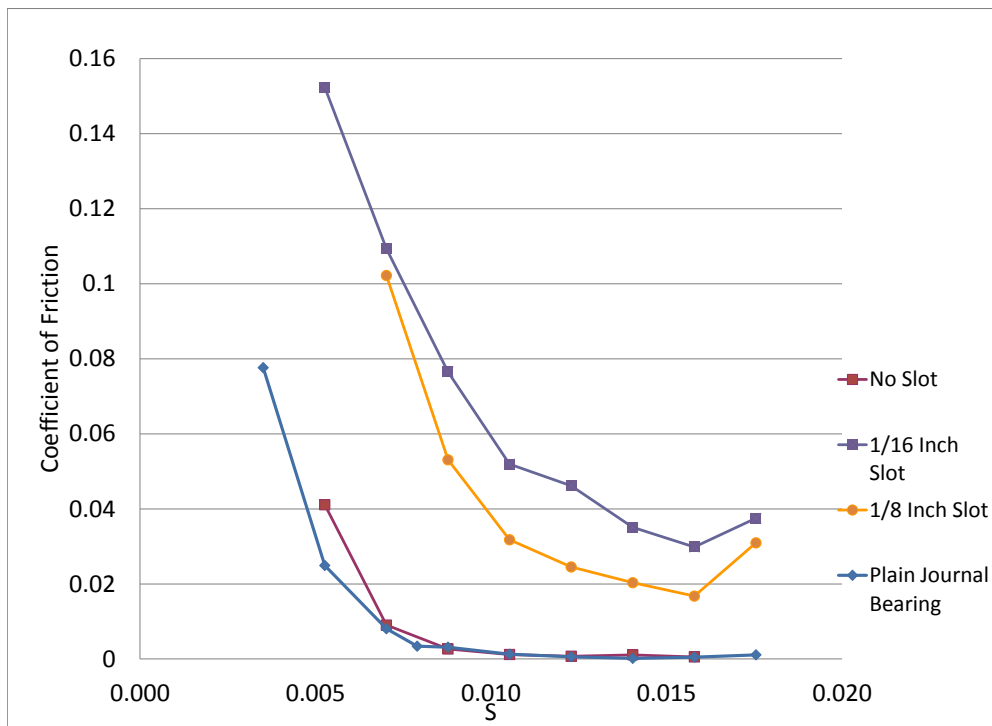
Figure 6-34: Comparison of clockwise friction coefficients for modified Centerlift bearings tested at 7 psi projected area load as a function of Sommerfeld number

through the bearing, interrupting the build up of film pressure illustrated in Figure 6-28. This results in a substantial reduction in hydrodynamic performance. Increasing the width of the slot further degrades the performance, but only marginally so. The introduction of the slot, no matter how small, is the cause of the majority of the decreased performance.
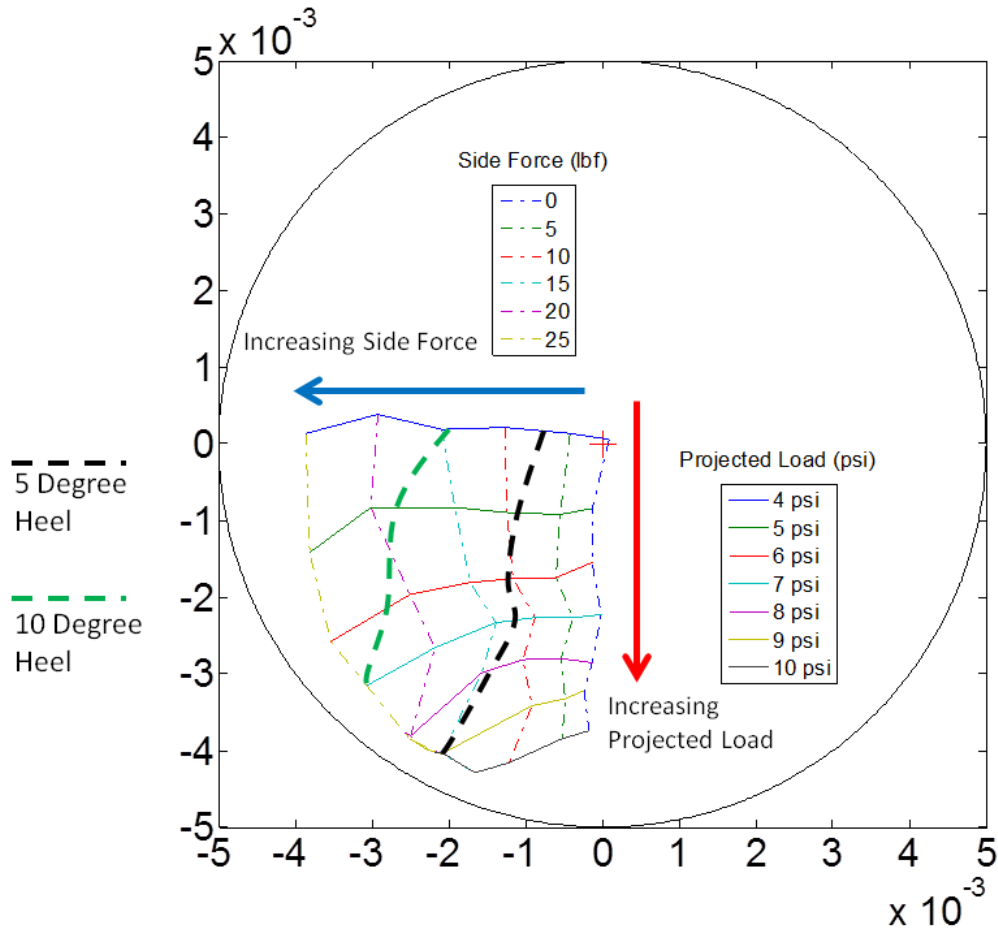
Figure 6-35: Locus of shaft positions (inches) for Centerlift bearing with 1/8 inch side flow ports at various projected loads and side forces

Side force testing during hydrostatic operation was conducted for the Centerlift bearing modified with side flow tubing. This testing was conducted using the revised side force testing apparatus, with results shown in Figure 6-35. The improved side force apparatus removed the tilting problem caused by the uneven torque, and the bearing was tested with higher side load forces. A noticeable response of the bearing

was that its ability to support higher side loads decreased at higher projected loads and eccentricities. For water-lubricated bearings that are designed to operate at high eccentricities, this reduction in side load support could be significant. Also noticeable was the offset between the clearance circle and when the bearing bottomed out on the bearing (when combined high projected area loads and high side forces were present). This is attributed to the offset between calibration in water, and the operation in a partially wetted condition - as described in section 4.5.4. The same pressure trends that were seen in Figure 6-31 were also seen during this test.

The Centerlift bearing was a dramatic improvement over the previous 3 port designs. It was easier to build, had superior hydrostatic performance, had adequate ability to support side loads, and (in the original design condition) had almost the same hydrodynamic performance as a plain journal bearing. Because of concerns with effectiveness of the compensating features in the bearing, an improvement to the basic design philosophy was attempted - the Two-Port Bearing.

6.6 Two-Port Bearing

6.6.1 Design Basis and Description

The Centerlift bearing was a success, but with the concerns over the effectiveness of the surface self-compensating features in that bearing identified during side force testing, a different bearing was conceived to provide a more direct pathway for the compensating grooves to the load pads. This was done to minimize the effect that leakage from the lifting section might have on the compensation network or any pressure drop due to very long grooves. The Two-Port design utilized the same basic principle as the Centerlift bearing - the inlet flow and pressure was used primarily to provide vertical load support, while the compensation network used residual pressure to provide side to side centering of the bearing. Figure 6-36 shows one of the original sketches and the final CAD design of the bearing.
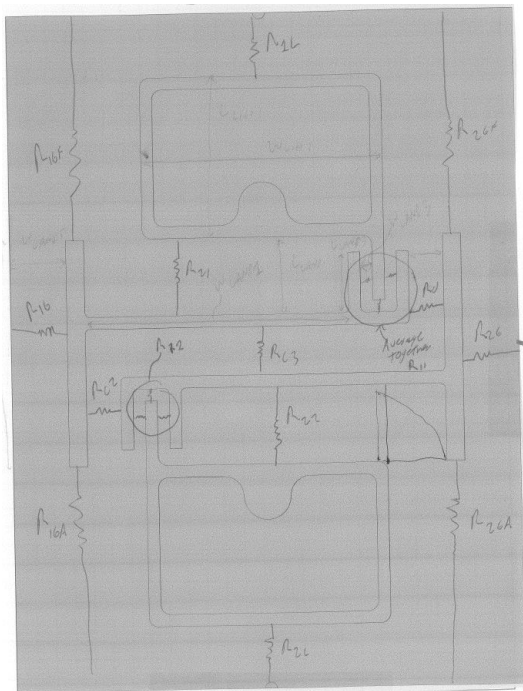
(a) Working Sketch of Two-Port Bearing Design   (b) Cad Design of Two-Port Bearing
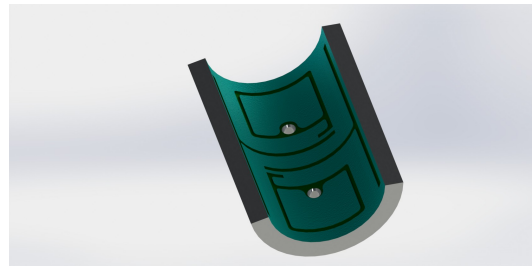
Figure 6-36: Two-Port Bearing Design

Previous bearings were designed for compensator resistance ratios (ζ) of approxi-

mately 1 using the flat plate approximation. The Two-Port bearing was the first bearing that an attempt was made to design for a non-concentric shaft by using the full integral equations. This proved very difficult due to the large variation in resistance across the compensating lands for eccentricity ratios deviating from zero. As figures 3-5 and 3-6 illustrate, there is significant increase in resistance with eccentricity ratio for lands that are located on the bottom portion of the bearing. For lands located at approximately 90 degrees from BDC, there is minimal change in resistance with increased eccentricity ratio. Because the compensating lands are located at approximately 30 degrees from BDC and the majority of leakage lands are located on the circumferential edge of the bearing, the resistance ratio is therefore expected to increase dramatically with eccentricity ratio.
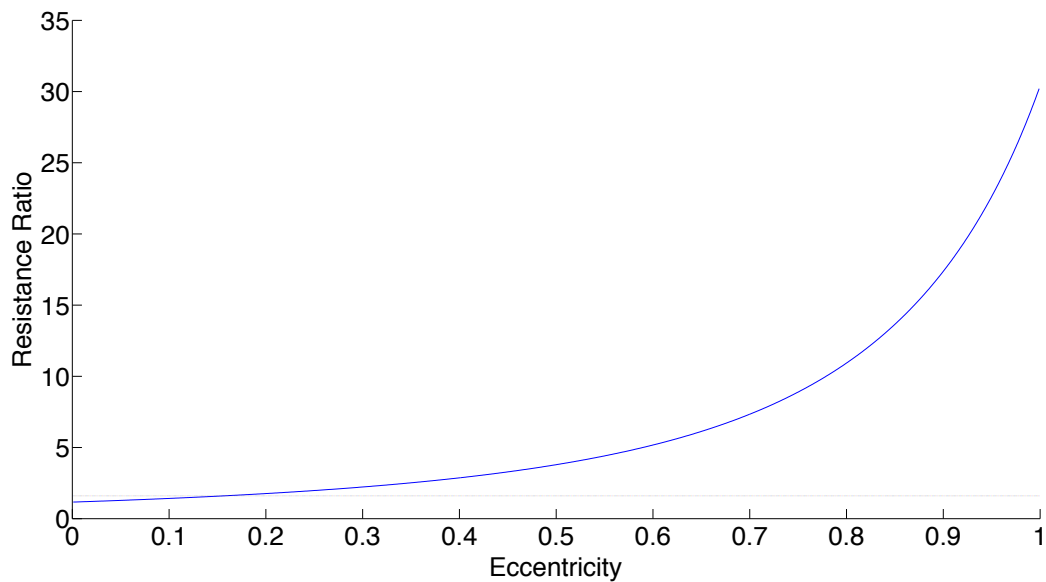
Figure 6-37: Change in resistance ratio (ζ) as a function of eccentricity ratio for Two-Port bearing

Figure 6-37 shows the change in resistance ratio in the Two-Port design versus eccentricity ratio. The horizontal line is the line where ζ is equal to one. Given the constrained locations of the compensating lands and the primary leakage lands, it is impossible to design the bearing to have a consistent resistance ratio over a complete

range of eccentricity ratios. There is only one operating point where that will occur, but the graph shows if operation is limited to relatively small eccentricity ratio deviations from zero, the resistance ratio is fairly flat. Unfortunately, water-lubricated bearings typically operate at very high eccentricities. Consideration was given to designing the bearing specifically for large eccentricities, but this would have resulted in extremely low resistance ratios at low eccentricities.
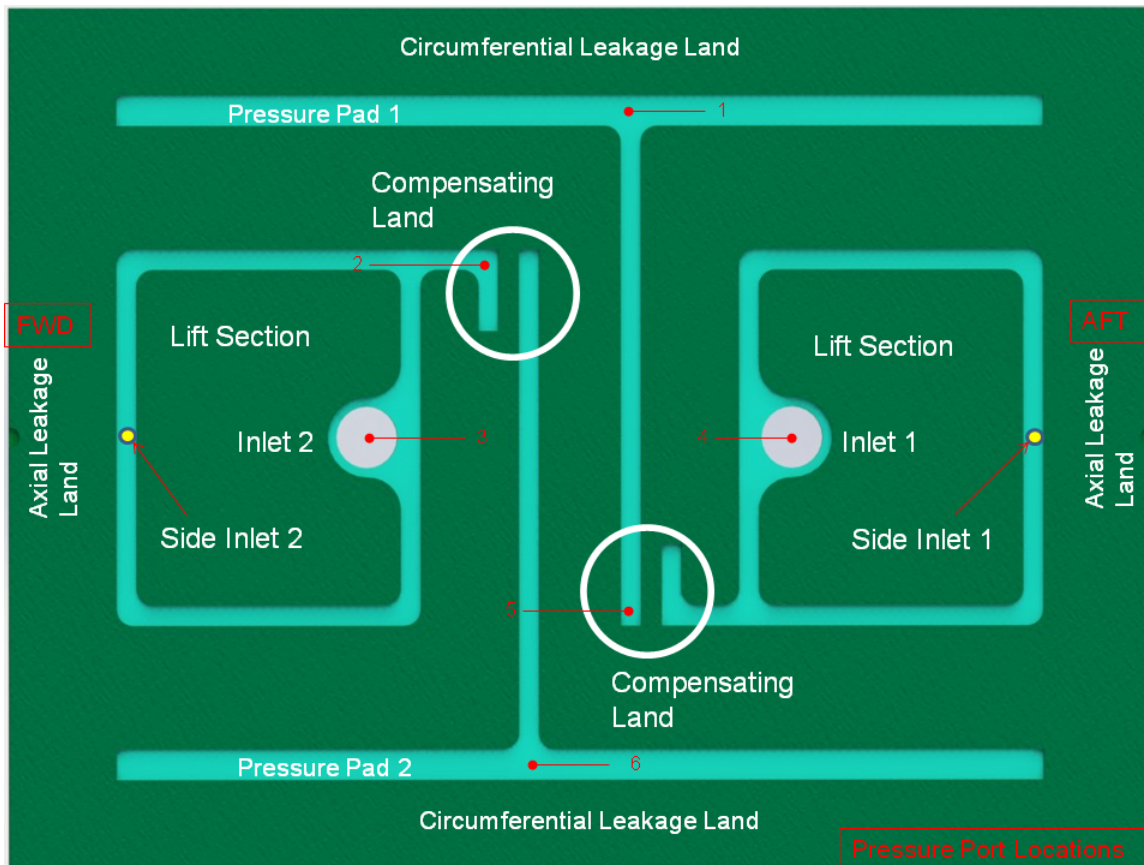
Figure 6-38: Two-Port bearing layout with side inlet flow connections

The Two-Port bearing was manufactured in similar fashion to the Centerlift bearing, using the same master shaft and general clearance ratio. Table 6.7 shows the specifications, and Figure 6-38 shows the layout and nomenclature of the bearing. There are two inlets supplying fluid pressure to independent lifting sections surrounded by a supply groove. There are small side inlet lines connected to the feed lines to the inlets by 1/8 inch flexible tubing. These are used in a similar fashion to the Centerlift bear-

ing side flow modification, augmenting the main flow of fluid from the inlets. There are compensation lands fed by the lifting section grooves that provide the controlled pressure drop to the compensating grooves and pressure pads.

An additional benefit of the Two-Port design is that there are two separate, independent lifting and compensating regions in the bearing. For longer bearings, additional independent sections could be added along the axis of the bearing. Unlike the Centerlift bearing, if a deep score were to occur in lands of the bearing, effectively creating a ground in the hydraulic resistance to atmosphere, there is still a section of the bearing that may be able to work.

Table 6.7: Two-Port Bearing Specifications

Bearing Configuration	Two-Port Bearing	
Material	Turcite	
Diameter	3.241	Inches
Radial Clearance	0.0052	Inches
Clearance Ratio	308	
Engagement Arc	170	degrees
L/D Ratio	2	

6.6.2 Test Results

Hydrostatic testing was conducted with the centrifugal pump in several different configurations for projected loads between 3 and 12 psi. This included running two independent fluid lines to each inlet port from the manifold, as well as one supply line split immediately before the inlets. For both of these cases there was a connection to the side inlets. An additional configuration was tested where there was a single supply line without side flow connections. In this condition the side flow connections were used as pressure ports. The pressure port locations used in this test configuration is shown in Figure 6-39.

The overall hydrostatic performance performance of the bearings were similar to the

243
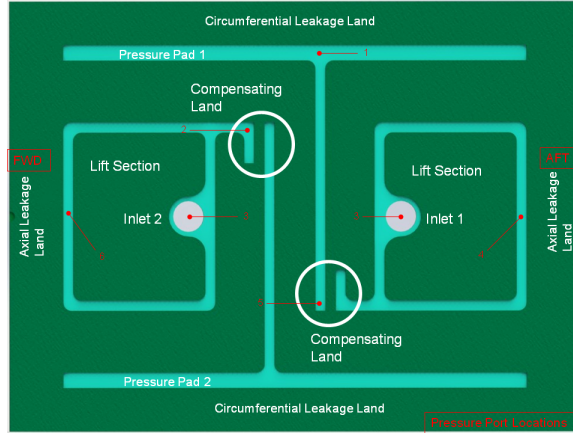
Figure 6-39: Two-Port bearing layout without side inlet flow connections and single supply line

Centerlift bearing, but with slightly less load carrying capacity. Hydrostatic loads on the order of 10 psi projected load were capable of being supported with the centrifugal pump and load efficiencies were on the order of 35 percent. Eccentricities were slightly higher for given projected area loads, and flow rates were significantly higher than with the Centerlift bearing. This resulted in a bearing that had higher pump power requirements and was less efficient with its use of flow. Table 6.8 shows the hydrostatic performance comparison between the different test configurations at a standardized eccentricity ratio of 0.75. Using two independent supply lines and connecting the supply to the side inlet ports does increase load capacity, but at the expense of increased flow.

Table 6.8: Hydrostatic Performance Comparison of Two-Port Bearings at 0.75 Eccentricity Ratio

Configuration	Projected Load (psi)	Load Carrying Efficiency	Total Flow (gpm)	Inlet Pressure (psi)	Flow Power (HP)
Side Flow - 2 Flowpaths	8.3	35.2%	2.95	23.5	0.0404
Side Flow - 1 Flowpaths	8.0	37.9%	2.70	21.0	0.0331
No Side Flow - 1 Flowpaths	7.5	33.6%	2.41	22.4	0.0314

The pressure response of the Two-Port bearing revealed a large pressure drop be-

tween the bearing inlet and the supply side of the compensating land. This indicates that a pressure drop was occurring in the grooves. A remedy to this would be to increase the depth and/or width of the grooves to lower their hydraulic resistance. Kotilainen's analysis found that grooves should have depth on the order of 10-15 times the clearance, while Rowe suggests a recess depth of approximately 20 times the gap[15, 26]. The groove depth was selected to be 0.05", which places the ratio between nominal fluid film thickness and groove depth at approximately 10:1. This value increases with higher eccentricities, with the ratio going to approximately 20:1 for eccentricities of 0.5. The depths of the grooves in the bearings were ultimately limited by the thickness of the Turcite®, which is 3/32" thick. Machining deeper than this thickness would not allow the manufacturing process of milling the features in a flat condition, as there would be no barrier to prevent epoxy from reaching the bearing surface. To increase groove or recess depths greater than this requires thicker bearing material (and boring out the housing to accommodate it), or milling the features into the cylindrical face of the bearing after manufacture.

Hydrodynamic testing was conducted at speeds varying between 50 and 500 rpm for 3, 5, 7, 9, and 11 psi projected loads. Overall, the Two-Port bearing showed poor hydrodynamic performance. Figure 6-40 shows the hydrodynamic friction as function Sommerfeld number. Although friction coefficients reach relatively low values at higher speeds, there are no definitive points of minimum friction that indicate a clear transition to the hydrodynamic lubrication. The response was similar in in the counter-clockwise direction. The large number of grooves interrupted the ability to develop a hydrodynamic film. Contributing to this was that the large number of grooves in the surface of the bearing resulted in many areas were edge effects from the manufacturing process (see section 5.3.2) caused small depressions in the bearing surface, further hindering the formation of a hydrodynamic film. Figure 6-41 shows the relative performance compared to a plain journal bearing at a 7 psi projected area load. The position of the isolation valve to the inlet to the bearing during hydrodynamic testing had no noticeable affect on hydrodynamic performance.
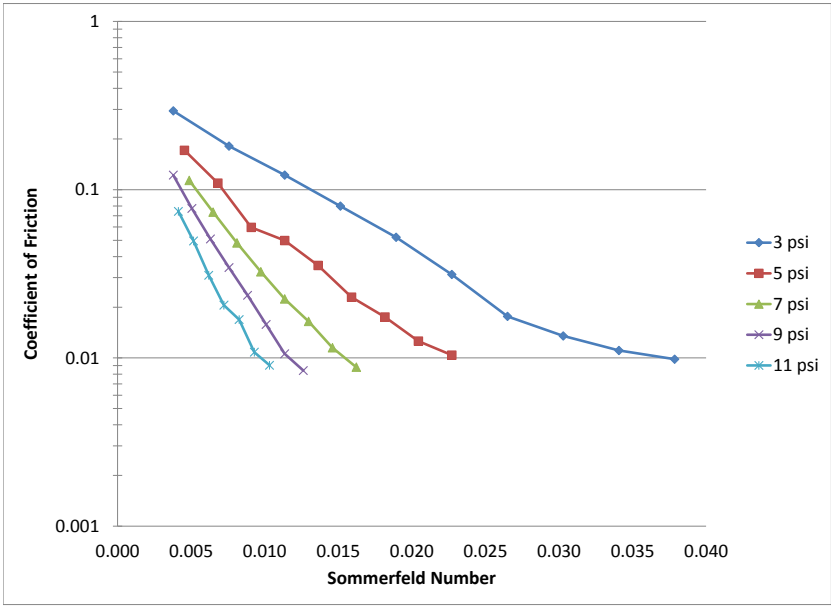
Figure 6-40: Clockwise friction curves of Two-Port bearing for various projected area loads as a function of Sommerfeld number
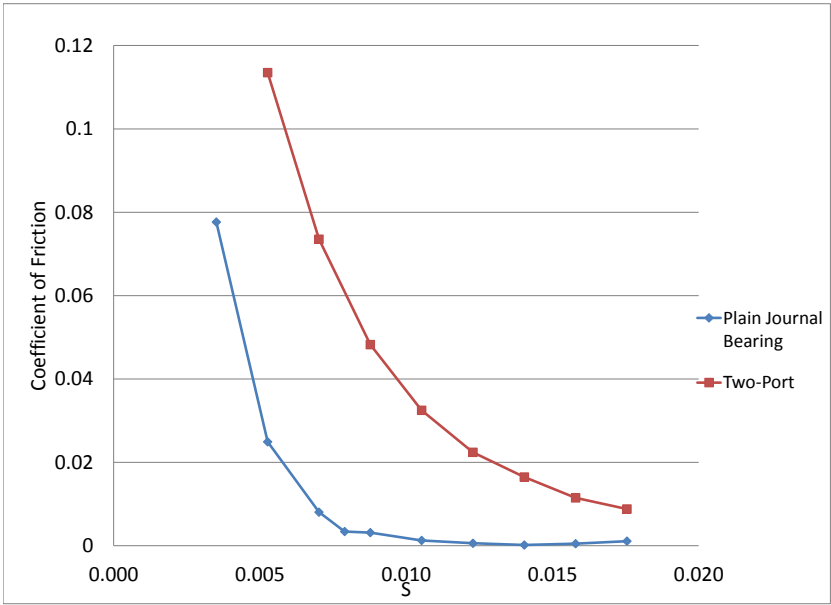
Figure 6-41: Comparison of clockwise friction coefficients for Two-Port bearing tested at 7 psi projected area load as a function of Sommerfeld number
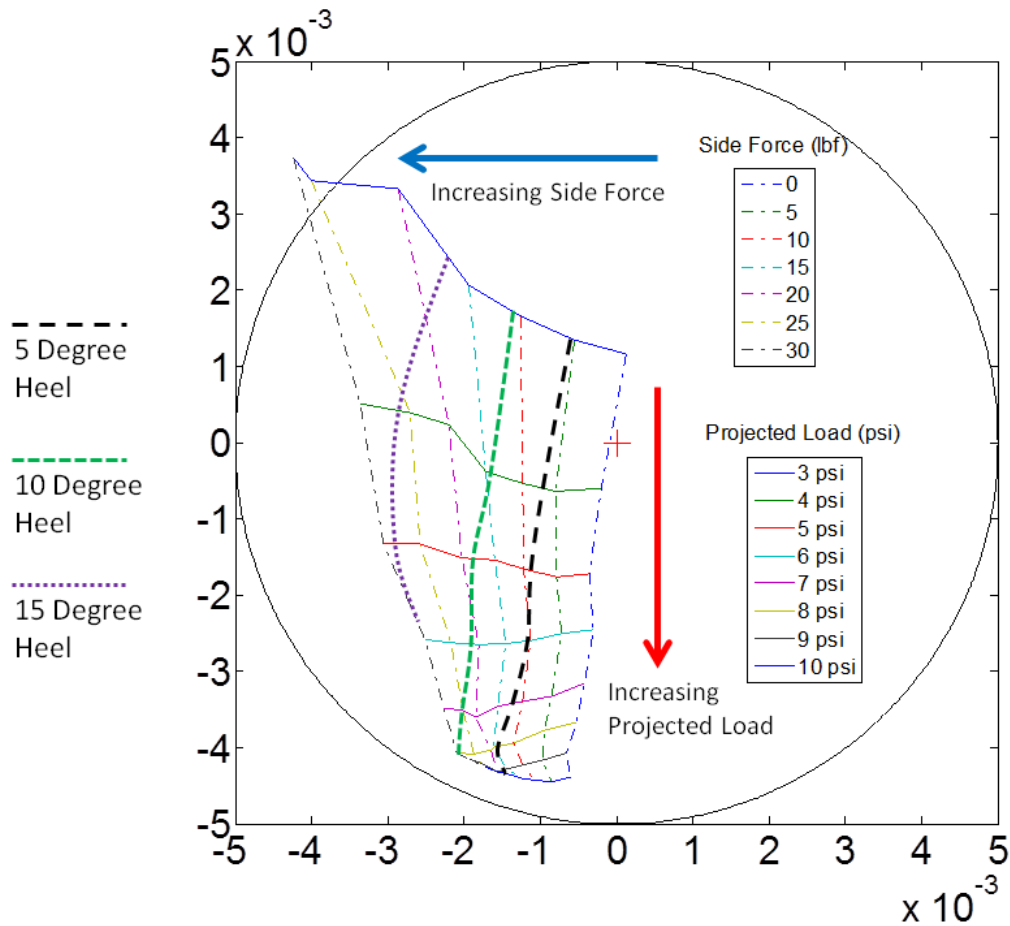
Figure 6-42: Locus of shaft positions (inches) for Two-Port bearing without side flow at various projected loads and side forces

Side force testing was conducted on the Two-Port bearing in the configuration with a single fluid supply line and no side flow connections. The bearing was tested for various projected area loads with side forces up to 30 lbf. The bearing displayed a greater ability to support side loads than the Centerlift bearing, with a fluid film maintained for all conditions except for those with a combination of high projected area loads and large side force. Figure 6-42 shows the displacement of the shaft relative to the bearing with an applied side force.

Figure 6-43 shows the fluid pressure response to a side load at 6 psi projected area load (nomenclature of pressure ports is specified in Figure 6-39). Based on the self-
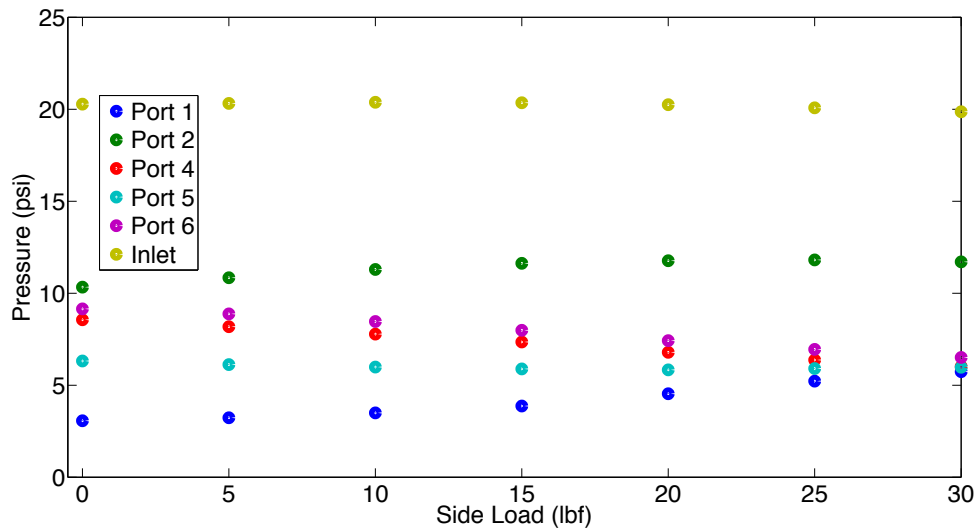
Figure 6-43: Two-Port bearing pressure response to side force at 6 psi projected area load

compensation theory, it was expected that port 1 and port 5 pressures would increase with side load. Port 1 pressure did increase with side force, but the port 5 pressure was generally flat. This indicated that although the build up of pressure in port 1 was providing the support needed to resist the applied side force, there was some other dominating factor driving the pressure increase other than the compensating land next to pressure port 5 - the reason for this would be discovered during testing of the Hydrostatic Lift bearing. Also interesting to note was that inlet pressure remained relatively constant, while pressure ports 4 and 6 located at the axial ends of the lifting sections saw a decrease in pressure with greater side force. This last observation is attributed to the opening gap on the one side of the lifting lands that prevents pressure from building up in that section of the bearing.

Additional testing on the Two-Port bearing was done using the side force test apparatus to apply moments on the bearing by using combinations of different weights on the individual monofilament lines connected to the support lanyards. This was done to determine bearing response to misalignment forces. Because of the manner in which the moments were applied, they were not pure moments, but rather a
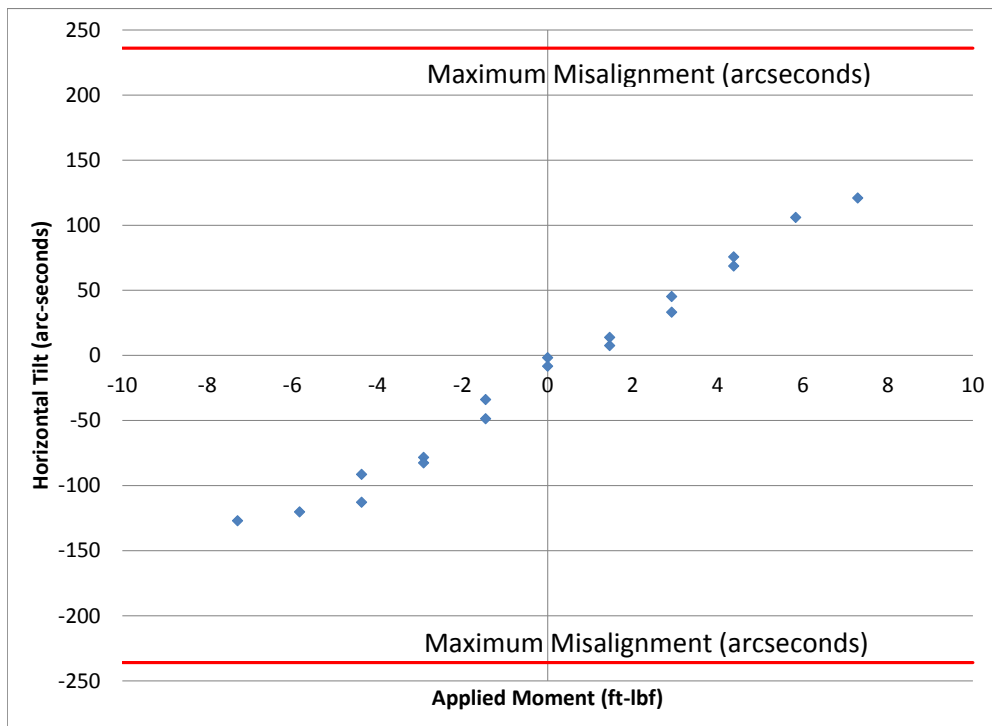
Figure 6-44: Horizontal tilt response to applied moments for Two-Port bearing at 7 psi projected area load

combination of side force and moments. Testing was conducted at a projected area load of 7 psi in a pure hydrostatic mode of operation. The bearing proved to be very receptive to applied moments on the bearing, as shown by Figure 6-44. On this figure the maximum misalignment that the bearing can support based on the bearing clearance, bearing length, and eccentricity ratio at 7 psi projected load (eccentricity ratio of approximately 0.71) is shown. There are no clear indications of the shaft coming up hard on the sides of the bearing, indicating that a fluid film is maintained throughout the bearing.

It should be noted that the maximum misalignment values are a driven by a combination of bearing eccentricity ratio and radial gap. A bearing operating at a high eccentricity ratio has a reduced capacity to accept misalignment before impacting the sides of a bearing. This is discussed in more detail in section 7.5.
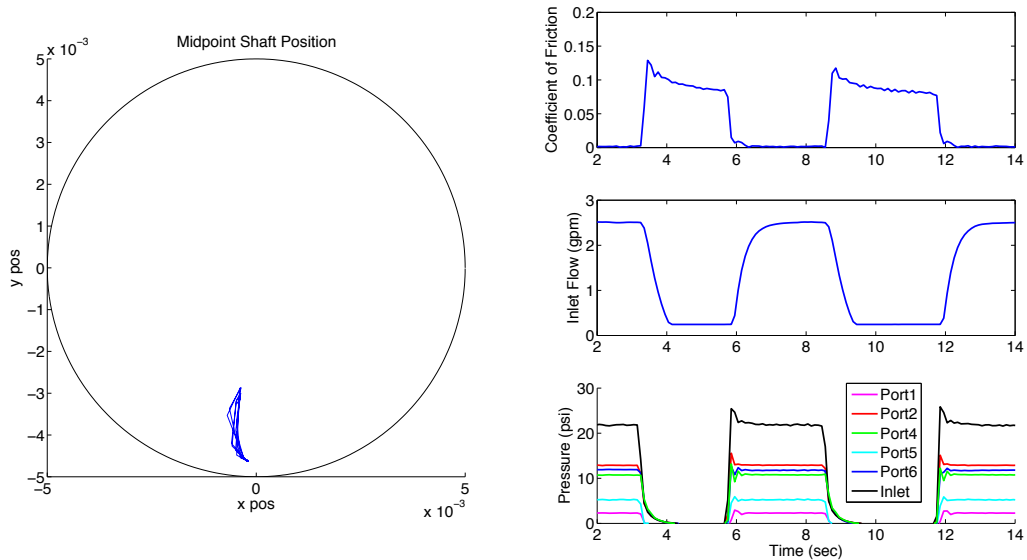
Figure 6-45: Transient response of Two-Port bearing to starting and securing of hydrostatic flow for 7 psi projected area load and 250 rpm

Hybrid testing of the bearing done at 7 psi projected area load revealed the same flat torque curve seen in previous bearings. The hybrid configuration was with the

250

single fluid supply line and no side flow connections. Additional hybrid testing of the bearing was conducted to determine the transitional response of the bearing when hydrostatic flow is secured and started in a rotating shaft under load. These tests were very dynamic and the results are best viewed with a timed-based video showing the response of the bearing. Figure 6-45 shows the time based response of the bearing to rapidly securing and starting hydrostatic flow in the bearing by closing a quick acting ball valve. There is a rapid jump in friction as the valve is closed and the shaft transitions to hydrodynamic operation.[9] The response of the flowmeters is delayed - actual staring and stopping of flow occurs much quicker than the figure indicates. The locus of shaft movement is also shown in the figure, with the bearing moving within a consistent range throughout the cycles. Testing was also conducted for 150 and 500 rpm speed conditions with similar responses.
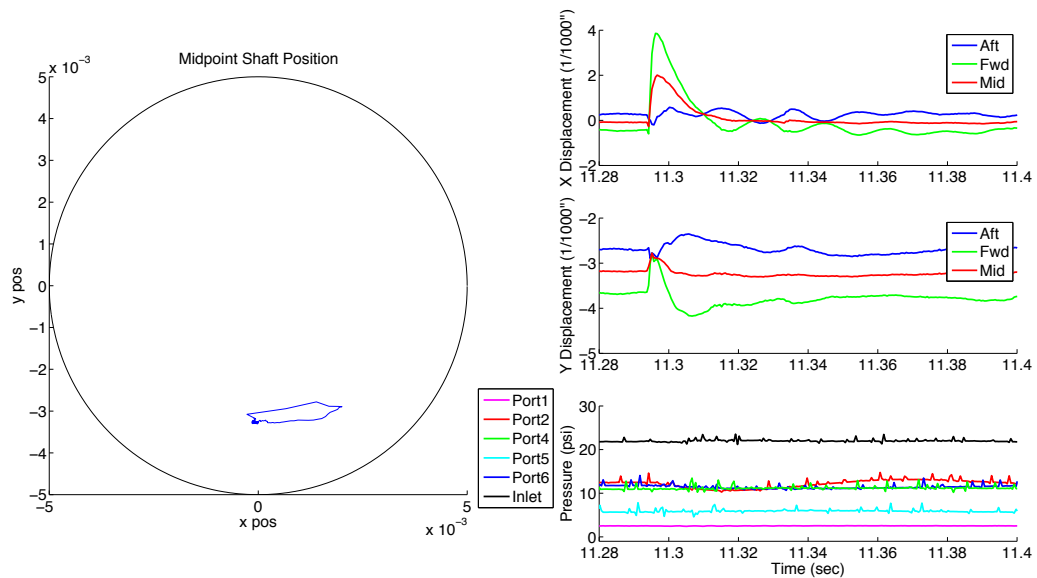
Figure 6-46: Response of Two-Port bearing to side impact at 7 psi projected area load during hydrostatic operation

The final testing that was done on the Two-Port bearing consisted of recording the short term response of the bearing to an impact load. To accomplish this, the bear-

[9]The Two-Port bearing was not capable of operating in the hydrodynamic lubrication regime at this projected load and speed

ing was operated hydrostatically at 7 psi projected load above water when an impact to the side was initiated with a lead hammer. Figure 6-46 shows the response of the bearing. Because of the short duration application of the load, it was expected that the stiffness in the bearing would be a result of the squeeze film response in the bearing. The pressure plots show no change pressures over the response period of the bearing with the exception of pressure port 2, which responds at a frequency much lower than the response of the bearing to the load. With the long flexible tubing between bearing and the pressure sensors, it is unlikely that any of the short term squeeze film effects would be seen by the sensors. The bearing did not contact the sides of the bearing, indicating the bearing is capable of handling a certain amount of shock load without sustaining damage due to the shaft impacting the bearing. Because of the manner in which the load was applied, further quantifying the dynamic response of the bearing was not done.

The Two-Port bearing had a better capacity to support side loads, but required higher flow rates and was not capable of achieving hydrodynamic lubrication even at the speed limits of the test rig. The bearing did display the ability to accommodate moments from misalignment as well as provide a satisfactory response to an impact load. Overall, the bearing design is not particularly suitable for use as a bearing for shipboard applications due to the poor hydrodynamic performance.

6.7 Stave Bearing

6.7.1 Design Basis and Description

The poor hydrodynamic performance of the Two-Port bearing generated a desire to have a baseline for comparison between bearings. Since a significant portion of water-lubricated bearings are stave bearings, a bearing made of Turcite® in the stave configuration was designed and built. Staves come in standard sizes, with channels between the staves for lubrication. Typical large ship stave bearings typically have either 5 or 6 staves for every 90 degree arc of the bearing.
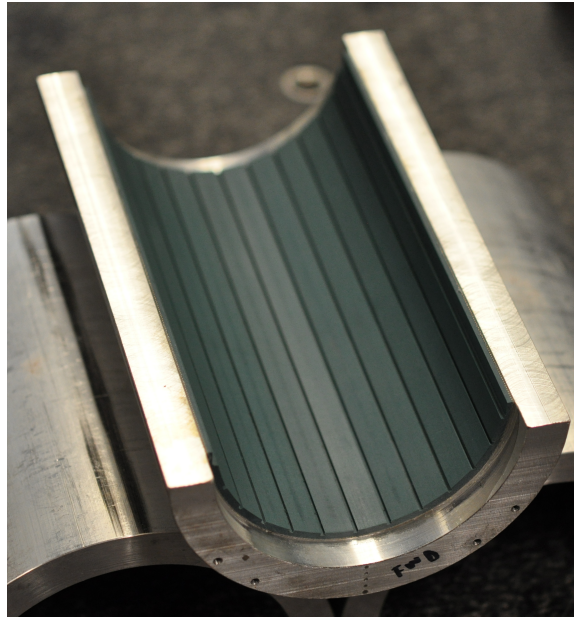
Figure 6-47: Turcite® Stave Bearing

To design the layout of this bearing, the groove width was selected to be 1/16" wide - corresponding to the smallest single flute downcut endmill available. The other variables driving dimensions for this bearing were the desired arc length of approximately 170 degrees and to have 12 staves within the arc of the bearing. The manufacturing process used for this bearing was the same as for previous bearings, with the grooves milled in the flat condition and the bearing material wrapped and epoxied to an aluminum housing. The only change was the orientation of the Turcite®

253

extrusion. Because wear-in testing was planned for this bearing, the bearing material was placed such that the axis of the extrusion was 90 degrees offset from the direction of shaft rotation. This was done to provide a more noticeable effect on the ability of the shaft to wear down high asperities on the bearing surface during a break in period. Figure 6-47 shows the resulting stave bearing built for this project. Because this bearing would undergo purely hydrodynamic testing, no pressure ports were fabricated into the surfaces of the staves. As shown in Figure 5-28(a), the stave bearing had significant edge effects.

Table 6.9: Stave Bearing Specifications

Bearing Configuration	Stave Bearing	
Material	Turcite	
Diameter	3.2390	Inches
Radial Clearance	0.0042	Inches
Clearance Ratio	380	
Engagement Arc	168	degrees
L/D Ratio	2	

6.7.2 Test Results

A break-in period was conducted before any specific hydrodynamic testing was conducted. After a very brief cycling of the bearing in both directions at very low loads, the stave bearing underwent a break-in consisting of operation at a counter-clockwise rotation of 500 rpm and 7 psi projected area load. The break-in period was 100,000 cycles (shaft rotations), or approximately 200 minutes of operation.

Figure 6-48 shows the friction coefficient as a function of cycles plotted on normal and semi-log graphs. There is a very quick reduction in friction followed by a gradual leveling off in friction. The initial drop is due to the extreme asperities of the bearing material being worn down by the interaction between shaft and bearing.

Figure 6-49 shows the radial displacement that occurs with the increase in cycles of
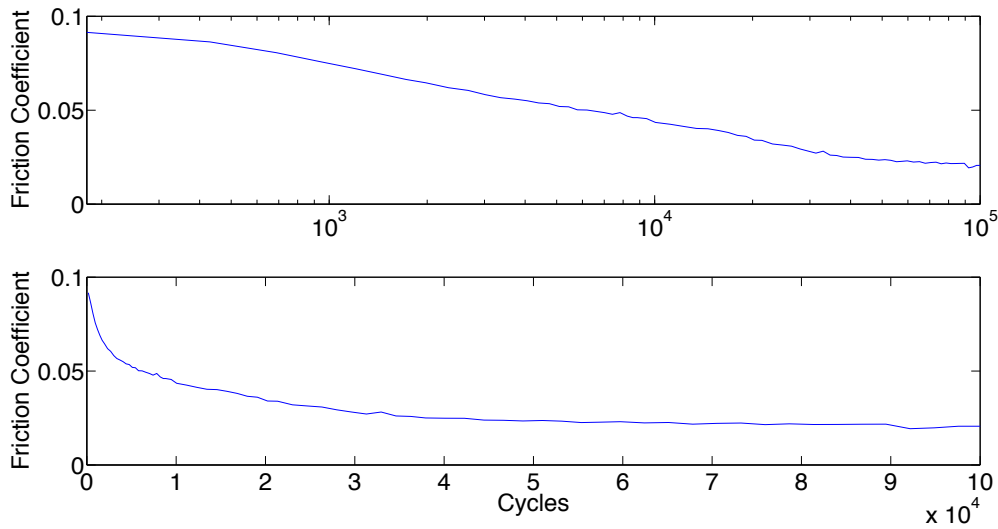
Figure 6-48: Counter-clockwise hydrodynamic coefficient of friction for stave bearing at 7 psi projected load and 500 rpm as a function of cycles, showing wear-in is required

the bearing. This is an indicator of the amount of wear-in that occurs as material is worn away. There is a wear down of approximately 0.0001 inches seen in the figure. Surface roughness measurements of the Turcite® showed a average roughness (R_a) value of around 50 μinch and maximum peak-to-valley heights (R_t) of around 400 μinch. This leaves approximately 0.0002" of peaks above the mean surface of the material to be worn down, although only a portion of this would be expected to actually occur. Therefore, the amount of wear measured during testing makes sense. This amount was later verified with post-testing measurements by the CMM, which indicated an increase in diameter near the bearing BDC of 0.0001 to 0.0002 inches.

The drop in friction over the break-in period was significant. This testing reinforced the importance in conducting a proper break-in for a bearing if it is going to be used in actual service.

After the wear-in testing, a series of normal hydrodynamic tests were conducted at various projected loads for speeds up to 500 rpm. The performance of the bearing was poor, with no clear point of minimum friction to mark the transition to the hydrodynamic lubrication regime with the exception of one projected load. Figure

255
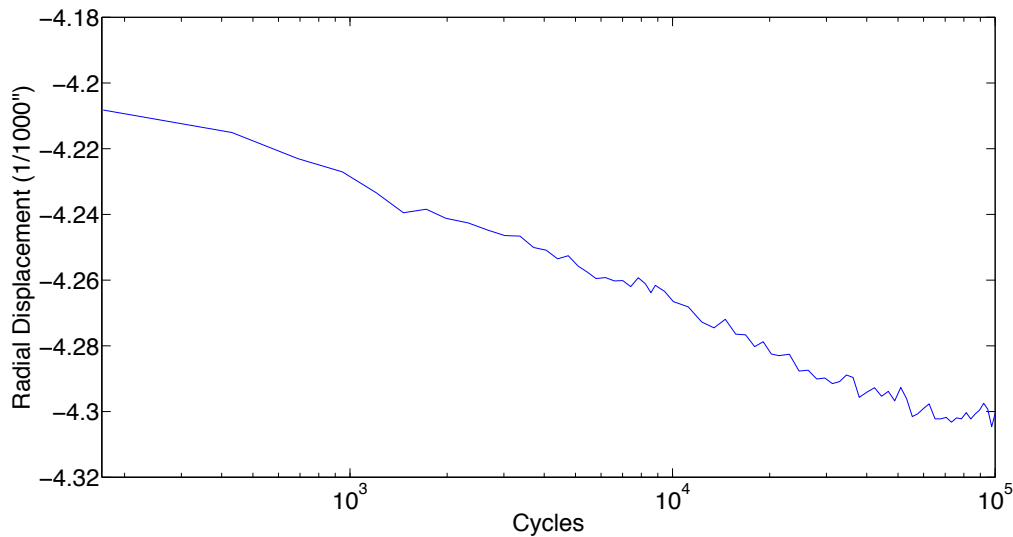
Figure 6-49: Change in radial shaft location of stave bearing at 7 psi projected load and 500 rpm as a function of cycles

6-50 shows the hydrodynamic response of the bearing for several load conditions in both clock-wise and counter-clockwise rotations. An interesting finding was that although the bearing was symmetric, there was higher friction coefficients seen in the clockwise direction. This is significant because the preceding wear-in was conducted in the counter-clockwise direction. This would indicate that to get a good wear-in, the bearing must be operated in all of the intended modes of operation.

The stave bearing was a success in that the ability of the bearings to have improved performance with a proper break in was seen. The overall hydrodynamic performance of the stave bearing was disappointing, but Orndorff's remarkable paper on the development of the water-lubricated rubber bearings illustrated that the performance of such bearings is influenced dramatically by the thickness and geometry of the material[21]. The use of a different material and deviations from the geometry that typical rubber staves have are likely significant contributers to this bearings poor performance.
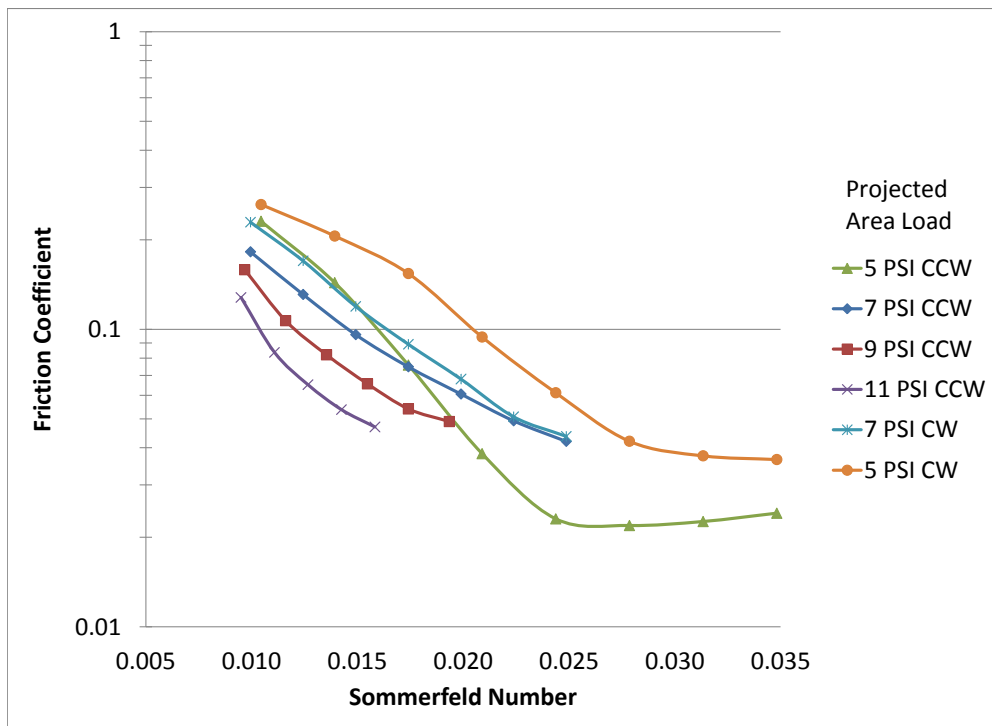
Figure 6-50: Comparison of friction coefficients for Stave bearing tested at various projected area loads as a function of Sommerfeld number

6.8 Comb Bearing

6.8.1 Design Basis and Description

There were concerns over how robust the hydrostatic bearings that possess axial grooves were. Scoring of the bearing due to debris could cause a direct path to atmosphere, effectively creating a short in the hydraulic resistance to flow and degrading the performance of the bearing. To address this, a 'Comb' style bearing was designed and built. The bearing design consists of a series of alternating circumferential grooves that are designed to provide inlet flow to the bearing and distribute pressure to the bearing. The layout of pressure port locations in the bearing is shown in Figure 6-51.
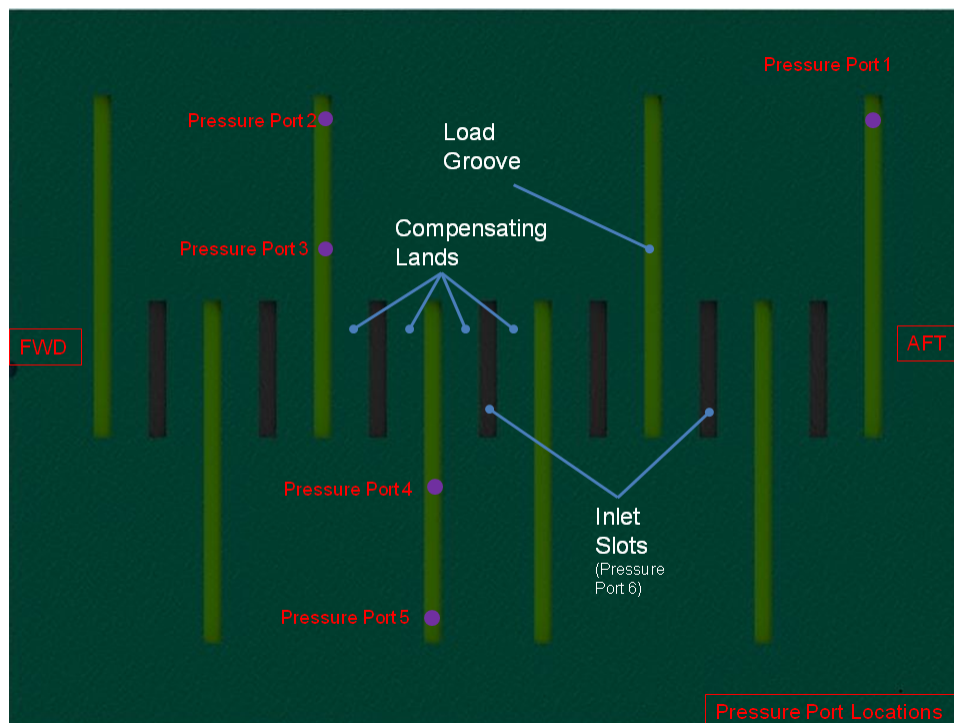
Figure 6-51: Conceptual Layout of Comb Bearing

Unlike previous self-compensation bearings where the change in resistance across the compensating lands is a dominant factor, this bearing response is designed to be driven by a varying leakage resistance. This is best described by Figure 6-52, which shows a simplified lumped parameter resistance model of the bearing. Consider a

258

case where the shaft moves towards the top of Figure 6-51. Because the inlets and compensating lands are located at the BDC of the bearing, the hydraulic resistance to flow across the compensating lands are relatively constant. The leakage resistance on the top side of Figure 6-51 will increase due to a smaller gap, while the leakage resistance on the bottom of Figure 6-51 will decrease due to a larger gap. The net result is that the pressure in the top grooves increase and the pressure in the bottom groove decreases, resulting in a restoring force.
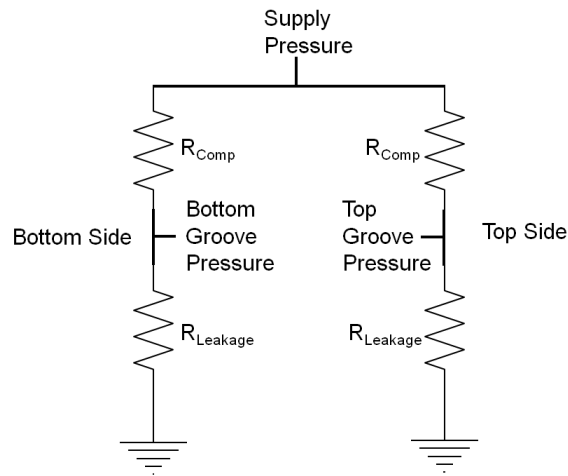
Figure 6-52: Simplified Resistance Model of Comb Bearing

This bearing is shown in Figure 5-30 and its unique construction described in section 5.4. The specifications for the bearing are provided in Table 6.10

Table 6.10: Comb Bearing Specifications

Bearing Configuration	Comb Bearing	
Material	Turcite	
Diameter	3.2398	Inches
Radial Clearance	0.0046	Inches
Clearance Ratio	347	
Engagement Arc	175	degrees
L/D Ratio	2	

6.8.2 Centrifugal Pump Test Results

The Comb bearing was hydrostatically tested with the centrifugal pump. It was found to have decent load capacity, with the ability to support projected area loads up to approximately 8 psi and achieving load efficiencies on the order of 35 percent. The bearing did display a rapid collapse at higher eccentricity ratios, with hydrostatic operation not possible at eccentricity ratios between 0.5 and 1. This is shown in Figure 6-53. Flow rates were very high, with flow above 3 gpm seen in the bearing. There also appeared to be a large pressure drop between the inlet and the manifold. There is a slight offset in the bearing during hydrostatic testing. This is believed to be due to either a slight misalignment in the bearing during manufacturing or the force from the flexible tubing influencing the bearing.
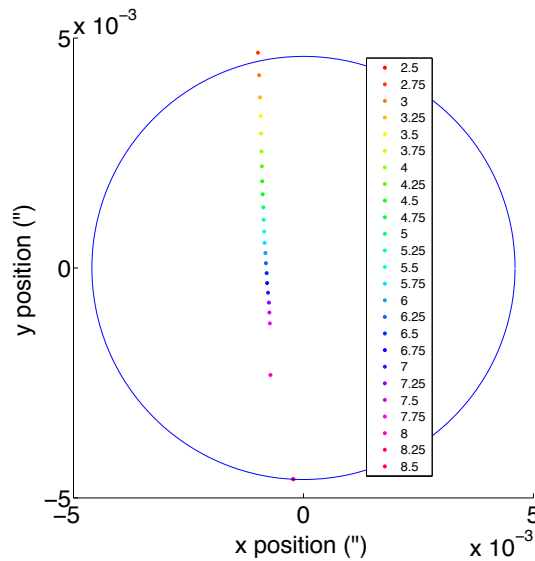
Figure 6-53: Locus of shaft position in Comb bearing during hydrostatic testing for various projected area loads (inches)

Side force testing conducted on the bearing revealed a good capacity to support side loads, as shown in Figure 6-54. The pressure response was as expected, with the closing gap side of the bearing (pressure ports 1, 2, and 3) experiencing an increase in pressure, while the opening gap side of the bearing (pressure ports 4 and 5) experienced a decrease in pressure. This indicated that the bearing compensation was

operating as designed.[10]
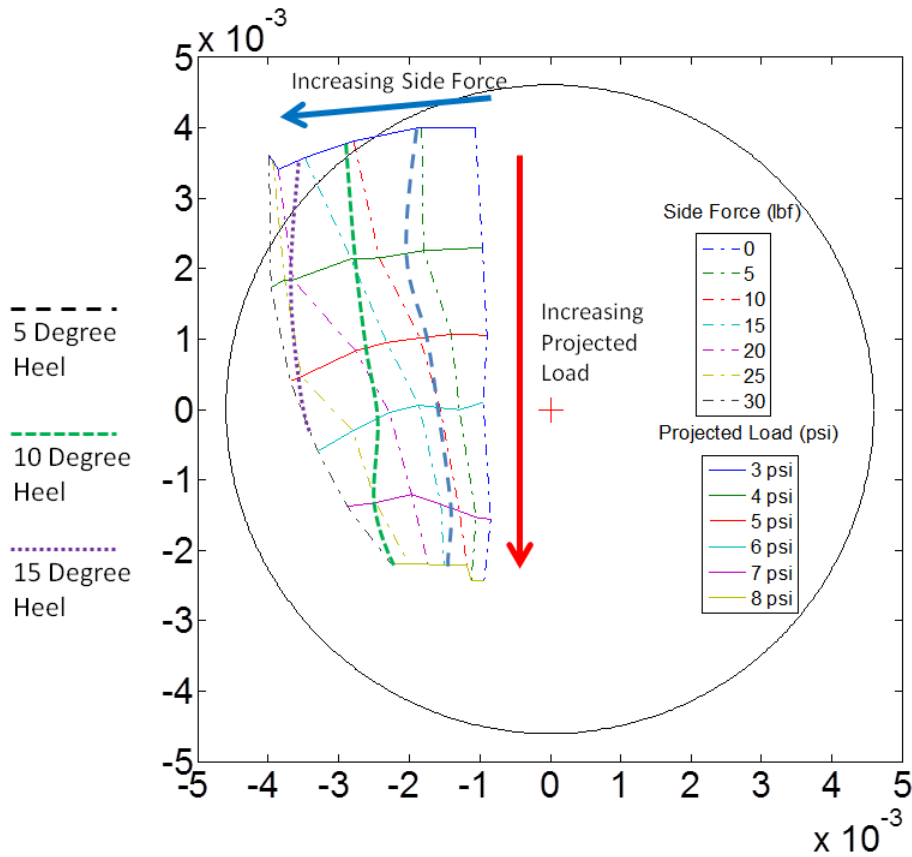
Figure 6-54: Locus of shaft positions (inches) for Comb bearing without side flow at various projected loads and side forces

In addition to side force testing, the response of the bearing to applied moments that can be caused by misalignment was conducted. Figure 6-56 shows the tilt response of the bearing at a 7 psi projected area load during hydrostatic operation. As with the Two-Port bearing, the figure shows the maximum misalignment the bearing can support at its operating eccentricity ratio (approximately 0.46). The response of the bearing is relatively linear, with no indications that the bearing grounds itself on one side of the bearing.

---

[10]There are additional effects contributing to this response, as was determined for the Hydrostatic Lift Bearing.
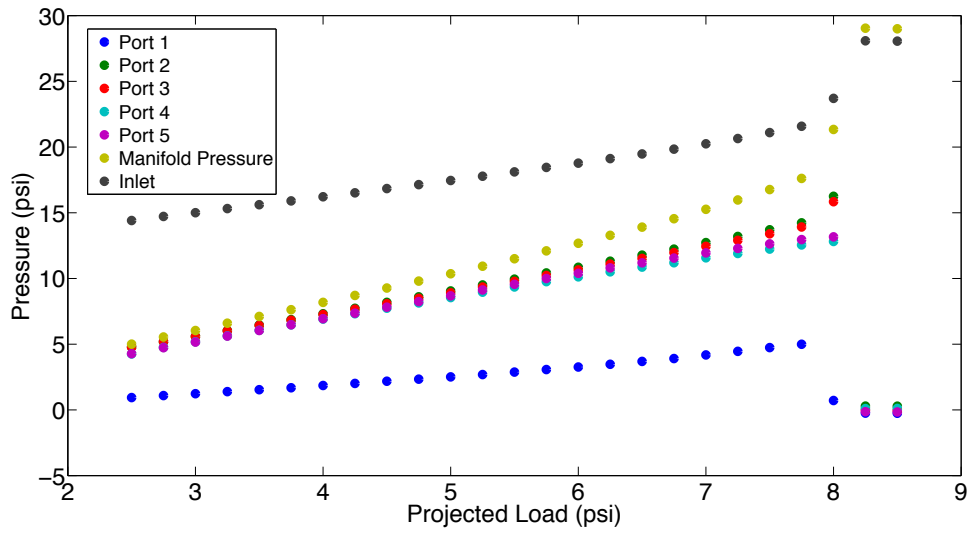
Figure 6-55: Comb bearing hydrostatic pressure response to various projected area loads
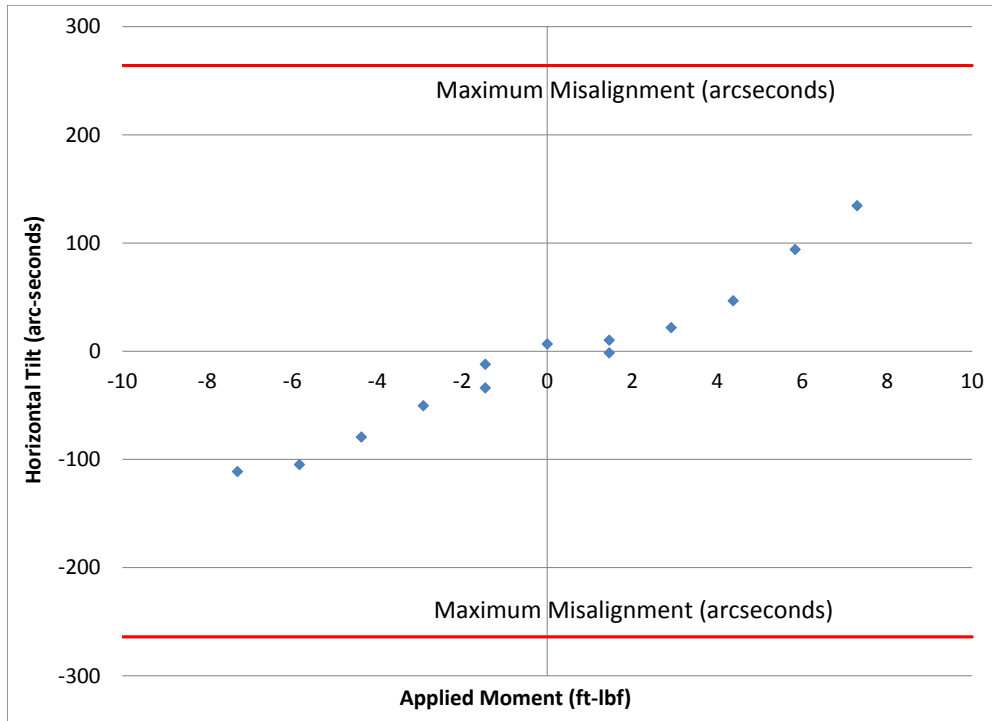
Figure 6-56: Horizontal tilt response to applied moments for Comb bearing at 7 psi projected area load

Hydrodynamic testing of the bearing was conducted for projected area loads of 5, 7, and 9 psi for speeds up to 500 rpm. Overall hydrodynamic performance was poor, with the friction response similar to that of the Stave bearing. Figure 6-57 shows the friction response of the bearing. The main reason for the poor hydrodynamic capability was because the design has a series of circumferential grooves. These grooves effectively split the bearing into stacks of very short bearings. There has been much research to show that hydrodynamic bearing performance degrades as the length decreases, due to the ability of pressure to leak out the axial ends of the bearing. Figure 6-58 shows the response of hydrodynamic bearings as a function of eccentricity ratio and L/D ratio. The side leakage load coefficient used by Fuller is proportional to the amount of load the bearing can support. The Comb bearing has a distance between grooves of 0.275 inches so each individual section has L/D ratios of approximately 0.085, which is off the chart. Extrapolating the lines in the figure make it clear that there is very little load that can be supported by bearings with such a low L/D and explains the reason for the Comb bearings poor hydrodynamic response.

Overall, the Comb bearing displayed unacceptable performance. During hydrostatic testing flow rates were excessive and the bearing displayed an unstable response at high eccentricites. Hydrodynamic response was completely unacceptable. Although the bearing did display the capability to support side loads and moments, the other performance metrics were not good enough to make this a viable bearing. Insight was gained, however, on the effectiveness of splitting the bearings into short L/D segments.
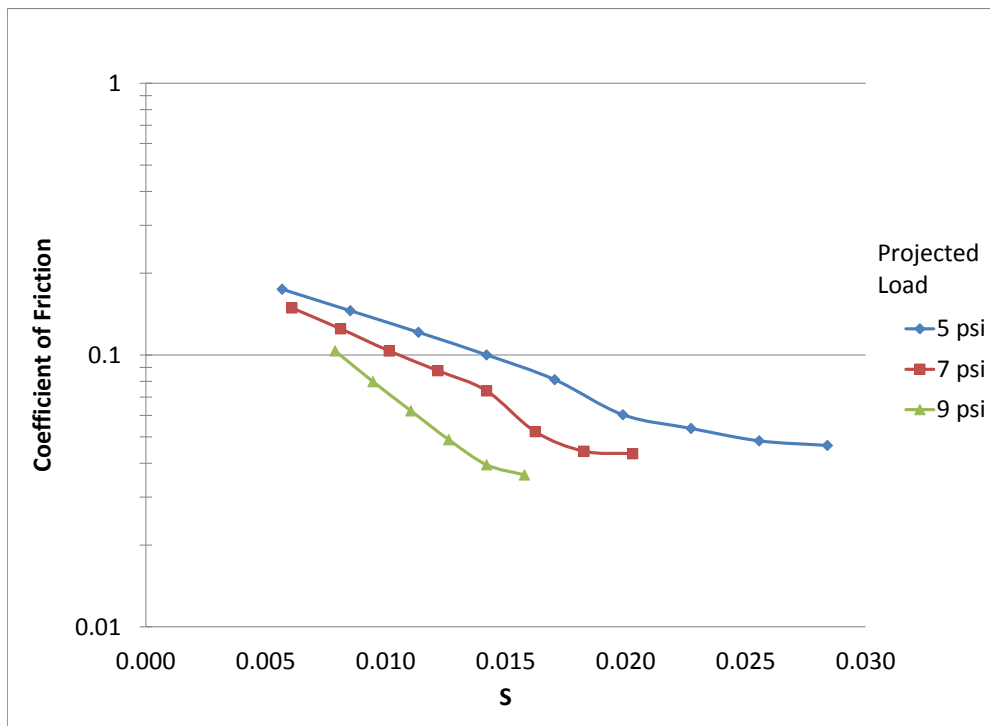
Figure 6-57: Comparison of counter-clockwise friction coefficients for Comb bearing tested at various projected area loads as a function of Sommerfeld number
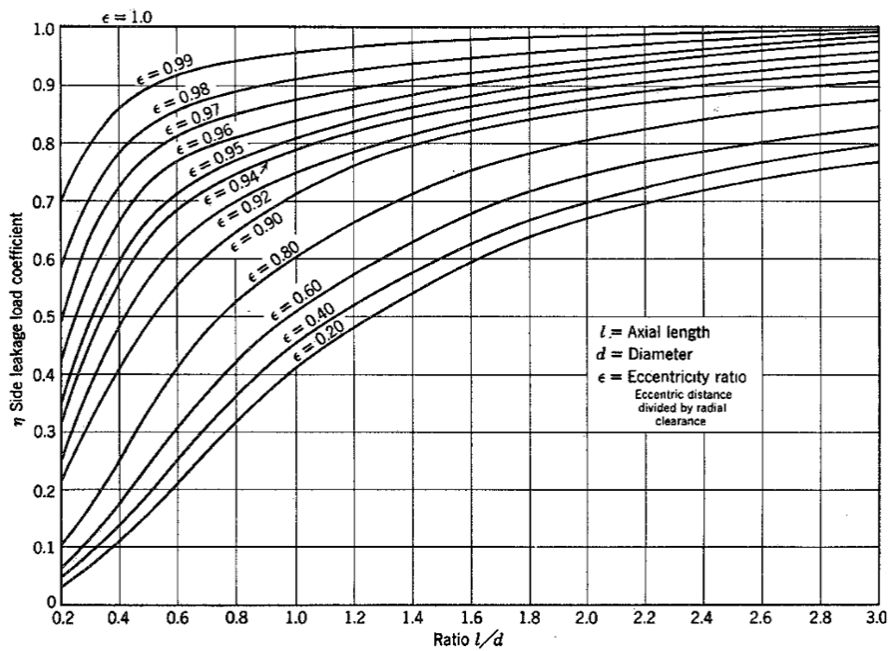
FIG. 6-9. Side-leakage factors for journal bearings.

Figure 6-58: Side-leakage factors as a function of eccentricity ratio and L/D ratio[8]

6.9 Hydrostatic Lift Bearing

6.9.1 Design Basis and Description

The Centerlift bearing design provided a good combination of hydrostatic and hydrodynamic performance, as well as a decent amount of side load capacity. It was desired to benchmark the capabilities of the Centerlift bearing (and other bearings built and tested) against an industry standard bearing design that is sometime used in hydrodynamic bearings - the Hydrostatic Lift (or "Oil Lift"). An oil lift consists of a single supply groove or recess along the BDC of the bearing where high pressure fluid can be introduced to lift the shaft from the bearing and support it with a fluid film. They are used for hydrodynamic bearings to reduce friction during start-up, shut-down, and reversal of direction as well as reduce the amount of wear that can occur during those conditions.

Such bearing designs are normally only used for large hydroelectric generators or turbine generators that are expected to see load in a constant direction[14]. Conventional wisdom suggests that the ability of such bearings to support a side load is negligible and should not be used in applications where those types of loads are expected, with the rationale being that a side load will cause the shaft to contact one side of the bearing, thereby interrupting the fluid film. Rippel's often cited hydrostatic design manual states that "The transverse, or side load-carrying capacity of a single-recess journal bearing is extremely limited, being approximately 1 or 2 per cent of applied radial load"[25]. The author has not come across any literature or application of such bearings where the ability to support any significant side load is either mentioned or realized. For a ocean vehicle subjected to varying heel and roll angles, such a bearing would not be viable. With this preconceived knowledge, this bearing was built with the expectation that it would only be able to support a vertical load and serve as a comparison point against the other bearings in that respect.

The original Hydrostatic Lift designed for this bearing consisted of a 3-inch long slot
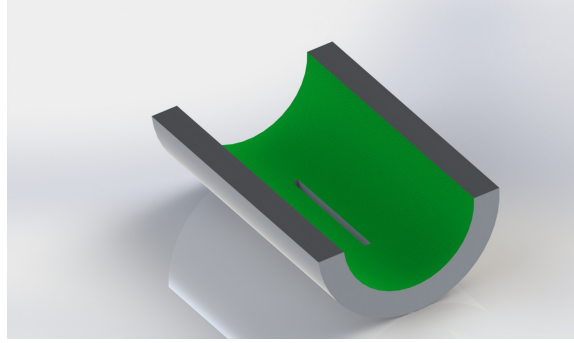
Figure 6-59: CAD representation of Hydrostatic Lift bearing with 3 inch slot

along the BDC of the bearing. The slot width was selected to be 0.015 inches wide. The 0.015 inch slot was created using a 1/8 inch single flute downcut endmill in the bearing material. This slot is fed lubricant through a 1/4 inch NPT threaded connection to a 1/2 inch push-to-connect fitting. The bearing was first fabricated, then tested as a plain journal bearing. Because of the simple geometry of the single groove in the Hydrostatic Lift, the 3 inch long slot was milled after the bearing was manufactured - a departure from earlier bearings where the grooves were cut into the bearing material in the flat condition. Figure 6-59 shows the layout of the bearing and Table 6.11 shows the specifications of the Hydrostatic Lift bearing.

Table 6.11: Hydrostatic Lift Specifications

Bearing Configuration	Hydrostatic Lift Bearing	
Material	Turcite	
Diameter	3.2391	Inches
Radial Clearance	0.0043	Inches
Clearance Ratio	376	
Engagement Arc	175	degrees
L/D Ratio	2	

6.9.2   Test Results

Initial hydrostatic testing of the 3-inch slot configuration was conducted with the centrifugal pump. Efficiencies at hydrostatic supported loads were on the order of 25 percent and flow rates were fairly small for a given eccentricity ratio. Similar to the

Comb bearing, it displayed an inability to operate at high eccentricity ratios. This is displayed in Figure 6-60. As the figure illustrates, the bearing collapses rapidly with a marginal increase in projected area load from 6.5 to 6.75 psi. Accompanying this collapse is the stopping of fluid flow through the bearing as the shaft effectively seals off the fluid supply groove. This unstable response in the vertical direction due to higher loads was found to be a function of the shape of the gap in the bearing. This behavior was first identified by Heller and Shapiro, who called the phenomena "Lockup"[12].
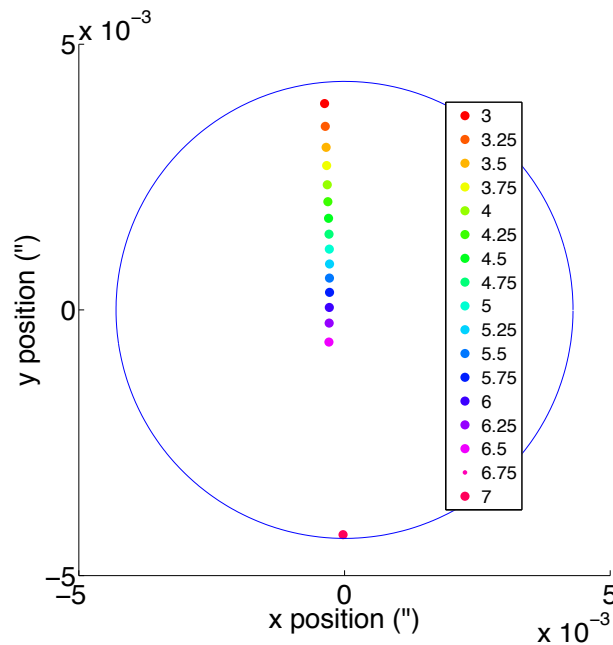
Figure 6-60: Locus of shaft position (inches) in Hydrostatic Lift bearing (3 inch slot configuration) during hydrostatic testing for various projected area loads (psi) using centrifugal pump

For a concentric shaft and bearing, the fluid gap between the inlet of the pressure groove at the bearing BDC and the circumferential exits of the bearing is a constant height - allowing the bearing to be modeled as a two flat plates consisting of the shaft and bearing over the arc length of the bearing. As the shaft eccentricity increases, however, the fluid gap becomes more and more of a diverging wedge shape. This change in the gap shape has a dramatic impact on the pressure profile of the bearing.

Figures 6-61 and 6-62 show the dramatic difference in pressure profiles that can be expected due to the changing gap shape from different eccentricities.[11] These figures assume a constant inlet pressure of 30 psi for illustrative purposes only.

Figure 6-61: Effect of gap shape on pressure profile of Hydrostatic Lift bearing for eccentricity ratio of 0 and constant pressure supply of 30 psi

The pressure profile graphs were generated from a model developed using the pressure gradient derived in section 3.2.1 for circumferential flow over lands in an eccentric shaft. As can be seen for the concentric shaft condition (Figure 6-61), there is a linear decrease in the pressure profile from the inlet to the edges of the bearing. For the eccentric condition (Figure 6-62), the pressure gradient has a rapid initial decrease in pressure. In all conditions, the common boundary conditions are atmospheric pres-

[11]The clearance depicted in these figures is oversized for illustrative purposes only.
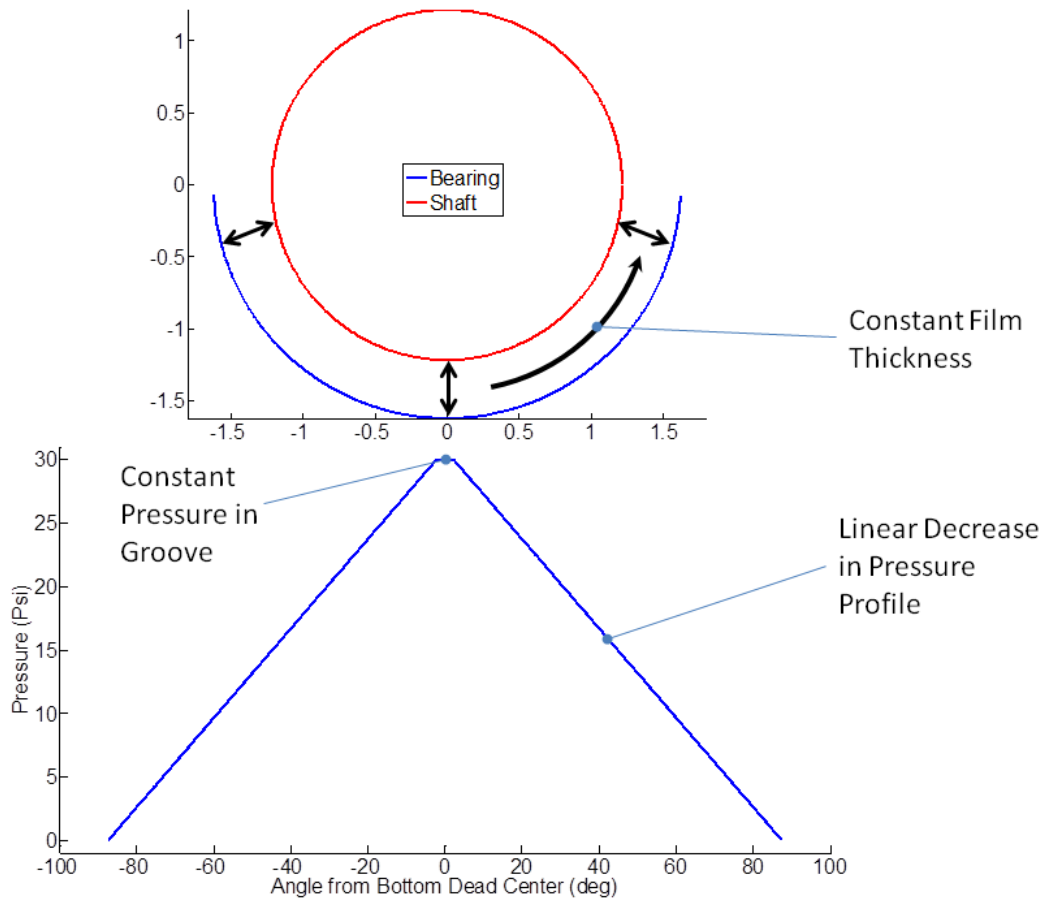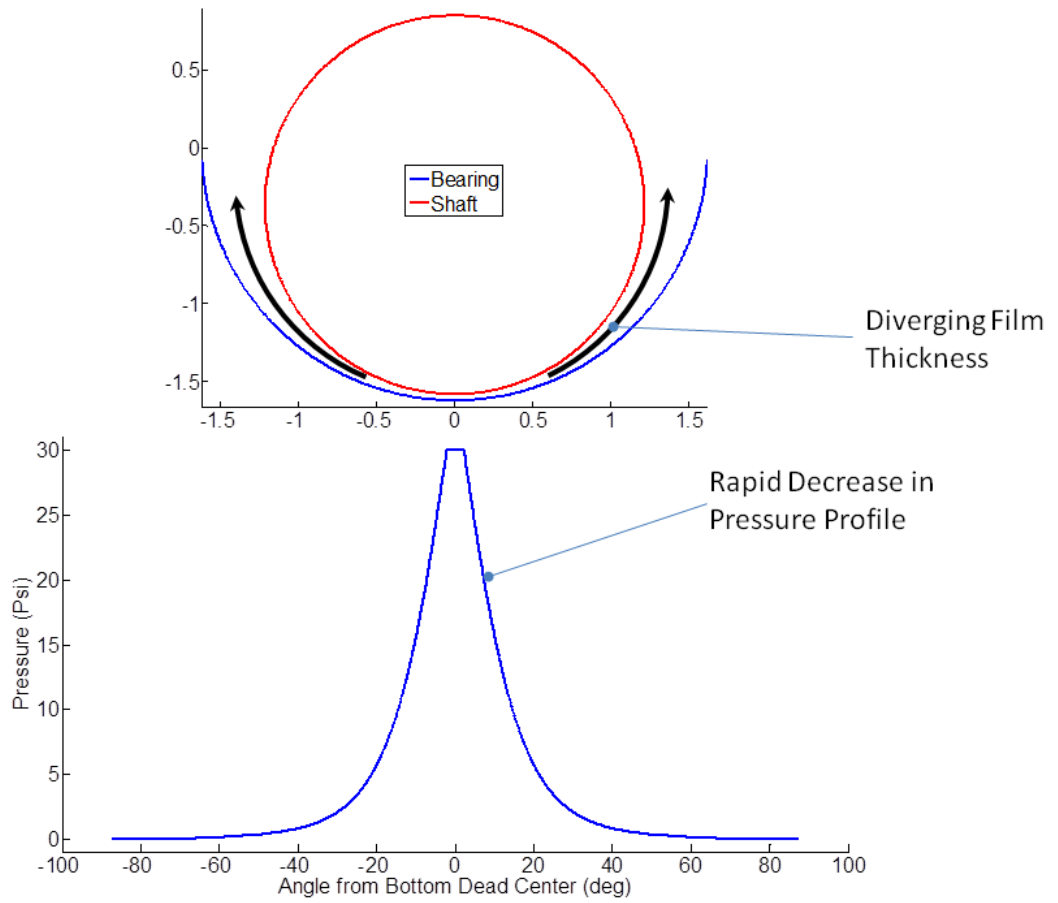
Figure 6-62: Effect of gap shape on pressure profile of Hydrostatic Lift bearing for eccentricity ratio of 0.9 and constant pressure supply of 30 psi

sure at the circumferential edge of the bearing and the inlet pressure at the supply groove. Since the pressure in the film is what develops the load support in the bearing, the vertical support is a function of the pressure at a point times the cosine of the angle from BDC at that point. Integrating that product over the entire bearing provides the total vertical support capacity of the bearing. From those figures, it is clear that the eccentric shaft has less pressure acting on it to support loads, which results in the collapse of the bearing (or 'Lockup').
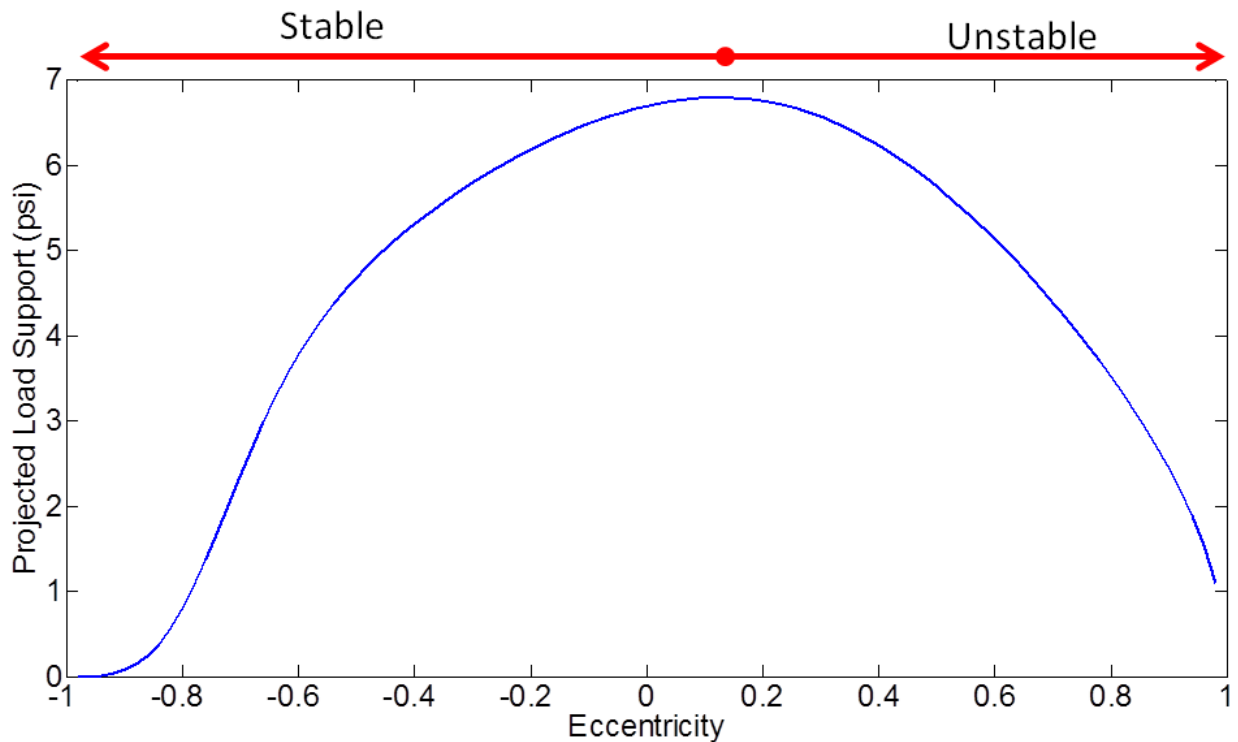
Figure 6-63: Projected load prediction for Hydrostatic Lift bearing (3 inch slot configuration) as a function of eccentricity ratio using the centrifugal pump

Figure 6-63 shows the predicted load support using the centrifugal pump in the 3 inch Hydrostatic Lift bearing using a simplified 2 dimensional model. It is clear that the bearing is inherently unstable in the vertical direction. Consider the case of a shaft

operating concentric to the bearing:

1. The bearing is operating at a stable point, but the external load is increased. This increased load results in a increase in eccentricity ratio.

2. This increase in eccentricity ratio results in more load support being developed by the bearing until it is equal to the external load.

3. This continues until approximately an eccentricity ratio of 0.13.

4. For increases in load that result in eccentricity ratios greater than 0.13, the load support capacity of the bearing decreases until the shaft bottoms out on the bearing.

This behavior was seen quite clearly during hydrostatic operation. There are errors between the model prediction and experimental results that can be attributed to at least two things. The first is that the model is 2 dimensional, while the bearing is 3 dimensional. To accurately model the bearing requires a finite difference program or computational fluid dynamics, but for illustrative purposes and predicting the general response of the bearing, the 2 dimensional model is adequate. The second factor contributing to error is the fact that the actual bearing had a slight vertical tilt during operation of approximately 20 arc seconds. The experimental results showed the model to be stable up to an eccentricity ratio of approximately 0.27.

Side force testing conducted on the Hydrostatic Lift configuration with a 3 inch slot revealed a remarkable capacity for supporting a transverse load, which was unexpected, as mentioned above. It is theorized that the cause of the load support is due to the changing shape of the fluid gap with eccentricity and attitude angle - similar to the effects seen with the instability of the bearing. Figure 6-64 represents the expected change in pressure profile due to the changing film shape for a bearing experiencing a transverse load. The converging film prevents a significant drop in pressure until the edge of the bearing. On the diverging film side of the bearing, there is a rapid drop in pressure from the supply groove to the edge of the bearing. The

transverse load support of the bearing is a function of the product of pressure and the sine of the angle from BDC of the bearing. This makes it clear that this pressure profile will allow a correcting force to the side to counteract the applied load. This pressure profile exists because this bearing is a partial arc configuration that forces atmospheric boundary conditions at the circumferential edges of the bearing. A full 360 degree bearing has no such forcing conditions, so the pressure profile in such a bearing is more of a 3 dimensional problem and may not necessarily have the same response.
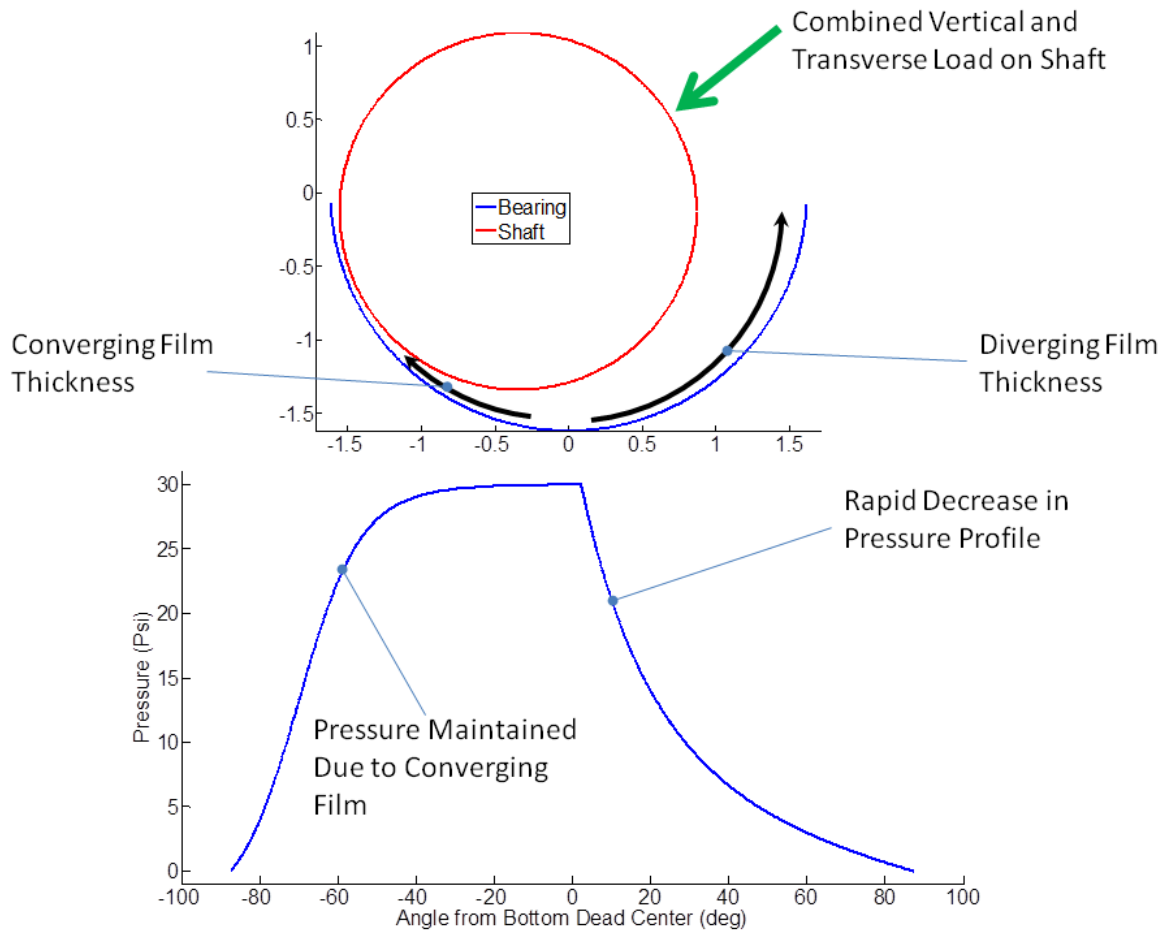

Figure 6-64: Effect of gap shape on pressure profile of Hydrostatic Lift bearing for eccentricity ratio of 0.9, attitude angle of -70 degrees, and constant pressure supply of 30 psi

The Hydrostatic Lift bearing was tested in its original plain journal configuration

273

to allow direct comparisons of hydrodynamic performance with other bearings with similar clearance ratios. The results of this testing are used in the comparison of the Centerlift bearing (section 6.5) and Two-Port bearing (section 6.6). Figure 6-65 shows the friction response of the bearing to various projected area loads in the counter-clockwise direction. As expected, the performance is very good, with the transition to the hydrodynamic lubrication regime clearly delineated by the point of minimum friction.
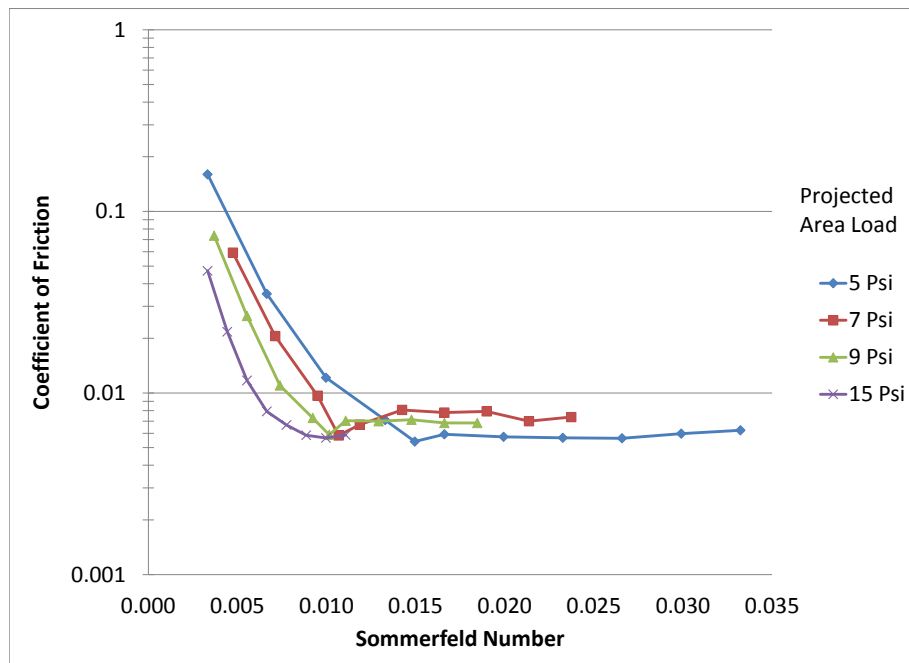
Figure 6-65: Counter-clockwise friction curves of Hydrostatic Lift bearing (in plain journal configuration) for various projected area loads as a function of Sommerfeld number

The bearing was also hydrodynamically tested after the milling of the 3 inch supply groove to determine the effect that the groove had on its response. This testing included two configurations. The first had the fluid inlet valve closed, allowing for pressure to build up in the groove of the bearing due to the hydrodynamic effect of

the bearing. The second configuration left the fluid inlet valve open, preventing the buildup of hydrodynamic fluid pressure in the supply groove. The differences in the bearings was very noticeable. In general, the slot had little effect on performance if the valve was shut. In fact, the lowest recorded friction was for the bearing with the slot configuration in the clockwise direction.[12] Leaving the inlet valve open had a degrading effect on performance, with a higher overall friction curve and the transition to hydrodynamic lubrication occurring at a higher speed.
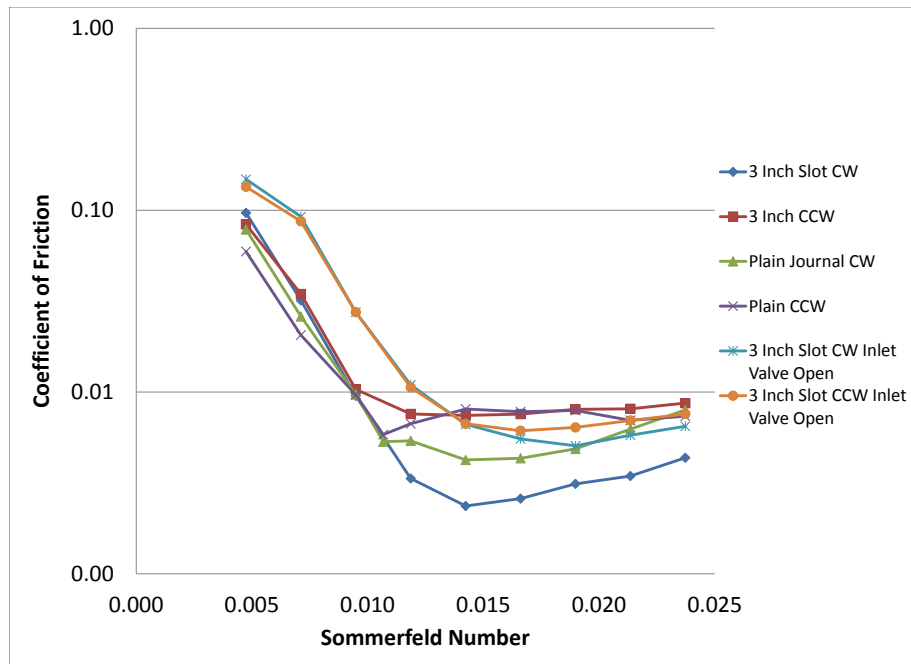
Figure 6-66: Comparison of friction coefficients for Hydrostatic Lift bearing (3 inch slot configuration) tested at 7 psi projected area loads as a function of Sommerfeld number

The build up of pressure in the slot with the valve closed was not instantaneous.

---

[12]These results must be analyzed taking into consideration the fact that the slot configuration was tested after the plain configuration. As seen with the stave bearing, the effects of wear-in has a significant impact of the friction seen in the bearings. It would be expected that the friction values would go down with later tests if all other considerations (including modifications to the bearing) are equal.

Transient responses were tested by cycling the supply valve open and shut with the pump secured. Figure 6-67 shows the time dependent response of the Hydrostatic Lift at 7 psi projected load. It is clear that it takes time (approximately 60 seconds) for pressure to build up completely in the slot from the hydrodynamic action of the bearing. During this period of pressure build up, the friction drops until around 20 seconds at which point the bearing is fully in the hydrodynamic lubrication regime and friction does not drop any further with pressure build up. This analysis provides key insights that are useful for a system level design. Incorporating a check valve or isolation valve in the fluid supply system is vital to achieving maximum hydrodynamic performance. If such valves are present, then the slot has a very negligible effect. If they are absent or not used, then a degraded hydrodynamic response can be expected.
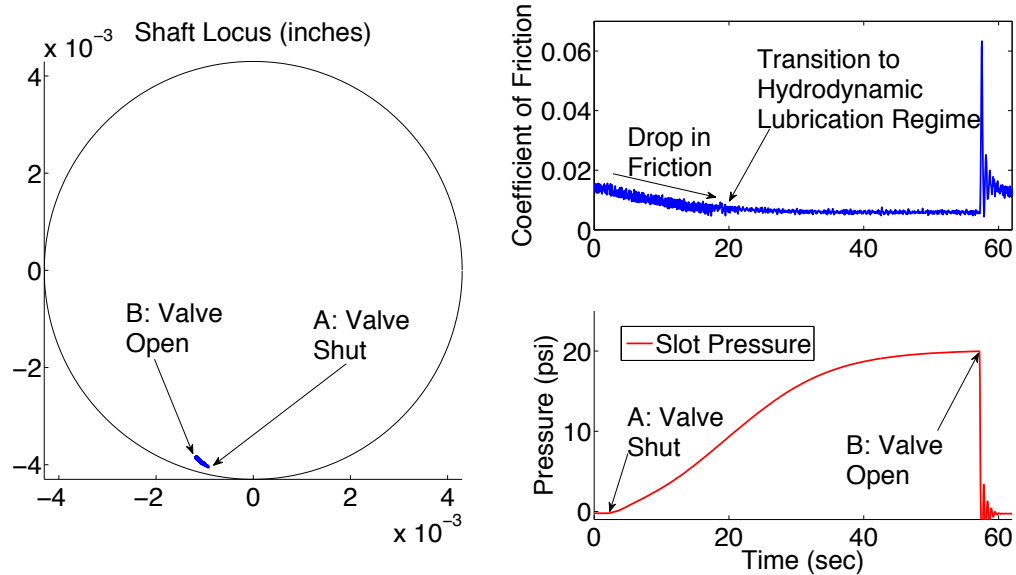
Figure 6-67: Time based response of Hydrostatic Lift bearing (3-inch slot configuration) to cycling of supply inlet valve at 7 psi projected load and 250 rpm in clockwise direction

Additional tests on the 3 inch slot configuration using the centrifugal pump included hybrid operation, applying moments to the bearing during hydrostatic operation, and side impact response during hydrostatic operation. As with previous bearings, the friction curve is generally flat during hybrid operation. Impact testing revealed the

bearing was capable of withstanding a certain amount of shock without the shaft contacting the sides of the bearing and causing damage. The bearing also showed a capacity to support moments caused by misalignment, shown in Figure 6-68. The slope of the tilt is higher than for the Two-Port and Comb bearings, which would indicate that the Hydrostatic Lift bearing can not accommodate as much misalignment force. This may not be entirely correct because this bearing was operating at a lower eccentricity ratio - providing more fluid film that can be compressed due to the misalignment forces.

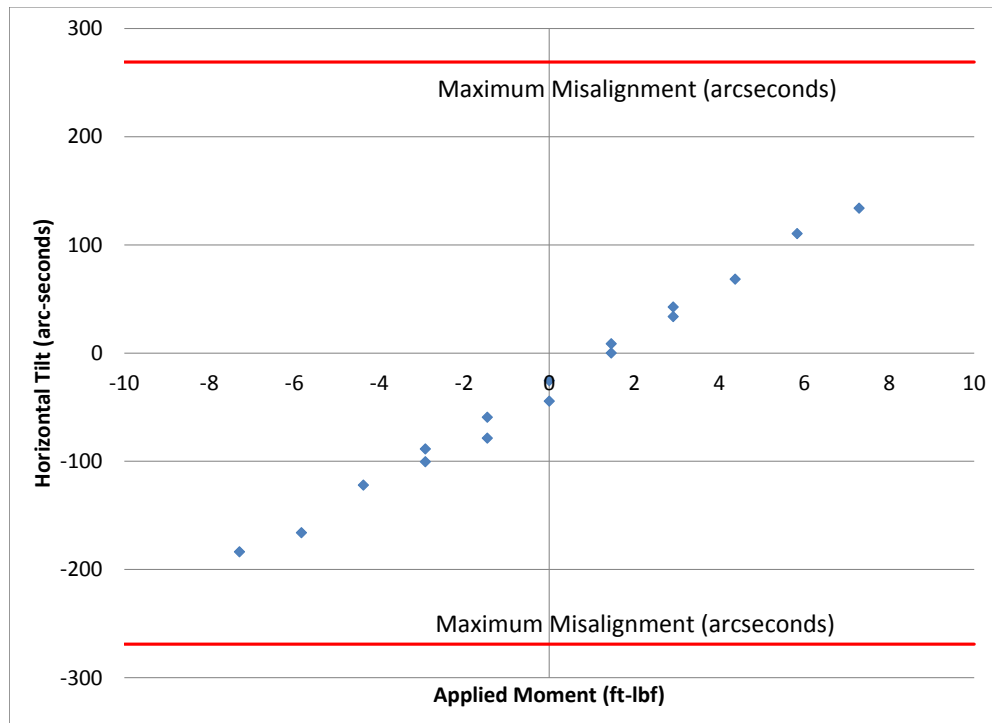Figure 6-68: Horizontal tilt response to applied moments for Hydrostatic Lift bearing (3 inch slot configuration) at 6 psi projected area load

Overall, the hydrostatic lift showed remarkable promise. The fact that it was inherently stable in response to transverse loads was remarkable in that no literature has ever suggested that such was the case. The ability of the changing gap shape to influ-

ence the pressure profile and respond to side forces removes the need for surface self compensating features in the bearing, greatly simplifying the design and manufacture of these bearings. Also revealing is that in previous bearings there was clearly some other factor at work other than self-compensation that was allowing the bearings to achieve such a high transverse load capacity - the enabler of this and what turns out to be the dominant factor is the changing gap/pressure profile in the bearings.

The simplified nature of the Hydrostatic Lift bearing provided a hydrodynamic performance approaching that of the plain journal configuration. This indicated that very little hydrodynamic capabilities needed to be sacrificed in order to achieve beneficial hydrostatic features. The major drawback to the basic Hydrostatic Lift design remained its inability to operate at high eccentricity ratios. This is important, because flow rates (and therefore pumping power) increases greatly with lower eccentricity ratios. To make an economical hybrid bearing, the flow rate should be minimized as much as possible. To do so requires either a smaller gap[13], or to operate at a higher eccentricity ratio. This last option was a driving reason behind the building of the gear pump device and the modifications to the 3-inch slot hydrostatic bearing discussed in the next section.

6.9.3 Centrifugal Pump Test Results

As described in section 4.4.3, a positive displacement gear pump device was built to support hydrostatic testing. This was driven by the limitations of operating at higher eccentricity ratios in the Hydrostatic Lift bearing. Switching to a different type of pump allowed for more direct control over the operation of the test rig by allowing flow rate to be independently controlled. In addition to the change in pump configuration, pressure ports were fabricated into the surface of the bearing along the axial midpoint to allow the pressure profile to be determined during operation. These pressure ports required aligning of the bearing by hand in a vice, so the placement of the ports was imprecise, but the actual locations of them were later determined

---

[13]See section 7.1 for more discussion on the ability to reduce gap size in water-lubricated bearings

accurately by CMM. Figure 6-69 shows the location and nomenclature of the pressure probes. Other probes not illustrated include probe 1, which had a failure and was inoperable for the remainder of testing and probe 6, which was used to record the inlet pressure to the supply groove.
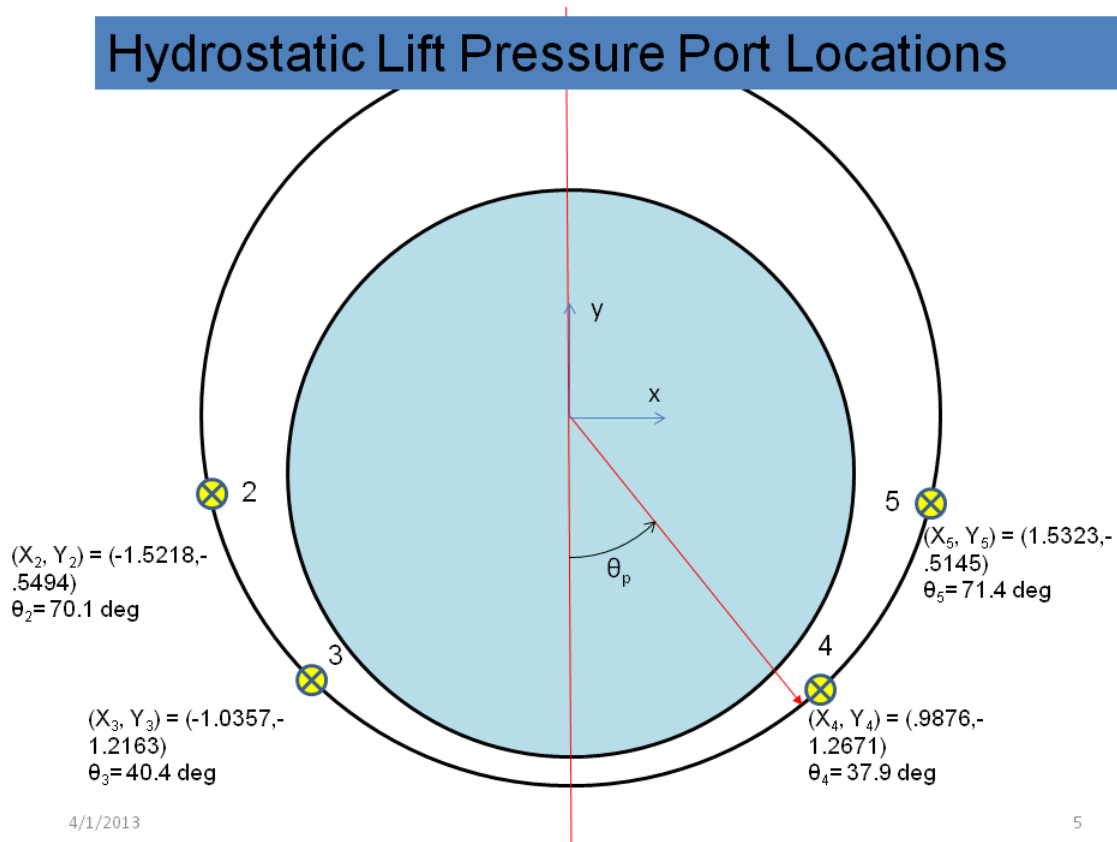
Figure 6-69: Pressure Probe Locations in the Hydrostatic Lift Bearing

Hydrostatic, hybrid, and hydrodynamic tests were repeated on the 3 inch slot configured Hydrostatic Lift bearing. The hydrostatic testing involved a systematic testing scheme where various projected loads were tested at various gear pump speeds. The gear pump motor was varied in approximately 10 percent speed increments (i.e. 100, 90, 80, etc. percent of full speed) until the bearing bottomed out. Although the exact eccentricity of the bearing is not known real time, it is clear when the shaft collapses onto the bearing because flow is secured to the bearing by the shaft sealing the groove. Testing with the gear pump showed the ability to achieve slightly higher

operating eccentricities, but could not attain ratios greater than approximately 0.5. Figures 6-70, 6-71, and 6-72 show some performance curves of the bearing at various eccentricities as a function of projected area load and gear pump speeds. Eccentricity ratios where the shaft was floating above the bearing and where the shaft is bottomed on the bearing are not shown. From the graphs, the truncation of eccentricity ratios greater than approximately 0.5 are a result of the unstable collapse behavior of the bearing. Flow rates are lower than previous bearings at these eccentricity ratios, while the load efficiency of the bearings is relatively flat.

Figure 6-70: Flow rates in Hydrostatic Lift bearing (3 inch slot configuration) during hydrostatic operation at various projected area loads and gear pump speeds as a function of eccentricity ratio

There does appear to be an optimum eccentricity ratio for load efficiency for each

Figure 6-71: Load efficiency in Hydrostatic Lift bearing (3 inch slot configuration) during hydrostatic operation at various projected area loads and gear pump speeds as a function of eccentricity ratio
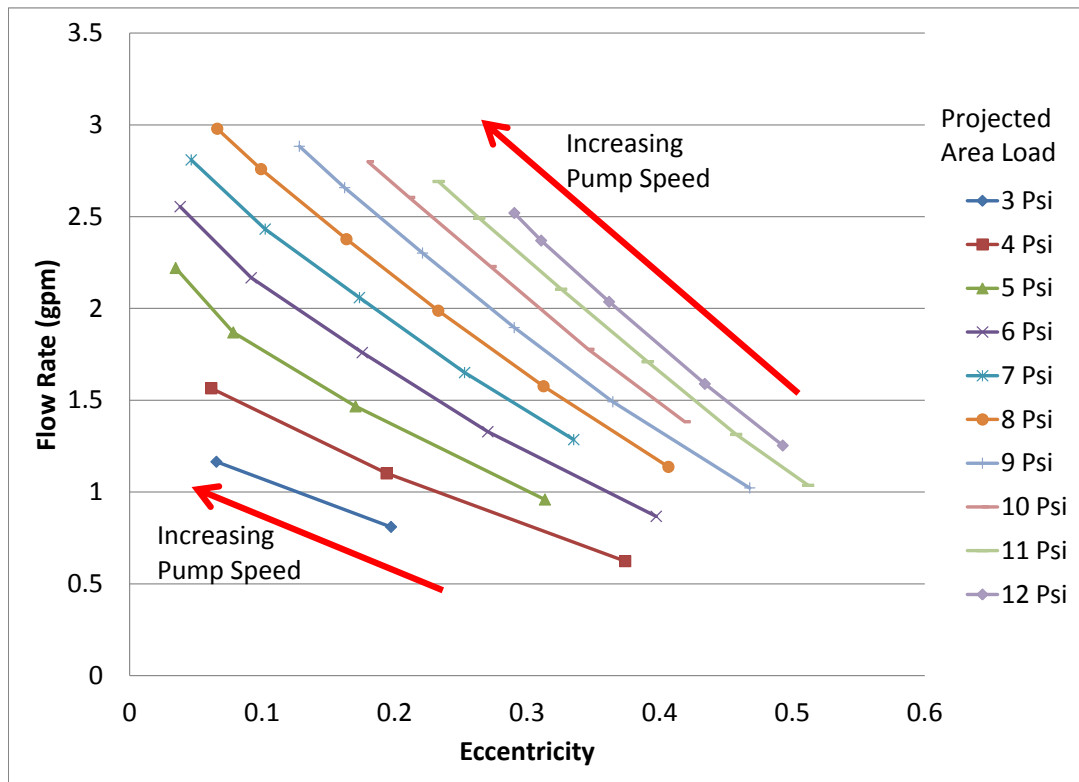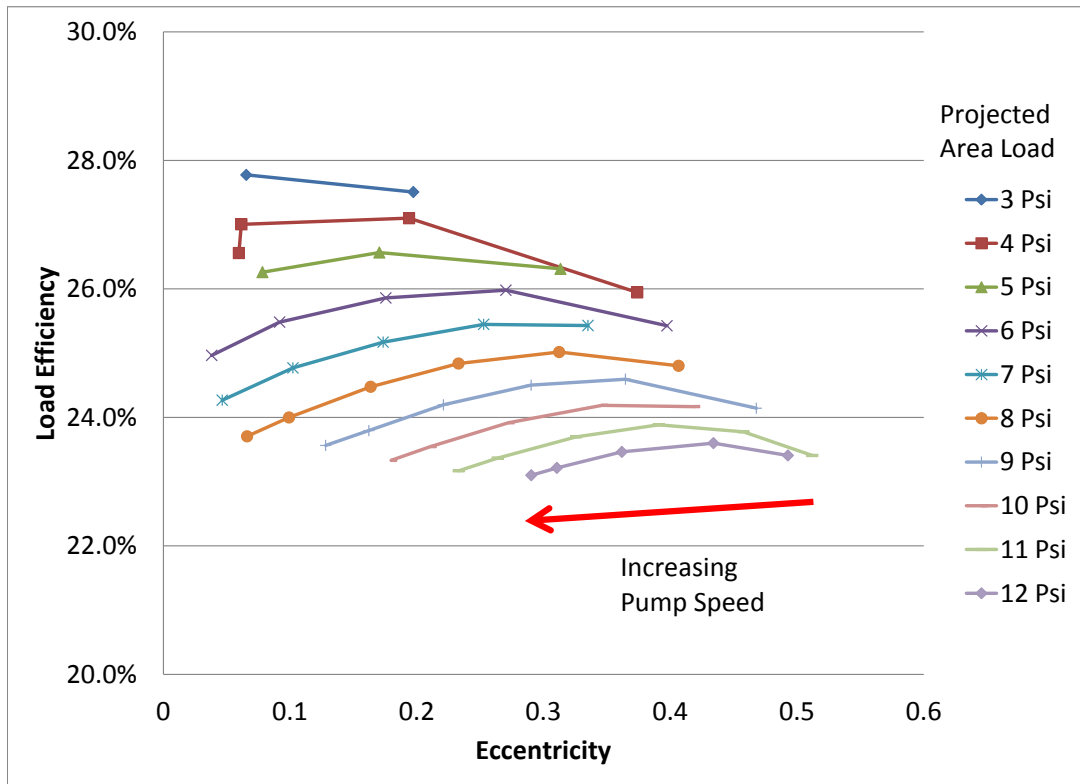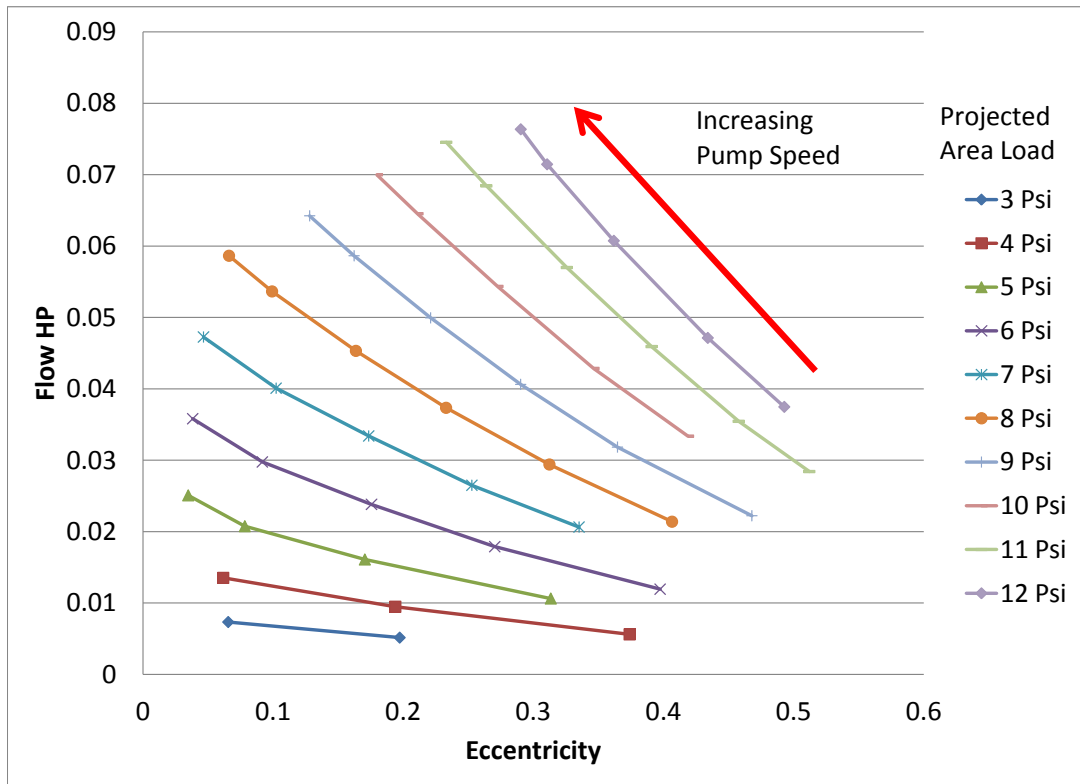
Figure 6-72: Flow power in Hydrostatic Lift bearing (3-inch slot configuration) during hydrostatic operation at various projected area loads and gear pump speeds as a function of eccentricity ratio

projected area load, but this is largely irrelevant because the dominant measure of efficiency will be the flow horsepower. Operating the shaft at eccentricity ratios lower than than those required to provide a complete fluid film is not needed, and only results in an excess flow power requirement. Because of this, the eccentricity should be small enough such that the shaft and bearing do not contact each other, but otherwise as large a possible. There should also be some margin to ensure that effects from misalignment, damage to the bearing surface, or dynamic effects do not result in contact between shaft and bearing.

Side force testing on the bearing was conducted at 7 psi projected area load for various pump speeds. The ability to vary the speed of the pump made it unnecessary to change projected loads to obtain a good indication of the bearing response. Figure 6-73 shows the shaft displacement from that testing. The bearing shows a remarkable ability to accommodate transverse loading. At the full 35 lbf side load this represents the ability to support a transverse load approaching 25 percent of the vertical load - an order of magnitude higher than the 1 or 2 percent suggested by Rippel[25].

The comparison of the experimental pressures and theoretical predictions from the simplified 2 dimensional model are shown in Figure 6-74 for a case of 7 psi projected area load, 35 lbf side force with the gear pump at 45 percent of maximum speed. The 2D model under predicts the pressures in the bearing, but the general shifting of the pressure profile is quite clear. This reinforces the assertion that it is the changing gap shape altering the pressure profile in the bearing that results in the ability to support side loads.

Comparisons were made against the model for other load transverse loads and eccentricities. Figure 6-75 show the experimental versus model pressure distributions in the bearing for two different operating conditions. The model provides an adequate ability to predict the vertical load support in the bearing (on the order of 10 percent error), but under predicts the amount of side force the bearing can handle. Predicted
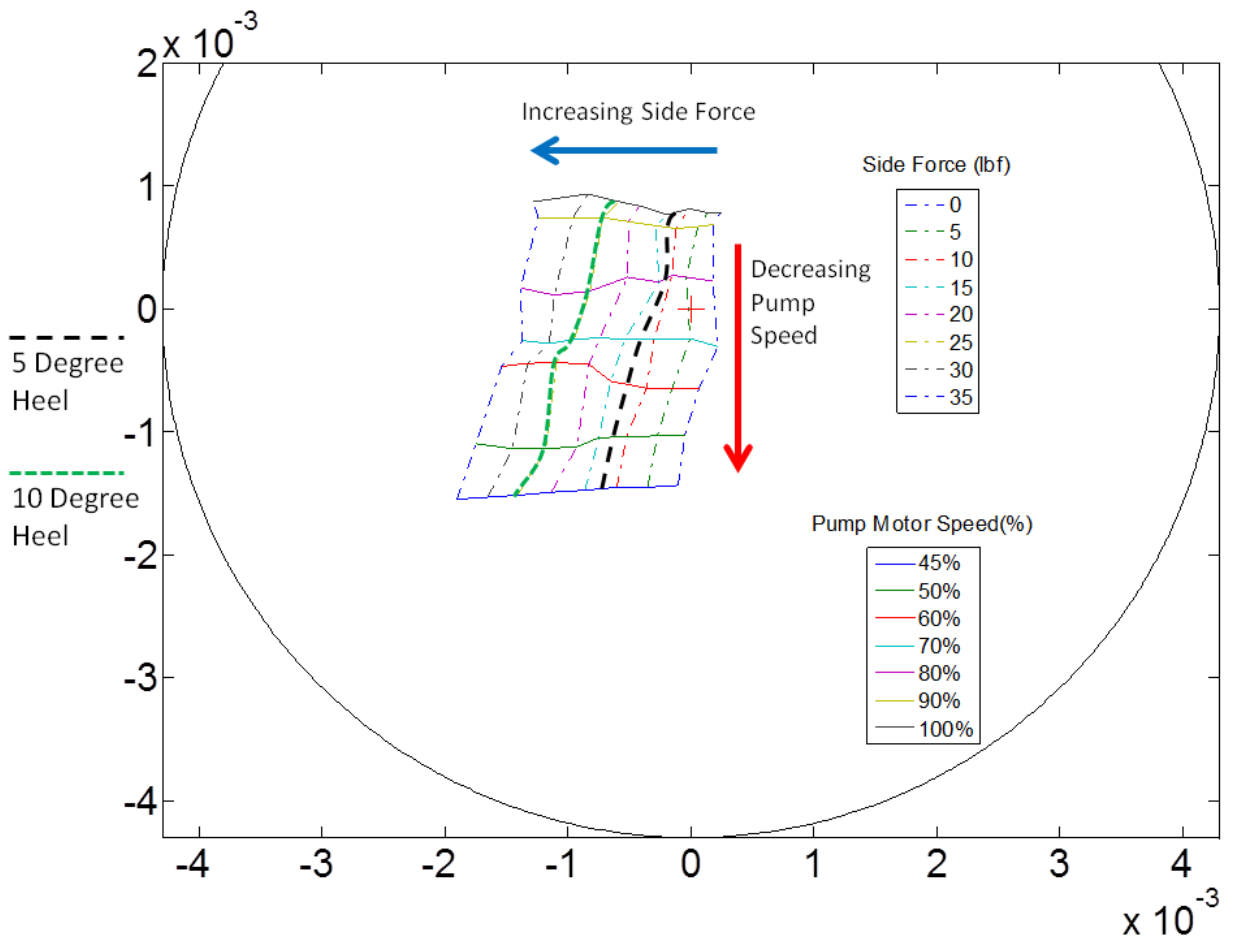
Figure 6-73: Locus of shaft positions (inches) for Hydrostatic Lift bearing (3-inch slot configuration) at 7 psi projected loads, various gear pump speeds and various side forces
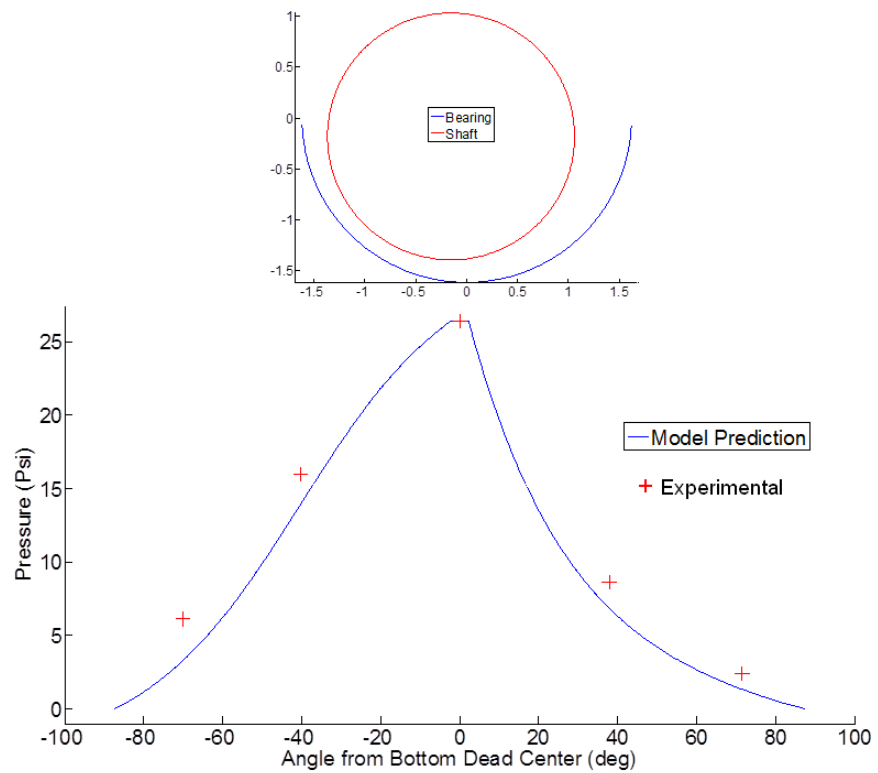
Figure 6-74: Pressure profile in bearing for Hydrostatic Lift bearing (3-inch slot configuration) for 7 psi projected load, 35lbf side force, and 45 percent pump speed

flow of the model consistently under predicted the amount of flow seen in the bearing. The driving reason behind this is the simplification of the process to a 2D model, when the bearing is a complex 3D system. The affects of leakage at the axial ends in particular will have a dramatic impact of the ability to maintain pressure on the diverging gap side of the bearing, especially if there is a tilt in the bearing. As stated earlier, to accurately model the bearing a finite difference program or computational fluid dynamics code would be needed.
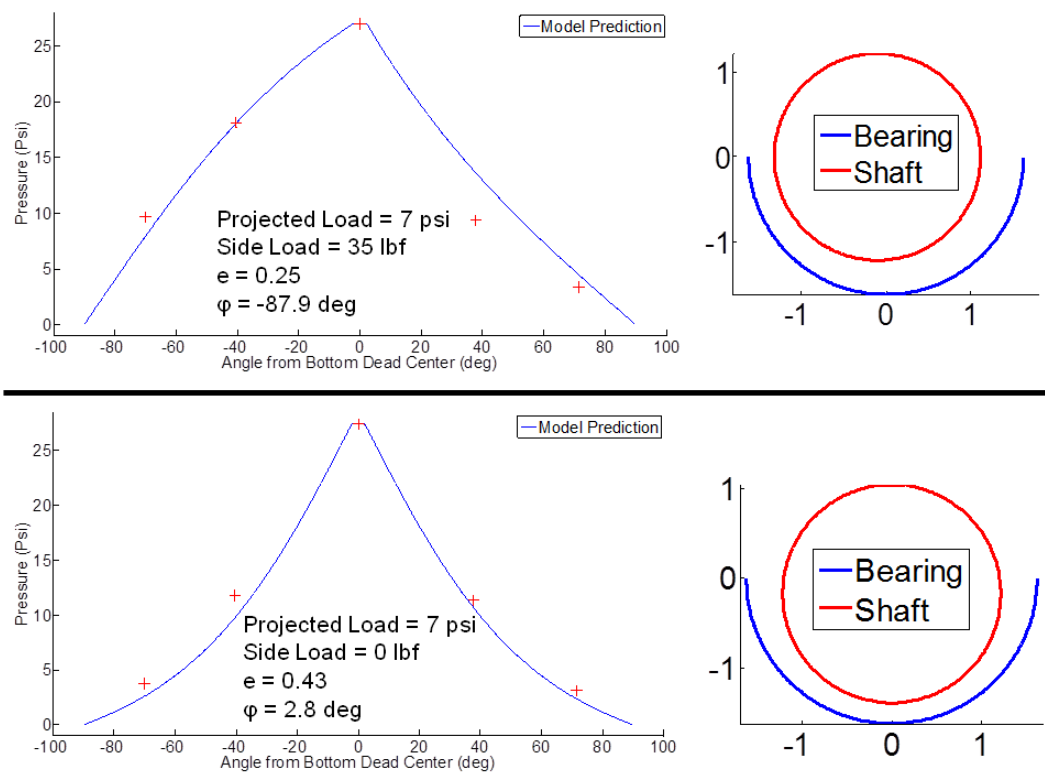
Figure 6-75: Pressure profiles in Hydrostatic Lift bearing (3 inch slot configuration) for different side loads, eccentricity ratios, and attitude angles

An additional concern with the unstable collapse behavior of the Hydrostatic Lift bearing was that it required a very large pressure in order to initially lift the shaft off the bearing. If the shaft is lifted and operating hydrostatically, there is the entire surface of the bearing for fluid pressure to influence, but once the shaft is grounded on the BDC of the bearing the effective pressure the supply fluid has to work on

Figure 6-76: Time based response of Hydrostatic Lift bearing (4 inch slot configuration) at 7 psi projected load and 20 percent gear pump speed illustrating shaft lift off and vertical instability

drops down to the area of the inlet groove. For this project, a variable called lift off pressure ratio (Δ) was defined as:

$$\Delta = \frac{P_{lift}}{P_{projected}} \tag{6.3}$$

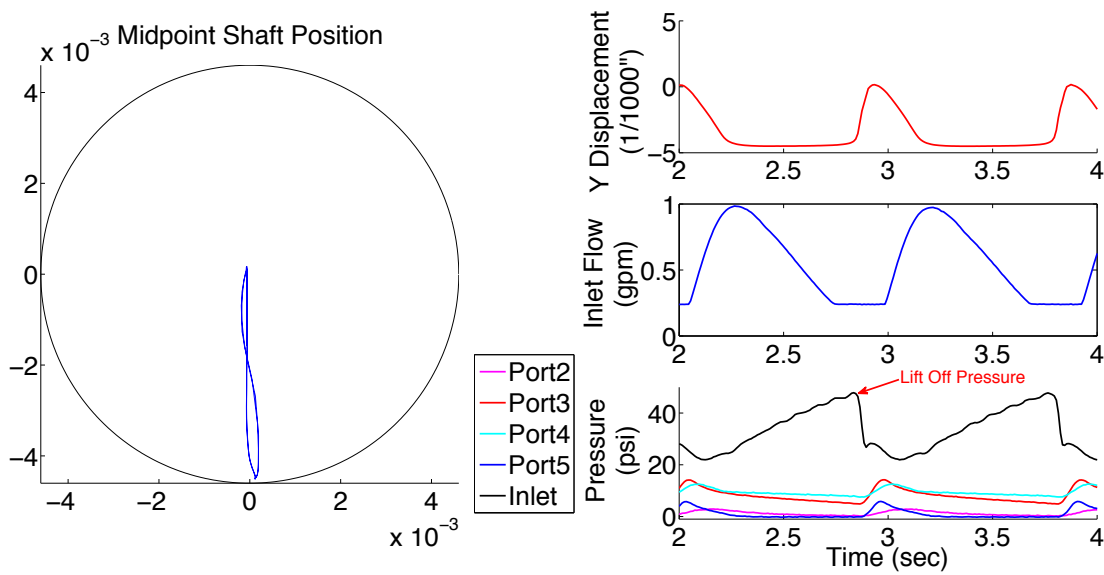where P_{lift} is the fluid supply pressure required to lift the shaft off the bearing surface and $P_{projected}$ is the projected area load of the bearing. During testing it was found that the bearing had a lift off pressure ratio (Δ) of approximately 15 to 20. For a nominal bearing designed to operate at 40 psi projected area load the maximum pump pressure capacity would need to be on the order of 600 to 800 psi. This would greatly complicate the overall system complexity of such a bearing, with piping systems, pumps, and accumulators designed to handle such high pressures during the starting transients. In addition to the large initial pressure needed to lift the bearing, the pumps need to supply sufficient flow and pressure to ensure the shaft operates at a stable eccentricity ratio. If insufficient flow power is provided, the shaft will immediately collapse back onto the bearing after lift off. This is shown in Figure 6-

76, which shows the transient response of a Hydrostatic Lift bearing with insufficient flow to achieve stable operation. This figure is for a modification of the bearing described in the next section. The instability seen at higher eccentricity ratios and the large lift off pressure ratio led to a series of design iterations and modifications to the Hydrostatic Lift bearing.

6.9.4 Modifications to Hydrostatic Lift and Results

To address the inability to operate at higher eccentricities, several modification were made to the Hydrostatic Lift bearing:

1. *4 Inch Slot Modification.* The slot was first extended to 4 inches to provide more axial groove length.

2. *2 Finger Modification.* Two short 1 inch long circumferential grooves feeding off the ends of the bearing were added (Figure 6-77).
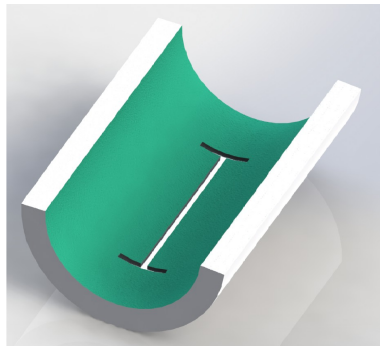
Figure 6-77: 2 Finger Modification to Hydrostatic Lift

3. *Greek Cross Modification.* An additional 1.75 inch long circumferential groove was placed along the axial midpoint of the bearing (Figure 6-78).

These modifications were able to reduce the lift off pressure ratio significantly, as shown in Figure 6-79. A trend seen in all of the bearings was the decrease in the pressure ratio with an increase in projected area load. The reason for this is that the soft compliant nature of the bearing material the area in the vicinity of the grooves deflects locally, allowing pressure to act upon a larger region of the shaft and reducing

Figure 6-78: Greek Cross Modification to Hydrostatic Lift

the lift off pressure.

Although lift off pressure ratios were successfully reduced through modifications, the ability to operate the bearing at higher eccentricity ratios was not reali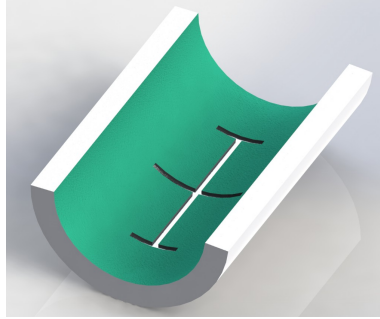zed. The bearing still collapsed at higher eccentricity ratios, with values greater than approximately 0.5 showing instability for all of the Hydrostatic Lift modifications.

As was expected, testing of the modified bearings showed that increasing the amount of grooves in the Hydrostatic Lift had an adverse affect on hydrodynamic performance, as shown in Figure 6-80. The largest degradation is due to the existence of the 3 inch slot. Increasing the slot length and adding circumferential fingers off the slot further degrade hydrodynamic performance, but only marginally. During the hydrodynamic testing of the modified Hydrostatic Lift bearings, they were configured for use with the gear pump, which did not have an isolation valve between the pump and the bearing. This prevented the hydrodynamic pressure from building up in the bearing grooves. As mentioned earlier, this build up of pressure provides the ability of the bearing to perform very closely to the plain journal configuration.
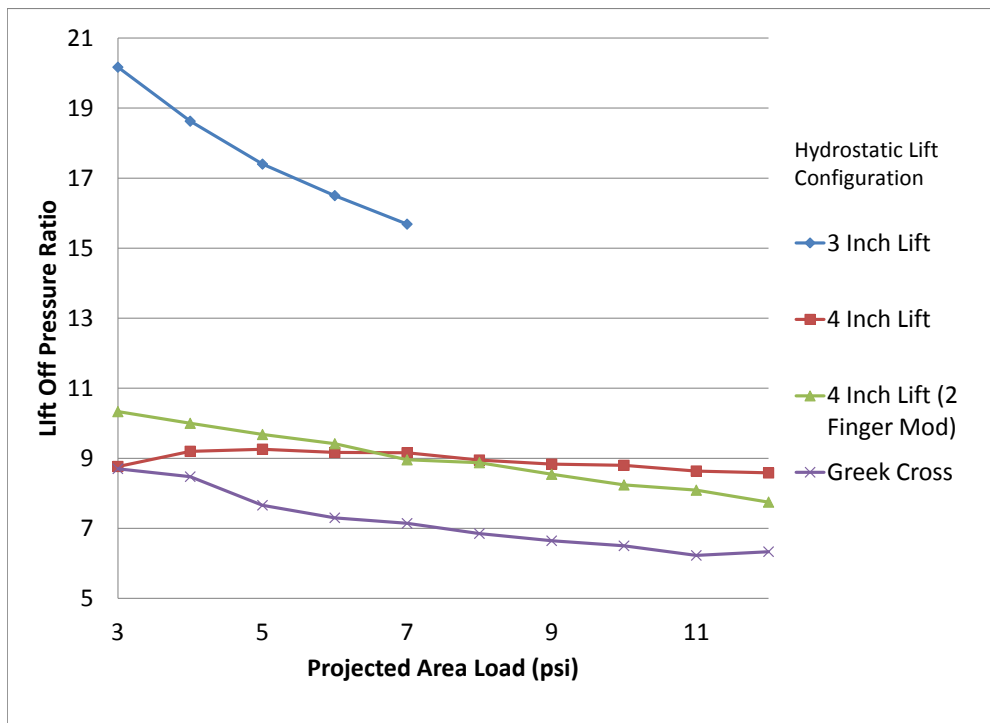
Figure 6-79: Lift off pressure ratio for Hydrostatic Lift modifications as a function of projected area load
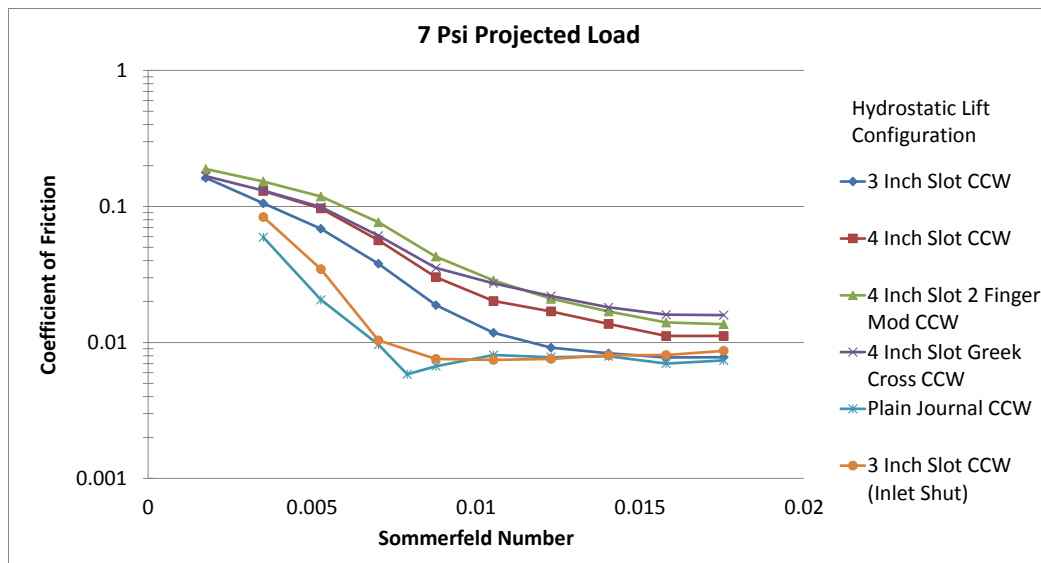
Figure 6-80: Comparison of friction coefficients for Hydrostatic Lift bearing modifications for 7 psi in the counter-clockwise rotation as a function of Sommerfeld number

6.10   Two-Slot Bearing

6.10.1   Design Basis and Description

A new bearing was designed to allow for the operation of the shaft at higher eccentricity ratios. This design, called the Two-Slot bearing, consists of two 1/8" wide by 4" long fluid supply grooves running axially and located approximately 30 degrees from the bearing BDC. The location of these grooves allows approximately 60 degrees of uninterrupted arc length to promote hydrodynamic lubrication, yet should provide a 60 degree arc of constant pressure between the grooves to provide load support during hydrostatic operation. The self-compensating characteristics against side forces due to the changing fluid film profile identified during the Hydrostatic Lift testing is used in this bearing. Figure 6-81 shows the layout of the bearing and the location of the pressure ports used during testing.
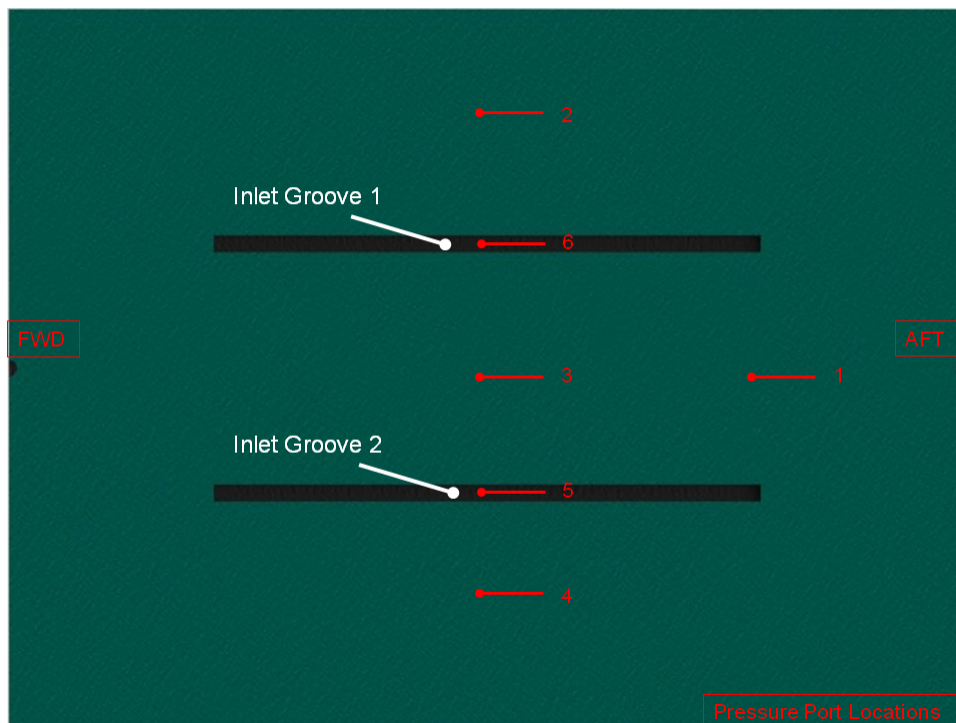

Figure 6-81: Layout of Two-Slot Bearing

The bearing was constructed in a fashion similar to that of the Hydrostatic Lift

bearing. A plain journal bearing was first fabricated, then the fluid grooves were milled into the surface of the bearing. The specifications of the Two-Slot bearing is provided in Table 6.12.

Table 6.12: Two-Slot Bearing Specifications

Bearing Configuration	Two-Slot Bearing	
Material	Turcite	
Diameter	3.2397	Inches
Radial Clearance	0.0046	Inches
Clearance Ratio	351	
Engagement Arc	175	degrees
L/D Ratio	2	

6.10.2   Test Results

The use of two slots allowed for the bearing to be tested in two configurations. The first involved the use of one supply line split immediately before the inlets without any form of flow restriction to each line. The second used two supply lines - each fed by a different gear pump - to provide two independent constant flow sources to the bearing. Simplified schematics of the two configurations is shown in Figure 6-82.

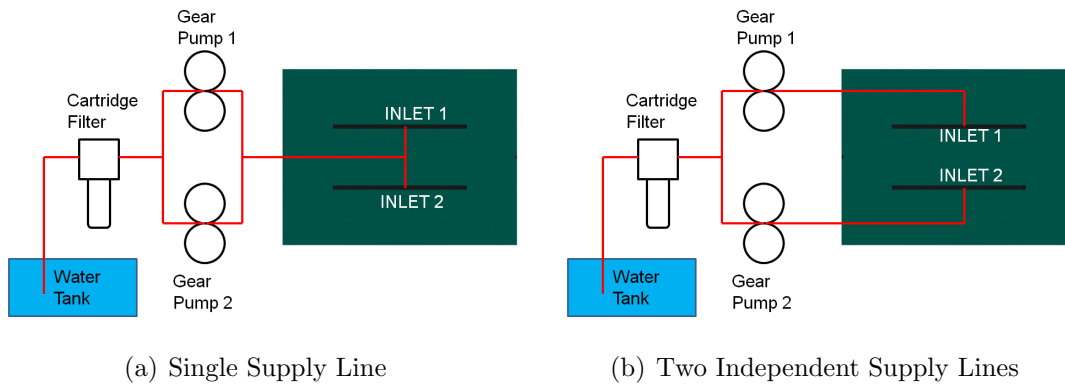(a) Single Supply Line   (b) Two Independent Supply Lines

Figure 6-82: Two-Slot Bearing Flow Configuration Schematic

6.10.2.1 Single Supply Line

In the single supply line configuration, the resistance seen by the two inlets are linked. A 'short' or lower hydraulic resistance in one groove will have a tendency to have an increased flow through that groove at the expense of the other. This could lead to an instability in the bearing and grounding of the shaft. Such instability is detrimental to performance, but this bearing was tested in this configuration to determine the ability of the self-compensating effects of the changing fluid film shape to overcome this.

Hydrostatic testing of the single supply line configured bearing revealed that there was no vertical collapse in the bearing similar to what was seen in the Hydrostatic Lift bearings. Load efficiencies were excellent, with values on the order of 42 to 44 percent. There was, however, horizontal instability seen at higher eccentricities where the shaft grounded to the side of the bearing. This testing showed that a single supply line configuration is very stable if the bearing operates at eccentricity ratios of approximately 0.65 or lower. This is because at higher eccentricity ratios, the bearing gap is diverging between the grooves and the circumferential ends of the bearing on both the left and right side of the bearing. The pressure between grooves is relatively constant since the groove pressures are equal. Lower eccentricity ratios allows for one side to have a converging film shape, while the other has a diverging film shape. As was seen in the Hydrostatic Lift bearings these differences in film shapes promote horizontal stability in the bearing. There is, therefore, an upper limit on the operating eccentricity ratio of a Two-Slot bearing with a single supply line.

Figure 6-83 shows the hydrostatic response of the bearing without a side load at 7 psi projected load. The bearing is able to maintain a centered position for low eccentricity ratios, but at a gear pump speed of approximately 40 percent (corresponding to an eccentricity ratio of roughly 0.6), the shaft starts to move to the right until it touches down with an offset to the side. There are small external forces from the
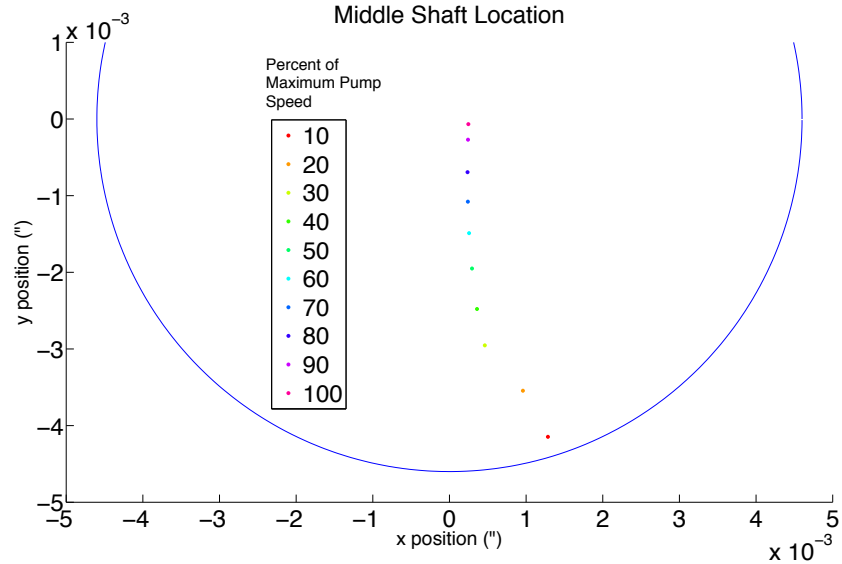
294

Figure 6-83: Locus of shaft position in Two-Slot bearing with single supply line for 7 psi projected load and various gear pump speeds during hydrostatic operation

flexible inlet lines that result in the movement of the shaft to that side, but the plot shows the ability to compensate for such forces at the lower eccentricity ratios.

Figure 6-84 shows the pressure and flow response of the bearing in hydrostatic operation. At low eccentricities, the small offset to the shaft to the right results in a slightly higher pressure on the right side (pressure port 4) than the left (pressure port 2) due to the right side being slightly convergent in shape while left side is divergent. This difference in pressure allows the bearing to remain relatively centered. At higher eccentricities, the shaft offset to the right does not alter the shape of the film enough to have an appreciable change in the pressure profile to allow the shaft to find a stable position. In fact, pressure port 4 decreases as the shaft moves to the right at high eccentricities - leading to the shaft grounding on the bottom right side of the bearing.

The ability to support side loads is shown in Figure 6-85. As can be seen, the side load capacity of the bearing is significant for low eccentricity ratios, but degrades at higher eccentricity ratios. For pump motor speeds less than approximately 40 percent (corresponding to an eccentricity ratio of approximately 0.63 in the graph), the shaft
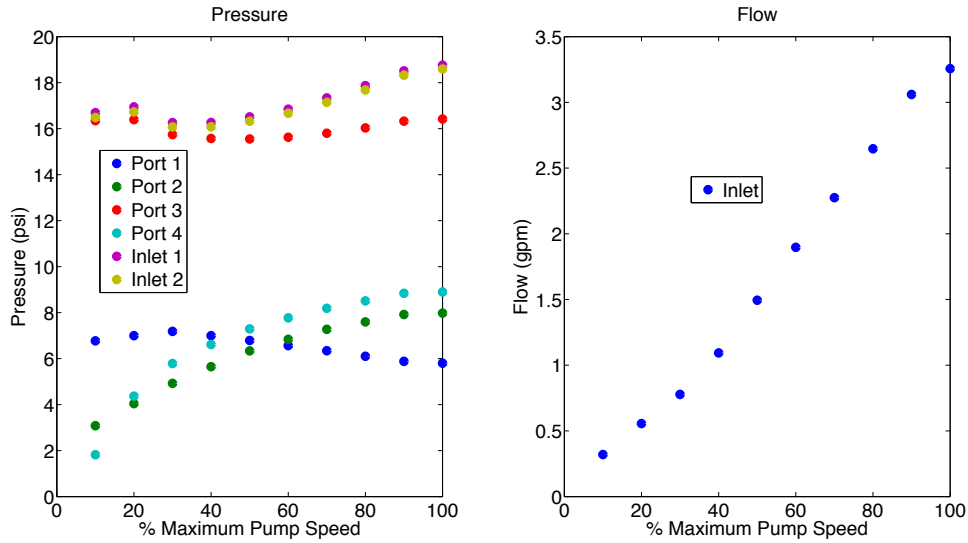
Figure 6-84: Pressure and flow response in Two-Slot bearing with single supply line for 7 psi projected load and various gear pump speeds during hydrostatic operation

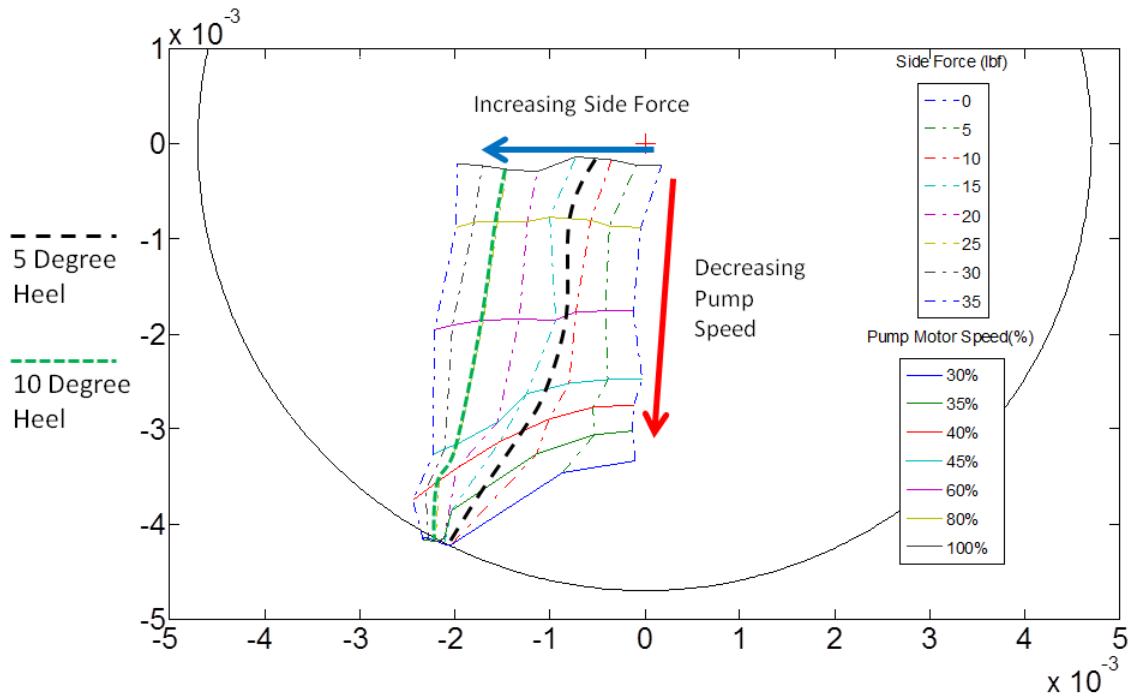
Figure 6-85: Locus of shaft positions (inches) for Two-Slot bearing with single supply line for 7 psi projected loads, various gear pump speeds and various side forces

is displaced to the side and grounds against the bearing with relatively small side forces. This illustrates the limitations of using a single supply line in a Two-Slot bearing if high operating eccentricity ratios are desired.

6.10.2.2 Two Independent Supply Lines

The Two-Slot bearing was also tested using supply lines from separate gear pumps. The gear pumps are identical and driven from the same shaft, so the flow to the slots should be equal in independent of the fluid resistance in the bearing. It is in effect, very close to a perfect flow divider. In actual calibration of flow, there was a slight difference in flow rates of approximately 0.1 gpm between the gear pumps at higher flows and virtually none at lower flows. This is attributed to minor variations between the pumps due to manufacturing tolerances. These differences did not appear to have any noticeable effect on bearing performance, however.
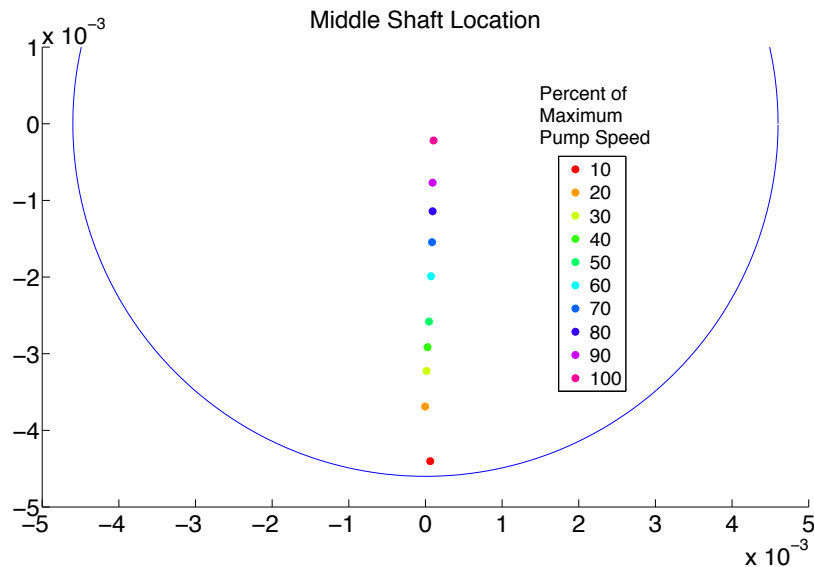
Figure 6-86: Locus of shaft position in Two-Slot bearing with two independent supply lines for 7 psi projected load and various gear pump speeds during hydrostatic operation

The hydrostatic response of the bearing can be seen in Figure 6-86 for 7 psi projected load. The ability to operate at higher eccentricities appears to be very good from the standpoint of the axial midpoint of the shaft. The bearing does, however, display a decreasing ability to support a horizontal misalignment at very high eccentricities. During testing, the bearing operated with a horizontal tilt of approximately 25 to 40 arcseconds over most of the testing range. This was most likely due to a consis-
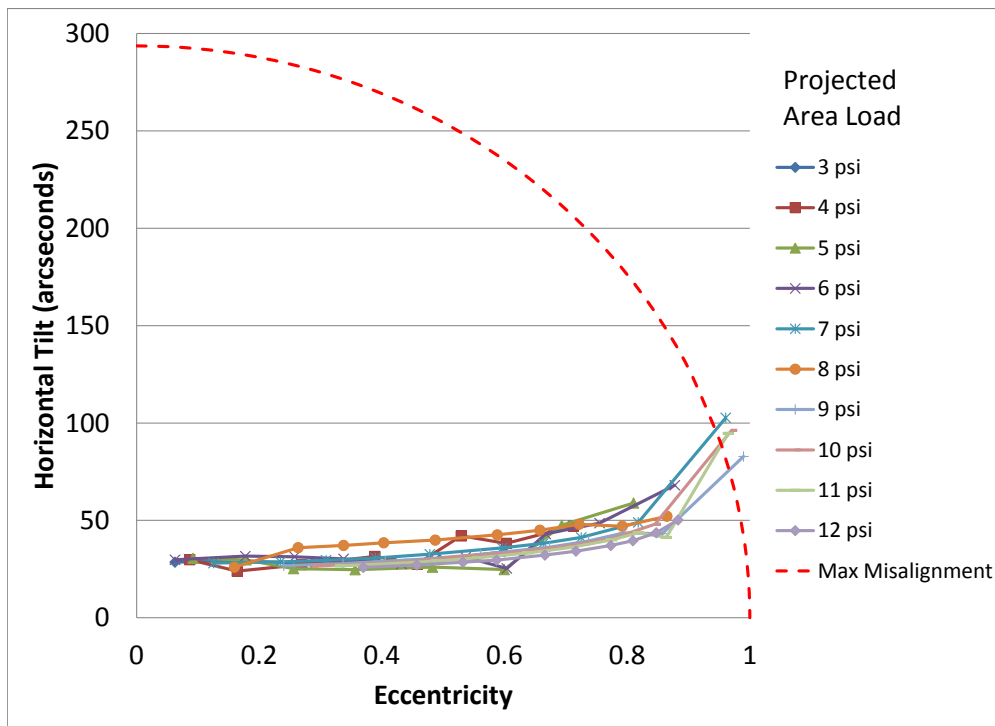
Figure 6-87: Horizontal tilt in Two-Slot bearing with two independent supply lines for various psi projected loads

tent moment imparted on the bearing by the support mechanism. Although it was designed to remove any external moments or forces, there will inevitably be some. The ability of the bearing to accommodate moments was tested, but a problem was noticed at very high eccentricity ratios (greater than 0.9). This response is shown in Figure 6-87. The figure shows that the horizontal tilt of the shaft is steady at lower eccentricity ratios and a large increase in tilt for eccentricity ratios approaching 1. Superimposed on the graph is maximum horizontal misalignment the bearing can accommodate before the shafts impact opposing corners of the bearing. This max misalignment is a function of bearing clearance, eccentricity ratio, and bearing length. It is clear from the graph that even for the Two-Slot bearing with two independent flow sources, there is an upper limit on eccentricity ratio that are acceptable for the bearing.
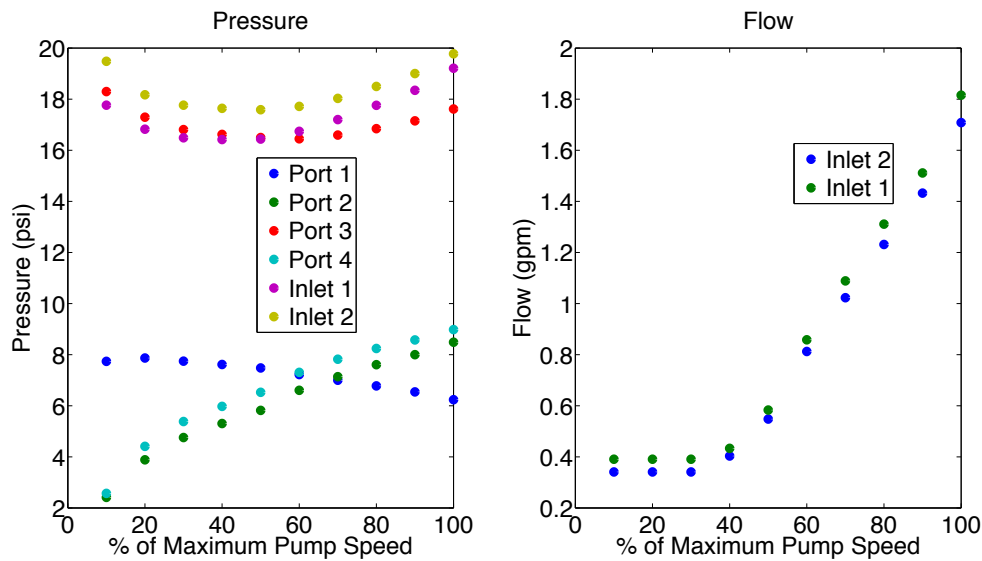
Figure 6-88: Pressure and flow response in Two-Slot bearing with two independent supply lines for 7 psi projected load and various gear pump speeds during hydrostatic operation

Hydrostatic load efficiencies were slightly lower than the single supply line configuration, with values on the order of 37 to 41 percent. The high load efficiencies for the Two-Slot bearing is primarily due to the fact that the area between the slots is a relatively constant pressure. This can be seen in Figure 6-88, which shows the pressure

and flow response in hydrostatic operation. Pressure port 3, located directly between the inlet grooves, has a pressure roughly equal to the groove pressures because there is very little pressure gradient circumferentially between the grooves. The axial pressure gradient between the midpoint and the ends of the bearing is very appreciable, as can be seen by the large drop in pressure between pressure port 3 and pressure port 1.

Flow rates are also low if the bearing operates at high eccentricity ratios. The ability to measure flows at the higher eccentricities was not possible due to the flowmeters reaching their lower limits. This is also seen in Figure 6-88 for pump speeds of 30 percent and lower.
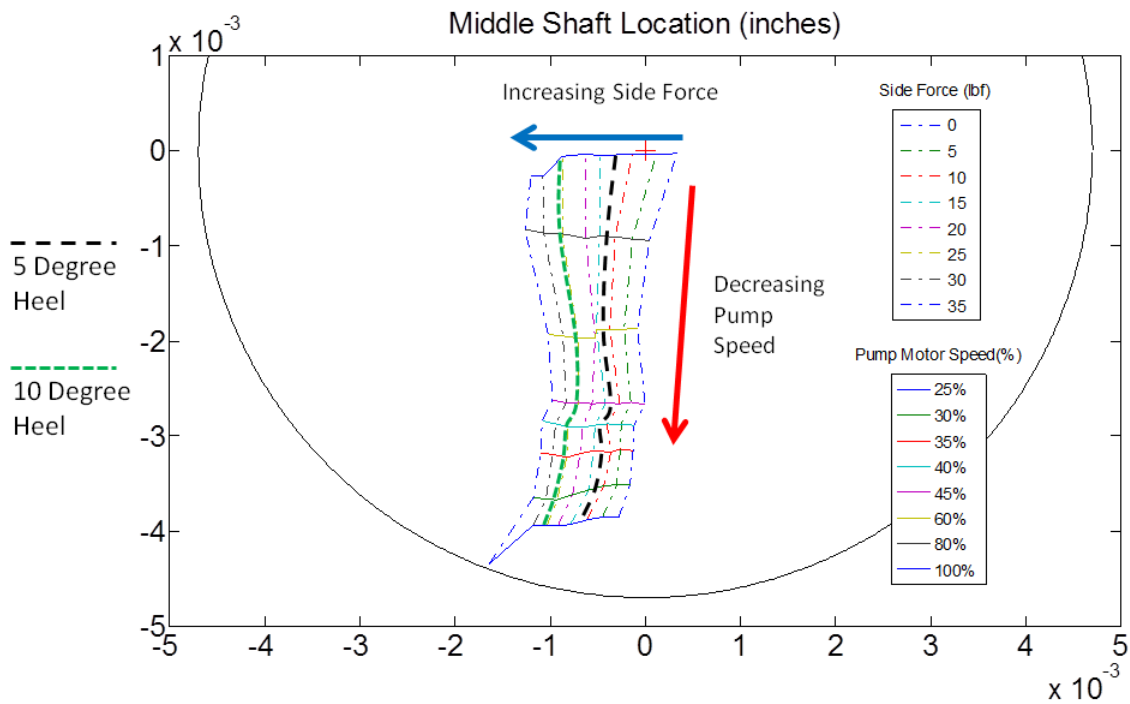

Figure 6-89: Locus of shaft positions (inches) for Two-Slot bearing with two independent supply lines for 7 psi projected loads, various gear pump speeds and various side forces

The bearing also showed a remarkable capacity to support side loads, even at high

301

eccentricity ratios. Figure 6-89 shows the response of the bearing to side loads at 7 psi projected load. Deflections of the shaft to the side are modest even for large loads. It is not until very high eccentricity ratios and side loads that the shaft loses support and grounds to the bearing. These results imply that normal operating eccentricity ratios of up to 0.8 can easily be used.
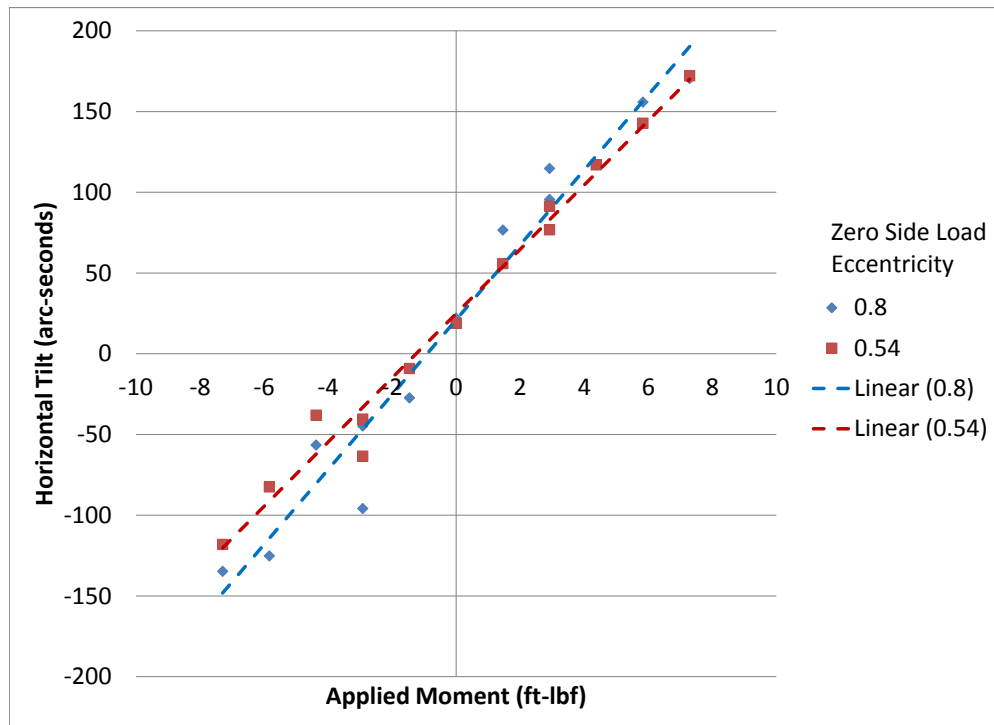
Figure 6-90: Horizontal tilt response to applied moments for Two-Slot bearing with two independent supply lines at 7 psi projected load for two different eccentricities

The poor ability of the bearing to handle misalignment at high eccentricity ratios was initially identified during hydrostatic testing. The tilt stiffness was therefore checked at two different eccentricities to quantify the bearings response to applied moments. The response of the bearing was fairly linear for both eccentricity ratios so a linear trend line was fit to the data, shown in Figure 6-90. The slope of the fitted trend line is the inverse of the horizontal tilt stiffness. As expected, the bearing is less stiff

at higher eccentricities, but not by an excessive amount. Operating at eccentricity ratios higher than 0.8 or 0.9 may result in difficulties and poor performance from an increasing likelihood that the shaft will contact the bearing due to misalignment. The combined effects of a lower tilt stiffness and a rapidly decreasing maximum alignment that the bearing can accept (as shown in Figure 6-87) are the major reasons for this.
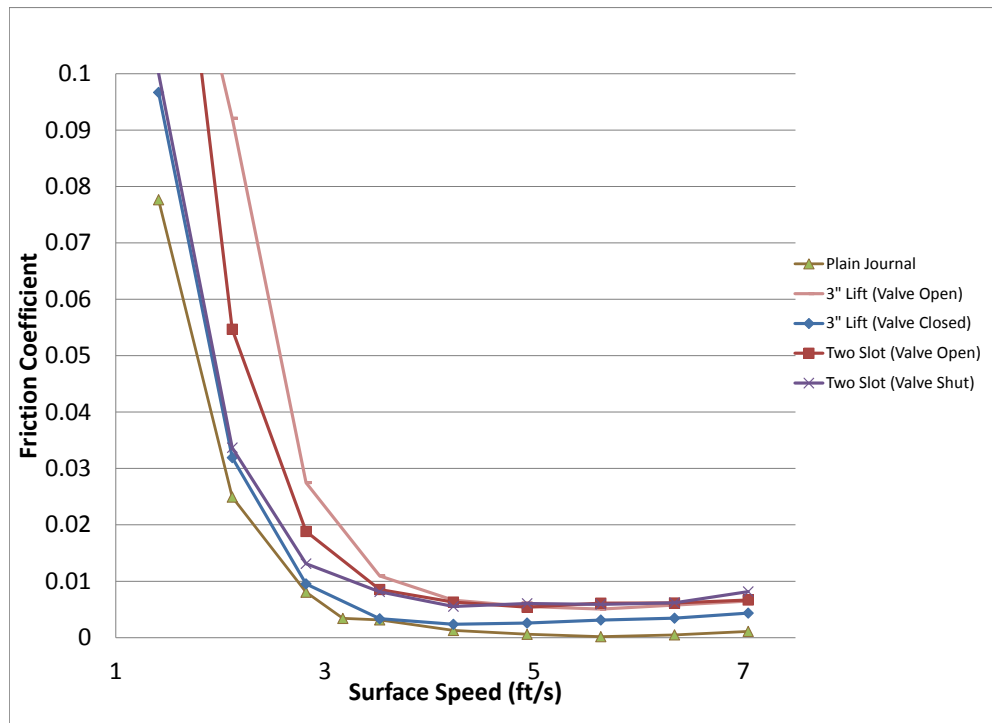
Figure 6-91: Comparison of hydrodynamic friction coefficient versus Sommerfeld number for Two-Slot bearing in clockwise rotation and 7 psi projected area load

Although there is 60 degrees of uninterrupted arc length of the bearing for hydrodynamic lubrication, the existence of the axial grooves does result in a noticeable and appreciable degradation in hydrodynamic response. Figure 6-91 shows the 7 psi projected load hydrodynamic characteristic for the Two-Slot bearing, with comparison to the plain journal and 3-inch Hydrostatic Lift configuration for clockwise rotation. Testing revealed a performance similar to that of the Hydrostatic Lift with a 3 inch

slot when the isolation valve is open, preventing pressure from building up in the grooves. Isolating the inlet grooves with a valve resulted in a significant improvement in performance - similar to what was seen with the 3-inch Hydrostatic Lift configuration. This verified that for these bearing designs, the presence of a check valve or isolation valve between bearing and pumps significantly improves the performance of the bearing.
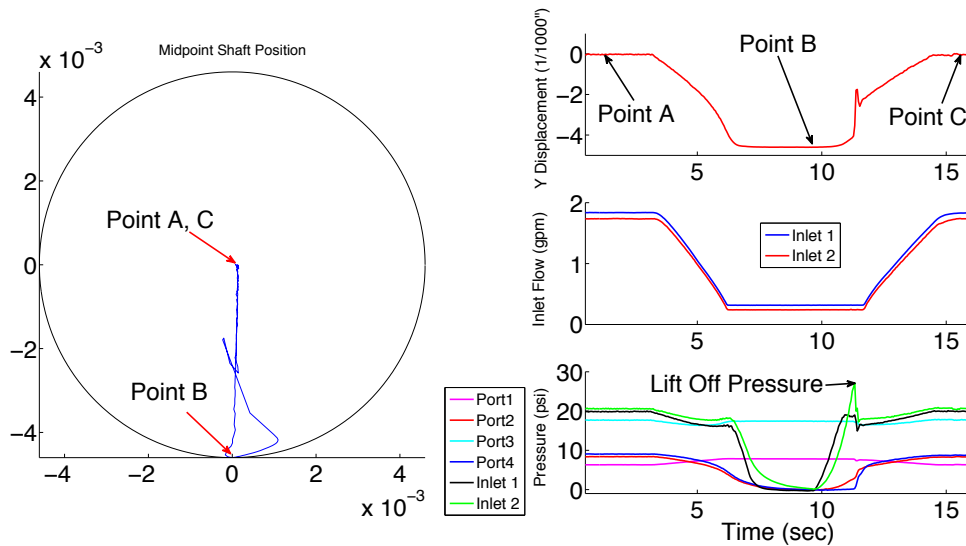

Figure 6-92: Time based response of Two-Slot bearing with two independent supply lines at 7 psi projected load illustrating shaft lift off

Testing was also conducted to determine if there is a substantial difference between lift off and operating pressures, similar to what was seen in the Hydrostatic Lift bearing (Figure 6-92. The pressure required to lift the bearing was approximately the same pressure required to operate the bearing in a normal hydrostatic mode of operation, indicating that a pump capable of handling significantly large pressures is not required. During initial lift off, the shaft did not move directly upward. Instead it moved to the right towards inlet 2 until enough flow was in the bearing to fully float the shaft at an eccentricity ratio high enough that the self-centering capabilities of the bearing started to work. Contributing to this is the fact that pressure and flow built up more quickly through inlet 1, which would push the shaft to the right.

This slight delay in the pressure buildup between grooves is most likely due to slight manufacturing differences in the gear pumps. Similar testing was done for the single supply line configuration, with results showing no significant lift off pressure required in that configuration either.

The Two-Slot bearing was a great success. It had multiple positive attributes that would make it feasible for use as a hybrid water-lubricated journal bearing, including good hydrodynamic and hydrostatic performance, the ability to operate at higher eccentricity ratios, and the relative ease of construction.

6.11 Summary of Bearing Testing

The battery of tests done on the various bearings revealed several key insights and lessons learned that can be used to aid the designer of future hybrid water-lubricated bearings. These findings include the utility of surface self-compensation, design variables that affect hydrodynamic performance, and key operating characteristics that will drive the selection and design of associated systems needed to operate such bearings.

Many of the initial designs were focused on the concept of surface self-compensation, which was born of full cylindrical hydrostatic bearings for machine tool spindles. In those applications, they are subjected to loads in all directions and accuracy is of paramount importance. Because of this they are designed to operated at minimum eccentricities. For the unique case of marine propulsion shafts that are loaded with a constant unidirectional force that varies within a very small range due heel or roll it was discovered that such compensation is not needed. This conclusion was reached primarily from the great success from the Hydrostatic Lift and Two-Slot bearing designs, which showed that a partial arc bearing has an inherent stability against side loads due to the changing fluid film shape. The significance of this finding cannot be understated. This was a concept that was heretofore never documented, and can have impacts far beyond a niche application in marine bearings.

The use of hydrostatic lifts have been generally limited to applications where the bearing is loading only in the direction of the lift groove, such as turbine generator bearings. As was seen, such bearings have a remarkable capacity to support transverse loads. The simplicity of their design over the multi-pad bearings that are sometimes used when transverse loads need to be supported make them particularly suitable for use for many more applications.

For all the positive benefits associated with the hydrostatic lift design, there were

significant drawbacks with the design. The vertical instability seen at high eccentricity ratios, or 'lockup', is a particular problem for marine water-lubricated bearings. Although these bearings operate satisfactory at low eccentricity ratios, the fluid gap is quite high, resulting in very large fluid flow rates. This can be addressed by reducing the nominal bearing gap, but the ability to do so is limited for marine bearings due to thermal expansion problems between shaft and bearings that have to successfully operate in extreme environments. For more industrial applications that use metallic bearing materials, this may not necessarily be a problem.

The significant lift-off pressures seen in the hydrostatic lift bearings also pose difficulties in respect to the overall system design. The pumps and piping systems must be appropriately sized to handle not only the low flow and high fluid supply pressures during startup, but also the high flow and lower fluid supply pressure conditions that exist during normal operation. The design iterations in this project showed the effectiveness of various ways to reduce the lift-off pressure ratio, primarily by increasing the overall groove area through circumferential fingers or extending the axial length of the groove. The use of positive displacement pumps for these types of bearings simplifies the design and improves performance because the pump can achieve whatever pressure is needed to provide the lift off force during startup.

The Two-Slot bearing is a derivative of the hydrostatic lift design, and has the capacity to operate at high eccentricity ratios, allowing for a large reduction in flow rates due to smaller fluid film gaps. This design did show a very high load efficiency, which allows for lower required pump pressures. When the lower flow rates and pressures in this design are combined, this bearing design provides a much more power efficient bearing than the Hydrostatic Lift variant. To operate at the highest eccentricity ratios, some form of flow compensation is required. In the case of this project, synchronized positive displacement gear pumps were used to provide nearly identical flow rates to each inlet groove. Alternative methods could employ either flow-control valves, a flow-dividing valves, or some other form of compensating element such as

a capillary tube or orifice restriction. Any of these alternative methods come with a penalty in that there is a significant pressure drop across them, and the potential for bearing failure should one of these elements get clogged with debris in the fluid line.

To effectively operate as a hybrid bearing, there needs to be as minimal an impact as possible on hydrodynamic performance. Those bearing designs that had large amounts of recesses or broke the bearing up into very small L/D ratios had significantly degraded hydrodynamic responses. For the more simple bearings such as the Hydrostatic Lift and the Two-Slot bearing, the introduction of axial grooves did degrade performance, but not excessively. It was also identified that by using isolation valves in between the bearing inlets and the fluid supply system, the adverse effect that these grooves have on hydrodynamic performance can be greatly minimized - to the point where they can perform almost as well as a plain journal bearing.

Chapter 7

Factors in Bearing Design and Performance

7.1 Clearance Effects

Equation 3.1 shows that flowrate is proportional to the cube of the nominal fluid film gap h:

$$Q = -\frac{L_z h^3}{12\mu}\frac{\partial p}{\partial x} \tag{??}$$

The hydrostatic bearings tested in this work all had substantial flowrates. Using bearings similar to these in a full scale application, where diameters are on the order of 20 to 30 inches, results in requirements for very large capacity pumps during hydrostatic operation. An argument could be made for designing smaller clearances in the bearings to reduce the required flowrate; doubling the clearance ratio from a value of 350 to 700 would result in roughly an 800 percent reduction in required hydrostatic flowrate. Since load carrying efficiencies are largely independent of bearing clearance, this also means that the hydrostatic pumping power would be reduced by approximately 800 percent. This reduced hydrostatic flowrate and power comes at the expense of increased friction during hydrodynamic operation. Petroff's law (equation 2.10) shows an inverse relationship between hydrodynamic friction and bearing

clearance.

$$f = 2\pi^2 \frac{\mu N}{P} \frac{r_b}{c} \tag{2.10}$$

These competing effects between hydrodynamic friction and hydrostatic flow/power imply that there is an optimum bearing clearance for a given set of operating parameters (i.e. shaft speed and loading) to minimize total shaft power consumed by a bearing. For the application of maritime vessels, this would be largely an academic endeavor since there are much more important considerations driving large bearing clearances for water-lubricated outboard bearings.

Marine water-lubricated bearings typically have clearances much larger than those normally specified in other bearing applications. An often used thumbrule for oil-fed non marine journal bearings is to use a clearance ratio of 1000[10]. Other suggestions are to use either the American Standards Association 'medium fits' (yielding clearance ratios on the order of 750 to 2200 for shafts from 3.25 inches to 8 inches), or to use a formula from Albert Kingsbury (yielding clearance ratios on the order of 620 to 930)[8]. All of these guidelines result in much smaller clearances than would be acceptable for marine applications of water-lubricated bearings.

For metal bearings, maritime classification societies specify a minimum clearance (in mm) defined by[18]:

$$C > \frac{Bearing Diameter}{1000} + 1.0mm \tag{7.1}$$

This equation results in clearance ratios from extremely low values of 76 for the 3.2305" test shaft to values on the order of 416 for a nominal 28" full size shaft. For synthetic bearings that can have substantial thermal expansion effects and swelling due to water absorption, minimum clearances are even more generous. Most classification societies specifically determine these based on the material properties of the bearing materials, but have an absolute minimum clearance of 1.5mm, which would correspond to a clearance ratio of 55 for the test shaft.

The guidance for naval vessels also dictates relatively large bearing clearances. For partial arc outboard bearings, an acceptable range of clearance ratios is typically in the range of 280 to 405. The clearance ratio is even larger for stave bearings with required values all below 367[17].

The majority of water-lubricated bearings used in the marine industry are synthetic polymers that can have a very significant thermal coefficient of expansion (α_T). Because the thermal coefficient of the bearing material is typically much larger than that of the shafting material, the relative geometric changes between the shaft and bearing can have an appreciable effect on the actual running clearance of the bearing. Synthetic polymers can also absorb water when submerged for long periods of time, which can further lead to decreased running clearances in bearings. The effects of temperature and water swelling must be taken into account not only in designing clearances in the bearings, but also the effect that they will cause on the interference between the bearing material and the bearing housing (typically Navy Brass with a much lower α_T). The issue can be further complicated for ship builders and designers when they have to account for the effect that an interference fitted bearing has on the clearance due to bore closure or the effects of machining tolerances on the final dimensions of a bearing.

Table 7.1 shows the properties of some common synthetic marine water-lubricated bearing materials. Also shown are the thermal expansion coefficients for Naval Brass (commonly used for bearing housings) and MIL-S-23284A Class I steel (a Ni-Mo steel commonly used for propulsion shafting in naval vessels). For an ocean vessel that can be expected to operate in extreme environments ranging from the arctic (where seawater temperatures can be below 32^oF) to equatorial waters (where seawater temperatures can exceed 95^oF), large variations in bearing temperature can be expected due to ambient conditions alone. Factoring in the heat build-up that can occur from viscous shearing of water during hydrodynamic bearing operation can result

311

Table 7.1: Properties of Synthetic Bearing, Housing, and Shafting Materials

Material	α_T (in/in-^{o}F)	Swell in Water (by Volume)
Thordon® XL	$8.2X10^{-5}$	1.30%
Thordon® SXL	$8.4X10^{-5}$	1.30%
Wartsila® Envirosafe	$1.1X10^{-5}$	0.20%
Orkot® TLM	$5.25X10^{-5}$	0.10%
Orkot® TXM	$5.25X10^{-5}$	0.10%
Duramax® ROMOR I	$9.4X10^{-5}$	Negligible
Vesconite®	$2.8X10^{-5}$	0.50%
Turcite B®	$3.2X10^{-5}$	<0.01%
UHMW PE	$13.9X10^{-5}$	0.01%
Bronze	$10.0X10^{-6}$	N/A
Naval Brass	$11.8X10^{-6}$	N/A
Aluminum	$12.3X10^{-6}$	N/A
MIL-S-23284A Class I	$6.4X10^{-6}$	N/A

in even greater ranges of possible bearing temperatures. A bearing that is expected to perform satisfactorily throughout this range must be capable of accommodating such changes.

Although decreasing the bearing gap is advantageous for hydrostatic bearing operation in that flow and power requirements are reduced, there is a limit to how small the gap may be for ocean vessels as long as typical synthetic water-lubricated bearing materials are utilized. Potential alternative designs that may allow for smaller gaps include:

- Using a non-metallic shaft that has a similar α_T as the bearing material could be used. This would be a significant deviation from normal ship and submarine designs, but could have the added benefit of removing corrosion concerns that metallic shafts currently have. Such a shaft would have to have similar swelling properties as the bearing material due to water exposure.

- Metallic bearing materials with an α_T closer to that of the shaft could be used. White metal (Pb-Sb-Sn Babbitt) is typically used for oil-lubricated bearings,

312

but is probably a poor candidate for water-lubrication. In the marine indus-
try, bronze is used frequently in water-lubricated rudder bearings. The shaft
material could be selected to match the α_T of the bearing material.

- A synthetic bearing polymer with a much lower α_T could be developed. Ideally
such a polymer would have very little or no swelling due to water.

7.2   Surface Roughness Measurements

As explained in chapter 2.1.1, the surface roughness of the bearing and shafting mate-
rial have a significant impact on the minimum film thickness. The surface roughness
of the Turcite® bearing material and other common polymer bearing materials were
tested to quantify the quality of the material finish. The shaft, described in section
4.3.2, has a nickel-plated high quality finish.

The polymer bearing materials were inspected on two machines. One machine, a
TENCOR P16 stylus surface profilometer (shown in Figure 7-1(a)) was used to mea-
sure Turcite®, UHMW PE, and Duramax ROMOR II® materials. The second ma-
chine, a Zygo vertical scanning interferometer (shown in Figure 7-1(b)) was used
to measure Turcite®, UHMW PE, Nylon, and ABS materials. The interferometer,
which requires a degree of reflectivity in the material in order to obtain a good sam-
ple, had difficulty obtaining measurements with the Turcite® material due to its dull
finish. In spite of this there was good agreement between average calculated surface
roughness values for the Turcite® (approximately a 2 to 4 percent error between
profilometer and interferometer values). The UHMW PE had a larger error between
roughness values of approximately 25 percent.

Table 7.2 shows the average measured values of the roughness. The complete set
of data and profile views is provided in appendix C. It is clear that the Turcite®
material has a significantly lower quality finish than the other bearing materials.
Other notable observations are that the materials (with the exception of ABS) have
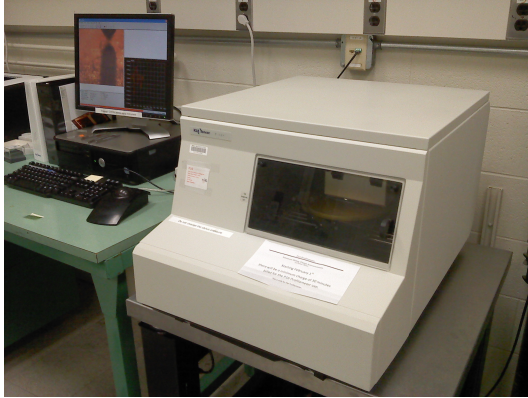
(a) Tencor P16 Stylus Profilometer

(b) Zygo Vertical Scanning Interferometer

Figure 7-1: Surface Roughness Metrology Machines

Table 7.2: Average Measured Surface Roughness Values (in μinches)

	R_t	R_q	R_a	$\frac{R_q}{R_a}$	Notes
Turcite®	426.14	67.45	50.22	1.34	Stylus Profilometer
UHMW PE	92.92	15.16	11.70	1.30	Stylus Profilometer
ROMOR II	62.18	9.21	7.24	1.27	Stylus Profilometer
ABS	71.40	3.41	2.30	1.49	Vertical Scanning Interferometer
Nylon	48.94	1.20	0.91	1.33	Vertical Scanning Interferometer
Test Shaft		5	4.00		Precision Ground Finish

fairly consistent $\frac{R_q}{R_a}$ values in a range of 1.27-1.34, slightly above the ratio for a gausian distribution of 1.25. A sample surface profile of Turcite® material is shown in Figure 7-2. This figure is for a profile that runs along the length of the material extrusion. There exist a significant difference in roughness of the Turcite® depending on the orientation with respect to the extrusion path. Profiles across it have a roughness that is approximately 67 percent worse than profiles taken along the extrusion. For this reason, during manufacturing of Turcite® bearings, the extrusion length is oriented to coincide with the direction of shaft rotation[1].
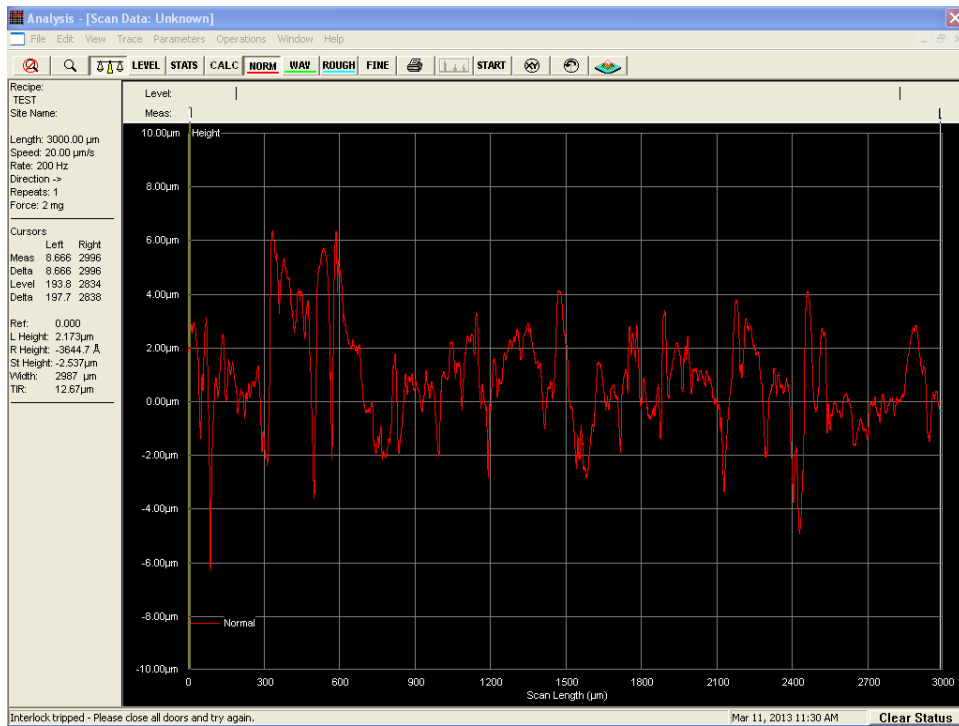
Figure 7-2: Profile of Turcite® Sample

Another observation regarding the Turcite® material is that the surface is 'pocketed', with deep holes located randomly on the surface of the material. For most machine tool applications of Turcite®, these holes provide areas for oil to collect during slow speed operation. This allows oil to be maintained on the bearing surface for improved

---

[1]One bearing was fabricated with the extrusion length counter to the direction of shaft. This bearing was the stave bearing configuration and was tested partially to determine the effects of wear-in on a Turcite® bearing. Configuring the extrusion to be counter to the shaft rotation allowed for more wear to occur in the bearing.

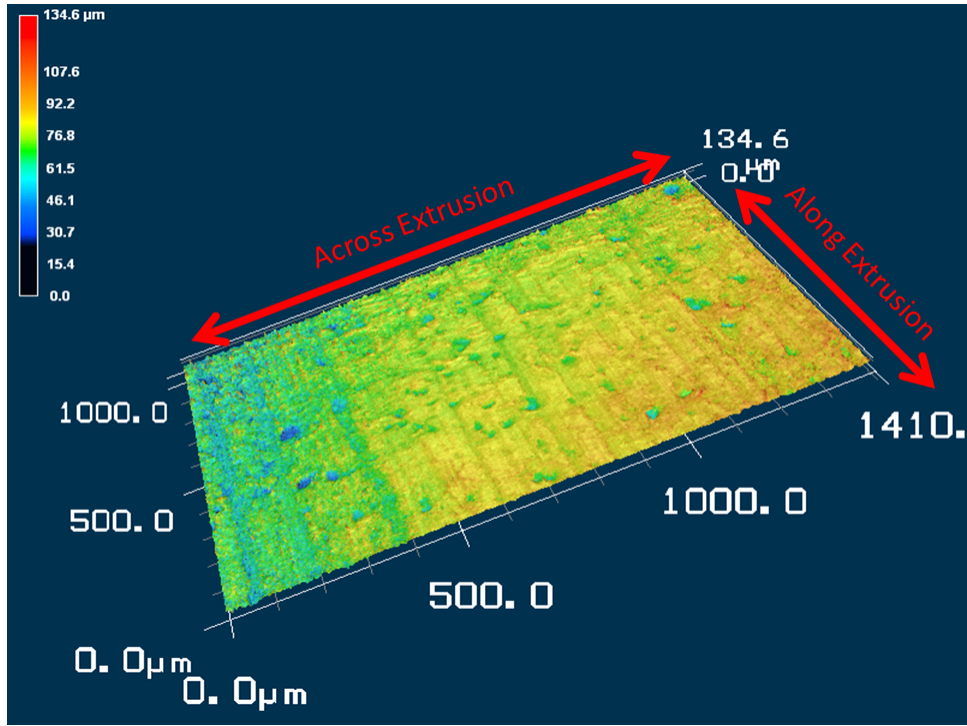Figure 7-3: SEM Image of Turcite® Material

operation in the boundary and mixed lubrication regimes. For water-lubricated bearing purposes, these holes are not advantageous and can rupture the thin fluid films required for hydrodynamic lubrication. The presence of these holes can be easily seen in Figure 7-3, which is a 50X magnified image of Turcite® under a scanning electron microscope (SEM). In the SEM image, the orientation of the extrusion is also readily discernible.

Combining the surface finish of the shaft and the different bearing materials into equation 2.1, the minimum film thicknesses (h_{min}) for hydrodynamic lubrication is estimated based on the discussion in chapter 2.1.1. For Turcite® material, using a Λ value of 5 provides a predicted h_{min} of 338 μinches. The surface finish of the shaft is of such high quality relative to the Turcite® that it has almost no appreciable effect on the hydrodynamic performance of the bearings. This is excellent for testing purposes because any effects from roughness can be attributed to the Turcite® material. In application, however, this could result in a waste of resources if time and money is

spent improving the surface finish of a shaft if a relatively rough bearing material is used.
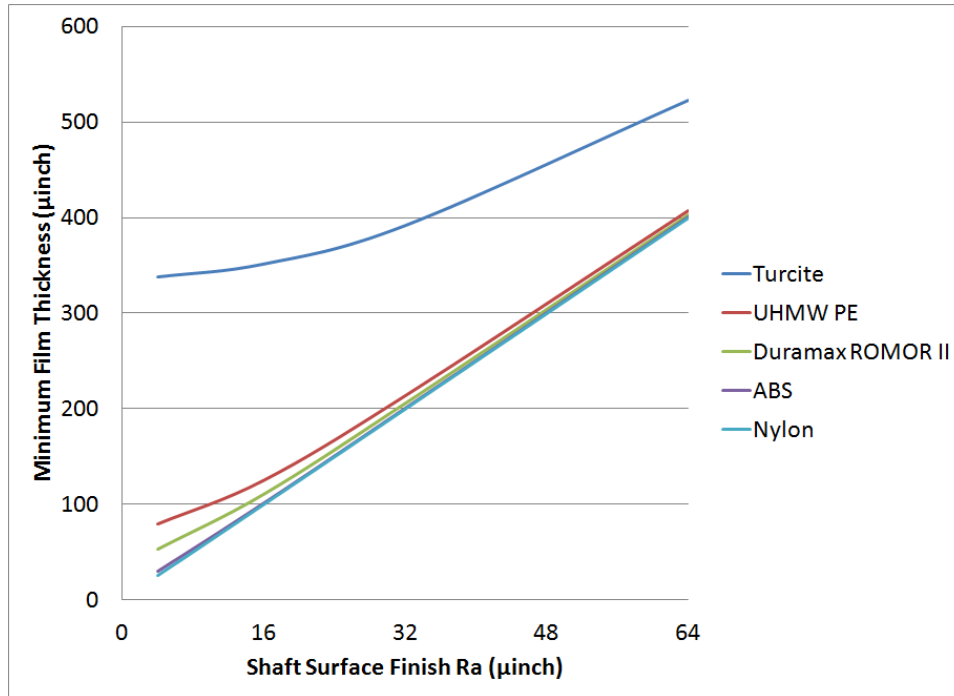
Figure 7-4: Effect of Shaft Roughness on (h_{min}

In Figure 7-4, Λ is assumed to be constant at 5 and the surface finish of the shaft is varied between a R_a value of 4 and 64. For the Turcite® material that has an R_a value of approximately 50, there is little to be gained from increasing the surface finish of a shaft more than 32μinches. Shaft surface finishes with values above 32 become progressively worse as the shaft roughness is of the same order of that of the Turcite® bearing material. The same is not true of the other bearing materials, which have a surface finish on the order of that of the test shaft. In that case, a decrease in the quality of shaft surface finish has an immediate and detrimental effect on the minimum film thickness. As the roughness of the shaft becomes much worse than that of the bearing materials, the shaft roughness becomes dominant and the slope of the graph approaches the value of ΛR_q. This illustrates that it is desirable for both the shaft or bearing roughnesses to be of the same order of magnitude[2].

[2]Figure 7-4 and the predicted minimum film thickness of 338 μinches for Turcite® do not take

7.3 Wettability

The Reynolds equation is based on the assumption that there are no-slip boundary conditions at the shaft and bearing surfaces. This assumption, however, becomes increasingly invalid for extremely hydrophobic surfaces that will have fluid slipping. To classify the Turcite® material, samples were measured for wettability with a goniometer. It was found to have a contact angle of approximately 90 degrees, a value at the transition between hydrophilic and hydrophobic materials. This contact angle is for Turcite® that has not been machined or worked to reduce the surface finish. It would be expected that a bearing with a less rough surface (such as one with a worn in surface) would have an even lower contact angle. This implies that the material is not hydrophobic enough to invalidate the no-slip boundary conditions in the Reynolds equation. The full contact angle testing results are shown in appendix E.

The no-slip boundary condition is vital to generating shear stresses in the fluid film. This in turn generates the pressure gradient that creates the buildup in the film pressure, allowing a bearing to support an applied shaft load. A slip condition at one of the surfaces would therefore be expected to reduce the shear stresses in the fluid and result in a lower pressure gradient in the fluid film and therefore a lower film thickness. This reduction in shear stresses would, however, result in lower frictional losses in the fluid. Theoretical work has shown that such is expected to be the case [7, 16]. Compared to a normal bearing, a bearing with a hydrophobic lining is characterized by:

- A reduction in stiffness and damping

- A reduction in frictional losses in the bearing

- An increase in the critical Taylor number value

- Lower film thicknesses

---

into account the wear in effect, where the high asperities of the bearings are worn down, effectively polishing and improving the surface finish of the bearings. This effect can be very appreciable.

Although reduced frictional losses are attractive for full fluid film lubrication, the impact that reduced film thicknesses have on bearing performance is the dominant effect. With a reduced film thickness, the transition between mixed and hydrodynamic lubrication for a given bearing will be delayed until a higher surface speed (RPM) is achieved. This is illustrated quite clearly in Figure 7-5, which shows that non fully wetted (NfW, i.e. Hydrophobic) surfaces have a shift in the stribeck curve down and to the right compared to fully wetted (FW, i.e. Hydrophilic) surfaces. The net result would be that by utilizing a highly hydrophobic bearing surface for a hybrid bearing, the bearing would need to operate in a hydrostatic mode of operation over a longer range of speeds. When combined with the typically poor wear resistance of highly hydrophobic materials, the usefulness of them in a hybrid bearing is questionable.
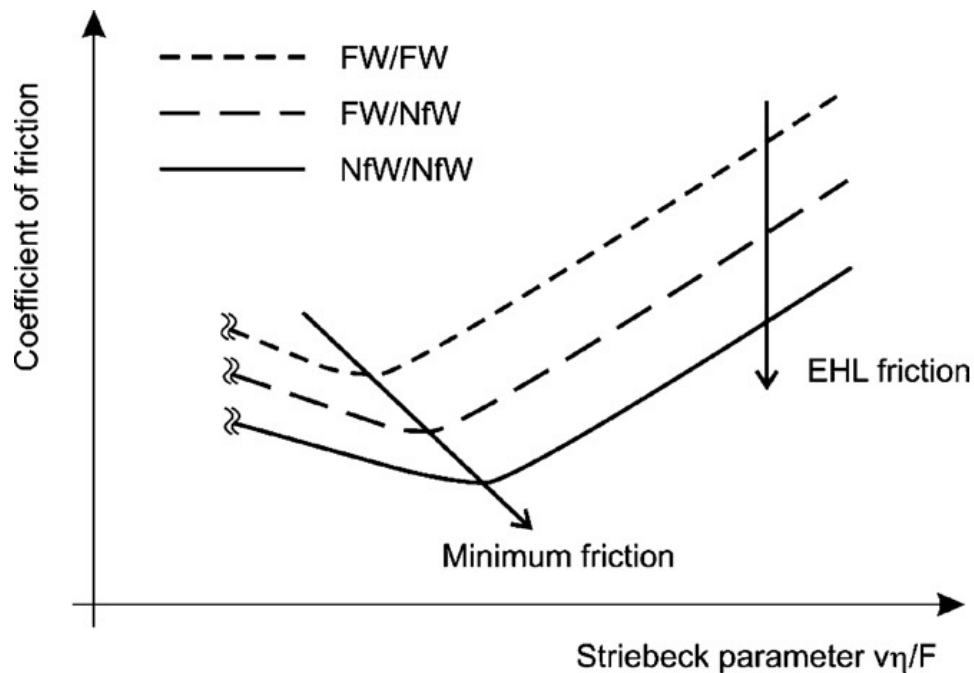
Figure 7-5: Effect of Hydrophobic Surfaces on Stribeck Curve [16]

7.4   Projected Area Loading

The allowable projected area load for water-lubricated bearings is much less than that of oil-lubricated bearings. ABS, for example, allows projected loads of white metal

319

bearings up to 116 psi with the bearing L/D ratio to be no less than 1.5. Pressure requirements are not specifically called out for water-lubricated bearings, but typically require a L/D ratio of at least 4. The net result is that projected area loads for water-lubricated bearings has historically been below 40 psi[19].[3] More recent non-stave configured water bearings (such as Thordon and Orkot) have type approval certificates from classification societies for L/D ratios as low as 2, resulting in projected area loads approaching 80 psi.

The benefit of higher loads is that the bearings can be shorter, making installation, alignment, and replacement easier. The drawback is operation at a lower Sommerfeld number and more localized stress on the bearing materials. This can lead to the transition to hydrodynamic lubrication occurring at higher speeds and increased bearing wear. For a hybrid bearing, an increased projected area load requires a higher pressure system to support the shaft in hydrostatic operation. This higher pressure will also result in a higher specific flowrate through the bearing, compounding the effect of a increased projected load. As will be seen in equation 7.10, the total pump power requirement will increase with the square of the projected area load. This will be partially offset by the fact that the bearing can be shorter which will tend to reduce flowrate. This large increase in required power must be considered when consideration is given to increasing the projected load of a hybrid bearing.

7.5   Bearing Alignment

A proper alignment of the propulsion train is critical for components to operate as designed. A misaligned shaft and bearing combination is the most common reason for premature failure of those components[30]. It is common knowledge that longer bearings are more difficult to align properly. It is partially for this reason that many

---

[3]ABS does provide a caveat for 'bearings of rubber, reinforced resins, or plastic materials, the length of the bearing, next to and supporting the propeller, may be less than four times, but not less than two times the required tail shaft diameter, provided the bearing design is being substantiated by experimental tests to the satisfaction of ABS'.

commercial ships use oil-lubricated bearings with a L/D ratio as low as 1.5.

During ship construction, a static alignment of the propulsion shaft is typically done through various sighting methods using lasers or piano wires, then bearing reaction loads are checked with the Sag and Gap method. In some cases, the stern-tube bearing is mounted with epoxy once the shaft is installed to ensure proper location and in others the bearing is slope-bored after installation for alignment[1]. These methods can help ensure a proper alignment during construction, but once in operation the alignment may become unsatisfactory due to a number of reasons. Different load conditions can cause the hull to sag or hog (particularly for liquid cargo carriers), or there may be dynamic misalignment that can occur from propeller induced vibrations (especially in twin screw vessels), or during severe hull deflecting maneuvers.
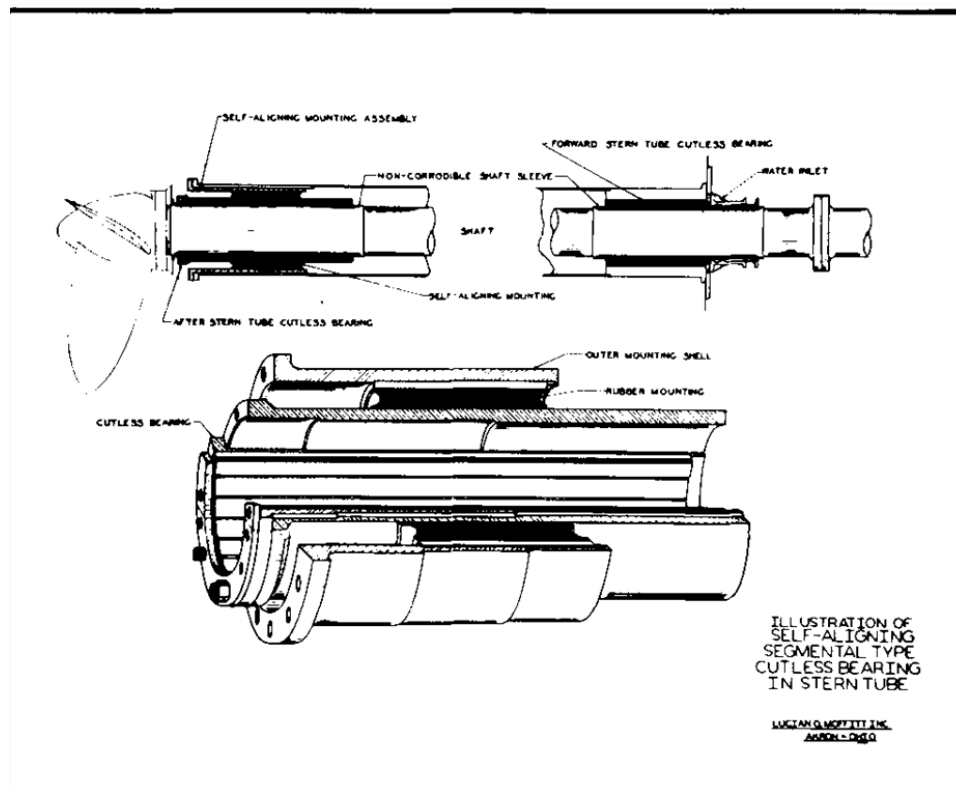
Figure 7-6: Self-Aligning Bearing Mount[21]

There are different ways used to address this issue. The use of a resilient bearing

material such as rubber assists in the alignment of stave bearings. Increasing the gap between bearing and shaft is another method, and one of the major reasons water-lubricated bearings have such generous clearances. A method used in some U.S. Navy ships is the use of a self-aligning mount, which consists of a rubber ring connecting the bearing housing and the ship structure. This mount provides the bearing the freedom to align itself with the shaft and allows the radial, friction, and tilt loads on the bearing to be transmitted through to the hull (see Figure 7-6)[21].
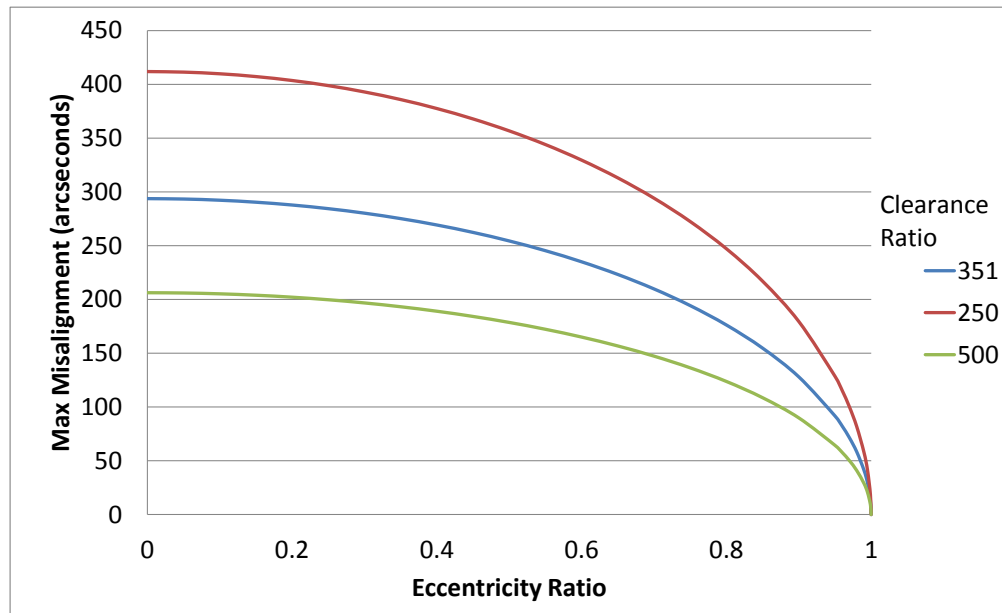
Figure 7-7: Maximum angular misalignment in bearing for $L/D = 2$ as a function of eccentricity ratio and clearance ratio

The test rig employs a similar mount concept that allows for the bearing to align itself. Using a self-aligning mount for a hybrid journal bearing in a ship application is likely a necessity. Although the test bearings did display an ability to support side loads and moments, the bearings were tested with very little misalignment and with

a L/D ratio of 2. Employing a longer bearing without the freedom to tilt would likely result in a major degradation of hydrostatic performance with any misalignment.

An additional consideration addressed during testing with applied moments is that the maximum angular misalignment the bearing can support without coming into contact with the shaft is very much a function of clearance ratio, eccentricity ratio, and L/D ratio. Figure 7-7 shows the effects that eccentricity ratio and clearance ratio have on allowable misalignment. The L/D ratio has an inversely proportional effect on alignment (i.e. the misalignment curves in the figure will be half the magnitude for an L/D ratio of 4). It is clear that there is a penalty paid by choosing to operate at high eccentricity ratios in that alignment becomes more critical.

7.6   Break-in and Wear

As seen in section 6.7, a proper break-in is vital to maximizing hydrodynamic performance. This process may take days or weeks of operation to occur depending on the operational cycle of a ship. A reduction in friction in and around the mixed lubrication regime, and a more distinct transition to hydrodynamic lubrication can be expected for most materials after a break-in period. These are beneficial attributes that come at the expense of a slight wear down of the material. Even after a modest break-in period in the stave bearing (section 6.7), a small but measurable amount of wear was seen. If the wear becomes too great, the shape of the bearing may change enough that the hydrostatic performance of the bearing changes.

The hybrid bearing concept is predicated on the idea that pumps will support hydrostatic operation at speeds less than those required for full hydrodynamic lubrication. It may be warranted to operate such a bearing without hydrostatic pump pressure at low speeds to conduct a break-in of the bearing surface. This may provide longer term benefits by allowing the pumps to be turned off at lower speeds than they otherwise would if no break-in had occurred.

7.7 Power, Friction, and Temperature

For a hybrid journal bearing, the total power is a combination of power supplied by the pump and the power dissipated in the bearing due to friction. For the pump that must pressurize the fluid to an elevated pressure with a given flow the pumping power (H_p) is:

$$H_p = P_s Q \tag{7.2}$$

where P_s is pump supply pressure and Q is total flow rate. This is the total power in a bearing operating in a pure hydrostatic mode without shaft rotation. The power due to frictional losses comes from the shearing of the fluid due to movement between surfaces. This friction results in a torque on a shaft. Recalling equation 2.9:

$$T_{friction} = fWr_s = 2fr_s^2 LP \tag{2.9}$$

Torque is related to friction power (H_f) by the relationship:

$$H_f = T_{shear}\omega \tag{2.7}$$

where ω is the angular velocity of the shaft. This comprises the total power in a bearing operating hydrodynamically without pump pressure. The total power (H_t) in a hybrid bearing can be summarized as:

$$H_t = H_p + H_f \tag{7.3}$$

Rowe provides an alternative expression for the total power:

$$H_t = H_p(1 + K) \tag{7.4}$$

where K is a 'power ratio' defined as:

$$K = \frac{H_f}{H_k} \tag{7.5}$$

The power ratio can be lumped into three general categories[26].

1. K = 0 to 1: Pure hydrostatic operation, or operation at low to moderate speeds.

2. K = 1 to 3: High-speed optimized hybrid hydrostatic bearings.

3. K = 3 to 9: High speed hydrostatic bearings for higher loads.
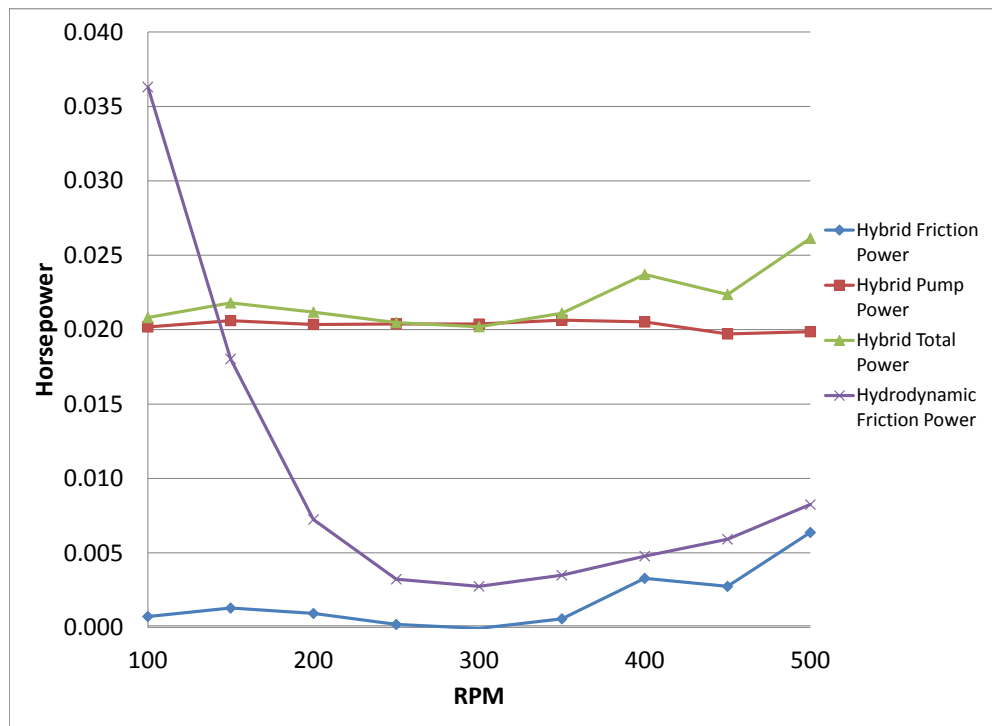
Figure 7-8: Components of power losses in bearing for Hydrostatic Lift (3" slot configuration) for 7 psi projected area load, clockwise rotation operating in both pure hydrodynamic and hybrid (with ϵ=0.34) modes of operation

Since the operating speeds at which hydrostatic pump pressure is needed are relatively low, it is expected that the K value would be very low. Experimental results verified this. Figure 7-8 shows the power components for the Hydrostatic Lift bearing with a 3" slot configuration operating hydrodynamically, and in a hybrid condition with an eccentricity ratio of approximately 0.34. The dominant power component is

the pump power. Even at the maximum speed of 500 rpm, the value of K is only 0.32. The value of K will vary with eccentricity ratio. This is because as the shaft becomes more eccentric, the fluid gap decreases resulting in more hydraulic resistance, lower flow rates, and therefore lower pumping power. At the same time, the friction power in the bearing increases with a greater eccentricity ratio due to the decreasing film gap. These two effects cause the value of K to increase with eccentricity ratio, as show in Figure 7-9.[4] The concept of the hybrid bearing assumes that pumps will be secured at speeds high enough to have hydrodynamic lubrication. This would imply that values of K can be expected to be very low in all cases where the pumps would be expected to run, making the bearing power dominated by pump power.

The operating temperature of a bearing is a very important factor that effects performance. As was illustrated in section 7.1, the variation in the temperature of the bearing materials can have a very significant and dominating effect on the actual operating clearance in bearing. In addition to this, the temperature of the fluid will have an impact on viscosity. All analysis done in this project used a constant viscosity model, assuming a design temperature of 70 degrees.[5] To estimate the temperature rise in the bearing fluid in a single pass, the assumption is made that all of the power is converted to heat:

$$\Delta T = \frac{H_t}{Q \rho c} = \frac{H_p(1 + K)}{Q \rho c} \tag{7.6}$$

where c in this case is the specific heat capacity, and ρ is the density of water at 70^oF. There are flow terms in both numerator and denominator, allowing further simplification:

$$\Delta T = \frac{P_s(1 + K)}{\rho c} \tag{7.7}$$

In the case of no shaft rotation (K=0), the expected temperature rise in the fluid

---

[4]The dip in K for 450 rpm is attributed to measurement noise due to the very low torque values seen during hybrid operation.

[5]The experimental test tank temperature was consistently within a degree or two of 70 degrees.
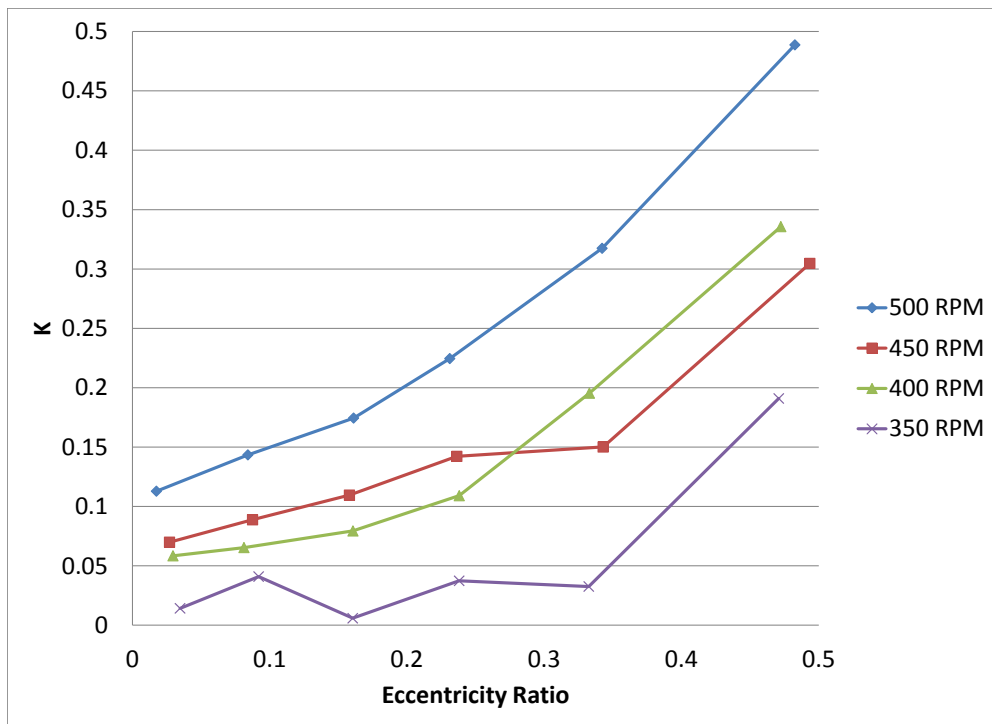
Figure 7-9: Variation in power ratio (K) as a function of eccentricity ratio for Hydrostatic Lift (3" slot configuration) for 7 psi projected area load, clockwise rotation, and various speeds operating in a hybrid mode of operation

would be expected to be:

$$\Delta T \approx 0.003 P_s \tag{7.8}$$

For a nominal bearing with a projected area load of 40 psi and a pump supply pressure of 125 psi, the expected temperature rise would be on the order of 0.4 ^{o}F. Even adding heat generated from friction losses in the bearing leads to very low increases in bearing temperatures during hybrid operation, therefore justifying the constant viscosity model.

When the pumps are secured and the bearing is operating hydrodynamically, a means of supplying cooling water to the bearing should be available. Flowrates for flushing and cooling of hydrodynamic values are usually expressed as functions of bearing diameter or length. Typical navy specifications are 2 gpm for every foot of bearing length, while ORKOT$^{\circledR}$ recommends 0.66 gpm for every inch of shaft diameter with typical supply pressures between 10 and 25 psi. Both of these would result in a flow rate of approximately 18 to 19 gpm for a nominal 28 inch diameter bearing with a L/D ratio of 4. This flow rate requires a pumping power of approximately 0.1 to 0.3 horsepower - about two orders of magnitude less than a hydrostatic bearing.

7.8 Scaling

Most references for hydrostatic bearings use non-dimensional parameters to correlate performance between different size bearings. This same concept can be applied for the work in this project. There are three parameters that are of particular use.

1. Load efficiency (η_{Load}) was previously defined:

$$\eta_{Load} = \frac{P_{projected}}{P_{inlet}} \tag{6.1}$$

2. Flow coefficient (q_f) can be used to define the total flow (Q) through the bearing:

$$Q = q_f P_{projected} \frac{c^3}{\mu} \qquad (7.9)$$

3. Pumping power coefficient (h_f) can be used to determine the power required by the pump in a bearing:

$$H_p = h_f P_{projected}^2 \frac{c^3}{\mu} \qquad (7.10)$$

where $h_f = \frac{q_f}{\eta_{Load}}$.

These non-dimensional parameters are based on the assumption that bearings are geometrically similar in regards to the placement of their pressure supply grooves, load pads, lands, clearance ratio, etc. Several key observations can be made regarding the effect that certain design variables have on a bearing.

- The flow rate is directly proportional to the projected area load.

- The flow rate is a cubed function of the bearing clearance.

- Pump power is proportional to the square of the projected area load and the cube of the clearance.

Figure 7-10 shows the load efficiency (η_{Load}) as a function of eccentricity ratio. Figure 7-11 shows the variation in the flow coefficient as a function of eccentricity ratio for the Two-Slot bearing configuration. The graph shows good consistency over the various projected area loads with the exception of very lightly loaded bearings. The horizontal lines that spur off at higher eccentricities are the result of the flow meters reaching their 'floor' values. The values from these graphs allow the flow and required pressure to be estimated for a different scale bearing. Consider the performance predictions for a nominal full scale bearing, shown in table7.3.
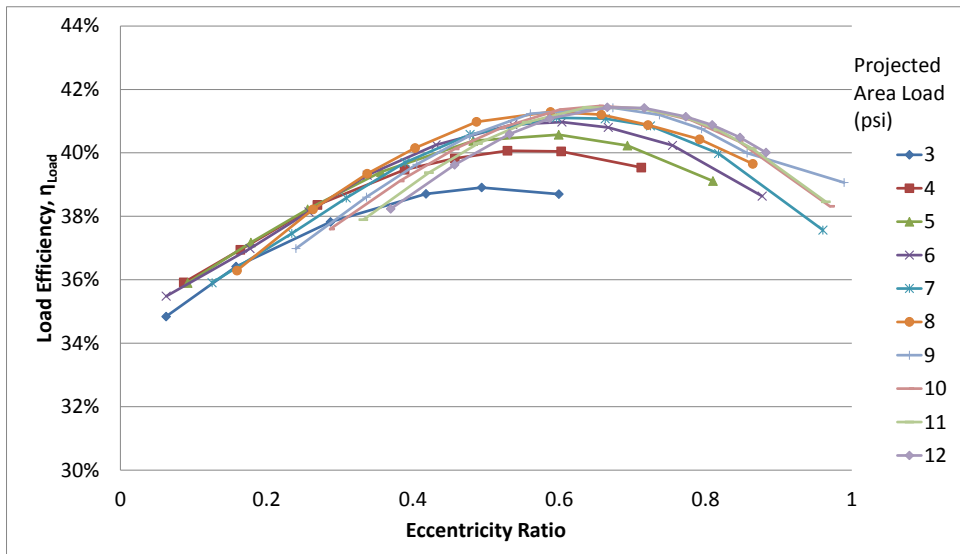
Figure 7-10: Load efficiency (η_{Load}) as a function of eccentricity ratio for Two-Slot bearing with two independent supply lines
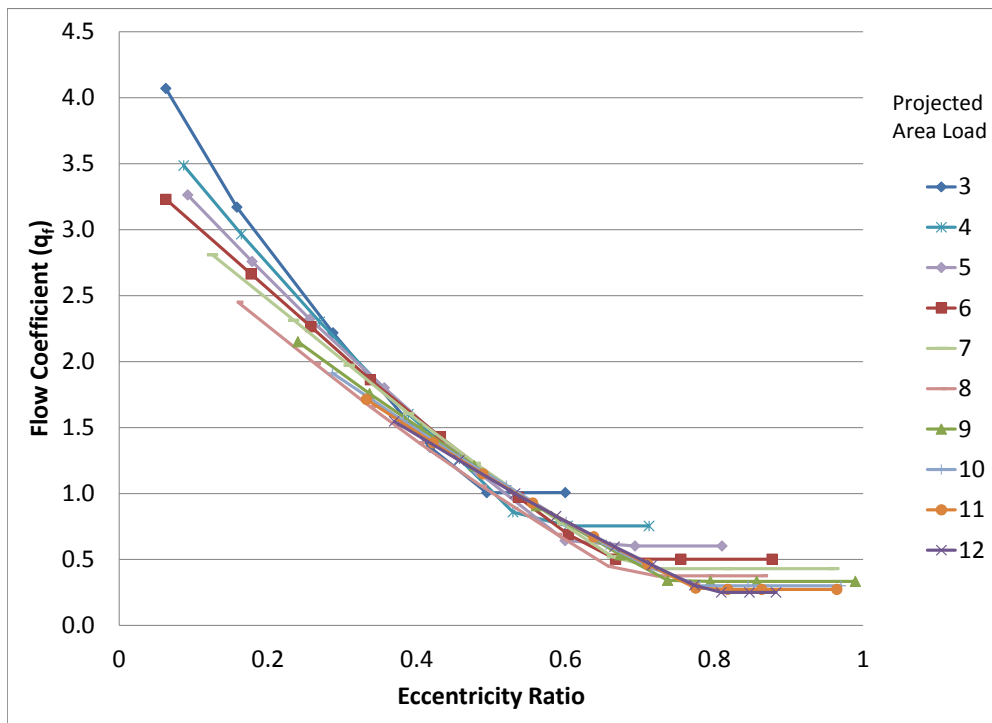
Figure 7-11: Flow coefficient (q_f) as a function of eccentricity ratio for Two-Slot bearing with two independent supply lines

Table 7.3: Nominal Full Scale Two-Slot Bearing

Bearing Configuration	Two-Slot Bearing	
Scale	8.67	
Nominal Shaft Diameter	28	Inches
Clearance Ratio	351	
Radial Clearance	0.040	inches
Engagement Arc	175	degrees
L/D Ratio	2	
Projected Area Load	40	psi
Design Eccentricity Ratio	0.75	
Load Efficiency	41.5	%
Flow Coefficient	0.375	
Hydrostatic Operation		
Inlet Pressure	96.4	psi
Flow Rate	1750	gpm
Flow Power	98.4	hp
Hydrodynamic Operation		
Supply Pressure	25	psi
Flow Rate	19	gpm
Flow Power	0.28	hp

For this bearing with a design eccentricity ratio of 0.75, a relatively modest inlet pressure of 96.4 psi is required due to the high efficiency in the Two-Slot bearing. The full scale flow rate of 1750 gpm is certainly large, but within the range of pumps commonly used on ships and submarines for seawater cooling, firefighting, and cargo handling. The required power is also appreciable, especially when motor and pump inefficiencies are taken into account, but it is less than the frictional power losses in a conventional water-lubricated bearing when hydrodynamic conditions do not exist.

The validity of these non-dimensional parameters relies heavily on bearings being in similar flow regimes. The hydrodynamic check of the Reynolds number in section 2.3.4 revealed that the test bearings were laminar for all speeds in the test rig. Full scale bearings should be in the laminar regime for speeds up to around 20 rpm. For this condition, the Reynolds number must calculated for the pure hydrostatic condition where the fluid flow is pressure driven. This is a difficult problem due to the fact that with an eccentric shaft there is not a consistent characteristic length. For sim-

plicity, a flat plate assumption (i.e. concentric shaft and bearing) is used to calculate the Reynolds number for the circumferential flow through the bearing.

For infinite parallel flat plates, the characteristic length is twice the distance between the plates. Applying this to the bearing, the characteristic length becomes twice the radial clearance. This leaves only the fluid velocity as an unknown. If the assumption is made that all the flow is circumferential and distributed over the length of the bearing, with flow split between the two sides then the average velocity of the fluid can be estimated by dividing half the total flow by the cross sectional area in the clearance gap:

$$V_{hydrostatic} \approx \frac{Q}{2Lc} \tag{7.11}$$

This velocity can then be plugged into the Reynolds equation for the parallel plate condition:

$$Re = \frac{2V_{hydrostatic}c}{\nu} \tag{7.12}$$

This simplified analysis does not account for axial flow or changes in fluid gaps due to eccentricity. A check of the test bearings reveal that they would be expected to lie within the laminar flow regimes with Reynolds numbers generally below 2000. For the full scale condition, the fluid velocity will increase directly with the scale of the bearing. Compounding this increased flow velocity with the increase in the characteristic length of the bearing gap means that the Reynolds number is proportional to the square of the scaling ratio. This means that in hydrostatic operation, a full scale bearing would be expected to be in the turbulent flow regime.

Any full scale extrapolations of performance must be made with the understanding that there will be significant errors in predictions due to the turbulent effects of the the flow that will exist in the larger scale bearings. Not only those impacts, but also the impact that dynamic pressures due to high flow velocities may have on performance

must be examined. These uncertainties reinforce the need for larger scale testing.

7.9   Fluid Supply System

The addition of a hydrostatic pressure supply system adds cost and complexity to a ship. A complex system of pumps, piping, filtration, and valves must be added in a logical fashion.

1. **Pressure Source.**

   Both centrifugal and positive displacement pumps could be utilized as a pressure source. Positive displacement gear pumps have the benefit of being able to provide very high pressures if needed and the ability to have a constant flow. Multiple gear pumps can be driven from a common shaft and power source - providing the capability to have matched flow into various inlets. This would provide almost perfect flow compensation for any bearing. For the Hydrostatic Lift bearing configurations, a gear pump or pumps would be an excellent choice.

   Utilizing the Two-Slot bearing configuration would allow for the use of single stage centrifugal pumps due to the fact that the lift-off pressure needed to initially unseat the bearing is approximately that of the relatively low operating pressure. Centrifugal pumps are commonly used in seawater associated systems for ships and submarines and can reliably operate with continuous duty. A pair of centrifugal pumps for the Two-Slot configuration would provide flow compensation and result in smaller pumps that can be easier to locate in a machinery room.

2. **Piping System.**

   Long runs of piping will be required to supply the inlet ports of a propeller or strut bearing that is located outside of the pressure hull. Systems need to be appropriately sized such that the head losses in the pipe runs allow the required inlet pressure to be delivered to the bearings. The hydrodynamic testing in this

project revealed the benefit of an isolation valve between the pressure supply and the bearing inlet port. The use of check valves and remotely operated isolation valves would be needed to achieve this.

For submarine applications where the submergence pressure varies with operating depth, a fluid system that has a closed loop with the environment should be used. This would allow the use of single stage centrifugal pumps because they would not have to elevate fluid pressure several hundreds of psi above the interior atmospheric pressure inside the hull. Such a system would require robust hull isolation valves to ensure watertight integrity should any failures occur to the pumps and piping systems inside the hull.

Due to relatively small clearances in the bearing, appropriately sized filtration is needed. For a full scale bearing operating at an eccentricity ratio of 0.75, the smallest gap size would be on the order of 0.01", requiring a filtration system of at least 250 microns. Hydrodynamic operation results in even smaller clearances, so better filtration would be prudent.

7.10 Economic Impact

A detailed economic impact of installing a hybrid bearing system was not completed, but general observations can be made regarding the system and factors that need to be considered.

- The initial cost of a hybrid bearing would be significantly more than that of a standard water-lubricated partial arc or stave bearing.

- The additional friction from a hybrid bearing at high operational shaft speeds should be minimal due to the bearings operating in the hydrodynamic lubrication regime. The pumping power required at lower speeds (where the hydrostatic system would be employed is of the same order of magnitude as the

friction power seen in the mixed and boundary lubrication regimes. This was seen in Figure 7-8. This implies that there would be minimal impact on overall operating costs due to increased fuel usage.

- The costs associated with bearing failures and replacements will be the driving reason for using a hybrid system. Chapter 1 showed probabilities and estimated economic costs of such failures. As designed, a hybrid bearing should prevent the majority of such failures from occurring. If the Net Present Value of the costs associated with bearing failures is higher than the initial capital costs of a hybrid system, then the installation of such a system will make it worthwhile.

- The costs of fines due to leakage of oil-lubricated bearing systems will likely continue to increase due to more stringent environmental regulations. This is a large reason behind the increasing use of water-lubricated bearings in general, and would only make a hybrid water-lubricated bearing system even more attractive.

Chapter 8

Conclusions and Future Work

8.1 Summary

This project investigated the feasibility of using a partial arc water-lubricated hybrid bearing to support the main propulsion shaft of an ocean vessel. The ultimate goal was to provide a sufficient understanding of the impacts that different design variables and configurations have on bearing performance. This allows for future studies and testing to be appropriately focused such that full scale applications can be realized.

Chapter 2 provided a brief overview on the theory behind fluid film bearings. The different lubrication regimes of hydrodynamic bearings was presented, as were fundamental fluid equations that form the basis for analyzing their performance. The principles behind hydrostatic lubrication were presented, including the need for flow compensation and the concept of surface self-compensation.

Chapter 3 showed the common modeling techniques used for hydrostatic bearings, including the lumped parameter method. An analytic approach to handle the effect that an eccentric shaft has on the fluid film, pressure distribution and flow rates through a bearing was presented, including discussion on how it was applied for specific bearings in this project. Additionally, a summary of the attempts at numerical modeling of the hydrostatic bearings was provided.

Chapter 4 provided an in-depth look into the design and construction of the bearing test rig used in this project. The individual mechanical and fluid system components of the apparatus were discussed, including the reasoning behind their use. The calibration procedures and data collection process used before and during test runs was addressed.

Chapter 5 discussed the need and basis behind the development of a unique manufacturing process for partial-arc bearings. The evolution of the construction process from its initial (and unsuccessful) trials through to its final mature state that is capable of producing highly accurate and precise bearings is presented, including all relevant lessons learned. Each individual step in the process is shown along with fundamental analysis to provide a future reader with the tools and understanding needed to replicate the manufacturing process. In addition, a summary of the accuracy of the bearings produced in this project is provided along with a discussion regarding the uncertainty associated with those measurements.

Chapter 6 starts with an introduction into the different types of bearing testing conducted during this project. It follows with a breakdown of every bearing tested in this project. For each bearing, the basis and reasoning behind its individual design is provided. The significant findings for the individual test results are presented along with how those findings influenced the design of the next bearing. This chapter shows the evolution of the surface self-compensated bearing designs from ones with unacceptable performance through to designs that provided marked improvements. Hydrodynamic bearings developed as benchmarks for comparison were built and tested. The key finding of hydrostatic lift bearings being able to inherently support substantial side loads when in a partial arc configuration is discussed, as is the instability displayed by such bearings at higher eccentricity ratios and the high lift off pressures required. Attempts to reduce the lift off pressures and allow operation at high eccentricity ratios for hydrostatic lifts were partially successful. Finally, a derivative of the hydrostatic

lift designs - the Two-Slot bearing - was designed, tested, and found to be particularly suitable for use as a hybrid bearing.

Chapter 7 provides an overview into many ancillary factors that can impact the use and applicability of a hybrid partial arc water-lubricated bearing in large ocean vessels. Specific discussion into the key bearing parameters such as clearance ratio, projected area load, and bearing lengths are addressed to include how they impact the ultimate performance of a hybrid bearing. Material finishes of the test bearings impact the interpretation and use of hydrodynamic test results in this project. A proper bearing break-in is required for optimal hydrodynamic performance. The key issue of power dissipation in the bearings is broken down by friction and pumping components along with how such power influences temperature and viscosity of the fluid. Using the results of this project for a full scale application is presented. This includes discussion of possible errors associated with different flow regimes, the need for large scale testing to verify behavior, and the impact such bearings will have on required ship systems. Finally, a brief overview of the driving economic factors that will be applicable in determining the value in implementing a hybrid bearing is provided.

8.2   Principle Contributions

8.2.1   Effect of Flat Plate Assumption in Hydrostatic Bearing Designs

Hydrostatic journal bearings are usually designed for operation with zero eccentricity, and for simplicity the resistance network uses the assumption that bearing and shaft surfaces can be modeled as flat plates - this assumption is valid for very low eccentricities. Previous studies have assumed that the errors are small until very high eccentricity ratios are reached and if very low land lengths are used. Section 3.2.3 showed that using the flat plate assumption leads to large errors for even mod-

est eccentricity ratios. For example, the predicted resistance using the flat plate approximation for a land located at the BDC of the bearing will have an error of approximately 100 percent at eccentricity ratio of only 0.25. In addition to this, the length of the land was found to have very little impact on the magnitude of the error. Although using the flat plate approximation when creating lumped parameter models to design hydrostatic journal bearings has been successful in the past, blind adherence to such simplifications could result in significant deviations in predicted performance for even modest eccentricity ratios.

8.2.2 Partial Arc Bearing Manufacturing Process

The manufacturing process outlined in chapter 5 solves many issues that can present difficulty in constructing partial arc bearings with hydrostatic surface grooves and features. It is a novel approach that utilizes only one precision engineering step (manufacturing of the master shaft with a lathe) to produce highly precise and accurate bearings. This process provides a cost-effective alternative to the use of expensive 4 or 5 axis CNC machines and allows for the relatively quick construction of bearings with unique surface features.

8.2.3 Inherent Transverse Load Support of Hydrostatic Lift Partial Arc Bearings

A key finding that hydrostatic lifts in the partial arc configuration are capable of supporting large side loads had a major impact on the direction of this project and has applicability far beyond the intended scope of this work. This side load capacity is a result of two factors. The first is the atmospheric pressure boundary conditions at the circumferential exits of the bearing. The second is the change in the fluid film to a diverging shape on one side and a converging shape on the other resulting from a side load. When combined, this creates a pressure profile in the film capable of countering those side loads. In no literature source found has this concept been identified. In fact Rippel - one of the most commonly cited sources in regards to hydrostatic bearings -

specifically states that the side load-carrying capacity of such bearings is extremely limited[25].[1] This thesis disproved analytically and experimentally the long held belief that a single inlet slot or pocket located at BDC could not support side load. Identifying the ability of such bearings to withstand significant side loads opens their use up for applications other than for uniaxial loads.

8.2.4 Identification of a Suitable Geometry for Hybrid Bearings in Ocean Vessels

An overarching goal of this work was to identify the dominant drivers behind bearing performance. In many cases, the features that make a journal bearing with good hydrostatic performance are not the same as the features required to make a journal bearing with good hydrodynamic performance. Increasing the amount of grooves, especially in the vicinity of the BDC of the bearing significantly degrades hydrodynamic performance of the bearing. This can be offset to a large extent through the use of isolation valves (or check valves) in supply lines to the grooves. Placing two grooves off the BDC in the Two-Slot bearing had the benefit of minimizing the degradation in hydrodynamic performance, while at the same time providing for a very good hydrostatic response. This was driven largely due to the pressure in between the slots being roughly that of the inlet pressure - generating a large lifting force. The Two-Slot design provided a very good combination of hydrostatic and hydrodynamic performance, making it particularly suitable for use as a hybrid bearing. Furthermore, this bearing is relatively simple to make and also robust since if a scratch does occur, the length of the scratch will be very long and hence the chance of a great loss of pocket pressure will be low.

---

[1]This may be due to the fact that Rippel might have assumed the slot is a relatively large pocket instead of a narrow slot.

8.3 Recommendations for Future Work

This work has made substantial progress towards the realization of a hybrid water-lubricated partial arc bearing. Testing of more bearings on the test rig developed for this project could be conducted, as could parametric studies on the Two-Slot bearing design making small variations in the geometry such as slot lengths, slot locations and bearing clearance. Doing so would make marginal gains in the understanding of these types of bearings. Far more important are some fundamental areas of research that would provide larger advances in hybrid bearing knowledge.

8.3.1 Large Scale Testing

The testing conducted in this project were all done for laminar flow conditions. Although at low speed hydrodynamic operation the full scale bearings should also be laminar, it was seen that turbulent flow conditions can be expected during hydrostatic operation due to high flow velocities of the fluid. Being able to accurately predict performance when turbulence is present is always a challenge. Extrapolating the experimental results from this project to estimate full scale performance will have errors because of this. Testing at larger scales (or ideally full scale) where turbulent flow conditions would be present can reduce the uncertainty of these errors and provide designers with more accurate information regarding the appropriate selection of fluid supply systems and bearing geometry.

8.3.2 Acoustic Performance

The impact that hybrid bearings will have on the acoustic signature of a vessel is of particular importance to naval vessels. Although a hybrid bearing will remove the noise associated with stick-slip shaft motion, the high anticipated flow rates may result in unacceptably large noises. Even during hydrodynamic lubrication the grooves may excite harmonics that can further degrade acoustic signature. These issues would be best solved through larger scale model testing or installing a hybrid bearing on an auxiliary vessel with acoustic instruments capable of quantifying the acoustic impact

these bearings have on a vessel. Such testing is warranted given the great potential benefit of reducing noise and wear at low rpms when conventional bearings operate in the boundary or mixed lubrication regimes.

8.3.3 Numerical Analysis

By using a simple geometry such as the Two-Slot bearing, the difficulty in modeling the bearing using CFD is probably greatly reduced. CFD may be able to account for turbulence in the bearings and provide the ability to investigate the effect of parametric variations in the nominal geometry of the bearing on performance. With a large set of empirical data from this project to compare against, validating the accuracy CFD model would be possible. Developing a finite element model would also be worthwhile for comparison against the empirical data, but such a model would have to include turbulence terms into the Reynolds equation to be applicable to a full scale application.

8.3.4 Materials

The use of polymer materials has a significant impact on how small the bearing clearances can be due to differences in thermal coefficients of expansion. Investigating or developing wear-resistance materials with low thermal coefficients that are also suitable for water lubrication would provide tremendous value. The use of a metallic bearing material such as bronze could be considered and tested, as could the use of a non-metallic propulsion shaft. Thermo-centric designs may also be investigated, where a higher coefficient of thermal expansion material on the outside of the bearings' structural housing could offset the effect of the bearing material on the inside of the housing [28].

Another option is to close the structural loop of the partial arc housing with a partial arc structure bolted to the top. In this case a large clearance (e.g. 10mm or more) would be used, and at TDC, a spring-loaded keeper bearing could be used to prevent

catastrophic uplift of the propeller shaft in an extreme event.

Appendix A

Modeling

A.1   Geometry Effects of Eccentric Shafts

The following MATLAB script provides the code used to determine the effects of eccentric shafts with circumferential (3.2.1) and axial (3.2.2) flows.

```matlab
1  clear all;
2  clc;
3
4  % Brian Heberley
5  % 20 Feb 2013
6
7  % Tool for determining geometric accuracy of reynolds equation ...
       flat plate
8  % simplifications
9
10 % Loop for Theta_C (Location of Land Center)
11
12 r_b = 3.2305/2;
13
14 for k = 1:7
15 theta_c = (k-1)*pi/6;    %+pi/2;    % Add +pi/2 to span the ...
       half-bearing or
```

```matlab
16                                       % remove pi/2 to plot full ...
                                            journal behavior
17 theta_deg(k) = theta_c*180/pi;

18

19      % Sets the land length/radius ratio
20      L_R = 1;
21      L_land = L_R*r_b;

22

23          % Loop for eccentricity
24          % Set spacing for eccentricity
25          n=100;
26          for i = 1:(n-1)          % Adjust for max eccentricity

27

28          e(i) = i/n;              % Range of eccentricities

29

30          x = -L_land/2:.0001:L_land/2;

31

32             % Equation for Axial Flow
33             ya = (1-i./n.*cos(theta_c+x./r_b)).^3;
34             Ya(k,i) = trapz(x,ya);
35             Ra(k,i) = 1/Ya(k,i);

36

37             % Equation for Circumferential Flow
38             yc = 1./(1-i./n.*cos(theta_c+x./r_b)).^3;
39             Yc(k,i) = trapz(x,yc);
40             Rc(k,i) = Yc(k,i);

41

42

43          end

44

45 end
46 % Plot of resistance ratios for various land length/radius ratios and
47 % eccentricities
48 %  figure(1)
49 %  subplot(2,1,1)
50 %  plot(e,L_land.*Ra)
```

```matlab
51 %  ylim([0,15])
52 %  subplot(2,1,2)
53 %  plot(e,Rc./L_land)
54 %  ylim([0,15])
55 %  theta_deg=theta_deg';
56 %  label=num2str(theta_deg);
57 %  legend(label)
58
59   figure(2)
60   plot(e,L_land.*Ra)
61   ylim([0,5])
62   xlabel('Eccentricity','FontSize',18)
63   ylabel('Resistance Ratio','FontSize',18)
64   theta_deg=theta_deg';
65   label=num2str(theta_deg);
66   legend(label)
67   set(gca,'FontSize',16)
68
69   figure(3)
70   plot(e,Rc./L_land)
71   ylim([0,5])
72   xlabel('Eccentricity','FontSize',18)
73   ylabel('Resistance Ratio','FontSize',18)
74   theta_deg=theta_deg;
75   label=num2str(theta_deg);
76   legend(label)
77   set(gca,'FontSize',16)
78
79 % Routine to get the min, max, and mean values to the resistance ...
       ratio of
80 % full journal solution over flat plate simplification
81 % min(R(:,i))
82 % max(R(:,i))
83 % [R(:,n-10),theta_deg]
84 % mean(R(:,n-1))
```

A.2   2 Dimensional Hydrostatic Lift Calculation Tool

The following MATLAB script provides the code used for simplified modeling of the response in a hydrostatic lift bearing circumferential (3.2.1) and axial (3.2.2) flows.

```matlab
1
2
3  % Brian Heberley
4  % Design tool for hydrostatic lift bearing
5
6
7  close all;
8  clear all;
9  clc;
10
11 %% CONSTANTS
12 global mu1 rho
13 mu1 = 2.034*10^-5/144;      %[lb-s/in^2], dynamic viscosity of ...
       fresh water at 70F
14 rho = 62.3;                 %[lb/ft^3], density of fresh water at 70F
15
16 %% INPUT
17
18 %% General Dimensions%%%%%%%%%
19 D = 3.2305;               %[in], Diameter of shaft
20 Ho = .0043;                %[in], Nominal bearing gap based on ¬...
       325:1 radial clearance ratio
21 Arc_b =170;               %[deg], Total Arc Length of Bearing
22 C_b = Arc_b/180*D*pi/2;   %[in], Circumference of bearing with ...
       180 degree arc
23 L_b = D*2;                %[in], Length of bearing with L/D = 2
24 r_b = D/2+Ho;             %[in], Bearing Radius
25
26 %% Hydrostatic Lift Groove Dimensions
27 L_g = 3;                  %[in], Length of lift groove
```

```matlab
28  W_g = 1/8;                   %[in], Width of lift groove
29  A_g = L_g*W_g;               %[in^2], Area of lift groove
30
31  %% Projected Area Load
32  W_proj = 40;                  %[psi], Projected area load
33  W = W_proj*2*D^2;            %[lbf], Applied load
34
35  %% Pump Information
36  P_d = 125;                    %[psi], Pump deadhead pressure
37
38  %%
39  %%%%%%%%%%%%%%%%  Hydrostatic Lift Numerical Integration %%%%%%%%%
40
41  %% Index Length
42  n =1000;
43
44  %% Shaft Location Point
45  e = .25;                     %[ND], Eccentricity
46  theta_c = -87.9;              %[deg], Relative angle from minimum ...
        clearance
47
48  %% Inlet Pressure Condition
49  P_inlet = 28.6;        %[psi], Bearing Inlet Pressure
50
51  %%%%%%%%%% Calculations of Angles %%%%%%%%%%%%%%%%
52  % Angles measured from relative angle from minimum clearance
53
54  %% Flow Exit Angles
55  theta_s2R = ((Arc_b/2)-theta_c);      %[deg], Angle of right ...
        circumferential exit
56  theta_s2L = -((Arc_b/2)+theta_c);     %[deg], Angle of left ...
        circumferential exit
57
58  %% Inlet Entrance Angles
59  theta_s1R = (((W_g/(2*r_b))*180/pi)-theta_c);     %[deg], Angle ...
        of right inlet groove
```

349

```matlab
60  theta_s1L = -(((W_g/(2*r_b))*180/pi)+theta_c);      %[deg], Angle ...
        of left inlet groove
61
62
63  %% Flow through bearing
64
65   Flow_R = Flow(e,r_b,Ho,L_g,P_inlet,theta_s1R,theta_s2R)   ...
         %[gpm], Flow through right side of bearing
66   Flow_L = Flow(e,r_b,Ho,L_g,P_inlet,theta_s1L,theta_s2L)   ...
         %[gpm], Flow through right side of bearing
67   Flow_total = Flow_R+Flow_L
68
69
70   %% Velocities at Bearing Exit
71   Velocity_R = Flow_R*231/60/(Ho*(1-e*cos(theta_s2R*pi/180))*L_g);
72   Velocity_L = Flow_L*231/60/(Ho*(1-e*cos(theta_s2L*pi/180))*L_g);
73  %% Pressures and Forces
74
75  % Arc Length Calculations
76  s_0 = -pi*r_b*theta_c/180;              %[in], Arc length from ...
        minimum clearance angle
77
78  % Loop for location of S
79
80   for i=1:n
81
82       % Angle from BDC
83       theta(i) = ((i-1)/n)*Arc_b/2;         %[deg]
84       theta_s(i) = theta(i)*pi/180;         %[rad]
85
86       % Finding Pressure Distributions
87
88       % Right side of bearing
89       % Angle moving from inlet to circumferential exit
90       theta_s3R(i) = theta(i)+theta_s1R-(180*W_g/(2*r_b*pi));
91       % Pressure Distribution and Force Distribution
```

```matlab
92          % If/Then for groove or landed section
93          % In Groove
94          if theta_s3R<theta_s1R
95              p1(i) = P_inlet;
96              px1(i) = P_inlet*sin(pi*(theta_s3R(i)-theta_c)/180);
97              py1(i) = P_inlet*cos(pi*(theta_s3R(i)-theta_c)/180);
98
99          % In Land
100         else
101
102             [p1(i),px1(i),py1(i)] = ...
                    Press_Force(e,r_b,Ho,L_g,Flow_R,P_inlet,theta_s1R,theta_s3R(i));
103
104         end
105
106         % Left side of bearing
107         % Angle moving from inlet to circumferential exit
108         theta_s3L(i) = -theta(i)+theta_s1L+(180*W_g/(2*r_b*pi));
109         % Pressure Distribution and Force Distribution
110             % If/Then for groove or landed section
111         % In Groove
112         if theta_s3L>theta_s1L
113             p2(i) = P_inlet;
114             px2(i) = P_inlet*sin(pi*(theta_s3L(i)-theta_c)/180);
115             py2(i) = P_inlet*cos(pi*(theta_s3L(i)-theta_c)/180);
116
117         % In Land
118         else
119
120             [p2(i),px2(i),py2(i)] = ...
                    Press_Force(e,r_b,Ho,L_g,Flow_L,P_inlet,theta_s1L,theta_s3L(i));
121
122         end
123     end
124
125
```

351

```matlab
126   % Individual Force Components
127   % Right side of Bearing over length of groove
128   Fx1 = cumsum(px1)*L_g*(r_b*Arc_b/(2*n))*pi/180;
129   Fy1 = cumsum(py1)*L_g*(r_b*Arc_b/(2*n))*pi/180;
130   % Left side of Bearing over length of groove
131   Fx2 = cumsum(px2)*L_g*(r_b*Arc_b/(2*n))*pi/180;
132   Fy2 = cumsum(py2)*L_g*(r_b*Arc_b/(2*n))*pi/180;
133   % Inlet Port Contribution
134
135
136   % Force Components from grooved section
137   FX = (Fx1+Fx2);
138   FY = (Fy1+Fy2);
139
140   %  % Force addition from Ends (assumes triangular pressure ...
          profile on both axial ends)
141   %  Fx_end = Fx*(L_b-L_g)/(L_g);
142   %  Fy_end = Fy*(L_b-L_g)/(L_g);
143   %
144   %  % Total Force components
145   %  FX = Fx+Fx_end;
146   %  FY = Fy+Fy_end;
147
148
149
150   %%%% Add in Experimental Results
151   % Probe Locations
152   theta_pb4 = 71.4;
153   theta_pb3 = 37.9;
154   theta_pb2 = -40.4;
155   theta_pb1 = -70.1;
156   theta_inlet = 0;
157   % Probe Pressures
158   press_pb4 = 3.35;
159   press_pb3 = 9.4;
160   press_pb2 = 18.45;
```

```matlab
161 press_pb1 = 9.69;
162 press_inlet = P_inlet;
163
164 % Plot of Pressure Distribution
165  figure(1)
166  hold on
167  plot(theta,p1,'LineWidth',1.5)
168  plot(-theta,p2,'LineWidth',1.5)
169  plot(theta_pb4,press_pb4,'r*',theta_pb3,press_pb3,'r*',theta_pb2,press_pb2,'r*',thet
170  legend('Model Prediction')
171  set(gca,'FontSize',30);
172  xlabel('Angle from Bottom Dead Center (deg)');
173  ylabel('Pressure (Psi)');
174  ylim([-1,P_inlet+1])
175
176 %% Graphical representation of Shaft and Bearing
177 pnts = 0:0.01:2*pi;
178 xb = r_b*cos(pnts);
179 yb = r_b*sin(pnts);
180 r_s = r_b*.75;
181 xs = r_s*cos(pnts)+(r_b-r_s)*e*sin(theta_c*pi/180);
182 ys = r_s*sin(pnts)-(r_b-r_s)*e*cos(theta_c*pi/180);
183 pnts = pi+(180-Arc_b)*pi/(2*180):0.01:2*pi-(180-Arc_b)*pi/(2*180);
184 xb = r_b*cos(pnts);
185 yb = r_b*sin(pnts);
186
187 figure(2)
188 hold on
189 plot(xb,yb,'b','LineWidth',3)
190 plot(xs,ys,'r','LineWidth',3)
191 set(gca,'FontSize',30);
192 legend('Bearing','Shaft')
193 axis equal
194
195
196 %% Flat Plate Calculations
```

```matlab
197
198  % Flat Plate Flow
199  Q_flat = 2*Qflat(Ho,L_g,r_b,P_inlet,theta_c,Arc_b/2)
200
201  %%
202  %%%%%%%%%%%%%%%%%%% Generalized Fuller ...
          Equations%%%%%%%%%%%%%%%%%%%%%%%%%%
203
204  %% Single Point Comparison
205
206      A_bar = A(e,L_g,L_b);
207      B_bar = B(e,L_g,D);
208
209
210      W_f = P_inlet*L_b*D*A_bar
211      Flow_f = (P_inlet*Ho^3*B_bar/mu1)*60/231
212
213
214  disp('Results');
215  table1 = ...
          [P_inlet,e,theta_c,Flow_total,FY(n),FY(n)/(L_b*D),FX(n);P_inlet,e,theta_c,Flow_f,
216  fprintf('Inlet Press(psi)\t e\t\t angle(deg)\t Flow(gpm)\t ...
          Vertical Force(lbf)\t Projected Load(psi)\t Side Force(lbf)\n');
217  fprintf('%3.3f\t\t\t\t %3.3f\t %3.3f\t\t %3.3f\t\t %3.3f\t\t\t\t ...
          %3.3f\t\t\t\t\t %3.3f\t\n',table1');
218
219  function [P,Px,Py] = ...
          Press_Force(e,r_b,Ho,L_g,Flow,P_inlet,theta_s1,theta_s3)
220  % Brian Heberley 13 Feb 2013
221  % Compute the pressure at a point through a hydrostatic lift one ...
          side of the bearing
222
223  % e = Eccentricity [n/d]
224  % r_b = Bearing radius [in]
225  % Ho = Nominal clearance [in]
226  % L_g = Length of inlet groove [in]
```

```matlab
227  % Flow = Flow to particular side of the bearing [gpm]

228  % P_inlet = Bearing inlet pressure [psi]

229  % theta_s1 = Angle of inlet port edge [deg]

230  % theta_s3 = Angle of integration end point [deg]

231

232

233  global mu1

234  %% Conversion to/from GPM from in^3/sec

235  Convert = 60/231;        % 60 sec/min & 231 in^3=gallon

236

237  %% Convert Angles to arc lengths

238  % Inlet Port

239  s1 = pi*r_b*theta_s1/180;

240  % Location of Integration

241  s3 = pi*r_b*theta_s3/180;

242

243

244  %% Range of integration

245

246  % For right side of bearing

247  if s1<s3

248  x_0 = s1;

249  x_1 = s3;

250

251  % For left side of bearing

252  else

253  x_0 = s3;

254  x_1 = s1;

255  end

256

257  %% Integration to find pressure

258

259  % Integrand for Pressure

260  fun_P = @(x) 1./(1-e.*cos(x./r_b)).^3;

261

262  % Integration equation for pressure (in Psi)
```

355

```matlab
263  P = ...
         P_inlet-(1/Convert)*((12*mu1*Flow)/(L_g*Ho^3))*integral(fun_P,x_0,x_1);
264
265  %% Calculation of Force Distribution
266
267  % Pressure in X,Y directions (Psi)
268  Px = P*sin((s3-s1)/r_b);
269  Py = P*cos((s3-s1)/r_b);
270
271  end
272
273  function Q = Flow(e,r_b,Ho,L_g,P_inlet,theta_s1,theta_s2)
274  % Brian Heberley 13 Feb 2013
275  % Compute the flow through a hydrostatic lift one side of the bearing
276
277  % e = Eccentricity [n/d]
278  % r_b = Bearing radius [in]
279  % Ho = Nominal clearance [in]
280  % L_g = Length of inlet groove [in]
281  % P_inlet = Bearing inlet pressure [psi]
282  % theta_s1 = Angle of inlet port edge [deg]
283  % theta_s2 = Angle of circumferential exit [deg]
284
285  global mu1
286  %% Convert Angles to arc lengths
287  % Inlet Port
288  s1 = pi*r_b*theta_s1/180;
289  % Circumferential Exit
290  s2 = pi*r_b*theta_s2/180;
291
292  %% Conversion to GPM from in^3/sec
293  Convert = 60/231;        % 60 sec/min & 231 in^3=gallon
294
295  %% Integration to find flow
296
297  fun = @(x) 1./(1-e.*cos(x./r_b)).^3;
```

```matlab
298
299  % For right side of bearing
300  if s1<s2
301  x_1 = s1;
302  x_2 = s2;
303
304  % For left side of bearing
305  else
306  x_1 = s2;
307  x_2 = s1;
308  end
309
310  Q = (Convert)*((L_g*P_inlet*Ho^3)/(12*mu1))/integral(fun,x_1,x_2);
311
312  end
```

Appendix B

DATA ANALYSIS

B.1   Eddy-Current Sensitivity Effects

The following MATLAB script provides the code to determine the eddy-current sensitivity effects shown in figures 4-31 and 4-33.

```matlab
1  % Brian Heberley
2  % 14 August 2012
3  % Eddy Current Probe Diameter Sensativity Effects
4
5
6  %% Plots for varying distances and gap heights
7  clear all;
8  clc;
9
10 % Shaft Diameter
11 D = 82.0547;
12 % Probe Diameter
13 d = 8;
14
15 for k = 1:6
16     % Vary h from 5 to 30% of probe diameter
17     h(k) = .05*d*k;
```

```matlab
18      % h as a percent of probe diameter
19      Gap_percent(k) = .05*k;
20
21      n=1000;
22      for i = 1:n
23          % Vary region of interest from probe center to 3X probe ...
                diameter
24          d2(i) = 1.5*d*i/n;
25          % Distance as a percent of probe diameter
26          x_percent(i)= i*.3;
27
28          % Height y from shaft center to shaft at x = 3d diameter
29          D1(k,i) = ((D/2)^2 - (d2(i))^2)^.5;
30
31          % Distance from virtual flat plate to shaft at 3X probe ...
                diameter
32          D2(k,i) = D/2 - D1(k,i);
33
34          % Distance from probe to shaft
35          D3(k,i) = h(k)+D2(k,i);
36
37          % Error Calculation at x positions
38          Error_3(k,i) = 100*(h(k)+D3(k,i)-h(k))/h(k);
39
40          % WEIGHTED ERROR CALCULATION
41          TA(i) = pi*(d2(i))^2;
42
43          % % Weighted Distance
44
45          if i==1
46          D4(k,i) = D3(k,i)*pi*(d2(i)^2);
47          D5(k,i) = D4(k,i);
48          else
49          D4(k,i) = D3(k,i)*pi*(d2(i)^2-d2(i-1)^2);
50          D5(k,i) = D4(k,i)+D5(k,i-1);
51          end
```

```
52
53          % Weighted Error
54          D6(k,i) = D5(k,i)/TA(i);
55          Error_w(k,i) = 100*(h(k)+D6(k,i)-h(k))/h(k);
56      end
57  end
58
59  % Plot of distance from probe to shaft
60  figure(1)
61  plot(x_percent,D3)
62  H=Gap_percent';
63  label=num2str(H);
64  legend(label)
65
66  % Plot of Error at radial point
67  figure(2)
68  plot(x_percent,Error_3)
69  H=Gap_percent';
70  label=num2str(H);
71  legend(label)
72
73  % Plot of Weighted Error at radial points
74  figure(3)
75  plot(x_percent,Error_w)
76  H=Gap_percent';
77  label=num2str(H);
78  legend(label)
```

B.2   Eddy-Current Calibration

The following MATLAB script provides the calibration routine described in section 4.5.2.

```
1  % Calibration for Hydrostatic Bearing Testing
```

361

```matlab
% Eddy Current Probes
% Brian Heberley
% 21 June 2012

clear all;
clc;

% Read in low load, no rotation test run
% Only relative movement can be detected between test runs.  It ...
    is assumed
% the shaft finds the minimum energy point in bearing which is at ...
    BDC of
% the bearing.  The probes will be assumed to be at the 45 degree ...
    corners
% of the bearing surfaces (135, 225 degrees from TDC).

%[filename,pathname] = uigetfile('.txt','Choose Data File');

[names,PathName,FilterIndex] = uigetfile('.txt','MultiSelect','on');


for i = 1:length(names)
data = dlmread(char(names(i)));

% Pull in Data for Eddy Current Probes
time = data(:,1);
% 8mm Rear Eddy Current Probes
p1 = data(:,4);
p2 = data(:,5);
s8 = 127;       % Volts per inch

% 8mm Front Eddy Current Probes
p3 = data(:,6);
p4 = data(:,7);
%s8 = 127;       % Volts per inch

```

```matlab
35  % Plot of calibration data for continuity check
36  figure(1)
37  subplot(length(names),1,i)
38  plot(p1)
39
40  % Average values of probes in volts.
41  P1(i) = mean(p1(i));
42  P2(i) = mean(p2(i));
43  P3(i) = mean(p3(i));
44  P4(i) = mean(p4(i));
45  end
46
47  disp(names')
48
49  % Display mean values of individual runs, Z Scores, ensemble mean ...
        and STD
50  table1 = [P1' zscore(P1)' P2' zscore(P2)' P3' zscore(P3)' P4' ...
        zscore(P4)'];
51  table2 = [mean(P1) std(P1) mean(P2) std(P2)/127 mean(P3) std(P3) ...
        mean(P4) std(P4)];
52  fprintf('P1\t\t\t Z1\t\t\t P2\t\t\t\t Z2\t\t P3\t\t\t\t Z3\t\t\t ...
        P4\t\t\t\t Z4\t \n');
53  fprintf('%4.5f\t\t %4.2f\t\t %4.5f\t\t %4.2f\t %4.5f\t\t ...
        %4.2f\t\t %4.5f\t\t %4.2f\t \n', table1');
54  fprintf('\n');
55  fprintf('P1 Mean\t\t P1 STD\t\t P2 Mean\t\t P2 STD\t P3 Mean\t\t ...
        P3 STD\t\t P4 Mean\t\t P4 STD\t\n');
56  fprintf('%4.5f\t\t %4.4f\t\t %4.5f\t\t %4.4f\t %4.5f\t\t ...
        %4.4f\t\t %4.5f\t\t %4.4f\t \n\n', table2');
57
58
59  % Calculate differences from the mean in terms of distances and ...
        plot them
60  G1(:,1) = (std(P1)*zscore(P1)/s8)';
61  G1(:,2) = (std(P2)*zscore(P2)/s8)';
62  %disp('Distance of calibration runs from Mean Value:');
```

363

```matlab
63  %disp(G1);

64

65  figure(2)
66  gscatter(G1(:,1),G1(:,2),names')
67  axis equal

68

69  G2(:,1) = (std(P3)*zscore(P3)/s8)';
70  G2(:,2) = (std(P4)*zscore(P4)/s8)';
71  %disp('Distance of calibration runs from Mean Value:');
72  %disp(G2);

73

74  figure(3)
75  gscatter(G2(:,1),G2(:,2),names')
76  axis equal

77

78  g = input('Enter nominal radial gap in inches= (0.002" default)');
79  if isempty(g)
80          g = .002;                      % Nominal gap in inches (¬800:1 ...
                 R/C)
81  end

82

83  D_a = input('Enter axial distance between probes in inches= ...
         (8.46" default)');
84  if isempty(D_a)
85          D_a = 8.46;                    % Axial distance between probes ...
                 (6.46"+2")
86  end

87

88  % Configure Geometry such that probes are "located" at bearing ...
         surface at
89  % 135 and 225 degrees from TDC.  (0,0) point is geometric center of
90  % bearing.

91

92  D = 3.2305/2 + g;

93

94  % 'Absolute Coordinates' of Probes
```

```matlab
95  X1 = D*sqrt(2)/2;
96  Y1 = -D*sqrt(2)/2;
97  X2 = -D*sqrt(2)/2;
98  Y2 = -D*sqrt(2)/2;
99
100 % Determine the reference distance from the virtual probe ...
        location to the
101 % shaft center
102 x1 = D*sqrt(2)/2;
103 y1 = -D*sqrt(2)/2 + g;
104 r1 = (x1^2+y1^2)^.5;     %Reference distance from probe to shaft ...
        center
105
106 x2 = -D*sqrt(2)/2;
107 y2 = -D*sqrt(2)/2 + g;
108 r2 = (x2^2+y2^2)^.5;     % Reference distance from probe to shaft ...
        center
109
110 r3 = r1;                % Geometry is same for forward probes
111 r4 = r2;                % Geometry is same for forward probes
112 X3 = X1;                % Geometry is same for forward probes
113 X4 = X2;                % Geometry is same for forward probes
114 Y3 = Y1;                % Geometry is same for forward probes
115 Y4 = Y2;                % Geometry is same for forward probes
116
117 P1 = mean(P1);
118 P2 = mean(P2);
119 P3 = mean(P3);
120 P4 = mean(P4);
121
122 [P1 P2 P3 P4 r1 r2 r3 r4 X1 X2 X3 X4 Y1 Y2 Y3 Y4 s8 g];  % Passed ...
        to cal
123 clear p1 p2 p3 p4 G1 G2 D x1 x2 y1 y2 i names data ans table1 ...
        table2 time
124 clear PathName FilterIndex
125 save eddycal
```

Appendix C

SURFACE ROUGHNESS MEASUREMENTS

Surface roughness measurements of various bearing materials are provided. Measurements were conducted with a Tencor P16 Surface Profilometer and a Zygo Vertical Scanning Interferometer.

C.1 Turcite

Instrument ZYGO Vertical Scanning Interferometer
Material Turcite
Notes: Difficulty obtaining measurements due to low reflectivity

Measurement	μm			Spot Size (mm)	Spot	Notes
	R_t	R_{RMS}	R_a			
1	11.141	3.325	2.889	.32x.26	A	Not counted b/c poor resolution
2	15.204	2.215	1.74	.36x.27	B	
3	15.124	2.016	1.527	.36x.27	B	Good Resolution
4	20.148	1.857	1.308	.36x.27	B	
5	37.355	2.214	1.425	.36x.27	C	
6	15.072	1.347	1.039	.36x.28	D	Good Resolution
7	15.608	1.36	1.076	.36x.29	E	Best Resolution
8	10.405	1.406	1.036	.36x.30	F	
9	11.088	1.474	1.074	.34x.27	F	
Average (μm)	19.12137	1.678067	1.224			
Average (μinch)	752.8097	66.06562	48.18898			
R_{RMS}/R_a Ratio			1.371			

Instrument Tencor KLA P16 Contact Profilometer
Material Turcite
Notes: With Extrusion Length

Measurement	μm			Sample Length (μm)
	R_t	R_{RMS}	R_a	
1	8.085	1.39352	1.01281	600
2	8.67278	1.53805	1.23486	1000
3a	18.4117	2.40443	1.52379	1000
3b	6.43514	1.12922	0.93366	1000
4a	13.38	1.97371	1.45167	1000
4b	8.89781	1.5988	1.19304	1000
5	14.6984	1.89181	1.48711	1000
6	12.6695	1.77578	1.367	3000
Average (μm)	10.82401	1.713165	1.275493	
Average (μinch)	426.1422	67.44744	50.21624	
R_{RMS}/R_a Ratio			1.343	

Tencor KLA P16 Contact Profilometer

Material   **Turcite**

Notes: **Against Extrusion Length**

Measurement	R_t	R_{RMS}	R_a	Sample Length (µm)
	µm	µm	µm	
1	27.5667	4.20957	2.97485	1000
2a	31.2742	3.05606	1.97594	2000
2b	13.7173	2.07694	1.64398	2000
3a	20.0602	2.59085	1.95821	3000
3b	15.4327	2.52493	2.03957	3000
Average (µm)	21.61022	2.89167	2.11851	
Average (µinch)	850.7961	113.8453	83.40591	
R_{RMS}/R_a Ratio			1.365	
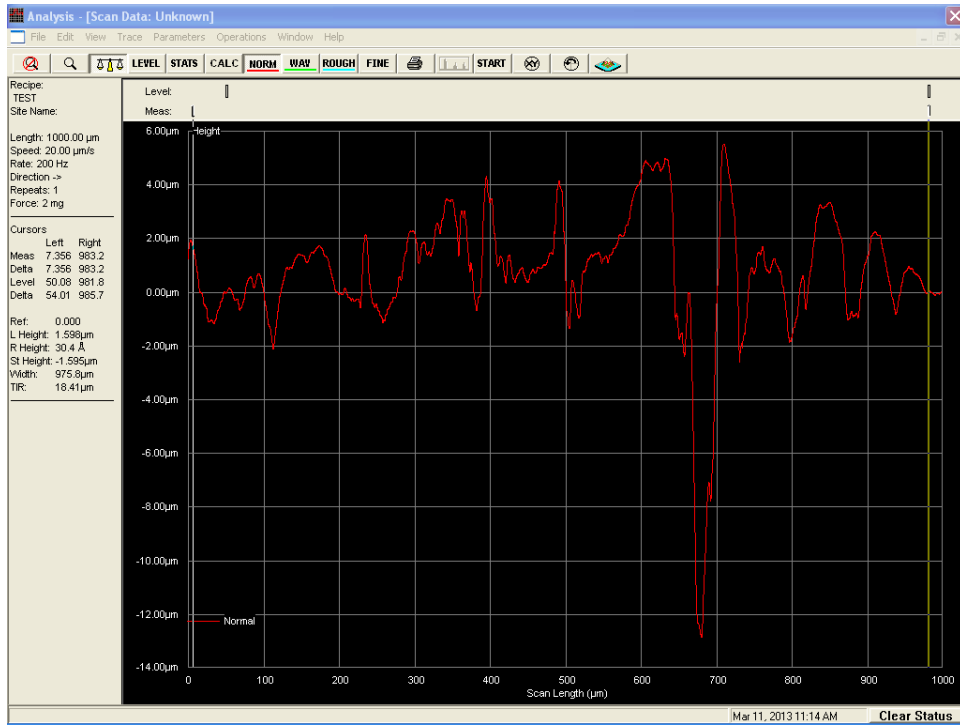
Figure C-1: Turcite Sample 3 (With Extrusion)
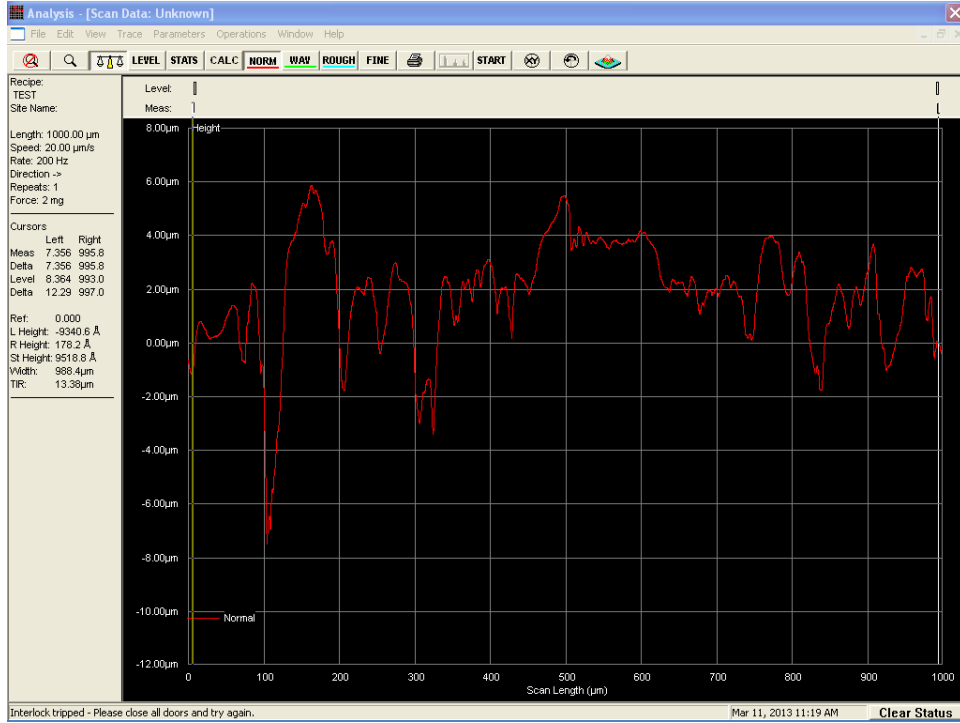
Figure C-2: Turcite Sample 4 (With Extrusion)
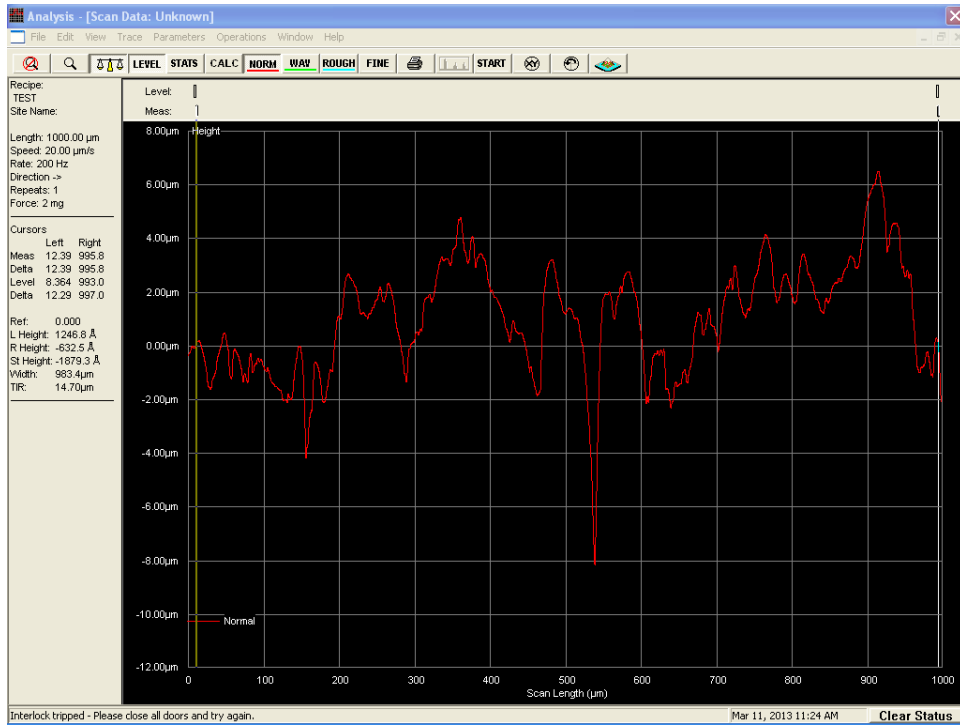
Figure C-3: Turcite Sample 5 (With Extrusion)
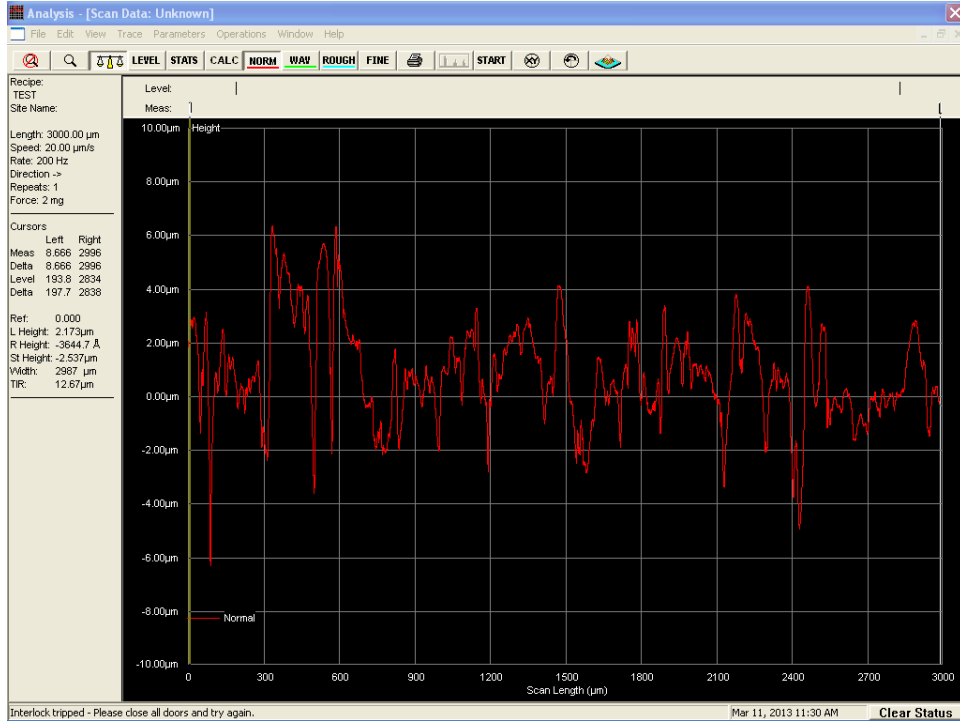
Figure C-4: Turcite Sample 6 (With Extrusion)
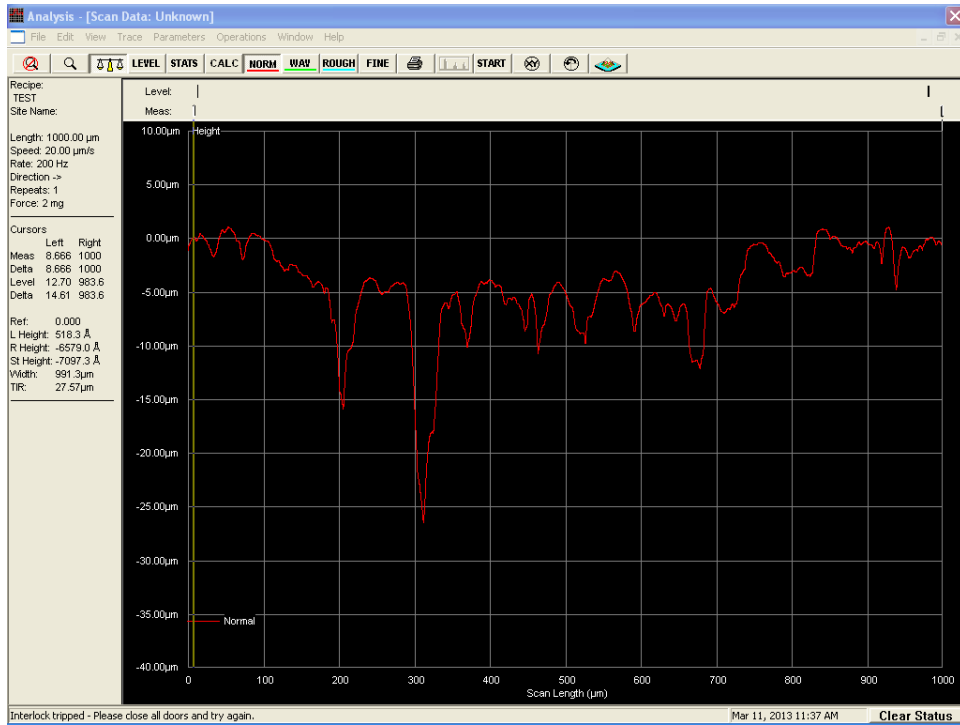
Figure C-5: Turcite Sample 1 (Across Extrusion)
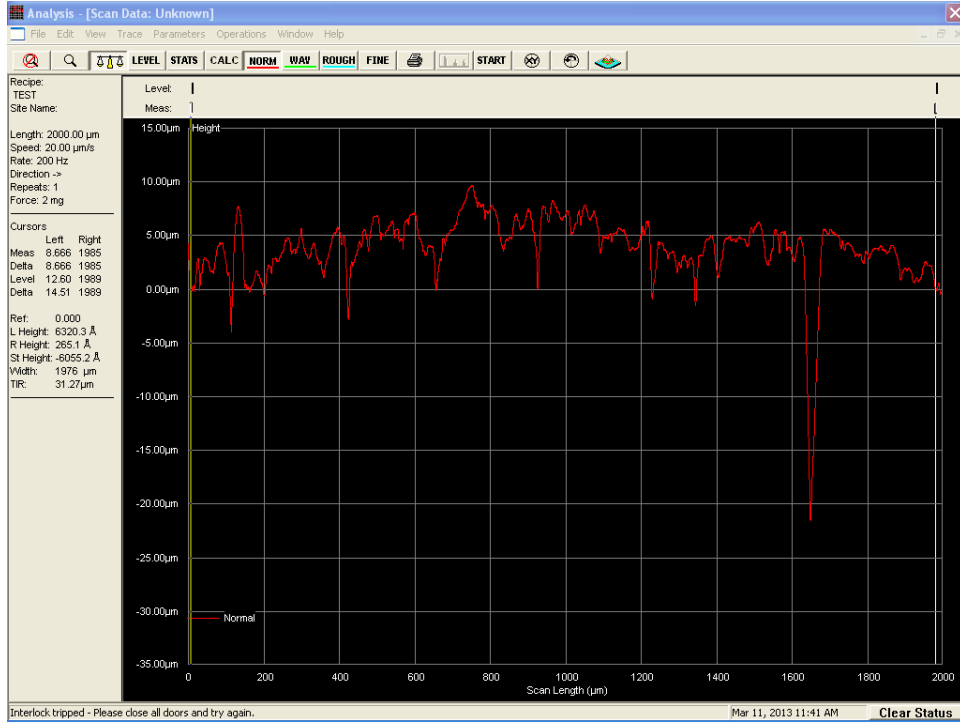
Figure C-6: Turcite Sample 2 (Across Extrusion)
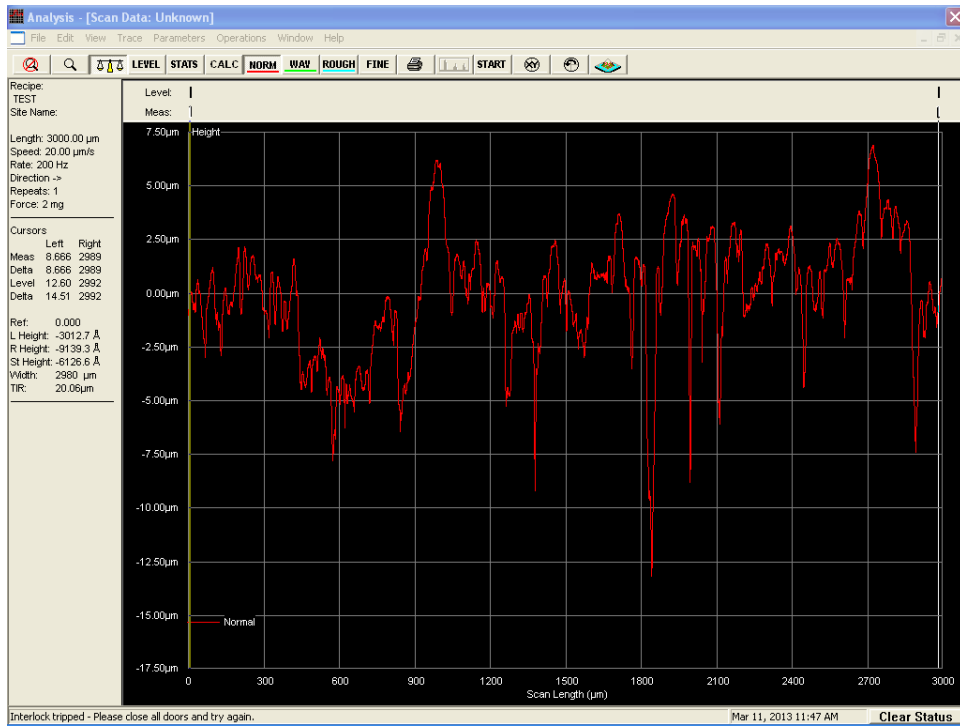
Figure C-7: Turcite Sample 3 (Across Extrusion)
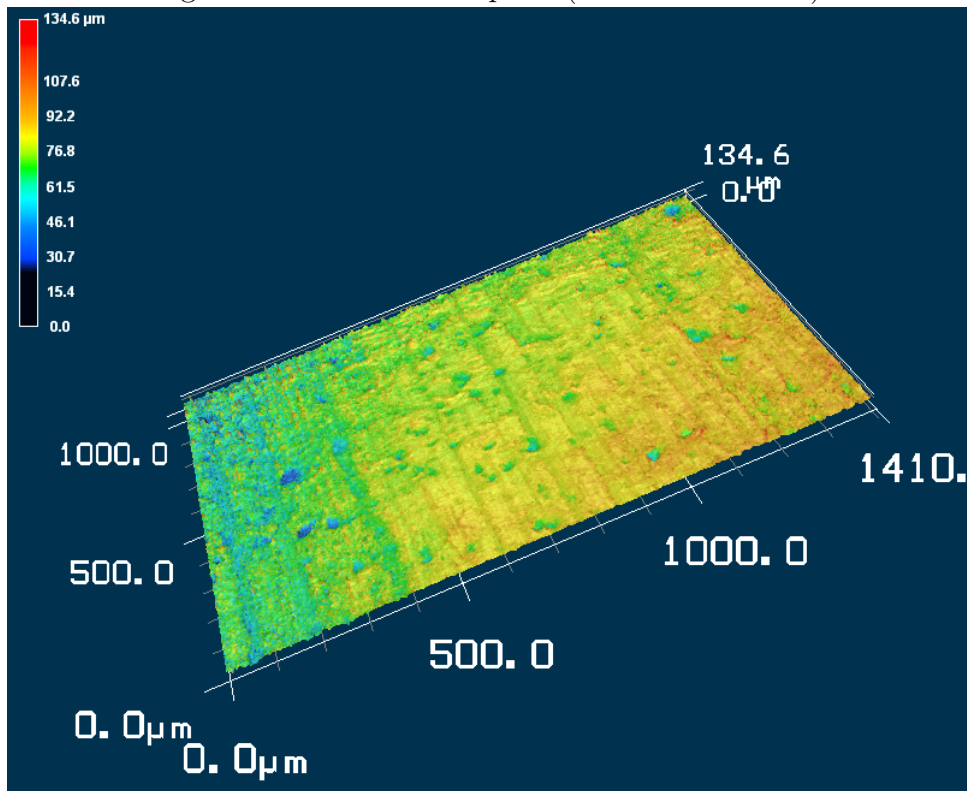
Figure C-8: Turcite SEM 3D 10X Image
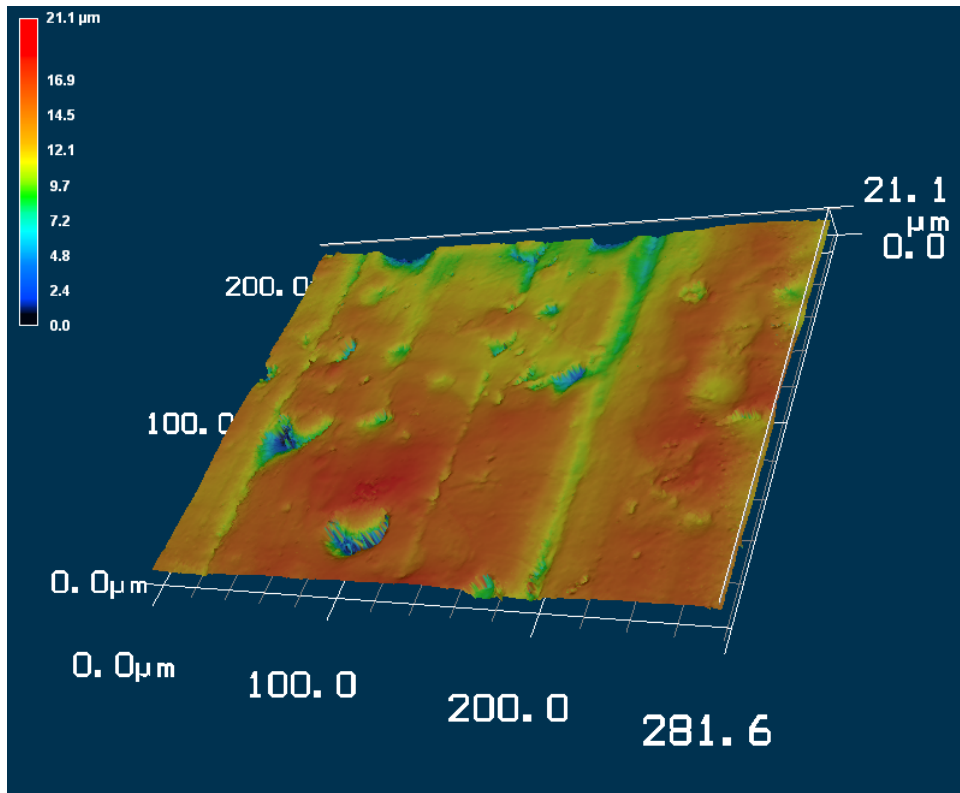
Figure C-9: Turcite SEM 3D 50X Image
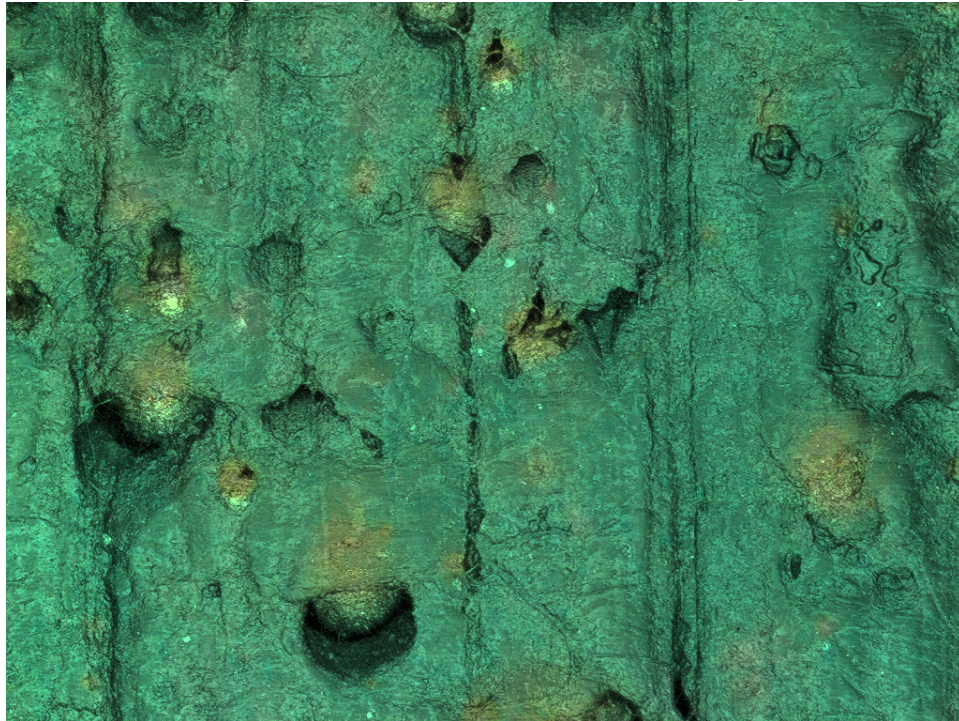
Figure C-10: Turcite Optical 50X Image

C.2 Ultra High Molecular (UHMW) Polyethylene (PE)

Instrument: ZYGO Vertical Scanning Interferometer
Material: UHMW Polyetheylene

Measurement	μm			Spot Size (mm)	Spot	Notes
	R_t	R_{RMS}	R_a			
1	2.9	0.326	0.26	.36x.26	A	
2	2.646	0.343	0.272	.36x.27	A	
3	2.04	0.224	0.173	.36x.27	B	
4	2.916	0.303	0.232	.36x.27	C	
Average (μm)	2.576333	0.287167	0.223667			
Average (μinch)	101.4304	11.30577	8.805774			
R_{RMS}/R_a Ratio			1.283905			

Instrument: Tencor KLA P16 Contact Profilometer
Material: UHMW

Measurement	μm			Sample Length (μm)
	R_t	R_{RMS}	R_a	
1	2.2124	0.4022	0.3147	2000
2	1.93245	0.25498	0.20002	2000
3(full)	3.61729	0.6544	0.512	2000
3(left)	0.96054	0.15912	0.1266	2000
3(right)	2.03658	0.28101	0.21435	2000
3(mid)	3.40167	0.5588	0.41539	2000
Average (μm)	2.360155	0.385085	0.297177	
Average (μinch)	92.91949	15.16083	11.69987	
R_{RMS}/R_a Ratio			1.295812	
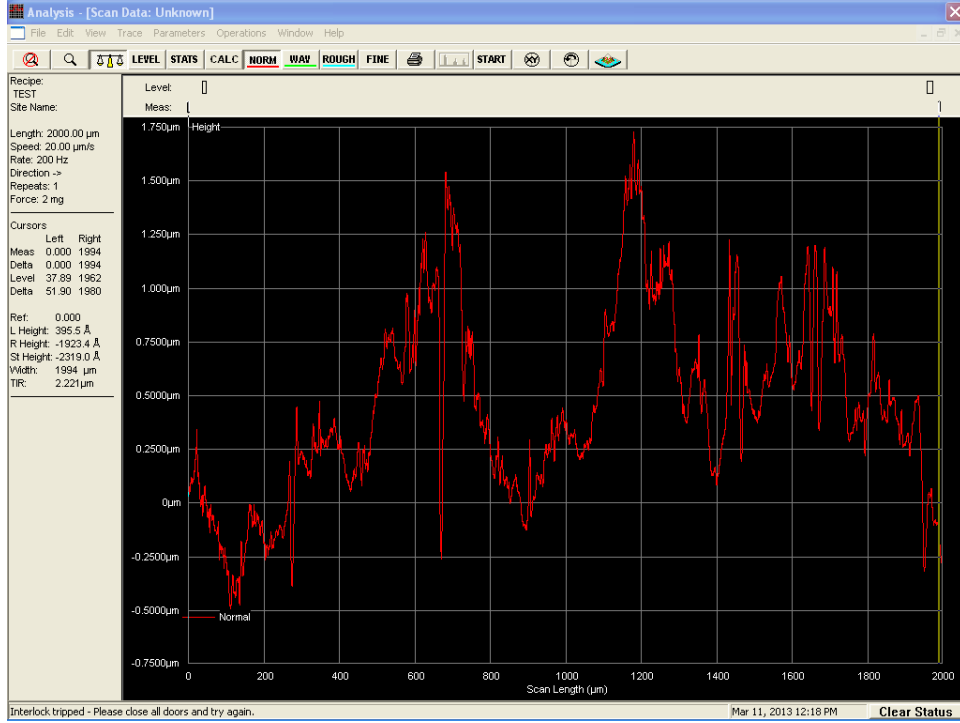
Figure C-11: UHMW PE Sample 1
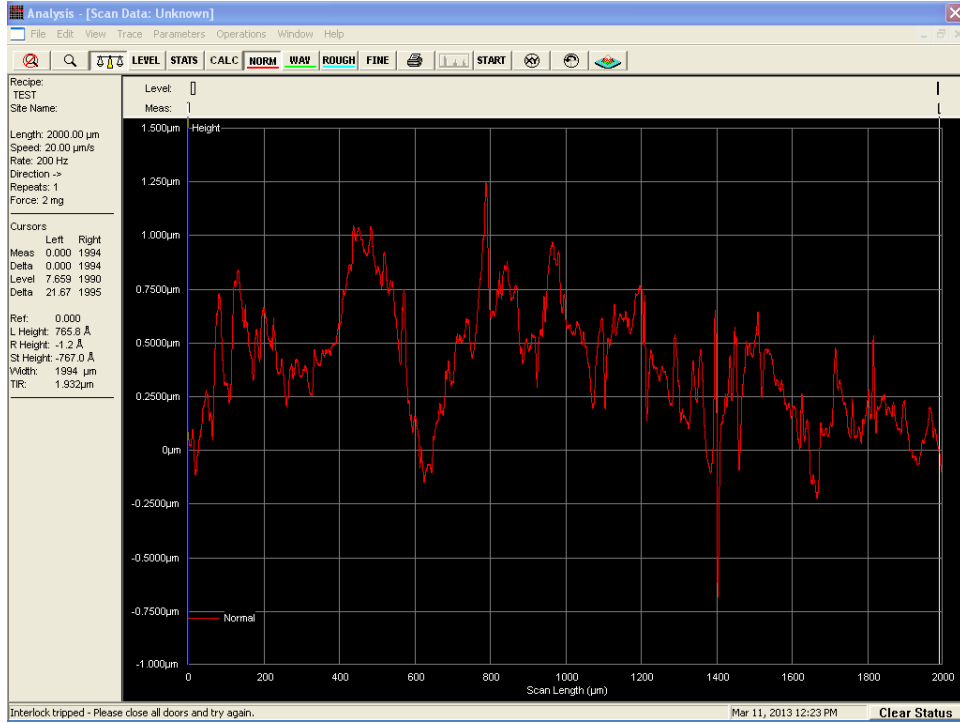
Figure C-12: UHMW PE Sample 2
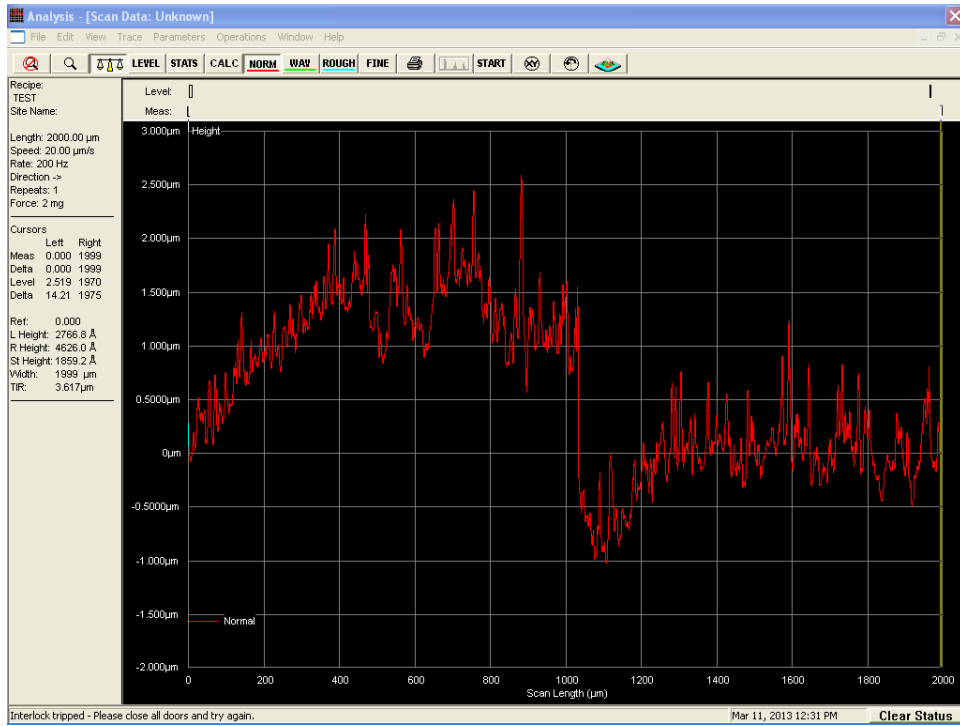
Figure C-13: UHMW PE Sample 3

C.3 DURAMAX ROMOR II

Instrument: Tencor KLA P16 Contact Profilometer
Material: DURAMAX ROMOR II

Measurement	μm			Sample Length (μm)
	R_t	R_{RMS}	R_a	
1a	2.29976	0.23813	0.179	2000
1b	1.03097	0.16702	0.12939	2000
2a	2.4713	0.48358	0.40705	2000
2b	2.07564	0.30956	0.21664	2000
3	1.59919	0.20569	0.17131	2000
Average (μm)	1.579477	0.233997	0.183898	
Average (μinch)	62.18412	9.212467	7.240092	
R_{RMS}/R_a Ratio			1.272424	
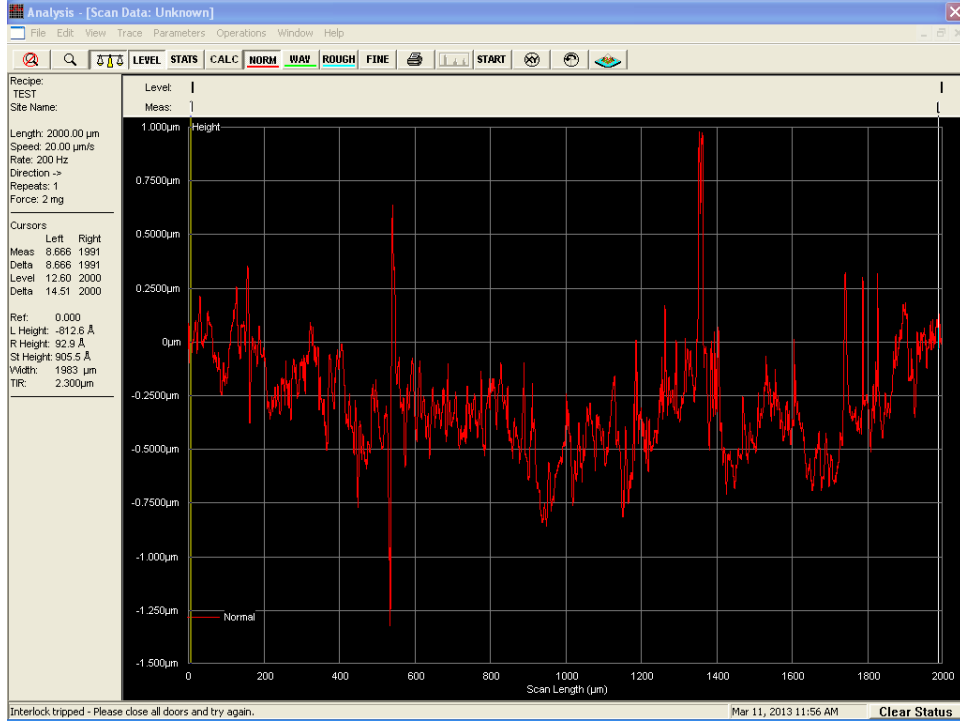
Figure C-14: ROMOR Sample 1
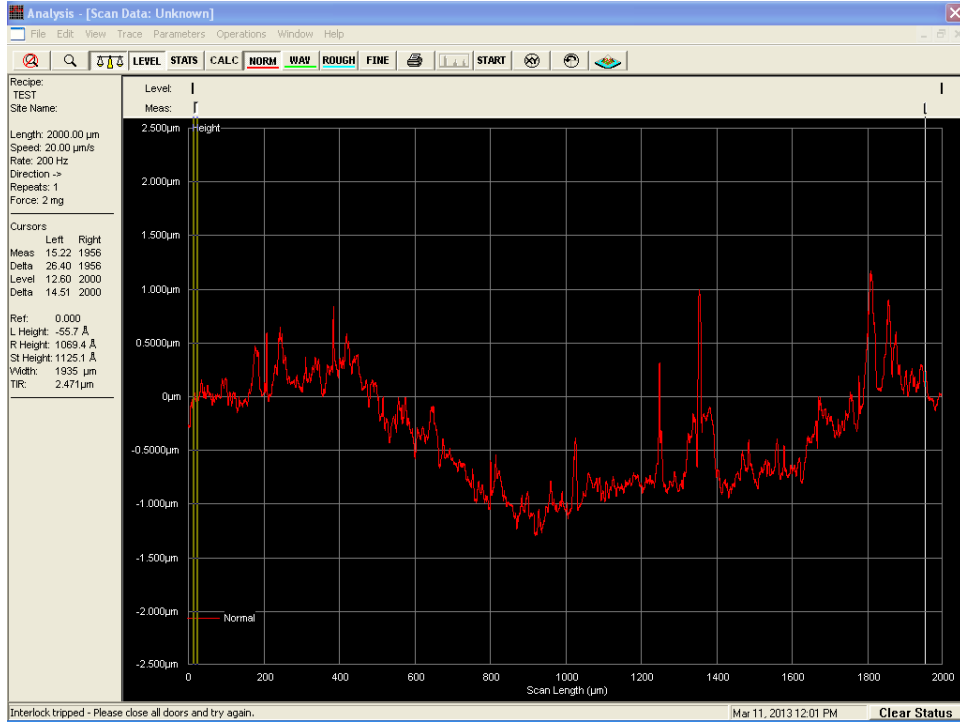
Figure C-15: ROMOR Sample 2
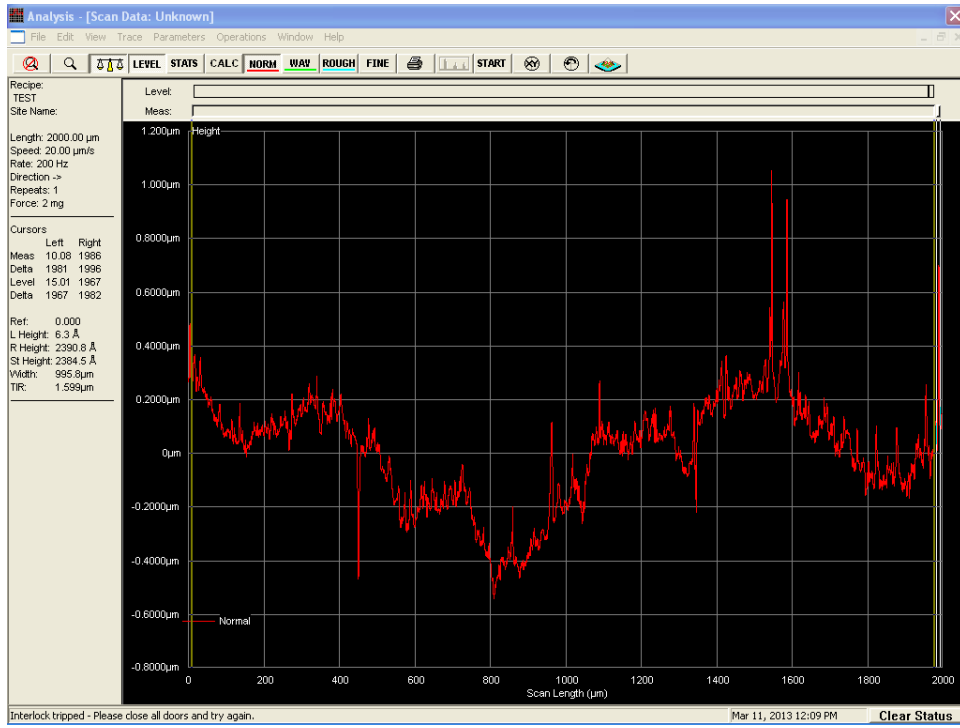
Figure C-16: ROMOR Sample 3

C.4 Nylon

Instrument: ZYGO Vertical Scanning Interferometer
Material: Nylon

Measurement	µm			Spot Size (mm)	Spot	Notes
	R_t	R_{RMS}	R_a			
1	0.804	0.027	0.021	.36x.26	A	
2	1.682	0.034	0.025	.36x.27	A	
Average (µm)	1.243	0.0305	0.023			
Average (µinch)	48.93701	1.200787	0.905512			
R_{RMS}/R_a Ratio			1.326087			

C.5 ABS

Instrument: **ZYGO Vertical Scanning Interferometer**
Material: **ABS**

Measurement	μm			Spot Size (mm)	Spot	Notes
	R_t	R_{RMS}	R_a			
1	1.417	0.086	0.061	.36x.26	A	
2	1.308	0.086	0.061	.36x.27	A	
3	3.047	0.097	0.054	.36x.27	B	
4	1.031	0.077	0.06	.36x.27	C	
Average (μm)	1.8135	0.086667	0.058333			
Average (μinch)	71.39764	3.412073	2.296588			
R_{RMS}/R_a Ratio			1.485714			

Appendix D

Spring Effects from Split Aluminum Tubing

The dimensional changes in cylindrical tubing due to being axially split are tabulated and illustrated. Tubes are 6061 T651 Aluminum of 7.5" in length, 3.5" ID, and 4.5" OD.

Table D.1: Geometric Accuracy and Form Error of ID for Split Tubes (inches)

Housing	Piece	y = 0.0" End Diameter	y = 0.0" End Roundness	y=7.5" End Diameter	y=7.5" End Roundness
1	Full Tube	3.4936	0.0028	3.4935	0.0065
1	Part A	3.4887	0.0018	3.4806	0.0031
1	Part B	3.4896	0.0016	3.4825	0.0016
2	Full Tube	3.4929	0.0022	3.4917	0.0051
2	Part A	3.4928	0.0012	3.4961	0.0023
2	Part B	3.4935	0.0022	3.4959	0.0016

Housing 1: 0.0" End
(3.49" Nominal Diameter)

Part B
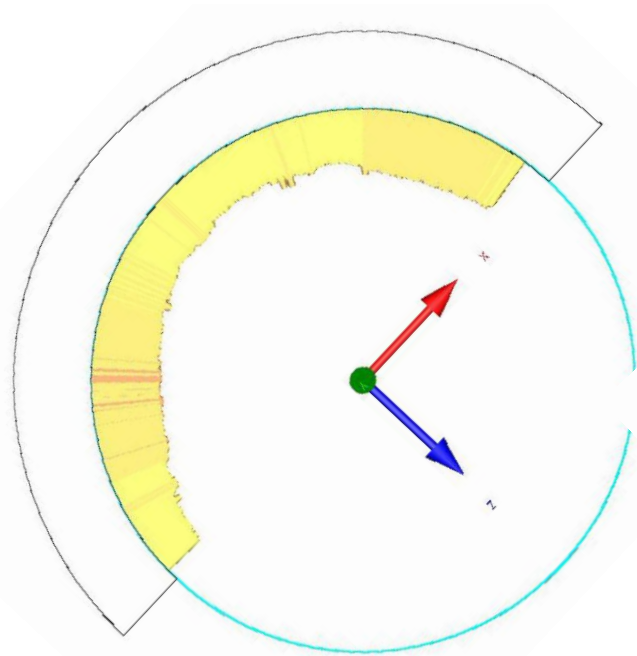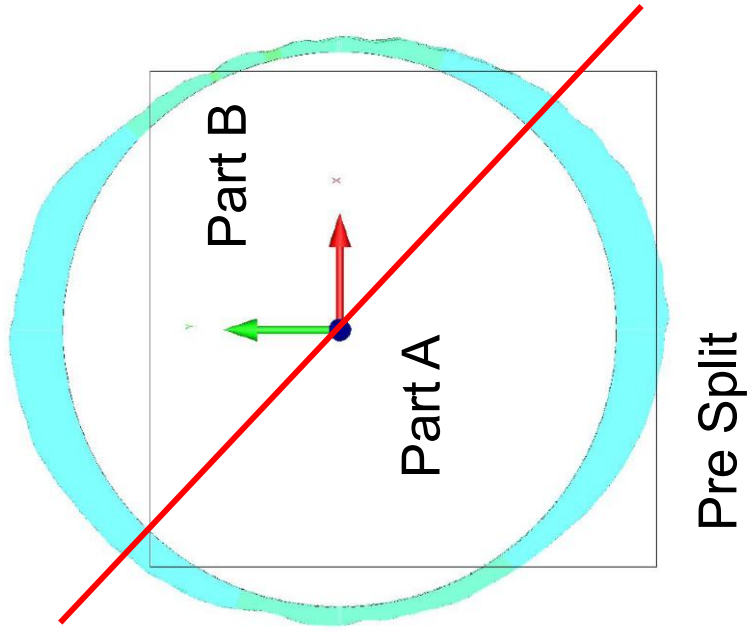
Part A

Part B
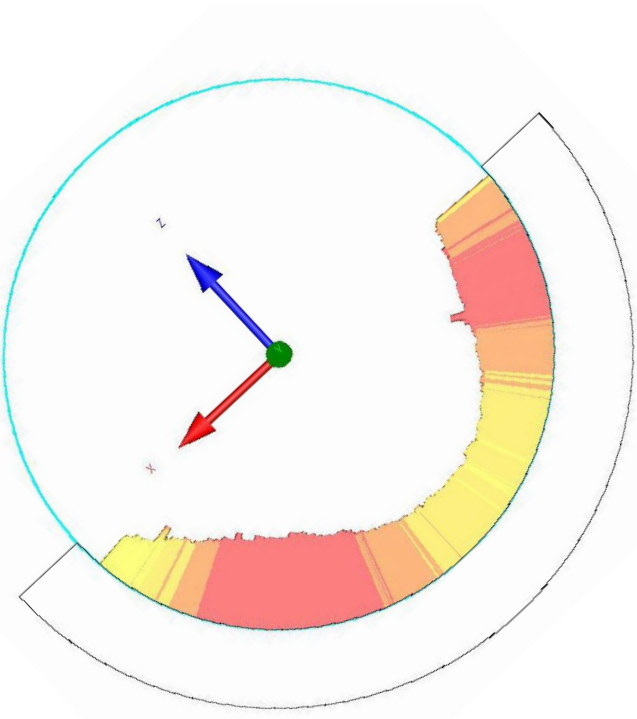
Part A

Pre Split

Housing 1: 7.5" End
(3.49" Nominal Diameter)

Part B

Part A

Pre Split

Part B

Part A
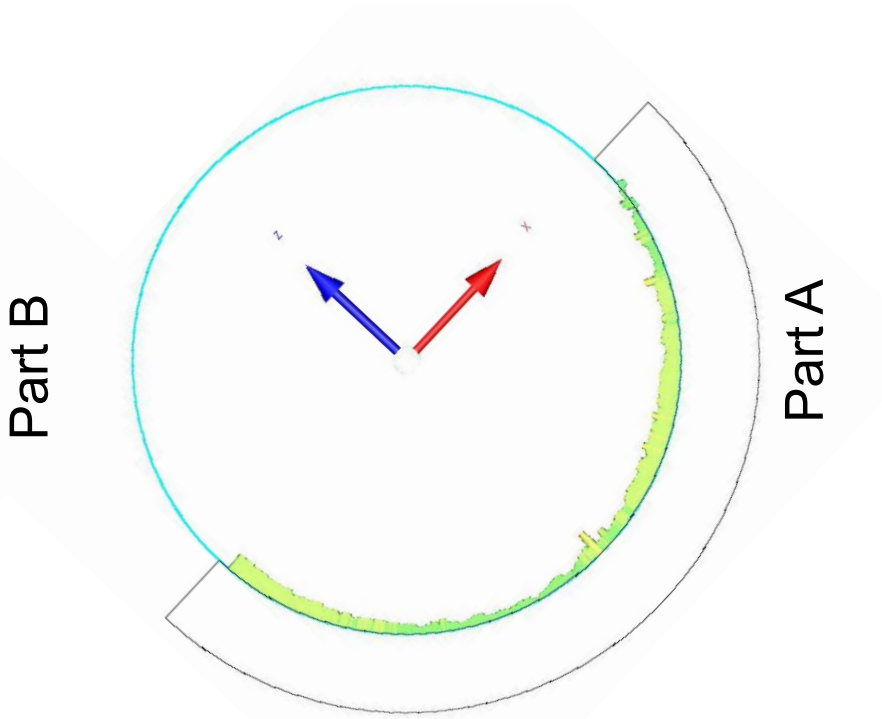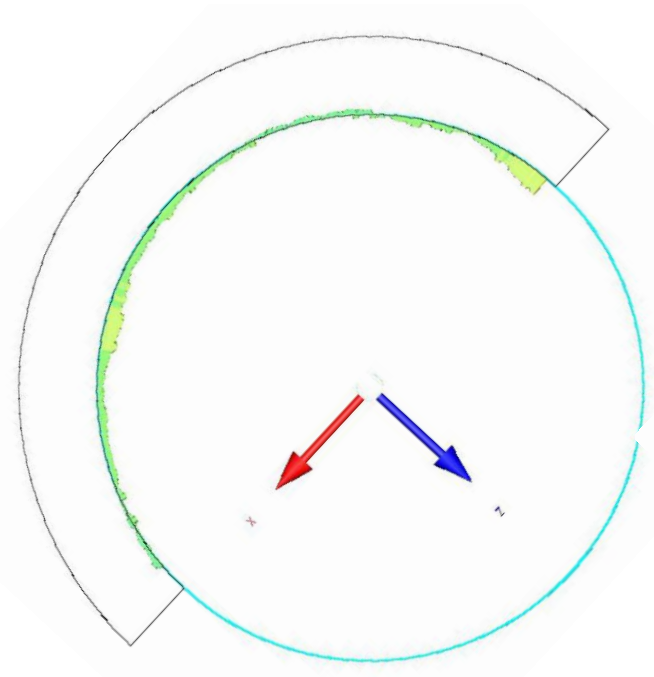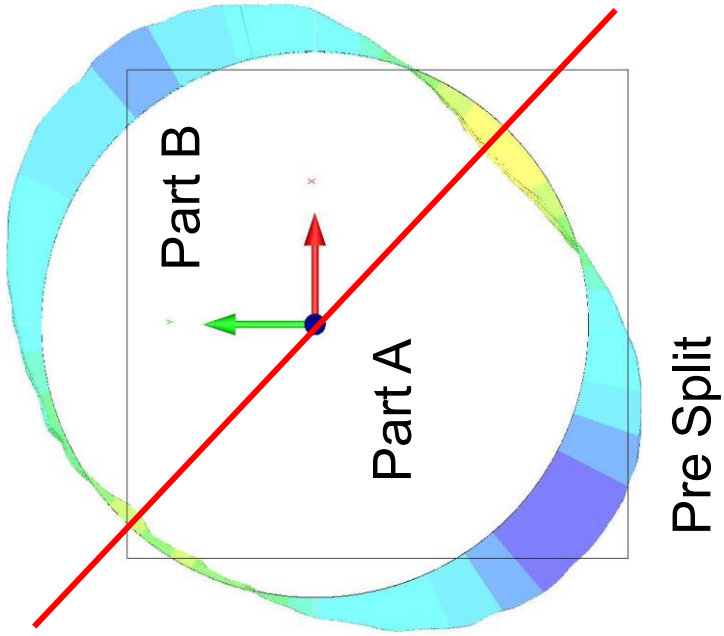
Housing 2: 0.0" End
(3.49" Nominal Diameter)

Part B

Part A

Pre Split

Part B

Part A

0.0050
0.0044
0.0038
0.0031
0.0025
0.0019
0.0013
0.0006
0.0000
-0.0006
-0.0013
-0.0019
-0.0025
-0.0031
-0.0038
-0.0044
-0.0050
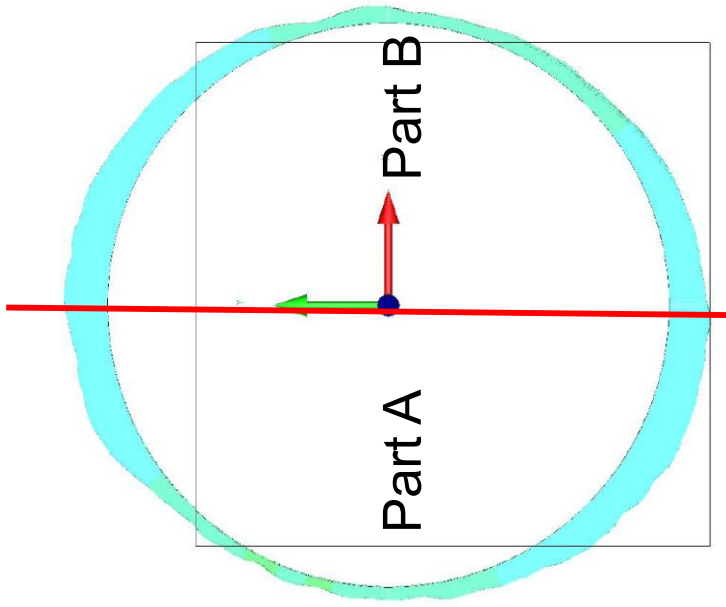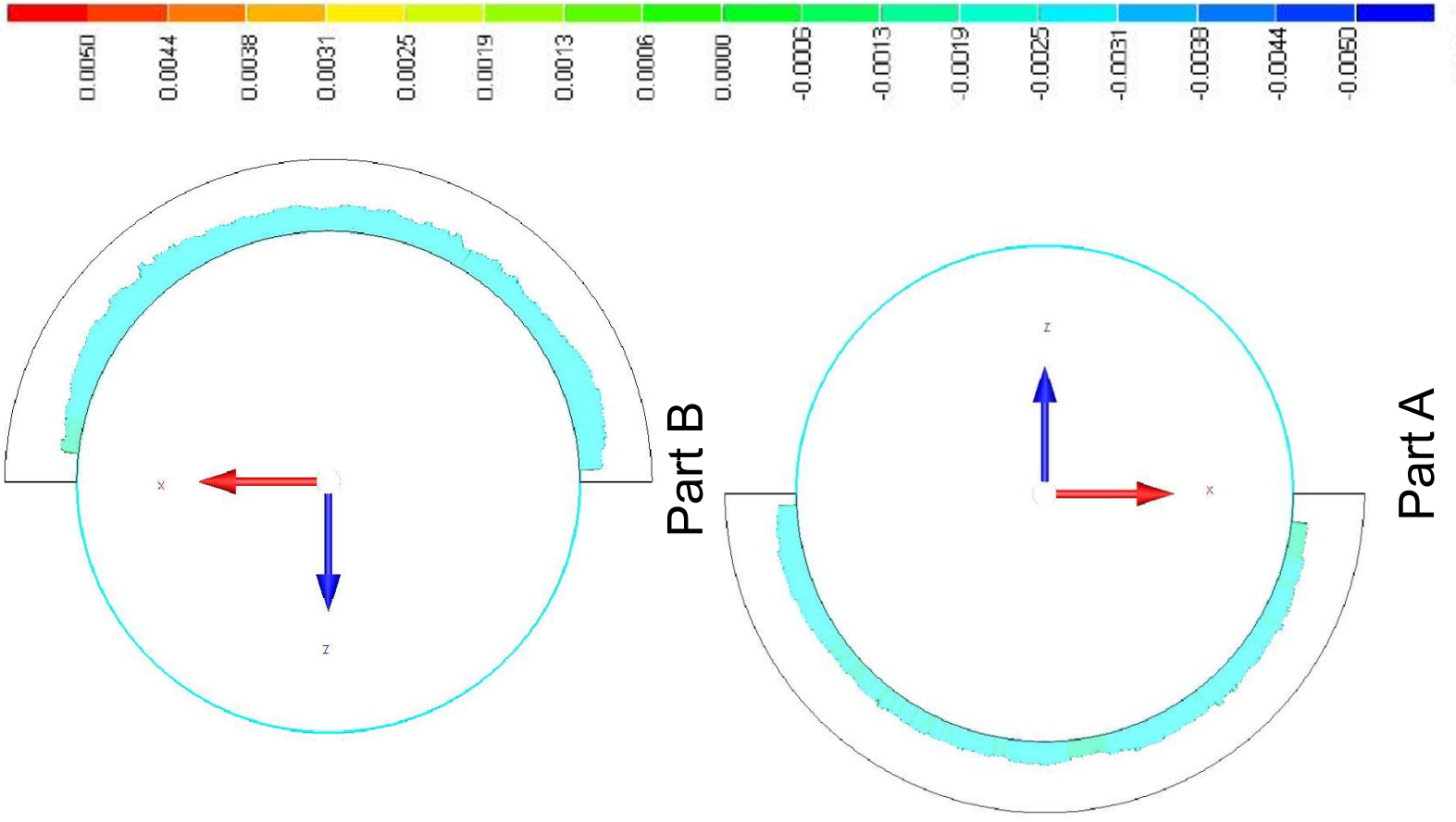
Housing 2: 7.5" End
(3.49" Nominal Diameter)

Part B

Part A

Pre Split

Part A

Part B

0.0050
0.0044
0.0038
0.0031
0.0025
0.0019
0.0013
0.0006
0.0000
-0.0006
-0.0013
-0.0019
-0.0025
-0.0031
-0.0038
-0.0044
-0.0050
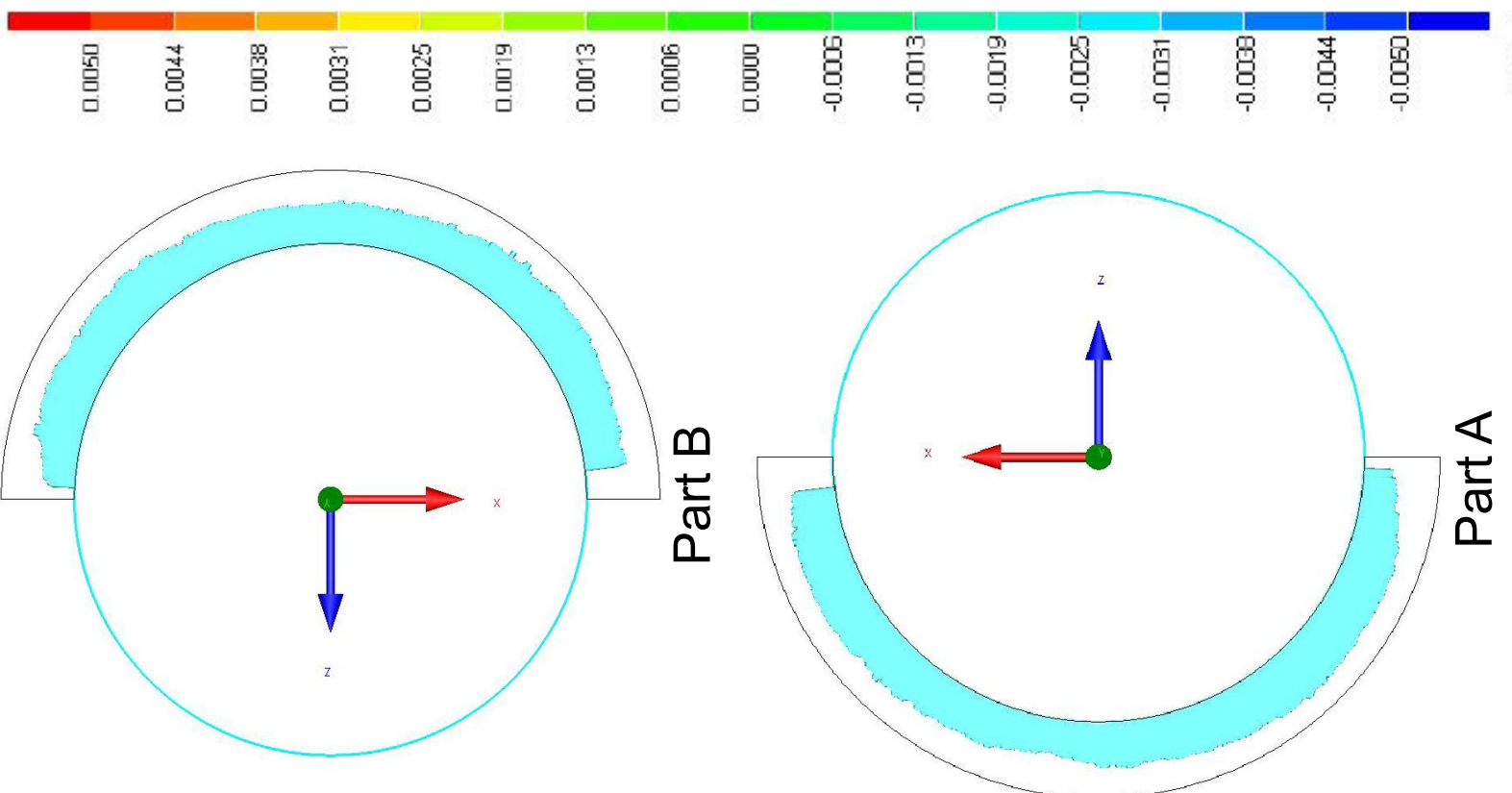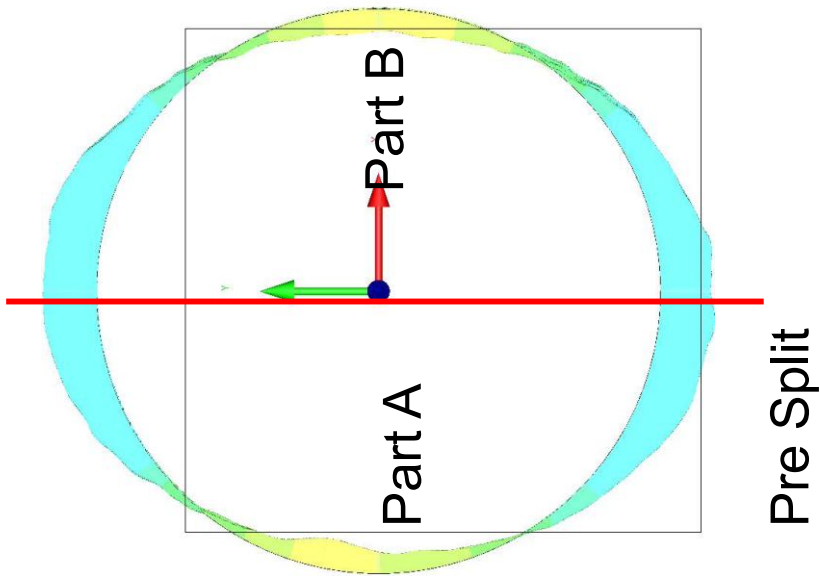
Appendix E

Wettability

A sample of Turcite® was tested for its wettability with water using a contact angle measurement instrument. The first two measurements are deemed to be reliable. The 3rd measurement had not been cleaned before testing and is therefore not considered representative of the material. The summary of the results is provided in table **??**. Figure E-1 shows a picture a water droplet on the material.

Table E.1: Results of Contact Angle Measurements

Test	Left Side	Right Side	Mean
1	93.0	85.6	89.3
2	89.5	90.9	90.2
3	74.9	75.4	75.2
Mean (1-2)	91.2	88.2	89.7
Mean (1-3)	85.8	84.0	84.9
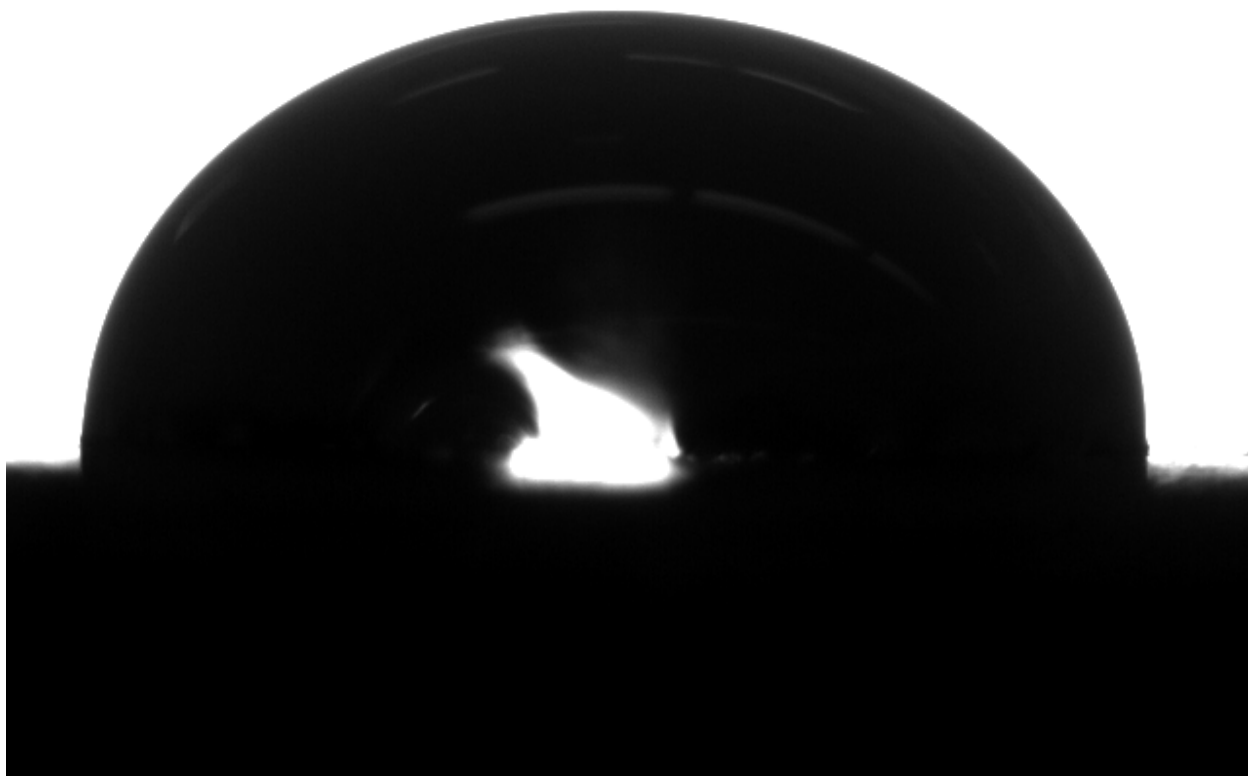
Figure E-1: Contact Angle Image

No.	Time	Tilt	Theta(L)	Theta(R)	Mean	Dev.	Height	Width
1	0	0	92.97	85.73	89.35	3.62	2.292	5.525
2	0.1	1.80E+301	93	85.75	89.38	3.63	2.292	5.525
3	0.2	3.20E+291	92.96	85.74	89.35	3.61	2.292	5.525
4	0.3	0	93.1	85.56	89.33	3.77	2.292	5.525
5	0.4	0	93.06	85.74	89.4	3.66	2.292	5.525
6	0.5	0	93.06	85.74	89.4	3.66	2.292	5.525
7	0.6	0	93.04	85.66	89.35	3.69	2.292	5.525
8	0.7	0	93.05	85.67	89.36	3.69	2.292	5.525
9	0.8	0	93.08	85.55	89.31	3.77	2.292	5.525
10	0.9	0	92.94	85.76	89.35	3.59	2.291	5.525
11	1	0	93.07	85.57	89.32	3.75	2.291	5.525
12	1.1	0	93.13	85.51	89.32	3.81	2.292	5.525
13	1.2	0	93.07	85.65	89.36	3.71	2.292	5.525
14	1.3	0	93.08	85.55	89.31	3.77	2.292	5.526
15	1.4	0	92.87	85.73	89.3	3.57	2.291	5.526
16	1.5	0	93.08	85.66	89.37	3.71	2.291	5.526
17	1.6	0	93.08	85.69	89.38	3.7	2.291	5.525
18	1.7	0	93.11	85.6	89.35	3.75	2.292	5.526
19	2	0	93.09	85.68	89.39	3.71	2.291	5.526
20	2.1	0	92.97	85.75	89.36	3.61	2.291	5.526
21	2.2	0	93.01	85.67	89.34	3.67	2.291	5.526
22	2.2	0	93	85.71	89.35	3.64	2.291	5.526
23	2.3	0	92.97	85.65	89.31	3.66	2.291	5.526
24	2.4	0	93.14	85.49	89.32	3.82	2.291	5.526
25	2.5	0	93.04	85.67	89.35	3.68	2.29	5.526
26	2.5	0	93.05	85.57	89.31	3.74	2.291	5.526
27	2.6	0	93.08	85.67	89.37	3.7	2.291	5.526
28	2.7	0	93.08	85.5	89.29	3.79	2.29	5.526
29	2.8	0	93.05	85.72	89.39	3.67	2.29	5.526
30	2.9	0	93.07	85.59	89.33	3.74	2.291	5.526
31	3	0	93.04	85.56	89.3	3.74	2.29	5.526
32	3.1	0	93.08	85.54	89.31	3.77	2.29	5.526
33	3.2	0	93.03	85.6	89.31	3.72	2.29	5.527
34	3.3	0	92.97	85.58	89.27	3.69	2.291	5.527
35	3.4	0	92.98	85.73	89.35	3.63	2.29	5.527
36	3.5	0	93.09	85.47	89.28	3.81	2.29	5.527
37	3.8	0	93.06	85.61	89.34	3.72	2.29	5.527
38	3.9	0	92.98	85.63	89.3	3.67	2.29	5.527
39	4	0	92.99	85.48	89.23	3.76	2.29	5.527
40	4.1	0	93.06	85.52	89.29	3.77	2.29	5.527
41	4.1	0	93.02	85.61	89.32	3.71	2.29	5.527
42	4.2	0	93.02	85.58	89.3	3.72	2.29	5.527
43	4.3	0	93.03	85.56	89.29	3.74	2.29	5.527
44	4.3	0	93	85.52	89.26	3.74	2.29	5.527
45	4.4	0	93.01	85.6	89.3	3.71	2.29	5.527
46	4.5	0	92.97	85.57	89.27	3.7	2.29	5.527
47	4.6	0	92.94	85.49	89.21	3.73	2.29	5.528
48	4.7	0	92.99	85.58	89.28	3.71	2.29	5.527
49	4.8	0	92.85	85.75	89.3	3.55	2.29	5.527
50	4.9	0	92.93	85.66	89.3	3.64	2.29	5.527
51	5	0	92.88	85.78	89.33	3.55	2.289	5.527
52	5.1	0	93.03	85.53	89.28	3.75	2.289	5.527
53	5.2	Nan	93.02	85.55	89.28	3.73	2.289	5.527
54	5.3	0	92.93	85.63	89.28	3.65	2.289	5.527
55	5.6	0	92.86	85.55	89.21	3.66	2.289	5.528
56	5.7	0	92.95	85.53	89.24	3.71	2.289	5.527
57	5.8	0	92.98	85.64	89.31	3.67	2.289	5.527
58	5.9	0	92.97	85.5	89.23	3.73	2.289	5.527
59	5.9	0	92.91	85.64	89.27	3.63	2.289	5.527
60	6	0	92.99	85.65	89.32	3.67	2.289	5.527
61	6.1	0	92.98	85.72	89.35	3.63	2.289	5.527
62	6.1	0	92.93	85.73	89.33	3.6	2.289	5.527

No.	Time	Tilt	Theta(L)	Theta(R)	Mean	Dev.	Height	Width
63	6.2	0	92.83	85.71	89.27	3.56	2.289	5.528
64	6.3	0	92.91	85.69	89.3	3.61	2.289	5.528
65	6.4	0	92.96	85.53	89.24	3.72	2.289	5.527
66	6.5	0	92.88	85.74	89.31	3.57	2.289	5.527
67	6.6	0	92.94	85.6	89.27	3.67	2.289	5.528
68	6.7	0	92.93	85.65	89.29	3.64	2.289	5.528
69	6.8	0	92.95	85.53	89.24	3.71	2.289	5.528
70	6.9	0	92.86	85.75	89.31	3.56	2.289	5.527
71	7	0	92.89	85.71	89.3	3.59	2.289	5.527
72	7.1	0	92.95	85.53	89.24	3.71	2.288	5.527
73	7.4	0	92.91	85.46	89.19	3.73	2.289	5.528
74	7.5	0	92.9	85.77	89.34	3.56	2.288	5.527
75	7.6	0	92.98	85.57	89.27	3.7	2.288	5.527
76	7.7	0	93	85.43	89.21	3.79	2.288	5.528
77	7.7	0	92.99	85.47	89.23	3.76	2.288	5.527
78	7.8	0	92.97	85.47	89.22	3.75	2.288	5.528
79	7.9	0	92.95	85.63	89.29	3.66	2.288	5.527
80	8	0	92.85	85.72	89.29	3.56	2.288	5.527
81	8	0	92.94	85.47	89.2	3.73	2.287	5.528
82	8.1	0	92.93	85.54	89.23	3.7	2.288	5.528
83	8.2	0	92.91	85.5	89.2	3.7	2.288	5.528
84	8.3	0	92.84	85.69	89.26	3.57	2.288	5.527
85	8.4	0	92.91	85.72	89.31	3.59	2.287	5.527
86	8.5	0	92.91	85.52	89.21	3.69	2.288	5.528
87	8.6	0	92.94	85.7	89.32	3.62	2.287	5.527
88	8.7	0	92.96	85.49	89.23	3.73	2.287	5.528
89	8.8	0	92.86	85.79	89.32	3.53	2.287	5.527
90	8.9	0	92.81	85.71	89.26	3.55	2.287	5.527
91	9.2	0	92.93	85.54	89.23	3.69	2.287	5.527
92	9.3	0	92.88	85.76	89.32	3.56	2.287	5.527
93	9.4	0	92.83	85.79	89.31	3.52	2.287	5.527
94	9.4	0	92.94	85.54	89.24	3.7	2.287	5.527
95	9.5	0	92.91	85.63	89.27	3.64	2.287	5.527
96	9.6	0	93.05	85.53	89.29	3.76	2.287	5.527
97	9.7	0	93.06	85.44	89.25	3.81	2.287	5.527
98	9.8	0	92.85	85.74	89.29	3.56	2.286	5.527
99	9.9	0	92.91	85.71	89.31	3.6	2.287	5.527
100	9.9	0	92.8	85.71	89.25	3.54	2.286	5.528

Mean:			92.98	85.62	89.3	3.68	2.289	5.527
Stand.dev.:			0.01	0.01	0	0.01	0	0

No.	Time	Tilt	Theta(L)	Theta(R)	Mean	Dev.	Height	Width
1	0	3.00E+166	89.54	90.79	90.16	0.63	2.332	5.926
2	0.1	0	89.58	91.38	90.48	0.9	2.33	5.924
3	0.2	0	89.51	90.87	90.19	0.68	2.332	5.926
4	0.3	0	89.44	90.7	90.07	0.63	2.331	5.926
5	0.4	0	89.56	91.15	90.35	0.79	2.33	5.925
6	0.5	0	89.51	91.24	90.37	0.87	2.33	5.925
7	0.6	0	89.54	91.14	90.34	0.8	2.33	5.925
8	0.7	0	89.6	90.96	90.28	0.68	2.33	5.925
9	0.8	0	89.52	91.44	90.48	0.96	2.329	5.924
10	0.9	0	89.49	91.39	90.44	0.95	2.329	5.925
11	1	0	89.55	91.13	90.34	0.79	2.329	5.926
12	1.1	0	89.54	91.06	90.3	0.76	2.329	5.926
13	1.2	0	89.5	91	90.25	0.75	2.33	5.926
14	1.3	0	89.44	90.86	90.15	0.71	2.329	5.927
15	1.4	0	89.44	90.91	90.18	0.73	2.329	5.927
16	1.5	0	89.41	91.29	90.35	0.94	2.328	5.927
17	1.6	0	89.52	91.36	90.44	0.92	2.329	5.927
18	1.7	0	89.58	91.28	90.43	0.85	2.329	5.927
19	1.8	0	89.48	91.25	90.36	0.89	2.328	5.928
20	2.1	0	89.45	91.35	90.4	0.95	2.327	5.928
21	2.2	0	89.53	91.05	90.29	0.76	2.327	5.928
22	2.3	0	89.48	91.15	90.32	0.84	2.327	5.928
23	2.3	0	89.51	91.14	90.32	0.82	2.326	5.928
24	2.4	0	89.49	91.2	90.34	0.86	2.326	5.928
25	2.5	0	89.49	91.25	90.37	0.88	2.326	5.928
26	2.9	0	89.42	91.3	90.36	0.94	2.325	5.928
27	3	0	89.49	91.08	90.28	0.79	2.325	5.929
28	3	0	89.42	90.96	90.19	0.77	2.325	5.929
29	3.1	0	89.54	91.17	90.35	0.82	2.325	5.929
30	3.2	0	89.51	91.18	90.34	0.83	2.325	5.929
31	3.2	0	89.39	90.93	90.16	0.77	2.325	5.93
32	3.3	0	89.45	91.11	90.28	0.83	2.325	5.929
33	3.4	0	89.48	91.1	90.29	0.81	2.324	5.929
34	3.4	0	89.51	91	90.26	0.74	2.324	5.929
35	3.5	0	89.39	90.98	90.19	0.79	2.324	5.93
36	3.6	0	89.48	91.04	90.26	0.78	2.324	5.929
37	3.6	0	89.52	91.08	90.3	0.78	2.323	5.929
38	4	0	89.48	91.11	90.3	0.82	2.324	5.929
39	4	0	89.38	91.11	90.24	0.87	2.323	5.93
40	4.1	0	89.43	91.03	90.23	0.8	2.323	5.93
41	4.2	0	89.57	91.08	90.33	0.75	2.324	5.929
42	4.2	0	89.58	91.06	90.32	0.74	2.323	5.929
43	4.3	0	89.47	91.09	90.28	0.81	2.323	5.929
44	4.4	0	89.48	91.02	90.25	0.77	2.323	5.93
45	4.4	0	89.53	90.88	90.2	0.67	2.323	5.93
46	4.5	0	89.48	91.27	90.38	0.89	2.323	5.929
47	4.6	0	89.49	91.11	90.3	0.81	2.322	5.929
48	4.7	0	89.46	91.08	90.27	0.81	2.322	5.93
49	4.8	0	89.57	91.05	90.31	0.74	2.323	5.929
50	4.9	0	89.44	91.05	90.24	0.81	2.323	5.93
51	5	0	89.5	91.29	90.39	0.9	2.322	5.929
52	5.1	0	89.48	91.46	90.47	0.99	2.322	5.929
53	5.2	0	89.59	91.46	90.52	0.93	2.322	5.929
54	5.3	0	89.57	90.83	90.2	0.63	2.322	5.932
55	5.4	0	89.5	90.8	90.15	0.65	2.322	5.932
56	5.7	Nan	89.57	91.34	90.45	0.88	2.322	5.933
57	5.8	0	89.54	91.09	90.31	0.77	2.321	5.933
58	5.9	0	89.49	91.04	90.26	0.77	2.322	5.934
59	5.9	0	89.59	91.19	90.39	0.8	2.321	5.933
60	6	0	89.51	91.18	90.34	0.84	2.321	5.936
61	6.1	0	89.54	90.43	89.99	0.44	2.321	5.941
62	6.1	0	89.46	90.37	89.92	0.45	2.321	5.942

No.	Time	Tilt	Theta(L)	Theta(R)	Mean	Dev.	Height	Width
63	6.2	0	89.59	90.17	89.88	0.29	2.321	5.942
64	6.3	0	89.52	90.4	89.96	0.44	2.32	5.942
65	6.4	0	89.55	90.32	89.93	0.39	2.321	5.942
66	6.5	0	89.55	90.1	89.82	0.28	2.321	5.943
67	6.6	0	89.45	90.07	89.76	0.31	2.32	5.944
68	6.7	0	89.48	90.02	89.75	0.27	2.32	5.944
69	6.8	0	89.55	90.07	89.81	0.26	2.319	5.944
70	6.9	0	89.61	90.19	89.9	0.29	2.319	5.944
71	7	0	89.64	90.13	89.88	0.24	2.318	5.944
72	7.1	0	89.5	90.19	89.84	0.35	2.319	5.944
73	7.2	0	89.55	90.26	89.9	0.35	2.318	5.944
74	7.5	Nan	89.58	90.37	89.97	0.39	2.317	5.944
75	7.6	Nan	89.52	90.13	89.83	0.3	2.318	5.944
76	7.7	Nan	89.6	90.4	90	0.4	2.317	5.944
77	7.8	Nan	89.51	90.32	89.92	0.41	2.317	5.944
78	7.8	Nan	89.54	90.48	90.01	0.47	2.317	5.944
79	7.9	Nan	89.57	90.52	90.05	0.48	2.317	5.943
80	8	Nan	89.6	90.4	90	0.4	2.317	5.944
81	8.1	Nan	89.55	90.53	90.04	0.49	2.316	5.944
82	8.1	Nan	89.61	90.6	90.11	0.5	2.316	5.943
83	8.2	Nan	89.56	90.46	90.01	0.45	2.316	5.944
84	8.3	Nan	89.56	90.57	90.07	0.51	2.316	5.944
85	8.4	Nan	89.51	90.51	90.01	0.5	2.315	5.944
86	8.5	Nan	89.56	90.59	90.07	0.51	2.314	5.944
87	8.6	Nan	89.54	90.62	90.08	0.54	2.314	5.944
88	8.7	Nan	89.63	90.68	90.16	0.52	2.314	5.943
89	8.8	Nan	89.54	90.68	90.11	0.57	2.314	5.943
90	8.9	Nan	89.55	90.63	90.09	0.54	2.314	5.944
91	9	Nan	89.59	90.72	90.16	0.57	2.314	5.943
92	9.3	Nan	89.64	90.99	90.32	0.67	2.314	5.943

Mean:			89.5190217	90.8675	90.1928261	0.67413043	2.32268478	5.93371739
Stand.dev.:			0.05789456	0.39133366	0.1890539	0.2059561	0.00490779	0.00741594

No.	Time	Tilt	Theta(L)	Theta(R)	Mean	Dev.	Height	Width
1	0	8.90E+252	74.81	75.58	75.2	0.38	1.903	6.419
2	0.1	0	74.63	75.77	75.2	0.57	1.902	6.419
3	0.2	0	74.89	75.42	75.15	0.27	1.902	6.419
4	0.3	0	75.26	75.24	75.25	0.01	1.903	6.419
5	0.4	0	75.24	75.23	75.23	0	1.903	6.419
6	0.5	0	75	75.39	75.19	0.19	1.902	6.419
7	0.6	0	74.87	75.47	75.17	0.3	1.902	6.419
8	0.7	0	74.96	75.51	75.23	0.28	1.902	6.419
9	0.8	0	75.21	75.27	75.24	0.03	1.902	6.419
10	0.9	0	75	75.43	75.21	0.22	1.902	6.419
11	1	0	74.78	75.63	75.21	0.42	1.902	6.419
12	1.1	0	74.92	75.44	75.18	0.26	1.901	6.419
13	1.2	0	75.1	75.25	75.18	0.07	1.901	6.419
14	1.3	0	75	75.58	75.29	0.29	1.902	6.419
15	1.4	0	74.95	75.46	75.21	0.25	1.901	6.419
16	1.5	0	75.18	75.29	75.24	0.06	1.901	6.419
17	1.6	0	74.74	75.64	75.19	0.45	1.901	6.419
18	1.7	0	74.66	75.72	75.19	0.53	1.901	6.419
19	1.8	0	74.87	75.48	75.18	0.3	1.9	6.418
20	2.1	0	75.14	75.36	75.25	0.11	1.9	6.419
21	2.2	0	74.65	75.62	75.14	0.48	1.9	6.419
22	2.3	0	74.94	75.47	75.2	0.26	1.9	6.419
23	2.3	0	75.1	75.2	75.15	0.05	1.9	6.419
24	2.4	0	74.54	75.67	75.11	0.56	1.9	6.419
25	2.5	0	74.82	75.62	75.22	0.4	1.9	6.418
26	2.6	0	74.94	75.27	75.1	0.17	1.9	6.419
27	2.7	0	74.56	75.78	75.17	0.61	1.901	6.418
28	2.7	0	74.89	75.41	75.15	0.26	1.899	6.419
29	2.8	0	74.82	75.42	75.12	0.3	1.899	6.419
30	2.9	0	74.86	75.43	75.14	0.28	1.899	6.419
31	3	0	74.79	75.51	75.15	0.36	1.9	6.419
32	3.1	0	74.86	75.31	75.09	0.23	1.899	6.419
33	3.2	0	74.98	75.33	75.15	0.17	1.899	6.419
34	3.3	0	74.87	75.42	75.15	0.27	1.899	6.419
35	3.4	0	74.76	75.57	75.17	0.4	1.9	6.418
36	3.5	0	74.9	75.5	75.2	0.3	1.9	6.418
37	3.6	0	74.93	75.52	75.23	0.29	1.899	6.418
38	3.9	0	75.25	75.23	75.24	0.01	1.899	6.418
39	4	0	74.64	75.68	75.16	0.52	1.899	6.418
40	4.1	0	74.77	75.52	75.15	0.38	1.898	6.418
41	4.1	0	75.07	75.27	75.17	0.1	1.899	6.418
42	4.2	0	74.89	75.48	75.18	0.29	1.899	6.418
43	4.3	0	74.91	75.44	75.18	0.27	1.898	6.418
44	4.4	0	74.94	75.37	75.15	0.22	1.898	6.418
45	4.5	0	74.93	75.48	75.21	0.27	1.899	6.418
46	4.5	0	75	75.34	75.17	0.17	1.899	6.418
47	4.6	0	74.76	75.54	75.15	0.39	1.898	6.418
48	4.7	0	74.83	75.45	75.14	0.31	1.898	6.418
49	4.8	0	74.9	75.47	75.19	0.29	1.898	6.418
50	4.9	0	74.93	75.34	75.14	0.2	1.898	6.418
51	5	0	75.01	75.28	75.15	0.14	1.898	6.418
52	5.1	0	74.92	75.43	75.17	0.26	1.898	6.418
53	5.2	0	74.68	75.53	75.11	0.43	1.898	6.418
54	5.3	0	74.89	75.5	75.2	0.3	1.898	6.418
55	5.4	0	74.92	75.32	75.12	0.2	1.898	6.418
56	5.8	0	75.14	75.22	75.18	0.04	1.898	6.418
57	5.9	0	74.81	75.62	75.21	0.41	1.897	6.418
58	6	0	74.69	75.68	75.19	0.5	1.897	6.418
59	6	0	75.25	75.1	75.17	0.08	1.897	6.418
60	6.2	0	75.13	75.25	75.19	0.06	1.897	6.418
61	6.2	0	74.67	75.59	75.13	0.46	1.897	6.418

No.	Time	Tilt	Theta(L)	Theta(R)	Mean	Dev.	Height	Width
62	6.3	0	74.97	75.26	75.12	0.14	1.897	6.419
63	6.4	0	74.77	75.6	75.19	0.41	1.896	6.418
64	6.5	0	74.54	75.76	75.15	0.61	1.896	6.419
65	6.6	0	75.09	75.29	75.19	0.1	1.897	6.419
66	6.7	0	75.18	75.18	75.18	0	1.897	6.418
67	6.8	0	74.94	75.56	75.25	0.31	1.896	6.418
68	6.9	0	74.94	75.61	75.27	0.33	1.896	6.418
69	7	0	75.1	75.27	75.19	0.09	1.897	6.418
70	7.1	0	75.3	75.16	75.23	0.07	1.897	6.418
71	7.2	0	74.93	75.44	75.19	0.26	1.896	6.418
72	7.3	0	74.83	75.67	75.25	0.42	1.896	6.418
73	7.4	0	74.99	75.37	75.18	0.19	1.896	6.418
74	7.7	0	75.14	75.17	75.15	0.02	1.896	6.418
75	7.8	0	74.58	75.79	75.19	0.6	1.894	6.418
76	7.9	0	75.02	75.4	75.21	0.19	1.896	6.418
77	8	Nan	74.73	75.61	75.17	0.44	1.895	6.418
78	8.1	0	74.77	75.61	75.19	0.42	1.895	6.418
79	8.2	0	74.92	75.34	75.13	0.21	1.896	6.419
80	8.3	0	74.84	75.58	75.21	0.37	1.895	6.418
81	8.4	0	75.17	75.22	75.2	0.03	1.896	6.418
82	8.5	0	74.57	75.78	75.18	0.61	1.894	6.418
83	8.6	0	74.82	75.51	75.17	0.34	1.895	6.419
84	8.7	0	75.33	75.05	75.19	0.14	1.895	6.418
85	8.7	0	74.89	75.33	75.11	0.22	1.896	6.418
86	8.9	0	74.75	75.6	75.18	0.42	1.895	6.418
87	9	0	74.83	75.46	75.14	0.31	1.895	6.419
88	9	0	75.13	75.25	75.19	0.06	1.895	6.418
89	9.1	0	74.98	75.34	75.16	0.18	1.896	6.418
90	9.2	0	74.99	75.32	75.16	0.16	1.895	6.418
91	9.3	0	74.93	75.36	75.14	0.21	1.895	6.418
92	9.7	0	74.79	75.46	75.13	0.33	1.895	6.418
93	9.8	0	74.98	75.37	75.17	0.2	1.895	6.418
94	9.9	0	74.87	75.38	75.13	0.26	1.895	6.418
95	10	0	74.93	75.48	75.2	0.28	1.894	6.418
96	10.1	0	74.92	75.37	75.14	0.23	1.895	6.418
97	10.2	0	74.75	75.57	75.16	0.41	1.894	6.418
98	10.3	0	74.8	75.57	75.18	0.39	1.894	6.418
99	10.4	0	74.87	75.37	75.12	0.25	1.894	6.418
100	10.5	0	74.84	75.47	75.16	0.31	1.894	6.418

Mean:			74.91	75.44	75.18	0.27	1.898	6.418
Stand.dev.:			0.02	0.02	0	0.02	0	0

Appendix F

Master Shaft Measurements
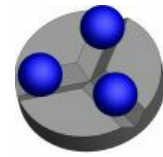
The measurements of the Master Shafts by CMM are provided below:

Table F.1: Manufacturing Tolerances in Master Shafts

Shaft	1	2	3	
Designed D/C Ratio	800	250	400	
Nominal Design Diameter	3.2345	3.2434	3.2386	Inches
Mean Measured Diameter	3.2345	3.2431	3.2389	Inches
Manufacturing Difference	0.0000	0.0003	-0.0003	Inches
Actual Diametrical Gap	0.004	0.0126	0.0084	Inches
Actual D/C Ratio	808	256	385	
Measured Roundness Error	0.0002	0.0002	0.0002	Inches

Precision Engineering Research Group
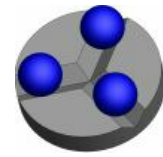
Plan Name			**Date**				
3.2345 Shaft			April 9, 2013				
Drawing No.			**Time**				
* drawingno *			3:31:50 pm				
Operator			**Incremental Part Number**				
Master			20120816 3.2345 Shaft1				

Name	ID	Actual	Nominal	pos Tol	neg Tol	Diff	<--|-->
Overall Result							
All Characteristics:		15					
Out of tolerance:		0					
Over Warning Limit:		0					
Not Calculated:	0						
Shaft Diameter	D	3.2345	3.2345	0.0010	-0.0010	0.0000	|
Shaft Cylindricity	GDT Cyl	0.0003	0.0000	0.0004		0.0003	|---
Diameter_Circle180	D	3.2345	3.2345	0.0010	-0.0010	0.0000	-|
Diameter_Circle158	D	3.2345	3.2345	0.0010	-0.0010	0.0000	-|
Diameter_Circle136	D	3.2344	3.2345	0.0010	-0.0010	-0.0001	-|
Diameter_Circle114	D	3.2344	3.2345	0.0010	-0.0010	-0.0001	-|
Diameter_Circle92	D	3.2346	3.2345	0.0010	-0.0010	0.0001	|-
Diameter_Circle70	D	3.2347	3.2345	0.0010	-0.0010	0.0002	|-
Roundness_Circle180	GDT Roun	0.0001	0.0000	0.0004		0.0001	|--
Roundness_Circle158	GDT Roun	0.0001	0.0000	0.0004		0.0001	|--
Roundness_Circle136	GDT Roun	0.0001	0.0000	0.0004		0.0001	|--
Roundness_Circle114	GDT Roun	0.0001	0.0000	0.0004		0.0001	|--
Roundness_Circle92	GDT Roun	0.0001	0.0000	0.0004		0.0001	|--
Roundness_Circle70	GDT Roun	0.0001	0.0000	0.0004		0.0001	|--
Locating Cylinder	GDT Cyl	0.0002	0.0000	0.0004		0.0002	|--

1

Precision Engineering Research Group

Plan Name	**Date**	
3.244 Shaft1	September 28, 2012	
Drawing No.	**Time**	
* drawingno *	10:06:51 am	
Operator	**Incremental Part Number**	
Master	3.244 Shaft Top	

Name	ID	Actual	Nominal	pos Tol	neg Tol	Diff	<--|-->
Overall Result							
All Characteristics:		15					
Out of tolerance:		1					
Over Warning Limit:		0					
Not Calculated:		0					
Shaft Diameter	D	3.2432	3.2440	0.0010	-0.0010	-0.0008	----|
Shaft Cylindricity	GDT Cyl	0.0005	0.0000	0.0004		0.0005	0.0001
Diameter_Circle180	D	3.2431	3.2440	0.0010	-0.0010	-0.0009	----|
Diameter_Circle158	D	3.2430	3.2440	0.0010	-0.0010	-0.0010	----|
Diameter_Circle136	D	3.2430	3.2440	0.0010	-0.0010	-0.0010	----|
Diameter_Circle114	D	3.2431	3.2440	0.0010	-0.0010	-0.0009	----|
Diameter_Circle92	D	3.2434	3.2440	0.0010	-0.0010	-0.0006	---|
Diameter_Circle70	D	3.2435	3.2440	0.0010	-0.0010	-0.0005	--|
Roundness_Circle180	GDT Roun	0.0002	0.0000	0.0004		0.0002	|---
Roundness_Circle158	GDT Roun	0.0003	0.0000	0.0004		0.0003	|---
Roundness_Circle136	GDT Roun	0.0002	0.0000	0.0004		0.0002	|---
Roundness_Circle114	GDT Roun	0.0002	0.0000	0.0004		0.0002	|---
Roundness_Circle92	GDT Roun	0.0002	0.0000	0.0004		0.0002	|---
Roundness_Circle70	GDT Roun	0.0002	0.0000	0.0004		0.0002	|---
Locating Cylinder	GDT Cyl	0.0003	0.0000	0.0004		0.0003	|---

Precision Engineering Research Group

Plan Name	Date
3.244 Shaft1	September 28, 2012

Drawing No.	Time
* drawingno *	10:48:27 am

Operator	Incremental Part Number
Master	3.244 Shaft Bottom

Name	ID	Actual	Nominal	pos Tol	neg Tol	Diff	<--|-->
Overall Result							
All Characteristics:		15					
Out of tolerance:		1					
Over Warning Limit:		0					
Not Calculated:		0					
Shaft Diameter	D	3.2430	3.2440	0.0010	-0.0010	-0.0010	----|
Shaft Cylindricity	GDT Cyl	0.0003	0.0000	0.0004		0.0003	|---
Diameter_Circle180	D	3.2430	3.2440	0.0010	-0.0010	-0.0010	----|
Diameter_Circle158	D	3.2430	3.2440	0.0010	-0.0010	-0.0010	----|
Diameter_Circle136	D	3.2430	3.2440	0.0010	-0.0010	-0.0010	----|
Diameter_Circle114	D	3.2430	3.2440	0.0010	-0.0010	-0.0010	----|
Diameter_Circle92	D	3.2429	3.2440	0.0010	-0.0010	-0.0011	-0.0001
Diameter_Circle70	D	3.2430	3.2440	0.0010	-0.0010	-0.0010	----|
Roundness_Circle180	GDT Roun	0.0002	0.0000	0.0004		0.0002	|---
Roundness_Circle158	GDT Roun	0.0002	0.0000	0.0004		0.0002	|---
Roundness_Circle136	GDT Roun	0.0002	0.0000	0.0004		0.0002	|---
Roundness_Circle114	GDT Roun	0.0002	0.0000	0.0004		0.0002	|---
Roundness_Circle92	GDT Roun	0.0002	0.0000	0.0004		0.0002	|---
Roundness_Circle70	GDT Roun	0.0002	0.0000	0.0004		0.0002	|---
Locating Cylinder	GDT Cyl	0.0001	0.0000	0.0004		0.0001	|--

Precision Engineering Research Group
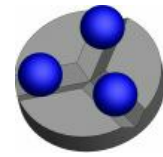
Plan Name 3.2386 Shaft	**Date** October 26, 2012
Drawing No. * drawingno *	**Time** 8:27:25 am
Operator Master	**Incremental Part Number** 3.2386 Shaft Discontinuity Up2
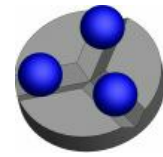
Name	ID	Actual	Nominal	pos Tol	neg Tol	Diff	<--|-->
Overall Result							
All Characteristics:		16					
Out of tolerance:		0					
Over Warning Limit:		0					
Not Calculated:		0					
Shaft Diameter	D	3.2388	3.2386	0.0010	-0.0010	0.0002	|-
Shaft Cylindricity	GDT Cyl	0.0002	0.0000	0.0004		0.0002	|---
Diameter_Circle180	D	3.2389	3.2386	0.0010	-0.0010	0.0003	|--
Diameter_Circle158	D	3.2389	3.2386	0.0010	-0.0010	0.0003	|--
Diameter_Circle136	D	3.2388	3.2386	0.0010	-0.0010	0.0002	|-
Diameter_Circle114	D	3.2388	3.2386	0.0010	-0.0010	0.0002	|-
Diameter_Circle92	D	3.2388	3.2386	0.0010	-0.0010	0.0002	|-
Diameter_Circle70	D	3.2388	3.2386	0.0010	-0.0010	0.0002	|-
Roundness_Circle180	GDT Roun	0.0002	0.0000	0.0004		0.0002	|--
Roundness_Circle158	GDT Roun	0.0002	0.0000	0.0004		0.0002	|--
Roundness_Circle136	GDT Roun	0.0002	0.0000	0.0004		0.0002	|--
Roundness_Circle114	GDT Roun	0.0002	0.0000	0.0004		0.0002	|--
Roundness_Circle92	GDT Roun	0.0002	0.0000	0.0004		0.0002	|--
Roundness_Circle70	GDT Roun	0.0002	0.0000	0.0004		0.0002	|--
Locating Cylinder	GDT Cyl	0.0003	0.0000	0.0004		0.0003	|----

Precision Engineering Research Group

Plan Name	**Date**
3.2386 Shaft	October 26, 2012
Drawing No.	**Time**
* drawingno *	8:10:03 am
Operator	**Incremental Part Number**
Master	3.2386 Shaft Discontinuity Down2

Name	ID	Actual	Nominal	pos Tol	neg Tol	Diff	<--|-->
Overall Result							
All Characteristics:		15					
Out of tolerance:		0					
Over Warning Limit:		0					
Not Calculated:	0						
Shaft Diameter	D	3.2389	3.2386	0.0010	-0.0010	0.0003	|--
Shaft Cylindricity	GDT Cyl	0.0004	0.0000	0.0004		0.0004	|----
Diameter_Circle180	D	3.2389	3.2386	0.0010	-0.0010	0.0003	|--
Diameter_Circle158	D	3.2388	3.2386	0.0010	-0.0010	0.0002	|-
Diameter_Circle136	D	3.2388	3.2386	0.0010	-0.0010	0.0002	|-
Diameter_Circle114	D	3.2389	3.2386	0.0010	-0.0010	0.0003	|--
Diameter_Circle92	D	3.2390	3.2386	0.0010	-0.0010	0.0004	|--
Diameter_Circle70	D	3.2392	3.2386	0.0010	-0.0010	0.0006	|---
Roundness_Circle180	GDT Roun	0.0002	0.0000	0.0004		0.0002	|--
Roundness_Circle158	GDT Roun	0.0002	0.0000	0.0004		0.0002	|--
Roundness_Circle136	GDT Roun	0.0002	0.0000	0.0004		0.0002	|--
Roundness_Circle114	GDT Roun	0.0002	0.0000	0.0004		0.0002	|--
Roundness_Circle92	GDT Roun	0.0002	0.0000	0.0004		0.0002	|--
Roundness_Circle70	GDT Roun	0.0002	0.0000	0.0004		0.0002	|---
Locating Cylinder	GDT Cyl	0.0003	0.0000	0.0004		0.0003	|----

Appendix G

Coordinate Measuring Machine Bearing Metrology Results

The metrology of the Turcite® bearings manufactured in this project are provided. All measurements were with a ZEISS Eclipse 550 Coordinate Measuring Machine (CMM) with a VAST XXT scanning probe. Tabulated measurement results are provided for each bearing, as is a graphical picture of the results at 200 times error magnification. Each graphical result has a scale to the right that is color coded to show variation from a nominal diameter. This provides direct insight into the variability in measurements of the bearing surface. A summary of the results is provided below:

Table G.1: CMM Measured Diameters of Bearings (Inches)

Bearing Configuration	Master Shaft Diameter			Diameter Error	Notes
	3.2345	3.2431	3.2389		
Plain Journal Bearing	3.2346			0.0001	1,3
180 Degree 3 Port Bearing	3.2356			0.0011	2,3
165 Degree 3 Port Bearing		3.2434		0.0003	2,3
Center Lift Bearing			3.2401	0.0012	2
2 Port Bearing			3.2410	0.0021	2
Stave Bearing			3.2390	0.0001	2
Comb Bearing			3.2398	0.0009	2
Hydrostatic Lift Bearing			3.2391	0.0002	1
2 Slot Bearing			3.2397	0.0008	1,4
Max Error				0.0021	
Average Error				0.0008	

G.1   Plain Journal Bearing

- The Plain Journal Bearing was replicated on the 3.2345" master shaft.

- 'Diameter1' is the measured bearing cylindrical diameter.

- The visual graph shows the bearing with a nominal diameter of 2.2345".

Precision Engineering Research Group

Plan Name
Turcite Bearing1

Drawing No.

Operator
Master

Date
April 9, 2013

Time
3:38:43 pm

Incremental Part Number
20120808 Turcite Plain Journal

Name	ID	Actual	Nominal	pos Tol	neg Tol	Diff	<--|-->
Overall Result							
All Characteristics:		12					
Out of tolerance:		0					
Over Warning Limit:		0					
Not Calculated:	0						
Diameter_Circle1	D	3.2347	3.2345	0.0059	-0.0059	0.0002	|-
Diameter_Circle2	D	3.2347	3.2345	0.0059	-0.0059	0.0002	|-
Diameter_Circle3	D	3.2346	3.2345	0.0059	-0.0059	0.0001	|-
Diameter_Circle4	D	3.2349	3.2345	0.0059	-0.0059	0.0004	|-
Diameter_Circle5	D	3.2347	3.2345	0.0059	-0.0059	0.0002	|-
Diameter1	D	3.2346	3.2345	0.0010	-0.0010	0.0001	|-
Cylindricity1	GDT Cyl	0.0009	0.0000	0.0010		0.0009	|----
Roundness1	GDT Roun	0.0005	0.0000	0.0005		0.0005	|----
Roundness_Circle2	GDT Roun	0.0004	0.0000	0.0005		0.0004	|---
Roundness_Circle3	GDT Roun	0.0005	0.0000	0.0005		0.0005	|----
Roundness_Circle4	GDT Roun	0.0005	0.0000	0.0005		0.0005	|----
Roundness_Circle5	GDT Roun	0.0004	0.0000	0.0005		0.0004	|---

Programme All Characteristics	Plan Name Turcite Bearing1		Temperature workpiece	Drawing No.
Incremental Part Number 20120808 Turcite Plain Journal1	Audit-No.: * vda_auditno *	Date April 9, 2013	Operator Master	Revision Date August 8, 2012 4:07:26 pm
		Time 3:43:05 pm		

0.0005
0.0004
0.0004
0.0003
0.0002
0.0002
0.0001
0.0001
0.0000
-0.0001
-0.0001
-0.0002
-0.0002
-0.0003
-0.0004
-0.0004
-0.0005

0.6 inch
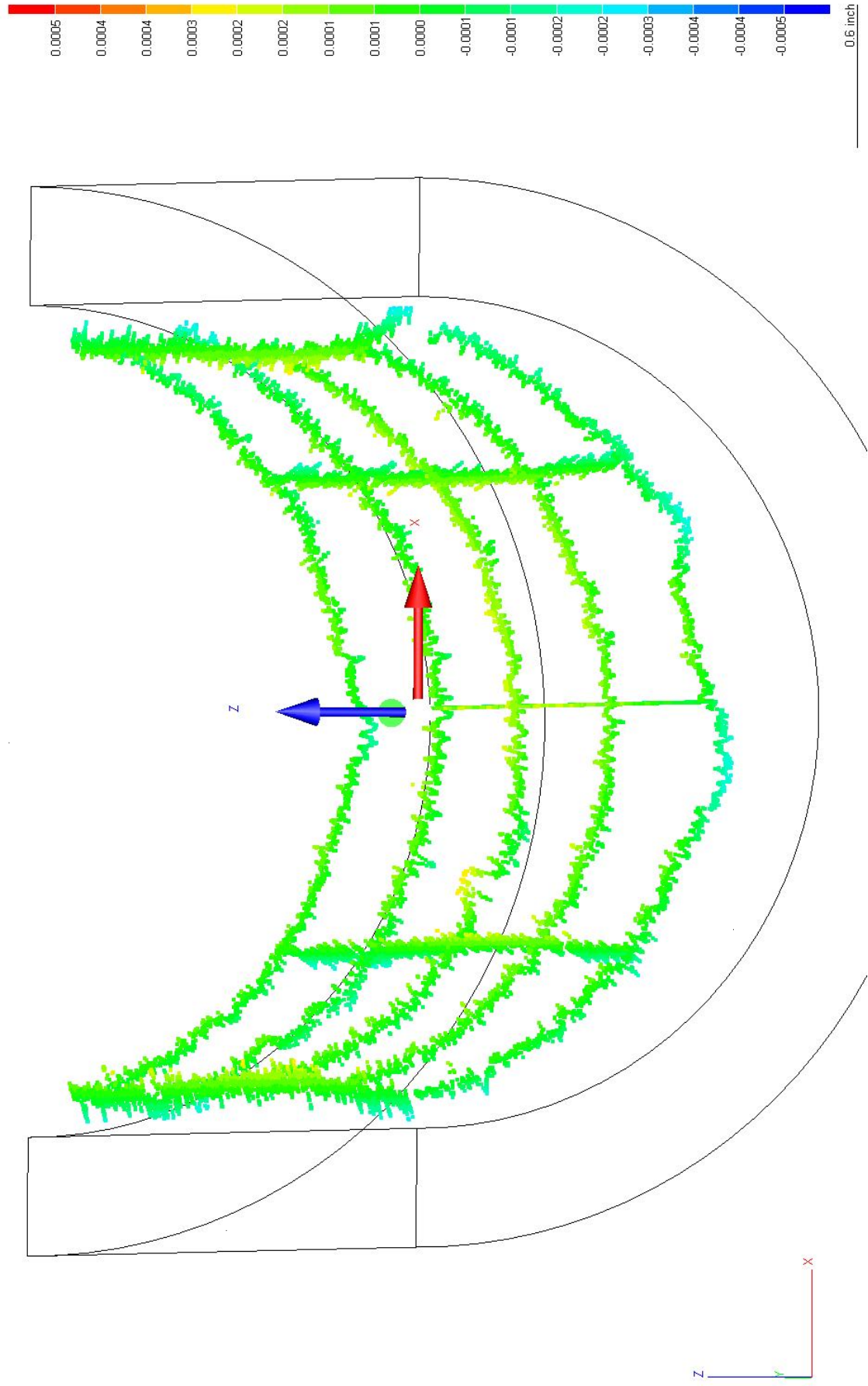
G.2 180 Degree 3 Port Bearing

- The 180 Degree 3 Port Bearing was replicated on the 3.2345" master shaft.

- 'Diameter-Lands' is the measured bearing cylindrical diameter.

- The visual graph shows the bearing with a nominal diameter of 2.2345".

- Edge effects can be seen quite clearly as depressed areas on the surface of the lands.

- A freeform scan of the landed regions was used for measuring the bearing.

Precision Engineering Research Group

Plan Name Turcite Bearing 3	**Date** April 9, 2013
Drawing No. * drawingno *	**Time** 4:13:07 pm
Operator Master	**Incremental Part Number** 180 3 Port Bearing

Name	ID	Actual	Nominal	pos Tol	neg Tol	Diff	<--|-->
Overall Result							
All Characteristics:		2					
Out of tolerance:			1				
Over Warning Limit:			0				
Not Calculated:		0					
🟨 Diameter_Lands	D	3.2356	3.2346	0.0010	-0.0050	0.0010	|---- |
🟥 Cylindricity_Lands	GDT Cyl	0.0091	0.0000	0.0010		0.0091	0.0081

Programme	Plan Name	Date	Temperature workpiece	Drawing No.
All Characteristics	Turcite Bearing 3	April 9, 2013		* drawingno *
Incremental Part Number	Audit-No.:	Time	Operator	Revision Date
180 3 Port Bearing	* vda_auditno *	4:13:07 pm	Master	September 19, 2012 5:36:31 pm

0.0010
0.0006
0.0002
-0.0001
-0.0005
-0.0009
-0.0013
-0.0016
-0.0020
-0.0024
-0.0027
-0.0031
-0.0035
-0.0039
-0.0043
-0.0046
-0.0050

0.6 inch
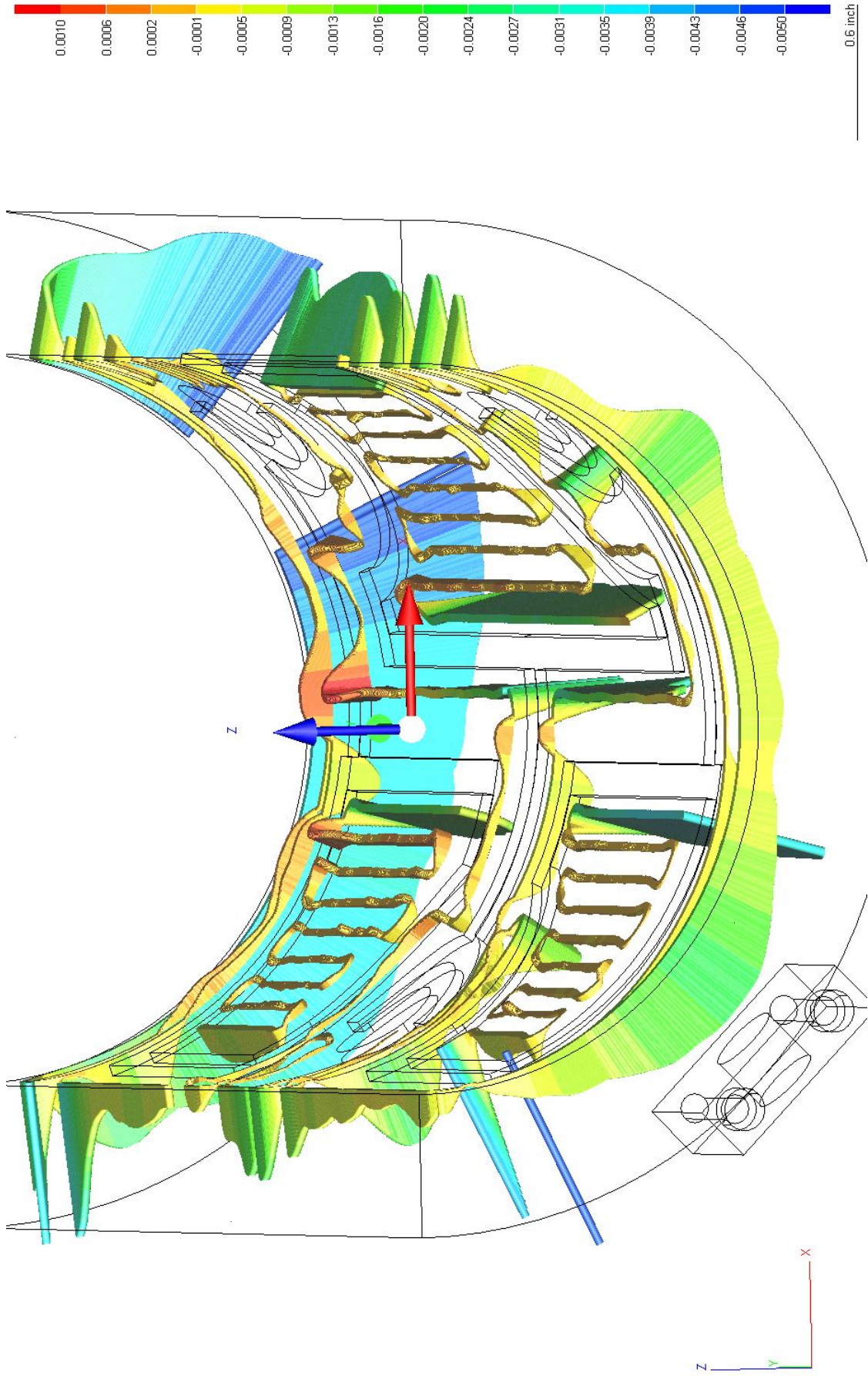
G.3   165 Degree 3 Port Bearing

- The 165 Degree 3 Port Bearing was replicated on the 3.2431" master shaft.

- 'Diameter-Cylinder1' is the measured bearing cylindrical diameter.

- The visual graph shows the bearing with a nominal diameter of 2.2410".

- Edge effects can be seen as depressed areas on the surface of the lands.

- A grid of individual points was used to map the surface of the landed regions.

Precision Engineering Research Group
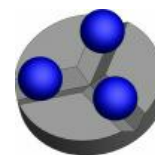
Plan Name	Date
165 Turcite	October 9, 2012

Drawing No.	Time
* drawingno *	1:16:51 pm

Operator	Incremental Part Number
Master	9 Oct 2020

Name	ID	Actual	Nominal	pos Tol	neg Tol	Diff	<--|-->
Overall Result							
All Characteristics:		1					
Out of tolerance:		0					
Over Warning Limit:		0					
Not Calculated:	0						
Diameter_Cylinder1	D	3.2434	3.2410	0.0030	-0.0030	0.0024	|----

0.0030
0.0026
0.0022
0.0019
0.0015
0.0011
0.0008
0.0004
0.0000
-0.0004
-0.0008
-0.0011
-0.0015
-0.0019
-0.0022
-0.0026
-0.0030

0.7 inch

ZEISS

G.4   Centerlift Bearing

- The Centerlift Bearing was replicated on the 3.2389" master shaft.

- 'Cylinder Diameter' is the measured bearing cylindrical diameter.

- The visual graph shows the bearing with a nominal diameter of 2.2390".

- Edge effects can be seen as depressed areas on the surface of the lands, especially very close to the intersection of groove and land.

- A grid of individual points was used to map the surface of the landed regions.

Precision Engineering Research Group

Plan Name		**Date**
Center Lift31 Oct 2013 Circles		April 9, 2013
Drawing No.		**Time**
* drawingno *		4:41:04 pm
Operator		**Incremental Part Number**
Master		31 Oct 2012 Circle Slices1

Name	ID	Actual	Nominal	pos Tol	neg Tol	Diff	<--|-->
Overall Result							
All Characteristics:		19					
Out of tolerance:		2					
Over Warning Limit:		0					
Not Calculated:	0						
🟥 Cylindricity1	GDT Cyl	0.0096	0.0000	0.0000		0.0096	0.0096
🟩 Cylinder Diameter	D	3.2401	3.2430	0.0030	-0.0030	-0.0029	----|
🟩 0.1 Inch Diameter	D	3.2412	3.2430	0.0059	-0.0059	-0.0018	--|
🟩 0.2 Inch Diameter	D	3.2395	3.2430	0.0059	-0.0059	-0.0035	---|
🟩 0.3 Inch Diameter	D	3.2392	3.2430	0.0059	-0.0059	-0.0038	---|
🟩 0.4 Inch Diameter	D	3.2393	3.2430	0.0059	-0.0059	-0.0037	---|
🟩 0.5 Inch Diameter	D	3.2400	3.2430	0.0059	-0.0059	-0.0030	---|
🟩 0.6 Inch Diameter	D	3.2406	3.2430	0.0059	-0.0059	-0.0024	--|
🟩 6.9 Inch Diameter	D	3.2436	3.2430	0.0059	-0.0059	0.0006	|-
🟩 6.8 Inch Diameter	D	3.2403	3.2430	0.0059	-0.0059	-0.0027	--|
🟩 6.7 Inch Diameter	D	3.2395	3.2430	0.0059	-0.0059	-0.0035	---|
🟩 6.6 Inch Diameter	D	3.2401	3.2430	0.0059	-0.0059	-0.0029	--|
🟩 6.5 Inch Diameter	D	3.2416	3.2430	0.0059	-0.0059	-0.0014	-|
🟩 6.4 Inch Diameter	D	3.2431	3.2430	0.0059	-0.0059	0.0001	|-
🟩 Stripe Diameter	D	3.2366	3.2381	0.0030	-0.0030	-0.0015	--|
🟩 Land 1 Diameter	D	3.2423	3.2386	0.0059	-0.0059	0.0037	|---
🟩 Land 1 Outer Diameter	D	3.2428	3.2386	0.0059	-0.0059	0.0042	|---
🟥 Land 2 Diameter	D	3.2559	3.2430	0.0059	-0.0059	0.0129	0.0070
🟩 Land 2 Outer Diameter	D	3.2436	3.2386	0.0059	-0.0059	0.0050	|----

Programme			Plan Name		Temperature workpiece	Drawing No.
All Characteristics			Center Lift31 Oct 2012			* drawingno *
Incremental Part Number		Audit-No.:	Date	Operator		Revision Date
31 Oct 2012 Points 0.1 from Edges		* vda_auditno *	December 16, 2012	Master		November 1, 2012 8:31:19 am
			Time			
			5:08:25 pm			

ZEISS

0.0010
0.0007
0.0004
0.0001
-0.0002
-0.0006
-0.0009
-0.0012
-0.0015
-0.0018
-0.0021
-0.0024
-0.0027
-0.0031
-0.0034
-0.0037
-0.0040

0.7 inch

G.5   2 Port Bearing

- The 2 Port Bearing was replicated on the 3.2389" master shaft.

- 'Cylinder Diameter' is the measured bearing cylindrical diameter.

- The visual graph shows the bearing with a nominal diameter of 2.2400".

- Edge effects are very noticeable in areas where grooves intersect. These effects propagate along axial lines extending beyond the axial grooves.

- A combination of a grid of individual points and scanned circumferential circles was used to map the surface of the landed regions.

Precision Engineering Research Group
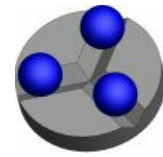
Plan Name 2 Port Center Hybrid	**Date** April 9, 2013
Drawing No. * drawingno *	**Time** 4:50:17 pm
Operator Master	**Incremental Part Number** 2 Port Inlet

Name	ID	Actual	Nominal	pos Tol	neg Tol	Diff	<--|-->
Overall Result							
All Characteristics:		11					
Out of tolerance:		1					
Over Warning Limit:		0					
Not Calculated:	0						
🟩 Diameter Mid Fwd	D	3.2465	3.2430	0.0059	-0.0059	0.0035	|---
🟩 Diameter Mid	D	3.2464	3.2430	0.0059	-0.0059	0.0034	|---
🟩 Diameter Mid Aft	D	3.2451	3.2430	0.0059	-0.0059	0.0021	|--
🟩 Diameter 6.386	D	3.2401	3.2430	0.0059	-0.0059	-0.0029	--|
🟩 Diameter 0.1	D	3.2393	3.2430	0.0059	-0.0059	-0.0037	---|
🟩 Diameter 6.286	D	3.2410	3.2430	0.0059	-0.0059	-0.0020	--|
🟩 Diameter 0.2	D	3.2403	3.2430	0.0059	-0.0059	-0.0027	--|
🟩 Diameter 6.186	D	3.2416	3.2430	0.0059	-0.0059	-0.0014	-|
🟩 Diameter 0.3	D	3.2414	3.2430	0.0059	-0.0059	-0.0016	--|
🟥 Cylindricity1	GDT Cyl	0.0118	0.0000	0.0000		0.0118	0.0118
🟩 Cylinder Diameter	D	3.2410	3.2413	0.0059	-0.0059	-0.0003	-|

Programme	Plan Name		Temperature workpiece	Drawing No.
All Characteristics	2 Port Center Hybrid			* drawingno *
Incremental Part Number	Audit-No.:	Date	Operator	Revision Date
2 Port Inlet	* vda_auditno *	April 9, 2013	Master	December 18, 2012 11:13:02 am
		Time		
		4:50:17 pm		

0.0030
0.0025
0.0020
0.0015
0.0010
0.0005
0.0000
-0.0005
-0.0010
-0.0015
-0.0020
-0.0025
-0.0030
-0.0035
-0.0040
-0.0045
-0.0050

0.8 inch
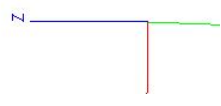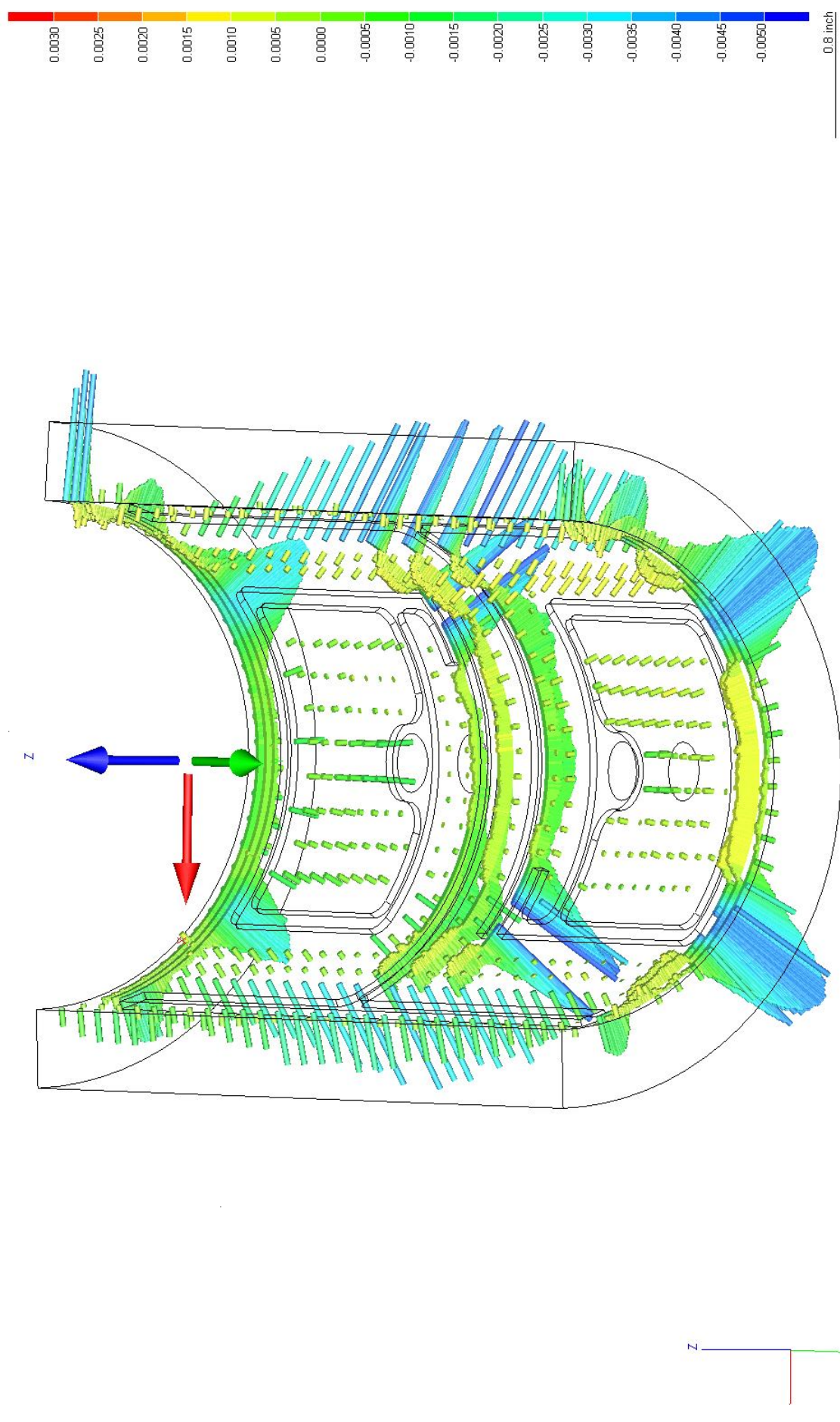
G.6   Stave Bearing

- The Stave Bearing was replicated on the 3.2389" master shaft.

- 'Diameter1' is the measured bearing cylindrical diameter and is based on the center section of the lands to remove the edge effects on diameter.

- The visual graph shows the bearing with a nominal diameter of 2.2390".

- Edge effects are extremely noticeable on the end view shot.

- Scanned linear paths were used to map the center surface of the lands.

- Circumferential scans were done to illustrate the edge effects.

Precision Engineering Research Group

Plan Name	**Date**	
Stave Bearing3	April 11, 2013	
Drawing No.	**Time**	
* drawingno *	7:02:12 pm	
Operator	**Incremental Part Number**	
Master	30 Dec 2030	

Name	ID	Actual	Nominal	pos Tol	neg Tol	Diff	<--|-->
Overall Result							
All Characteristics:		3					
Out of tolerance:			0				
Over Warning Limit:			0				
Not Calculated:		0					
■ Diameter1	D	3.2390	3.2390	0.0005	-0.0005	0.0000	|-
■ Cylindricity1	GDT Cyl	0.0010	0.0000	0.0010		0.0010	|----

Programme		Plan Name		Date		Temperature workpiece		Drawing No.
All Characteristics		Stave Bearing3		April 11, 2013				* drawingno *
Incremental Part Number		Audit-No.:		Time		Operator		Revision Date
30 Dec 2030		* vda_auditno *		7:02:12 pm		Master		April 11, 2013 6:30:16 pm

0.0004
0.0004
0.0003
0.0002
0.0002
0.0001
0.0001
0.0000
0.0000
-0.0000
-0.0001
-0.0001
-0.0002
-0.0002
-0.0003
-0.0004
-0.0004

0.8 inch

Programme All Characteristics	Plan Name Stave Bearing	Date January 19, 2013	Temperature workpiece	Drawing No. * drawingno *
Incremental Part Number 19 Jan 2013	Audit-No.: * vda_auditno *	Time 2:57:14 pm	Operator Master	Revision Date January 24, 2013 10:40:46 am

0.0010
0.0006
0.0002
-0.0001
-0.0005
-0.0009
-0.0013
-0.0016
-0.0020
-0.0024
-0.0027
-0.0031
-0.0035
-0.0039
-0.0043
-0.0046
-0.0050

0.4 inch
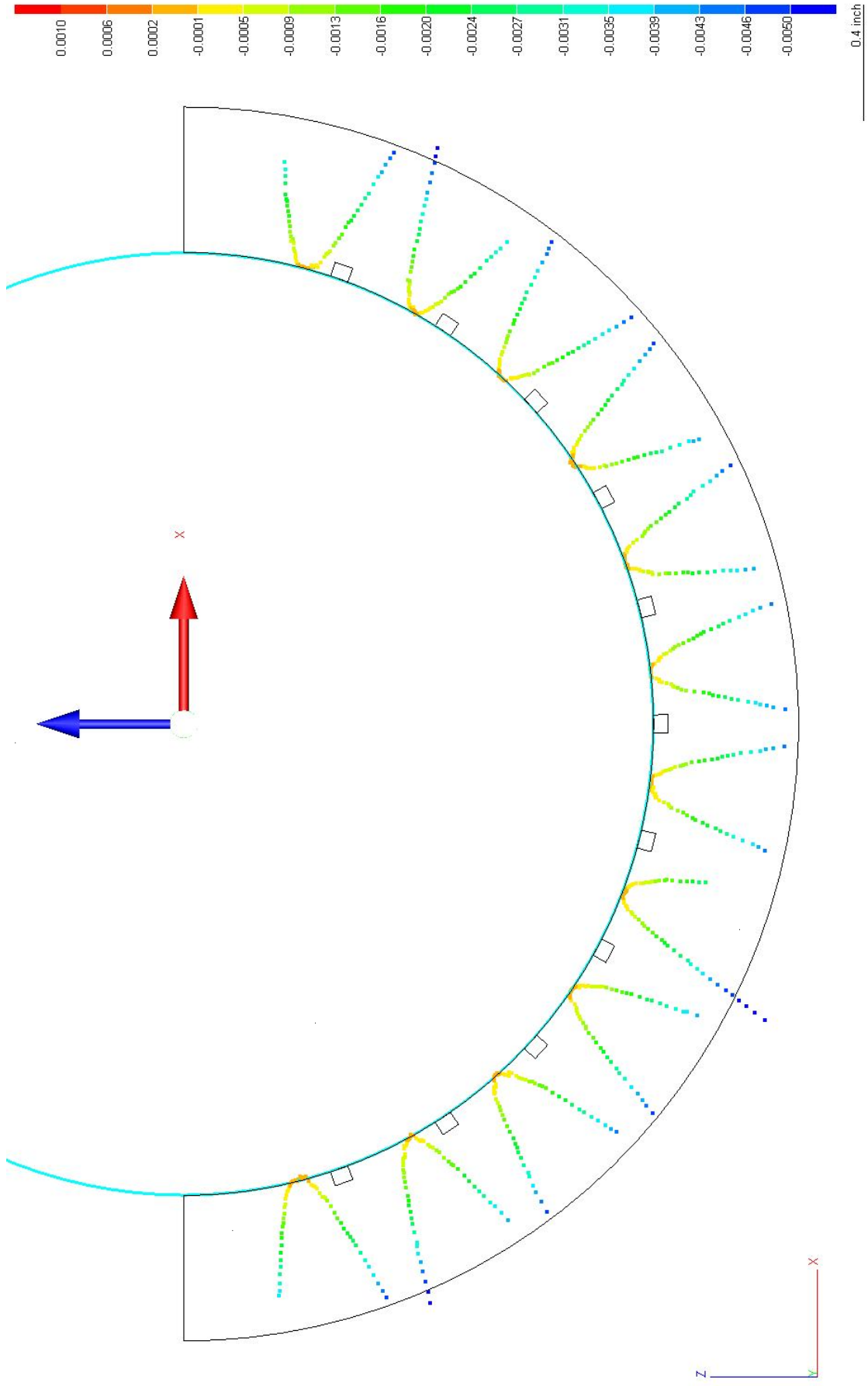
G.7   Comb Bearing

- The Comb Bearing was replicated on the 3.2389" master shaft.

- 'Cylinder Diameter' is the measured bearing cylindrical diameter.

- The visual graph shows the bearing with a nominal diameter of 2.2398".

- A series of scanned circumferential circles was used to map the surface of the bearing.

- No significant edge effects are seen due to scan lines being placed in the middle of grooves.

- There appears to be a very minor axial line of depression towards the bottom dead center of the bearing.

Precision Engineering Research Group

Plan Name Comb Bearing 20 Feb	**Date** April 10, 2013
Drawing No. * drawingno *	**Time** 8:40:51 am
Operator Master	**Incremental Part Number** 20 Feb 2013

Name	ID	Actual	Nominal	pos Tol	neg Tol	Diff	<--|-->
Overall Result							
All Characteristics:		18					
Out of tolerance:		1					
Over Warning Limit:		0					
Not Calculated:		0					
🟥 Cylindricity1	GDT Cyl	0.0012	0.0000	0.0000		0.0012	0.0012
🟩 Cylinder Diameter	D	3.2398	3.2400	0.0059	-0.0059	-0.0002	-|
🟩 0.3 Diameter	D	3.2401	3.2400	0.0059	-0.0059	0.0001	|-
🟩 .839 Diameter	D	3.2402	3.2400	0.0059	-0.0059	0.0002	|-
🟩 1.244 Diameter	D	3.2401	3.2400	0.0059	-0.0059	0.0001	|-
🟩 1.644 Diameter	D	3.2399	3.2400	0.0059	-0.0059	-0.0001	-|
🟩 2.049 Diameter	D	3.2399	3.2400	0.0059	-0.0059	-0.0001	-|
🟩 2.449 Diameter	D	3.2396	3.2400	0.0059	-0.0059	-0.0004	-|
🟩 2.854 Diameter	D	3.2398	3.2400	0.0059	-0.0059	-0.0002	-|
🟩 3.254 Diameter	D	3.2397	3.2400	0.0059	-0.0059	-0.0003	-|
🟩 3.659 Diameter	D	3.2398	3.2400	0.0059	-0.0059	-0.0002	-|
🟩 4.059 Diameter	D	3.2397	3.2400	0.0059	-0.0059	-0.0003	-|
🟩 4.464 Diameter	D	3.2399	3.2400	0.0059	-0.0059	-0.0001	-|
🟩 4.864 Diameter	D	3.2397	3.2400	0.0059	-0.0059	-0.0003	-|
🟩 5.269 Diameter	D	3.2398	3.2400	0.0059	-0.0059	-0.0002	-|
🟩 5.669 Diameter	D	3.2398	3.2400	0.0059	-0.0059	-0.0002	-|
🟩 6.074 Diameter	D	3.2395	3.2400	0.0059	-0.0059	-0.0005	-|
🟩 6.5 Diameter	D	3.2396	3.2400	0.0059	-0.0059	-0.0004	-|

Programme	Plan Name		Temperature workpiece	Drawing No.
All Characteristics	Comb Bearing 20 Feb			* drawingno *
Incremental Part Number	Audit-No.:	Date		Revision Date
20 Feb 2013	* vda_auditno *	April 10, 2013		February 20, 2013 11:25:19 am
		Time	Operator	
		8:40:51 am	Master	

0.0010
0.0009
0.0008
0.0006
0.0005
0.0004
0.0002
0.0001
0.0000
-0.0001
-0.0002
-0.0004
-0.0005
-0.0006
-0.0008
-0.0009
-0.0010

0.8 inch
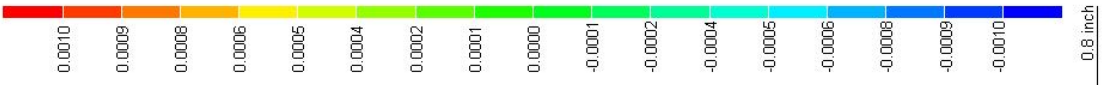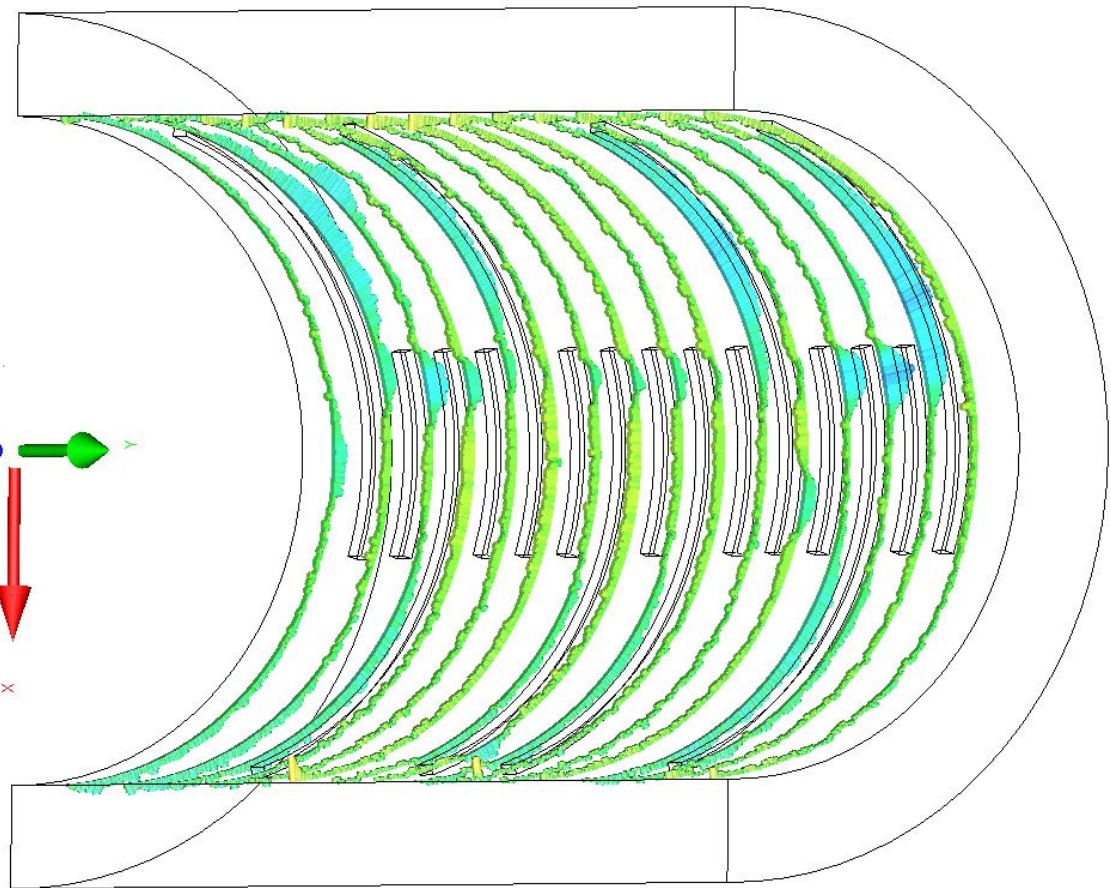
G.8 Hydrostatic Lift Bearing

- The Hydrostatic Lift Bearing was replicated on the 3.2389" master shaft.

- 'Bearing Cylinder' is the measured bearing cylindrical diameter.

- The visual graph shows the bearing with a nominal diameter of 2.2390".

- A series of scanned circumferential circles was used to map the surface of the bearing.

- The scan lines are particularly uniform, with maximum deviations in diameter on the order of 0.0002" which is on the order of accuracy of the machine.

Precision Engineering Research Group
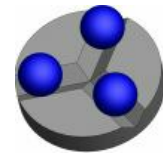
Plan Name	Date
Plain Journal Full2	April 9, 2013

Drawing No.	Time
* drawingno *	5:23:51 pm

Operator	Incremental Part Number
Master	31 Jan 2015

Name	ID	Actual	Nominal	pos Tol	neg Tol	Diff	<--|-->
Overall Result							
All Characteristics:		11					
Out of tolerance:		2					
Over Warning Limit:		0					
Not Calculated:	0						
Bearing Cylinder	D	3.2391	3.2390	0.0003	-0.0003	0.0001	|--
0.5 Diameter	D	3.2390	3.2390	0.0002	-0.0002	0.0000	|-
1.5 Diameter	D	3.2390	3.2390	0.0002	-0.0002	0.0000	|--
2.5 Diameter	D	3.2389	3.2390	0.0002	-0.0002	-0.0001	--|
3.5 Diameter	D	3.2389	3.2390	0.0002	-0.0002	-0.0001	---|
4.5 Diameter	D	3.2392	3.2390	0.0002	-0.0002	0.0002	|----
6.5 Diameter	D	3.2393	3.2390	0.0002	-0.0002	0.0003	0.0001
0.1 Diameter	D	3.2431	3.2390	0.0059	-0.0059	0.0041	|---
6.772 Diameter	D	3.2419	3.2390	0.0059	-0.0059	0.0029	|--
Excess Margin Diameter	D	3.2408	3.2390	0.0059	-0.0059	0.0018	|--
5.5 Diameter	D	3.2393	3.2390	0.0002	-0.0002	0.0003	0.0001

Programme	Plan Name		Temperature workpiece	Drawing No.
All Characteristics	Plain Journal Full2			* drawingno *
Incremental Part Number	Audit-No.:	Date	Operator	Revision Date
31 Jan 2014	* vda_auditno *	April 9, 2013	Master	January 31, 2013 10:19:04 am
		Time		
		5:17:31 pm		

0.0003
0.0003
0.0002
0.0002
0.0001
0.0001
0.0001
0.0000
0.0000
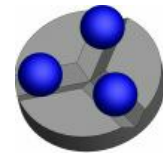-0.0000
-0.0001
-0.0001
-0.0002
-0.0002
-0.0003
-0.0003

0.9 inch

G.9   2 Slot Bearing

- The 2 Slot Bearing was replicated on the 3.2389" master shaft.

- 'Diameter1' is the measured bearing cylindrical diameter.

- The visual graph shows the bearing with a nominal diameter of 2.2397".

- A series of scanned circumferential circles was used to map the surface of the bearing.

- The scan lines are particularly uniform, with typical deviations in diameter on the order of 0.0002" with some exceptions.

- There are edge effects that can be seen towards the circumferential edge of the bearing. This might also be due to the probe riding on an edge of the the bearing.

- There are some grooved areas visible at one axial end of the bearing that resulted from slight damage that occurred during the fabrication process.

- There is an area of depression at one section in the middle of the bearing at approximately 45° from bottom dead center (BDC). The suspected cause of this is due to a thick puddle of release agent that was sprayed onto the master shaft during fabrication.

Precision Engineering Research Group

Name	ID	Actual	Nominal	pos Tol	neg Tol	Diff	<--|-->
Overall Result							
All Characteristics:	8						
Out of tolerance:	0						
Over Warning Limit:	0						
Not Calculated:	0						
Diameter1	D	3.2397	3.2400	0.0010	-0.0010	-0.0003	--|
0.5 Diameter	D	3.2403	3.2390	0.0059	-0.0059	0.0013	|-
1.5 Diameter	D	3.2398	3.2390	0.0059	-0.0059	0.0008	|-
2.5 Diameter	D	3.2397	3.2390	0.0059	-0.0059	0.0007	|-
3.5 Diameter	D	3.2395	3.2390	0.0059	-0.0059	0.0005	|-
4.5 Diameter	D	3.2395	3.2390	0.0059	-0.0059	0.0005	|-
5.5 Diameter	D	3.2400	3.2390	0.0059	-0.0059	0.0010	|-
6.5 Diameter	D	3.2407	3.2390	0.0059	-0.0059	0.0017	|--

ZEISS

Programme	Plan Name	Date	Temperature workpiece	Drawing No.
All Characteristics	Plain Journal Full	April 9, 2013		* drawingno *
Incremental Part Number	Audit-No.:	Time	Operator	Revision Date
25 March 2020	* vda_auditno *	5:30:42 pm	Master	March 25, 2013 1:08:30 pm

0.0010
0.0009
0.0008
0.0006
0.0005
0.0004
0.0002
0.0001
0.0000
-0.0001
-0.0002
-0.0004
-0.0005
-0.0006
-0.0008
-0.0009
-0.0010

0.8 inch

Bibliography

[1] American Bureau of Shipping. *Guidance Notes on Propulsion Shafting Alignment*, 2006.

[2] ANSI. *Preferred Metric Limits and Fits*. American National Standards Institute, b 4.2 edition, 1978.

[3] D. Arpi and L. Winn. A statistical and economic evaluation of stern tube bearing and seal failures. In *Proceedings; Fourth Ship Technology and Research (STAR) Symposium*, pages 121–133. SNAME, 1979.

[4] R. Bassani and B. Piccigallo. *Hydrostatic Lubrication*, volume 22. Elsevier, New York, 1992.

[5] CRANE Corporation. *Technical Paper No. 410: Flow of fluids through valves, fittings, and pipe*. Crane Co., Long Beach, CA, 1999.

[6] Lion Precision Corporation. Eddy current probes, August 2012.

[7] M. Kozubkova F. Pochyly, S. Fialova. Journal bearings with hydrophobic surface. In *13th International Scientific and Engineering Conference "Hervicon-2011"*, 2011.

[8] D.D. Fuller. *Theory and practice of lubrication for engineers*. Wiley, New York, 2nd ed edition, 1984.

[9] B.J. Hamrock, S.R. Schmid, and B.O. Jacobson. *Fundamentals of fluid film lubrication*, volume 169 of *Mechanical engineering*. Marcel Dekker, New York, 2nd ed edition, 2004.

[10] A. Harnoy. *Bearing design in machinery: engineering tribology and lubrication*, volume 147 of *Mechanical Engineering*. Marcel Dekker, New York, 2003.

[11] R.L Harrington. *Marine Engineering*. Society of Naval Architects and Marine Engineers, Jersey City, N.J., 1992.

[12] S. Heller. A numerical solution for incompressible hybrid journal bearing with cavitation. *Journal of Lubrication Technolody*, 91(3), 1969.

[13] P. Keenan. Interview with navsea supervisor of salvage and diving. Personal communication, December 2011.

[14] M.M. Khonsari and E.R. Booser. *Applied Tribology: Bearing Design and Lubrication*. Tribology series. Wiley, Chichester, England, 2nd ed edition, 2008.

[15] M.S. Kotilainen. *Design and Manufacturing of Modular Self-Compensating Hydrostatic Journal Bearings*. PhD thesis, Massachusetts Institute of Technology, 2000.

[16] J. Vizintin M. Kalin, L. Velkavrh. The stribeck curve and lubrication design for non-fully wetted surfaces. *Wear*, 267:1232–1240, 2009.

[17] Naval Sea Systems Command. *Naval Ship's Technical Manual Chapter 244: Propulsion Bearings and Seals*, revision 7 edition, May 2002.

[18] International Association of Classification Societies (IACS), March 2013.

[19] American Bureau of Shipping. *ABS Rules for Steel Vessels*, 2013.

[20] OMEGA. Turbine and paddlewheel flowmeters. October 2012.

[21] R.L. Orndorff. Water-lubricated rubber bearings, history and new developments. *Naval Engineers Journal*, 97(7):39–52, 1985.

[22] O. Pinkus and B. Sternlicht. *Theory of hydrodynamic lubrication*. McGraw-Hill, New York, 1961.

[23] A.A. Raimondi and John Boyd. A solution for the finite journal bearing and its application to analysis and design. *ASLE*, 1(1):159–209, 1958.

[24] Rayleigh. Notes on the theory of lubrication. *Philsophical Magazine and Journal of Science*, 6, 1918.

[25] H.C. Rippel. *Cast bronze hydrostatic bearing design manual*. Cast Bronze Bearing Institute, Inc., 1963.

[26] W.B. Rowe. *Hydrostatic, Aerostatic and Hybrid Bearing Design*. Butterworth - Heinemann, 2012.

[27] A.H. Slocum. High speed hydrostatic spindle design. US Patent 5466071, 14 November 1995.

[28] A.H. Slocum. *Precision Machine Design*. Society of Manufacturing Engineers, Dearborn, Michigan, 1992.

[29] A.H. Slocum. Self-compensating hydrostatic bearings for supporting shafts and spindles and the like for rotary and translational motion and methods therefor. US Patent 5281032, 25 January 1994.

[30] D. Sverko. Discussions regarding abs bearing experiences. Personal communication, March 2013.

[31] G. Vogelpohl. Thermal effects and elasto-kinetics in self-acting bearing lubrication. *Proceedings of Internation Symposium on Lubrication and Wear*, pages 766–815, 1965.

[32] KL Wasson. *Hydrostatic Machine Tool Spindles.* PhD thesis, Massachusetts Institute of Technology, 1996.

[33] A. Wong. Design of a low cost hydrostatic bearing. Master's thesis, Massachusetts Institute of Technology, June 2012.